Technische Universität München
TUM School of Life Sciences

Designed Aβ-derived peptides as effective inhibitors of amyloid self-assembly of both IAPP and Aβ

Karin Taş

Vollständiger Abdruck der von der TUM School of Life Sciences der Technischen Universität München zur Erlangung einer

Doktorin der Naturwissenschaften (Dr. rer. nat.)

genehmigten Dissertation.

Vorsitz: Prof. Dr. Dmitrij Frischmann

Prüfer*innen der Dissertation:

1. Prof. Dr. Aphrodite Kapurniotu
2. Prof. Dr. Johannes Buchner

Die Dissertation wurde am 22.06.2022 bei der Technischen Universität München eingereicht und durch die TUM School of Life Sciences am 05.11.2022 angenommen.

Zusammenfassung

Die Fehlfaltung und Aggregation von Polypeptiden oder Proteinen in amyloide Fibrillen steht in Zusammenhang mit zahlreichen zelldegenerativen Erkrankungen wie zum Beispiel Alzheimer (AD) oder Typ 2 Diabetes (T2D). Die Schlüsselkomponenten der beiden Krankheiten sind das Amyloid-β Peptid (Aβ) bzw. das Insel-Amyloid-Polypeptid (IAPP) und es gibt zunehmend mehr Hinweise, dass AD und T2D sowohl auf pathophysiologischer als auch auf molekularer Ebene miteinander in Verbindung stehen. Interaktionen zwischen unterschiedlichen amyloidogenen Polypeptiden, so genannte „*cross*-amyloide" Interaktionen, sind zentrale Modulatoren bei der Amyloidogenese und könnten eine Verbindung verschiedener Protein-Fehlfaltungserkrankungen miteinander darstellen. Die Kreuz-Interaktion zwischen IAPP und Aβ wird auch tatsächlich bereits als molekulares Bindeglied zwischen T2D und AD in Betracht gezogen. Daher könnten Moleküle, die die amyloide Selbst-Assemblierung von Aβ und IAPP sowie deren Fähigkeit zum gegenseitigen „*Cross-Seeding*" unterbinden, vielversprechende Leitsubstanzen für zukünftige, gegen Amyloidbildung gerichtete Medikamentenforschung sein. Allerding stellt das Designen von hocheffektiven Inhibitoren gegen pathogene Protein- und Peptidfehlfaltung nach wie vor eine große Herausforderung dar.

In dieser Arbeit wird das Design, die Synthese, sowie Struktur-Funktions-Studien einer neuartigen Klasse von hochwirksamen Inhibitoren der Amyloidbildung, genannt *Aβ amyloid core mimics* oder ACMs, vorgestellt. ACMs stellen konformativ eingeschränkte Peptide dar, die basierend auf der Aβ-IAPP Interaktionsfläche und dem amyloiden Kernsegment Aβ(15-40) als Vorlage entworfen wurden. Zuerst wurden die Eigenschaften und das Inhibitionspotential verschiedener von Aβ(15-40) abgeleiteten Peptide mittels CD-Spektroskopie sowie ThT-Bindungs- und MTT-Reduktions-Experimenten charakterisiert. Diese Untersuchungen konnten zeigen, dass der Austausch bestimmter Aminosäuren sowie die Einführung von *N*-Methylierungen essentiell für die Entwicklung von IAPP-Inhibitoren ist. Obwohl sie auf dem amyloidogenen Aβ Kernsegment 15-40 basieren, sind ACMs selbst nicht toxisch und nicht amyloidogen und binden IAPP und Aβ mit hoher Affinität. Die ACMs unterdrückten die zytotoxische Amyloid-Selbstassemblierung von IAPP und Aβ42 sowohl unter nicht mit Fibrillen angeimpften als auch unter selbst- und kreuz-geseedeten Bedingungen.

Es stellte sich heraus, dass die ACMs IAPP und Aβ42 inhibieren, indem sie mit beiden Polypeptiden co-assemblieren und fibrilläre, gemischte IAPP/ACM- oder Aβ42/ACM-Aggregate ausbilden. Um diese molekular zu charakterisieren, wurden hochauflösende Mikroskopie-Methoden wie confokale Laser-Scanning-Mikroskopie (CLSM), *stimulated emission depletion* (STED) Mikroskopie, Zwei-Photon Mikroskopie (2-PM) und *fluorescence lifetime imaging* Mikroskopie (FLIM)-basierte Förster Resonanzenergietransfer (FRET) (FLIM-FRET) Analysen verwendet. Darüber hinaus wurden Immunogold-Transmissions-Elektronenmikroskopie (IG-TEM) und Pulldown-Experimente durchgeführt. Zusätzliche Untersuchungen bezüglich des Entstehungsmechanismus von gemischten IAPP/ACM- und Aβ42/ACM-Fibrillen zeigten auf, dass ACMs mit IAPP oder Aβ42 zuerst amorphe Heterokomplexe bilden, welche sich anschließend zu Fibrillen reorganisieren. Die Bildung von

IAPP/ACM Heterofibrillen scheint ausgehend von der Interaktion der ACMs mit monomerem oder präfibrillärem IAPP initiiert zu werden. Die Bildung von fibrillären Aβ42/ACM Co-Aggregaten kann ausgehend von der Interaktion mit monomerem oder präfibrillärem Aβ42 eingeleitet werden und es entstehen dabei Fibrillen, die signifikant länger sind als Aβ42 Fibrillen. Mit Hilfe von Peptid-Arrays wurden zudem die Peptid-Segmente identifiziert, die für die Ausbildung der IAPP/ACM und der Aβ42/ACM Interaktionsfläche wichtig sind. Verglichen mit IAPP oder Aβ42 Fibrillen zeigen die gemischten IAPP/ACM- und Aβ42/ACM-Fibrillen mehrere vorteilhafte Eigenschaften: keine Zytotoxizität, keine „*Seeding*"-Fähigkeit, sowie Thermolabilität und gesteigerte Anfälligkeit gegenüber Proteolyse.

Zusammenfassend kann festgehalten werden, dass die ACMs in hocheffektiver Weise die amyloide Selbst-Assemblierung von IAPP und Aβ42 und die damit verbundenen cytotoxischen Effekte inhibieren und zusätzlich deren gegenseitiges „*Cross-Seeding*" unterbinden können und dabei einem neuartigen Inhibitionsmechanismus folgen. All das macht sie zu nützlichen Templaten und vielversprechenden Leitmolekülen für zukünftige Medikamentenentwicklung, die gegen die Amyloidbildung bei den beiden bisher unheilbaren Erkrankungen AD und T2D gerichtet sein könnten.

Abstract

Misfolding and aggregation of intrinsically disordered polypeptides or proteins into amyloid fibrils is closely associated to numerous cell-degenerative diseases, including Alzheimer's disease (AD) and type 2 diabetes (T2D). The key amyloid polypeptides in T2D and AD are islet amyloid polypeptide (IAPP) and β-amyloid peptide (Aβ), respectively, and increasing evidence suggest that AD and T2D are connected, both on a pathophysiological and a molecular level. Interactions between different amyloidogenic polypeptides, so-called "cross-amyloid interactions", are crucial modulators of amyloidogenesis and might provide the link between different protein misfolding diseases to each other. In fact, the IAPP-Aβ cross-interaction has been proposed as a molecular link between T2D and AD. Hence, molecules that block amyloid self-assembly of both Aβ and IAPP and their reciprocal cross-seeding abilities could be promising leads for future anti-amyloid drug candidates. However, the design of highly effective inhibitors of pathogenic protein and peptide misfolding is still a great challenge.

This work presents design, synthesis, and structure-function studies of a novel class of potent amyloid inhibitors termed Aβ amyloid core mimics or ACMs. ACMs are conformationally constrained peptides designed based on the Aβ-IAPP interaction interface using the Aβ(15-40) amyloid core segment as a template. Firstly, properties of various different Aβ(15-40)-derived peptides and their inhibitory potential were characterised using CD spectroscopy, ThT binding, and MTT reduction assays. These studies elucidated the importance of specific amino acid exchanges and *N*-methylation introductions for generating IAPP inhibitors. Despite being derived from the Aβ40 amyloid core segment Aβ(15-40), ACMs were non-amyloidogenic and non-toxic themselves, and they bound IAPP and Aβ with high affinity. ACMs suppressed cytotoxic amyloid self-assembly of IAPP and Aβ42 under both unseeded and self- or cross-seeded conditions.

Remarkably, ACMs inhibited IAPP and Aβ42 by co-assembling with them into mixed IAPP/ACM or Aβ42/ACM fibrillar species. For their molecular characterisation, advanced microscopy methods including confocal laser scanning microscopy (CLSM), stimulated emission depletion (STED) microscopy, two-photon microscopy (2-PM), and fluorescence lifetime imaging microscopy (FLIM)-based Förster resonance energy transfer (FRET) (FLIM-FRET) analysis were performed. In addition, immunogold transmission electron microscopy (IG-TEM) and pulldown studies were done. Additional studies on the formation mechanism of IAPP/ACM and Aβ42/ACM fibrillar co-assemblies revealed that ACMs first form amorphous heterocomplexes with IAPP or Aβ42 which subsequently transform into fibrils. In case of IAPP/ACM fibrillar co-assemblies, their formation seems to be templated by the interaction of ACMs with monomeric or prefibrillar IAPP species. Formation of Aβ42/ACM fibrillar co-assemblies can be initiated from interaction with monomeric or prefibrillar Aβ42 and results in fibrils which are significantly longer than fAβ42. Using peptide arrays, important regions of IAPP/ACM and Aβ42/ACM interaction interfaces were identified. Compared to IAPP or Aβ42 fibrils, mixed fibrillar co-assemblies displayed several beneficial properties like attenuated

toxicity, seeding-incompetency, thermolability, and increased susceptibility to protease digestion.

In conclusion, ACMs effectively suppress amyloid self-assembly of IAPP and Aβ42, their reciprocal cross-seeding events, and related cell-damaging effects by a novel mechanism which makes them useful templates and promising leads for future anti-amyloid drugs targeting the two as yet incurable diseases AD and T2D.

Acknowledgements

Firstly, I would like to express my thanks to Prof. Dr. Aphrodite Kapurniotu for giving me the opportunity to perform my PhD work under her supervision at the Professorship of Peptide Biochemistry of the TUM School of Life Sciences. I thank her for her scientific advice, for providing guidance and feedback throughout this project, the helpful discussions, and the constant supervision of my scientific work.

I would also like to thank Prof. Dr. Jürgen Bernhagen (Chair of Vascular Biology, LMU) for his advice and in particular for giving me the possibility to perform 2-PM and FLIM-FRET measurements in his lab.

I thank also my former and current colleagues in the working group, Michael Kracklauer, Alexandros Grammatikopoulos, Anna Spanopoulou, Christos Kontos, Simon Hornung, Hendrik Wunderlich, Beatrice Dalla Volta, Valentina Armiento, Denise Naltsas, Maria Bakou, Eleni Maldideli and Kathleen Hille for providing a great working atmosphere, the valuable discussions during the years, and numerous funny coffee breaks. I would like to additionally thank Beatrice Dalla Volta for her input to this project by providing me with her data on some donor-alone controls for FLIM-FRET experiments. Kathleen Hille, Valentina Armiento, Beatrice Dalla Volta, Christos Kontos, Maria Bakou, Anna Spanopoulou and the Bavarian Center for Biomolecular Mass Spectrometry (BayBioMS) at TUM I thank for MALDI analyses. In addition, I thank Kathleen Hille for her support with peptide syntheses and HPLC purifications. Special thanks go to Kathleen Hille, Eleni Malideli, and Maria Bakou, who quickly turned from colleagues into friends and enriched the every-day lab business with their spirit, humour, and support.

Additionally, I would like to thank Remco T.A. Megens from the Institute for Cardiovascular Prevention (Prof. C. Weber group) and Omar El Bounkari (Prof. J. Bernhagen group) for their help and support with CLSM, STED, 2-PM, and FLIM-FRET measurements, for introducing me to these methods, and for spending all these hours in front of the microscopes with me. I also thank Christine Krammer (Prof. J. Bernhagen group) for peptide microarray work-up and development. Moreover, I would like to thank the coworkers of the Electron Microscopy group (Prof. S. Weinkauf) Carsten Peters, Benjamin Rossa, and Christoph Kaiser, for help with TEM. I also thank Burghard Cordes from the TUM Department of Chemistry (Zentralanalytik) for performing ESI-IT-MS analyses.

Last but not least, thanks to my family and my beloved husband who always stood behind me with their love and support.

Some of the Figures shown in this thesis are included in the following manuscript submitted for publication to Nature Communications:

Karin Taş, Beatrice Dalla Volta, Christina Lindner, Omar El Bounkari, Kathleen Hille, Yuan Tian, Xènia Puig-Bosch, Markus Ballmann, Simon Hornung, Martin Ortner, Sophia Prem, Laura Meier, Gerhard Rammes, Martin Haslbeck, Christian Weber, Remco T.A. Megens, Jürgen Bernhagen, Aphrodite Kapurniotu

Designed peptides as nanomolar cross-amyloid inhibitors acting *via* supramolecular nanofiber co-assembly.

Nature Communications (currently under revision at the day of thesis submission)

Data in this thesis that are also shown in manuscript figures are indicated in the corresponding figure legends.

Table of content

List of figures

List of tables

Abbreviations

1xb buffer	10 mM NaH_2PO_4, pH 7.4
2-PM	two-photon microscopy
a7nAChR	nicotinic acetylcholine receptor
AA	amino acid
Ac_2O	acetic anhydride
ACA	ε-aminocaproic acid
ACM	Aβ amyloid core mimics
ACN	acetonitrile
AD	Alzheimer's disease
ADP	Aβ-derived peptide
AICD	APP intracellular domain
APH-1	anterior pharynx defective 1
APP	amyloid-precursor-protein
app. k_D	apparent binding affinity
Aβ	amyloid-β peptide
BACE	Beta-site APP-cleaving enzyme
BCA	bicinchoninic acid
BOC	*tert*-Butyloxycarbonyl
BSA	bovine serum albumin
BSA	bovine serum albumin
$CaCl_2$	calcium chloride
CD	circular dichroism
CGRP	calcitonin gene-related peptide
CL	cross linking
CLSM	confocal laser scanning microscopy
CPE	carboxypeptidase E
DAC	7-diethylaminocoumarin-3-carbonyl
DB	dot blot
DCM	dichlormethane
DIEA	*N,N*-diisopropylethylamine
DMF	*N,N*-dimethylformamide
DMSO	dimethyl sulfoxide
DNA	desoxyribonucleic acid
DTT	dithiothreitol
EDT	ethanedithiol
EGCG	epigallocatechin gallate
EM	electron microscopy
EPR	electron paramagnetic resonance
eq.	equivalent
ER	endoplasmic reticulum
ESI-IMS-MS	electrospray ionisation-ion mobility spectrometry-mass spectrometry
ESI-IT-MS	electrospray ionization ion-trap mass spectrometry
Et_2O	diethylether
FAD	familial Alzheimer's disease
fAβ40	Aβ40 fibrils
fAβ42	Aβ42 fibrils
FCS	fetal calf serum
fIAPP	IAPP fibrils
FITC	Fluorescein-isothiocyanate
FLIM	fluorescence lifetime imaging
Fluos	5,6-carboxyfluorescein
Fmoc	fluorenylmethoxycarbonyl
FRET	Förster's resonance energy transfer
GdnHCl	guanidinium hydrochloride
GLUT	glucose transporter
HATU	2-(7-aza-1H-benzotriazole-1-yl)-1,1,3,3-tetramethyluronium-hexafluorophosphate
HBTU	2-(1H-Benzotriazol-1-yl)-1,1,3,3-tetramethyluronium-hexafluorophosphate
HCl	hydrochloric acid
HD	Huntington's disease
HEPES	4-(2-hydroxyethyl)-1-piperazineethanesulfonic acid
hf-Aβ42/ACM	fibrillar co-assemblies containing Aβ42 and ACM
hf-IAPP/ACM	fibrillar co-assembly containing IAPP and ACM
HFIP	1,1,3,3,3,3-hexafluoro-2-isopropanol
HMW	high-molecular weight
HNT	Buffer containing HEPES, NaCl, and Triton X-100
HOBt	1-Hydroxybenzotriazole
HPLC	high performance liquid chromatography
HRP	horse-radish peroxidase
IAPP	islet-amyloid polypeptide

IDE	insulin-degrading enzyme
IGF	insulin growth factor
IG-TEM	immunogold- transmission electron microscopy
ISM	interaction surface mimic
KCl	potassium chloride
KCN	potassium cyanide
KH_2PO_4	potassium dihydrogenphosphate
LDS	lithium dodecyl sulphate
LMW	low-molecular weight
LTP	long-term potentiation
LTS	loop tripeptide segment
MALDI-TOF-MS	Matrix-assisted laser desorption ionization time-of-flight mass spectrometry
MBP	maltose-binding protein
MD	molecular dynamics
MMP	matrix metalloproteinase
mRNA	messenger ribonucleic acid
MTP	microtiter plate
MTT	3-[4,5-dimethylthiazol-2-yl]-2,5-diphenyl-tetrazolium bromide
MW	molecular weight
Na_2HPO_4	disodium hydrogenphosphate
$NaBH_4$	sodium borohydride
NaCl	sodium chloride
NaH_2PO_4	sodium dihydrogenphosphate
NaOH	sodium hydroxide
NEAA	non-essential amino acids
NH_4CO_3	ammonium carbonate
NMDAR	*N*-methyl-D-aspartic acid receptor
NMe	*N*-methylation
NMR	nuclear magnetic resonance
OtBu	*tert*-butylester
p75NTR	p75 neurotrophin receptor
Pbf	2,2,4,6,7-pentamethyl-dihydrobenzofuran-5-sulfonyl
PBS	phosphate-buffered saline
PC1/3	prohormone convertase 1/3
PC2	prohormone convertase 2
PD	Parkinson's disease
PEN-2	presenilin enhancer 2
PK	proteinase K
PSEN	presenilin
ROI	region of interest
ROS	reactive oxygen species
RP-HPLC	reversed-phase high performance liquid chromatography
RP-HPLC	reversed-phase high performance liquid chromatography
rpm	rounds per minute
RT	room temperature
SDS	sodium dodecyl sulphate
SDS-PAGE	sodium dodecyl sulphate polyacrylamide gel electrophoresis
SEC	size exclusion chromatography
SL	substitution level
SN	supernatant
SPPS	solid-phase peptide synthesis
SSC	saline sodium citrate
T1D	type 1 diabetes mellitus
T2D	type 2 diabetes mellitus
TAMRA	5- or 5,6-carboxy-tetramethylrhodamine
TBS	Tris-buffered saline
TBS-T	Tris-buffered saline with Tween-20
tBu	*tert*-butyl
TCA	trichloroacetic acid
TEM	transmission electron microscopy
TFA	trifluoroacetic acid
TFSMA	trifluoromethane sulfonic acid
ThT	Thioflavin-T
ThT assay buffer	50 mM sodium phosphate with 100 mM NaCl, pH 7.4
TIS	triisopropylsilane
TRIS	*Tris*(hydroxymethyl)aminomethane
TrT	trityl
WB	Western blot

1 Introduction

1.1 Protein folding, misfolding, amyloid formation, and disease

Proteins are synthesised by ribosomes from mRNA based on the genetic information encoded in a cell's DNA and the basic structure of each protein is a linear amino acid chain. Correct folding of such a polypeptide chain into a particular three-dimensional structure is not only crucial for the biological activity of the protein but is also coupled to other biological processes such as the trafficking of molecules to specific cellular locations or the regulation of cell growth and differentiation[1]. Although protein folding has been extensively studied for decades, the exact mechanism by which proteins "know" how to fold from their linear amino acid chain into their unique 3D structure is not fully understood yet, but fundamental events might involve the interaction of a relatively small number of residues to form a folding nucleus about which the remainder of the structure rapidly condenses[1]. Folding can occur co-translational or posttranslational and is often assisted by molecular chaperones and other folding catalysts to ensure efficiency of the process and to avoid misfolding and aggregation[1]. Although different quality-control mechanisms exist within the cell to assure detection of incorrectly folded proteins and their targeting for degradation, sometimes proteins escape all the protective mechanisms and subsequently form aggregates inside cells or the extracellular space[1].

Uncontrolled misfolding and associated protein aggregation can result in the formation of different large aggregates, as native-like deposits, amorphous deposits, or amyloid fibrils, all of which have links to pathological states in human disease[2]. Most deposits associated with such so-called protein misfolding diseases consist of amyloid fibrils. Three criteria define a protein aggregate as an amyloid fibril: the fibrillar morphology, the characteristic cross-β structure, and the ability to be stained by specific dyes (Congo Red, Thioflavin-T)[2]. Amyloid fibrils are usually 7-13 nm in diameter, microns in length, and generally comprise 2-8 protofilaments that can twist around each other or associate laterally[2]. The β-strands in the fibrils are orientated perpendicularly to the fibril axis and are assembled into β-sheets that are arranged parallelly to the fibril axis (cross-β structure), displaying typical X-ray diffraction patterns of 4.7-4.8 Å (meridional reflection) and 10 Å (equatorial reflection), corresponding to the inter-strand and stacking distances in the β-sheet[3,4]. Formation of fibrils during a protein aggregation reaction often follows sigmoidal kinetics that can generally be divided in three distinct phases: the lag phase, the exponential or growth/elongation phase, and the plateau or saturation phase[2]. To describe the aggregation pathway from an intrinsically disordered or globular protein monomer into amyloid fibrils, different models involving different nucleus formation mechanisms as starting point for further aggregation have been applied: the nucleated polymerisation model, the nucleated conformational conversion, and native-like aggregation[2].

More than 30 peptides and proteins have been found to form amyloid deposits in human pathologies, including for example Alzheimer's disease (AD), Parkinson's disease (PD), Huntington's disease (HD), type II diabetes (T2D), a number of systemic amyloidoses, and many more[2]. While most of these peptides/proteins are secreted and resulting deposits are

thus found in the extracellular space, a minority is also cytosolic and lead to the formation of intracellular inclusions[2]. Some of the described peptides/proteins adopt a well-defined fold in the native state while others are intrinsically disordered[2]. Seven peptides/proteins were described to from deposits in the central nervous system causing neurodegenerative conditions as for instance observed in AD and PD, but the majority forms aggregates in other tissues and resulting disorders are therefore non-neuropathic[2]. 50 % of these peptides/proteins causing non-neuropathic diseases deposit in a range of tissues, leading to systemic amyloidoses, while the other 50 % deposit in one of a variety of specific tissues, like for example islet-amyloid polypeptide (IAPP) in the pancreas in T2D. Many amyloid-related diseases occur mainly sporadic although some hereditary forms have also been described, but some of them also exclusively occur hereditary, like HD and some apolipoprotein-associated amyloidoses[2]. In case of familial forms of amyloid-related diseases, mutations are often located in the gene encoding the peptide or protein undergoing amyloid fibril formation and lead to a direct or indirect increase in the propensity of the peptide/protein to aggregate, e. g. by increasing the intrinsic aggregation rate, destabilising a folded state, or causing alternative mRNA splicing resulting in an mRNA coding for a more amyloidogenic protein variant[2].

While amyloid formation was usually associated with disease, evidence emerged during the last years that amyloid might also have useful features in bacteria, fungi, and even mammals[5]. Such so-called functional amyloids can play roles in chemical storage of peptide hormones, fulfil structural functions, or lead by their formation to an intended loss- or gain-of-function of the respective protein[5]. In contrast to disease-associated amyloids, functional amyloids are non-toxic, a feature that might be explained by structural differences and/or a highly controlled and fast aggregation mechanism that avoids toxicity or the generation of toxic oligomer intermediates[5].

1.2 Type 2 diabetes (T2D) and the islet amyloid polypeptide (IAPP)

1.2.1 Hallmarks of T2D and the origin of islet amyloid

Every tenth adult is currently living with diabetes, meaning 537 million people worldwide[6]. The main forms of diabetes mellitus are gestational diabetes, type 1 diabetes (T1D), and type 2 diabetes (T2D), the latter accounting for ~90 % of cases and being clearly associated with aging and obesity[7]. Insulin resistance, β-cell failure, and chronic hyperglycemia are typical features of T2D. β-cell dysfunction and the continuous reduction of β-cell mass are attributed to factors like glucolipotoxicity, inflammation, cholesterol accumulation, and islet amyloid formation[8]. Islet amyloid deposits around pancreatic β-bells in the islets of Langerhans is the most characteristic morphological islet feature of T2D, is considered a hallmark of T2D since it has been observed in ~90 % of patients suffering from this disease, and seems also to be an important contributor to the failure of islet cell transplants[9-11]. The major protein component of islet amyloid is the 37-residue polypeptide hormone known as islet amyloid polypeptide (IAPP), or amylin[12,13].

IAPP is not only existing in humans but has been also found in several other mammals so far. Although variations are existing, its sequence is strongly conserved between species[7,8]. These variations correlate with the ability to form amyloid *in vivo*, e. g. formation of IAPP islet amyloid has been observed in humans, primates, and cats, but not in rodents and dogs[8]. Of note, human IAPP and rat IAPP differ at six positions, five of which are between residues 23-29 and three of which are prolines (residues 25, 28, and 29). Therefore, the inability of rat IAPP to form amyloid was attributed to the proline substitutions and led to the assumption that the ability of human IAPP to form amyloid is controlled by its region comprising amino acids 20-29[14]. Notably, a S20G mutation is a naturally occurring variation of the human IAPP sequence and might be associated with an early onset form of T2D and with an increased aggregation propensity *in vitro*[15,16]. Though it was found e. g. by proline substitutions or introduction of *N*-methylations in IAPP segment 20-29[17-19] that this region is important for amyloid formation, meanwhile also other segments of human IAPP were reported to be able to form amyloid and thus IAPP(20-29) is not the only determinant of amyloidogenicity[20-25].

Whether islet amyloid has an intracellular or extracellular origin *in vivo* is debated since some time and controversial reports are existing in literature[9]. Paulsson *et al.* proposed the following hypothesis concerning the sequence of events initiating islet amyloidosis[26]: Factors such as continuously high levels of fatty acids and glucose first affect the processing of proIAPP which starts to aggregate and form fibrils within the granules. By time, these granules fuse and form intracellular amyloid-like deposits which continuously grow until most of the cell is replaced and the cell dies. Cell death releases the proIAPP amyloid into the extracellular space where it can act as seed for further amyloid formation of mature IAPP released from neighbouring β-cells.

1.2.2 Structural changes of monomeric IAPP during its aggregation process

Self-assembly and aggregation of IAPP into amyloid fibrils occurs via a common nucleation-growth mechanism[27]: During the lag phase, soluble IAPP monomers start to assemble into oligomers that can vary in size and structure (primary nucleation). Such oligomers can further associate into higher-order species and subsequently generate a critical assembly nucleus. After the nucleus has formed, rapid polymerisation into amyloid fibrils follows (growth or elongation phase). Existing fibrils can additionally enhance the fibrillation rate by catalysing the formation of new oligomers on their surface, and/or by fragmentation that generates more fibril ends (secondary nucleation). In the end of the process, soluble peptide is in equilibrium with the fibrils (stationary phase).

Monomeric IAPP was shown to be an intrinsically disordered peptide that adopts a random coil structure in solution, but it can also exhibit partially helical conformations, especially in the presence of membranes[28-31] (Figure 1-1a-c). When aggregating, IAPP undergoes several structural changes, including the transition from random coil structure to helix and then to β-sheet, to finally adopt the cross-β sheet structure observed in mature fibrils[32]. Earlier IAPP fibril models based on solid-state NMR studies, X-ray diffraction studies of IAPP-fragment microcrystals forming steric zippers, amide H/D exchange measurements, two-dimensional infrared studies, and EPR studies were in line with a U-shaped structure of the IAPP monomer

containing two β-sheets within the fibrils, while more recent cryo-EM findings now suggest a S-shaped fold[8,33-35] (Figure 1-1d,e).

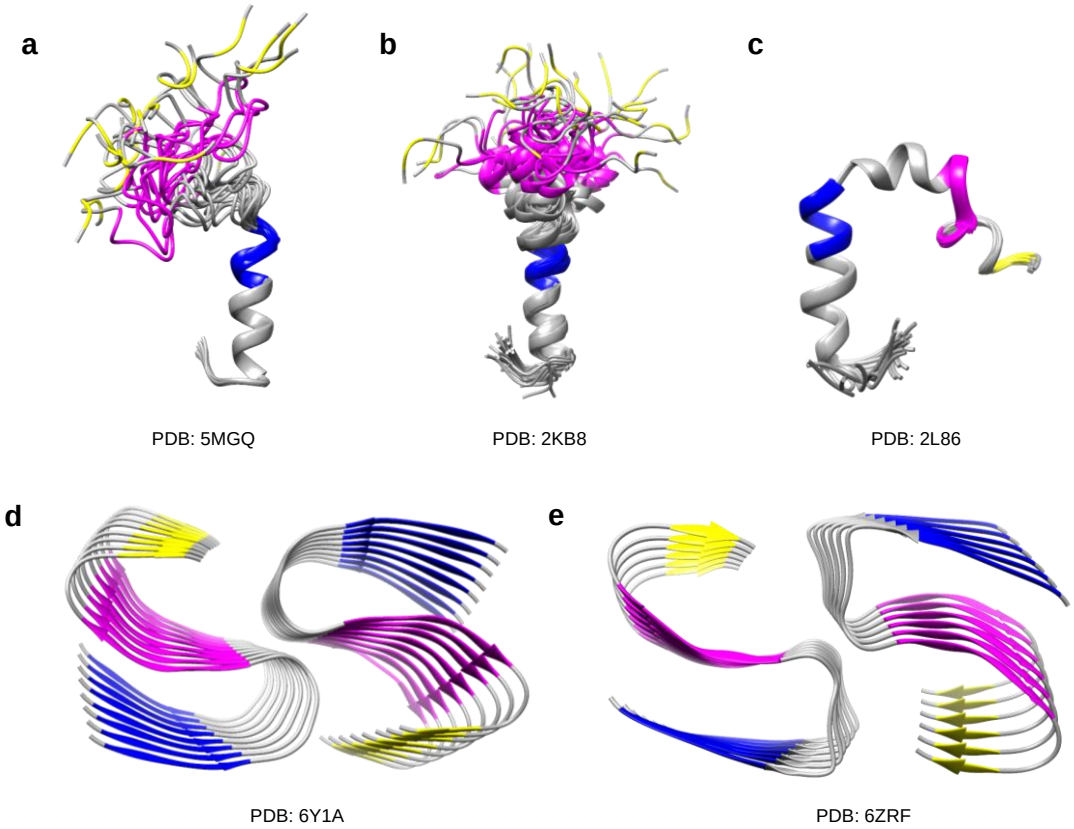

Figure 1-1: Exemplary structures of monomeric and fibrillar IAPP. (**a**) IAPP structure in solution reported by Camargo *et al.*[29] (solution-state NMR, pH 5.3, 4 °C). (**b**) IAPP structure in solution in the presence of SDS micelles reported by Patil *et al.*[36] (solution-state NMR, pH 4.6, 37 °C). (**c**) IAPP structure in solution in the presence of SDS micelles reported by Nanga *et al.*[37] (solution-state NMR, pH 7.3, 25 °C). (**d**) IAPP fibril structure reported by Röder *et al.*[33] (cryo-EM). (**e**) IAPP fibril structure reported by Gallardo *et al.*[34] (cryo-EM). The three IAPP regions forming the β-strands in the S-shaped fibril structure are coloured in blue (IAPP(14-18)), magenta (IAPP(26-31)), and yellow (IAPP(35-36)). Structures were taken from the PDB database, accession codes as indicated.

1.2.3 IAPP production, homeostasis, and its physiological and pathological functions

Understanding the natural mechanisms by which IAPP production and degradation is controlled, and its aggregation is prevented might be of great importance for the circumvention of β-cell loss in T2D since IAPP amyloid formation is toxic to β-cells. IAPP belongs to the calcitonin related peptide family that further comprises calcitonin, α-/β-calcitonin gene-related peptide (CGRP), adrenomedullin, and intermedin[38,39]. Within the family, IAPP is most similar to CGRP and all peptides share an amidated C-terminus and a intramolecular disulphide-bridge located near the N-terminus. IAPP is synthesised as prepro-hormone consisting of 89 amino acids, including a signal peptide and a N-terminal and C-terminal flanking peptide (Figure 1-2). The 22-amino acid signal peptide is cleaved off when the peptide entered the endoplasmic reticulum (ER) to yield the proform (67 amino acids)[8,9]. Further processing to remove the two flanking peptides is conducted by the two endoproteases prohormone

convertase 2 (PC2) and prohormone convertase 1/3 (PC1/3) and by carboxypeptidase E (CPE) in the Golgi apparatus and the β-cell secretory granules[8,9]. Biologically active, mature IAPP has a disulphide-bridge between residues 2 and 7, and a C-terminal amidation.

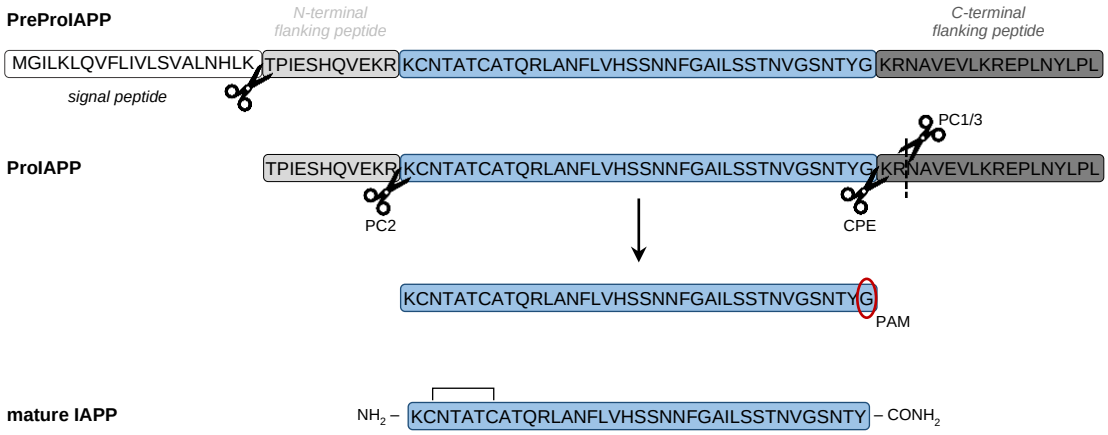

Figure 1-2: Processing of human PreProIAPP to mature IAPP. The 22-residue signal peptide is removed in the ER yielding proIAPP. ProIAPP is further processed in the Golgi apparatus and the β-cell secretory granules by the proteases PC2, PC1/3 and CPE. The C-terminal glycine residue (red circle) is then used for amidation and an intramolecular disulphide-bridge is generated yielding biologically active, mature IAPP. PC2: prohormone convertase 2; PC1/3: prohormone convertase 1/3; CPE: carboxypeptidase E; PAM: peptidyl amidating monooxygenase complex. Figure modified from references [8] and [9].

IAPP and insulin expression is regulated by similar mechanisms including the same transcription factor, and proIAPP and proinsulin are processed by the same proteases[9,32]. The two peptides are stored together in the secretory granules of β-cells at a 1-2:50 to 1:100 molar ratio and are co-secreted e. g. in response to glucose[9,32]. Insulin is known to have suppressive effects on IAPP fibrillogenesis since many years and might thus be considered an endogenous IAPP aggregation inhibitor[40]. Long exposure to hyperglycemia has a stronger effect on IAPP synthesis and secretion than on insulin's and might thus cause an imbalance in the IAPP:insulin ratio, triggering amyloid formation[41]. Insufficiently processed proIAPP was proposed to form the first amyloid within β-cells acting subsequently as seeds for further IAPP amyloid formation and a primary defect in the prohormone processing machinery was suggested to participate in T2D pathogenesis[9,26,42]. Hyperlipidemia, which is observed in T2D and obesity, was reported to increase IAPP production and also impaired IAPP degradation might be a critical step to trigger amyloid formation[41]. Several enzymes have already been reported to potentially play a role in IAPP clearance, e. g. the matrix metalloproteinases MMP-2 and MMP-9, neprilysin, the Beta-site APP-cleaving enzymes BACE1 and BACE2 (β-secretases), and the insulin-degrading enzyme (IDE)[7]. Of note, despite one exception, all the described cleavage sites targeted by these proteases lie within IAPP region 8-28[7], the segment forming major parts of the surface involved in IAPP self-assembly and fibril formation[30,43]. Additionally, ubiquitin-dependent proteasomal degradation and autophagic processes may play a role in IAPP clearance[7].

Several physiological roles have been suggested for IAPP[32]. Under normoglycemic conditions, IAPP acts in concert with insulin to control blood sugar levels by stimulating glucose uptake and suppressing its production. To reach its binding sites in the central nervous system it can also cross the blood-brain barrier, where it stimulates specific receptors and thereby

suppresses pancreatic glucagon release, promotes satiation, and regulates gastric emptying. In addition, functions in the proliferation of pancreatic β-cells, in the regulation of blood pressure, kidney function, the cardiovascular system, and the process of bone resorption have been ascribed to IAPP. Under hyperglycemic conditions as observed in T2D when IAPP starts to aggregate and accumulate, the situation inverses and IAPP exerts its cytotoxic effects via various mechanisms[32]. Toxic IAPP species can lead to cell death by inducing cell membrane disruption, ER stress, mitochondrial membrane damage and dysfunction, oxidative stress, islet inflammation, DNA damage, and prevention of autophagy.

1.3 Alzheimer's disease (AD) and the amyloid-β peptide (Aβ)

1.3.1 AD progression, pathology, and genetic factors

In 2015, already 46.8 million people worldwide were living with dementia and this number is predicted to almost double every 20 years, to reach 131.5 million in 2050[44]. Alzheimer's disease (AD), first described by the German psychiatrist Alois Alzheimer in 1907[45], represents the most common form of dementia, accounting for 60-70 % of cases according to the World Health Organisation (WHO) and is accompanied with continuous neuronal loss and cognitive decline. AD pathology is not only associated with memory loss but also with non-amnestic focal syndromes. Symptoms reflect the area of the brain's atrophy and can induce language deficits, visuospatial deficits, and behavioural alterations[46]. Clinical phases of AD can be group into 4 classes[47]: In the pre-clinical stage (1) memory loss is mild, clinical signs and symptoms of AD are absent, and daily activities are not impaired. In the early stage (2) symptoms like loss of concentration and memory, disorientation (place & time), and changes in mood start to appear. In the moderate stage (3) memory loss increases and difficulties in recognising family and friends, reading, writing, and speaking are observed. In late stages (4) progressive functional and cognitive impairment occurs, patients cannot recognise family members anymore and might become bedridden. The rate of AD progression is heterogenous and can range from a rather slow disease course lasting for more than 10 years to a rapid worsening and subsequent death within 2 years, but factors influencing disease progression are not completely understood[46,48,49]. Current AD therapy consists of four drugs, three of which are inhibitors of acetylcholinesterase, and one is an *N*-methyl-D-aspartic acid receptor (NMDAR) antagonist[46,47]. All medication is just symptomatic leading to improved memory and alertness but does not cure the disease or prevent its progression.

Neuropathological hallmarks of AD are extracellular amyloid neuritic plaques and intracellular neurofibrillary tangles observed in AD patients' brains, and neuroinflammation. The principal components of the amyloid plaques are 40- and 42-residues long amyloid-β peptides (Aβ40 and Aβ42) and Aβ is considered to play a central role in neuronal cell death causing the brain atrophy observed in AD pathology[46]. Although AD develops largely sporadic and with increasing age, familial forms (FAD) with earlier disease onset do also occur. Known pathogenic gene mutations associated with AD are located on three genes, 51 of them on the amyloid-precursor-protein (APP) gene coding for the transmembrane protein from which Aβ is

derived of, and 235 of them on the presenilin 1 or 2 gene (PSEN1/2) which are components of the γ-secretase complex responsible for cellular Aβ production[46] (see also chapter 1.3.2). Mutations of the PSEN1 gene represent 70 % of causes of FAD and are associated with youngest age of onset and the shortest disease duration[46,50]. With only one exception, mutations in the APP gene show an autosomal-dominant inheritance pattern and are often located in the protein's N- or C-terminal part close to or in α- and γ-secretase cleavage sites, leading to an increase in total Aβ content or shifting the production of Aβ peptides to the more amyloidogenic form Aβ42[46]. Genome-wide association studies (GWAS) meanwhile also identified several genetic risk factors for sporadic AD in addition to the longer and well-known ε4-allele of apolipoprotein E[46,47].

1.3.2 Aβ's biological source and its pathological and physiological roles

Aβ is produced through the proteolytic processing of APP, a transmembrane protein that is expressed in many tissues, especially in the synapses of neurons[51]. Human APP can be processed via two alternative pathways, the non-amyloidogenic and the amyloidogenic one, differing mainly in the cleavage step occurring first[51] (Figure 1-3). During the non-amyloidogenic pathway, APP is first cleaved by the α-secretase, while in the amyloidogenic pathway it is first cleaved by the β-secretase. Both cleavage steps leave a membrane-anchored α- or β-C-terminal fragment (CTFα/β) and release a soluble part (sAPPα/β). The second cleavage step in both pathways is executed by the γ-secretase, a complex that is composed of the four components presenilin 1 or 2, nicastrin, anterior pharynx defective 1 (APH-1), and presenilin enhancer 2 (PEN-2). In the non-amyloidogenic pathway, this cleavage leads to the release of a 3 kDa (P3) fragment and an APP intracellular domain (AICD), while in the amyloidogenic pathway the 4 kDa Aβ peptide is released instead of P3.

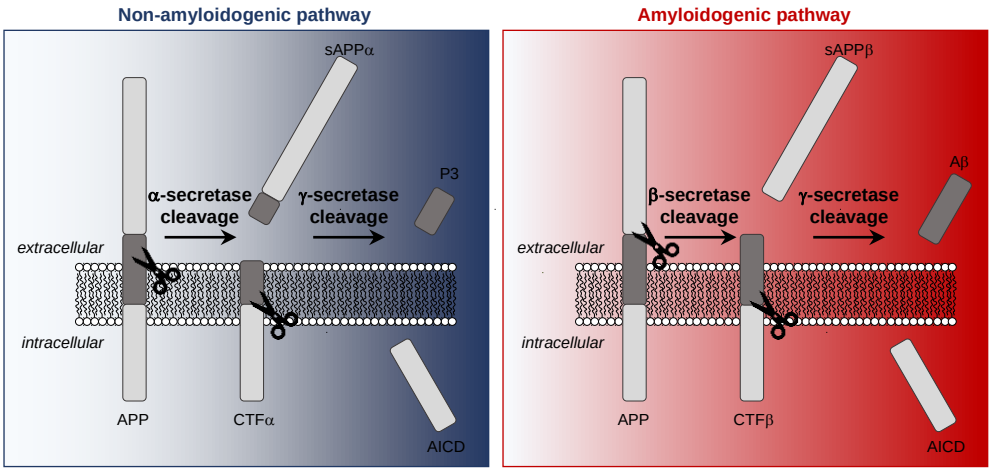

Figure 1-3: Pathways of proteolytic APP cleavage. Non amyloidogenic processing of APP is carried out first by α-secretase cleavage leading to a membrane bound C-terminal fragment CTFα and a soluble fragment sAPPα. CTFα is subsequently cleaved by γ-secretase to release the 3 kDa peptide fragment P3 and the APP intracellular domain (AICD). In amyloidogenic processing, APP is first cleaved by β-secretase yielding membrane bound CTFβ and soluble sAPPβ. In the second step, CTFβ is cleaved by γ-secretase and the Aβ peptide is released. Figure modified from reference [51].

The Aβ monomer is believed to be primarily unstructured in solution but there is also some evidence that it might be a mixture of random coil and helical parts depending on experimental conditions[52,53]. In its fibrillar form, Aβ40 adopts a U-turn fold with parallel β-sheets and two- or three-fold symmetries were described for the protofilaments constituting a fibril[54,55]. The structure of Aβ42 was determined by cryo-EM as being composed of two LS-shaped twisted protofibrils composed of Aβ42 molecules stacked in a parallel, in-register cross-β structure[56]. Aβ can aggregate rapidly to form fibrils that deposit into the amyloid plaques observed in AD brains. Therefore, the initial "amyloid cascade hypothesis" proposed that the Aβ aggregation into plaques leads to neurotoxicity and dementia in AD[57], while nowadays it is widely believed that soluble Aβ oligomers produced along the aggregation pathway rather than insoluble fibrils or plaques trigger synaptic failure and memory impairment[58]. Indeed, Aβ oligomers have been shown to exert cytotoxicity via divers mechanisms, e. g. by binding to a variety of receptors such as the a subunit containing nicotinic acetylcholine receptor (a7nAChR), the N-methyl-D-aspartic acid receptor (NMDAR), or the Aβ-binding p75 neurotrophin receptor (p75NTR), or by membrane disruption, or impairment of key intracellular processes[51,59]. However, fibrils also have proven not to be completely innocuous material, as they can deplete key components of the proteostasis network, serve as reservoir and thereby releasing source for Aβ oligomers, and can catalyse the generation of toxic oligomers via secondary nucleation[2].

Also failure of several anti-amyloid targeted therapies in clinical trials has challenged the amyloid cascade hypothesis over the last years and raised the need for an updated version[60]. Future AD therapies are no longer only amyloid-centred but also novel targets receive more and more attention[60,61]. Nevertheless, aducanumab[62], an anti-amyloid antibody targeting aggregated Aβ and clears amyloid, was recently approved in the US by the Food and Drug Administration (FDA) for AD treatment[63] and thus also provides clinical validation of the utility of targeting Aβ amyloid in AD patients.

Despite its negative role in AD pathology, Aβ was also described to exert some positive physiological functions under certain conditions and might thus not be only an incidental catabolic by-product. For instance, it was found to maybe act as endogenous antioxidant, have neuroprotective effects, is necessary for synaptic plasticity and memory, and might even act as antimicrobial peptide[64-66]. Benign and malign effects in the nervous system may not necessarily be mutually exclusive, and physiological roles might turn into pathological, toxic effects when under certain circumstances production or clearance of the Aβ peptide is altered[64].

1.4 Connections between T2D and AD

1.4.1 Pathophysiological links

Clinical studies suggest that patients suffering from T2D have an increased risk of additionally developing AD and *vice versa*[67,68] and the two diseases share several pathophysiological features[69,70]. For instance, T2D is associated with increasing insulin resistance and also during

AD, the brain's ability to respond to insulin and insulin growth factor (IGF) and to metabolise glucose decreases[71-73], leading to a "brain diabetes phenotype"[74]. Due to this similarity and other significant shared mechanisms between AD and T2D, researcher even came to propose the term "Type-3-Diabetes" for AD[70]. For maintaining normal metabolic functionality of the brain, availability of glucose is inevitable. Since glucose cannot passively diffuse through the blood-brain barrier, specific glucose transporters (GLUTs) are required to assure trafficking of glucose to the brain and into the intracellular environment of neurons and glia cells, a process in which insulin has a key regulating role[75]. When the availability of glucose in the brain decreases due to insulin resistance, neuronal synaptic transmission is seriously affected by this, since key precursors for the synthesis of the main neurotransmitter related to cognition – acetylcholine – such as coenzyme A and succinyl coenzyme A cannot be metabolised anymore from glucose in sufficient quantity[75]. Additionally, insulin resistance might stimulate the generation of Aβ and the hyperphosphorylation of tau[75]. Beside its generally known role in maintaining glucose homeostasis, insulin has also important neuroprotective and neuromodulating functions in the brain, mainly by activating the AKT and extracellular signal-regulated kinase (ERK-1/2) pathways in neurons[75]. Further evidence of the role of insulin resistance in AD pathogenesis comes from various promising trials to apply antidiabetic treatments in context of AD, that e. g. hint that insulin or insulin-sensitising drugs might have neuroprotective effects[75]. Interestingly, injections of IAPP resulted in reduced amyloid burden and lower Aβ brain concentrations in AD mouse models, improved learning and memory of these animals, reduced neuroinflammation, and positively influenced abnormal gene expression in mice brains linked with amyloid pathology[76,77]. Thus, not only insulin but also IAPP might intrinsically have protective effects against AD pathology.

Despite the abnormalities in insulin signalling, there are also other factors like altered neuronal levels of GLUTs, mitochondrial dysfunction and oxidative stress, and autophagic processes that pathophysiologically connect T2D with AD[75].

1.4.2 The role of IAPP in AD

As described before (see chapter 1.3), the presence of extracellular Aβ amyloid plaques and intracellular tangles comprised of hyperphosphorylated tau in patients' brains are the classical diagnostic markers of AD. Recently, IAPP has emerged as a novel player in AD, but mechanisms by which IAPP contributes to AD pathology are not solved yet[78]. Increased IAPP secretion (hyperamylinemia) as observed in T2D might be a trigger for IAPP misfolding and aggregation, leading to toxic gain-of-function of aggregates, the loss of physiological functions, and a dyshomeostasis also affecting the brain, dependently and independently of Aβ[78]. IAPP dyshomeostasis may worsen Aβ's toxic effects by increasing ROS production or the breakdown of IDE activity, an enzyme that is not only degrading insulin but also IAPP and Aβ [78]. AD patients can have IAPP brain deposits even without clinical manifestation of diabetes, and IAPP deposition was shown to impair brain function[78]. IAPP dysregulation may also have important implications in neuronal function, since it was shown to cross the blood-brain barrier, act on brain receptors, promote neurogenesis, and to potentially exert presynaptic effects[78].

1.4.3 Molecular links via the involved polypeptides IAPP and Aβ

Increasing evidence suggests that T2D and AD are also linked on a molecular level, mediated by IAPP and Aβ, which play major roles in the two diseases. Indeed, both peptides share analogies: IAPP and Aβ are both intrinsically disordered in their monomeric state and their sequences are 25 % identical and 50 % similar, a property that even increases to 39 % and 65 %, respectively, when only Aβ regions important for fibril formation (Aβ(15-37)) are considered[79]. Moreover, both peptides aggregate into fibrils and deposit in human tissue, and their accumulation is associated with progressive cell degeneration and death. Early pre-fibrillar and non-toxic IAPP and Aβ were also shown to interact with nanomolar affinity and this interaction delays them from amyloid self-aggregation by sequestering the peptides into initially non-fibrillar and non-toxic co-assemblies[80]. This hetero-association could mutually protect the peptides *in vivo* from misfolding and self-aggregation[80] and indeed, both IAPP and Aβ are present in human serum and cerebrospinal fluid[81-83], making such a scenario possible. Unbalancing of this heterocomplex formation e. g. by competing self-association, seeding, or cross-seeding events (see also below) could shift the equilibrium from hetero-association to self-association and thereby lead to the peptides' aggregation and accumulation[80,84]. A follow-up study indeed suggested that initially non-fibrillar and non-toxic IAPP/Aβ hetero-assemblies can further aggregate to form heteromeric fibrils and cytotoxic assemblies *in vitro*[84]. Thus, such cross-interactions between IAPP and Aβ could be the basis for the molecular link of T2D and AD. In fact, a very recent study confirmed the heterologous interaction of IAPP and Aβ in living cells and showed that co-expression of the two peptides leads to their co-deposition into mixed amyloid aggregates in *Drosophila melanogaster* brains, significantly reducing the fly longevity[85].

Addition of preformed Aβ40 or Aβ42 fibrils (fAβ40, fAβ42) to monomeric IAPP solutions (heterologous seeding or cross-seeding) enhances IAPP fibrillation comparably strong as homologous seeding by IAPP fibrils[79]. While this study identified IAPP fibrils (fIAPP) as only poor seeds for Aβ40 cross-seeding, other reports could show clear cross-seeding effects also of fIAPP seeds on Aβ40 and Aβ42 fibrillation[86,87]. The findings indicate that IAPP and Aβ cannot only interact in their native, unfolded state but also when once aggregated. Homologous and heterologous seeding experiments conducted *in vivo* confirmed that IAPP amyloid formation can be enhanced in both ways. Single intravenous injections of preformed fIAPP or fAβ42 to human IAPP transgenic mice resulted in ~10-fold and 5-fold increase in IAPP amyloid-containing pancreatic islets, respectively, suggesting that local IAPP amyloid cannot only be seeded but also cross-seeded via blood[88]. This study further provided morphological analyses of pancreases from T2D subjects and brain from AD patients revealing colocalization of IAPP and Aβ in cerebral plaques. This finding agrees with previous results presented by Jackson *et al.* that showed that IAPP accumulates in AD patients' brains and forms independent plaques or co-precipitates with Aβ to form mixed IAPP-Aβ plaques[89], and was further confirmed by studies from Martinez-Valbuena *et al.*[90] and Moreno-Gonzalez *et al.*[87]. The latter group could demonstrate that IAPP ad Aβ were both detectable in amyloid brain plaques in transgenic mice models and that intracerebral inoculation of IAPP aggregates promotes Aβ aggregation and enhances memory impairment[87], a finding that further substantiates the cross-seeding

potential of fIAPP toward Aβ fibrillation. While the morphological analyses by Oskarsson *et al.*[88] did only show the presence of IAPP in brain plaques but could not detect Aβ in islet amyloid deposits in the endocrine pancreas from T2D patients, three other studies showed that Aβ indeed also co-deposits with IAPP and is present in pancreatic islets both in human and in mouse models[90-92].

A possible reason for the high-affinity interaction between IAPP and Aβ and their potential for mutual cross-seeding is the above-mentioned high degree of sequence identity and similarity, as well as their fibril fold which has recently been proposed to share significant similarities[33,35,43,56,79]. A study using membrane-bound peptide arrays of 10-residue Aβ40 or IAPP sequences (covering full-length peptide lengths and positionally shifted by one residue) identified IAPP(8-18) and IAPP(22-28) and Aβ(19-22), Aβ(27-32), and Aβ(35-40) as "hot regions" crucial not only for the self-assembly of the two peptides but also for their hetero-association[43]. Of note, these regions are also regions with highest sequence identity and similarity[43,79]. The fibrillar spines IAPP(19-29) S20G and Aβ(24-34) were investigated by Eisenberg and co-workers and were found to be structurally similar and could both seed full-length IAPP and Aβ42 fibril formation, thus being good candidates for self- and cross-interacting segments of their two parent peptides[93]. The group suggested a hetero-assembly model of the two spine peptides that may represent an actual interface between IAPP and Aβ able to cross-template aggregation by conferring a similar structural motif[93]. Superimposition of the IAPP fibril structure that was obtained shortly after by the Eisenberg group with different Aβ fibril structures further confirmed this predicted cross-seeding core, since high structure similarities of their IAPP fold at IAPP(21-26) with Aβ(26-31) were observed[35]. Simultaneously to Eisenberg and co-workers, the IAPP fibril structure was also solved via cryo-EM by two additional groups[33,34]. By superimposing their IAPP fibril structure with their recently solved Aβ42 fibril structure[56], Schröder and co-workers could identify the segments with high structural similarity being IAPP(23-27) with Aβ(28-32) and IAPP(14-22) with Aβ(16-24)[33], which is in very good agreement with findings of the Eisenberg group. The authors postulated that the similarity between IAPP and Aβ42 fibril folds regarding topology and size might promote cross-seeding at the fibril end[33]. Also MD simulations indicated that IAPP may be a good template for the growth of Aβ and vice versa, and that lateral association of IAPP and Aβ oligomers might be preferred over double-layer conformations, while in double-layer conformations IAPP can have stabilising or destabilising effects on the Aβ oligomer depending on the arrangement[94]. Other MD simulations revealed cross-seeding IAPP-Aβ assemblies with high structural stability and favourable interfacial interactions constituted by IAPP(11-19) with Aβ(33-42) (parallel double-layer arrangement) or IAPP(9-17) with Aβ(18-24) (antiparallel double-layer arrangement)[95]. Also these results do agree with the other findings concerning the IAPP-Aβ cross-interaction and cross-seeding interface.

In conclusion, the significant overlap of T2D and AD regarding both pathophysiological and molecular events raises the need of new common therapeutic strategies, optimally considering treatments able to simultaneously tackle both diseases. Peptide-based inhibitors of amyloid self-assembly of both polypeptides ("cross-amyloid" inhibitors, see also chapter 1.5) could be such promising leads for developing anti-amyloid drugs for both T2D and AD.

1.5 Peptide-based strategies to inhibit IAPP and Aβ amyloid formation and toxicity

Future drug candidates must fulfil several requirements like target-specificity, solubility, or proteolytic stability[96]. Designing potent anti-amyloid inhibitors as therapeutic leads is even more challenging due to the following reasons: the absence of a defined target structure due to a often intrinsically unfolded nature of amyloidogenic peptides, the dynamic structure of self-assembly, the plasticity of amyloid assemblies as well as the large size of involved surfaces, and the requirement of high affinity inhibitors[96]. Most of the reported inhibitors of amyloid formation can be categorised as antibody/protein, small organic molecule, or peptide/peptidomimetic[96]. Peptide-based compounds are frequently designed by either resorting to molecular recognition principles of amyloid self-assembly, where the inhibitor sequence is derived from an amyloid self-recognition site, or to cross-amyloid interactions, where the inhibitor is derived from another amyloidogenic peptide that is known to cross-interact with the target peptide, or to known interactions with non-amyloidogenic peptides, like e. g. chaperones[96]. Notably, until now only few inhibitors were reported to be able to interfere with amyloid self-assembly of both IAPP and Aβ. The two polyphenolic compounds epigallocatechin gallate (EGCG) and resveratrol, belonging to the group of "small organic compounds", were shown to exert inhibitory effects on IAPP and Aβ by redirecting fibril formation toward amorphous aggregates and suppress cytotoxic effects, but with resveratrol being a much less effective agent against IAPP aggregation compared to EGCG[97-100]. Originating from the "chaperone-based" design strategy, the BRICHOS domain of the chaperone Bri2 has emerged as a potent IAPP and Aβ inhibitor able to interfere with aggregation, fibril formation, and cytotoxicity of the peptides both *in vitro* and *in vivo*[101-103]. Concerning the "peptide or peptidomimetic" group of amyloid inhibitors, Krotee *et al.*, Frydman-Marom *et al.*, and Kellock *et al.* have described steric zipper structure-based peptides, D-Trp-Aib dipeptides and specific α-sheet forming hairpins that could act on both IAPP and Aβ amyloidogenicity[93,104,105]. Interestingly, the D-Trp-Aib dipeptide and β-hairpin peptides bearing both Trp and Tyr residues were reported to inhibit not only IAPP but also αSynuclein[106], the key polypeptide related to Parkinson's disease (PD). This is an important finding since T2D was not only found to increase the risk for AD (see chapter 1.4.1) but also for PD[107]. Thus, such molecules could also provide an attractive basis for a future two-in-one directed solution of disease treatments. Eisenberg and co-workers presented further peptide-based inhibitors designed from steric zipper motifs in amyloid fibril cores that were able to concomitantly inhibit Aβ and tau fibrillation[108], but these two peptides belong to the same protein misfolding disease, namely, AD. Of note, none of the inhibitors affecting both IAPP and Aβ mentioned so far has anything to do sequence-wise with one of the target peptides but they rather tackle a special conformational signature common in different amyloids. Many peptide-based amyloid inhibitors have been already described that were derived from the sequence of Aβ or IAPP and therefor able to interfere with the self-assembly of its progenitor[96]. In contrast, very few have been reported that were based on the sequence of an amyloidogenic peptide being able to inhibit its parent and simultaneously its cross-interaction partner.

Around 15 years ago, work by the Kapurniotu group showed that IAPP-GI, a designed double *N*-methylated, non-amyloidogenic, and non-toxic IAPP analogue, was able to block not only IAPP but also Aβ amyloid self-assembly and was thus the first reported peptide cross-amyloid inhibitor of both IAPP and Aβ[19,80] (Figure 1-4a,b). After, more double *N*-methylated full-length IAPP analogues followed[109]. IAPP-GI was also identified as nanomolar inhibitor of non-native insulin aggregation without affecting its function, awarding this peptide not only double but triple functionality[110]. Having identified the IAPP "hot segments" involved not only in IAPP self-recognition but also in its cross-interaction with Aβ[43], "interaction surface mimics" (ISMs) were generated based on this knowledge[111] (Figure 1-4c). These peptides were made by connecting the IAPP "hot segments" with structurally biased linkers and introducing the beneficial *N*-methylation pair identified during IAPP-GI design and presented strong cross- or target-selective inhibition of Aβ and/or IAPP. Some of them were even able to block fAβ40-mediated cross-seeding of IAPP[111]. One ISM, R3-GI, a potent cross-amyloid inhibitor of Aβ, was taken as lead for further development and improvements (Figure 1-4d). Stepwise cyclisation, sequence truncation, reduction of the sequence to minimal IAPP-derived recognition elements, and systematic L-/D-amino acid exchanges led in the end to a macrocyclic peptide termed **2e**, that was not only a potent and selective Aβ inhibitor but also showed high plasma stability and could even pass the blood-brain barrier in a human cell model[112] (Figure 1-4e). Notably, out of this variety of peptides generated during the years only some ISMs displayed the ability to inhibit cross-seeding of IAPP by Aβ40 fibrils but none of them was shown to block both fAβ42-mediated IAPP cross-seeding and fIAPP-mediated Aβ42 cross-seeding.

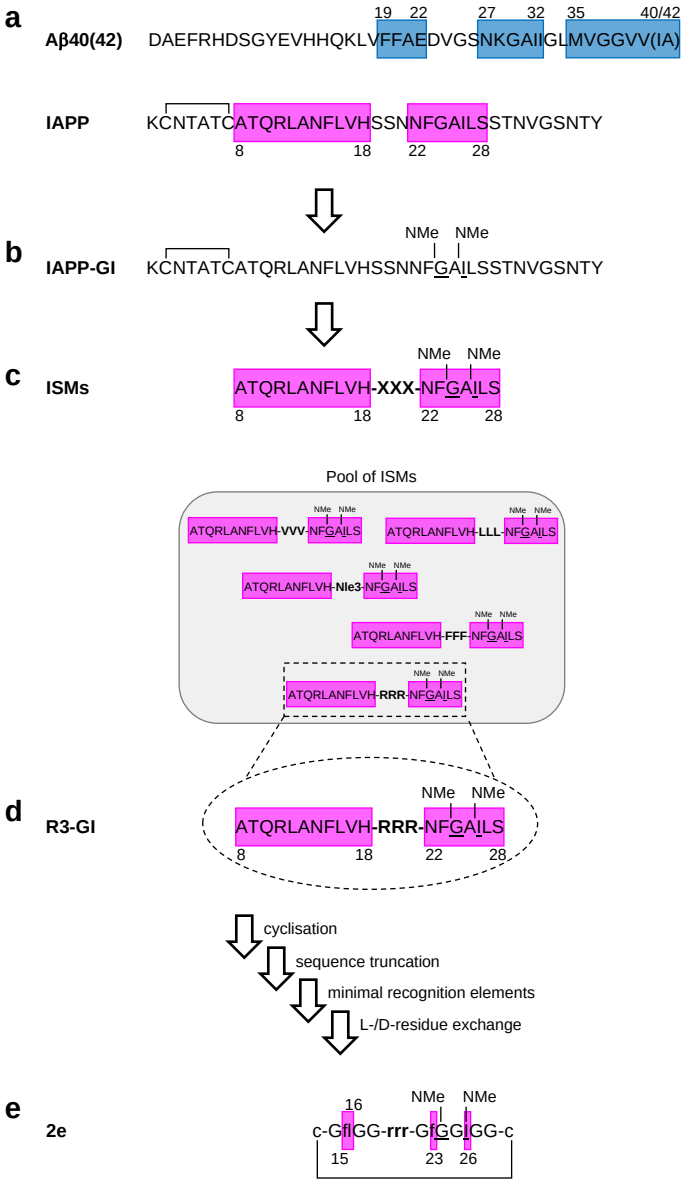

Figure 1-4: IAPP-derived IAPP and Aβ cross-amyloid inhibitors developed by the Kapurniotu group. (**a**) Primary sequences of IAPP and Aβ40(42). "Hot regions"[43] involved in self- and hetero-assembly are highlighted with coloured boxes. (**b**) Primary sequence of the non-toxic and non-amyloidogenic IAPP analogue IAPP-GI. N-methylated residues (NMe) are underlined. IAPP-GI inhibits both IAPP and Aβ and is the first reported peptide cross-amyloid inhibitor[19,80]. (**c**) "Interaction surface mimics" (ISMs)[111] created from the IAPP "hot regions". -XXX- indicates variable linker sequences. (**d**) Primary sequence of R3-GI, a potent cross-amyloid inhibitor of Aβ emerged from the pool of ISMs. This peptide was taken as lead for further improvements. (**e**) Primary sequence of the macrocyclic peptide **2e**[112]. The minimised and optimised sequence kept cross-amyloid inhibitor properties against Aβ and showed high proteolytic stability and BBB permeability. Lower-case letters indicate D-amino acids, coloured boxes and numbers highlight key residues left as minimal recognition elements from the initial IAPP "hot segments". *N*-methylated residues (NMe) are underlined.

2 Aims

Building on previous studies of our group[80,111,112], this thesis aimed to rationally design potent cross-amyloid inhibitors derived from the Aβ sequence which can inhibit IAPP and Aβ amyloid self-assembly both in unseeded and self- or cross-seeded scenarios (Figure 2-1). In summary, the aims of this thesis were the following:

1) Design and synthesis of potential inhibitors of IAPP and/or Aβ40(42) amyloid self-assembly from the Aβ(15-40) template by suitable sequence changes and introduction of *N*-methylations (termed Aβ-derived peptides or ADPs).
2) Investigations of biophysical properties of ADPs.
3) Studies on interactions and effects of the peptides on IAPP, Aβ42, and Aβ40 fibril formation and cytotoxicity.
4) Identification of the crucial motives making an ADP to an inhibitor (termed Aβ amyloid core mimic or ACM).
5) Studies on the effects of inhibitors on self-seeded IAPP and Aβ42 amyloid formation.
6) Studies on the effects of inhibitors on cross-seeded IAPP and Aβ42 amyloid formation.
7) Studies on the mechanism of action of peptides related to inhibition of amyloid self-assembly of IAPP and Aβ42.
8) Studies on the interaction interface in heterocomplexes of inhibitors and IAPP or Aβ42.

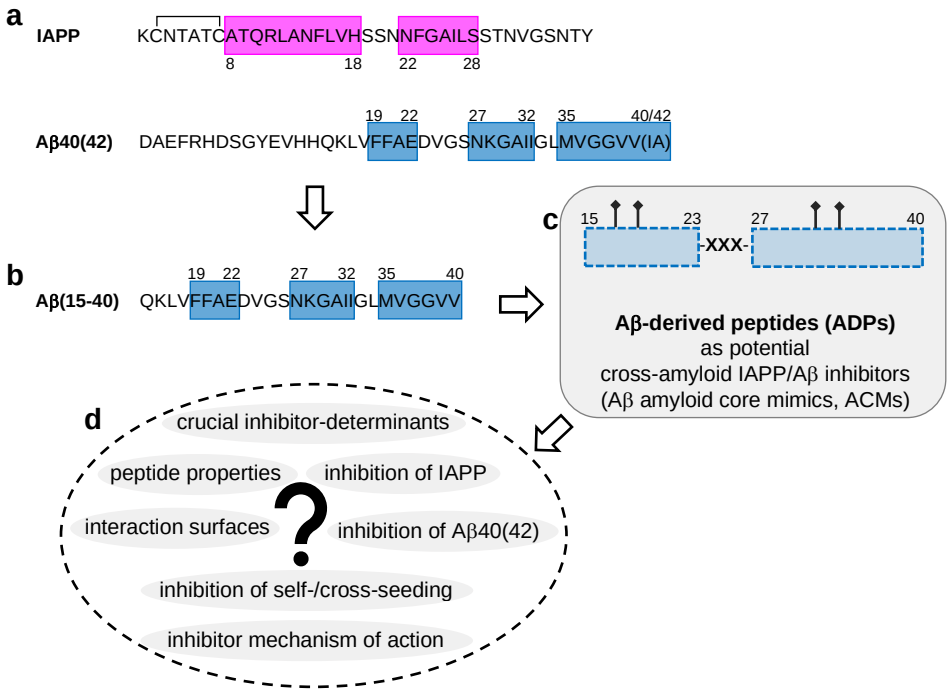

Figure 2-1: Inhibitor design strategy and aims of this thesis. (**a**) Primary sequences of IAPP and Aβ40(42). "Hot regions"[43] involved in self- and hetero-assembly are highlighted with coloured boxes. (**b**) Primary sequence of Aβ(15-40), the segment that was used for designing Aβ-derived peptides (ADPs) studied within this thesis. "Hot regions"[43] involved in self- and hetero-assembly with IAPP are marked with coloured boxes. (**c,d**) For designing ADPs, different loop tripeptide segments (-XXX-) were introduced in Aβ region Aβ(24-26) and additional optimisations were done on the sequence template Aβ(15-40) (see also chapter 4.1); sticks: *N*-methylations. ADPs that could successfully inhibit IAPP and Aβ amyloid self-assembly were termed Aβ amyloid core mimics (ACMs). Key questions addressed in this thesis are shown.

3 Material and Methods

3.1 Material

3.1.1 Resins, amino acids, and peptide labels for SPPS

Fluorenylmethoxycarbonyl (Fmoc)-based solid-phase peptide synthesis (SPPS) was conducted using either WANG resin or Tentagel R PHB resin to obtain final products as C-terminal carboxylic acids (Table 3-1). The resin that was used for the different peptides studied in this thesis is specified in chapter 3.2.1. The amino acids used for the syntheses are summarised in Table 3-2, including specifications of their N^{α}-terminal and side chain protecting groups. For special applications (e. g. fluorescence spectroscopic titrations or CLSM/2-PM imaging), fluorescent labels (see Table 3-3) were introduced N^{α}-terminally to the peptides after full assembly of the peptide chain.

Table 3-1: Resins used for SPPS. WANG or Tentagel R PHB resin was used to obtain peptides as C-terminal carboxylic acids. Which resin was used for which peptides is defined in chapter 3.2.1.

Resin name	Peptide C-terminus	Company
WANG resin	Carboxylic acid (-COOH)	Iris Biotech, Marktredwitz, DE
Tentagel R PHB resin	Carboxylic acid (-COOH)	Rapp Polymere, Tübingen, DE

Table 3-2: Amino acids used for SPPS. All amino acids are L-amino acids. TrT: trityl; Boc: *tert*-Butyloxycarbonyl; OtBu: *tert*-butylester; tBu: *tert*-butyl; Pbf: 2,2,4,6,7-pentamethyl-dihydrobenzofuran-5-sulfonyl.

Amino acid	Company
Fmoc-Ala-OH * H_2O	Iris Biotech, Marktredwitz, DE
Fmoc-Arg(Pbf)-OH	Iris Biotech, Marktredwitz, DE
Fmoc-Asn(Trt)-OH	Iris Biotech, Marktredwitz, DE
Fmoc-Asp(OtBu)-OH	Iris Biotech, Marktredwitz, DE
Fmoc-Gln(Trt)-OH	Iris Biotech, Marktredwitz, DE
Fmoc-Glu(OtBu)-OH	Iris Biotech, Marktredwitz, DE
Fmoc-Gly-OH	Iris Biotech, Marktredwitz, DE
Fmoc-Ile-OH	Iris Biotech, Marktredwitz, DE
Fmoc-Leu-OH	Iris Biotech, Marktredwitz, DE
Fmoc-Lys(Boc)-OH	Iris Biotech, Marktredwitz, DE
Fmoc-Nle-OH	Iris Biotech, Marktredwitz, DE
Fmoc-NMeGly-OH	Iris Biotech, Marktredwitz, DE
Fmoc-NMeIle-OH	Iris Biotech, Marktredwitz, DE
Fmoc-NMeLeu-OH	Iris Biotech, Marktredwitz, DE
Fmoc-NMePhe-OH	Iris Biotech, Marktredwitz, DE
Fmoc-NMeVal-OH	Iris Biotech, Marktredwitz, DE
Fmoc-Phe-OH	Iris Biotech, Marktredwitz, DE
Fmoc-Ser(tBu)-OH	Iris Biotech, Marktredwitz, DE
Fmoc-Val-OH	Iris Biotech, Marktredwitz, DE

Table 3-3: Fluorescent labels and tags for SPPS. Labels were introduced to peptides N^{α}-terminally after full assembly of the peptide chain.

Name	Abbreviation	Company
5,6-Carboxyfluorescein	Fluos	Sigma-Aldrich, St. Louis, USA
5,6-Carboxytetramethylrhodamine	TAMRA	Novabiochem/Merck, Darmstadt, DE
7-diethylaminocoumarin-3-carbonyl	DAC	Sigma-Aldrich, St. Louis, USA
Atto647N-carboxy	Atto647N	ATTO-TEC, Siegen, DE
Fmoc-6-aminohexanoic acid	ACA	Iris Biotech, Marktredwitz, DE
Biotin	-	Sigma-Aldrich, St. Louis, USA

3.1.2 Chemicals

Table 3-4: Overview of applied chemicals. For explanations on the abbreviations see the chapter “Abbreviations”.

Chemical	Company
5,6-Carboxyfluorescein (Fluos)	Sigma-Aldrich, St. Louis, USA
5,6-Carboxytetramethylrhodamine (TAMRA)	Novabiochem/Merck, Darmstadt, DE
7-diethylaminocoumarin-3-carbonyl (DAC)	Sigma-Aldrich, St. Louis, USA
Ac_2O	Sigma-Aldrich, St. Louis, USA
Acetaldehyde	Roth, Karlsuhe, DE
Acetone	Thermo Fisher, Waltham, USA
ACN	VWR, Radnor, USA
Ammoniumacetate	Merck, Darmstadt, DE
ANS	Sigma-Aldrich, St. Louis, USA
Atto647N-carboxy	ATTO-TEC, Siegen, DE
BOP	Novabiochem/Merck, Darmstadt, DE
Bradford reagent	Sigma-Aldrich, St. Louis, USA
BSA	Roth, Karlsuhe, DE
$CaCl_2$	Roth, Karlsuhe, DE
Chloranil	Fluka, Seelze, DE
DCM	Fluka, Seelze, DE
DIC	Iris Biotech, Marktredwitz, DE
DIEA	Iris Biotech, Marktredwitz, DE
DMF	CLN, Niederhummel, DE
DMSO (≥ 99.8 %)	Roth, Karlsuhe, DE
DMSO (for SPPS)	Roth, Karlsuhe, DE
DTT	Sigma-Aldrich, St. Louis, USA
EDT	Sigma-Aldrich, St. Louis, USA
Et_2O	Thermo Fisher, Waltham, USA
Ethanol	Roth, Karlsuhe, DE
Ethanol (96 %, denatured)	CLN, Niederhummel, DE
Formic acid	Roth, Karlsuhe, DE
GdnHCl	Roth, Karlsuhe, DE
Glutaraldehyde (25 % aqueous solution)	Sigma-Aldrich, St. Louis, USA
Glycine	Fluka, Seelze, DE
H_2O_2	Sigma-Aldrich, St. Louis, USA
HATU	Bachem, Bubendorf, CH
HBTU	Iris Biotech, Marktredwitz, DE
HCl (37 %, fuming)	Roth, Karlsuhe, DE
HEPES	Roth, Karlsuhe, DE
HFIP (≥ 99%)	Sigma-Aldrich, St. Louis, USA
HOBt	Sigma-Aldrich, St. Louis, USA
Isopropanol	Thermo Fisher, Waltham, USA
KCl	Merck, Darmstadt, DE
KCN	Sigma-Aldrich, St. Louis, USA
KH_2PO_4 anhydr.	Fluka, Seelze, DE
Methanol	VWR, Radnor, USA
Micro BCA Protein Assay Kit	Thermo Fisher, Waltham, USA
Milk powder	Applichem, Darmstadt, DE
MTT	Sigma-Aldrich, St. Louis, USA
Na_2HPO_4 * 2 H_2O	Merck, Darmstadt, DE
$NaBH_4$	Roth, Karlsuhe, DE
NaCl	Roth, Karlsuhe, DE
NaH_2PO_4	Roth, Karlsuhe, DE
NaOH	Roth, Karlsuhe, DE
NH_4CO_3	Fluka, Seelze, DE
Ninhydrin	Sigma-Aldrich, St. Louis, USA
NMP	Biosolve, Valkenswaard, NL
Phenol	Sigma-Aldrich, St. Louis, USA
Piperidine	Iris Biotech, Marktredwitz, DE
Poly-L-lysine	Sigma-Aldrich, St. Louis, USA
Prolong Diamond Antifade Mountant	Thermo Fisher, Waltham, USA
Pyridine	Roth, Karlsuhe, DE
SDS	Roth, Karlsuhe, DE
SSC buffer	Sigma-Aldrich, St. Louis, USA
TCA	Roth, Karlsuhe, DE
Tert-butyl-methylether	Merck, Darmstadt, DE
TFA (99 %, for HPLC)	Sigma-Aldrich, St. Louis, USA
TFA (for SPPS)	Iris Biotech, Marktredwitz, DE
Thioanisole	Sigma-Aldrich, St. Louis, USA
ThT	Sigma-Aldrich, St. Louis, USA
TIS	Sigma-Aldrich, St. Louis, USA
TRIS	Roth, Karlsuhe, DE
Triton X-100	Sigma-Aldrich, St. Louis, USA
Tween-20	Roth, Karlsuhe, DE
Uranylacetate	Sigma-Aldrich, St. Louis, USA
β-mercaptoethanol	Roth, Karlsuhe, DE

3.1.3 Aqueous buffers used for preparation of peptide incubations

The buffers that were used in this thesis to prepare the different peptide incubations are summarised in Table 3-5. Aqueous buffers were made with distilled water (ddH_2O). Their composition is additionally given in the explanations on the assay that they were used in (see Methods), respectively. Peptide incubations were prepared using either 1xb buffer (10 mM NaH_2PO_4, pH 7.4), ThT assay buffer (50 mM sodium phosphate with 100 mM NaCl, pH 7.4), or a 50 mM ammonium acetate stock solution (for Aβ42-related assays), with or without addition of HFIP. 1xb buffer was made by dissolving NaH_2PO_4 in ddH_2O to a concentration of 10 mM and adjusting the pH to 7.4 using 4 M aqueous NaOH. The ammonium acetate stock solution was made by dissolving ammonium acetate to a concentration of 50 mM and adjusting the pH to 8.5 with 4 M aqueous NaOH. For preparing the ThT assay buffer, $Na_2HPO_4 * 2\ H_2O$ was dissolved to a concentration of 500 mM in ddH_2O and aqueous NaH_2PO_4 (500 mM) was used to adjust its pH to 7.4. This solution was diluted 1:10 with ddH_2O to obtain 50 mM sodium phosphate buffer. 100 mM NaCl were added to this solution to obtain ThT assay buffer. Both 1xb buffer and ThT assay buffer were autoclaved and filtered over a 0.2 µm filter before usage, the 50 mM ammonium acetate stock solution was only filtered. Composition of other buffers and solutions are specified in the Methods sections of the assays they were used in.

Table 3-5: Peptide incubation buffers. The compositions of the aqueous incubation buffers are additionally stated in the corresponding Methods section of the assays they were used in. For details on the preparation of the buffers see the text.

1xb buffer	10 mM NaH_2PO_4, pH 7.4
ThT assay buffer	50 mM sodium phosphate with 100 mM NaCl, pH 7.4
Ammonium acetate stock solution	50 mM ammonium acetate, pH 8.5

3.1.4 Reagents and buffers for SDS-PAGE, WB, and pulldown

Purchased reagents for SDS-PAGE, WB, and pulldown assays are summarised in Table 3-6. Before usage, NuPAGE MES SDS running buffer (20x) was diluted with ddH_2O to 1x (referred to as “MES running buffer” in the corresponding Methods sections for SDS-PAGE/WB/pulldown, see chapters 3.2.16 and 3.2.17). NuPAGE transfer buffer (20x) was mixed with methanol (10 % v/v final) and diluted with ddH_2O to 1x (referred to as “transfer buffer” in the corresponding Methods sections for SDS-PAGE/WB/pulldown, see chapters 3.2.16 and 3.2.17). NuPAGE LDS sample buffer (4x) was diluted with ddH_2O to 1x and DTT was added to a final concentration of 50 mM (referred to as “reducing NuPAGE sample buffer” in the corresponding Methods sections for SDS-PAGE/WB/pulldown, see chapters 3.2.16 and 3.2.17). The buffers used for SDS-PAGE, WB, and pulldown assays were made with distilled water (ddH_2O) and their composition is shown in Table 3-7.

Table 3-6: Reagents for SDS-PAGE, WB, and pulldown. NuPAGE LDS sample buffer (4x), NuPAGE MES SDS running buffer (20x), and NuPAGE transfer buffer (20x) were diluted to 1x with ddH2O before usage. Additionally, DTT (50 mM) was added to NuPAGE LDS sample buffer to obtain reducing NuPAGE sample buffer and methanol (10 % v/v) was added to NuPAGE transfer buffer (see also text). The other reagents were used as purchased.

Name	Company
NuPAGE LDS sample buffer (4x)	Invitrogen/ Thermo Fisher, Waltham, USA
NuPAGE MES SDS running buffer (20x)	Invitrogen/ Thermo Fisher, Waltham, USA
NuPAGE transfer buffer (20x)	Invitrogen/ Thermo Fisher, Waltham, USA
NuPAGE 4-12 % Bis-Tris gel (10 or 15 well)	Invitrogen/ Thermo Fisher, Waltham, USA
Novex sharp pre-stained Protein standard	Invitrogen/ Thermo Fisher, Waltham, USA
Dynabeads M-280 streptavidin	Invitrogen/ Thermo Fisher, Waltham, USA
Super Signal West Dura Extended Duration Substrate	Invitrogen/ Thermo Fisher, Waltham, USA

Table 3-7: Buffers for SDS-PAGE, WB, and pulldown. pH of the aqueous solutions was adjusted with aqueous 4 M NaOH or 4 M HCl.

Name	Composition
TBS-T	20 mM Tris/HCl, 150 mM NaCl, and 0.05 % Tween-20, in ddH_2O, pH 7.3
Stripping buffer	2 % SDS, 100 mM β-mercaptoethanol, 50 mM Tris/HCl, in ddH_2O, pH 6.8
HNT buffer	25 mM HEPES, 0.1 M NaCl, and 0.5 % Triton X-100, in ddH_2O
1xPBS	137 mM NaCl, 2.7 mM KCl, 1.5 mM KH_2PO_4, 8.1 mM Na_2HPO_4* 2 H_2O, in ddH_2O, pH 7.2

3.1.5 Cell culture media and additives

Medium and additives used for culturing RIN5fm and PC-12 cells are summarised in Table 3-8. For cultivating RIN5fm cells, RPMI 1640 medium was supplemented with 10 % heat-inactivated fetal calf serum (FCS), 2 mM L-glutamine, 0.1 mM non-essential amino acids (NEAA), 1 mM sodium pyruvate, 1 mg/ml glucose, and 0.1 mg/ ml penicillin/streptomycin. RPMI 1640 medium for cultivating PC-12 cells was supplemented with 10 % heat-inactivated horse serum, 5 % FCS, and 0.1 mg/ml penicillin/streptomycin. Heat-inactivation of FCS used for RIN5fm cells was done in our lab (30 min at 56 °C in the water bath) while heat-inactivated horse serum used for PC-12 cells was purchased in ready-to-use form.

Table 3-8: Cell culture media and additives.

Name	Company
RPMI 1640 (with phenol red)	Gibco/Thermo Fisher, Waltham, USA
L-glutamine 200 mM	Gibco/Thermo Fisher, Waltham, USA
D(+)-glucose 100g/l	Sigma-Aldrich, St. Louis, USA
Penicillin/streptomycin (10000 U/ml)	Gibco/Thermo Fisher, Waltham, USA
Sodium pyruvate 100 mM	Gibco/Thermo Fisher, Waltham, USA
MEM NEAA 100x	Gibco/Thermo Fisher, Waltham, USA
Horse Serum, heat-inactivated	Gibco/Thermo Fisher, Waltham, USA
FCS	Gibco/Thermo Fisher, Waltham, USA

3.1.6 Consumables

Table 3-9: Consumables.

Name	Company
1.5 ml reaction vessel (Eppendorf tube)	Sarstedt, Nümbrecht, DE
Cell culture microplate, 96 well, PS, Cellstar	Greiner Bio-One, Frickenhausen, DE
Cell culture microplate, 96 well, poly-L-lysine coated, cellGrade plus	Brand, Wertheim, DE
Cell culture T75 flask, Cellstar	Greiner Bio-One, Frickenhausen, DE
FluoroNunc 96-well microtiter plate, black	Thermo Fisher, Waltham, USA
Glas vial, 1.5 ml (for ESI-IT-MS)	Zefa, Grasbrunn, DE
Microscope cover glasses, high prescision, 170±5 µm, No. 1.5H	Marienfeld, Lauda-Königshofen, DE
Millex-FG Millipore filter units, PTFE, 0.2 µm	Zefa, Grasbrunn, DE
Nitrocellulose membrane, 0.2 µm, Amersham Protran	GE Healthcare, Chicago, USA
Protective film filmolux 609	Roth, Karlsuhe, DE
Single-use cuvettes, 2.5 ml, PS	Brand, Wertheim, DE
SPOT-membrane, modified cellulose	Intavis, Tübingen, DE
SuperFrost plus microscope slide	Thermo Fisher, Waltham, USA
Syringe filters ROTILABO®, Cellulose acetate, 0.2 µm	Roth, Karlsuhe, DE
Syringe for SPPS 2/10/20 ml, BD Discardit II	Vetter, Ammerbuch, DE
Syringe frits, pore width 35 µm	Vetter, Ammerbuch, DE
TEM grids, FCF300-CU, formvar/carbon 300 mesh, copper	Electron Microscopy Siences, Hatfield, USA

3.1.7 Antibodies, purchased peptides/proteins, and peptides made in-house by the lab

An overview of the antibodies used in this thesis can be found in Table 3-10. The dilutions and incubation times applied within different assays are specified in the corresponding Methods sections. Purchased peptides or proteins are summarised in Table 3-11. For peptides that were made in-house by the research group refer to Table 3-12.

Table 3-10: Primary and secondary antibodies.

Antibody	Company	Order number
Rabbit Anti-Amylin (Human) IgG	Peninsula Laboratories, San Carlos, USA	T-4149
Anti-IAPP (fibril specific), from mouse, Clone 91E7	Synaptic Systems, Göttingen, DE	none
Anti-β-Amyloid Protein (1-40) antibody produced in rabbit	Sigma-Aldrich, St. Louis, USA	A8326-.5ML
Anti-amyloid beta (1-17) [6E10], IgG1, from mouse	Biozol, Eching, DE	ABA-AB00714-1.1-BT
Streptavidin-POD conjugate	Sigma-Aldrich, St. Louis, USA	11089153001
anti-Rabbit IgG, peroxidase-linked species-specific whole antibody (from donkey), Secondary Antibody	Thermo Fisher, Waltham, USA	10794347
Goat Anti-Mouse IgG H&L, Secondary Antibody	Abcam, Cambridge, UK	ab6789
Stabilized Goat Anti-Mouse HRP-conjugated, Secondary Antibody	Pierce/ Thermo Fisher, Waltham, USA	1858413
Anti-rabbit IgG (whole molecule), gold conjugate 10 nm, produced in goat	Sigma-Aldrich, St. Louis, USA	G-3779-.4ML
Anti-mouse IgG (whole molecule), gold conjugate 5 nm, produced in goat	Sigma-Aldrich, St. Louis, USA	G7527-.4ML

Table 3-11: Purchased peptides or proteins.

Name	Company	Order number
5-TAMRA-Aβ42 (TAMRA-Aβ42)	Bachem, Bubendorf, CH	4090153.0100
FITC-β-Ala-Aβ42 (FITC-Aβ42)	Bachem, Bubendorf, CH	4033502.0500
HiLyte647-Aβ42	Hölzel Diagnostika, Köln, DE	AS-64161
Proteinase K	Sigma-Aldrich, St. Louis, USA	1.24568.0100

Table 3-12: Peptides made in-house by the research group.

Name	SPPS/purification described in chapter
Fluos-IAPP	3.2.1 and 3.2.5
TAMRA-IAPP	3.2.1 and 3.2.5
TAMRA-IAPP-GI	3.2.1 and 3.2.5
Biotin-IAPP	3.2.1 and 3.2.5
DAC-Aβ40	3.2.1 and 3.2.7
Biotin-Aβ40	3.2.1 and 3.2.7
IAPP	3.2.1 and 3.2.5
IAPP-GI	3.2.1 and 3.2.5
rat-IAPP (rIAPP)	3.2.1 and 3.2.5
Aβ40	3.2.1 and 3.2.7
Aβ42	3.2.6

3.1.8 Cuvettes

Table 3-13: Cuvettes used for UV absorption, CD experiments, and fluorescence titrations.

Type	Company
Quartz glas ultra-micro cell, QS, black, 10 mm	Hellma Analytics, Müllheim, DE
Quartz glas micro cell, 115F-QS, 10x2 mm	Hellma Analytics, Müllheim, DE
Quartz glass macro cell, QS, 2 mm	Hellma Analytics, Müllheim, DE
Quartz glass macro cell, QS, 5 mm	Hellma Analytics, Müllheim, DE
Quartz glass macro cell, QS, 10 mm	Hellma Analytics, Müllheim, DE

3.1.9 Instruments, devices, HPLC systems, and chromatography columns

Table 3-14: Instruments and devices.

Name	Company
2030 Multilabel Reader ViktorX3	Perkin Elmer, Waltham, USA
Spectrophotometer V-630	Jasco, Pfungstadt, DE
Spectropolarimeter J-715	Jasco, Pfungstadt, DE
Spectrofluorometer FP-6500	Jasco, Pfungstadt, DE
MultiPep RSi peptide synthesizer	Intavis, Tübingen, DE
CS336X peptide synthesizer	C S Bio, Menlo Park, USA
Freeze Dryer Freeze Zone 2.5 Plus	Labconco, Kansas City, USA
Freeze Dryer Alpha 1-2 LD plus	Christ, Osterode, DE
TKA MicroPure water system	TKA Wasseraufbereitungssysteme/Thermo Fisher, Waltham, USA
MALDI-TOF Massenspektrometer	Bruker Daltonics, Bremen, DE
Centrifuge Labofuge Ae	Heraeus Sepatech, Hanau, DE
Centrifuge 5417C	Eppendorf, Hamburg, DE
Orbital shaker CAT S20	Zefa, Grasbrunn, DE
Microscope CKX41	Olympus, Shinjuku, J
Two-photon TCSPC SP8 DIVE microscope	Leica, Wetzlar, DE
SP8 STED 3X microscope	Leica, Wetzlar, DE
Intelli Mixer Rotator Type RM-2M	Neoloab, Heidelberg, DE
Magnetic Particle Concentrator DynaMag-2	Invitrogen/ Thermo Fisher, Waltham, USA
XCell II Blot Module	Invitrogen/ Thermo Fisher, Waltham, USA
LAS-400mini instrument	Fujifilm, Minato, J
Ultrasonic bath Sonorex	Bandelin, Berlin, DE
Thermostat cabinet TC140 G, 2-40 °C	Aqualytic, Dortmund, DE
Drying cabinet Heraeus Type 6	Heraeus Sepatech, Hanau, DE
CO2 incubator MCO-17AIC	Sanyo, Osaka, J

Table 3-15: HPLC systems.

Components HPLC system 1	Jasco, Gross-Umstadt, DE
Hardware-connection PC/System	LC Net II/ ADC
Low pressure gradient unit	LG-2080-02S
Degaser	DG-2080-53
UV/Vis-Detector	UV-2077 Plus
Pump	PU-2080 Plus
Components HPLC system 2	Jasco, Gross-Umstadt, DE
UV/Vis-Detector	UV-2075
Pump	PU-2089
Components HPLC system 3	Thermo Fisher, Waltham, USA
UV/Vis-Detector	Dionex Ultimate 3000, RS variable wavelength
Pump	Dionex Ultimate 3000

Table 3-16: Columns used for peptide purification and SEC. All HPLC columns have a length of 25 cm and an inner diameter (ID) of 8 mm and were used with corresponding pre-columns (ID: 8 mm, length 33 mm). For details about purification strategies and which column was used for which peptide refer to Table 4-3 in chapter 4.2. Bed dimensions of the SEC column (Superdex 75 10/300 GL) are 10x300-310 mm.

Column	**Company**
Nucleosil 100 C18; particle size: 7 µm	Grace, Columbia, USA
Reprosil Gold 200 C18; particle size: 10 µm	Dr. Maisch, Ammerbuch-Entringen, DE
Vydac 150HC C18; particle size: 10 µm	Grace, Columbia, USA
Superdex 75 10/300 GL; particle size: 13 µm	GE Healthcare, Chicago, USA

3.1.10 Software

Table 3-17: Software used for data acquisition and processing.

Software	**Company/Source**
OriginPro 2016G	OriginLab, Northampton, USA
LAS-X	Leica, Wetzlar, DE
ImageJ	Wayne Rasband, NIH, Bethesda, USA
Prism 5	GraphPad, San Diego, USA
GraFit (v5)	Erithacus Software, East Grinstead, UK
Chimera	UCSF Resource for Biocomputing, Visualization, and Informatics, San Francisco, USA
SwissSidechain database	Swiss Institute for Bioinformatics, Lausanne, CH
Perkin Elmer 2030	Perkin Elmer, Waltham, USA
Spectra Manager	Jasco, Gross-Umstadt, DE
LAS-4000 Image Reader	Fujifilm, Minato, J
Chromeleon (v7)	Thermo Fisher, Waltham, USA
ChromPass Chromatography Data System	Jasco, Gross-Umstadt, DE

3.2 Methods

3.2.1 Solid-phase peptide synthesis (SPPS)

Coupling of the first amino acid on WANG resin

Before coupling of the first amino acid (Fmoc-Val-OH), WANG resin (substitution level (SL) = 1.1 mmol/g or 0.99 mmol/g) was shaken for 30 min in *N,N*-dimethylformamide (DMF) for swelling. After, 3 equivalents (eq.) of Fmoc-protected amino acid (AA) were mixed with 3 eq. of 2-(1H-Benzotriazol-1-yl)-1,1,3,3-tetramethyluronium-hexafluorophosphate (HBTU) and 3 eq. of 1-Hydroxybenzotriazole (HOBt), dissolved in DMF and added to the resin. Following addition of 6 eq. of *N,N*-diisopropylethylamine (DIEA), the coupling reaction was performed for 2 h (shaking). Coupling reagents were discarded and the resin was washed with

DMF (3x 1 min) and diethylether (Et_2O) (2x 1 min) and dried in the desiccator. WANG resin was used for synthesising all ADPs with exception of Nle3, R3, and G3-VF, and for the N- and C-terminal ADP fragments of ADP(15-23)-VF and ADP(27-40). Approximate substitution level (SL) after coupling of the first amino acids was 0.3-0.5 mmol/g.

Coupling of the first amino acid on Tentagel R PHB resin

For synthesising the peptides Nle3, R3, and G3-VF Tentagel R PHB resin was used, and the syntheses were performed by Kathleen Hille. Tentagel R PHB resin (SL = 0.21 mmol/g) was swelled for 20 min in DMF (shaking) before further usage. Two couplings were performed to load the C-terminal amino acid (Fmoc-Val-OH). The first coupling was performed for 3 h (shaking; 3 eq. AA/3 eq. HBTU/ 3 eq. HOBt, dissolved in DMF; 6 eq. DIEA). After removal of the coupling solution and washing of the resin with DMF (1x 1 min), the coupling was repeated (overnight reaction, shaking). Coupling reagents were discarded and the resin was washed with DMF (3x 1 min) and Et_2O (2x 1 min) and dried in the desiccator. Approximate SL after coupling of the first amino acids was 0.16 mmol/g.

Determination of the substitution level and capping of the resin

To determine the resulting substitution level (SL) of the resin after coupling of the first amino acid, three samples of the resin (~2 mg each) were taken and transferred to 10 ml volumetric flasks. 25 % piperidine in DMF was added and the resin was incubated for 10 min (RT). Absorbance of the three samples at 290 nm was measured in UV cuvettes using 25 % piperidine in DMF as background value. The new SL of the resin can be calculated by:

$$SL\ \left[\frac{mmol}{g}\right] = \frac{A * volume\ [ml]}{\varepsilon\ [M^{-1} * cm^{-1}] * cuvette\ length\ [cm] * mass\ of\ resin\ [g]}$$

where A is the measured absorbance at 290 nm and ε is the molar extinction coefficient at 290 nm (5800 $M^{-1}*cm^{-1}$). SL was calculated for all three samples. The mean of the three values gives the final new SL. Approximate SL after coupling of the first amino acids were 0.3-0.5 mmol/g for WANG resin and 0.16 mmol/g for Tentagel R PHB resin.

Afterwards, remaining reactive positions of the resin were capped by acetylation using 10 eq. acetic anhydride (Ac_2O) and 10 eq. DIEA (in DMF; equivalents corresponding to the resin's initial SL). The reaction was conducted for 40 min (shaking) and the resin was washed with DMF (3x 1 min) thereafter.

Fmoc-cleavage and coupling of further amino acids

Before addition of the next amino acid, the resin was Fmoc-deprotected using 25 % piperidine in DMF. With increasing peptide chain length, deprotection times were increased from 1x 5 min and 1x 10 min to 1x 5 min and 1x 20 min. *N*-methylated amino acids were deprotected shorter, namely, 1x 2 min and 1x 7 min, to avoid diketopiperazine formation[113]. After Fmoc-deprotection, resins were washed with DMF (4x 1 min) before the next amino acid was

coupled. Kaiser test or chloranil test was performed to assure complete deprotection of the resin.

Generally, double-couplings were performed (40-60 min 3 eq. AA/3 eq. HBTU/4.5 eq. DIEA). In between couplings, the resin was washed with DMF (1x 1 min). To introduce amino acids in difficult positions, either 2-(7-aza-1H-benzotriazole-1-yl)-1,1,3,3-tetramethyluronium-hexafluorophosphate (HATU) was used instead of HBTU, reactions were conducted applying higher molar excess (4- to 6-fold) of protected amino acid or triple-couplings were performed. This applied for the following positions: Lys16, Leu17, Val18, Phe19, Lys28, Ile31 and Ile32. For coupling Ala30 to NMeIle31, five coupling steps (1 h each) were necessary (6 eq. AA/6 eq. HATU/9 eq. DIEA). *N*-methylated amino acids were introduced as follows: NMePhe20, NMePh19, NMeVal18 or NMeLeu17 were coupled via double-coupling using first 6 eq. AA/6 eq. HATU/9 eq. DIEA and after 3 eq. AA/3 eq. HATU/4.5 eq. DIEA. NMeGly29, NMeIle31 and NMeGly33 were coupled via double-couplings with first amino acid/activator/DIEA = 4/4/6-fold excess and after amino acid/activator/DIEA = 3/3/4.5-fold excess. The region comprising the LTS (Aβ(24-26)) was synthesized differently depending on the amino acid composition: the native LTS ValGlySer was coupled (double-coupling) using 3 eq. AA/3 eq. HBTU/4.5 eq. DIEA; G3- and L3-loops were introduced using double- or triple-couplings applying 3 eq. AA/3 eq. HATU/4.5 eq. DIEA; Nle3-, F3-, and R3-loops were introduced using double- or triple-couplings with either amino acid/HATU/DIEA = 3/3/4.5-fold excess or amino acid/HATU/DIEA = 6/6/9-fold excess. Synthesis plans for ADPs are shown in Table 7-1 to Table 7-7 in the Appendix.

After finishing the coupling reactions, resins were washed with DMF (3x 1 min). Kaiser test or chloranil test was performed to assure sufficient coupling of the amino acid to the resin (see paragraph “Kaiser test and chloranil test” later in this chapter). Acetylation was done for 15 min, using 10 eq. Ac_2O and 10 eq. DIEA in DMF. The resin was washed with DMF (3x 1 min) afterwards and the next coupling cycle was started. Syntheses were usually interrupted – when necessary – in the end of the day after the capping step to be continued the next day. Then, resins were additionally washed with Et_2O (2x 1 min).

Following the same principles, parts of the peptides were also synthesised in an automated peptide synthesizer (C S Bio, model CS336X). Peptide segments composed of (non-methylated) amino acids 21-40 were well suitable for automated synthesis, while automated synthesis was generally avoided for amino acids 15-20 or C-terminal peptide segments including *N*-methylated amino acids, since better results (less by-products) were obtained by manual synthesis of these regions.

Coupling of fluorescence labels

Fluorescence labels were introduced N^{α}-terminally to peptides following assembly of the fully protected peptide chain, N^{α}-Fmoc-cleavage (25 % piperidine in DMF, 1x 5 min, 1x 20 min), and washing of the resin with DMF (4x 1 min). After coupling of the labels, resins were washed with DMF (3x 1 min) and Et_2O (2x 1 min) and dried in the desiccator.

ADPs were labelled with 5,6-Carboxyfluorescein (Fluos) or with Atto647N (carboxy-derivate). Fluos-couplings (double coupling) were performed using 3 eq. of the label, 3 eq. HATU, and

4.5 eq. DIEA (in DMF) (2x 2 h). The coupling of Atto647N to Nle3-VF was performed by Kathleen Hille. Atto647N was either introduced via a single coupling (2 h) using 2 eq. of Atto647N-carboxy, 2 eq. HATU, and 3 eq. DIEA in DMF or via a double coupling (2x 2 h) using 1 eq. of Atto647N-carboxy, 1 eq. HATU, and 1.5 eq. DIEA in DMF. Both coupling protocols yielded similarly good results. Note that Atto647N-coupling requires intensive DMF-washing after the coupling step is done, to assure complete removal of unbound label.

IAPP was labelled with Fluos (Fluos-IAPP) or 5,6-carboxytetramethylrhodamine (TAMRA-IAPP). IAPP-GI was labelled with TAMRA (TAMRA-IAPP-GI). SPPS of Fluos-IAPP was performed within our research group by Kathleen Hille, Denise Naltsas, and Alexandros Grammatikopoulos. The Fluos-label was introduced by double couplings using 3 eq. of the label, 3 eq. HATU, and 4.5 eq. DIEA (in DMF) (2x 2 h), based on previous protocols[19]. TAMRA-IAPP was synthesized in context of Ricardo Keller's research internship[114] and re-synthesized by Kathleen Hille, who also synthesized TAMRA-IAPP-GI. TAMRA was coupled via an overnight reaction applying 3 eq. of label, 3 eq. HBTU, and 4.5 eq. DIEA in DMF.

The synthesis of 7-diethylaminocoumarin-3-carbonyl labelled Aβ40 (DAC-Aβ40) was done within our research group by Kathleen Hille, Michael Kracklauer, and Alexandros Grammatikopoulos. The coupling was performed using 3 eq. of label in the presence of 3 eq. HBTU and 4.5 eq. DIEA in DMF (2x 2 h).

Synthesis of biotinylated peptides

The N^{α}-biotinyl label, spaced by a ε-aminocaproic acid (ACA) moiety, was introduced to ADPs, Aβ40, and IAPP after assembly of the fully protected peptide chain. Biotin-Aβ40 and Biotin-IAPP were synthesized within our research group by Kathleen Hille according to previously published protocols[19,80]. After Fmoc-deprotection (25 % piperidine in DMF; 1x 5 min, 1x 20 min) and washing with DMF (4x 1 min), the spacer was coupled using 3 eq. ACA, 3 eq. HBTU, and 4.5 eq. DIEA in DMF. Double couplings were performed, lasting 1 h each. The resin was washed with DMF 3x for 1 min and Fmoc-deprotection of the ACA-spacer was performed (25 % piperidine in DMF, 1x 5 min and 1x 20 min). Triple couplings (1 h each) were performed to introduce the biotin label. 3 eq. biotin in combination with 3 eq. HBTU and 4.5 eq. DIEA in DMF were applied. After coupling of the label, the resin was washed with DMF (3x 1 min) and Et_2O (2x 1 min) and dried in the desiccator.

Kaiser test and chloranil test

For performing the Kaiser test[115] or the chloranil test[116], resins were washed 4x for 1 min (after Fmoc-deprotection) or 3x for 1 min (after couplings) with DMF. A small amount of resin was transferred to a test glass and mixed with three drops of each of the test solutions (see Table 3-18). For Kaiser tests, mixtures were boiled for 5 min at 110 °C and then visually inspected. For chloranil test, visual inspection was done 2-3 min after the mixture was prepared (no boiling). The 2-3 min of incubation were established as modification of previously existing protocols of our lab, since it was observed that results were often not clear directly after addition of the test reagents in case of ADPs. Of note, Kaiser tests started not to be reliable

anymore with increasing peptide chain length in case of the majority of synthesised ADPs. In these cases, coupling of a new amino acid was verified by re-assuring the SL and Kaiser tests were skipped thereafter.

Table 3-18: Content of the solutions used for Kaiser test and Chloranil test. KCN, potassium cyanide; DMF, dimethylformamide.

Kaiser test	
Solution 1	50 mg/ml ninhydrin in ethanol
Solution 2	4 g/ml phenol in ethanol
Solution 3	20 mM KCN in 98 % pyridin and ddH_2O
Chloranil Test	
Solution 1	2 % (w/v) chloranil in DMF
Solution 2	2 % (v/v) acetaldehyde in DMF

Cleavage of the peptides from the resin

20-40 mg of resin were transferred to a 2 ml-syringe. After swelling the resin in DMF (10-15 min), the N^{α}-terminal Fmoc-group was removed using 25 % piperidine in DMF (1x 5 min, 1x 20 min), and the resin was washed thereafter with DMF 4x for 1 min. The resin was dried by washing 3x for 1 min with Et_2O and subsequent placing in the desiccator for ~30 min. Cleavage of the peptides was done by incubating the resin for 3 h (shaking) either with 95 % TFA in ddH_2O or with reagent K (TFA/water/thioanisole/ethandithiol/phenol, 83/4.5/4.5/2/6 (v/v/v/v/w))[117]. For 40 mg of resin, 1 ml of the respective cleavage cocktail was used. ADPs containing RRR loop tripeptide segments (LTS), Fluos-labelled, and Biotin-labelled ADPs were cleaved with reagent K. The other unlabelled ADPs and Atto647N-Nle3-VF were cleaved with 95 % TFA in ddH_2O, but cleavage trials using reagent K also yielded similar results.

After cleavages using 95 % TFA in ddH_2O, the reaction mixture was filtered over the syringe frit and mixed with 10-15 ml of ddH_2O. The peptide solution was frozen at -80 °C and lyophilised to obtain crude product. Crude peptides were stored at -20 °C until RP-HPLC purification.

After cleavages using reagent K, the reaction mixture was filtered over the syringe frit into a centrifuge tube and mixed with 5-6 ml of ddH_2O. Afterwards, extraction with ice-cold ether was performed (3x). Therefor, the tube was filled with ice-cold Et_2O, turned upside down to mix the phases, and then centrifuged for 2 min at 3500 rpm. The ether phase was removed, and the procedure repeated twice. Finally, the tube was filled with ddH_2O, and the peptide solution was frozen, lyophilised and stored as explained before for cleavages using 95 % TFA in ddH_2O.

3.2.2 Purification of ADPs via reversed-phase (RP)-HPLC

For purification via RP-HPLC, crude products were usually dissolved in TFA/80 % B (1/4) at a concentration of 1 mg/ml, where “80 % B” is defined as a mixture of 80 % of HPLC elution solvent B and 20 % HPLC elution solvent A (see below). For the special case of biotin-labelled Nle3-VF, Nle3, and VGS-VF, crude product was dissolved in DMSO/80 % B (1/1). 500 µg crude peptide were injected per run. Peptides were chromatographed using Nucleosil 100 C18

or Reprosil Gold 200 C18 columns at a flow rate of 2 ml/min, using the following elution solvents: A, 0.058% (v/v) TFA in water and B, 0.05% (v/v) TFA in 90% (v/v) CH_3CN and water. Four different gradients were mainly applied: “schnellAβ”, “10-100 % B”, “langsamAβ”, and “langsam40-70 % B”. A fifth gradient, “50-100 % B in 30 min”, was designed especially for purifying Atto647N-Nle3-VF. For details on the gradients see Table 3-19 and Figure 3-1. Peptides were detected via their UV absorbance at 214 nm. Elution peaks containing the desired product were manually collected, immediately frozen on dry-ice, and lyophilised. Amounts of pure lyophilised products were quantified by weigh, bicinchoninic acid (BCA) assay, Bradford assay, or UV spectroscopy (fluorescently labelled analogues) (see chapter 3.2.4). Aliquots of pure lyophilised peptides were stored at -20 °C until further usage. For details on the purification strategy for the different ADPs and their HPLC retention times see Table 3-20 and Table 3-21.

Table 3-19: HPLC gradients used for purification of ADPs. Solvent A: 0.058% (v/v) TFA in ddH_2O; solvent B: 0.05% (v/v) TFA in 90% (v/v) CH_3CN and ddH_2O.

	Time (min)	solvent A	solvent B
schnellAβ	0	90 %	10 %
	1	90 %	10 %
	31	10 %	90 %
	Time (min)	**solvent A**	**solvent B**
10-100 % B	0	90 %	10 %
	1	90 %	10 %
	20	0 %	100 %
	30	0 %	100 %
	Time (min)	**solvent A**	**solvent B**
langsamAβ	0	70 %	30 %
	7	70 %	30 %
	37	40 %	60 %
	Time (min)	**solvent A**	**solvent B**
langsam40-70 % B	0	60 %	40 %
	7	60 %	40 %
	37	30 %	70 %
	Time (min)	**solvent A**	**solvent B**
50-100 % B in 30 min	0	50 %	50 %
	7	50 %	50 %
	37	0 %	100 %
	47	0 %	100 %

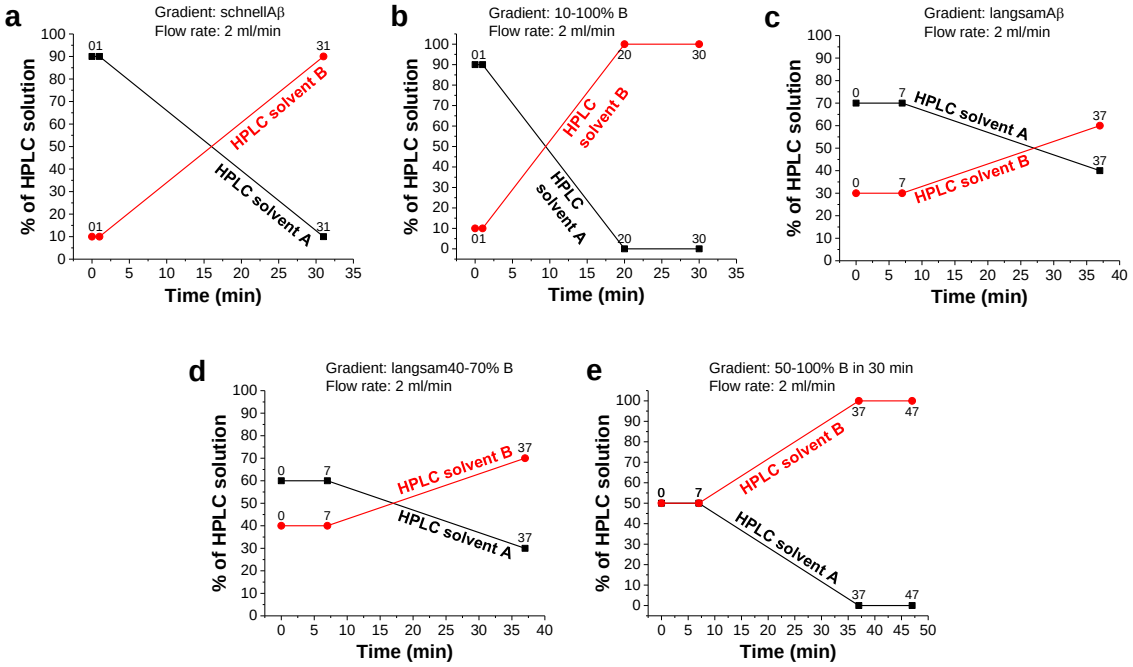

Figure 3-1: HPLC gradients used to purify 1st and 2nd generation ADPs. Gradients were run with a flow rate of 2 ml/min. The HPLC solution used to chromatograph the peptides is a mixture of HPLC solvent A (0.058 % (v:v) TFA in ddH_2O) and HPLC solvent B (0.05 % (v:v) TFA in 90 % ACN: ddH_2O). Gradient time courses are shown for the programs called "schnellAβ" (**a**), "10-100 % B" (**b**), "langsamAβ" (**c**), "langsam40-70 % B" (**d**), and "50-100 % B in 30 min" (**e**).

Table 3-20: Overview on purification strategies for ADPs. Peptides were purified via reverse-phase (RP)-HPLC. In general, gradients were run on a Nucleosil 100 C18 column. Cases in which gradients were run on a Reprosil Gold 200 C18 column are marked by asterix (*). For details on gradients see Figure 3-1 and Table 3-19. ADP(15-23)-VF and ADP(27-40) were purified by Kathleen Hille and she also assisted in purification of other ADPs. Abbreviations: pur., purification; rep, re-purification; RT, retention time.

Peptide	Gradient pur.	RT pur. (min)	Gradient rep.	RT rep. (min)
VGS	schnellAβ	22.5	-	-
VGS-LF	langsamAβ	29.1	schnellAβ	21.5
VGS-VF	langsamAβ	29.2	schnellAβ	21.9
VGS-GI	schnellAβ	22.3	schnellAβ	22.3
VGS-GG	langsamAβ*	23	-	-
R3	langsamAβ*	20.9	schnellAβ*	18.9
R3-LF	langsamAβ	24	-	-
R3-VF	langsamAβ	25	langsamAβ	25
R3-GI	schnellAβ	20.6	-	-
R3-GG	schnellAβ	20	-	-
G3	langsamAβ	28	schnellAβ*	20.1
G3-VF	langsamAβ	27.3	-	-
L3	10-100% B	18.3	-	-
L3-LF	schnellAβ	25.4	-	-
L3-VF	schnellAβ	24.8	langsam40-70% B	26.2
Nle3	10-100% B	18	10-100% B	18
Nle3-LF	schnellAβ	25.6	schnellAβ	25.2
Nle3-VF	schnellAβ	24.9	langsam40-70% B	25.6
Nle3-GI	schnellAβ	24.3	schnellAβ	24.5
Nle3-GG	langsam40-70% B	20.8	-	-
F3-LF	schnellAβ	25.4	langsam40-70% B	27.8
F3-VF	schnellAβ	24.8	langsam40-70% B	27.1
ADP(15-23)-VF	schnellAβ	25.4	langsamAβ	19.4
ADP(27-40)	schnellAβ*	19.5	-	-

Table 3-21: Overview on purification strategies for labelled ADPs. Peptides were purified via reverse-phase (RP)-HPLC. In general, gradients were run on a Nucleosil 100 C18 column. Cases in which gradients were run on a Reprosil Gold 200 C18 column are marked by asterix (*). For details on gradients see Figure 3-1 and Table 3-19. Abbreviations: pur., purification; rep, re-purification; RT, retention time.

Peptide	Gradient pur.	RT pur. (min)	Gradient rep.	RT rep. (min)
Fluos-VGS	schnellAβ	25.5	-	-
Fluos-VGS-LF	10-100% B	17.3	langsamAβ	34.5
Fluos-VGS-VF	10-100% B*	16.5	langsamAβ*	31
Fluos-VGS-GI	schnellAβ	25	schnellAβ	23.5
Fluos-VGS-GG	schnellAβ	25.8	-	-
Fluos-R3-LF	langsamAβ	28.5	-	-
Fluos-R3-VF	langsamAβ*	29	-	-
Fluos-G3-VF	schnellAβ	23.5	-	-
Fluos-L3	10-100% B*	19.9	-	-
Fluos-L3-LF	10-100% B*	18.1	10-100% B	19.6
Fluos-L3-VF	langsam40-70% B*	26.5	10-100% B*	17.5
Fluos-Nle3	10-100% B	22.6	-	-
Fluos-Nle3-LF	10-100% B	20.4	10-100% B	21.4
Fluos-Nle3-VF	schnellAβ	28	langsam40-70% B	34
Fluos-Nle3-GI	10-100% B	19.6	10-100% B	19.6
Fluos-Nle3-GG	10-100% B	19.1	10-100% B	19.1
Fluos-F3-LF	10-100% B	19.4	-	-
Fluos-F3-VF	langsam40-70% B*	28	schnellAβ*	25.5
Atto647N-Nle3-VF	10-100% B*	19.6	50-100% B	22.6
Biotin-Nle3-VF	langsam40-70% B*	24.4	langsam40-70% B	30.4
Biotin-Nle3-GG	langsam40-70% B*	27.2	-	-
Biotin-Nle3	10-100% B	21.6	10-100% B	22.8
Biotin-VGS-VF	langsam40-70% B*	16.9	langsam40-70% B*	16.9

3.2.3 Verification of peptide purity by MALDI-TOF and ESI-IT mass spectrometry

To verify peptide identity and purity after RP-HPLC purification, matrix-assisted laser desorption ionisation - time of flight mass spectrometry (MALDI-TOF-MS) was used in most cases. For some peptides, MALDI-TOF-MS generated artefact peaks and electrospray ionisation - ion trap mass spectrometry (ESI-IT-MS) was used alternatively (see Table 4-3 and Table 4-4 in chapter 4.2). For MALDI-TOF-MS analysis, a small amount of lyophilised peptide was dissolved in 30 % acetonitrile (ACN) in ddH_2O with 0.1 % TFA or in 97 % acetone in ddH_2O with 0.1 % TFA. Samples were mixed with α-cyano-4-hydroxycinnamic acid matrix which was dissolved in the corresponding solvent. Analyses were performed by various co-workers of our group (Kathleen Hille, Valentina Armiento, Beatrice Dalla Volta, Christos Kontos, Maria Bakou, Anna Spanopoulou) at the MALDI facility of the Bavarian Center for Biomolecular Mass Spectrometry (BayBioMS) at TUM. For ESI-IT-MS, 20 µg of lyophilised peptide were transferred into a 1.5 ml glass vial. 80 % ACN in ddH_2O was used as solvent. Peptides were dissolved directly before analysis. Analyses were performed by Burghard Cordes at the TUM Department of Chemistry – Zentralanalytik.

3.2.4 Determination of peptide amounts and stock preparation

Obtained amounts of pure peptides was mostly determined by weight. Pures were aliquoted and then stored at -20 °C until further usage. Peptide stock solutions were prepared in 1,1,3,3,3,3-hexafluoro-2-isopropanol (HFIP) on ice. Left-overs of ADP stock solutions were frozen and kept at -20 °C for later re-usage. When the yield of pure peptide was too little to be weighed correctly by an analytical balance (<1 mg), amounts were determined by the BCA

assay (see next paragraph). Stock concentrations of fluorescently labelled peptides and of IAPP/IAPP-GI/rat-IAPP were determined by UV spectroscopy (see Table 3-22 later in this chapter and chapter 3.2.5).

BCA assay

Peptides were dissolved in 80 % B (on ice) to a concentration of ~1 µg/µl. 20 µl (~20 µg) were transferred to an Eppendorf tube, frozen, and lyophilised. The lyophilised sample was dissolved in 40 µl HFIP. A control peptide (e. g. the same peptide from a previous purification lot) of known amount (20 µg) was treated in the same way and used as control. 10 µl, 5 µl, and 2 µl corresponding to 5 µg, 2.5 µg, and 1 µg of the control peptide, were pipetted for both samples in duplicates into a 96-well cellStar microplate. HFIP was evaporated and 50 µl of 1xb buffer (10 mM NaH_2PO_4, pH 7.4) were added to each well. Samples were incubated for 10 min at RT to assure complete dissolving (slow shaking at 200 rpm). 150 µl of the BCA kit solution (25/24/1-mixture of reagents A, B, and C; Micro BCA Protein Assay Kit) were added to each sample and mixtures were incubated at 37 °C for 2 h. Samples were then cooled for 3-5 min at -20 °C and UV absorbance at 570 nm was measured thereafter. Correct peptide amounts of samples were determined by using the absorbance values of the included control peptide as a reference standard curve.

UV spectroscopy

UV spectroscopy was performed using a JASCO Spectrophotometer V-630. Stocks of fluorescently labelled peptides were made in HFIP, on ice. For FITC-, Fluos-, TAMRA-, Atto647N-, and DAC-labelled peptides, stock concentrations could be determined via UV spectroscopy using the molar extinction coefficients listed in Table 3-22 and the Lambert-Beer law. Therefor, a small amount of peptide was transferred into an Eppendorf tube and dissolved in HFIP. For fluorescence spectroscopic titrations, stocks were freshly prepared directly before the experiment and solutions were filtered over 0.2 µm filters (Millipore) before UV absorbance measurements. Non-filtered stocks were used for other experiments.

Table 3-22: Molar extinction coefficients used for concentration determinations of fluorescently labelled peptides. Molar extinction coefficients for FITC, Fluos, and DAC were taken from references [118] and [119]. Molar extinction coefficients for TAMRA and Atto647N were determined by using HFIP-solutions of known label concentration.

Label	Wavelength (nm)	ε ($M^{-1}*cm^{-1}$)
FITC	432	22770
Fluos	432	22770
TAMRA	547	71391
Atto647N	639	236454
DAC	445	75938

3.2.5 Preparation of IAPP, rat-IAPP, and IAPP-GI, and their labelled analogues

HPLC purification of IAPP was performed for the research group by myself, Eleni Malideli, Denise Naltsas, and Simon Hornung. Purified IAPP-GI, TAMRA-IAPP-GI, and Biotin-IAPP were provided by Kathleen Hille. TAMRA-IAPP was synthesised and purified by Ricardo Keller during his research internship[114] and by Kathleen Hille. Fluos-IAPP was purified by Kathleen

Hille, Denise Naltsas, and Alexandros Grammatikopoulos for the research group. Crude products were air-oxidized (0.5 mg/ml; in aqueous 0.1 M NH_4CO_3; with 6 M (IAPP, Biotin-IAPP, TAMRA-IAPP, TAMRA-IAPP-GI) or 3 M GdnHCl (IAPP-GI, rat-IAPP); for IAPP-GI and rat-IAPP with 10% DMSO) and purified using a Vydac 150HC C18 or Nucleosil 100 C18 column. Details on the purification strategies of these peptides are summarised in Table 3-23, Figure 3-2 shows MALDI-TOF-MS spectra of purified products. Rat-IAPP was synthesised by Erika Andreetto and the HFIP stock solution that I used was taken from Li-Mei Yan (MALDI-TOF-MS see Figure 3-2). IAPP and IAPP-GI stock solutions (100-350 µM) were prepared in HFIP (4°C), filtered over 0.2 µm filters (Millipore), and concentrations were determined by UV spectroscopy[19,28] (ε(274 nm)=1440 $M^{-1}*cm^{-1}$). Labelled IAPP-analogs were cleaved, oxidized, and purified via RP-HPLC as described above for unlabelled IAPP, stocks were made in HFIP (4 °C) and their concentration was determined via UV spectroscopy (see chapter 3.2.4).

Table 3-23: Overview on purification strategies for IAPP, rat-IAPP, IAPP-GI, and their labelled analogues. Peptides were purified via reverse-phase (RP)-HPLC with contributions of various colleagues of our lab (see chapter 8). Unlabelled and labelled IAPP, and TAMRA-IAPP-GI were purified using a Vydac 150HC C18 column, IAPP-GI was purified usind a Nucleosil 100 C18 column. For details on gradients see Figure 3-1 and Table 3-19. Molecular weights of purified peptides were controlled by MALDI-TOF mass spectrometry ([a]: $M+H^+$). MALDI solvent A: 97 % acetone in ddH_2O with 0.1 % TFA; MALDI solvent B: 30 % ACN in ddH_2O with 0.1 % TFA. MALDI matrix: α-Cyano-4-hydroxycinnamic acid (HCCA). RT, retention time; MW, molecular weight.

Peptide	Gradient	RT (min)	MW calc. ($M+H^+$) (g/mol)	MW found (g/mol)	MALDI solvent
IAPP	langsamAβ	27.4	3901.86	3902.41[a]	B
IAPP-GI	langsamAβ	22.2	3929.92	3930.47[a]	B
Fluos-IAPP	langsamAβ	29.4	4260.16	4260.48[a]	A
TAMRA-IAPP	langsamAβ	32.0	4314.29	4313.95[a]	B
TAMRA-IAPP-GI	langsamAβ	28.7	4342.35	4342.41[a]	A
Biotin-IAPP	langsamAβ	28.7	4240.19	4241.13[a]	B

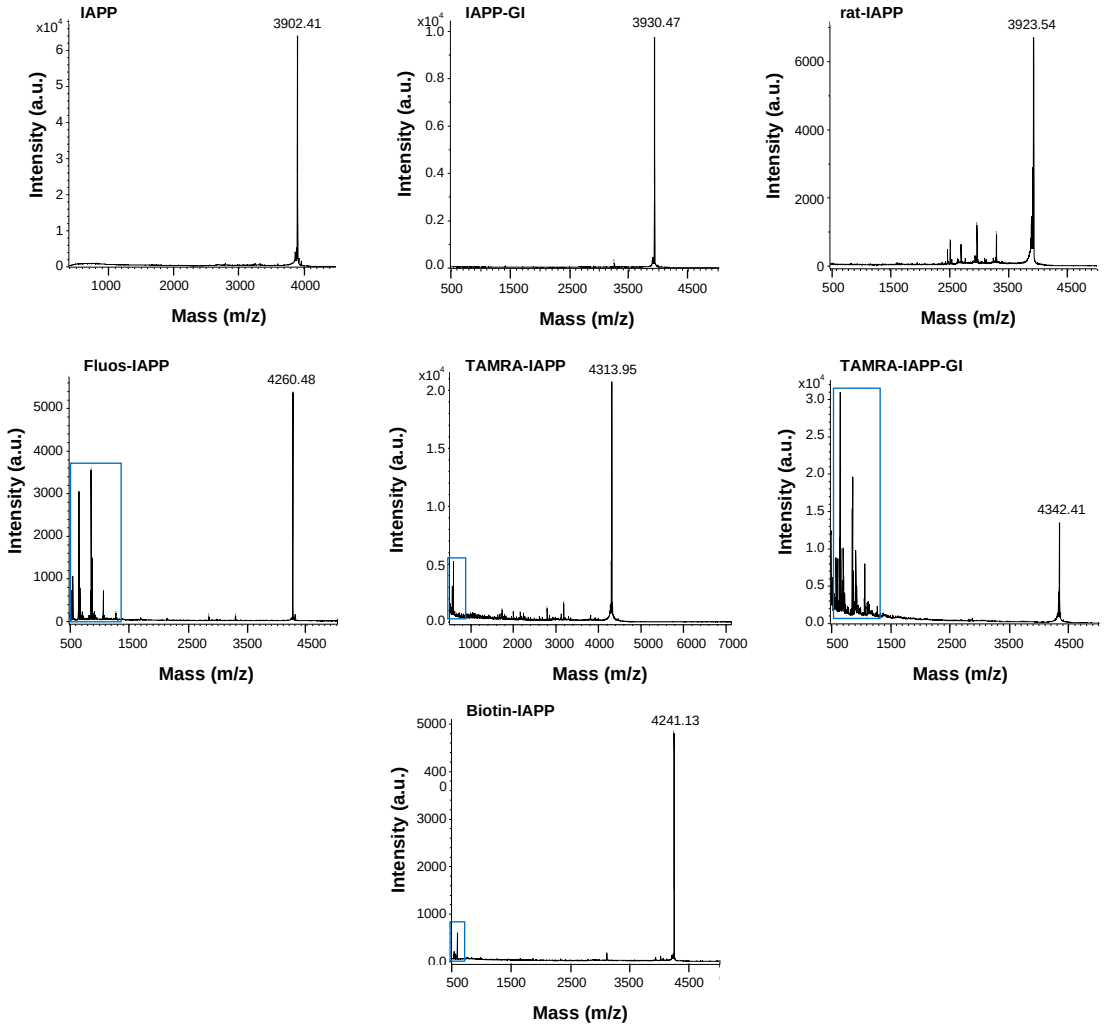

Figure 3-2: Mass spectrometric characterisation of IAPP, IAPP-GI, rat-IAPP, and their labelled analogues. MALDI-TOF-MS spectra of the peptides that were HPLC-purified according to the strategies presented in Table 3-23. Samples of all peptides except Fluos-IAPP and TAMRA-IAPP-GI were dissolved in 30 % ACN in ddH_2O with 0.1 % TFA. Fluos-IAPP and TAMRA-IAPP-GI were dissolved in 97 % acetone in ddH_2O with 0.1 % TFA. The theoretical calculated masses ($M+H^+$) are: 3901.86 g/mol (IAPP), 3918.96 g/mol (rat-IAPP), 3929.92 g/mol (IAPP-GI), 4260.16 g/mol (Fluos-IAPP), 4314.29 g/mol (TAMRA-IAPP), 4342.35 g/mol (TAMRA-IAPP-GI), 4240.19 g/mol (Biotin-IAPP). Blue boxes indicate peaks that are due to the matrix (see Figure 7-5 in Appendix).

3.2.6 Preparation of Aβ42 and its labelled analogues

Aβ42 was synthesised group by Kathleen Hille by Fmoc-based SPPS on Tentagel R PHB resin (SL=0.1776 mmol/g) using previously published protocols[19,117,120]. Double couplings (3 eq. AA/3 eq. HBTU/ 4.5 eq. DIEA) were performed. HATU was used instead of HBTU in the second coupling step of Leu17, Val18 and Phe19. Crude product was obtained by treating the resin with reagent K (3 h) (see chapter 3.2.1). Ether extraction was performed on ice with centrifugation steps at 4 °C. Crude product was purified by PSL (Heidelberg) (TFA salt). Purity of the product was confirmed by the company via ESI-MS (see Figure 3-3). To obtain seed-free aqueous stock solutions (10-20 µM) of Aβ42 for the experiments, I performed size-exclusion chromatography (SEC) based on protocols of Walsh *et al.*[121] and Jan, Hartley & Lashuel[122]. Briefly, pure product was dissolved in 5 M GdnHCl in 10 mM TRIS/HCl pH 6.0 (1 mg/ml), loaded onto a Superdex 75 10/300 GL column (400 µg/run), and chromatographed using 50 mM ammonium acetate (pH 8.5) as elution buffer and a flow rate of 0.5 ml/min. The

monomeric Aβ42 elution peak was collected on ice, concentrations were determined via UV spectroscopy (ε(275 nm)=1400 $M^{-1}*cm^{-1}$). Stock solutions were stored at 4 °C and consumed within one week. Fluorescein-isothiocyanate-β-Ala-labelled Aβ42 (FITC-Aβ42) and 5-Carboxytetramethylrhodamine-labelled Aβ42 (TAMRA-Aβ42) were from Bachem, HiLyte647-Aβ42 from AnaSpec. Stock solutions were prepared in HFIP (4 °C) and concentrations of FITC-Aβ42 and TAMRA-Aβ42 were determined by UV spectroscopy (see chapter 3.2.4).

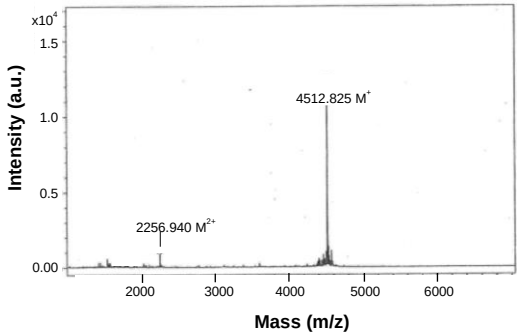

Figure 3-3: Verification of Aβ42 purity by mass spectrometry. Elector-spray mass spectrometry (ESI-MS) spectrum of Aβ42 that was HPLC-purified by PSL (Heidelberg). The spectrum was provided by the company. The theoretical calculated mass $[M+H]^+$ is 4512.28; the experimentally obtained masses are 2256.94 $(M+2H^+)^{2+}$ and 4512.83 $(M+H^+)^+$.

3.2.7 Preparation of Aβ40 and its labelled analogues

Aβ40 was synthesised and purified by Kathleen Hille. For SPPS, a Tentagel R PHB resin (Rapp Polymere) (SL=0.146 mmol/g) was used, and synthesis and cleavage from the resin was done according to the Aβ42 protocol (see chapter 3.2.6). Crude product was dissolved in TFA/80 % B (20/80) and purified by RP-HPLC on a Nucleosil 100 C18 column (TFA salt), using the elution program “langsamAβ40” (see chapter 3.2.2). Yields were determined by Kathleen Hille applying the BCA assay (see chapter 3.2.4). For usage in the experiments, I freshly prepared Aβ40 stocks (1 mg/ml) in HFIP (4 °C).

The N^{α}-terminal DAC-label and biotin-label were introduced into Aβ40 as described in chapter 3.2.1 . Purified DAC-Aβ40[43] and Biotin-Aβ40[43] were provided for the research group by Kathleen Hille (DAC-Aβ40, Biotin-Aβ40), Michael Kracklauer (DAC-Aβ40), and Alexandros Grammatikopoulos (DAC-Aβ40) using the following protocols: DAC-Aβ40 and Biotin-Aβ40 were cleaved as their unlabelled counterpart and purified by RP-HPLC on a Nucleosil 100 C18 column (DAC-Aβ40) or on a Reprosil Gold 200 C18 column (Biotin-Aβ40). Crude DAC-Aβ40 was dissolved in 6 M aqueous GdnHCl. Crude Biotin-Aβ40 was dissolved in TFA/80 % B (2.5/97.5) containing 10 mM DTT and incubated in this solution for 15 min at 40 °C. Both DAC-Aβ40 and Biotin-Aβ40 were chromatographed on a Nucleosil 100 C18 column using the elution program “schnellAβ” (see chapter 3.2.2). For a summary on the purification strategies for Aβ40, DAC-Aβ40, and Biotin-Aβ40 and their mass spectrometric characterisation see Table 3-24 and Figure 3-4.

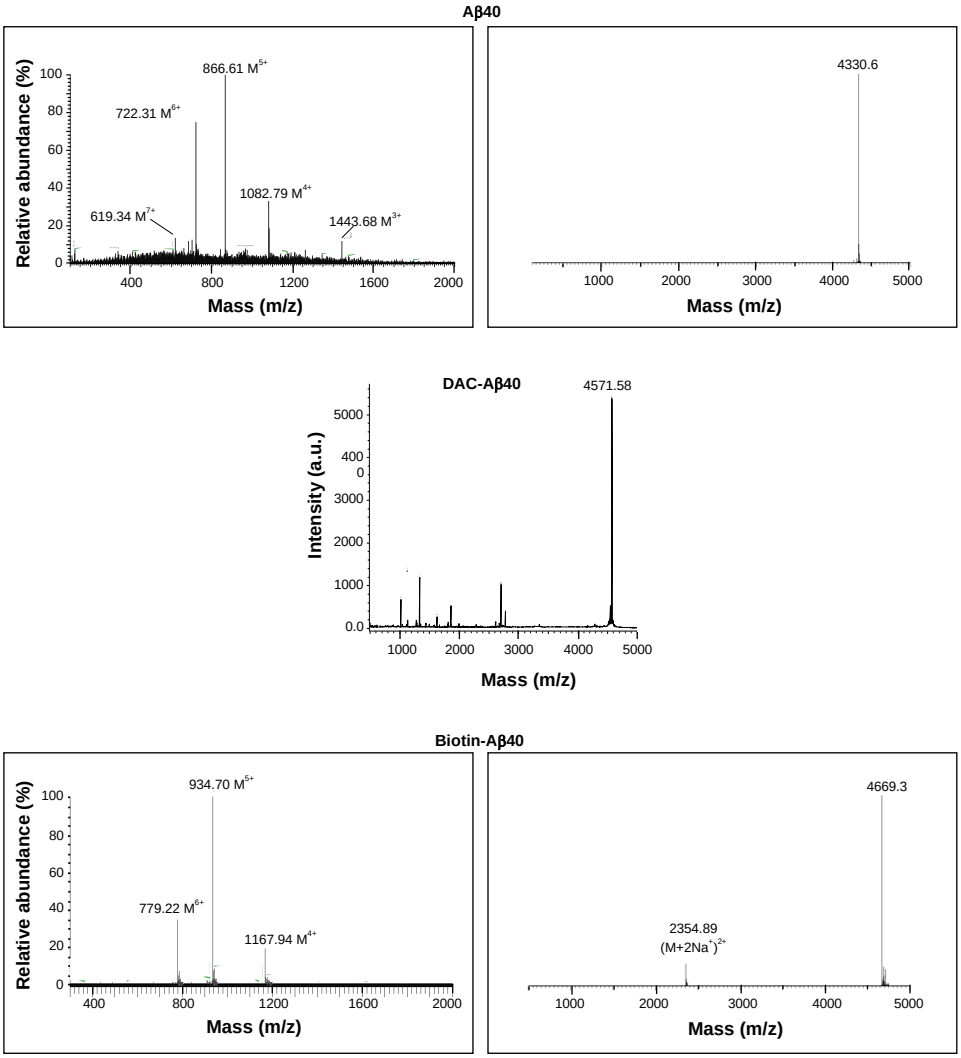

Figure 3-4: Mass spectrometric characterisation of Aβ40, DAC-Aβ40, and Biotin-Aβ40. MALDI-TOF-MS and ESI-IT-MS spectra of the peptides that were HPLC-purified according to the strategies presented in Table 3-24. Samples of Aβ40 and Biotin-Aβ40 were dissolved in 80 % ACN in ddH2O and analysed via ESI-IT-MS, DAC-Aβ40 was dissolved in a formic acid/isopropanol/ddH_2O-solution (1/2/3) and analysed via MALDI-TOF-MS. The theoretical calculated masses ($M+H^+$) are: 4328.15 g/mol (Aβ40), 4571.42 g/mol (DAC-Aβ40), 4666.48 g/mol (Biotin-Aβ40). Additional peaks (between 1000 – 3000 g/mol) present in the spectrum of DAC-Aβ40 were proven to be MALDI-artefacts that were not present in ESI analysis. The ESI spectrum is not shown since the product got oxidised during ESI analysis.

Table 3-24: Overview on purification strategies for Aβ40, DAC-Aβ40, and Biotin-Aβ40. Peptides were purified via reverse-phase (RP)-HPLC on a Nucleosil 100 C18 column using the gradients "schnellAβ" and "langsamAβ" (see Figure 3-1 and Table 3-19) by various colleagues of our lab (see chapter 8). Molecular weights of purified peptides were controlled by MALDI-TOF or ESI-IT mass spectrometry ([a]: $M+H^+$). MALDI solvent ("A"): formic acid/isopropanol/ddH_2O-solution (1/2/3); ESI solvent ("B"): 80 % ACN in ddH_2O. MALDI matrix: α-Cyano-4-hydroxycinnamic acid (HCCA). RT, retention time; MW, molecular weight.

Peptide	Gradient	RT (min)	MW calc. ($M+H^+$) (g/mol)	MW found (g/mol)	MALDI/ESI solvent
Aβ40	langsamAβ	23.5	4328.15	4330.60[a]	B
DAC-Aβ40	schnellAβ	21.5	4571.42	4571.58[a]	A
Biotin-Aβ40	schnellAβ	19.5	4666.48	4669.30[a]	B

3.2.8 Far-UV CD spectroscopy

Far-UV CD spectroscopy was carried out using a Jasco 715 spectropolarimeter. Spectra between 195 and 250 nm were recorded immediately (at RT) after sample preparation in the cuvette. Each spectrum represents an average of 3 spectra, collected at 0.1 nm intervals and

a response time of 1 s. CD spectra (ellipticities or mean residue ellipticities) are presented after subtracting the spectra of buffer alone. MRE values were calculated according to the following formula:

$$MRE\left[\frac{deg * cm^2}{dmol}\right] = \frac{100 * \theta}{c * d * n} \quad (1)$$

c: peptide concentration in mol/l
d: path length of cuvette in cm
θ: ellipticity in degree
n: number of amino acids

To evaluate structural changes occurring upon interaction of two peptides or upon heterocomplex/ heterofibril formation, the spectra obtained for the mixture were compared with theoretical spectra obtained by mathematical addition of the spectra measured for the single peptides.

Concentration dependence studies

Concentration-dependent CD studies were performed using freshly prepared (on ice) peptide HFIP stocks. Stocks were diluted with 1xb buffer (10 mM NaH_2PO_4, pH 7.4) to obtain a final concentration of 1 % HFIP and peptide concentrations between 5 µM and 100 µM. Solutions were prepared in the cuvette, mixed, and immediately measured (RT).

Studies of interactions of Aβ40 and ADPs

Stocks of Aβ40 and ADPs were prepared in HFIP on ice and 1:1-mixtures of the peptides were made from HFIP stocks. Mixed peptide solutions (in HFIP) were diluted thereafter with 1xb buffer (10 mM NaH_2PO_4, pH 7.4) to obtain a final concentration of 1 % HFIP and peptide concentrations of 5 µM each. Solutions were prepared in the cuvette, mixed, and immediately measured (RT). Samples containing either 5 µM of Aβ40 or ADP alone were prepared similarly and measured in parallel for comparison.

Studies of interactions of Aβ42 and ADPs

Aβ42 stocks in 50 mM ammonium acetate (pH 8.5) were obtained by SEC as described in chapter 3.2.6 and handled on ice. Stocks of ADPs were made in HFIP (on ice). Aβ42 was diluted to 5 µM in the CD cuvette using ddH_2O, leading to a final ammonium acetate concentration of 20 mM. Addition of ADPs (500 µM stocks in HFIP) to a concentration of 5 µM (1:1-mixture) resulted in a final amount of 1 % HFIP in the mixture. Solutions were mixed and immediately measured (RT). Samples containing either 5 µM of Aβ42 or ADP alone were prepared accordingly and measured in parallel for comparison.

Structure of IAPP/inhibitor heterocomplexes and heterofibrils

IAPP stocks were prepared in HFIP (on ice) as described in chapter 3.2.5, stocks of ADPs were made in HFIP, on ice. Incubations containing 16.5 µM IAPP and 33 µM ADP (1:2) were made in ThT assay buffer (0.5 % HFIP) as for ThT binding and MTT reduction assays (see chapters 3.2.10 and 3.2.13). To analyse heterocomplex structures, mixtures were either immediately transferred to cuvettes and measured (0 h) or incubated for 1 h at 20 °C and measured thereafter. To analyse heterofibril structures, mixtures were first incubated for 7 days at 20 °C before the measurement. All CD spectra were recorded at RT. Solutions containing only IAPP or ADP were prepared similarly and incubated and measured under the same conditions.

Structure of Aβ42/inhibitor heterocomplexes and heterofibrils

Aβ42 stocks in 50 mM ammonium acetate (pH 8.5) were obtained by SEC as described in chapter 3.2.6 and handled on ice. Stocks of ADPs were made in HFIP (on ice). Incubations containing 5 µM Aβ42 and 5 µM ADP (1:1) were made in 45 mM ammonium acetate (pH 8.5) as for MTT reduction studies (see chapter 3.2.13). For analysing heterocomplex structures, mixtures were immediately transferred to cuvettes and measured (0 h). To analyse heterofibril structures, mixtures were first incubated for 6 days at 37 °C before the measurement. All CD spectra were recorded at RT. Similar solutions containing only Aβ42 or ADP were prepared, incubated, and measured in parallel under the same conditions.

3.2.9 Fluorescence spectroscopic titrations

For fluorescence spectroscopic titrations a Jasco FP-6500 fluorescence spectrophotometer was used, and previously established methods were applied[19,80,111,112]. The apparent binding affinities (app. k_Ds) of all interactions were determined by titrating the fluorescently labelled binding partner with increasing amounts of peptide ligand. Measurements were conducted at RT. Freshly made and filtered stock solutions of labelled analogues in HFIP were used for the experiments. Stock solutions were kept on ice during the whole experiment. The following equations were applied to estimate the app. k_Ds:

$$F = F_0 + \frac{F_{max} - F_0}{1 + 10^{[(logk_D - L)\cdot m]}} \quad (2)$$

$$F = F_{min} + (F_{max} - F_{min}) * \frac{\sqrt{\frac{L + F_0 + k_D}{2} - \frac{(L + F_0 + k_D)^2}{4} - (L * F_0)}}{F_0} \quad (3)$$

F: measured fluorescence intensity
F_{min}/F_{max}: minimal/maximal fluorescence intensity
F_0: fluorescence intensity of the labelled peptide
k_D: dissociation constant
L: concentration of the ligand
m: slope of the curve

Equation (**2**) was used in cases where the app. k_D was higher than 20-times the concentration of the applied fluorescently labelled peptide (e. g. app. k_D >100 nM when the concentration of the fluorescently labelled partner was 5 nM) and fits were made with the OriginPro 2016G software. Equation (**3**) was used in cases where the app. k_D was lower than 20-times the concentration of the applied fluorescently labelled peptide and fits were made with the GraFit software. Experimental protocols are described in the following sections.

Self-assembly of ADPs, binding of ADPs to Fluos-IAPP or FITC-Aβ42, and binding of Fluos-labelled ADPs to unlabelled IAPP or Aβ40

Fluos-IAPP (5 nM) and FITC-Aβ42 (5 nM) were titrated with increasing amounts of unlabelled ADPs based on established methods[43,80,117]. Fluos-labelled ADPs (5 nM) were titrated with increasing amounts of their unlabelled counterpart for determining self-assembly affinities or with IAPP or Aβ40. HFIP stocks of ADPs and Fluos-labelled ADPs were prepared on ice as described in chapter 3.2.4. The preparation of HFIP stock solutions (on ice) for IAPP, Aβ40, and their labelled analogues is described in chapters 3.2.5 and 3.2.7. Measurements were performed in 1xb (10 mM NaH_2PO_4, pH 7.4) containing 1 % HFIP. Excitation was at 492 nm and fluorescence emission spectra were collected between 500 and 600 nm. Binding curves were generated using the fluorescence emission intensities at 522 nm or 519 nm for Fluos-IAPP/Fluos-ADPs or FITC-Aβ42, respectively.

Binding of DAC-Aβ40 to unlabelled ADPs

DAC-Aβ40 (10 nM) was titrated with increasing amounts of unlabelled ADPs as previously described[43,84]. Stocks in HFIP were prepared on ice as described in chapter 3.2.4. Measurements were performed in 1xb (10 mM NaH_2PO_4, pH 7.4) containing 1 % HFIP. Excitation was at 430 nm and fluorescence emission spectra were collected between 440 and 550 nm. Binding curves were generated using the fluorescence emission intensities at 465 nm.

Binding of Fluos-labelled ADPs to unlabelled Aβ42

Fluos-labelled ADPs (1 nM) were titrated with increasing amounts of unlabelled Aβ42. HFIP stocks of Fluos-labelled ADPs were prepared on ice as described in chapter 3.2.4. Aβ42 stocks in 50 mM ammonium acetate (pH 8.5) were obtained via SEC as described in chapter 3.2.6 and handled on ice. Measurements were performed in 50 mM ammonium acetate (pH 8.5) containing 1 % HFIP. Excitation was at 492 nm and fluorescence emission spectra were collected between 500 and 600 nm. Binding curves were generated using the fluorescence emission intensities at 522 nm.

3.2.10 Thioflavin T (ThT) binding assays

A 2030 Multilabel Reader VictorX3 was used to measure ThT fluorescence emission intensities. Samples were excited at 450 nm and fluorescence emission was determined at

486 nm after a short mixing interval (1 s). Details on the preparation of the incubations for different experimental setups, on the concentrations of applied ThT solutions, and on incubation/ThT mixing ratios are provided in the following chapters. Generally, incubations for Aβ42-related studies were prepared in black 96-well FluoroNunc microtiter plates, while incubations for Aβ40-related and IAPP-related studies were prepared in Eppendorf tubes if not stated otherwise. For more details on peptide stock preparation and assay buffers refer to chapters 3.2.4 to 3.2.7 and chapter 3.1.3.

Studies on the effect of ADPs on IAPP fibril formation, Eppendorf tube-system

Effects of ADPs on IAPP fibril formation were studied using previously established protocols[19,80,111]. IAPP and ADP (ratio 1:2) were transferred from their HFIP stocks to an Eppendorf tube (on ice). HFIP was evaporated with air and peptides were dissolved at RT in ThT assay buffer (50 mM sodium phosphate with 100 mM NaCl, pH 7.4) containing 0.5 % HFIP to obtain final concentrations for IAPP of 16.5 µM and for ADPs of 33 µM. Solutions were gently vortexed to mix and incubated at 20 °C. As controls, solutions containing only IAPP or ADP were prepared and incubated under the same conditions. ThT binding was determined by first gently vortexing the incubations and then mixing 30 µl-aliquots of each incubation with 170 µl of a 20 µM ThT solution (in aqueous 0.05 M glycine/NaOH, pH 8.5) in a black 96-well FluoroNunc microtiter plate. This results in a final ratio of 6.9 µmol ThT/ µmol peptide (respective to IAPP). Fluorescence emission was measured immediately. Buffer values were not subtracted from the measurements. The same procedure was applied for preparing incubations used in IC_{50} assays, but IAPP (16.5 µM) was mixed with gradually increasing amounts of inhibitors. For MTT reduction assays and TEM analysis, aliquots of the same above-described incubations containing IAPP, ADP, or both were used.

Studies on the effect of ADPs on IAPP fibril formation, microtiter plate-system

To follow the IAPP aggregation kinetics for longer than 7 days (see Figure 4-24i,j) or to do studies with only 1 µM of IAPP (see Figure 4-16), another ThT binding assay system was established on the basis of previous protocols[19,80,111] (see also previous paragraph) using black 96-well FluoroNunc MTPs. IAPP (1 µM or 16.5 µM) and inhibitors were mixed (from HFIP stocks) inside the wells (ratios as indicated in the figures). After HFIP evaporation, peptides were dissolved in 100 µl ThT assay buffer (0.5 % HFIP) and mixed with 100 µl of a ThT solution consisting of 13.7 µM (for 1 µM IAPP) or 226.7 µM (for 16.5 µM IAPP) ThT in 0.05 M glycine/NaOH (pH 8.5). This led to a final incubation buffer containing 25 mM sodium phosphate, 50 mM NaCl, 0.025 M glycine/NaOH, 6.9 or 113.4 µM ThT and 0.25 % HFIP (pH 7.5), and a final ratio of 6.9 µmol ThT/ µmol peptide (respective to IAPP). Incubations were prepared on ice and incubated at 20 °C without agitation. ThT fluorescence was measured by placing the MTP containing the incubations in the 2030 Multilabel Reader VictorX3 and reading the emission at 486 nm after excitation at 450 nm, as for the other ThT binding studies. Buffer values were not subtracted from the measurements. For TEM analysis, aliquots of these incubations or of equivalent ones prepared for MTT reduction studies (w/o ThT, see chapter 3.2.13) were used.

Studies involving seeded IAPP

Effects of ADPs on fIAPP-self-seeded IAPP

Experiments were performed essentially as previously published[19]. Briefly, for generating the fIAPP seeds, IAPP (12 µM) was incubated for 4-7 days in ThT assay buffer containing 0.5 % HFIP at 20 °C (fibril formation confirmed by TEM). IAPP and ADPs (ratio 1:2) were transferred from their HFIP stocks to Eppendorf tubes (on ice). HFIP was evaporated with air and peptides were dissolved at RT in ThT assay buffer (0.5 % HFIP), before fIAPP seeds were added (10 %). Final concentrations of peptides and seeds were: IAPP 12 µM, inhibitor 24 µM, fIAPP seeds 1.2 µM. Seeded and unseeded IAPP and inhibitor as well as seeds alone were incubated in parallel as controls. Incubation was performed at RT. ThT fluorescence emission was measured by mixing 30 µl-aliquots of each incubation with 170 µl of a 20 µM ThT solution (in aqueous 0.05 M glycine/NaOH, pH 8.5) in a black 96-well FluoroNunc MTP. Buffer values and values obtained for the fIAPP seeds alone were subtracted from the measurements (10 % fIAPP seeds showed a ThT signal different from buffer alone).

Effects of ADPs on fAβ40-cross-seeded IAPP

Seeding experiments using fAβ40 were performed based on established protocols[111]. For generating the fAβ40 seeds, Aβ40 was transferred from its HFIP stock to an Eppendorf tube (on ice). HFIP was evaporated with nitrogen and the peptide was dissolved in ThT assay buffer containing 1 % HFIP (to 16.5 µM). Following a 1 h-period of agitated incubation (200 rpm on an orbital shaker; CAT S20) at RT, Aβ40 was further incubated at RT w/o shaking for 6-8 days. TEM confirmed fibril formation. Fibrils were sonicated for 5 min prior to usage. To test for inhibition of fAβ40-mediated cross-seeding of IAPP, IAPP and ADPs (ratio 1:2) were transferred from their HFIP stocks to Eppendorf tube (on ice) and HFIP was evaporated with air. Peptides were dissolved at RT in ThT assay buffer (0.5 % HFIP) before fAβ40 seeds were added (10 %). Final concentrations of peptides and seeds were: IAPP 12 µM, inhibitor 24 µM, fAβ40 seeds 1.2 µM. Seeded and unseeded IAPP and inhibitor as well as seeds alone were incubated in parallel as controls. Incubation was performed at RT. ThT fluorescence emission was measured by mixing 30 µl-aliquots of each incubation with 170 µl of a 20 µM ThT solution (in aqueous 0.05 M glycine/NaOH; pH 8.5) in a black 96-well FluoroNunc MTP. Buffer values and values obtained for the fAβ40 seeds alone were subtracted from the measurements (10 % fAβ40 seeds did not show a ThT signal different from buffer alone).

Effects of ADPs on fAβ42-cross-seeded IAPP

For generating fAβ42 seeds, lyophilised pure Aβ42 was first dissolved in HFIP (on ice) to obtain a stock solution. The required amount of Aβ42 stock was transferred to an Eppendorf tube (on ice) and HFIP was evaporated with nitrogen. Aβ42 was re-dissolved in a small amount of HFIP (1 % of the final incubation volume) and diluted with ThT assay buffer to a final concentration of 88 µM. This Aβ42 solution (in ThT assay buffer with 1 % HFIP) was incubated for 18-19 days at 37 °C (fibril formation confirmed by TEM). To investigate the inhibitors' potential to block fAβ42-mediated cross-seeding of IAPP, IAPP and ADPs (ratio 1:2) were transferred from their HFIP stocks to Eppendorf tubes (on ice). HFIP was evaporated with air and peptides were dissolved at RT in ThT assay buffer (0.5 % HFIP). fAβ42 seeds (10 %) were added thereafter.

Final concentrations of peptides and seeds were: IAPP 12 µM, inhibitor 24 µM, fAβ42 seeds 1.2 µM. Seeded and unseeded IAPP and inhibitor as well as seeds alone were incubated in parallel as controls. Incubation was performed at RT. ThT fluorescence emission was measured by mixing 30 µl-aliquots of each incubation with 170 µl of a 20 µM ThT solution (in aqueous 0.05 M glycine/NaOH, pH 8.5) in a black 96-well FluoroNunc MTP. Buffer values and values obtained for the fAβ42 seeds alone were subtracted from the measurements (10 % fAβ42 seeds showed a ThT signal different from buffer alone).

Seeding of IAPP by inhibitor-coated fIAPP

To generate fIAPP seeds, IAPP (12 µM) was incubated for 4-7 days in ThT assay buffer (0.5 % HFIP) at 20 °C. For coating the fibril surface of the seeds with inhibitor, the inhibitor was transferred to an Eppendorf tube (on ice), HFIP was evaporated with air, and fIAPP seeds (12 µM) were mixed with the dried peptide to obtain a final inhibitor concentration of 24 µM (1:2). The solution was pre-incubated for 1 day at 20 °C prior to its usage in the seeding experiment. To examine if pre-treatment of the fIAPP seeds blocks IAPP self-seeding and fibril formation, IAPP was transferred from its HFIP stock to an Eppendorf tube (on ice), HFIP was evaporated with air and IAPP was dissolved at RT in ThT assay buffer containing 0.5 % HFIP to 12 µM. The inhibitor-coated fIAPP seeds (10 %) were added thereafter. Incubations containing untreated fIAPP seeds were made and investigated in parallel for comparison. Final concentrations of peptides and seeds were: IAPP 12 µM, fIAPP seeds 1.2 µM, coated fIAPP seeds: 1.2 µM fIAPP + 2.4 µM inhibitor. Unseeded IAPP and seeds alone were incubated simultaneously as controls. Incubation was performed at RT. ThT fluorescence emission was measured by mixing 30 µl-aliquots of each incubation with 170 µl of a 20 µM ThT solution (in aqueous 0.05 M glycine/NaOH, pH 8.5) in a black 96-well FluoroNunc MTP. Buffer values and values obtained for the seeds alone were subtracted from the measurements.

Seeding of IAPP by heterofibrils

Heterofibrils were obtained by preparing mixtures of IAPP and ACMs (1:2) as described under “Studies on the effect of ADPs on IAPP fibril formation, Eppendorf tube-system” and aging them for 7 days in ThT assay buffer containing 0.5 % HFIP (20 °C). IAPP was transferred from its HFIP stock to an Eppendorf tube (on ice) and HFIP was evaporated with air. Thereafter, IAPP (12 µM) was dissolved at RT in ThT assay buffer (0.5 % HFIP) and heterofibrils seeds (10 %) were added. Seeding with fIAPP seeds was performed simultaneously for comparison. Final concentrations of peptides and seeds were: IAPP 12 µM, fIAPP seeds 1.2 µM, heterofibril seeds: 1.2 µM IAPP + 2.4 µM inhibitor. Unseeded IAPP and seeds alone were incubated in parallel as controls. Incubation was performed at RT. ThT fluorescence emission was measured by mixing 30 µl-aliquots of each incubation with 170 µl of a 20 µM ThT solution (in aqueous 0.05 M glycine/NaOH,pH 8.5) in a black 96-well FluoroNunc MTP. Buffer values and values obtained for the seeds alone were subtracted from the measurements.

Studies on the effect of ADPs on aged IAPP

To investigate the influence of inhibitors on already nucleated IAPP fibrillogenesis, IAPP solutions (16.5 µM) were prepared by transferring IAPP from its HFIP stock to an Eppendorf

tube (on ice), evaporating the HFIP with air, and dissolving the peptide at RT in ThT assay buffer containing 0.5 % HFIP. At different stages during the fibril formation process (0 h, 4 h, 6 h, 24 h), aliquots of these solutions were added to ACMs (33 µM, 1:2; dried with air from HFIP) as previously described[19,80,109,111] and ThT fluorescence was determined directly before and after mixing, and at several later time points. Incubation was performed at RT and ThT fluorescence was measured by mixing 30 µl-aliquots of each incubation with 170 µl of a 20 µM ThT solution (in aqueous 0.05 M glycine/NaOH, pH 8.5) in a black 96-well FluoroNunc MTP. Buffer values were not subtracted from the measurements.

ThT binding assay sensitivity determination

To evaluate the sensitivity of the applied ThT binding assay (see Figure 4-24c), IAPP fibrils (16.5 µM, 7 days) were prepared in ThT assay buffer containing 0.5 % HFIP as described under “Studies on the effect of ADPs on IAPP fibril formation, Eppendorf tube-system”. Fibrils were serially diluted into ThT assay buffer (0.5 % HFIP) to various concentrations and ThT fluorescence was determined as for standard inhibition assays by mixing 30 µl-aliquots of each incubation with 170 µl of a 20 µM ThT solution (in aqueous 0.05 M glycine/NaOH, pH 8.5). Buffer values were not subtracted from the measurements.

ThT binding competition assays

To study whether binding of ACMs on IAPP fibrils competes with ThT binding and thereby “hide” them from being detected, two different assays were performed. The first one aimed at investigating if increasing the ThT concentration by 10-times leads to a measurable ThT fluorescence signal for IAPP/ACM mixtures that are usually ThT-negative (see Figure 4-24e). The second assay compared ThT binding of IAPP fibrils before and after they were treated with inhibitor to potentially cover their surface and thereby block ThT binding and detection (see Figure 4-24f).

ThT binding of fIAPP and IAPP/ACM heterofibrils using 20 and 200 µM ThT

IAPP fibrils and IAPP/inhibitor heterofibrils were prepared by incubating IAPP (16.5 µM) with or without inhibitor (33 µM, 1:2) in ThT assay buffer containing 0.5 % HFIP (96 h, 20 °C; compare chapter “Studies on the effect of ADPs on IAPP fibril formation, Eppendorf tube-system”). ThT fluorescence was measured using 20 and 200 µM ThT solutions (in aqueous 0.05 M glycine/NaOH, pH 8.5). 30 µl of sample were mixed with 170 µl of ThT solution. Buffer values were subtracted from measurements.

ThT binding of fIAPP before and after coating with inhibitor

IAPP fibrils were prepared by incubating IAPP (16.5 µM) for 9 days in ThT assay buffer containing 0.5 % HFIP at 20 °C. For coating the fibril surface of the IAPP fibrils with inhibitor, the inhibitor was transferred to an Eppendorf tube (on ice), HFIP was evaporated with air, and the fibrils were mixed with the dried peptide to obtain a final inhibitor concentration of 33 µM (1:2). The solution was further incubated for 1 day at 20 °C. ThT binding of the IAPP fibrils was determined before mixing with inhibitors and after 1 day of co-incubation. Fluorescence

emission was measured after mixing 30 µl-aliquots of the samples with 170 µl of a 20 µM ThT solution (in aqueous 0.05 M glycine/NaOH, pH 8.5). Buffer values were not subtracted from the measurements.

Studies on the effect of ADPs on Aβ40 fibril formation

Aβ40 and ADP (ratio 1:1) were transferred from their HFIP stocks to an Eppendorf tube (on ice) and HFIP was evaporated with nitrogen. Peptides were dissolved at RT in ThT assay buffer containing 1 % HFIP to obtain final concentrations of 16.5 µM each. Solutions were gently vortexed to mix and incubated at RT w/o shaking after an initial 1 h-period of agitated incubation (200 rpm) at RT. As controls, solutions containing only Aβ40 or ADP were prepared and incubated under the same conditions. ThT binding was determined by mixing 30 µl-aliquots of each incubation with 170 µl of a 20 µM ThT solution (in aqueous 0.05 M glycine/NaOH, pH 8.5) in a black 96-well FluoroNunc MTP. Fluorescence emission was measured immediately. Buffer values were not subtracted from the measurements. For MTT reduction experiments and TEM analysis, aliquots of the same above-described incubations containing Aβ40, ADP, or both were used.

Studies on the effect of ADPs on Aβ42 fibril formation

The effects of ADPs on Aβ42 fibril formation were assessed using a ThT binding assay system in black 96-well FluoroNunc MTPs. Aβ42 stock solutions from SEC (see chapter 3.2.6) were diluted to 5 µM with 50 mM ammonium acetate (pH 8.5) and ThT (100 µM in ddH_2O) was added to a final concentration of 10 µM (final incubation buffer: 45 mM ammonium acetate pH 8.5 containing 10 µM ThT; 200 µl per well). For mixtures with peptides (1:1), ADPs were pipetted from their HFIP stocks into the wells and HFIP was evaporated with air. Dried peptides were mixed with 5 µM Aβ42 (in 50 mM ammonium acetate (pH 8.5)) inside the wells and ThT (100 µM in ddH_2O) was added to a final concentration of 10 µM as above to achieve the same incubation conditions. Control incubations containing the ADP alone were prepared in the same way, but instead of addition of Aβ42 the peptide was dissolved in the same buffer w/o Aβ42. The above-mentioned steps were done on ice with ice-cold buffers/ solutions to avoid Aβ42 aggregation during assay preparation. Plates were sealed with protective film (filmolux) and incubations were shaken (500 rpm on an orbital shaker; CAT S20) for 5 h at 37 °C and were incubated thereafter under non-agitated conditions (37 °C). For preparing incubations used in IC_{50} assays the same procedure was followed, but Aβ42 (5 µM) was mixed with gradually increasing amounts of inhibitors. To measure ThT fluorescence, the MTP containing the incubations was placed in the 2030 Multilabel Reader VictorX3 and emission at 486 nm was read out after excitation at 450 nm, as for the other ThT binding studies. Buffer values were not subtracted from the measurements. For TEM analysis, aliquots were taken from equivalent incubations (w/o ThT) prepared in parallel for MTT reduction studies (see chapter 3.2.13).

Studies involving seeded Aβ42

Effects of ADPs on fAβ42-self-seeded Aβ42

Aβ42 seeds (fAβ42) were produced as described in the previous chapter (5 µM, 6 days aged) but w/o ThT. Aliquots were added to incubations of Aβ42 (5 µM) or its mixtures with peptides (1:1; preparation see previous chapter) to a final seed concentration of 0.5 µM (10 %) before addition of ThT (10 µM final). Incubations of seeded and unseeded Aβ42, unseeded mixtures, 10 % fAβ42 seeds alone, and the examined peptide (5 µM) containing 10 % fAβ42 were included as controls. Buffer composition, assay preparation (on ice), incubation conditions, and the ThT fluorescence measurement procedure were as specified for standard inhibition assays (see previous chapter). Values obtained for the buffer and the fAβ42 seeds alone were subtracted from the measurements.

Effects of ADPs on fIAPP-cross-seeded Aβ42

fIAPP seeds were generated by incubating IAPP (128 µM) in ThT assay buffer containing 0.5 % HFIP for 9-12 days (20 °C; in Eppendorf tubes). Mixtures of Aβ42 and inhibitors (1:1 or 1:2) were prepared by mixing 10 µM Aβ42 (in 50 mM ammonium acetate, pH 8.5) with dried peptides (from HFIP) in MTP wells (compare chapter “Studies on the effect of ADPs on Aβ42 fibril formation”). fIAPP-seeds were added to these solutions to a final concentration of 2 µM (20 %) before addition of ThT (in ddH_2O; diluted 1:10 from 100 µM to 10 µM). Final buffer conditions were: 45 mM ammonium acetate pH 8.5 containing 10 µM ThT and a small amount of ThT assay buffer with 0.5 % HFIP (<2 %) resulting from the seeds’ incubation buffer. The same amount of ThT assay buffer with 0.5 % HFIP was added to incubations w/o seeds to guarantee identical buffer conditions in all samples. As for self-seeding studies, solutions of seeded and unseeded Aβ42, unseeded mixtures, 20 % fIAPP seeds alone and the examined peptide (20 µM) containing 20 % fIAPP were included as controls.

Using this setup (setup 1), Aβ42 was first mixed with inhibitor to allow complex formation before fIAPP seeds were added. In an additional second setup (setup 2), inhibitors were first mixed with the fIAPP seeds to allow interaction of the peptides with the fibril surface. This was done as follows: ADPs were pipetted from their HFIP stocks into the MTP well, HFIP was evaporated with air, and the peptide was dissolved (80 µM final) in 45 mM ammonium acetate buffer (pH 8.5) before fIAPP seeds (8 µM final) were added (10-fold excess of ACM over fIAPP seeds). This solution was diluted 1:4 while mixing it with Aβ42 (10 µM final). Final peptide concentrations in both setup 1 and 2 thus were: 10 µM Aβ42, 20 µM ADP, and 2 µM IAPP fibrils (20 %). The final buffer composition was as for setup 1 (see above).

Assay preparation (on ice), incubation conditions and the ThT fluorescence measurement procedure were as specified for standard inhibition assays (see chapter “Studies on the effect of ADPs on Aβ42 fibril formation”). Values obtained for the buffer and the fIAPP seeds alone were subtracted from the measurements.

Seeding of Aβ42 by heterofibrils

Heterofibrils were obtained by preparing mixtures of Aβ42 and ACMs (1:1) as described for the inhibition assay (see chapter “Studies on the effect of ADPs on Aβ42 fibril formation”) and

aging them for 6 days. Note that solutions were prepared w/o ThT. To examine if Aβ42/ACM heterofibrils can seed Aβ42 fibril formation, Aβ42 was diluted from its SEC-stock solution (see chapter 3.2.6) to 5 µM with 50 mM ammonium acetate (pH 8.5). Heterofibril seeds (10 %) were added before addition of ThT (100 µM in ddH_2O) to a final concentration of 10 µM. Seeding with fAβ42 seeds was performed simultaneously for comparison. Final concentrations of peptides and seeds were: Aβ42 5 µM, fAβ42 seeds 0.5 µM, heterofibril seeds: 0.5 µM Aβ42 + 0.5 µM inhibitor. Unseeded Aβ42 and seeds alone were incubated in parallel as controls. Buffer composition, assay preparation (on ice), incubation conditions, and the ThT fluorescence measurement procedure were as specified for standard inhibition assays (see chapter "Studies on the effect of ADPs on Aβ42 fibril formation"). Values obtained for the buffer and the seeds alone were subtracted from the measurements.

Studies on the effect of ADPs on aged Aβ42

Aβ42 solutions of 5 µM (with 10 µM ThT inside the well) were prepared and incubated as described for standard inhibition assays in chapter "Studies on the effect of ADPs on Aβ42 fibril formation". Aged solutions were mixed after with peptides (1:1, dried with air from HFIP) inside the MTP wells and ThT fluorescence was continued to be determined. Buffer composition, incubation conditions, and the ThT fluorescence measurement procedure were as specified for standard inhibition assays. Buffer values were not subtracted from the measurements.

For obtaining samples for TEM analysis to follow heterofibril elongation starting from nucleated Aβ42 time-dependently (see Figure 4-82a,b), solutions were prepared and incubated in the same way as above, but no ThT was added. Additional Aβ42 solutions (5 µM) were prepared and aged for 7 days before mixture with inhibitor (1:1), to study elongation of mature Aβ42 fibrils in mixture with inhibitor (see Figure 4-82a,c).

3.2.11 Studies on amyloidogenicity of ACMs and other ADPs

As ADPs might have an intrinsic amyloidogenic propensity due to their sequence origin, their potential fibril formation was always investigated by preparing control solutions containing peptides alone. These peptide solutions were incubated in parallel to their mixtures with IAPP or Aβ40 or Aβ42 during inhibition assays and their ThT binding was investigated in the same way (see chapter 3.2.10). ADPs were incubated at 33 µM in ThT assay buffer with 0.5 % HFIP (as controls in IAPP inhibition assays), at 16.5 µM in ThT assay buffer with 1 % HFIP (as controls in Aβ40 inhibition assays), or at 5 µM in 45 mM ammonium acetate (as controls in Aβ42 inhibition assays). Also TEM grids were prepared from such solutions to confirm results of the ThT binding assays.

Additionally, ACMs were incubated for 4 days at 100 µM in 1xb buffer containing 1 % HFIP to test for amyloidogenicity at higher concentrations. Aliquots of these incubations were used for TEM analysis. ThT binding was determined by mixing 30 µl-aliquots of each incubation with 170 µl of a 121 µM ThT solution (in aqueous 0.05 M glycine/NaOH,pH 8.5). Cytotoxic effects of ACMs incubated under these conditions were studied as described in chapter 3.2.13.

3.2.12 Cell culture for cell viability assays

Cultivating and plating RIN5fm cells

Based on previous protocols[123], the rat insulinoma cell line RIN5fm was cultured in RPMI 1640 medium (with phenol red) containing 10 % heat-inactivated fetal calf serum (FCS), 2 mM L-glutamine, 0.1 mM non-essential amino acids, 1 mM sodium pyruvate, 1 mg/ml glucose, and 0.1 mg/ ml penicillin/streptomycin, using T75 culture flasks (37 °C, humidified atmosphere with 5 % CO_2). For MTT reduction experiments, cells were plated in 96-well plates at a density of $6x10^5$ cells/ml (100 µl/well) and incubated for 24 h at 37 °C (humidified atmosphere with 5 % CO_2) before peptide samples were added.

Cultivating and plating PC-12 cells

The rat pheochromocytoma cell line PC-12 was cultured in RPMI 1640 medium (with phenol red) containing 10 % heat-inactivated horse serum, 5 % FCS, and 0.1 mg/ml penicillin/streptomycin, using poly-L-lysine-coated T75 culture flasks (37 °C, humidified atmosphere with 5 % CO_2), as described[80]. For MTT reduction experiments, cells were plated in poly-L-lysine-coated 96-well plates at a density of $1x10^5$ cells/ml (100 µl/well) and incubated for 24 h at 37 °C (humidified atmosphere with 5 % CO_2) before peptide samples were added.

3.2.13 MTT reduction assays

Cell viability of RIN5fm or PC-12 cells that were treated with IAPP, Aβ40, Aβ42, ADPs, or any mixtures of them, was determined by measuring the cellular reduction of 3-[4,5-dimethylthiazol-2-yl]-2,5-diphenyl-tetrazolium bromide (MTT) applying previously published protocols[19,80,123]. Of note, peptide solutions used for the MTT reduction assays were used in parallel also for the corresponding ThT binding assays (except for Aβ42-related experiments). After cells were incubated with peptides for 20-24 h (37 °C, humidified atmosphere with 5 % CO_2), 25 µl of MTT solution (5 mg/ml in 1x PBS; 137 mM NaCl, 2.7 mM KCl, 1.5 mM KH_2PO_4, 8.1 mM Na_2HPO_4*2 H_2O in ddH_2O, pH 7.2) were added to each well to a final concentration of 1 mg/ml. Thereafter, cells were further incubated for another 1.5 h (PC-12 cells) or 2 h (RIN5fm cells). Two different protocols were applied to read out the cellular MTT reduction for RIN5fm and PC-12 cells.

In case of RIN5fm cells, supernatants were taken off and cells were lysed by incubating them for 10 min (RT) with 0.04 N HCl in isopropanol (100 µl per well). After, solutions were mixed with 100 µl of ddH_2O and MTT reduction was quantified by measuring the absorbance at 570 nm using a 2030 Multilabel Reader VictorX3. In case of PC-12 cells, cells were lysed by addition of 70 µl lysis buffer (10 % SDS in 20 mM HCl, pH 4.5) per well. Following overnight incubation (RT, shaking 200 rpm), MTT reduction was quantified as for RIN5fm cells. Complete cell damage (0 % viability) was defined as the absorbance value measured in wells treated with 0.1 % Triton X-100. Full viability (100 % MTT reduction) was defined as the absorbance value obtained in wells containing medium alone. Cell viability (% of control) was calculated by:

$$\%\ MTT\ reduction = \frac{A_{sample} - A_{0.1\%\ Triton}}{A_{medium} - A_{0.1\%\ Triton}} * 100\% \quad (4)$$

For details on the preparation of incubations for different MTT reduction assay setups and dilutions/concentrations used to treat the cells see the following chapters. Assay buffers are specified in chapter 3.1.3.

Effects of ADPs on cell viability of PC-12 cells

Incubations were prepared in 1xb buffer containing 1 % HFIP using concentrations of 100 µM or 1 mM. Peptides were transferred from their HFIP stocks into Eppendorf tubes (on ice), HFIP was evaporated with air, and the peptides dissolved in the assay buffer. Following a 30 min-period of agitated incubation (200 rpm) at RT, solutions were further incubated at RT for 4 days. Serial dilutions of the peptide solutions were made in PC-12 cell culture medium. Dilutions were added to PC-12 cells (3-times to three different wells corresponds to three assays in technical triplicate), that were cultured and plated into 96-well plates as described in chapter 3.2.12, to the final concentrations indicated in the figures. Cell viabilities were assessed after 20-24 h by measuring the cellular reduction of MTT as described in the previous paragraph. Aliquots of the 100 µM peptide solutions were also used for TEM grid preparation.

Effects of inhibitor-coated fIAPP on cell viability of RIN5fm cells

IAPP (16.5 µM) was incubated for 7 days in ThT assay buffer containing 0.5 % HFIP at 20 °C to generate fibrils. For coating the IAPP fibril surface with inhibitor, the inhibitor was transferred from its HFIP stock to an Eppendorf tube (on ice), HFIP was evaporated with air, and the fibrils were mixed with the dried peptide to obtain a final inhibitor concentration of 33 µM (1:2). The solution was further incubated for 1 day at 20 °C. Solutions containing only fIAPP or inhibitor were examined in parallel as controls. Incubations were diluted with cell medium and applied onto RIN5fm cells (3-times to three different wells corresponds to three assays in technical triplicate), cultured and plated as described in chapter 3.2.12, to a final IAPP concentration of 500 nM. Cell viabilities were assessed after 20-24 h by measuring the cellular reduction of MTT as described in the top section of chapter 3.2.13.

Studies on the effect of ADPs on IAPP cytotoxicity, Eppendorf tube-system

Incubations to assess cytotoxic effects of IAPP, its mixture with ADPs, and of ADPs incubated in isolation as controls, were prepared as described for the corresponding ThT binding assays (see chapter 3.2.10, “Studies on the effect of ADPs on IAPP fibril formation, Eppendorf tube-system”). Preparation of the incubations in Eppendorf tubes was the main system used if not stated otherwise for specific assay applications (see next paragraph). After 24 h or 7 days of incubation, aliquots of the solutions were taken, diluted with RIN5fm cell medium, and applied onto RIN5fm cells at the final concentrations indicated in the figures (3-times to three different wells corresponds to three assays in technical triplicate). To define the IC_{50} values for the inhibitory effect of peptides towards the formation of cell damaging IAPP assemblies,

established protocols were used[109,111]. Briefly, IAPP (16.5 µM) was incubated with different molar ratios of the inhibitors as described for ThT binding studies (see chapter 3.2.10, “Studies on the effect of ADPs on IAPP fibril formation, Eppendorf tube-system”), and dilutions in cell medium were made as just described. IC_{50} values (24 h and 7 days) were calculated for a final IAPP concentration of 100 nM on the cells.RIN5fm cells were cultured and plated before into 96-well plates as described in chapter 3.2.12. Cell viabilities were determined after 20-24 h by measuring the cellular reduction of MTT as described in the top section of chapter 3.2.13.

Studies on the effect of ADPs on IAPP cytotoxicity, microtiter plate-system

To assess the effect of ADPs on IAPP cytotoxicity after long-term incubation (see Figure 4-24j), peptide solutions were prepared in black 96-well FluoroNunc MTPs as described for the corresponding ThT binding experiments in chapter 3.2.10 (“Studies on the effect of ADPs on IAPP fibril formation, microtiter plate-system”), but no ThT was added. After 14 days, incubations were gently mixed in the wells using the pipet, and 20 µl-aliquots were taken out for MTT reduction experiments. Dilutions were made with RIN5fm cell medium and applied onto RIN5fm cells at the concentrations indicated in the figure.

Studies on the effect of ADPs on Aβ40 cytotoxicity

Solutions of Aβ40, ADPs, or their mixture were prepared and incubated as described for the corresponding ThT binding studies. Aliquots of these solutions were taken after 72 h and 8 days of incubation, diluted into PC-12 cell culture medium, and added to PC-12 cells at the concentrations indicated in the figures.

Studies on the effect of ADPs on Aβ42 cytotoxicity

Solutions were prepared and incubated in black 96-well FluoroNunc MTPs as described for ThT binding assays (see chapter 3.2.10, “Studies on the effect of ADPs on Aβ42 fibril formation”) but did not contain ThT. Notably, solutions used for MTT reduction studies were incubated in parallel and on the same MTP as the corresponding solutions used for ThT binding studies. Aliquots of such incubations were also used for TEM analysis. After 6 days of aging, 170 µl-aliquots were taken out from the wells after gently mixing with the pipet. Dilutions were prepared with PC-12 cell medium and applied onto PC-12 cells. For calculating IC_{50} values for the inhibitory effect of peptides towards the formation of cytotoxic Aβ42 assemblies, Aβ42 (5 µM) was incubated with different molar ratios of the inhibitors as described for ThT binding studies (see chapter 3.2.10, “Studies on the effect of ADPs on Aβ42 fibril formation”), and dilutions in cell medium were made as just described. IC_{50} values were calculated for 6 days aged incubations and a final Aβ42 concentration of 1 µM on the cells.

3.2.14 Transmission Electron Microscopy (TEM)

Incubations of which samples were taken for TEM analysis were prepared under the buffer and incubation conditions described for the corresponding ThT binding and/or MTT reduction

assays in chapters 3.2.10, 3.2.11, and 3.2.13, and as indicated in the figures. 10-20 µl of solutions were applied after the incubation times indicated in the figures onto formvar carbon-coated copper grids and incubated for 3 min. When samples were taken from incubations prepared in ThT assay buffer or 45 mM ammonium acetate solution, grids were washed once (for few seconds) with ddH_2O before staining. When samples were taken from incubations prepared in 1xb, grids were not washed. Staining was performed for 1 min using aqueous 2% (w/v) uranyl acetate solution (in ddH_2O). Grid examination was done with a JEOL 1400 Plus electron microscope (120 kV).

3.2.15 Dot blot assays

Proteinase K digestion of fIAPP, IAPP/ACM heterofibrils and ACM-coated fIAPP

Proteinase K (PK) stock solutions were prepared in 50 mM TRIS/HCl pH 8.0 with 10 mM $CaCl_2$ at a concentration of 100 µg/ml. IAPP fibrils (16.5 µM, 7-8 days, 20 °C) and IAPP/ACM heterofibrils (IAPP + inhibitor 1:2, 7 days, 20 °C) were prepared in 1xb buffer. For generating inhibitor-coated IAPP fibrils, 6 days aged IAPP (16.5 µM, in 1xb, 20 °C) was mixed 1:2 with dried inhibitor (from HFIP) and incubated for one more day at 20 °C prior to digestion experiment. The PK digestion experiments were performed based on protocols by Ladiwala *et al.*[124] and Cho *et al.*[125]. After dotting the reference sample (100% undigested fibrils) onto a nitrocellulose membrane (0.2 µm), PK (final concentration: 0.5 µg/ml) was added to solutions by mixing 60 µl of the fIAPP or IAPP/ACM heterofibril incubations with 0.3 µl of the PK stock solution. Additional samples were taken and dotted after incubation for 0, 1, 3.5, 6, 24 and 30 h at 37 °C. The proteolytic reaction was quenched quickly as the membrane was dried after deposition. The IAPP amount per spot was 0.6 µg. Membranes were washed with TBS-T (20 mM Tris/HCl, 150 mM NaCl, and 0.05 % Tween-20, in ddH_2O, pH 7.3) and blocked overnight (10 °C) with 5 % milk in TBS-T. For detecting IAPP, the fibril-specific mouse anti-fIAPP antibody (Synaptic Systems, Cl. 91E7[29,98]) (1:500 in 5 % milk in TBS-T, 2 h, RT) was used. The peptide-component was detected using a polyclonal rabbit anti-Aβ40 antibody (1:2000 in 5 % milk in TBS-T, 2 h RT). Primary antibodies were combined with suitable peroxidase (POD)-coupled secondary antibodies (see Materials) to reveal samples using the Super Signal West Dura Extended Duration Substrate.

Proteinase K digestion of fAβ42 and Aβ42/ACM heterofibrils

Aβ42 fibrils (5 µM, 7 days) and related heterofibrils (Aβ42 + inhibitor 1:1, 7 days) were prepared and incubated in 45 mM ammonium acetate, pH 8.5, as described in chapter 3.2.10 (“Studies on the effect of ADPs on Aβ42 fibril formation”; w/o ThT). The PK digestion experiments were performed based on protocols by Ladiwala *et al.*[124] and Cho *et al.*[125]. Digestions were performed by mixing 200 µl of fAβ42 or Aβ42/ACM heterofibril solutions with 1 µl (final concentration: 0.5 µg/ml) or 0.2 µl (final concentration: 0.1 µg/ml) PK stock (100 µg/ml in 50 mM TRIS/HCl pH 8.0 with 10 mM $CaCl_2$). Solutions made as above but w/o PK were used as controls for 100% undigested fibrils. Besides the undigested control, samples (0.44 µg Aβ42) were taken and dotted after incubation for 0, 5, 10, 15, 30, 60, 120 and 420 min at 37 °C onto a nitrocellulose membrane (0.2 µm). Membranes were washed, blocked, and

developed as described for the corresponding IAPP-related assay in the previous paragraph. Aβ42-specific detection was assured by using the monoclonal mouse anti-Aβ(1-17) antibody (6E10) (1:2000 in 5 % milk in TBS-T, 2 h RT).

Confirmation of similar amounts taken out from solutions of IAPP and IAPP/inhibitor mixtures

To verify the presence of equal amounts of homo- and heteromeric fibrils in solutions of IAPP and its mixtures with ACMs, dot blot assays were used (see Figure 4-24b). Since such solutions were examined by various assays (ThT binding assay, MTT reduction assay, PK digestion assay etc.) for which different incubations buffers were used, 7 days aged IAPP (16.5 µM) and IAPP/ACM (1:2) incubations were prepared both in ThT assay buffer (0.5 % HFIP) and in 1xb buffer. Freshly prepared solutions (0 h) not containing fibrillar species according to TEM results were used as controls. Aliquots (20 µl total, containing 1.3 µg IAPP) were spotted onto 0.2 µm-nitrocellulose membranes. Membranes were washed, blocked, and developed as described in the previous paragraphs. IAPP in freshly prepared solutions (mainly monomeric or non-fibrillar) was revealed using a rabbit polyclonal anti-IAPP antibody (1:1000 in 5 % milk in TBS-T, 2 h RT). IAPP in 7 days aged solutions (mainly fibrils) was revealed using the fibril-specific mouse anti-fIAPP antibody (Synaptic Systems, Cl. 91E7[29,98]) (1:500 in 5 % milk in TBS-T, 2 h, RT).

Confirmation of fibril-specificity of the anti-fIAPP antibody (91E7)

IAPP (128 µM; 0.5 mg/ml) solutions were prepared as for the ThT binding assays (see chapter 3.2.10, “Studies on the effect of ADPs on IAPP fibril formation, Eppendorf tube-system”) in ThT assay buffer with 0.5 % HFIP and deposited onto nitrocellulose membranes (0.2 µm) either freshly (monomers) or after 4 days aging (fibrils). 1 µg and 10 µg-dots were made. Membranes were washed with TBS-T (20 mM Tris/HCl, 150 mM NaCl, and 0.05 % Tween-20, in ddH_2O, pH 7.3) and blocked for 3 h at RT with 5 % milk in TBS-T. Two identical membranes were either incubated with a rabbit polyclonal anti-IAPP antibody (1:1000) or with the fibril-specific mouse anti-fIAPP antibody (Synaptic Systems, Cl. 91E7[29,98]) (1:500) in 5 % milk in TBS-T (overnight, 10 °C). Primary antibodies were combined with suitable peroxidase (POD)-coupled secondary antibodies (see Materials) to reveal samples using the Super Signal West Dura Extended Duration Substrate, and binding strengths (spot intensities) obtained for the two different primary antibodies to monomeric and fibrillar IAPP were compared to assure fibril specificity of the anti-fIAPP antibody.

3.2.16 Cross-linking, NuPAGE, Western blot

A previously established assay system that was applied for characterisation of Aβ and IAPP homo- and hetero-assemblies was used for heterocomplex cross-linking studies in combination with NuPAGE and WB[80,109,111]. Experimental details are specified in the following sections.

Concentration dependence studies on the formation of homo- and hetero-assemblies in IAPP and its mixtures with ADPs

IAPP (30 µM) and IAPP/ADP-mixtures (1:1, 1:2, 1:4; as indicated in the figures) were made in 30 µl of 1xb buffer. Samples were cross-linked with 25 % aqueous glutaraldehyde (2 min, RT) either directly after their preparation or following 30 min or 7 days (as specified in the figures) of incubation at 20 °C and treated thereafter with a 2 M $NaBH_4$ solution (in 0.1 M NaOH, 20 min, RT). Following precipitation with chilled aqueous trichloroacetic acid (TCA, 10 %) for 30 min and centrifugation (10 min, 12000 g), pellets were dissolved in 45 µl reducing NuPAGE sample buffer (see chapter 3.1.4)., boiled (5 min, 95 °C) and 20 µl were subjected to NuPAGE gel electrophoresis in 4-12 % Bis-Tris gels with MES running buffer (see chapter 3.1.4). Equal amounts of IAPP (1.6 µg) were loaded in all lanes, peptide amounts per lane depended on the applied ratio (e. g. 1.1 µg Nle3-VF when a ratio of 1/1 was used). A molecular weight marker ranging from 3.5 to 260 kDa was electrophoresed in the same gels. A XCell II Blot Module blotting system was used for transferring peptides onto nitrocellulose membranes (0.2 µm) using transfer buffer (see chapter 3.1.4). Membranes were washed with TBS-T (20 mM Tris/HCl, 150 mM NaCl, and 0.05 % Tween-20, in ddH_2O, pH 7.3) and blocked overnight (10 °C) with 5 % milk in TBS-T. IAPP and IAPP-containing heterocomplexes were detected using a polyclonal rabbit anti-IAPP antibody (1:1000 in 5 % milk in TBS-T, 2 h RT) while peptides were detected using a polyclonal rabbit anti-Aβ40 antibody (1:2000 in 5 % milk in TBS-T, 2 h RT). All primary antibodies were combined with suitable peroxidase (POD)-coupled secondary antibodies to reveal complexes applying the Super Signal West Dura Extended Duration Substrate. Membranes were first developed with the anti-IAPP and corresponding secondary antibody to probe for IAPP and IAPP-containing heterocomplexes, and then stripped by incubating in stripping buffer (2 % SDS, 100 mM β-mercaptoethanol, 50 mM TRIS, pH 6.8) for 20 min at 60 °C and for 45 min at RT. After washing with TBS-T and blocking (overnight, 10 °C, 5 % milk in TBS-T), the same membranes were then re-developed with the anti-Aβ40 and corresponding secondary antibody to probe for ADPs and ADP-containing heterocomplexes.

Kinetic studies on the formation of homo- and hetero-assemblies in IAPP and its mixtures with ADPs

Solutions containing IAPP (30 µM), IAPP/ADP-mixtures (1:2) or ADPs alone (60 µM) were prepared in 1xb buffer. Freshly prepared and 24 h and 7 days aged (20 °C) incubations were cross-linked with 25 % aqueous glutaraldehyde. Further cross-linking procedure, NuPAGE, WB, and membrane development were done as described in the previous paragraph for concentration-dependence assays. For TEM analysis of species present in cross-linked samples of IAPP and IAPP/Nle3-VF mixtures, aliquots were taken from pellets dissolved in reducing NuPAGE sample buffer (see chapter 3.1.4) after the boiling step (5 min at 95 °C), and grids were prepared and analysed as described in chapter 3.2.14.

To compare IAPP homo-complex and IAPP/Nle3-VF heterocomplex composition in boiled and unboiled samples (see Figure 4-54), solutions were prepared, incubated, and cross-linked as described above. For unboiled samples, the pellet was resuspended in reducing NuPAGE

sample buffer (see chapter 3.1.4) and loaded on the gel without the previous boiling step. NuPAGE, WB, and membrane development were done as above.

3.2.17 Pulldown assays

Biotin-IAPP (16.5 µM) or its mixtures with Nle3-VF (1:2) were incubated in 200 µl 1xb buffer for 7 days at 20 °C. Pulldown assays were performed based on previous protocols[19,80,117] using streptavidin-coupled magnetic beads (Dynabeads M-280 Streptavidin) (20 µl). To control unspecific binding to the beads, incubations containing Nle3-VF alone (33 µM) were also included. Beads were washed with 1xPBS (137 mM NaCl, 2.7 mM KCl, 1.5 mM KH_2PO_4, 8.1 mM Na_2HPO_4*2 H_2O in ddH_2O, pH 7.2), TBS-T (20 mM Tris/HCl, 150 mM NaCl, and 0.05 % Tween-20, in ddH_2O, pH 7.3), and 0.25 % BSA in TBS-T, and blocked overnight with 0.25 % BSA in TBS-T (10 °C). Thereafter, beads were again washed with TBS-T and 1xPBS, pre-treated with assay buffer (1xb), and incubated after with the aged peptide solutions for 4 h (RT). Complexes that bound to the beads were isolated by magnetic affinity. Following washing with HNT buffer (25 mM HEPES, 0.1 M NaCl, and 0.5 % Triton X-100 in ddH_2O) and addition of reducing NuPAGE sample buffer (see chapter 3.1.4), beads were boiled (5 min, 95 °C) and supernatants containing complexes or peptides alone were subjected to NuPAGE electrophoresis in 4-12 % Bis-Tris gels with MES running buffer as described before for cross-linking experiments (see chapter 3.2.16). Equal amounts of peptide were loaded in each lane (100 % input: 11.2 µg Biotin-IAPP, 14.5 µg Nle3-VF). Loaded amounts for Nle3-VF control (freshly dissolved peptide without bead-incubation) was 1.8 µg (12.5 %). Peptide transfer onto nitrocellulose membranes and antibody development was done as for cross-linking assays (see chapter 3.2.16) using a polyclonal rabbit anti-IAPP antibody (1:1000 in 5 % milk in TBS-T, 2 h RT) and a polyclonal rabbit anti-Aβ40 antibody (1:2000 in 5 % milk in TBS-T, 2 h RT). Negligible non-specific binding to beads was found for Nle3-VF under the applied conditions.

3.2.18 Size exclusion chromatography (SEC) of IAPP/ADP heterocomplexes

Heterocomplex formation of IAPP and Nle3-VF or VGS-VF was studied based on earlier protocols by Yan *et al.*[19]. SEC was performed at RT as follows: Incubations of IAPP (16.5 µM) or mixtures with peptides (1:2; from HFIP stocks) were prepared in 200 µl ThT assays buffer containing 0.5 % HFIP, aged (20 °C) for the specified time (see figures) and centrifuged after for 1 min at 20000 g. Supernatants (200 µl, equates to 12.9 µg IAPP) were loaded onto a Superdex 75 10/300 GL column and chromatographed at 0.5 ml/min (eluent: ThT-buffer w/o HFIP). Chromatograms were recorded at 214 nm. The lowest value (in the depicted time frame between 10-60 min) was set to 0 and chromatograms were normalised after to the highest absorbance value. The Superdex column was calibrated using the elution volumes from proteins of known molecular weight (γ-globulin 670 kDa, ovalbumin 158 kDa, myoglobulin 44 kDa) in combination with the elution volumes observed for monomeric IAPP (3.9 kDa) and monomeric Nle3-VF (2.8 kDa) (see also chapter 4.5.2.2).

3.2.19 Immunogold-staining-TEM and gold particle counting

Solutions of IAPP/Nle3-VF heterofibrils for analysis via immunogold staining were prepared as described in chapter 3.2.10 ("Studies on the effect of ADPs on IAPP fibril formation, Eppendorf tube-system") and aged for the indicated time (see figures). Inhibitor-coated fIAPP was generated by incubating IAPP (16.5 µM) for 24 h in ThT assay buffer with 0.5 % HFIP (20 °C) and subsequent mixing with dried Nle3-VF (33 µM; 1:2; co-incubation for 4 days at 20 °C). 20 µl of the aged solutions were applied onto formvar carbon-coated copper grids for 3 min. After drying, the procedure was repeated once more. Immunogold-staining was performed based on previous protocols[84] applied for IAPP/Aβ hetero-assemblies as follows: Grids were washed with ddH_2O and 1xPBS (137 mM NaCl, 2.7 mM KCl, 1.5 mM KH_2PO_4, 8.1 mM Na_2HPO_4*2 H_2O in ddH_2O, pH 7.2) (1 min), blocked with 0.1 % BSA in 1xPBS for 15 min at RT and washed after again with 1xPBS (3x 1 min). For detecting fibrillar IAPP, a fibril-specific mouse anti-fIAPP antibody (Synaptic Systems, Cl. 91E7[29,98]) was used. ADPs were revealed by a rabbit anti-Aβ40 antibody. A solution containing one or both primary antibodies, depending on the underlying question, was deposited onto the grid and incubated for 20 min (RT, antibodies 1:10 in 0.1 % BSA in 1xPBS). Following washing with 1xPBS (3x 1 min), secondary antibodies (goat anti-rabbit gold-conjugate (10 nm) and goat anti-mouse gold-conjugate (5 nm)) were applied (1:10 in 0.1 % BSA in 1xPBS) and incubated in the same way. Finally, grids were washed with 1xPBS (3x 1 min) and ddH_2O (2x 1 min) and negatively stained using aqueous 2 % (w/v) uranyl acetate solution (1 min). Examination was performed on a JEOL 1400 Plus electron microscope at 120 kV. To quantify IAPP and Nle3-VF contents of fibrils, 5 and 10 nm gold particles were counted. "Antibody reactivity" is expressed as % of total number of gold particles bound. Significance was analysed by one-way ANOVA and Bonferroni.

3.2.20 2-Photon-Microscopy (2-PM) and FLIM imaging

Preparation of incubations

The different applied protocols are described in the following sections:

1) For 2-PM and FLIM-FRET analysis, IAPP homofibres and IAPP/inhibitor hetero-nanofibers were generated by using the synthetic N-terminal fluorescently labelled peptide analogues TAMRA-IAPP and Fluos-inhibitor (see chapters 3.2.5 and 4.2). Solutions of TAMRA-IAPP (16.5 µM) or TAMRA-IAPP/Fluos-inhibitor mixtures (1:2, from HFIP stocks) were made in 1xb buffer and incubated for 6-7 days (20 °C).
2) To follow the IAPP/Nle3-VF heterocomplex→hetero-nanofiber transition via 2-PM, the synthetic N-terminal fluorescently labelled peptide analogues TAMRA-IAPP and Fluos-Nle3-VF or Atto647N-Nle3-VF (see chapter 4.2) were used (HFIP stocks). Incubations were made in 1xb buffer and incubated for 0-48 h (20 °C) and contained mixtures of unlabelled (90 % of total) and labelled (10 % of total) peptides. Solutions of IAPP/Nle3-VF mixtures thus contained 14.85 µM IAPP, 1.65 µM TAMRA-IAPP, 29.7 µM Nle3-VF, and 3.3 µM Fluos-Nle3-VF or Atto647N-Nle3-VF, thereby maintaining a total IAPP concentration of 16.5 µM and a total inhibitor concentration of 33 µM as used in inhibition experiments and TEM studies.

3) For investigating the appearance of peptide-coated IAPP nanofibers via 2-PM, labelled nanofibers were generated by incubating TAMRA-IAPP (16.5 µM, from HFIP stock) for 7 days in 1xb (20 °C) (fibrillar species confirmed by TEM, see Figure 7-49a in Appendix). Thereafter, these nanofibers were mixed with dried Fluos-Nle3-VF or Fluos-VGS-VF (33 µM; 1:2; from HFIP stocks) and co-incubated for 1 day (20 °C) (see Figure 4-47c). In another attempt, labelled nanofibers were made from a mixed solution containing both TAMRA-labelled IAPP (1.65 µM; 10 %) and unlabelled IAPP (14.85 µM; 90 %), which was incubated for 2 days at 20 °C (in 1xb). These nanofibers were then added to a dried mixture of 3.3 µM Atto647N-Nle3-VF and 29.7 µM Nle3-VF and co-incubated for 1 day (20 °C) (see Figure 4-47d).
4) To follow the effect of monomeric/pre-fibrillar IAPP species on hetero-nanofiber formation via 2-PM and FLIM-FRET analysis, mixtures (from HFIP stocks) of Fluos-peptide (33 µM) and TAMRA-IAPP (1.65 µM; 5 %) were made in 1xb and incubated at 20 °C. Aliquots for sample preparation were taken after 48 h and 7 days of aging.
5) To follow the effect of fibrillar IAPP species on hetero-nanofiber formation via 2-PM and FLIM-FRET analysis, labelled IAPP nanofibers were made by incubating TAMRA-IAPP (16.5 µM, from HFIP stock) in 1xb for 5 days (20 °C). Freshly prepared Fluos-peptide solutions (33 µM, in 1xb) were mixed with 3.3 µM TAMRA-IAPP nanofibers (10 %) and incubated at 20 °C for 0-48 h.
6) Aβ42 homo-nanofibres and Aβ42/inhibitor hetero-nanofibers were made for 2-PM and FLIM-FRET analysis by using the N-terminal fluorescently labelled peptide analogues TAMRA-Aβ42 (purchased) and Fluos-inhibitor (synthetic) (stocks in HFIP). Solutions were prepared and incubated (4-6 days) as described for ThT binding studies (see chapter 3.2.10, “Studies on the effect of ADPs on Aβ42 fibril formation”) (w/o ThT) using an Aβ42/inhibitor ratio of 1:2 and were made with mixtures of labelled (50 % of total) and unlabelled peptides (50 % of total). Aβ42/inhibitor mixtures to generate hetero-nanofibers thus contained 2.5 µM Aβ42, 2.5 µM TAMRA-Aβ42, 5 µM unlabelled inhibitor, and 5 µM Fluos-inhibitor. Such mixtures are indicated in the text by “(TAMRA-)Aβ42/(Fluos-)inhibitor”, peptides alone as “(TAMRA-)Aβ42” or “(Fluos-)inhibitor”. For unlabelled Aβ42 its stock obtained from SEC was used (see chapter 3.2.6), while TAMRA-Aβ42 and the Fluos-peptide stocks were prepared in HFIP.
7) For mixing inhibitors with aged Aβ42 solutions, (TAMRA-)Aβ42 was prepared as described in the previous paragraph and aged for 1.75 h. The aged solution was then added to a dried mixture of 5 µM Fluos-inhibitor and 5 µM unlabelled inhibitor (from HFIP stocks).
8) For studies on fIAPP-mediated cross-seeding of Aβ42, the following labelled peptides were used: TAMRA-IAPP (synthetic), HiLyte647-Aβ42 (purchased), and Fluos-Nle3-VF (stocks in HFIP). Labelled IAPP nanofibers were made by incubating TAMRA-IAPP (128 µM) for 6 days in ThT assay buffer with 0.5 % HFIP (20 °C). Solutions were prepared and incubated (1.5 h) as described for ThT binding studies (see chapter 3.2.10, “Studies involving seeded Aβ42”; w/o ThT) using 10 µM Aβ42 and an Aβ42/inhibitor ratio of 1:2 and were made with mixtures of labelled (50 % of total) and unlabelled (50 % of total) Aβ42 and inhibitor. For instance, the Aβ42 alone solution thus contained 5 µM Aβ42 and 5 µM HiLyte647-Aβ42. The Aβ42/inhibitor mixture contained 5 µM Aβ42, 5 µM HiLyte647-Aβ42,

10 µM Nle3-VF, and 10 µM Fluos-Nle3-VF. TAMRA-IAPP seeds were added to a final concentration of 2 µM (20 %). For assay setup 1 (heterocomplex formation before addition of seeds), TAMRA-IAPP seeds were added after the Aβ42/ACM mixture was made; for assay setup 2 (coating of seed surface before addition to Aβ42), TAMRA-IAPP seeds were first added to a Fluos-inhibitor/unlabelled inhibitor solution (50 %/50 % of total) and subsequently mixed with Aβ42. For details on the preparation steps in assay setup 1 and 2 consider also the procedure for the corresponding ThT binding studies (chapter 3.2.10). For unlabelled Aβ42 its stock obtained from SEC was used (see chapter 3.2.6), while all other used peptide stocks were prepared in HFIP.

Slide preparation and imaging

30-40 µl aliquots of the above-mentioned solutions were used in case of IAPP-related samples to prepare slides for 2-PM and FLIM-FRET analysis. 50-100 µl aliquots were used for Aβ42-related samples. Solutions were applied onto SuperFrost Plus adhesion slides, air-dried, washed with ddH_2O (Aβ42-related studies only) and embedded with Prolong Diamond Antifade Mountant (Thermo Fisher) using a high precision cover glass (#1.5). For FLIM-FRET analysis Aβ42/Nle3-VF hetero-nanofibers, the solution was centrifuged (20 min, 20000 g) after incubation and the resuspended pellet (in 1xb) was spotted onto the adhesion slide to avoid disturbance of the measurement by the ammonium acetate salt of the incubation buffer.

Imaging was performed in Prof. Bernhagen's group (Vascular Biology) at the Institute for Stroke and Dementia Research under the supervision of Omar El Bounkari. Samples were imaged on a Leica TCS SP8 DIVE multispectral two (multi)-photon microscope with 4TUNE NDD detection module, LIGHTNING adaptive deconvolution, and fast lifetime contrast (FALCON) modality, equipped with extended IR spectrum tunable laser (680-1300 nm) (New InSight® X3™, Spectra-Physics) and fixed IR laser (1045 nm), advanced Vario Beam Expander (VBE), ultra-high-speed resonance scanner (8kHz), HC PL IRAPO 25x/1.0 WATER objective, and FLIM-FRET modality[126]. Images were collected in a sequential scanning mode using hybrid diode detectors (HyD-RLD, reflected light detection) (TAMRA: excitation 1100 nm/ emission 560-630 nm; Fluos: excitation 920 nm/ emission 480-550 nm; HiLyte647: excitation 1280 nm/ emission 635-715 nm). Images were handled using LAS-X software package. Deconvolutions were performed using Huygens Professional or the Leica Lightning application.

FLIM-FRET measurements

For fluorescence lifetime imaging (FLIM), up to 1000 photons per pixel were captured in a time-correlated single photon counting (TCSPC) mode. Fluorescence decay data was fit using Leica FALCON software applying multi-exponential models. The quality of the fit was assessed by randomly distributed residuals and by low Chi-square values. The number (n) of components used for the fittings was manually fixed to a value (n=2-4) that minimised the Chi-square statistic. In control experiments, the fluorescence lifetime of the donor fluorescent molecule (prepared under the same conditions as the corresponding mixture; by Beatrice Dalla Volta) in

absence of acceptor was acquired similarly. A multi-exponential model had to be applied as well to minimise the Chi-square statistic. As the donor fluorescent molecule (Fluos) showed multiexponential decay curves both in presence and absence of the acceptor fluorescent molecule (TAMRA), “amplitude-weighted average lifetime” (τAvAmp) was used to calculate FLIM-FRET efficiency. This lifetime value was extracted by the Leica FALCON software after fitting of the decay curves and is specified as $\tau AvAmp = \frac{\sum A_i * \tau_i}{\sum A_i}$ (A: amplitude, τ: lifetime). By comparing the amplitude weighted average lifetimes of the unquenched donor with the donor undergoing FRET, the software calculated the FLIM-FRET efficiency according to $FRET\ Eff\ (E) = 1 - \frac{\tau AvAmp}{\tau D}$ (with τAvAmp: amplitude-weighted average lifetime of the quenched donor (undergoing FRET); τD, amplitude-weighted average lifetime of the unquenched donor). To compare decay curves and lifetime distributions measured for the donor in presence and absence of acceptor, data were normalised to the highest obtained fluorescence intensity or occurrence value.

3.2.21 Confocal laser scanning microscopy (CLSM) and stimulated emission depletion (STED) imaging

Incubations of IAPP and IAPP/Nle3-VF mixtures contained 10 % N-terminal fluorescently labelled analogues (TAMRA-IAPP and Atto647N-Nle3-VF; see chapters 3.2.5 and 4.2), were made in 1xb buffer, and aged for 7 days (20 °C). Labelled and unlabelled peptides were mixed from their HFIP stocks (on ice), HFIP was evaporated with air, and peptides were dissolved in buffer. The total IAPP content was 16.5 µM, the total Nle3-VF content was 33 µM (1:2). 30-40 µl aliquots of these solutions were applied onto SuperFrost Plus adhesion slides, air-dried, and embedded with Prolong Diamond Antifade Mountant using a high precision cover glass (#1.5) as for 2-PM studies.

Stimulated emission depletion imaging (STED) was performed at the Institute for Cardiovascular Prevention under the supervision of Remco T.A. Megens. For 3D STED, samples were imaged on a Leica SP8 STED 3X microscope (Leica, Germany) equipped with a HC PL APO 93x/1.30 GLYC CORR STED objective. A tunable white light laser source was used to excite fluorophores. Depletion was performed at 660 nm and 775 nm for TAMRA and Atto647N, respectively. Depletion power and time-gated detection of the excited light were chosen to minimize damage to the sample while optimizing xy- and z-resolutions. Images were collected in a sequential scanning mode using hybrid diode detectors to maximize signal collection while minimizing cross-talk between the channels (TAMRA: excitation 552 nm/ emission 557-645 nm; Atto647N: excitation 646 nm/ emission 651-700 nm). 3D reconstructions and fibril measurements were performed using LAS-X software package (v1.2) and datasets were deconvolved using Leica’s Lightning application.

3.2.22 Thermostability of fIAPP and IAPP/ACM heterofibrils

IAPP homofibrils (16.5 µM) and IAPP/Nle3-VF heterofibrils (16.5 µM/ 33 µM; 1:2) were prepared as described for ThT binding studies (see chapter 3.2.10, “Studies on the effect of ADPs on IAPP fibril formation, Eppendorf tube-system”) and incubated for 7 days (20 °C). Fibrils formed in mixtures of IAPP and VGS-VF (1:2) were prepared as controls. TEM grids

were loaded with 2x 20 µl of solutions. Incubations were then boiled for 5 min (95 °C, water bath) and additional TEM grids were made (2x 20 µl loaded). Grids were stained and analysed as described in chapter 3.2.14. ThT binding of fIAPP, heterofibrils, and fibrils formed in IAPP/VGS-VF mixtures was assessed before and after boiling by mixing aliquots (30 µl) of boiled and unboiled incubations with 170 µl of 20 µM ThT (in aqueous 0.05 M glycine/NaOH in ddH20, pH 8.5), corresponding to the standard protocol described for ThT binding studies (see chapter 3.2.10). Buffer values were subtracted from all measurements.

3.2.23 Thermostability of fAβ42 and Aβ42/ACM heterofibrils

For assessing the thermostability of Aβ42 homofibrils and Aβ42/Nle3-VF heterofibrils, two slightly different experiments were performed. In the first experiment, fAβ42 and Aβ42/Nle3-VF heterofibrils were prepared as described in chapter 3.2.10 (“Studies on the effect of ADPs on Aβ42 fibril formation”) (5 µM Aβ42, 1:1 mixture with Nle3-VF, 10 µM ThT, 6 days aged). 200 µl fibril solutions were diluted 1:1 with aqueous 45 mM ammonium acetate (pH 8.5) and transferred into fluorescence cuvettes. ThT fluorescence was measured between 460 and 700 nm (1 nm intervals, 1 s response time) after excitation at 450 nm using a Jasco FP-6500 fluorescence spectrophotometer. To evaluate the experiment, the fluorescence emission obtained at 486 nm was used. After, fibril solutions were boiled inside the cuvettes for 5, 10, or 15 min at 95 °C and ThT fluorescence was determined again. In the second experiment, fibril solutions were made as above but w/o ThT. To measure ThT fluorescence of unboiled samples, 200 µl of fibril solution were transferred to a fluorescence cuvette and mixed with 22.2 µl of 100 µM ThT in ddH_2O to obtain a ThT concentration of 10 µM as in experiment 1. This solution was then diluted with aqueous 45 mM ammonium acetate (pH 8.5) as before and ThT fluorescence was measured. To measure ThT fluorescence of boiled samples, 200 µl of fibril solution were transferred to a fluorescence cuvette and boiled at 95 °C (5-15 min). Solutions were cooled on ice for 3 min before ThT and aqueous 45 mM ammonium acetate (pH 8.5) were added as before for unboiled samples.

Incubations for TEM analysis were prepared in parallel to incubations used in the fluorescence assay as described above (w/o ThT). Aliquots of unboiled samples were taken directly from the MTP and loaded onto TEM grids (3x 20 µl). Boiled samples were generated by transferring the fibril solutions to Eppendorf tubes and boiling them for 5-15 min at 95 °C. After boiling, 3x 20 µl were loaded onto TEM grids. For grid staining and analysis see chapter 3.2.14.

3.2.24 HPLC, DB, and ThT binding analyses to confirm that fibrils are main species in aged IAPP/inhibitor mixtures

In a first step, a dot blot assay was performed to confirm the presence of fibrillar species in pellet fractions of aged solutions of IAPP and its mixture with inhibitor (see Figure 4-25a). For this, solutions of IAPP (16.5 µM) or its mixture with Nle3-VF (1:2) were made in 1xb aged for 7 days at 20 °C to generate fibrils. Fibril solutions were centrifuged for 5 min at 7000 rpm and supernatants were discarded. Pellets were re-dissolved in 1xb buffer and dotted onto 0.2 µm nitrocellulose membranes (10 µg). Membranes were washed with TBS-T (20 mM Tris/HCl, 150 mM NaCl, and 0.05 % Tween-20, in ddH_2O, pH 7.3) and blocked overnight (10 °C) with

5 % milk in TBS-T. Two identical membranes were either incubated with a rabbit polyclonal anti-IAPP antibody (1:1000) to detect monomeric/prefibrillar IAPP or with the fibril-specific mouse anti-fIAPP antibody (Synaptic Systems, Cl. 91E7[29,98]) (1:500) (to detect fibrils) in 5 % milk in TBS-T (2 h, RT). Primary antibodies were combined with suitable peroxidase (POD)-coupled secondary antibodies (see Materials) to reveal samples using the Super Signal West Dura Extended Duration Substrate. Detection by the fibril-specific anti-fIAPP antibody but not by the anti-IAPP antibody confirmed the presence of fibrils as main species in pellet fractions of both IAPP and IAPP/Nle3-VF solutions.

In a second step, solutions (300 µl; in ThT assay buffer with 0.5 % HFIP) containing IAPP (16.5 µM) or its mixture with Nle3-VF (1:2) were analysed via HPLC either directly after their preparation (0 h) or after 7 days of aging at 20 °C. For this, solutions were first centrifuged for 10 min at 14000 rpm (20000 x g) and then SN fractions were taken off. In a previous trial in which ThT fluorescence of pellet and SN fractions of aged IAPP were measured, it was confirmed that IAPP fibrils are completely precipitated after this centrifugation step: an aliquot of IAPP fibrils (16.5 µM, in ThT assay buffer with 0.5 % HFIP, aged at 20 °C, 14 days) was taken and centrifuged for 10 min at 14000 rpm (20000 x g). The pellet was resuspended in 1xb buffer and resuspended pellet and SN were mixed with 200 µM ThT (in aqueous 0.05 M glycine/NaOH, pH 8.5). ThT fluorescence was measured with a 2030 Multilabel Reader VictorX3 at 486 nm after excitation at 450 nm. Measurements were compared to a non-centrifuged sample and the buffer control and confirmed precipitation of IAPP fibrils (see Figure 4-25b).

Before injection into the HPLC, SN fractions of aged IAPP and IAPP/Nle3-VF solutions (see above) were mixed with 50 µl TFA and corresponding pellet fractions were dissolved in 50 µl TFA and 450 µl 80 % B. Samples were chromatographed on a Reprosil Gold 200 C18 column using the elution program “schnellAβ” (see chapter 3.2.2). Soluble IAPP contents were quantified by peak areas (see Figure 4-25c). The sum of peak areas of IAPP SN and IAPP pellet at 0 h was considered as 100 %.

3.2.25 BCA, DB, and ThT binding analyses to confirm that fibrils are main species in aged Aβ42/inhibitor mixtures

Solutions containing Aβ42 fibrils or Aβ42/Nle3-VF heterofibrils were prepared in 45 mM ammonium acetate (pH 8.5) at 37 °C as described in chapter 3.2.10 (“Studies on the effect of ADPs on Aβ42 fibril formation”) (w/o ThT) using 5 µM Aβ42. Nle3-VF was applied with 2-fold excess (10 µM). After 8 days, solutions were transferred to Eppendorf tubes, centrifuged (20 min, 20000 x g) and supernatants were removed. Supernatants were analysed via DB, peptide amounts in pellets were quantified via BCA (see next paragraphs). In a preliminary trial it was confirmed that Aβ42 fibrils are completely precipitated after this centrifugation step. This experiment was done as follows: An aged Aβ42-solution (5 µM, 6 days aged, 37 °C, in 45 mM ammonium acetate, pH 8.5, w/o ThT) was transferred into an Eppendorf tube and centrifuged (20 min, 20000 x g). SN and pellet fractions were separated. ThT (100 µM in ddH_2O) was added to SN to a final concentration of 10 µM. The pellet fraction was resuspended in 45 mM ammonium acetate, pH 8.5, containing 10 µM ThT. ThT fluorescence

was measured with a 2030 Multilabel Reader VictorX3 at 486 nm after excitation at 450 nm. Measurements were compared to a freshly prepared Aβ42-solution (5 µM, in 45 mM ammonium acetate, pH 8.5) containing 10 µM ThT (w/o centrifugation). ThT fluorescence was only observed for the pellet fraction, confirming that Aβ42 fibrils fully precipitated (see Figure 4-76a).

For DB analysis of the SN, solutions were spotted stepwise onto 0.2 µm nitrocellulose membranes (4.5 µg). Membranes were washed with TBS-T (20 mM Tris/HCl, 150 mM NaCl, and 0.05 % Tween-20, in ddH_2O, pH 7.3) and blocked overnight (10 °C) with 5 % milk in TBS-T. Selective detection of Aβ42 was carried out using the mouse anti-Aβ(1-17) antibody (6E10) (1:2000 in 5 % milk in TBS-T, 2 h RT). The primary antibody was combined with a suitable peroxidase (POD)-coupled secondary antibody (see Materials) to reveal samples using the Super Signal West Dura Extended Duration Substrate. As control, a freshly prepared solution of Aβ42 (5 µM, w/o centrifugation) was spotted and analysed in parallel (see Figure 4-76b).

For quantifying peptide amounts in insoluble fractions (pellets) of Aβ42 fibril or Aβ42/Nle3-VF heterofibril solutions via BCA, remaining pellets from the dot blot assay were used. Pellets were resuspended in 200 µl of 45 mM ammonium acetate (pH 8.5) and mixed with 150 µl of the BCA kit solution (25/24/1-mixture of reagents A, B, and C; Micro BCA Protein Assay Kit). Mixtures were incubated at 37 °C for 3 h. Samples were then cooled for 3-5 min at -20 °C and UV absorbance at 570 nm was measured thereafter. Results are presented as raw data, after subtracting the buffer value, and as peptide amounts calculated relatively to the respective control sample (see Figure 4-76c-e). As controls, freshly prepared solutions of Aβ42 (5 µM) or an Aβ42/Nle3-VF mixture (1:2) were used (w/o centrifugation).

3.2.26 Peptide arrays

Applying previously published protocols[127], peptides were made by stepwise SPOT synthesis on modified cellulose disks using an Intavis MultiPep RSi/CelluSpot Array system. Planning, preparation, and performance of the SPOT synthesis was carried out together with Valentina Armiento, Kathleen Hille, and Christos Kontos. After finishing the stepwise SPOT synthesis, work-up and microarray development were performed by Christine Krammer (Prof. J. Bernhagen group).

Following SPOT synthesis, work-up was performed applying protocols of Intavis: Side chains were deprotected by incubating the peptide-cellulose disks for 2 h (RT) in a cleavage solution composed of TFA/DCM/TIS/ddH_2O (80/12/3/5 v/v). To dissolve cellulose disks and precipitate cellulose-peptide conjugates disks were first incubated for 16 h (RT) in a solvation solution containing TFA, trifluoromethanesulfonic acid (TFSMA), TIS, and ddH_2O (88.5/4/2.5/5 v/v). Then, the solution was mixed with cold tert-butyl-methylether and cooled at -20 °C for 2 h. Precipitated peptide-cellulose conjugates were spun down by centrifuging at 1100 x g for 20 min (4 °C), washed with tert-butyl-methylether, and centrifuged again (1100 x g for 20 min, 4 °C). After evaporation of the ether, conjugates were dissolved in DMSO. Prior to their deposition onto coated glass slides (CelluSpot slides) using an Intavis Slide Spotting Robot, peptide-conjugate solutions were diluted 1:1 with spotting solution (1x saline sodium citrate (SSC) buffer diluted 1:2 with DMSO). The SSC buffer stock (20x) consists of 3 M NaCl and

0.3 M Na3 citrate·2H_2O (pH 7.0) and was diluted 1:20 with ddH_2O before usage. One microarray is composed of two identical subarrays each carrying 383 different peptide sequences spotted in duplicates. For data analysis, one subarray was defined as one separate assay, meaning that the development of one microarray with biotinylated peptides (see below) yields results of two assays (Figure 3-5).

Glass microarrays were blocked (4 h, RT) in 50 mM Tris-buffered saline containing 0.1 % Tween-20 and 1 % BSA and washed after with TBS containing 0.1% Tween 20, as described[127]. Lyophilised biotinylated peptides were dissolved in HFIP, diluted to 0.5 µM or 3 µM with blocking solution (final HFIP amount: 0.6 %), and incubated with the microarrays overnight at 4 °C. Bound peptides were detected by with horse-radish peroxidase (HRP)-conjugated streptavidin in blocking buffer (1:5000, 2 h, RT). Chemiluminescent signals were measured by a LI-COR Odyssey® Fc imager. Spot intensities were corrected for spot-specific background signal. Influence of unspecific binding of the biotinylated peptides to the glass microarray was eliminated by subtracting chemiluminescent signals measured for a control spot where no peptide-cellulose conjugate is bound to. Spot intensities were normalised to the highest intensity value measured within a group of related peptide segments (example of a group: all IAPP decamer segments). Microarray raw data is shown in Figure 7-62 to Figure 7-64 in the Appendix.

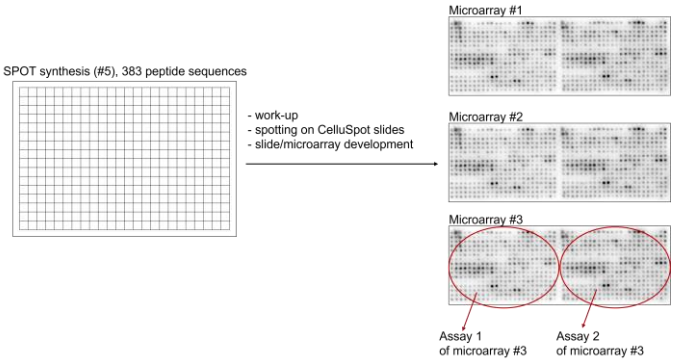

Figure 3-5: Definition of "1 assay" for peptide microarrays. Peptides were synthesised on modified cellulose disk via SPOT synthesis (synthesis #5 in my case). After work-up of the disks, peptides were spotted onto CelluSpot slides. One slide (= one microarray) thereby contains a duplicate of spots (left and right "window"). Thus, incubation of one microarray with biotinylated peptide and subsequent development leads to results from two assays.

3.2.27 Light microscopy imaging of IAPP/ACM heterofibrils

Mixtures of IAPP (16.5 µM) and Nle3-VF (33 µM; 1:2) to generate heterofibrils were made as for inhibition assays (see chapter 3.2.10, "Studies on the effect of ADPs on IAPP fibril formation, Eppendorf tube-system") in ThT assay buffer (0.5 % HFIP). After 7 days of aging (20 °C), 20 µl of the fibril solution were pipetted onto a SuperFrost Plus adhesion microscope slide, air-dried, and washed once with 50 µl ddH2O. The sample was inspected using an Olympus CXK41 microscope.

3.2.28 Measurement of fibril lengths and widths from TEM images using ImageJ

Images acquired during TEM analyses were opened in ImageJ (.tif-files) and the correct scale was assigned to them for defining the number of pixels making up a certain distance (e. g. for a magnification of 30000x the pixel size in nm is 0.553, meaning that 180.8 pixels make up a distance of 100 nm). Using the ImageJ line tool, lines were drawn along a fibril to measure its length and lines were drawn perpendicularly to the fibril axis from fibril edge to edge to measure its width. Lengths and widths values were displayed by using the ImageJ analysis tool “measure”.

3.2.29 Measurement of nanofiber widths from 2-PM, CLSM and STED images using LAS-X

Images acquired during fluorescence microscopy analyses were opened using Leica’s LAS-X software (.lif-files). For measuring nanofiber widths, the LAS-X line tool was used and lines were drawn perpendicularly to the fibril axis. Nanofiber widths were determined from the resulting intensity plots for the different channels by measuring the widths of fluorescence signal intensities at half-maximum height (see Figure 3-6). Measurements were performed in the same way for all the different fluorescence imaging techniques (2-PM, CLSM, STED).

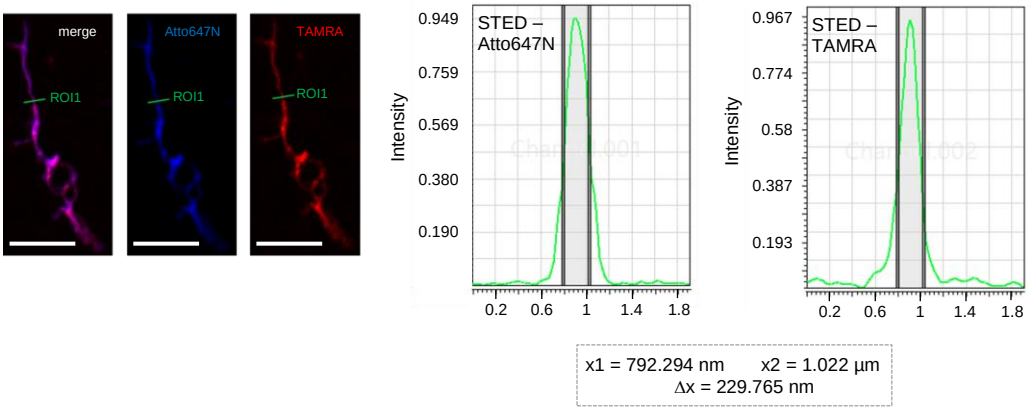

Figure 3-6: Exemplary measurement of nanofiber width from fluorescence intensity plots using LAS-X. Exemplary measurement of TAMRA-IAPP/Atto647N-Nle3-VF hetero-nanofiber thickness from STED images are shown. Scale bar: 5 µm. Green line highlights region of interest (ROI) chosen for measurement. Intensity plots obtained after using the line tool in LAS-X of both channels are depicted on the right. Widths are measured at half-maximum of the intensity peak height (grey area). Δx: Hetero-nanofiber width.

3.2.30 Construction of the proposed IAPP/Nle3-VF heterofibril model using Chimera and the SwissSidechain database

For constructing hypothetical IAPP/Nle3-VF heterofibril models shown in chapter 5.3, the Chimera software[128] and the SwissSidechain database[129] were used and published structures of IAPP and Aβ40(42) were applied. First, two artificial Nle3-VF constructs were generated based on the Aβ40(42) model structures PDB 5OQV[56] (Aβ42) and 2LMQ[55] (Aβ40) by deleting residues 1-14 and 41-42 or residues 11-14, respectively, and replacing residues V24, G25,

S26 and M35 by norleucine. With the help of the SwissSidechain database most probable norleucine rotamers were inserted that did not clash with surrounding atoms in the existing Aβ40(42) structure (no energy minimisation of the structure was done). Based on results from peptide arrays (see chapter 4.9), both Nle3-VF model constructs were manually overlayed with the IAPP fibril structure (PDB 6Y1A[33]) to match IAPP's NFLVH-segment with Nle3-VF's NKGAII-segment. Parallel and antiparallel alignment directions were tried. From the parallel overlays, two hypothetical IAPP/Nle3-VF heterofibrils were built, one representing a heterofibril co-assembled by mixed protofilaments consisting of both peptides (A; see Figure 5-7a) and the other representing a heterofibril built up by two self-sorted protofilaments forming a joint lateral assembly (B; see Figure 5-7b). For (A), the Nle3-VF construct generated from the Aβ42 fibril structure was inserted into the IAPP fibril structure by deleting an IAPP molecule in every second layer and manually replacing it by an Nle3-VF molecule. For (B), the Nle3-VF construct generated from the Aβ40 fibril structure was manually placed strand-by-strand next to the IAPP fibril structure to match Nle3-VF's NKGAII-region with IAPP's NFLVH-region.

4 Results

4.1 Design strategy of Aβ(15-40) analogues

Aβ-derived peptides (ADPs) as potential inhibitors of IAPP and/or Aβ40 or Aβ42 were designed based on previously in our lab identified "hot segments" of the Aβ sequence[43]. This study revealed that Aβ segments Aβ(19-22), Aβ(27-32) and Aβ(35-40) are "hot segments" in both Aβ self- and its cross-interaction interface with IAPP (Figure 4-1a). Additionally, Aβ(15-21) and Aβ(26-32) are the shortest sequences of Aβ with highest degrees of identity and similarity with IAPP[43,79]. Furthermore, solid-state NMR measurements identified Aβ(11-22) and Aβ(30-40) as the segments building up two β-strands which form separate, parallel β-sheets in the Aβ40 fibril[54,55,130,131] (Figure 4-1a,b). The two β-strands are connected by a loop region, forming the characteristic β-strand-loop-β-strand motif which is additionally stabilised by a D23/K28 salt-bridge[54,130]. N-terminal Aβ40 residues are more flexible and not part of the fibril core[54,55,130-132].

Capitalising on IAPP "hot segments"[43], our lab previously designed so-called IAPP interaction surface mimics (ISMs) which were potent inhibitors of amyloid self-assembly of both Aβ40(42) and/or IAPP[111]. In analogy to the ISM concept, ADPs should mimic Aβ40's intrinsic amyloid β-strand-loop-β-strand structure in an alternative, amyloid-like β-sheet/β-turn fold. In contrast to Aβ40, ADPs should additionally be non-toxic and non-amyloidogenic themselves, while maintaining the high-affinity self-/cross-interaction ability with IAPP and Aβ40(42) in order to inhibit the amyloid self-assembly of one or both polypeptides. Based on the above-mentioned knowledge, ADPs were designed as follows:

(a) Aβ40 residues Aβ(1-14) were omitted since the N-terminal amino acids are not part of the Aβ40 fibril core and the highest degree of identity and similarity of Aβ40's N-terminus with corresponding IAPP residues is observed in region Aβ(15-21). Additionally, Aβ(15-40) contains all three "hot segments".
(b) The loop tripeptide Aβ(24-26) was substituted by different structurally biased tripeptide segments[111]. Both small and large hydrophobic or polar tripeptides consisting of the same three amino acids were introduced. Tripeptides consisting of large hydrophobic residues were assumed to yield potent inhibitors due to their β-sheet propagating properties, according to the ISM concept[111]. Tripeptides consisting of small or polar residues were introduced for obtaining control peptides and evaluating the hypothesis.
(c) Met35 was substituted by norleucine to avoid the risk of uncontrolled oxidation of the peptides. The Met35Nle exchange is an equivalent substitution since it does not affect the structure of the Aβ monomer[133].

Steps a-c led to a first set of ADPs consisting of 5 peptides containing different loop tripeptide segments (LTS), i. e. VGS (native), RRR, GGG, LLL and NleNleNle (Figure 4-1c and Table 4-1). To reduce the potentially inherited propensity of ADPs to self-aggregate and form amyloids, pairs of *N*-methylations were introduced into the peptides' N- or C-termini when designing the next set of ADPs. Also, introduction of *N*-methylations has proved earlier to be a useful tool to generate inhibitors of Aβ amyloid formation[134-139]. Thus, such modulations were

envisioned to also enhance the inhibitory capacity of ADPs toward IAPP. This second set of ADPs comprised 17 potential inhibitors (Figure 4-1c and Table 4-2). Peptides out of this set which proved to indeed inhibit IAPP were termed Aβ amyloid core mimics (ACMs).

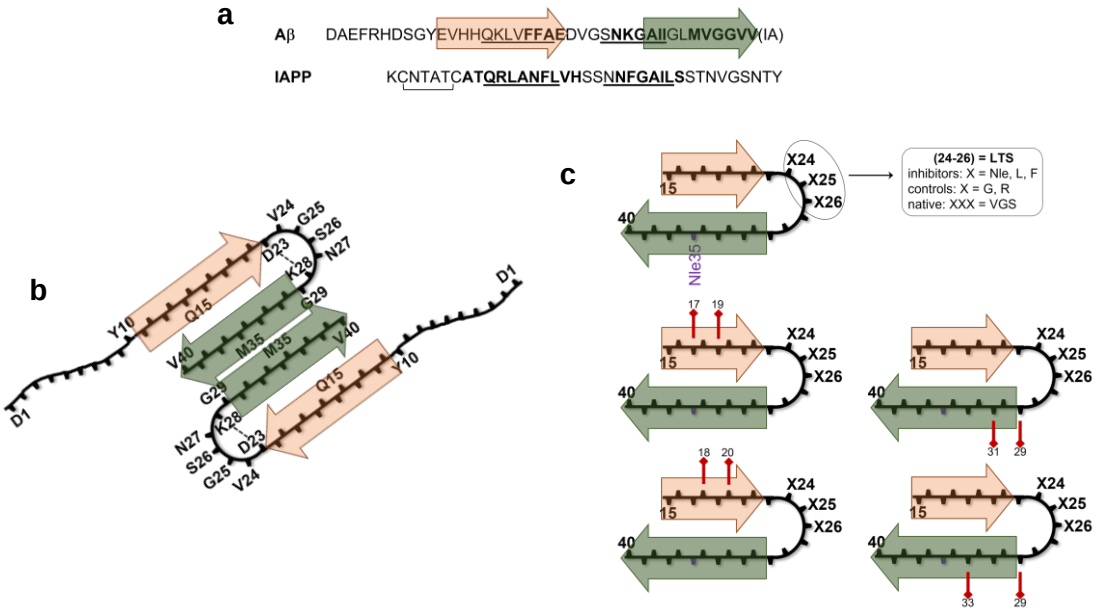

Figure 4-1: Peptide design strategy. (**a**) Primary sequences of Aβ40(42) and IAPP. Bold letters: "hot segments" of Aβ and IAPP self- and cross-interaction[43]. Underlined: shortest sequences with highest degrees of identity and similarity in Aβ and IAPP[43,79]. Coloured arrows indicate regions forming the N-terminal (orange) and C-terminal (green) β-strands in the Aβ40 fibril. (**b**) Structure and orientation of two Aβ40 molecules in one layer of the Aβ40 fibril model determined by Tycko and co-workers[54] that was used as a template. Dotted line indicates the salt-bridge formed between residues D23 and K28. (**c**) Design concept of the first (w/o methylation) and second set (with methylations) of ADPs. M35Nle exchange is highlighted in purple. Sticks indicate *N*-methylation positions. LTS: loop tripeptide segment. Figure is part of reference [140] (adapted version).

Table 4-1: Amino acid sequences of the first set of ADPs. All peptides have a free N-terminal amino group (NH_2-) and are C-terminal carboxylic acids (-COOH). Amino acid counting refers to the full-length Aβ40 sequence of which the peptides are derived from. M35Nle substitution is indicated by underline. Peptides were synthesised by Martin Ortner during his Bachelor thesis[141] and by Kathleen Hille. [a]: by Martin Ortner, [b]: by Kathleen Hille.

Peptide Sequence	Abbreviation
^{1}DAEFRHDSGYEVHH^{15}QKLVFFAED – VGS – NKGAIIGLMVGGVV^{40}	Aβ40[b]
^{15}QKLVFFAED – VGS – NKGAIIGLNleVGGVV^{40}	VGS[a]
^{15}QKLVFFAED – RRR – NKGAIIGLNleVGGVV^{40}	R3[a],[b]
^{15}QKLVFFAED – GGG – NKGAIIGLNleVGGVV^{40}	G3[a]
^{15}QKLVFFAED – LLL – NKGAIIGLNleVGGVV^{40}	L3[a]
^{15}QKLVFFAED – NleNleNle – NKGAIIGLNleVGGVV^{40}	Nle3[a],[b]

Table 4-2: Amino acid sequences of ACMs and other ADPs of the second design set. All peptides have a free N-terminal amino group (NH_2-) and are C-terminal carboxylic acids (-COOH). Amino acid counting refers to the full-length Aβ40 sequence of which the peptides are derived from. M35Nle substitution is indicated by underline. N-Me: *N*-methylation. Sophia Prem and Kathleen Hille contributed to the syntheses of several peptides (see chapter 8). The peptides VGS-GI, VGS-GG, R3-GI, R3-GG, Nle3-GI, Nle3-GG, and Nle3-LF were synthesised by me during my Master thesis[142] (*). A similar table is presented in reference [140].

Peptide Sequence	Abbreviation
^{1}DAEFRHDSGYEVHH^{15}QKLVFFAED – VGS – NKGAIIGLMVGGVV^{40}	Aβ40
^{15}QK**(N-Me)L**V**(N-Me)F**FAED – VGS – NKGAIIGL<u>Nle</u>VGGVV^{40}	VGS-LF
^{15}QKL**(N-Me)V**F**(N-Me)F**AED – VGS – NKGAIIGL<u>Nle</u>VGGVV^{40}	VGS-VF
^{15}QKLVFFAED – VGS – NK**(N-Me)G**A**(N-Me)I**IGL<u>Nle</u>VGGVV^{40}	VGS-GI*
^{15}QKLVFFAED – VGS – NK**(N-Me)**GAII**(N-Me)G**L<u>Nle</u>VGGVV^{40}	VGS-GG*
^{15}QK**(N-Me)L**V**(N-Me)F**FAED – RRR – NKGAIIGL<u>Nle</u>VGGVV^{40}	R3-LF
^{15}QKL**(N-Me)V**F**(N-Me)F**AED – RRR – NKGAIIGL<u>Nle</u>VGGVV^{40}	R3-VF
^{15}QKLVFFAED – RRR – NK**(N-Me)G**A**(N-Me)I**IGL<u>Nle</u>VGGVV^{40}	R3-GI*
^{15}QKLVFFAED – RRR – NK**(N-Me)**GAII**(N-Me)G**L<u>Nle</u>VGGVV^{40}	R3-GG*
^{15}QKL**(N-Me)V**F**(N-Me)F**AED – GGG – NKGAIIGL<u>Nle</u>VGGVV^{40}	G3-VF
^{15}QK**(N-Me)L**V**(N-Me)F**FAED – LLL – NKGAIIGL<u>Nle</u>VGGVV^{40}	L3-LF
^{15}QKL**(N-Me)V**F**(N-Me)F**AED – LLL – NKGAIIGL<u>Nle</u>VGGVV^{40}	L3-VF
^{15}QK**(N-Me)L**V**(N-Me)F**FAED – NleNleNle – NKGAIIGL<u>Nle</u>VGGVV^{40}	Nle3-LF*
^{15}QKL**(N-Me)V**F**(N-Me)F**AED – NleNleNle – NKGAIIGL<u>Nle</u>VGGVV^{40}	Nle3-VF
^{15}QKLVFFAED – NleNleNle – NK**(N-Me)G**A**(N-Me)I**IGL<u>Nle</u>VGGVV^{40}	Nle3-GI*
^{15}QKLVFFAED – NleNleNle – NK**(N-Me)**GAII**(N-Me)G**L<u>Nle</u>VGGVV^{40}	Nle3-GG*
^{15}QK**(N-Me)L**V**(N-Me)F**FAED – FFF – NKGAIIGL<u>Nle</u>VGGVV^{40}	F3-LF
^{15}QKL**(N-Me)V**F**(N-Me)F**AED – FFF – NKGAIIGL<u>Nle</u>VGGVV^{40}	F3-VF

4.2 Synthesis and purification of ADPs

ADPs were synthesised using previously developed Fmoc-SPPS protocols[19,120]. Standard double couplings were usually conducted using 3-fold molar excess protected amino acid and HBTU and 4.5-fold molar excess of DIEA in DMF. Couplings were generally performed for 40 min for amino acids in region Aβ(20-40) and for 50 min for amino acids in region Aβ(15-19). For regions in which I observed difficulties in couplings, several rounds of optimisation were performed to improve synthesis efficiency. Such cases were: sequence parts corresponding to Aβ(16-21) and Aβ(27-33), couplings of/to *N*-methylated amino acids, and within the LTS (final SPPS protocols see Table 7-1 to Table 7-7 in Appendix). For these difficult sequence parts either HATU was applied instead of HBTU, or 4-6-fold molar excess of protected amino acids was used, and/or triple couplings were performed (40-60 min). Due to their extraordinary difficulty, the following two couplings required specific attention: coupling of Ala30 to NMeIle31 in the C-terminus of Gly29Ile31-methylated peptides (see Table 7-3) and coupling of Leu17 to NMeVal18 in the N-terminus of Val18Phe20-methylated peptides (see Table 7-7). For coupling of Ala30 to NMeIle31, five coupling rounds (1 h each) using 6-fold excess of protected amino acid and HATU were required. Couplings needed to be performed in the minimum amount of DMF necessary to dissolve the amino acid/HATU mixture. Also for the coupling of Leu17 to NMeVal18 using the minimum amount of DMF necessary to dissolve the amino acid/HATU

mixture was crucial, otherwise more coupling steps than described in the protocol shown in Table 7-7 are required.

After full assembly of the peptide chains by SPPS and cleavage from the resin, lyophilised products were purified via RP-HPLC on Nucleosil 100 C18 or Reprosil Gold 200 C18 columns. The applied gradients were “schnellAβ”, “10-100 % B”, “langsamAβ”, “langsam40-70 % B“, and “50-100 % B in 30 min” (see Table 3-19 and Figure 3-1 in chapter 3.2.2 for details). Table 4-3 and Table 4-4 give an overview on the purification strategies applied for labelled and unlabelled ADPs and their molecular weights, calculated and verified by MALDI-TOF or ESI-IT mass spectrometry. Figure 4-2 to Figure 4-9 show representative HPLC chromatograms of purification and re-purification of the most important peptides Nle3-VF, Nle3-LF, L3-VF, L3-LF, F3-VF, F3-LF, VGS-VF and VGS-LF, as well as an HPLC chromatogram and the mass spectrometric analyses of the pure products. Mass spectrometric characterisation of other ADPs (labelled and unlabelled) after purification are shown in Figure 7-1 to Figure 7-5 in the Appendix.

Table 4-3: Overview on purification steps of 1st and 2nd set ADPs and their molecular weights. Peptides were purified via reverse-phase (RP)-HPLC. In general, gradients were run on a Nucleosil 100 C18 column. Cases in which gradients were run on a Reprosil Gold 200 C18 column are marked by asterix (*). For details on gradients see Figure 3-1 and Table 3-19 in chapter 3.2.2. Yield gives the percentage of pure peptide that was obtained from the total amount of purified crude product. Molecular weights of purified peptides were controlled by MALDI-TOF or ESI-IT mass spectrometry ([a]: $M+Na^+$, [b]: $M+H^+$). MALDI matrix: α-cyano-4-hydroxycinnamic acid (HCCA). MALDI solvent A: 97 % acetone in ddH_2O with 0.1 % TFA; MALDI solvent B: 30 % ACN in ddH_2O with 0.1 % TFA; ESI solvent (“C”): 80 % ACN in ddH_2O. For HPLC chromatograms and MALDI/ESI spectra of Nle3-VF, Nle3-LF, L3-VF, L3-LF, F3-VF, F3-LF, VGS-VF, and VGS-LF see Figure 4-2 to Figure 4-9. For MALDI/ESI spectra of other ADPs see Figure 7-1 and Figure 7-2 in the Appendix. ADP(15-23)-VF and ADP(27-40) were purified by Kathleen Hille and she also assisted in purification of other ADPs (see chapter 8). Abbreviations: pur., purification; rep, re-purification; RT, retention time; MW, molecular weight.

Peptide	Gradient pur.	RT pur. (min)	Gradient rep.	RT rep. (min)	Yield (%)	MW calc. ($M+H^+$) (g/mol)	MW found (g/mol)	MALDI/ ESI solvent
VGS	schnellAβ	22.5	-	-	25	2630.48	2652.35[a]	A
VGS-LF	langsamAβ	29.1	schnellAβ	21.5	9	2658.54	2680.47[a]	A
VGS-VF	langsamAβ	29.2	schnellAβ	21.9	19	2658.54	2681.37[a]	A
VGS-GI	schnellAβ	22.3	schnellAβ	22.3	5-10	2658.54	2658.65[b]	B
VGS-GG	langsamAβ*	23	-	-	15	2658.54	2680.79[a]	A
R3	langsamAβ*	20.9	schnellAβ*	18.9	7	2855.67	2855.97[b]	B
R3-LF	langsamAβ	24	-	-	12.5	2883.73	2883.99[b]	A
R3-VF	langsamAβ	25	langsamAβ	25	5	2883.73	2884.80[b]	C
R3-GI	schnellAβ	20.6	-	-	30	2883.73	2883.69[b]	A
R3-GG	schnellAβ	20	-	-	15	2883.73	2883.46[b]	A
G3	langsamAβ	28	schnellAβ*	20.1	25	2558.43	2580.42[a]	A
G3-VF	langsamAβ	27.3	-	-	15	2586.49	2609.00[a]	A
L3	10-100% B	18.3	-	-	13	2726.61	2727.00[b]	C
L3-LF	schnellAβ	25.4	-	-	20	2754.67	2776.87[a]	C
L3-VF	schnellAβ	24.8	langsam40-70% B	26.2	16	2754.67	2776.99[a]	A
Nle3	10-100% B	18	10-100% B	18	15	2726.61	2748.71[a]	A
Nle3-LF	schnellAβ	25.6	schnellAβ	25.2	20	2754.67	2776.83[a]	A
Nle3-VF	schnellAβ	24.9	langsam40-70% B	25.6	10	2754.67	2776.89[a]	A
Nle3-GI	schnellAβ	24.3	schnellAβ	24.5	6	2754.67	2776.50[a]	A
Nle3-GG	langsam40-70% B	20.8	-	-	24	2754.67	2777.13[a]	A
F3-LF	schnellAβ	25.4	langsam40-70% B	27.8	13	2856.63	2878.73[a]	A
F3-VF	schnellAβ	24.8	langsam40-70% B	27.1	17	2856.63	2878.92[a]	A
ADP(15-23)-VF	schnellAβ	25.4	langsamAβ	19.4	4	1124.62	1146.62[a]	A
ADP(27-40)	schnellAβ*	19.5	-	-	40	1309.81	1331.93[a]	A

Table 4-4: Overview on purification steps of labelled 1st and 2nd set ADPs and their molecular weights. Peptides were purified via reverse-phase (RP)-HPLC. In general, gradients were run on a Nucleosil 100 C18 column. Cases in which gradients were run on a Reprosil Gold 200 C18 column are marked by asterix (*). For details on gradients see Figure 3-1 and Table 3-19 in chapter 3.2.2. Molecular weights of purified peptides were controlled by MALDI-TOF mass spectrometry ([a]: $M+Na^+$, [b]: $M+H^+$, [c]: $M+K^+$). MALDI matrix: α-cyano-4-hydroxycinnamic acid (HCCA). MALDI solvent A: 97 % acetone in ddH_2O with 0.1 % TFA. For MALDI/ESI spectra of labelled ADPs see Figure 7-3 and Figure 7-4 in the Appendix. Kathleen Hille and Sophia Kalpazidou contributed to the purification of several peptides (see chapter 8). Abbreviations: pur., purification; rep, re-purification; RT, retention time; MW, molecular weight.

Peptide	Gradient pur.	RT pur. (min)	Gradient rep.	RT rep. (min)	MW calc. ($M+H^+$) (g/mol)	MW found (g/mol)	MALDI solvent
Fluos-VGS	schnellAβ	25.5	-	-	2987.78	3010.50[a]	A
Fluos-VGS-LF	10-100% B	17.3	langsamAβ	34.5	3016.84	3039.04[a]	A
Fluos-VGS-VF	10-100% B*	16.5	langsamAβ*	31	3016.84	3038.84[a]	A
Fluos-VGS-GI	schnellAβ	25	schnellAβ	23.5	3016.84	3038.61[a]	A
Fluos-VGS-GG	schnellAβ	25.8	-	-	3016.84	3039.46[a]	A
Fluos-R3-LF	langsamAβ	28.5	-	-	3242.03	3242.89[b]	A
Fluos-R3-VF	langsamAβ*	29	-	-	3242.03	3242.47[b]	A
Fluos-G3-VF	schnellAβ	23.5	-	-	2944.79	2967.02[a]	A
Fluos-L3	10-100% B*	19.9	-	-	3083.91	3107.01[a]	A
Fluos-L3-LF	10-100% B*	18.1	10-100% B	19.6	3112.97	3134.75[a]	A
Fluos-L3-VF	langsam40-70% B*	26.5	10-100% B*	17.5	3112.97	3134.94[a]	A
Fluos-Nle3	10-100% B	22.6	-	-	3084.91	3108.05[a]	A
Fluos-Nle3-LF	10-100% B	20.4	10-100% B	21.4	3112.97	3135.16[a]	A
Fluos-Nle3-VF	schnellAβ	28	langsam40-70% B	34	3112.97	3134.93[a]	A
Fluos-Nle3-GI	10-100% B	19.6	10-100% B	19.6	3112.97	3134.89[a]	A
Fluos-Nle3-GG	10-100% B	19.1	10-100% B	19.1	3112.97	3133.09[a]	A
Fluos-F3-LF	10-100% B	19.4	-	-	3214.93	3236.59[a]	A
Fluos-F3-VF	langsam40-70% B*	28	schnellAβ*	25.5	3214.93	3237.05[a]	A
Atto647N-Nle3-VF	10-100% B*	19.6	50-100% B	22.6	3382.57	3381.85[b]	A
Biotin-Nle3-VF	langsam40-70% B*	24.4	langsam40-70% B	30.4	3093.00	3116.33[a]	A
Biotin-Nle3-GG	langsam40-70% B*	27.2	-	-	3093.00	3116.03[a]	A
Biotin-Nle3	10-100% B	21.6	10-100% B	22.8	3064.94	3104.59[c]	A
Biotin-VGS-VF	langsam40-70% B*	16.9	langsam40-70% B*	16.9	2996.87	3020.15[a]	A

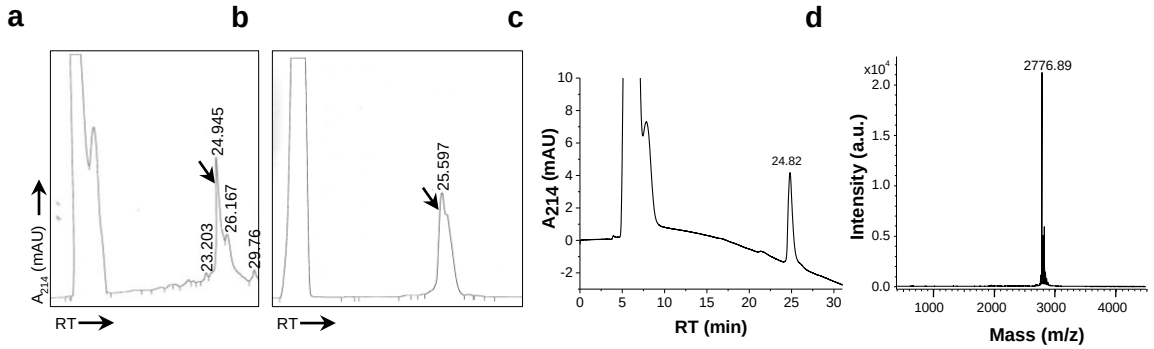

Figure 4-2: HPLC purification strategy for Nle3-VF. (**a**) Purification. Representative C18 HPLC chromatogram (schnellAβ, absorbance 214 nm) of Nle3-VF (500 µg crude product). The peak containing the correct product is marked with an arrow (retention time: 24.945 min). Numbers on peaks show their retention time in minutes. (**b**) Re-purification. Representative C18 HPLC chromatogram (langsam40-70 % B, absorbance 214 nm) of Nle3-VF. Product collected from the peak eluting at 24.945 min (see a) was re-injected. The peak containing the correct product is marked with an arrow (retention time: 25.597 min). Numbers on peaks show their retention time in minutes. (**c**) HPLC of pure product (20 µg). Gradient: schnellAβ, absorbance 214 nm. (**d**) MALDI-TOF-MS spectrum of HPLC-purified Nle3-VF. The theoretical calculated mass $[M+H]^+$ is 2754.67; the experimental mass $[M+Na^+]^+$ is 2776.89.

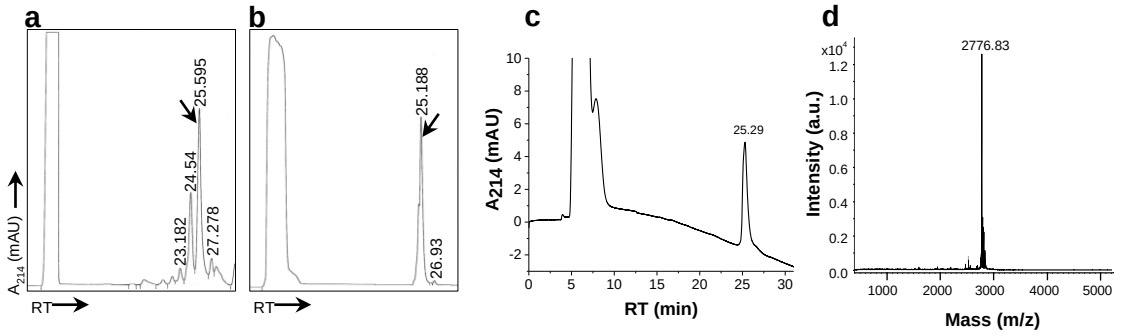

Figure 4-3: HPLC purification strategy for Nle3-LF. (**a**) Purification. Representative C18 HPLC chromatogram (schnellAβ, absorbance 214 nm) of Nle3-LF (500 µg crude product). The peak containing the correct product is marked with an arrow (retention time: 25.595 min). Numbers on peaks show their retention time in minutes. (**b**) Re-purification. Representative C18 HPLC chromatogram (schnellAβ, absorbance 214 nm) of Nle3-LF. Product collected from the peak eluting at 25.595 min (see a) was re-injected. The peak containing the correct product is marked with an arrow (retention time: 25.188 min). Numbers on peaks show their retention time in minutes. (**c**) HPLC of pure product (20 µg). Gradient: schnellAβ, absorbance 214 nm. (**d**) MALDI-TOF-MS spectrum of HPLC-purified Nle3-LF. The theoretical calculated mass $[M+H]^+$ is 2754.67; the experimental mass $[M+Na^+]^+$ is 2776.83.

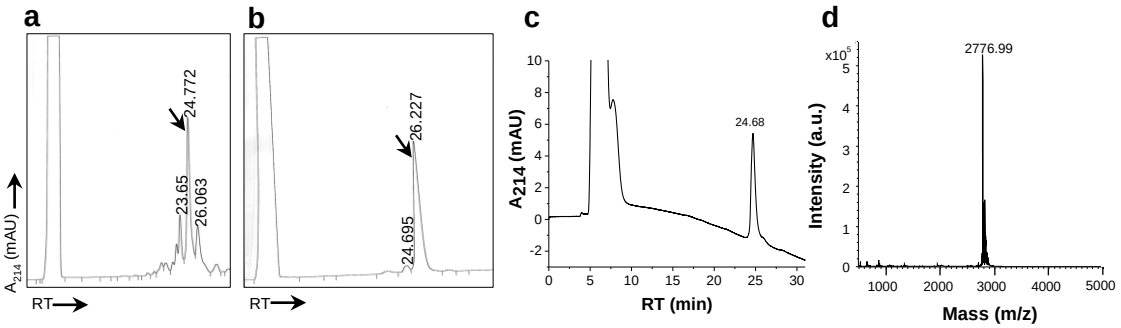

Figure 4-4: HPLC purification strategy for L3-VF. (**a**) Purification. Representative C18 HPLC chromatogram (schnellAβ, absorbance 214 nm) of L3-VF (500 µg crude product). The peak containing the correct product is marked with an arrow (retention time: 24.772 min). Numbers on peaks show their retention time in minutes. (**b**) Re-purification. Representative C18 HPLC chromatogram (langsam40-70 % B, absorbance 214 nm) of L3-VF. Product collected from the peak eluting at 24.772 min (see a) was re-injected. The peak containing the correct product is marked with an arrow (retention time: 26.227 min). Numbers on peaks show their retention time in minutes. (**c**) HPLC of pure product (20 µg). Gradient: schnellAβ, absorbance 214 nm. (d) MALDI-TOF-MS spectrum of HPLC-purified L3-VF. The theoretical calculated mass $[M+H]^+$ is 2754.67; the experimental mass $[M+Na^+]^+$ is 2776.99.

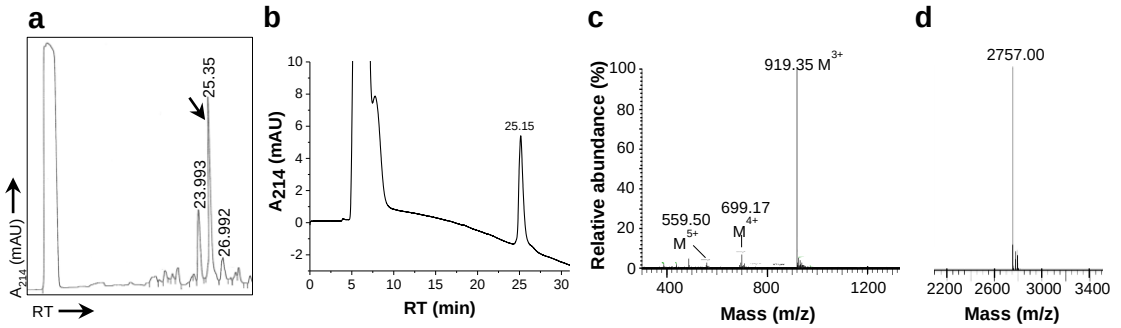

Figure 4-5: HPLC purification strategy for L3-LF. (**a**) Purification. Representative C18 HPLC chromatogram (schnellAβ, absorbance 214 nm) of L3-LF (500 µg crude product). The peak containing the correct product is marked with an arrow (retention time: 25.35 min). Numbers on peaks show their retention time in minutes. (**b**) HPLC of pure product (20 µg). Gradient: schnellAβ, absorbance 214 nm. (**c**) ESI-IT-MS spectrum of HPLC-purified L3-LF. The theoretical calculated mass $[M+H]^+$ is 2754.67; the experimental mass $[M+3H^+]^{3+}$ is 919.35 (main peak). (**d**) Deconvolved ESI-IT-MS spectrum from c).

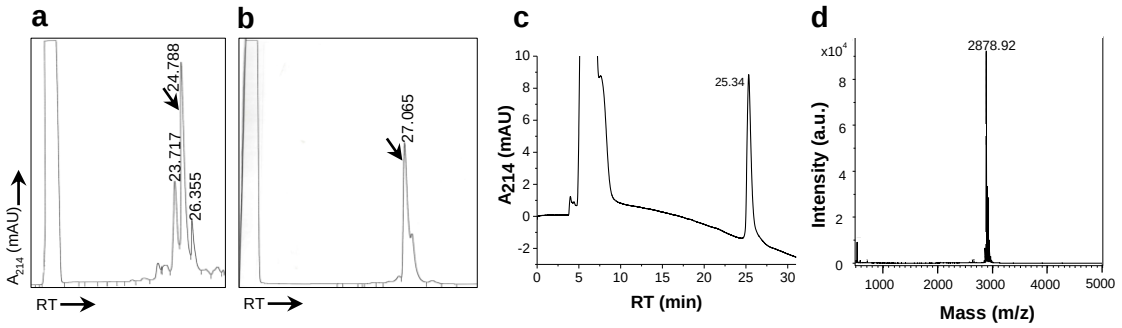

Figure 4-6: HPLC purification strategy for F3-VF. (**a**) Purification. Representative C18 HPLC chromatogram (schnellAβ, absorbance 214 nm) of F3-VF (500 µg crude product). The peak containing the correct product is marked with an arrow (retention time: 24.788 min). Numbers on peaks show their retention time in minutes. (**b**) Re-purification. Representative C18 HPLC chromatogram (langsam40-70 % B, absorbance 214 nm) of F3-VF. Product collected from the peak eluting at 24.788 min (see a) was re-injected. The peak containing the correct product is marked with an arrow (retention time: 27.065 min). Numbers on peaks show their retention time in minutes. (**c**) HPLC of pure product (20 µg). Gradient: schnellAβ, absorbance 214 nm. (**d**) MALDI-TOF-MS spectrum of HPLC-purified F3-VF. The theoretical calculated mass $[M+H]^+$ is 2856.63; the experimental mass $[M+Na^+]^+$ is 2878.92.

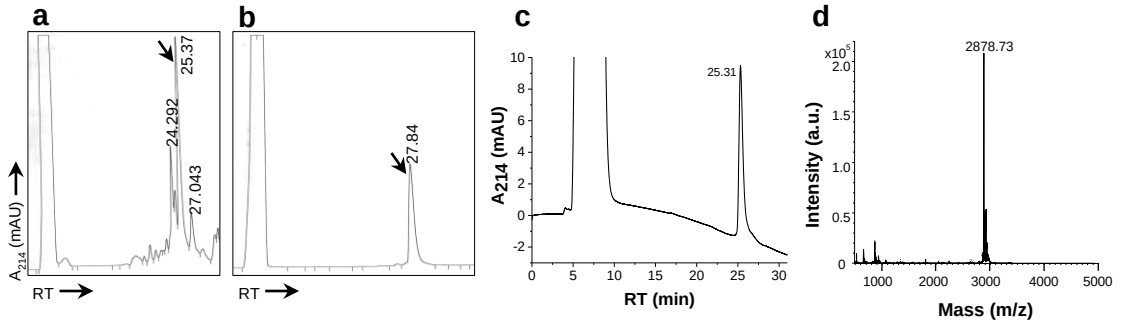

Figure 4-7: HPLC purification strategy for F3-LF. (**a**) Purification. Representative C18 HPLC chromatogram (schnellAβ, absorbance 214 nm) of F3-LF (500 µg crude product). The peak containing the correct product is marked with an arrow (retention time: 25.37 min). Numbers on peaks show their retention time in minutes. (**b**) Re-purification. Representative C18 HPLC chromatogram (langsam40-70 % B, absorbance 214 nm) of F3-LF. Product collected from the peak eluting at 25.37 min (see a) was re-injected. The peak containing the correct product is marked with an arrow (retention time: 27.84 min). Numbers on peaks show their retention time in minutes. (**c**) HPLC of pure product (20 µg). Gradient: schnellAβ, absorbance 214 nm. (**d**) MALDI-TOF-MS spectrum of HPLC-purified F3-LF. The theoretical calculated mass $[M+H]^+$ is 2856.63; the experimental mass $[M+Na^+]^+$ is 2878.73.

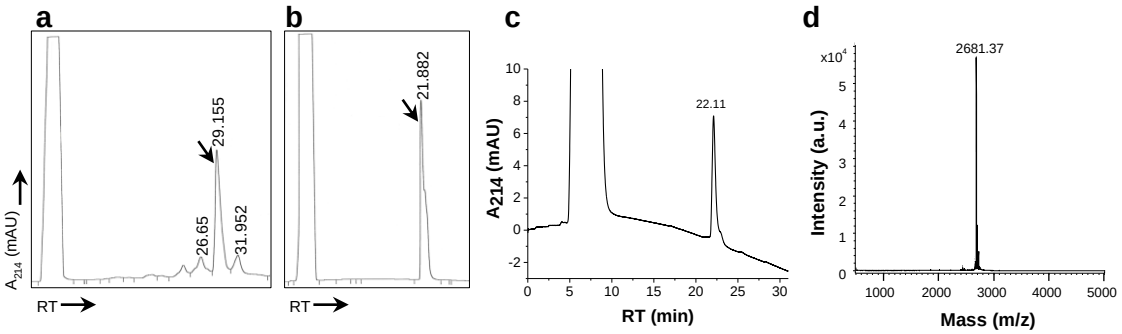

Figure 4-8: HPLC purification strategy for VGS-VF. (**a**) Purification. Representative C18 HPLC chromatogram (langsam40-70 % B, absorbance 214 nm) of VGS-VF (500 µg crude product). The peak containing the correct product is marked with an arrow (retention time: 29.155 min). Numbers on peaks show their retention time in minutes. (**b**) Re-purification. Representative C18 HPLC chromatogram (schnellAβ, absorbance 214 nm) of VGS-VF. Product collected from the peak eluting at 29.155 min (see a) was re-injected. The peak containing the correct product is marked with an arrow (retention time: 21.882 min). Numbers on peaks show their retention time in minutes. (**c**) HPLC of pure product (20 µg). Gradient: schnellAβ, absorbance 214 nm. (**d**) MALDI-TOF-MS spectrum of HPLC-purified VGS-VF. The theoretical calculated mass $[M+H]^+$ is 2658.54; the experimental mass $[M+Na^+]^+$ is 2681.37.

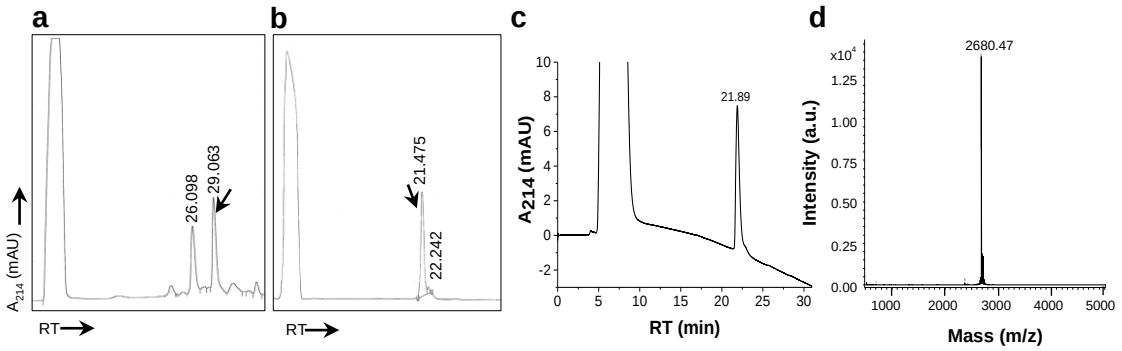

Figure 4-9: HPLC purification strategy for VGS-LF. (**a**) Purification. Representative C18 HPLC chromatogram (langsam40-70 % B, absorbance 214 nm) of VGS-LF (500 µg crude product). The peak containing the correct product is marked with an arrow (retention time: 29.063 min). Numbers on peaks show their retention time in minutes. (**b**) Re-purification. Representative C18 HPLC chromatogram (schnellAβ, absorbance 214 nm) of VGS-LF. Product collected from the peak eluting at 29.063 min (see a) was re-injected. The peak containing the correct product is marked with an arrow (retention time: 21.475 min). Numbers on peaks show their retention time in minutes. (**c**) HPLC of pure product (20 µg). Gradient: schnellAβ, absorbance 214 nm. (**d**) MALDI-TOF-MS spectrum of HPLC-purified VGS-LF. The theoretical calculated mass $[M+H]^+$ is 2658.54; the experimental mass $[M+Na^+]^+$ is 2680.47.

4.3 Studies on structural and cytotoxic properties of ADPs and their effect on IAPP fibril formation and toxicity

4.3.1 Inhibitory potential of ADPs towards IAPP aggregation depends on linker sequence

The first set of ADPs, created by combining the known Aβ40 "hot segments"[43] of the Aβ40-IAPP interaction interface within the Aβ(15-40) segment with different LTS (VGS, Nle3, L3, G3, R3), was first studied with regard to the structural properties of the peptides by circular dichroism spectroscopy (CD). In contrast to Aβ40, all peptides proved to be of high structural order: the peptides containing the native LTS VGS or the LTS L3, R3 and G3 showed minima at around 225 nm and maxima at around 200 nm being indicative for β-turns or (red-shifted) β-sheets, whereas the Nle3-linked peptide rather presented β-sheet contents (minimum at ~216 nm, maximum at ~195 nm)[143] (Figure 4-10). These results were in accordance with studies from Martin Ortners Bachelor's thesis[141].

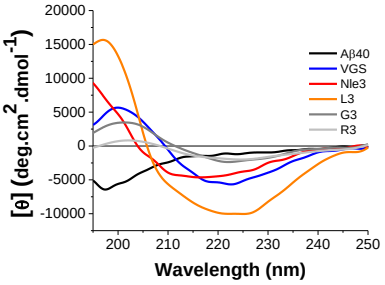

Figure 4-10: Structures of Aβ40 and differently linked ADPs determined by CD. CD spectra of 5 µM peptides were recorded in 1xb containing 1 % HFiP, pH 7.4. Baseline signals were subtracted from all measurements. CD spectra of VGS, Nle3, G3, and R3 were measured also by Martin Ortner during his Bachelor thesis[141]. Data in figure is part of a figure in reference [140].

Fluorescence titration experiments using Fluos-IAPP (5 nM) additionally showed that despite their altered structural properties, all peptides were still able to interact with IAPP; however, VGS and G3 exhibited weaker binding affinities to IAPP than Nle3, L3, and R3 (Table 4-5, Figure 4-12). For Nle3, L3 and R3, binding affinities were comparable to Aβ40 (Table 4-5, Figure 4-12). This feature could be important for IAPP inhibition. Therefore, all ADPs of the first design set were tested for their effect on IAPP fibril formation and cytotoxicity via the ThT-binding and the MTT reduction assay in rat insulinoma (RIN5fm) cells. Peptides with LTS consisting of bulky, hydrophobic residues (Nle3, L3) had a promising inhibitory capacity towards IAPP: L3 was able to delay IAPP fibril formation for 48 h, Nle3 even for 72 h (Figure 4-11a). Both peptides efficiently inhibited IAPP-mediated cell damage after 24 h of incubation but lost this property after 7 days (Figure 4-11b,c). In accordance with the inhibitor design concept, compounds containing the native LTS (VGS) or small, flexible (G3) or polar LTS (R3) were completely inactive.

Table 4-5: Binding affinities of ADPs from the first design set to Fluos-IAPP. Binding affinities (app. k_Ds) were determined in 1xb containing 1 % HFiP, pH 7.4. Fluos-IAPP (5 nM) was titrated with increasing amounts of indicated peptides. App. k_Ds were calculated from three binding curves (mean ± SD). * Data taken from reference[80] and shows mean ± SEM. Binding data of R3 and Nle3 were produced in my Master thesis[142].

Peptide	Aβ40*	VGS	Nle3	L3	G3	R3
app. k_D (nM)	48.5 ± 4.2	417.6 ± 23.3	198.5 ± 5.6	80.5 ± 2.3	> 5000	154.6 ± 10.9

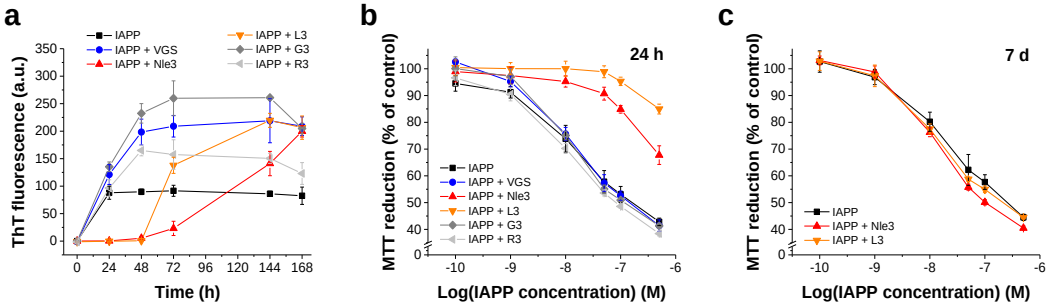

Figure 4-11: Effects of first set ADPs on IAPP amyloidogenicity. (**a**) Effect of ADPs on IAPP fibril formation was assessed using the ThT-binding assay. Incubations of IAPP (16.5 µM) or mixtures with peptides (1:2) were prepared in ThT assay buffer containing 0.5 % HFiP. Error bars represent means ± SD from three assays. Data was normalized to highest and lowest IAPP values in each assay. Preliminary studies on the effects of VGS, R3, G3, and Nle3 on IAPP fibril formation were also performed by Maria Bakou[144] and showed comparable results. (**b,c**) For measuring effects on IAPP-mediated cytotoxicity via the MTT reduction assay, aliquots from incubations in **a**, were taken after 24 h (**b**) and 7 d (**c**), diluted into cell medium and applied onto RIN5fm cells. Values for IAPP+G3 in **b**, were normalised to the IAPP shown in the graph due to variations of IAPP cytotoxicity in the original assay. Error bars represent means ± SD from three assays, n=3 each. Preliminary studies on the effects of VGS, R3, G3, and Nle3 on IAPP cytotoxicity were also performed by Maria Bakou[144] and showed comparable results. Data in figure part a) is part of a figure in reference [140].

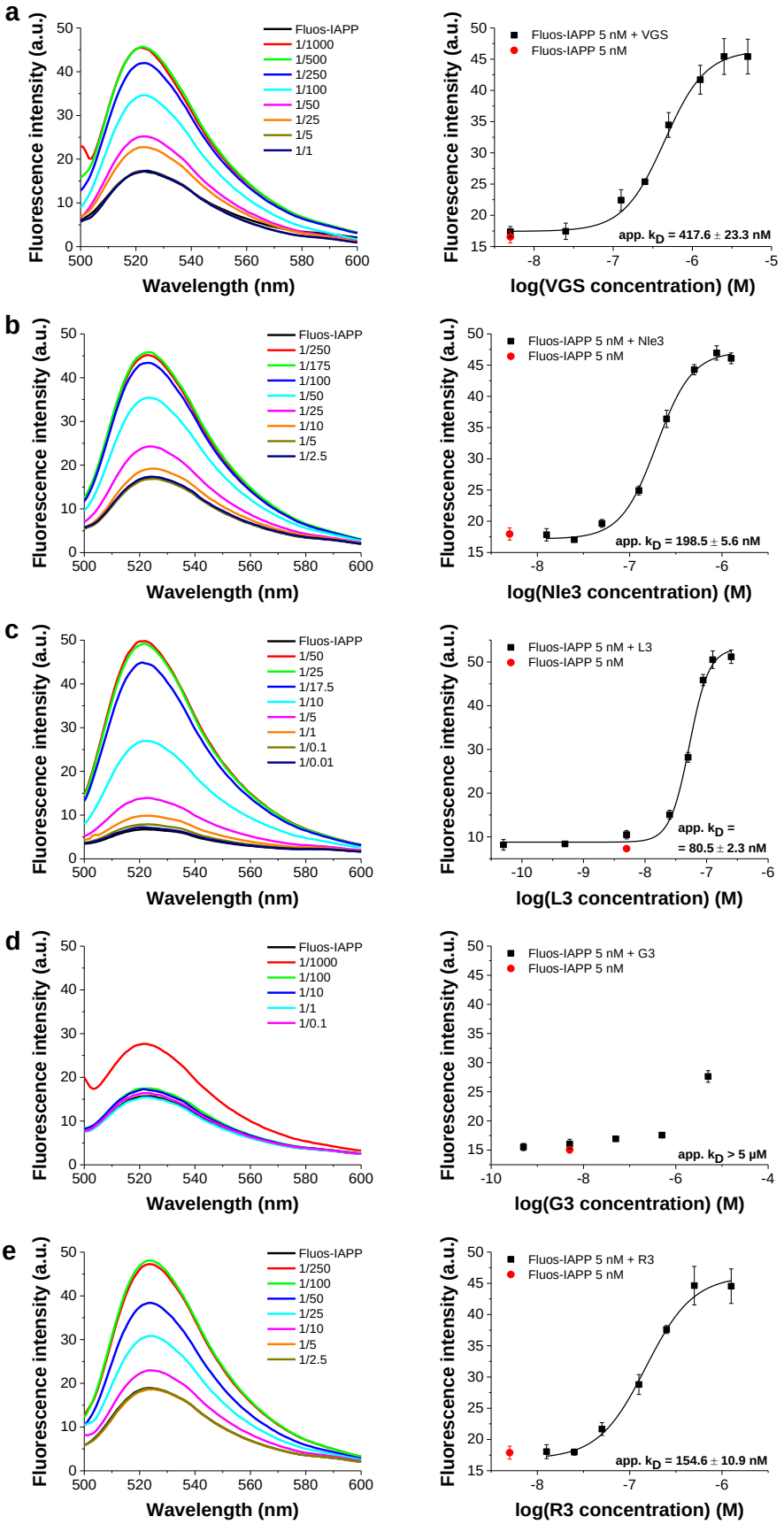

Figure 4-12: Fluorescence spectroscopic titrations of Fluos-IAPP with first set ADPs. *Left panels:* Fluorescence spectroscopic titrations were performed using Fluos-IAPP (5 nM). Fluorescence emission spectra of Fluos-IAPP alone and after titration with peptides were recorded in 1xb containing 1 % HFiP, pH 7.4. Shown is one representative data set. *Right panels:* App. k_D values (means ± SD) were calculated from three different binding curves. Fluorescence emission of Fluos-IAPP is shown as red dot for comparison. Data is shown for the following peptides: VGS (**a**), Nle3 (**b**), L3 (**c**), G3 (**d**) and R3 (**e**).

As Aβ40 is known to be highly neurotoxic, its derivatives might also share this for an inhibitory peptide undesirable property. Therefore, the peptides Nle3, L3 and the native segment control peptide VGS were tested for cytotoxicity on PC-12 cells. Both Nle3 and VGS did not display relevant toxic effects when incubated for 4 days at 100 µM and applied onto PC-12 cells at 20 µM, whereas Aβ40 was highly toxic under these conditions (Figure 4-13a). None of the three peptides Nle3, L3 and VGS caused significant cell damage at 20 µM even when incubated at 10-fold higher concentration (1 mM) (Figure 4-13b).

Taken together, ADPs from the first design set comprising a hydrophobic LTS (Nle3 and L3) did not only present promising inhibitory capacity against IAPP amyloidogenicity but also displayed the initially desired β-sheet/β-turn structure, showed nanomolar binding affinity to IAPP and were non-toxic. As Nle3's potency in blocking IAPP fibril formation was comparable to its full-length parent peptide Aβ40[80], this compound was chosen as a lead for further improvements.

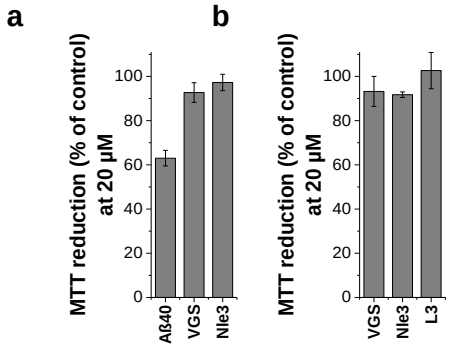

Figure 4-13: Effects of first set ADPs on cell viability of PC-12 cells. Aβ40 and peptides were incubated at 100 µM (**a**) or 1 mM (**b**) for 4 days in 1xb containing 1 % HFiP, diluted into cell medium and applied at 20 µM into cultured PC-12 cells. First set ADPs show no cytotoxicity compared to Aβ40 control. Error bars represent means ± SD from three assays, n=3 each. Values were corrected for effects of buffer alone (1xb 1 % HFIP). Effects of VGS and Nle3 (1 mM incubations) on PC-12 cell viability were studied during my Master thesis[142].

4.3.2 Inhibitory potential of ADPs towards IAPP aggregation depends on *N*-methylation position

As the introduction of *N*-methylations into the Aβ sequence was already found to be beneficial for blocking its own fibril formation and to design inhibitors[134-139] such modulations were assumed to also enhance inhibitory capacity of the peptides towards IAPP. Within the scope of designing a second set of ADPs, four different *N*-methylation pairs (L17F19, V18F20, G29I31 and G29G33) – indicated in the peptides' names as -LF, -VF, -GI and -GG – were tested for Nle3. N-terminally methylated Nle3-VF and Nle3-LF impressively reduced IAPP fibrillogenesis and cytotoxicity when added at 2-fold excess whereas C-terminally methylated Nle3-GG and Nle3-GI showed decreased inhibitory potential compared to the non-methylated peptide (Figure 4-14a-c). Because the introduction of N-terminal methylations led to great improvement of the Nle3 peptide, both methylation pairs were also tested with the L3 peptide. Additionally, another compound comprising a hydrophobic linker sequence was created by exchanging Aβ(24-26) with a phenylalanine tripeptide (F3) and tested for improvement by N-terminal methylations. All peptides – L3-VF, L3-LF, F3-VF and F3-LF – combining N-terminal

N-methylations with hydrophobic loops proved to be able to efficiently block IAPP fibril formation and related cell-damaging effects (Figure 4-14d-g). In contrast, none of the N-terminally methylated peptides containing small, polar LTS (VGS-VF, VGS-LF, G3-VF, R3-VF, R3-LF) showed effects towards IAPP amyloidogenicity when added at the same molar excess (2-fold) (Figure 4-14h,i). Also no improvement was observed when C-terminal methylations were introduced into these peptides (Figure 4-14j,k).

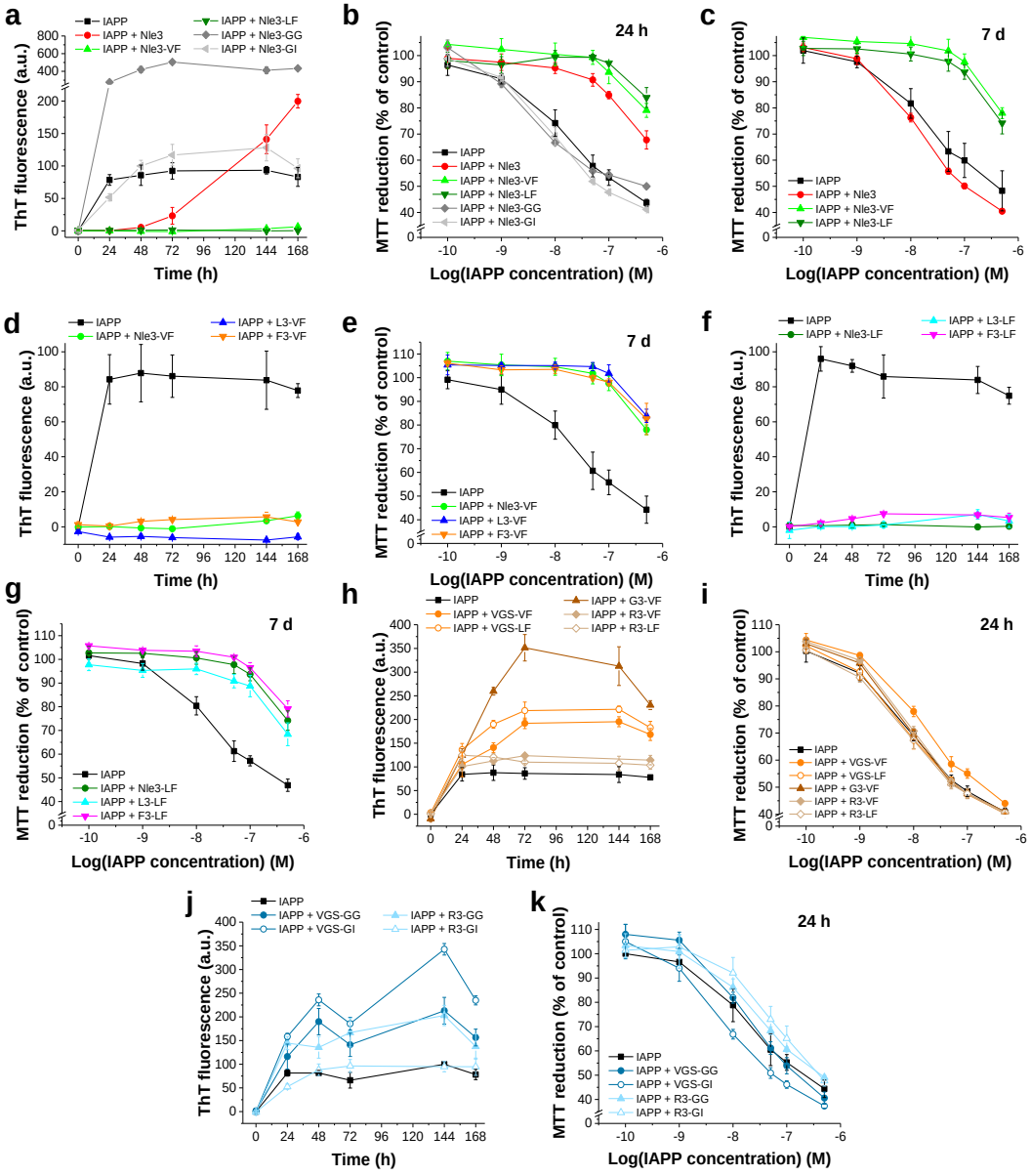

Figure 4-14: Effects of second set ADPs on IAPP amyloidogenicity. (**a,d,f,h,j**) IAPP fibril formation was followed in presence and absence of peptides (1:2; exception: L3-LF is 1:2.5) by ThT binding. Incubations were prepared in ThT assay buffer with 0.5 % HFiP containing 16.5 µM IAPP. Error bars represent means ± SD from three assays. Data was normalized to highest and lowest IAPP values in each assay. Note: y-axis is interrupted in **a**. (**b,c,e,g,i,k**) Aliquots from corresponding incubations in **a, d, f, h** or **j** were taken at 24 h (**b,i,k**) and 7 days (**c,e,g**) and applied into cultured RIN5fm cells after dilution into cell medium for assessing cell damage via the MTT reduction assay. Values for IAPP+R3-LF in i, were normalised to the IAPP shown in the graph due to variations of IAPP cytotoxicity in the original assay. Error bars represent means ± SD from three assays, n=3 each. Effects of R3-GG, R3-GI, VGS-GG, and VGS-GI on IAPP fibril formation and cytotoxicity and preliminary studies using Nle3-GG, Nle3-GI, and Nle3-LF are from my Master thesis[142]. Data in figure parts a), c), and d-i) are part of a figure in reference [140].

Of note, the partial ADP segments ADP(15-23)-VF and ADP(27-40) could not block IAPP fibril formation and cytotoxicity (Figure 4-15). These results led to the conclusion that for creating IAPP inhibitors from the Aβ(15-40) segment a hydrophobic loop tripeptide segment and the introduction of N-terminal *N*-methylations is crucial. Due to their design concept, these peptides were termed Aβ amyloid core mimics (ACMs).

The high potential of ACMs to inhibit IAPP cytotoxicity was further verified by determining their IC_{50} values. Both after 24 h and 7 days of incubation with IAPP all ACMs presented IC_{50} values in the low-nM range with Nle3-VF being the most potent one at 7 days (Table 4-6 and Figure 7-6 to Figure 7-9 in Appendix). Additionally, the molar excess necessary for the non-inhibitory (at 1:2) control peptides Nle3-GG, Nle3-GI and VGS-VF to become IAPP inhibitors was determined to specify the improvement obtained by changing linker sequence and *N*-methylation position in the ACM Nle3-VF. These ThT binding assays were performed in a microtiter plate system, where IAPP aggregation can still be followed at 1 µM (see chapter 3.2.10, "Studies on the effect of ADPs on IAPP fibril formation, microtiter plate-system"). When IAPP (1 µM) or its mixture with Nle3-VF (1:1) were incubated under the microtiter plate system conditions, similar results were obtained compared to findings from incubations prepared in Eppendorf tubes (with IAPP 16.5 µM) (Figure 4-16a; compare Figure 7-6a in Appendix). While Nle3-VF was able to block IAPP fibril formation when used in a 1:1 molar ratio, the C-terminally methylated analogue Nle3-GG was not inhibiting even when applied at 20-fold excess (Figure 4-16b). Also, the second C-terminally methylated analogue Nle3-GI had to be applied at 10-fold molar excess to fully block IAPP fibrillation but could at least reduce the final fibril load already when used in a 1:5 ratio (Figure 4-16c). The peptide sharing the same methylations

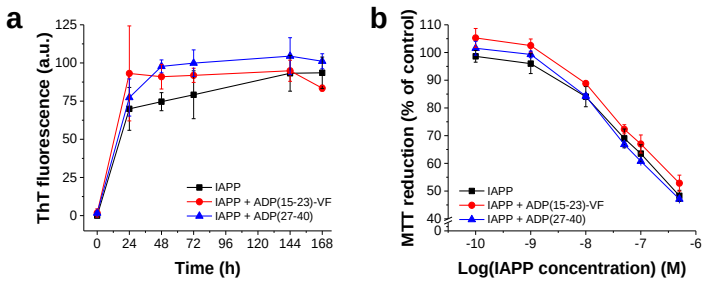

Figure 4-15: Effects of partial ADP segments ADP(15-23)-VF and ADP(27-40) on IAPP amyloidogenicity. (**a**) Effects on IAPP fibril formation were studied in solutions containing IAPP alone (16.5 µM) or its mixture with the partial ADP segments (1:2; in ThT assay buffer with 0.5 % HFIP) via the ThT binding assay. Error bars: means ± SD, n=3. Data was normalised to highest and lowest IAPP values in each assay. (**b**) Effects on IAPP cytotoxicity were studied via the MTT reduction assay. Following 24 h of aging, aliquots of solutions of a, were applied onto RIN5fm cells after dilution into cell medium. Error bars: means ± SD from three assays, n=3 each. Data in figure is part of a figure in reference [140].

Table 4-6: IC_{50} of inhibitory effects of ACMs on cytotoxic self-assembly of IAPP. IC_{50} means (±SD) from 3 titration assays (n=3 each) (IAPP, 100 nM). See Table 7-11 and Table 7-12 in Appendix for the three single IC_{50} values. Data for 24 h is part of a table in reference [140].

ACM	IC_{50} (±SD) (nM) 24 h	IC_{50} (±SD) (nM) 7 d
Nle3-VF	65.0 (± 5.2)	94.5 (± 4.5)
Nle3-LF	82.1 (± 10.2)	133.5 (± 11.6)
L3-VF	112.5 (± 8.1)	187.7 (± 8.7)
L3-LF	133.2 (± 29.0)	240.8 (± 8.0)
F3-VF	78.5 (± 13.6)	147.2 (± 0.8)
F3-LF	41.7 (± 4.1)	116.3 (± 7.1)

with Nle3-VF but containing the native LTS, VGS-VF, could not suppress IAPP aggregation at 4-fold excess and showed instable effects at 5-fold excess (Figure 4-16d). Results obtained when using VGS-VF in a 1:5 ratio under the microtiter plate system conditions ranged from almost full inhibition to no inhibition. Therefore, this experiment was repeated in the Eppendorf tube system (IAPP 16.5 µM; see 3.2.10, "Studies on the effect of ADPs on IAPP fibril formation, Eppendorf tube-system"). In this case, VGS-VF showed stable inhibition of IAPP fibril formation when applied at 5-fold molar excess (Figure 4-16e). In conclusion, moving the *N*-methylations from the C-terminus to the N-terminus in the Nle3 peptide leads to a 10 to 20 times more potent inhibitor. Changing the native LTS ValGlySer in VGS-VF into a Nle tripeptide renders the resulting peptide at least 5-times more potent. Both findings highlight again the importance of a hydrophobic linker sequence and a N-terminal methylation pair when designing IAPP inhibitors derived from the Aβ(15-40) segment. The rational design concept led to six potent amyloid inhibitors, the inhibitory potential of which is determined by their loop tripeptide segment and *N*-methylation position.

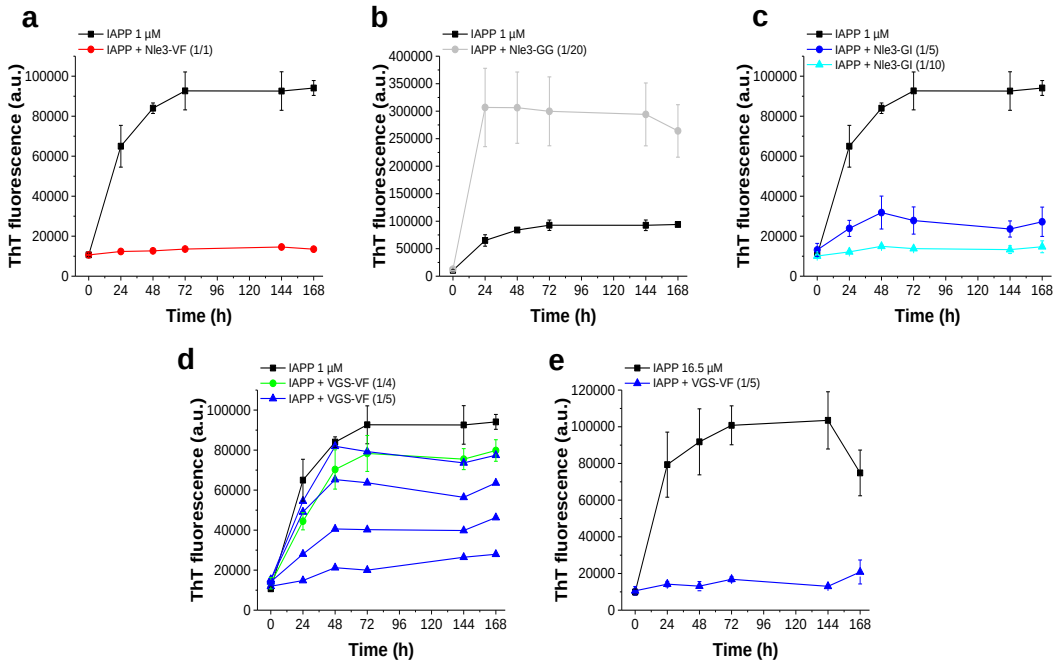

Figure 4-16: Determination of the critical molar excess for IAPP non-inhibitors to become inhibitors. (**a-d**) For being able to increase the peptides' molar excess to up to 20-fold and to simultaneously avoid solubility problems, ThT binding assays were performed in a microtiter plate system in which the IAPP concentration can be lowered to 1 µM. Incubations were prepared in an aqueous solution of 25 mM sodium phosphate, 50 mM NaCl and 25 mM Glycin/NaOH with 0.25 % HFiP and containing 6.9 µM ThT (pH 7.5). Shown are results for the ACM Nle3-VF (**a**), for the two corresponding C-terminally methylated peptides Nle3-GG (**b**) and Nle3-GI (**c**) and the native-LTS peptide VGS-VF (**d**) at indicated ratios. (**e**) Experiments for VGS-VF were repeated in the Eppendorf tube system (standard system; see chapter 3.2.10, "Studies on the effect of ADPs on IAPP fibril formation, Eppendorf tube-system") due to instable results found in the microtiter plate system. Incubations were prepared in an aqueous solution of 50 mM sodium phosphate and 100 mM NaCl (ThT assay buffer) with 0.5 % HFIP (pH 7.4) at 16.5 µM IAPP. All error bars in this figure represent means ± SD from three assays (meaning three independent incubations prepared in three different wells or Eppendorf tubes) with exception of IAPP + VGS-VF (1/5) in (**d**). Here, four different assays are shown, each performed once.

4.3.3 Structural and solubility properties of ACMs and their effect on PC-12 cell viability

ACMs were designed to mimic a structure similar to what Aβ40 can obtain in its fibrillar context. As the Aβ40 fibril core contains the Aβ(15-40) segment which is also important for the Aβ40-IAPP cross-interaction, this structural feature was assumed to be possibly important for Aβ40-derived IAPP inhibitors. Therefore, CD experiments were performed next to investigate the structures of ACMs and related non-inhibitory ADPs in order to maybe correlate a specific structural feature with the observed inhibitory properties. When comparing the CD spectra of Nle3 with the two ACMs Nle3-VF and Nle3-LF and the corresponding non-inhibitory peptides Nle3-GG and Nle3-GI, it turns out that introducing the G29G33 methylation pair in Nle3-GG results in a significantly less ordered peptide showing high amount of random coil content and some remaining β-sheet content (minima at ~200 nm and ~216 nm)[143] (Figure 4-17a). In contrast, introducing the N-terminal methylation pairs V18F20 and L17F19 or the C-terminal methylation pair G29I31 seems to lead to a rearrangement of the peptide from a β-sheet into a β-turn (minima shift from ~216 nm to ~ 225 nm)[143], with Nle3-VF being the most ordered one. Since β-sheet structures are known to present some spectral diversity in CD, this red-shift of the minima could alternatively be due to a change in β-sheet orientation (parallel/antiparallel) or twisting[145]. Therefore, this structural feature (minimum at ~225 nm) will be further referred to as "β-sheet/β-turn" structure. Also, all other ACMs display a β-sheet/β-turn structure, whereas their respective non-inhibitory control ADPs VGS-VF and VGS-LF additionally present significant amounts of random coil (Figure 4-17b,c). Similar results were found for V18F20- and L17F19-methylated non-inhibitory ADPs comprising small, or hydrophilic LTS (G3-VF, R3-VF and R3-LF) and the C-terminally *N*-methylated non-inhibitory ADPs VGS-GG, VGS-GI, R3-GG and R3-GI (Figure 4-17d,e). This indicates that an ordered β-sheet/β-turn structure is important for the ACMs' inhibitory effect towards IAPP. Nevertheless, this feature alone is not enough to define an inhibitor as e. g. the ACM Nle3-LF and the non-inhibitory ADP Nle3-GI have almost identical structures, but Nle3-GI seems to inhibit IAPP only at 10-fold excess or higher (see Figure 4-16c).

To analyse oligomerisation and solubility properties of ACMs and related non-inhibitory ADPs, CD spectra were recorded using increasing peptide concentrations. Nle3-LF, L3-VF, and L3-LF gained slightly more β-sheet/β-turn structure content when the concentration was increased from 5 µM to 10 µM, while other ACMs did not display differences (Figure 4-18). The decrease in signal intensity of the minimum at ~225 nm indicated that all 6 ACMs started to form soluble oligomers when their concentration was increased from 10 µM to 20 µM, but no precipitates were observed (Figure 4-18). For Nle3-VF, no insoluble aggregates were even observed at 100 µM. All other ACMs formed insoluble aggregates at 50 µM which precipitated in the cuvette. The non-inhibitory ADPs VGS-VF and VGS-LF showed similar properties as ACMs (Figure 4-18).

Next, ACMs and non-inhibitory ADPs were tested for cell-damaging effects on PC-12 cells. When incubated for 4 days at 100 µM and applied onto the cells at 20 µM, none of the 6 ACMs showed toxicity, while Aβ40 control lowered cell viability to approx. 60 % (Figure 4-19a). To investigate influences of different methylation pairs in peptides with different LTS in more detail,

peptides were additionally incubated at a 10-times higher concentration (1 mM) and tested once more for cytotoxic effects. In general, only the introduction of the N-terminal V18F20 methylations led to an increased cell damaging effect of ADPs compared to the non-methylated controls, while other methylation pairs did not show a negative effect (Figure 4-19b-e). One exception was observed when the G29G33 methylations were introduced to Nle3: this methylation pair rendered the peptide toxic even when diluted to 500 nM before applied onto the cells (Figure 4-19b and Figure 7-11 in Appendix).

Taken together, the introduction of the V18F20 methylation pair has advantageous and disadvantageous effects on ADPs. While they help to keep a more ordered structure in peptides with hydrophobic Nle3 or L3 LTPs compared to the L17F19-methylations (Figure 4-17b,c), they simultaneously increase ADP cytotoxicity when the peptides are incubated at higher concentrations (1 mM). Since an ordered β-sheet/β-turn structure seems to be important for ACMs to inhibit IAPP, this highlights the importance of keeping a balance between inducing certain structural features to the peptide and trapping it in a toxic conformation when adjusting the peptides' structure for improved IAPP inhibition. As ACMs needed to be applied at a concentration of only 33 µM (2-fold excess regarding IAPP at 16.5 µM) but the V18F20-methylation did not increase peptide cytotoxicity when ACMs were incubated at concentrations up to 100 µM, it still can be concluded that the beneficial effects of introducing this methylation pair exceed the disadvantageous one.

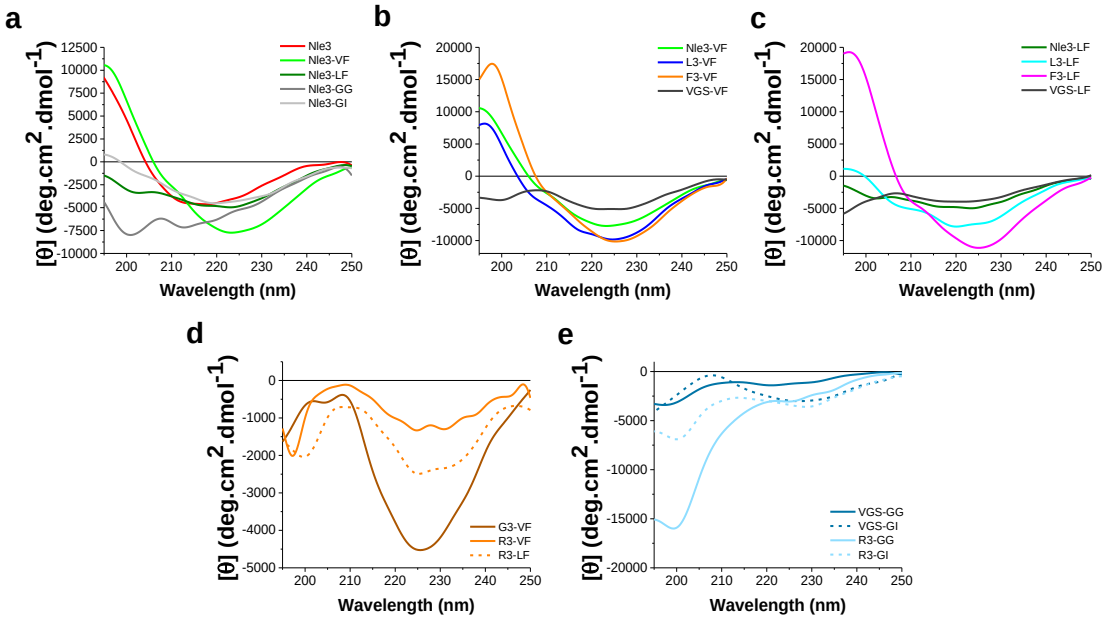

Figure 4-17: CD spectra of ACMs and non-inhibitory ADPs. CD spectra of 5 µM peptides were measured in 1xb containing 1 % HFiP, pH 7.4. Baseline signals were subtracted from all measurements. (a) Introduction of N- or C-terminal methylation pairs induce structural changes in Nle3. The structure of Nle3 was analysed also before by Martin Ortner during his Bachelor thesis[141]. Spectra of Nle3-LF, Nle3-GG, and Nle3-GI are from my Master thesis[142]. (b) V18F20 methylated ACMs show higher structural order than the control ADP VGS-VF. (c) L17F19 methylated ACMs show higher structural order than the control ADP VGS-LF. The structure of F3-LF was also investigated by Sophia Prem during her Bachelor thesis[146]. The spectrum of Nle3-LF is from my Master thesis[142]. (d) V18F20- or L19F20-methylated peptides comprising small or hydrophilic LTS are partially unstructured. Experiment for R3-VF was taken over from Sophia Prem's Bachelor thesis[146]. The structure of R3-LF was also investigated by Sophia Prem during her Bachelor thesis[146], the structure of G3-VF was also investigated by Sophia Kalpazidou during her Erasmus internship[147]; results were similar. (e) G29G33 or G29I31 methylated ADPs containing the native LTS or the R3-LTS show high random coil content. These spectra are from my Master thesis[142]. Data in figure parts b) and c) is part of a figure in reference [140].

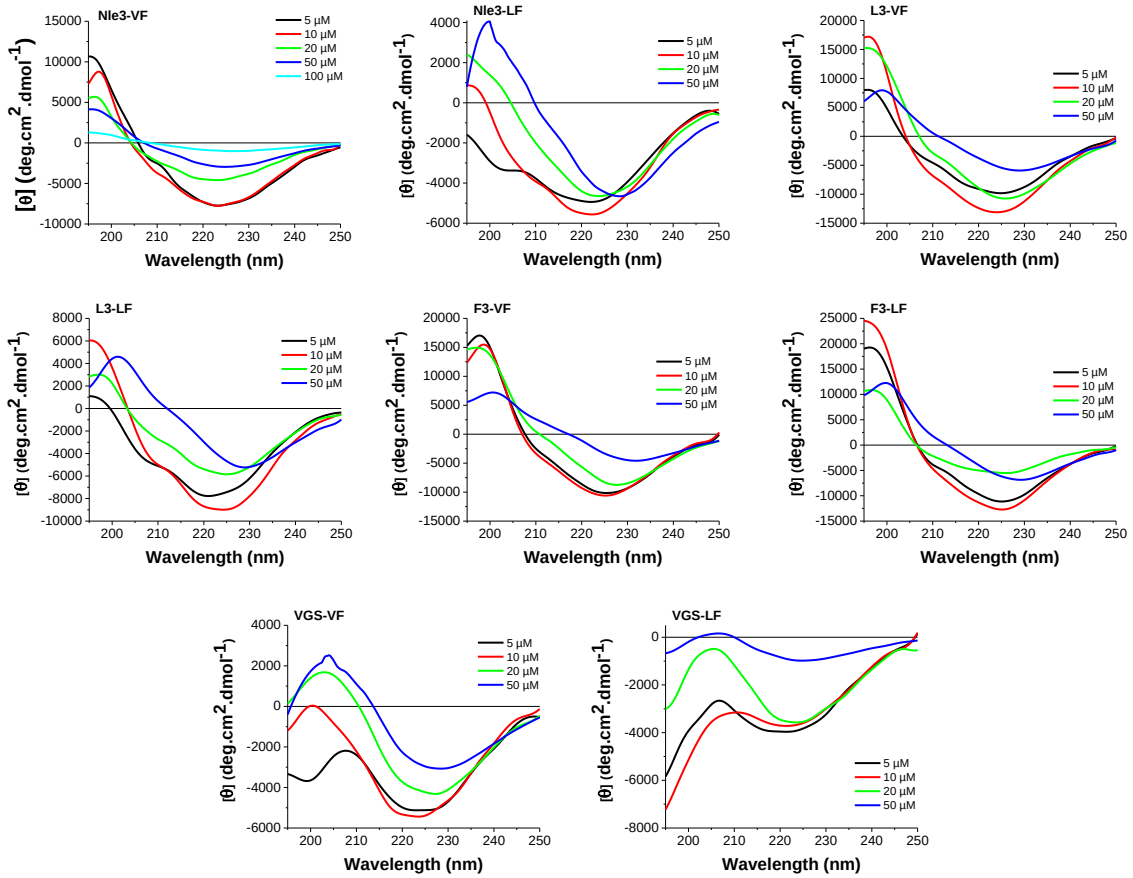

Figure 4-18: Concentration-dependent CD spectra of ACMs and non-inhibitory control ADPs VGS-VF and VGS-LF. CD spectra of the peptides were measured in 1xb containing 1 % HFiP, pH 7.4. Baseline signals were subtracted from all measurements. Nle3-VF did not show insoluble aggregates at 100 µM, while all other ACMs and the non-inhibitory control ADPs VGS-VF and VGS-LF formed insoluble oligomers at 50 µM which precipitated in the cuvette. Concentration-dependent structural properties of Nle3-LF were also studied during my Master thesis[142]. The CD spectrum of F3-LF was also measured previously by Sophia Prem during her Bachelor thesis[146]. Data of Nle3-VF is part of a figure in reference [140].

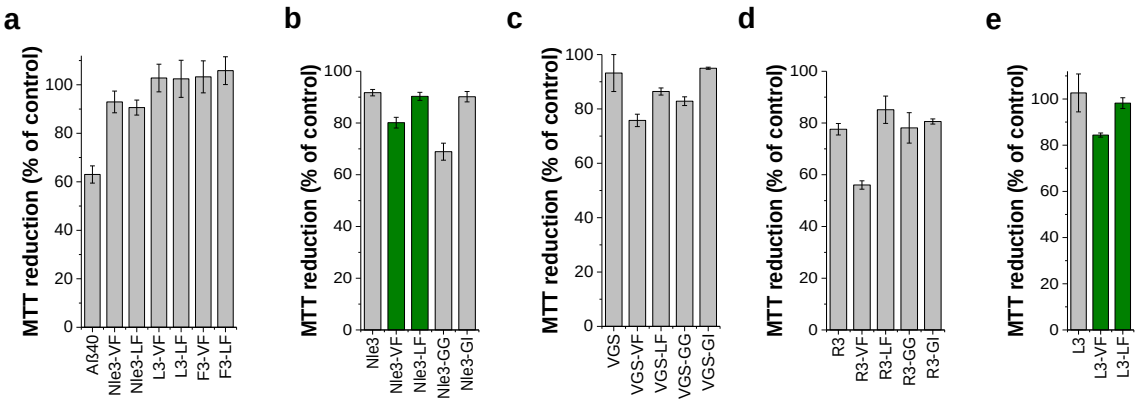

Figure 4-19: Effects of second set ADPs on cell viability of PC-12 cells. (**a**) Aβ40 and peptides were incubated at 100 µM for 4 days in 1xb containing 1 % HFiP, diluted into cell medium and applied at 20 µM into cultured PC-12 cells. ACMs display no cytotoxicity compared to Aβ40 control. (**b-e**) Peptides were incubated at 1 mM for 4 days in 1xb containing 1 % HFiP. Following dilution into cell medium, peptides were applied at 20 µM into cultured PC-12 cells. ACMs are highlighted in green. Depending on linker sequence, N- or C-terminal methylations influence the peptides' toxicity differently. Error bars represent means ± SD from three assays, n=3 each. Values were corrected for effects of buffer alone (1xb 1 % HFIP. Experiment for R3-VF was taken over from Sophia Prem's Bachelor thesis[146]. Cytotoxic effects of R3-LF were also investigated by Sophia Prem during her Bachelor thesis[146], the data presented in the figure are from my studies. Cytotoxic effects of the ADPs Nle3, Nle3-LF, Nle3-GG, VGS, VGS-GG, VGS-GI, R3, R3-GG, and R3-GI are from my Master thesis[142]. Data of a) is part of a figure in reference [140].

4.3.4 ACMs supress fIAPP-self- and fAβ40(42)-cross-seeded IAPP amyloid self-assembly

As ACMs proved to effectively inhibit IAPP fibril formation when mixed at pre-nucleated stages, it was next tested if their presence prevents IAPP also from accelerated fibrillation induced by pre-formed IAPP seeds. For this, IAPP (12 µM) was mixed with V18F20-*N*-methylated ACMs and the non-inhibitor VGS-VF (IAPP:ADP 1:2) and the mixtures were seeded by adding 10 % of preformed IAPP seeds (fIAPP). fIAPP significantly accelerated IAPP fibril formation, whereas fibril formation was suppressed in the presence of ACMs (Figure 4-20a). Also VGS-VF was able to block the fIAPP-mediated seeding effect but could not block IAPP fibrillation. Control experiments with incubations containing either ACMs alone or ACMs in presence of 10 % fIAPP showed that fIAPP does not induce fibril formation in case of ACMs (Figure 4-20a). Additionally, IAPP aggregation can also be induced by fAβ-mediated cross-seeding *in vitro* and *in vivo*[79,88]. Since IAPP self-seeding could be blocked by ACMs, their potential in blocking cross-seeding by fAβ42- and fAβ40 was also investigated. Similar to the previous experiments, IAPP (12 µM) was mixed with ACMs or VGS-VF (IAPP:ADP 1:2) and the mixtures were seeded with 10 % preformed Aβ42 or Aβ40 seeds. IAPP fibril formation was significantly accelerated by fAβ42 and fAβ40, but in presence of ACMs no seeding effect was observed, and fibril formation was blocked (Figure 4-20b,c). As found for IAPP self-seeding, VGS-VF could also

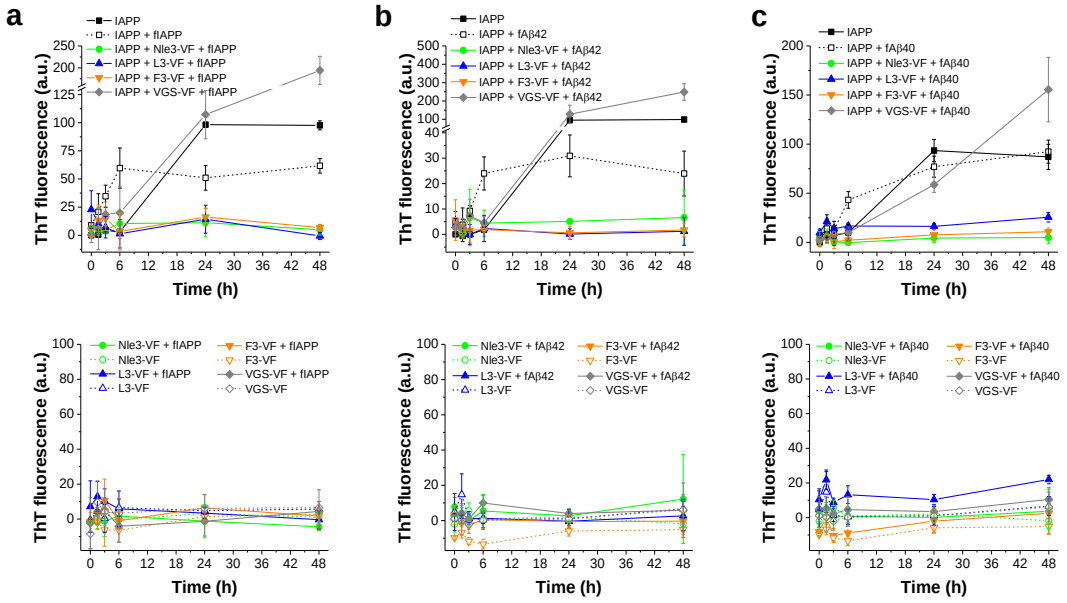

Figure 4-20: Inhibition of self- and cross-seeded IAPP by ACMs. (**a**) *Top,* Fibril formation of IAPP (12 µM) and IAPP/ADP mixtures (1:2) was followed via ThT binding in absence and presence of IAPP seeds (fIAPP, 10 %). Incubations were prepared in ThT assay buffer containing 0.5 % HFiP. Note: y-axis is interrupted. *Bottom,* Peptides (24 µM) were incubated as controls with and without 10 % fIAPP under the conditions described above. No seeding effect was observed for controls. Error bars represent means ± SD from three independent assays. As 10 % IAPP seeds showed ThT binding, buffer and seed values were subtracted from all measurements. Data was normalized to highest and lowest IAPP values in each assay. (**b**) *Top,* IAPP fibrillation (IAPP 12 µM) was followed in presence and absence of Aβ42 seeds (10 %) by ThT binding. Seeded mixtures (IAPP:peptide = 1:2) were incubated in parallel. Incubations were done in ThT assay buffer containing 0.5 % HFiP. Note: y-axis is interrupted. *Bottom,* As controls, peptides (24 µM) were incubated with and without Aβ42 seeds (fAβ42, 10 %) under the same conditions. No seeding effect was observed for controls. Error bars represent means ± SD from three independent assays (exceptions: IAPP and IAPP + fAβ42 n=6 independent assays). As 10 % Aβ42 seeds showed ThT binding, buffer and seed values were subtracted from all measurements. Data was normalized to highest and lowest IAPP values in each assay. (**c**) *Top,* Fibril formation of IAPP (at 12 µM) and IAPP/ADP mixtures was followed via ThT binding in absence and presence of Aβ40 seeds (fAβ40, 10 %). Incubations were done in ThT assay buffer containing 0.5 % HFIP. *Bottom,* Peptides were incubated at 24 µM with and without 10 % fAβ40 as controls under the same conditions. No seeding effect was observed for controls. Error bars represent means ± SD from three assays. Data was normalized to highest and lowest IAPP values in each assay. Data of upper panels of a) and b) is part of a figure in reference [140].

block the fAβ42- and fAβ40-mediated cross-seeding effect but failed to inhibit IAPP fibril formation. Despite that ACMs are derived from the Aβ40 sequence, neither fAβ42 nor fAβ40 could induce fibril formation when incubated with the peptides. Taken together, these results show that ACMs cannot only block IAPP fibrillation when applied at pre-nucleated stages but also can inhibit when fibril formation is favoured in presence of preformed seeds. This might be due to the formation of a non-seedable IAPP-ACM complex or to ACMs' binding to the seeds' surface.

4.4 The presence of ACMs leads to the formation of ThT-negative fibrils in mixtures with IAPP

Since ACMs were found to be potent inhibitors of IAPP amyloidogenicity by ThT binding assays and MTT reduction assays, results should be additionally verified by transmission electron microscopy (TEM). Surprisingly, TEM imaging did not only reveal fibrils being present in samples of IAPP alone and mixtures with non-inhibitory peptides but also in 7 days aged IAPP/ACM mixtures despite their negative ThT-binding result. To increase the reliability of the TEM-based conclusions regarding the presence of fibrillar assemblies as major species, 10-30 squares/grid were usually examined for this kind of studies. Interestingly, samples taken at earlier stages (24 h) only presented amorphous aggregates (Figure 4-21).

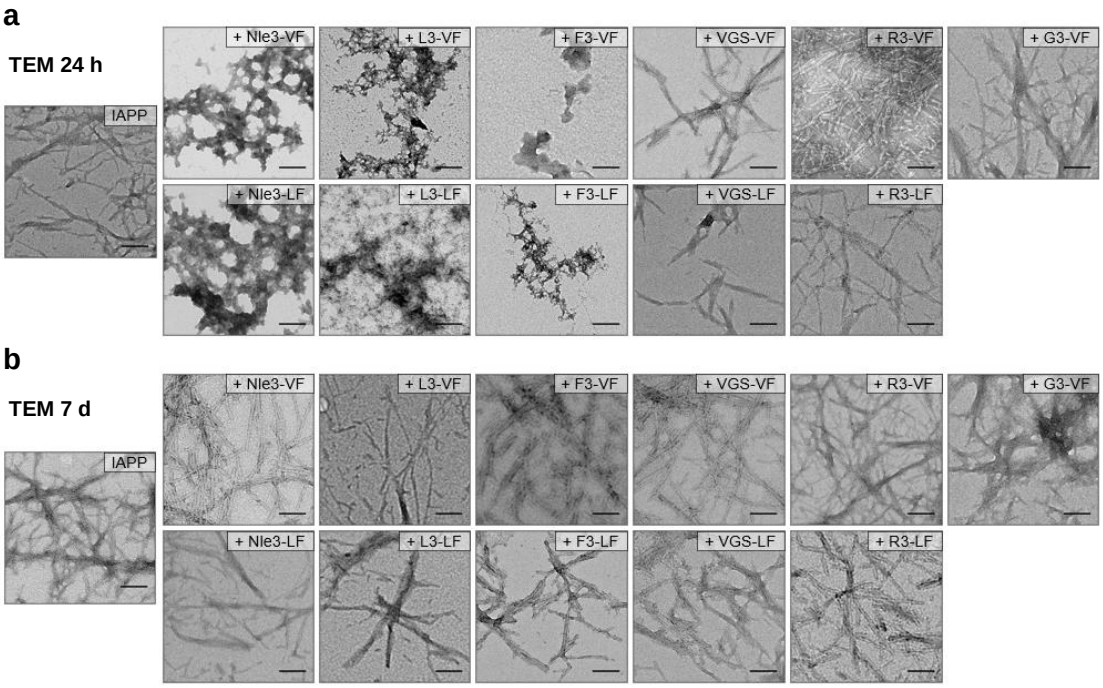

Figure 4-21: TEM pictures of IAPP and mixtures with ADPs. Negative stain TEM imaging was performed of samples containing either IAPP (16.5 µM) or IAPP/ADP mixtures (1:2) after 24 h (**a**) and 7 days (**b**) incubation. Samples were taken from respective ThT binding assay incubations (in ThT assay buffer with 0.5 % HFIP). Scale bars are 100 nm. Images of IAPP and IAPP + ACMs in a) and of IAPP, IAPP + ACMs, and IAPP + VGS-VF in b) are part of a figure in reference [140].

Even though the ACM design makes it rather unlikely that these fibrils are fibrils consisting only of ACM, this possibility should be excluded by TEM analysis of peptides incubated in isolation under the exact same conditions used for ThT binding and MTT reduction assays (33 µM, ThT assay buffer 0.5 % HFiP). TEM imaging of samples taken after 7 days incubation showed that ACMs do not form fibrils under these conditions (Figure 4-22a). In addition, ACMs were also incubated at a 3-fold increased concentration (100 µM in 1xb 1 % HFiP, 4 days) but no fibrils were found when samples were analysed via TEM (Figure 4-22b). Also, no fibrils were found when the non-inhibitory ADP VGS-VF was incubated in isolation (Figure 4-23). Thus, fibrils found in aged IAPP/ACM mixtures are not due to a fibril formation of ACMs themselves.

Since IAPP fibrils bind strongly ThT, fibrils found in IAPP/ACM mixtures could be fIAPP which escaped quantification by the ThT binding assay. This could have different reasons like (a) insufficient fibril quantification ability of the ThT binding assay or (b) competitive binding of ACMs and ThT to fibrillar IAPP hindering detection of fIAPP by ThT. Additionally, a “kinetic problem” could exist, meaning: ACMs are able to drastically reduce IAPP’s aggregation speed (lag-time at least 7 d longer) but after 7 days of incubation IAPP might slowly start to fibrillate nevertheless due to a weakening of inhibitor function. This would be invisible as the assay is generally stopped at 7 days but could be the reason for the presence of fibrils on grids of 7 days samples.

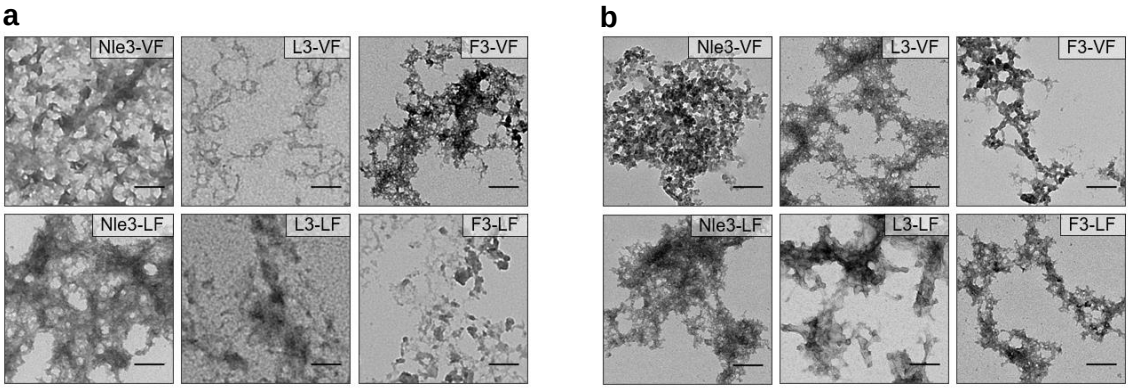

Figure 4-22: TEM pictures of ACMs incubated in isolation. Fibril formation of ACMs was excluded under two different conditions. ACMs were incubated in isolation either at 33 µM for 7 days (in ThT assay buffer 0.5 % HFiP corresponding to IAPP inhibition conditions) (**a**) or at 100 µM for 4 days (in 1xb 1 % HFiP) (**b**). Scale bars are 100 nm. Images of b) are part of a figure in reference [140].

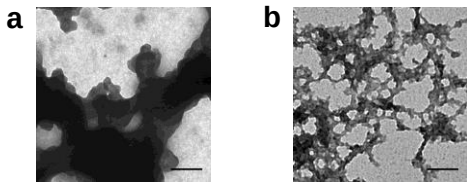

Figure 4-23: TEM pictures of the non-inhibitory ADP VGS-VF incubated in isolation. Fibril formation of VGS-VF was excluded under two different conditions. VGS-VF was incubated in isolation either at 33 µM for 7 days (in ThT assay buffer 0.5 % HFiP corresponding to IAPP inhibition conditions) (**a**) or at 100 µM for 4 days (in 1xb 1 % HFiP) (**b**). Scale bars are 100 nm.

Before ensuring that the ThT binding assay system is quantitative and sensitive enough to detect also smaller fibril quantities it was confirmed that similar IAPP amounts are present in samples of IAPP and IAPP/ACM mixtures used for ThT measurements (aliquots removed incubations made in from Eppendorf tubes). To investigate this, a newly developed antibody which specifically recognises fibrillar IAPP was used. Dot blot assays confirmed that this antibody (anti-fIAPP Cl. 91E7, Synaptic Systems[29,98]) is indeed able to detect fIAPP, while the normally used anti-IAPP antibody (from Peninsula, see chapter 3.1.7) mostly detects monomeric IAPP (Figure 4-24a). Equal volumes (containing 1.3 µg IAPP) of either freshly prepared or 7 days aged solutions of IAPP alone or its mixture with Nle3-VF (1/2) were dotted onto nitrocellulose membranes. Incubations were prepared in two different buffer systems mainly used in all other experiments: buffer 1 (ThT assay buffer containing 0.5 % HFiP) and buffer 2 (10 mM sodium phosphate buffer, pH 7.4 (1xb)). Membranes with freshly prepared samples (containing mainly monomeric IAPP) were developed using the standard anti-IAPP antibody, membranes with 7 days aged samples (containing mainly fibrillar species) were developed using the anti-fIAPP antibody. Similar spot intensities for both samples (IAPP alone vs. mix) indicate similar amounts taken from the incubation solution, excluding that differences in ThT signal intensities are due to different peptide amounts (Figure 4-24b).

Next, the fibril quantification ability of the ThT binding assay was examined. For this, IAPP fibrils were prepared at a concentration of 16.5 µM (7 days in ThT assay buffer 0.5 % HFIP) and serially diluted down to 0.165 µM. ThT measurements (with 20 µM ThT in 50 mM Glycin/NaOH) showed linear behaviour and a signal different from buffer control at 3.3 µM (20 %) (Figure 4-24c), confirming that the assay system is sufficiently quantifying fibrillar species. Of note, no fibrils could be detected when freshly made (0 h) IAPP solutions or IAPP/ACM solutions used in the ThT binding assay were examined by TEM (Figure 4-24d), suggesting that fibrils found in 7 days aged IAPP/ACM mixtures are not due to minor fIAPP amounts (<10 %) present already at 0 h.

To exclude that ACMs are competing with ThT for binding to IAPP fibrils and thereby make them “invisible” for the assay system, ThT measurements of 4 days aged solutions (in ThT assay buffer 0.5 % HFiP) of IAPP and its mixture with Nle3-VF (1/2) were performed using a 20 µM ThT solution and a 200 µM ThT solution (10x higher concentrated than usually). No significant differences were observed (Figure 4-24e). It was further confirmed that ThT binding ability of fIAPP does not change in the presence of inhibitors by measuring ThT fluorescence of IAPP fibrils before and after coating with ACMs. Therefor, inhibitors Nle3-VF and F3-VF were added (1/2) to preformed IAPP fibrils (9 days aged IAPP) and following incubation of the mixture for 24 h, ThT was added, and ThT binding was determined. No difference between ThT binding of fIAPP before and after addition of the inhibitors was found (Figure 4-24f).

To address the possible “kinetic” issue, several different strategies were followed: 1) The IAPP:ACM ratio was increased from 1:2 to 1:5. In the case fibrils found in the IAPP/inhibitor 1/2 mixtures were fIAPP formed due to a reduced inhibitor function in 7 days aged solutions, they should disappear when higher inhibitor/IAPP ratios are applied. This did not prove true. ThT-negative fibrils of similar appearance to fIAPP were major species in the 7 days aged mixtures even when inhibitors were present at a 5-fold excess (Figure 4-24g). 2) The IAPP concentration was reduced from 16.5 µM to 6 µM by keeping an IAPP:ACM ratio of 1:2. Using

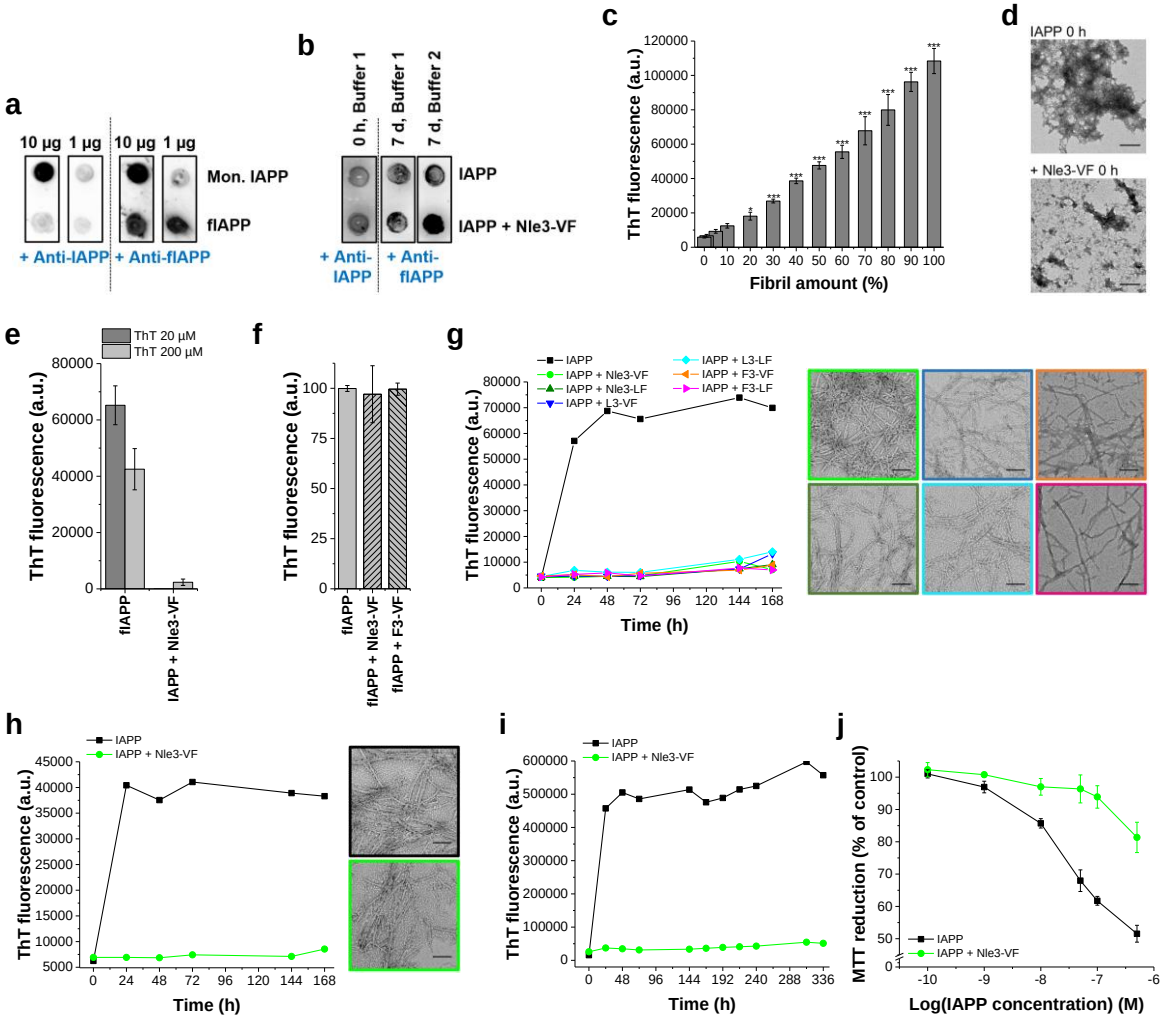

Figure 4-24: Fibrils in 7 days aged mixtures of IAPP and ACMs are no artefact. Dot blot assay confirming fibril specificity of anti-fIAPP antibody (Cl. 91E7). IAPP monomers (0 h) and fibrils (7 days) (128 µM) were prepared in ThT assay buffer 0.5% HFiP and spotted onto nitrocellulose membranes at indicated amounts. The fibril-specific anti-fIAPP antibody shows fibril binding whereas the anti-IAPP antibody mainly detects monomeric IAPP. Experiment for anti-fIAPP is representative of 4 different, experiment with anti-IAPP was done 1x as control. (**b**) Dot blot assay confirming similar peptide amounts taken out from incubations used for ThT binding, MTT reduction, and TEM experiments. Incubations were prepared in ThT assay buffer 0.5 % HFiP (Buffer 1) or 1xb (Buffer 2) and contained IAPP (16.5 µM) or its mixtures with Nle3-VF (1:2). Equal volumes (20 µl) were taken from both solutions and spotted onto nitrocellulose membranes (1.3 µg IAPP). Freshly prepared samples (containing mostly monomers) were revealed using the anti-IAPP antibody, 7 days aged samples (containing fibrillar species) were revealed using the fibril-specific anti-fIAPP antibody. Similar spot intensities for IAPP and mixture indicate similar amounts taken out. Assays were performed 1x in each buffer. (**c**) ThT binding study to test the sensitivity of the assay system. Fibrillar IAPP (16.5 µM, 7 days, in ThT assay buffer 0.5 % HFiP) was serially diluted into ThT assay buffer 0.5 % HFiP. ThT signals significantly different from buffer background were found for fIAPP concentrations >3.3 µM (20 %)). Error bars: means ± SD from three assays. *** P<0.01, * P<0.05 (one-way ANOVA & Bonferroni). (**d**) TEM images from IAPP (16.5 µM) and its mixture with Nle3-VF (1:2) at t=0 h. Samples were taken from incubations in ThT assay buffer (0.5 % HFiP). Scale bars: 100 nm. (**e**) ThT binding assay to examine possible competition between ThT and peptide binding to IAPP fibrils. IAPP (16.5 µM) or its mixture with Nle3-VF (1:2) were incubated in ThT assay buffer 0.5 % HFiP for 96 h. ThT fluorescence was measured after using two differently concentrated ThT solutions: 20 and 200 µM (in 50 mM Glycin /NaOH). Measurements with 10x higher concentrated ThT did not show higher ThT fluorescence in mixtures as usually observed (with 20 µM ThT), excluding a competitive effect of fibril binding between ThT and peptide. Error bars: means ± SD, n=3. Buffer values were subtracted. (**f**) ThT binding assay to investigate if coating of fibrillar IAPP by ACMs hinders ThT binding. IAPP fibrils (16.5 µM) were probed for ThT reactivity before and 1 day after coating with Nle3-VF and F3-VF (1:2). Error bars: means ± SD, n=3. Values were normalized to IAPP. (**g**) ThT binding assay using higher ACM ratios to exclude kinetic effects in fibril formation. Incubations were prepared in ThT assay buffer 0.5 % HFiP. IAPP was 16.5 µM, mixtures were 1:5. Assay was performed 1x. TEM samples of mixtures were taken after 168 h incubation. Colors correspond to colors in ThT binding assay. Scale bars: 100 nm. (**h**) ThT assay using a lower IAPP concentration to exclude kinetic effects in fibril formation. Incubations were prepared in ThT assay buffer 0.5 % HFiP. IAPP was 6 µM, mixture was 1:2. Assay was performed 1x. TEM sample of IAPP and mixture were taken after 168 h incubation. Colors correspond to colors in ThT binding assay. Scale bars: 100 nm. (**i**) Long-duration ThT binding assay to exclude kinetic effects in fibril formation. Assay was performed in a microtiter plate system with final buffer conditions of 25 mM Nappi/ 50 mM NaCl/ 25 mM Glycin (NaOH)/ 0.25 % HFiP containing 113.4 µM ThT (pH 7.5). IAPP was 16.5 µM, mixture was 1:2. Experiment is representative of 4 assays (meaning 4 independent incubations prepared in 4 different wells). (**j**) MTT reduction assay after 14 days of incubation to confirm non-toxic properties of IAPP/Nle3-VF (1:2). Incubations for MTT were performed similarly to incubations for ThT in (i) but no ThT was added. Solutions were diluted into cell medium and incubated with RIN5fm cells. Assay was performed 1x in technical triplicate and is representative of two assays (meaning 2 independent incubations prepared in 2 different wells). Data in b), c), e), and f) is part of a figure in reference [140].

a lower IAPP concentration should decelerate fibril formation and thus decrease inhibitor weakening after 7 days so that no fibrils are found on TEM grids. But, samples taken from these IAPP/Nle3-VF mixtures after 7 days of incubation displayed fibrils even though ThT binding was found to be negative (Figure 4-24h). 3) The MTP assay system was used allowing a longer follow-up of the IAPP fibrillogenesis (up to 14 days). Should fibrils found in the 7 days aged IAPP/ACM mixtures be due to a time-dependent weakening of inhibitor function, significantly higher ThT binding (due to increased fIAPP amounts) would be expected to be found at 14 days. The lack of ThT binding in IAPP/Nle3-VF mixtures even after 14 days of incubation (Figure 4-24i) further confirmed the long-lasting effect of ACMs on IAPP fibrillogenesis and suggested that the fibrils found in 7 days aged IAPP/ACM cannot be explained by a time-dependent reduction of inhibitory potency. In addition, Nle3-VF showed still strong effects on formation of cytotoxic IAPP assemblies after 14 days substantiating its inhibitory potency (Figure 4-24j). Moreover, in the MTP assay system both inhibitor and ThT (1/~3.4) are present simultaneously from the beginning of the IAPP fibrillogenesis process thus allowing them to compete for IAPP binding. The fact that also in this assay system IAPP/ACM mixtures do not show ThT binding is further supporting the notion that ACMs do not block binding of ThT to fIAPP.

Since fibrils were found to be the main species in 7 days aged IAPP/ACM mixtures by TEM but no ThT binding could be measured for these incubations even though it was shown that the assay system is sensitive enough to recognize also smaller fibril amounts, HPLC analyses of soluble fractions were performed to finally ascertain fibrils being indeed the main species. For this, IAPP (16.5 µM) or its mixtures with Nle3-VF (1/2) were incubated as usually done for ThT binding assays (in ThT assay buffer 0.5 % HFiP, 7 d, 20 °C). Dot blot analysis of similarly prepared incubations (in 1xb, 7 d, 20 °C) using the fibril-specific anti-fIAPP antibody confirmed again that only fibrillar species can be detected in such samples (Figure 4-25a). After incubation for 7 days, solutions were centrifuged for 10 min at 20000 g and supernatants were subjected to HPLC analysis. It was proven before by ThT binding studies of soluble and insoluble fractions, that fibrillar IAPP is precipitating completely under the applied centrifugation conditions (Figure 4-25b). Soluble IAPP fractions in incubations containing only IAPP or mixtures with Nle3-VF were quantified by peak areas. The results show that after 7 days almost no soluble IAPP is left anymore in incubations containing only IAPP (Figure 4-25c). 7 days aged mixtures show, that only ~30 % of the total IAPP amount is still in solution, meaning that the main part is precipitated into fibrils. Similar results (20 % IAPP left in solution after 7d in mixtures) were obtained by using more gentle centrifugation conditions (5 min 10000 g) (data not shown). Of note, already at 0 h soluble fractions of mixtures contain significantly less IAPP compared to soluble fractions of IAPP alone, which might be a sign of the formation of big IAPP/ACM complexes (later confirmed by CL and SEC experiments, see chapter 4.5.2).

Taking together, all these results support the notion that the fibrils found in 7 days aged mixtures of IAPP and inhibitors are neither ACM fibrils nor fIAPP which escaped quantification or developed due to inhibitor weakening. Nevertheless, fibrils are the main species that is formed. Consequently, it was hypothesised that ACMs might inhibit IAPP by co-assembling with it into distinct fibrillar species (heterofibrils).

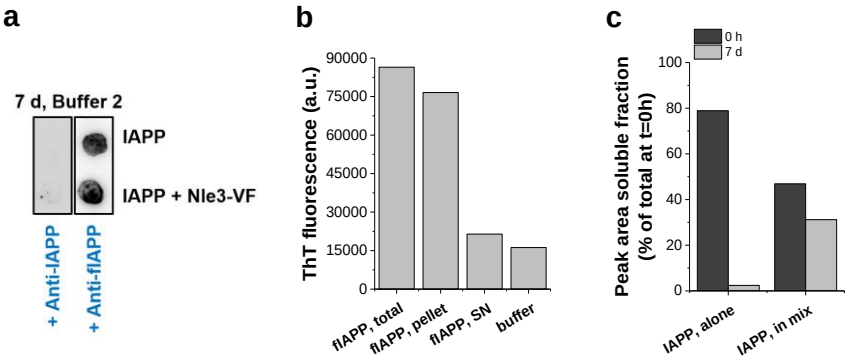

Figure 4-25: DB, ThT binding, and HPLC analyses confirming that fibrils are main species in aged IAPP/ACM mixtures. (**a**) Dot blot assay to confirm fibrillar species in 7 days aged samples. Incubations were prepared in 1xb (buffer 2) and aged for 7 days. Revealing samples (10 µg IAPP) with anti-IAPP anti-fIAPP (Cl. 91E7) antibodies showed that both samples only contain fibrillar species. Assay was performed once. (**b**) ThT fluorescence of pellet and supernatant (SN) fractions of fibrillar IAPP (16.5 µM) after 10 min centrifugation at 20000 g. Pellet was dissolved in assay buffer (ThT assay buffer 0.5 % HFiP) before mixing with ThT solution. SN and pellet were mixed with a 200 µM ThT solution (in 50 mM Glycin/NaOH). ThT fluorescence measurements were compared to non-centrifuged sample (fIAPP, total) and buffer control. Experiment was performed once and was done prior to the experiment shown in **c**, to ensure that the centrifugation conditions used in **c**, are sufficient to fully precipitate fIAPP. (**c**) Quantification of soluble IAPP amounts in incubations containing IAPP (16.5 µM) or its mixture with Nle3-VF (1:2) via HPLC. Incubations were prepared in ThT assay buffer 0.5 % HFiP and centrifuged 10 min at 20000 g. SN of 0 h or 7 days aged solutions were subjected to HPLC analysis and soluble IAPP content was quantified by peak areas. The sum of peak areas of IAPP SN and IAPP pellet at 0 h was considered as 100 %. Experiment is representative of 2.

4.5 Studies on the interaction and heterocomplex formation of ADPs with IAPP

4.5.1 ACMs show strong binding to monomeric IAPP

For dissecting a possible formation mechanism of IAPP/ACM-heterofibrils, firstly, fluorescence spectroscopy titrations were performed to gain information about peptides' self-assembly propensities and binding affinities toward IAPP. Experiments were carried out in 1xb containing 1 % HFiP using 5 nM N^{α}-aminoterminally fluorescein-labelled ADPs or IAPP (Fluos-IAPP). Apparent dissociation constants (app. k_Ds) of self-assembly of all ADPs were found to be in the low-nanomolar range, spanning from ~20 nM to ~200 nM with three exceptions: the peptides VGS-GG, VGS-GI and G3-VF did not self-assemble up to a concentration of 5 µM (Table 4-7). Notably, almost all other tested ADPs showed stronger self-assembly propensities than their parent Aβ40 (see x-fold changes in Table 4-7). Only Nle3 showed a similar self-assembly propensity. In contrast to the C-terminally methylated peptides VGS-GG and VGS-GI, the non-methylated analogue VGS and the N-terminally methylated analogues VGS-VF and VGS-LF showed very similar self-assembly properties (VGS: 16.8 ± 6.7 nM; VGS-VF: 24.2 ± 2.4 nM; VGS-LF: 78.9 ± 32.5 nM). This suggests that the self-association of these peptides involves their C-terminal part which gets blocked for interaction by introducing the G29G33- or G29I31-methylation. Interestingly, introduction of C-terminal methylations into the Nle3-linked peptide does not lead to a weakened self-assembly (Nle3-GG: 81.7 ± 1.9 nM; Nle3-GI: 28.5 ± 1.9 nM), indicating that the hydrophobic loop sequence might be sufficient to compensate for this effect. In case of G3-VF the lack of self-association might be due to its very flexible LTS, as all other ADPs comprising N-terminal methylations display strong self-interaction (see Table 4-7).

Table 4-7: App. k_Ds for self-assembly of ADPs and their binding to IAPP. Self-assembly was determined by titrations of synthetic N-terminally fluorescein-labelled ADPs (5 nM) with unlabelled ADPs. Bindings to Fluos-IAPP were determined by titrations of synthetic N-terminally fluorescein-labelled IAPP (5 nM) with unlabelled ADPs. Bindings to unlabelled IAPP were determined by titrations of synthetic N-terminally fluorescein-labelled ADPs (5 nM) with IAPP. Experiments were performed in 1xb containing 1 % HFiP. App. k_Ds are means (± SD) from three binding curves. Fluorescence emission spectra and binding curves can be found in Figure 7-12 to Figure 7-30 in the Appendix. See Table 7-14 to Table 7-16 in the Appendix for the three single app. k_Ds. Numbers in brackets give the approx. fold change compared to Aβ40 control. ACMs are highlighted in green. n.d.: not determined; No binding: no binding observed up to a ligand concentration of 5 µM; * done by Sophia Kalpazidou during her Erasmus internship[147]. Interactions of Fluos-IAPP with R3, R3-GG, R3-GI, Nle3, Nle3-GG, Nle3-GI, and Nle3-LF were studied during my Master thesis[142]. [a]: taken from reference [43], [b]: taken from reference [118], [c]: taken from reference [80]; [a], [b], and [c] show means ± SEM. Data of titrations of Fluos-IAPP with ACMs is included in a table in reference [140].

	Self-assembly	**IAPP**	**Fluos-IAPP**
Peptide	app. k_D (±SD) (nM)		
Aβ40	198 ± 43[a]	119 ± 13[b]	48.5 ± 4.2[c]
Nle3	198.1 ± 53.4 (1)	114.2 ± 10.6 (1)	198.5 ± 5.6 (4)
Nle3-VF	51.9 ± 4.5 (0.3)	17.8 ± 0.3 (0.2)	69.5 ± 1.4 (1.5)
Nle3-LF	24.1 ± 1.4 (0.1)	17.1 ± 0.7 (0.2)	55.4 ± 5.9 (1)
Nle3-GG	81.7 ± 1.9 (0.4)	7.1 ± 0.3 (0.1)	580.1 ± 24.8 (12)
Nle3-GI	28.5 ± 1.9 (0.1)	9.5 ± 0.6 (0.1)	236.5 ± 16.1 (5)
L3	34.1 ± 6.4 (0.2)	16.7 ± 0.2 (0.2)	80.5 ± 2.3 (1.5)
L3-VF	20.2 ± 0.6 (0.1)	6.1 ± 0.5 (0.05)	77.3 ± 2.9 (1.5)
L3-LF	48.1 ± 1.8 (0.2)	5.7 ± 0.1 (0.05)	143.2 ± 5.0 (3)
F3-VF	64.9 ± 11.6 (0.3)	13.1 ± 5.0 (0.1)	15.0 ± 1.9 (0.3)
F3-LF	47.0 ± 7.8 (0.2)	15.7 ± 3.9 (0.2)	37.6 ± 2.9 (1)
VGS	16.8 ± 6.7 (0.1)	5.00 ± 0.03 (0.05)	417.6 ± 23.3 (9)
VGS-VF	24.2 ± 2.4 (0.1)	1.8 ± 0.4 (0.01)	238.1 ± 4.2 (5)
VGS-LF	78.9 ± 32.5 (0.4)	1.3 ± 0.4 (0.01)	> 500
VGS-GG	No binding	> 5 µM	> 5 µM
VGS-GI	No binding	3.0 ± 1.3 (0.03)	154.1 ± 92.1 (3)
R3	n.d.	n.d.	154.6 ± 10.9 (3)
R3-VF	37.7 ± 9.1 (0.2)	9.9 ± 1.5 (0.1)	70.3 ± 17.9 (1.5)
R3-LF	20.8 ± 4.3 (0.1)	16.6 ± 4.6 (0.2)	41.6 ± 5.7 (1)
R3-GG	n.d.	n.d.	167.8 ± 18.7 (3.5)
R3-GI	n.d.	n.d.	539.1 ± 49.8 (11)
G3-VF	No binding	6.2 ± 3.1* (0.05)	49.6 ± 14.9* (1)

Since the app. k_Ds of self-assembly were higher than 5 nM for all tested ADPs, it can be assumed that by titrating 5 nM fluorescently labelled peptide with IAPP the binding to monomeric ADPs is followed. Except the binding of IAPP to Fluos-Nle3 (app. k_D 114.2 ± 10.6 nM) and to Fluos-VGS-GG (app. k_D >5 µM), all other titrations involving fluorescently labelled ADPs and IAPP resulted in app. k_Ds below or very close to the app. k_D found for IAPP self-association (~10 nM[19]) meaning that it is mainly a matter of monomer-to-monomer interaction (or peptide monomer to small IAPP oligomer) (Table 4-7). In addition, binding affinities were much stronger than for Aβ40 (except for Nle3 and VGS-GG; see x-fold changes in Table 4-7). Notably, binding affinities of IAPP towards fluorescently labelled ADPs did not show an observable trend linking the peptides' inhibitory property to their interaction potential. Therefore, next vice-versa titrations were performed using unlabelled ADPs and

fluorescently labelled IAPP (Fluos-IAPP, 5 nM). Under these conditions, IAPP was found to be present mainly as monomer[19]. Five out of six ACMs showed a strong binding to Fluos-IAPP (app. k_Ds <80 nM and similar to binding of Aβ40; see x-fold changes in Table 4-7), whereas most non-inhibitory ADPs bound significantly weaker (Table 4-7), indicating that binding to the IAPP monomer is crucial for the peptide's inhibitory potential. For the sixth ACM, L3-LF, an app. k_D of 143.2 ± 5.0 nM was calculated which is a little bit higher compared to the other ACMs. This correlates with the finding that L3-LF is the weakest out of all ACMs (a 2.5-fold molar excess is necessary to fully inhibit IAPP whereas all other ACMs show complete inhibition already at 2-fold excess). The fact that the non-inhibitors R3-VF, R3-LF and G3-VF bind to Fluos-IAPP with an affinity similar to ACMs (app. k_Ds 70.3 ± 17.9 nM, 41.6 ± 5.7 nM and 49.6 ± 14.9 nM, respectively) shows that binding to monomeric IAPP is very important for inhibition but is alone not enough to define an inhibitor. A similar conclusion was drawn already from CD experiments (see chapter 4.3.3), which revealed that an ordered β-sheet/β-turn structure is important for an inhibitory peptide, but this feature alone does also not determine an inhibitor. This suggests that an inhibitory peptide must be simultaneously equipped with the correct structure and a strong binding affinity towards monomeric IAPP. A random binding to IAPP is maybe not enough; a conformational selection might be necessary.

In conclusion, the binding studies indicate that inhibition by ACMs is based on a conformation-specific interaction involving an ACM conformer with ordered β-sheet/β-turn structure, which is able to bind a specific IAPP conformer. This IAPP conformer might be the one which is evolving prior to oligomer/fibril formation.

4.5.2 IAPP and ACMs form low- and high-molecular weight heterocomplexes

4.5.2.1 Heterocomplex formation revealed by CL experiments

For further investigations of heterocomplexes formed by IAPP and ADPs, glutaraldehyde-mediated cross linking (CL) of IAPP/ACM mixtures was performed followed by NuPAGE gel electrophoresis and Western blot (WB) analysis. For all three tested ACMs – Nle3-VF, L3-VF and F3-VF – the formation of low-molecular weight (LMW) heterocomplexes was observed accompanied by a huge smear in the upper part of the membrane caused by high-molecular weight (HMW) heterocomplexes (15 to >260 kDa) (Figure 4-26). Nle3-VF already showed formation of LMW heterocomplexes with IAPP already when applied at an equimolar ratio whereas for L3-VF and F3-VF a 2- or 4-fold molar excess was necessary. LMW heterocomplexes seemed to be hetero-dimers and -trimers as their bands migrated in between the IAPP monomer (MW=3901 g/mol) and dimer (MW=7802 g/mol) bands, and in between the IAPP dimer and trimer (MW=11703 g/mol) bands, respectively. Expected molecular weights for LMW IAPP/ACM heterocomplexes are summarised in Table 4-8. Molecular weights of LMW heterocomplexes were also estimated from their migration distance in the gel by using the protein standard as a reference. The results are shown in Table 4-9. The estimations might not be fully reliable since ACMs alone show an unnatural migration behaviour in the gels (see later in this chapter) and this might also affect ACM-containing heterocomplexes. Thus, it cannot be ruled out that the assumed hetero-trimer is actually a hetero-tetramer or a mixture

of both. Therefore, this species will be further referred to as “hetero-trimer/-tetramer”. In conclusion, the appearance of the mixtures is clearly different from the oligomerisation pattern observed for IAPP which mainly presents 1- to 7-mers and bigger oligomers ranging in mass from 30 to 80 kDa.

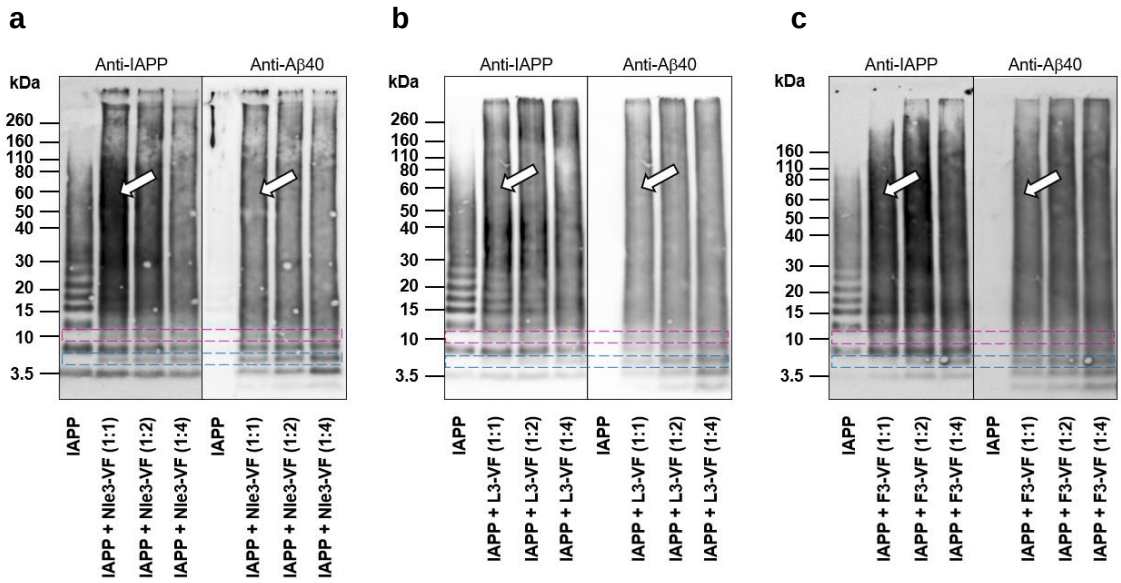

Figure 4-26: Concentration-dependence CL experiments of IAPP and its mixtures with ACMs. Characterisation of IAPP-peptide hetero-assemblies was performed via cross-linking with glutaraldehyde, NuPAGE gel electrophoresis and Western blot (WB) using an anti-IAPP antibody and an anti-Aβ40 antibody. Mixtures of IAPP (30 µM) and peptides (ratio 1:1, 1:2 or 1:4 as indicated) were incubated 30 min before cross linking. The highlighted areas between 3.5 and 10 kDa show hetero-dimer (blue) and -trimer/-tetramer (magenta) bands. Arrows highlight HMW hetero-assemblies. ACMs alone were not analysed in parallel in these gels/blots but representative results for the ACM Nle3-VF are shown in Figure 4-27. Results are shown for Nle3-VF (**a**), L3-VF (**b**) and F3-VF (**c**) and are representative of 6 experiments for Nle3-VF and of 3 experiments for L3-VF and F3-VF.

Table 4-8: Expected molecular weights of LMW hetero-assemblies formed by IAPP and ACMs. MWs of IAPP homoassemblies and hetero-assemblies with ACMs are sorted by their expected migration properties during gel electrophoresis. MW for ACM monomers can be found below for comparison.

	MW (g/mol)		MW (g/mol)		
	IAPP		**IAPP + Nle3-VF**	**IAPP + L3-VF**	**IAPP + F3-VF**
Trimer	11702.58				
		Hetero-tetramer 3	14456.25	14456.25	14558.21
		Hetero-tetramer 2	13309.06	13309.06	13512.98
		Hetero-tetramer 1	12161.87	12161.87	12467.75
		Hetero-trimer 2	10555.39	10555.39	10657.35
		Hetero-trimer 1	9408.20	9408.20	9612.12
Dimer	7801.72				
		Hetero-dimer	6654.53	6654.53	6756.49
Monomer	3900.86				
Nle3-VF monomer: 2753.67 g/mol		L3-VF monomer: 2753.67 g/mol		F3-VF monomer: 2855.63 g/mol	

Table 4-9: Experimentally determined molecular weights of IAPP/ACM hetero-dimers and -trimers/-tetramers observed in CL studies. Molecular weights were determined by measuring the migration length of the corresponding bands (see blue and magenta boxes in Figure 4-26; 1:2-mixtures were exemplary used) with ImageJ. Migration length was calibrated using the protein standard. Theoretical masses for IAPP/ACM hetero-dimers and -trimers/-tetramers can be found in Table 4-8.

	MW (g/mol)		
	IAPP + Nle3-VF	**IAPP + L3-VF**	**IAPP + F3-VF**
Hetero-dimer	5888	5830	6189
Hetero-trimer/-tetramer	8536	8344	8841

As the formation of LMW and HMW heterocomplexes with IAPP seems to be a common pattern observed for inhibitors, subsequently time-dependence CL experiments were performed to follow the development or possible changes of these complexes during the IAPP aggregation process. In accordance with previous ThT binding studies and MTT reduction assays, mixtures containing peptide at 2-fold molar excess were analysed and the following time points were chosen for cross linking: directly after mixing IAPP with the peptide (0 h) and after 24 h and 7 days of incubation. In the IAPP/Nle3-VF mixture LMW and HMW heterocomplexes are formed already at t=0 h (Figure 4-27a). The composition of the mixture is not noticeably changing by time, containing at 7 days still the same species which were found also directly after mixing. Also mixtures with other ACMs show a similar pattern when analysed after 7 days (Figure 7-48 in Appendix). Probing the membrane additionally with an anti-Aβ40 antibody confirmed the simultaneous presence of IAPP and Nle3-VF in the HMW heterocomplexes as for the same regions (> 110 kDa) in the IAPP and ACM control lanes no antibody binding was observed whereas the mixture stained for both peptides (Figure 4-27b). The heterogenic nature of the hetero-dimer and -trimer/-tetramer bands in the mixture is less obvious as also the ACM-alone control shows bands which migrated to similar levels. Nle3-VF presents one rather fade band below 3.5 kDa and three dominant ones between 3.5 kDa and 10 kDa (Figure 4-27b,c). The lowest band is supposed to represent the Nle3-VF monomer (MW = 2753.67 g/mol), the three higher bands are expected to contain dimeric (MW = 5507.34 g/mol), trimeric (MW = 8261.01 g/mol) and tetrameric (MW = 11014.68 g/mol) inhibitor. Interestingly, all three bands are found int the mass range of 3.5 to 10 kDa according to the molecular weight marker even though the Nle3-VF tetramer has a higher mass. Also, the Nle3-VF trimer band is running lower than expected, as it is actually assumed to run higher than or similar to the IAPP dimer (MW = 7801.72 g/mol) band. This unexpected behaviour might be explainable by the CL reaction itself: As Nle3-VF has three crosslinking-competent amino acids, intramolecular cross linking might occur. The denaturing step during the sample preparation procedure thus cannot convert the peptide anymore into its linear, fully extended form, which might lead to modified migration properties. As the peptide is not fully extended but partially folded it might appear smaller than it is.

Even though the Nle3-VF control presents similar bands compared to the mixture when analysed via the anti-Aβ40 antibody, direct comparison of the results for both antibody developments reveals small differences in the migration behaviour. While the third highest band found in the mixture when probed for Aβ is running at exactly the same level as the second highest band found in the mixture when probed for IAPP, the third highest band (trimer) in the Nle3-VF control is running a little bit higher (Figure 4-27c). Thus, the suspected hetero-dimer band found in the mixture can be claimed to indeed contain both IAPP and Nle3-VF as it has no corresponding equivalent in both peptide-alone control lanes. The same holds true for the hetero-trimer/-tetramer band.

Similar time-dependent experiments were performed with the non-inhibitory ADPs VGS-VF, Nle3-GG, R3-VF and G3-VF to investigate if the observations made so far for ACMs are indeed inhibitor-specific. Firstly, VGS-VF was tested. In fluorescence titration experiments this peptide showed a ~3.4-fold reduced affinity towards Fluos-IAPP compared to Nle3-VF suggesting that complex formation is less stable. Agreeing with these binding results, VGS-VF formed no

hetero-dimers and -trimers/-tetramers with IAPP and HMW hetero-assemblies were only observed at t=0 h but were not stable over time as found for ACMs (Figure 4-28a). As expected for a non-inhibitory ADP, the observed oligomerisation pattern in the mixture containing IAPP and VGS-VF was identical to IAPP when incubated alone at 24 h and 7 days as aggregation cannot be prevented. The development with the anti-Aβ40 specific antibody reveals that VGS-VF shows an oligomerisation pattern similar to Nle3-VF (3-4 bands in the mass range between 3.5 and 10 kDa) (Figure 4-28b). Alignment of bands found in 7 days aged solutions by probing for IAPP-containing (anti-IAPP) and by probing for VGS-VF-containing species (anti-Aβ40) further confirms absence of hetero-dimers and -trimers/-tetramers in the mixture: In the anti-IAPP development only bands are present which are also found in the IAPP-alone control and also all bands revealed by the anti-Aβ40 development can be attributed to bands found in the VGS-VF control lane which migrated to exact same levels (Figure 4-28c).

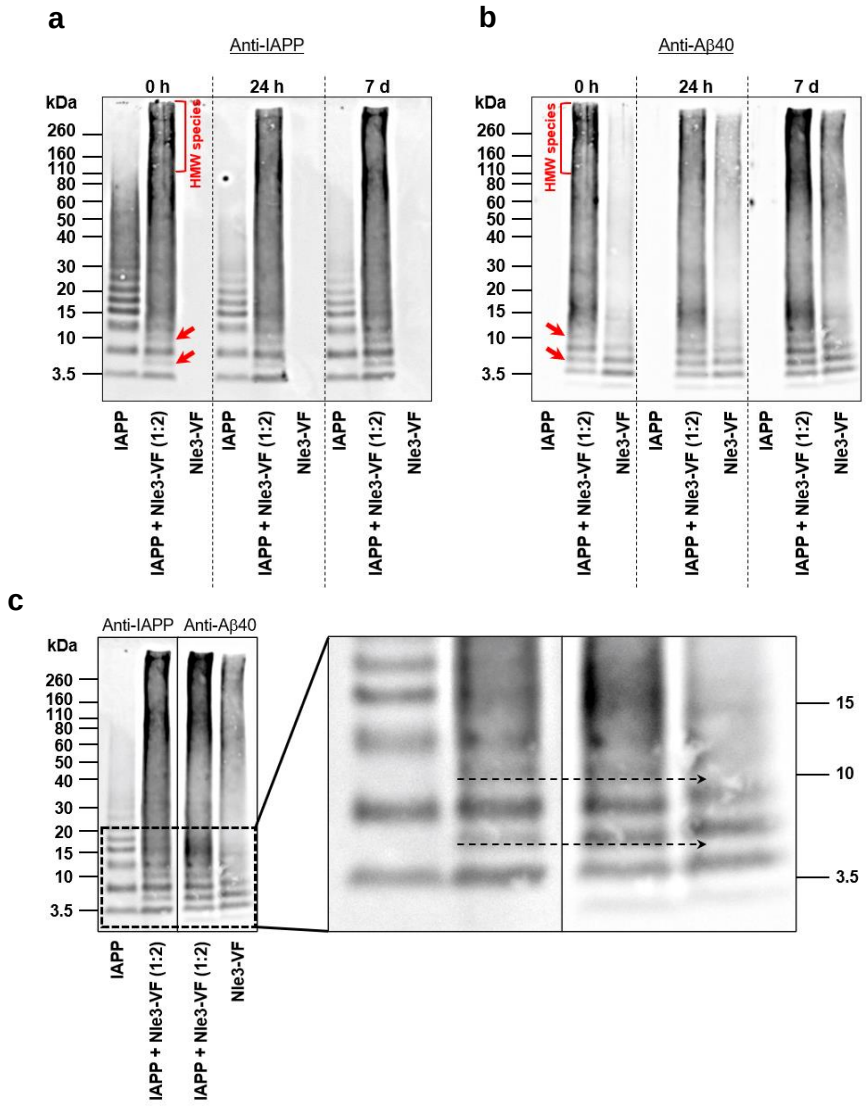

Figure 4-27: Time-dependent CL experiment of IAPP and its mixture with Nle3-VF. Glutaraldehyde-mediated cross linking was performed at indicated time points of samples containing either IAPP (30 µM), Nle3-VF (60 µM) or their mixture (1:2). Species were analysed by NuPAGE gel electrophoresis followed by Western blot analysis. Red arrows highlight hetero-dimers and -trimers/-tetramers, red brackets show HMW hetero-assemblies. (**a**) Membrane probed by anti-IAPP specific antibody. (**b**) Membrane probed by anti-Aβ40 specific antibody. (**c**) Direct comparison of both antibody developments at 7 days to confirm presence of both IAPP and Nle3-VF in the bands assumed to contain hetero-dimers and -trimers/-tetramers. Arrows in the magnified area highlight absence of Nle3-VF-related bands at the migration hight of the hetero-dimer and -trimer/-tetramer bands. Results are representative of 4 experiments. Data of a) and b) is part of a figure in reference [140].

Time-dependent CL experiments were also performed for mixtures of IAPP and the non-inhibitory ADP Nle3-GG sharing the same linker sequence with Nle3-VF but containing its methylation in the C-terminal peptide strand. Nle3-GG was found to form heterodimers and -trimers/-tetramers with IAPP at t=0 h similar to Nle3-VF but the hetero-dimer seems to be of a different nature/ conformation as it runs closer to the IAPP-dimer band than the one formed by IAPP and Nle3-VF (Figure 4-29a,b). The presence of both IAPP and Nle3-GG in the hetero-dimer is confirmed by direct alignment of the bands found in the anti-IAPP and the anti-Aβ40 development as the band of interest does not have a corresponding counterpart in one of the IAPP or Nle3-GG control lanes (Figure 4-29c). Additionally, the formation of HMW heterocomplexes at t=0 h is less pronounced than in mixtures with Nle3-VF or VGS-VF where also species >160 kDa were found. In case of Nle3-GG HMW heterocomplexes are only between 80 and 160 kDa in weight. As for VGS-VF, the heterocomplex formation is not permanently observed during time but the oligomerisation pattern of the mixture is adapting to the one observed for IAPP when inhibition is lost after 24 h/ 7 days. This is again in good agreement with the binding data which showed a ~8.3-fold decrease in binding affinity towards Fluos-IAPP for Nle3-GG.As the peptide R3-VF does not inhibit IAPP but shows a similar binding affinity towards Fluos-IAPP as Nle3-VF (chapter 4.5.1), the complex formation of this peptide with IAPP was investigated next. When freshly prepared mixtures (0 h) were crosslinked, mainly hetero-dimers and some bigger hetero-oligomers (mass between ~15 and 80 kDa) were found (Figure 4-30a). After 24 h and 7 days of incubation the oligomerisation pattern of the mixture looks identical to the one observed for IAPP as it was found also for the other non-inhibitors, with the exception that the hetero-dimer band is still present (but getting fader by time). In contrast to previously examined peptides, R3-VF mainly forms monomers and dimers as revealed by the anti-Aβ40 development of the membrane (Figure 4-30b). The mixture presents two bands at identical migration levels. Nevertheless, the heterogenic nature of the dimer in the mixture can be confirmed by having a closer look at the corresponding bands (Figure 4-30c): Only the upper half of the dimer band in the mixture has a corresponding signal in the anti-IAPP development whereas the lower half can be attributed to the R3-VF dimer as it does not show signal when developed anti-IAPP. The dimer band found in the mixture at t=0 h is thus most likely a combination of the R3-VF homo-dimer and the IAPP/R3-VF hetero-dimer. Due to very similar MWs (R3-VF homo-dimer: 5765.46 g/mol, IAPP/R3-VF hetero-dimer: 6783.59 g/mol) the two bands overlap and are not easily distinguishable. The finding that the hetero-dimer is still visible at 24 h and 7 days when R3-VF is not inhibiting IAPP anymore comes into good agreement with previously made observations from CD and fluorescence titration experiments. Even though R3-VF shows an app. k_D comparable to Nle3-VF and is able to form hetero-dimers with IAPP the resulting complex is not an inhibition-competent one as IAPP is able to “escape” from it and to self-aggregate thereafter which might be a result of the less ordered structure adopted by R3-VF. This indicates once more the importance of conformational specificity in the IAPP inhibition mechanism of ACMs.

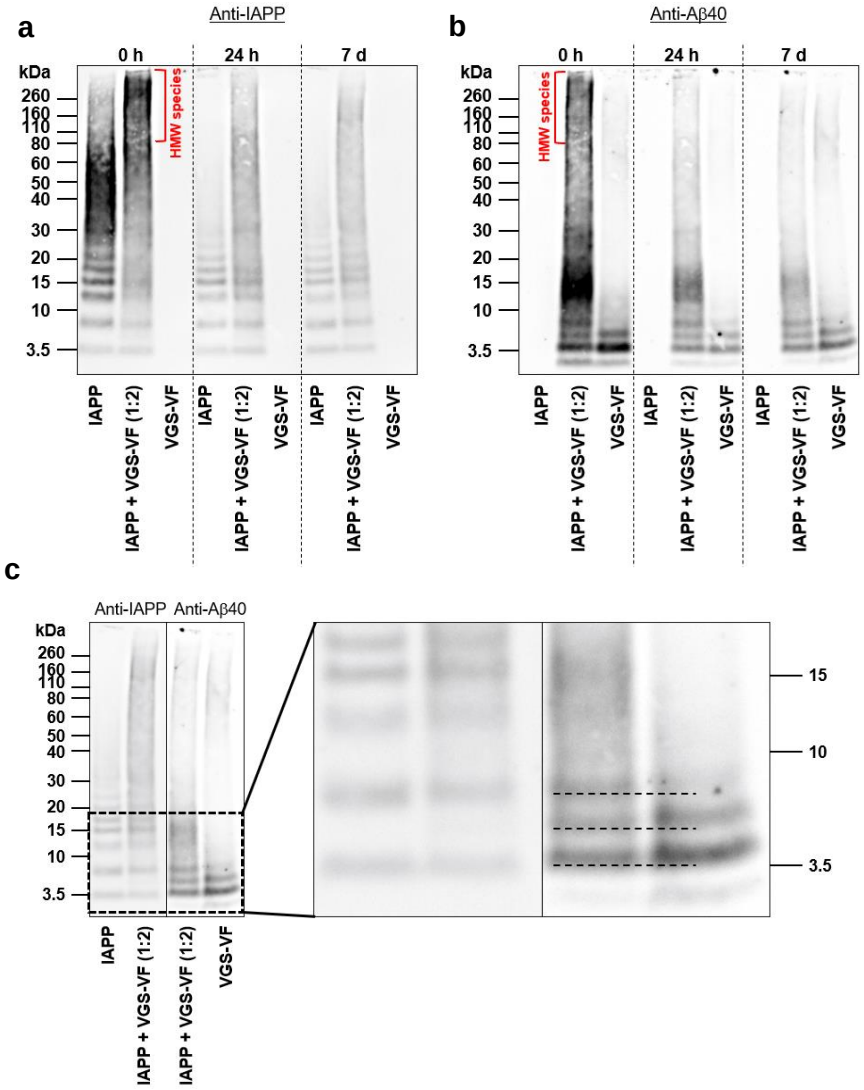

Figure 4-28: Time-dependent CL experiment of IAPP and its mixture with VGS-VF. Incubations containing either IAPP (30 µM), VGS-VF (60 µM) or their mixture (1:2) were cross linked at indicated time points using glutaraldehyde. Species were revealed by NuPAGE gel electrophoresis followed by Western Blot analysis using an anti-IAPP specific and an anti-Aβ40 specific antibody. Red brackets highlight HMW hetero-assemblies. (**a**) Membrane probed by anti-IAPP specific antibody. (**b**) Membrane probed by anti-Aβ40 specific antibody. (**c**) Direct comparison of both antibody developments at 7 days. No hetero-dimers/ -trimers/-tetramers are formed as bands found in mixtures can either be attributed to IAPP or to VGS-VF. Results are representative of 3 experiments. Christina Lindner contributed to the experiment in a-c) (see chapter 8).

.

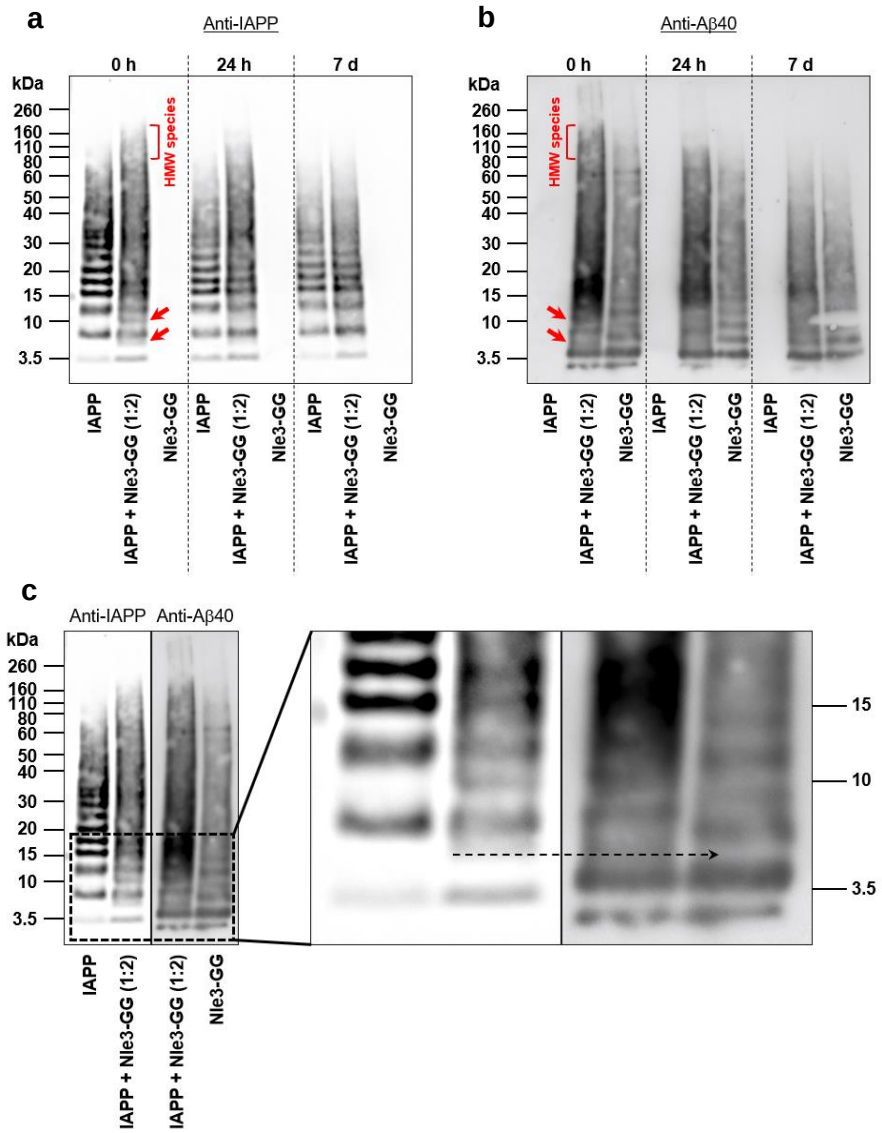

Figure 4-29: Time-dependent CL experiment of IAPP and its mixture with Nle3-GG. Characterisation of IAPP-Nle3-GG hetero-assemblies was performed via cross-linking with glutaraldehyde, NuPAGE gel electrophoresis and Western blot (WB). Species were revealed using an anti-IAPP antibody and an anti-Aβ40 antibody. Solutions containing either IAPP (30 µM), Nle3-GG (60 µM) or their mixture (1:2) were incubated for the indicated time before cross linking. Red arrows highlight hetero-dimers and -trimers/-tetramers, red brackets show HMW hetero-assemblies. (**a**) Membrane probed by anti-IAPP specific antibody. (**b**) Membrane probed by anti-Aβ40 specific antibody. (**c**) Direct comparison of both antibody developments at 0 h to confirm presence of both IAPP and Nle3-GG in the band assumed to contain a hetero-dimer. Arrow in the magnified area highlights absence of Nle3-GG-related bands at the migration hight of the hetero-dimer band. Results are representative of 2 experiments. Christina Lindner contributed to the experiment in a-c) (see chapter 8).

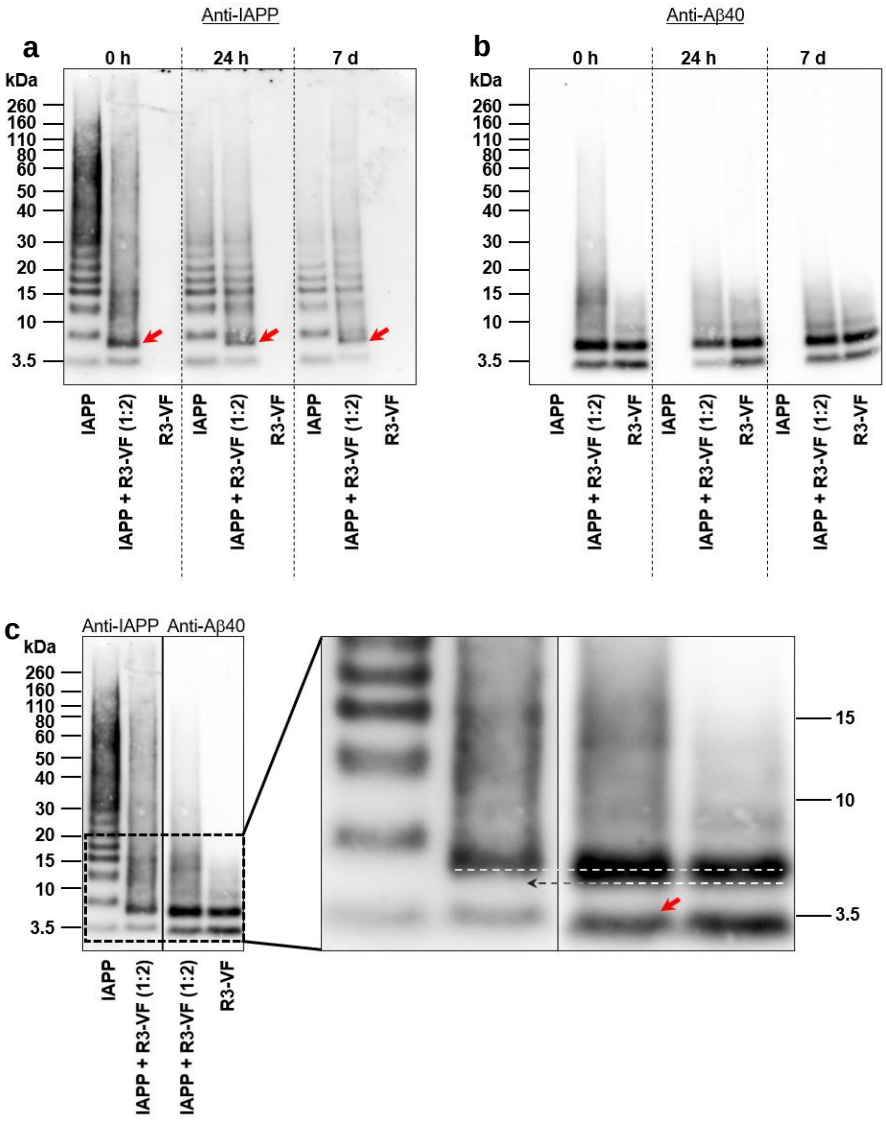

Figure 4-30: Time-dependent CL experiment of IAPP and its mixture with R3-VF. Cross linking was performed at indicated time points of samples containing either IAPP (30 µM), R3-VF (60 µM) or their mixture (1:2) using gluaraldehyde. Species were revealed by NuPAGE gel electrophoresis followed by Western blot analysis. (**a**) Membrane probed by anti-IAPP specific antibody. Arrows highlight the IAPP/R3-VF hetero-dimer band. (**b**) Membrane probed by anti-Aβ40 specific antibody. (**c**) Direct comparison of both antibody developments at 0 h to confirm presence of both IAPP and R3-VF in the hetero-dimer band. Dashed lines in the magnified area highlight absence and presence of IAPP and R3-VF in different parts of the dimer band in the mixture. The red arrow highlights the reduced amount of R3-VF monomer in the mixture. Results are representative of 2 experiments.

Similar conclusions can be drawn from results obtained by CL experiments using G3-VF, another non-inhibitory peptide sharing a similar binding affinity towards Fluos-IAPP with Nle3-VF. This peptide does not form form hetero-dimers with IAPP but shows a small number of hetero-trimers/-tetramers as well as HMW species at t=0 h. Similarly to the hetero-dimer formed by R3-VF, the IAPP/G3-VF hetero-trimer/-tetramer seems to be still present at 7 days, whereas the HMW smear vanished at 24 h. Hence, not only R3-VF but also G3-VF binds similarly to Fluos-IAPP as Nle3-VF and can form LMW heterocomplexes but both peptides are not able to establish an inhibition-competent complex with IAPP.

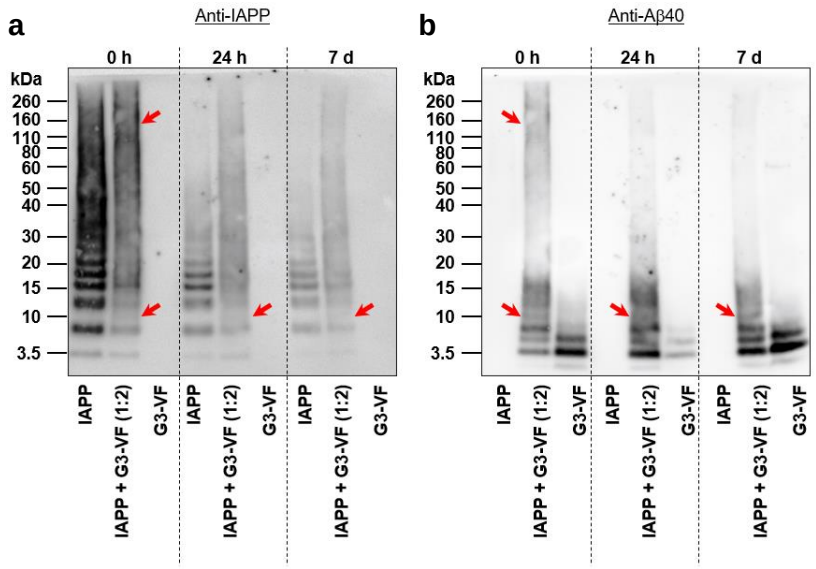

Figure 4-31: Time-dependent CL experiment of IAPP and its mixture with G3-VF. Glutaraldehyde-mediated cross linking was performed in incubations containing either IAPP (30 µM), G3-VF (60 µM) or their mixture (1:2) at indicated time points. Species were revealed by NuPAGE gel electrophoresis followed by Western Blot analysis using an anti-IAPP specific and an anti-Aβ40 specific antibody. Arrows highlight the IAPP/G3-VF hetero-trimer/-tetramer and HMW species. (**a**) Membrane probed by anti-IAPP specific antibody. (**b**) Membrane probed by anti-Aβ40 specific antibody. Results are representative of 2 experiments. Christina Lindner contributed to the experiment in a-c) (see chapter 8).

4.5.2.2 Heterocomplex formation proven by SEC analysis

Since formation of stable hetero-dimers/-trimers and HMW heterocomplexes was found to be an inhibitor-specific property by CL experiments, these results should be further confirmed via size exclusion chromatography (SEC). To be able to assign molecular weights to IAPP/ADP hetero-assemblies, the Superdex column was calibrated in a first attempt using a standard calibrant for globular proteins consisting of vitamin B12 (1.35 kDa), myoglobulin (17 kDa), ovalbumin (44 kDa), γ-globulin (158 kDa) and thyroglobulin (670 kDa). The standard was dissolved in ThT assay buffer and chromatographed as the IAPP-related samples (Figure 4-32a,b). For calculating the best-fit linear curve, thyroglobulin was excluded since it was not entirely separated from γ-globulin (column exclusion limit ~1 x 10^5 Da). Using the remaining components, the standard curve was calculated to be

$$y = -4{,}84941 \cdot x + 32{,}97472 \qquad (5)$$

where x represents the logarithmic molecular weight of the compound of interest and y its expected elution volume. Based on this equation, the IAPP monomer (logMW = 3.5912) should elute from the column with an elution volume of 15.56 ml (retention time: 31.1 min with flow rate 0.5 ml/min). However, when freshly dissolved IAPP was injected, three peaks were detected eluting at 35.25 min, 38.25 min and 43.75 min (Figure 4-32c,d). As the latest peak (43.75 min) is considered to be the IAPP monomer, the observed retention time differs by more than 12 min from the expected one. Since this could be due to a nonideal chromatographic behaviour of the analytes often observed especially for peptides[148], the firstly applied calibration method was not suitable here.

Therefore, the column was calibrated by using the elution volumes from γ-globulin, ovalbumin and myoglobulin in combination with the elution volumes observed for monomeric IAPP

(3.9 kDa, 43.75 min) and monomeric Nle3-VF (2.8 kDa, 53.25 min) or monomeric VGS-VF (2.7 kDa, 53.3 min), respectively, as a replacement for vitamin B12. The resulting best-fit linear curves were

$$y = -0.08599 \cdot x + 5.5786 \quad (6)$$

using Nle3-VF and

$$y = -0.08664 \cdot x + 5.58575 \quad (7)$$

using VGS-VF (Figure 4-32e-h). Applying these equations, a molecular weight could be assigned to all peaks observed in freshly prepared incubations of IAPP, Nle3-VF and VGS-VF (Figure 4-33 and Table 4-10). IAPP presented three peaks corresponding to its monomer, dimer and trimer. Both Nle3-VF and VGS-VF displayed peaks that could be assigned to species up to the size of a heptamer. Of note, Nle3-VF was found to be mainly dimeric, whereas the largest portion of VGS-VF seemed to be hexamers or heptamers.

Comparing chromatograms of freshly prepared IAPP/Nle3-VF or IAPP/VGS-VF mixtures with the corresponding peptide-alone controls revealed that IAPP/Nle3-VF mixtures contain LMW and HMW heterocomplexes already at t=0 h, whereas no heterocomplex formation was observed for IAPP/VGS-VF mixtures, which is in perfect agreement with CL findings (Figure 4-34). By using the previously established fitting curves (equation (6)) it was found that the peak of the IAPP/Nle3-VF mixture eluting at 40.62 min contains a LMW heterocomplex with a mass of ~6794 g/mol corresponding to the IAPP/Nle3-VF hetero-dimer (MW = 6654.53 g/mol). The peak eluting at 15.25 min accordingly contains HMW heterocomplexes with a mass of ~83739 g/mol corresponding to differently composed oligomers consisting of 22 to 30 molecules (Table 4-11). After 96 h of incubation, the IAPP/Nle3-VF hetero-dimer is still present but became less compared to the Nle3-VF homo-dimer (peak at 43.8 min) suggesting that it oligomerised further to form higher ordered species. Additionally, peaks corresponding to hetero 8- or 9-mers and to hetero 19- to 24-mers were observed at 96 h (Table 4-11), whereas no heterocomplex formation was found in mixtures with VGS-VF.

In conclusion, SEC experiments could nicely confirm previous findings from CL. The results strongly support the hypothesis that formation of specific hetero-dimers and -trimers/-tetramers as well as HMW heterocomplexes is a crucial feature underlying the mechanism by which ACMs block IAPP amyloidogenicity.

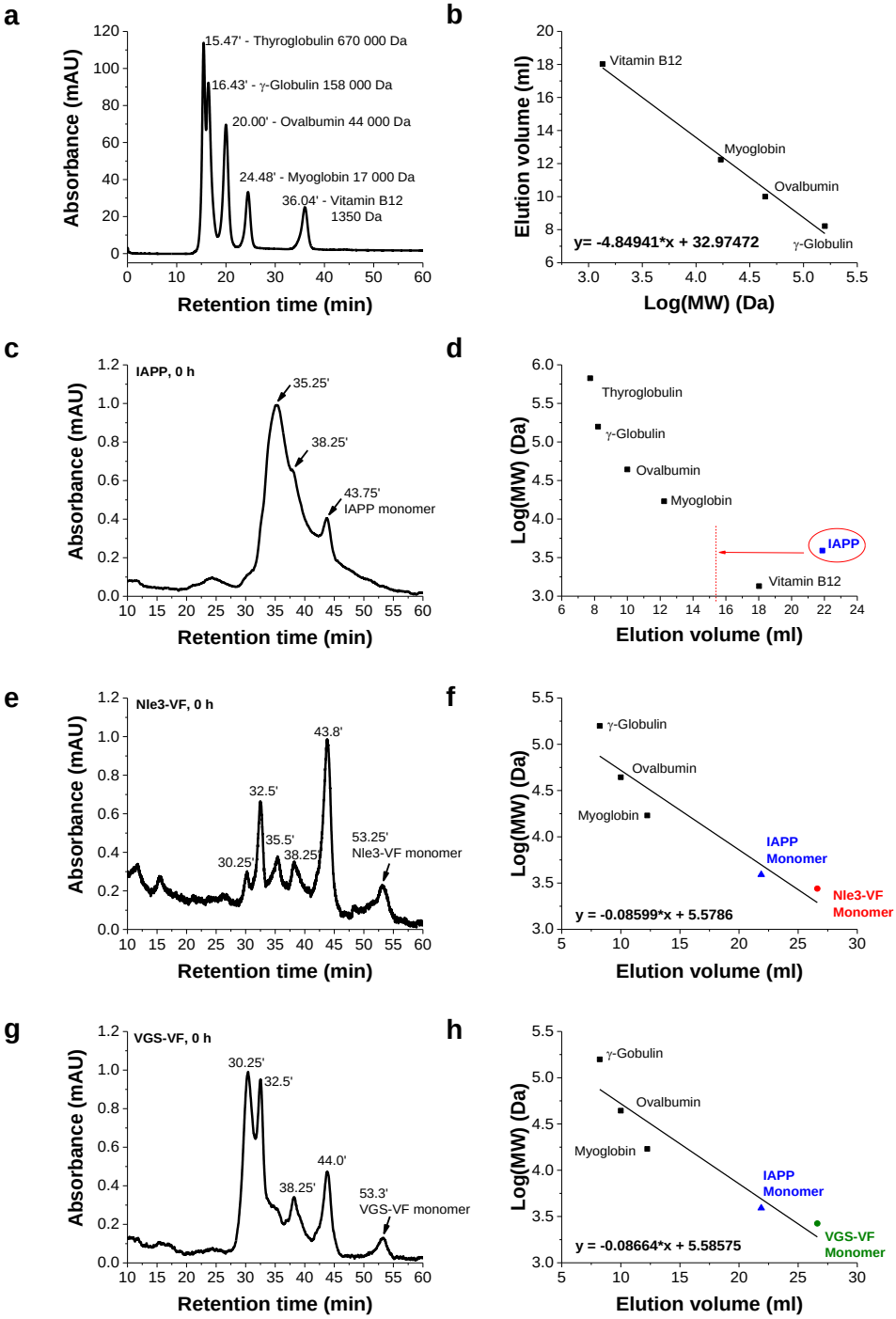

Figure 4-32: Calibration of the Superdex 75 10/300 GL SEC column. (**a,b**) Elution profile and resulting best-fit linear curve of the protein calibration standard. The standard was dissolved in ThT assay buffer and chromatographed as IAPP-related samples after (mobile phase: ThT assay buffer, 0.5 ml/min). (**c**) Chromatogram for freshly dissolved IAPP. Incubation was prepared in ThT assay buffer containing 0.5 % HFiP at a concentration of 16.5 µM. Sample was centrifuged for 1 min at 20000 g before injection of supernatant. (**d**) Comparison of observed and expected elution volume for monomeric IAPP. Doted line and arrow mark elution volume expected from fitting curve calculations, blue dot highlights observed elution volume. (**e, f**) Elution profile of freshly prepared Nle3-VF and best-fit linear curve using monomeric IAPP and Nle3-VF as additional calibrants. (**g,h**) Elution profile of freshly prepared VGS-VF and best-fit linear curve using monomeric IAPP and VGS-VF as additional calibrants. Absorbance values in c, e and g were normalised to the highest value after setting the lowest value within the time frame 10-60 min to 0.

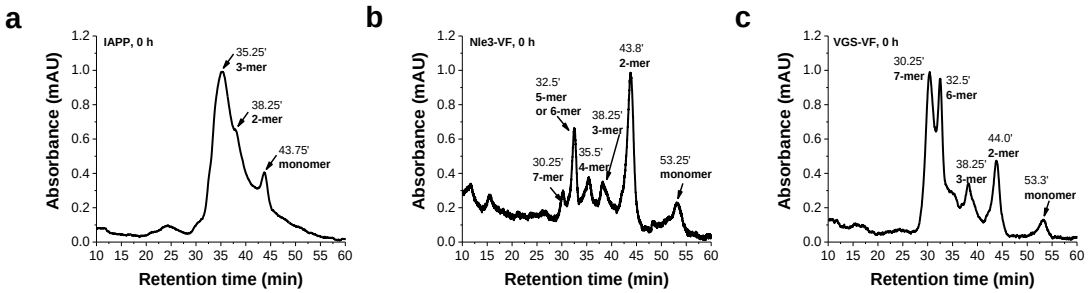

Figure 4-33: SEC elution profiles of freshly prepared IAPP, Nle3-VF and VGS-VF incubations. Samples were prepared in ThT assay buffer with 0.5 % HFiP and contained either IAPP (16.5 µM) (**a**) or Nle3-VF (33 µM) (**b**) or VGS-VF (33 µM) (**c**). All incubations were centrifuged for 1 min at 20000 g before the supernatant was loaded onto a Superdex 75 10/300 GL column. Samples were chromatographed using ThT assay buffer as mobile phase at a flow rate of 0.5 ml/min. Absorbance values were normalised to the highest value after setting the lowest value within the time frame 10-60 min to 0. Peaks are annotated with their corresponding retention time and the identified species affiliation.

Table 4-10: Experimentally determined and expected molecular weights for differently sized homo-oligomers found in freshly prepared IAPP, Nle3-VF and VGS-VF incubations. M_{found}: Mass calculated from fitting curve, $M_{exp.}$: expected mass.

	RT peak (min)	M_{found} (g/mol)	species	$M_{exp.}$ (g/mol)
IAPP	43.76	-	monomer per definition	3900.86
	38.25	8591	dimer	7801.60
	35.25	11562	trimer	11702.40
Nle3-VF	53.25	-	monomer per definition	2753.67
	43.8	4959	dimer	5507.34
	38.25	8591	trimer	8261.01
	35.5	11279	tetramer	11014.68
	32.5	15180	pentamer or hexamer	13768.35 or 16522.02
	30.25	18967	heptamer	19275.69
VGS-VF	53.3	-	monomer per definition	2657.54
	44.0	4783	dimer	5315.08
	38.25	8487	trimer	7972.62
	32.5	15061	hexamer	15945.24
	30.25	18850	heptamer	18602.78

Table 4-11: Experimentally determined and expected molecular weights for differently sized hetero-oligomers found in IAPP/Nle3-VF mixtures. M_{found}: Mass calculated from fitting curve, $M_{exp.}$: expected mass. n and m give the number of Nle3-VF or IAPP molecules, respectively, that form the hetero-oligomer. Summarised are possible hetero-oligomers the masses of which are in a range of ±400 g/mol compared to M_{found}. Corresponding SEC chromatograms see Figure 4-34a.

Time point	Retention time (min)	M_{found} (g/mol)	Hetero-oligomer (n Nle3-VF/ m IAPP)	$M_{exp.}$ (g/mol)
0 h	40.6	6794	1/1	6655
	15.3	83739	12/13	83761
			29/1	83767
			2/20	83528
			5/18	83988
			19/8	83534
			22/6	83994
96 h	40.5	6875	1/1	6655
	26.5	27404	3/5	27767
			7/2	27080
	17.0	70418	10/11	70451
			17/6	70224
			3/16	70678
			20/4	70684

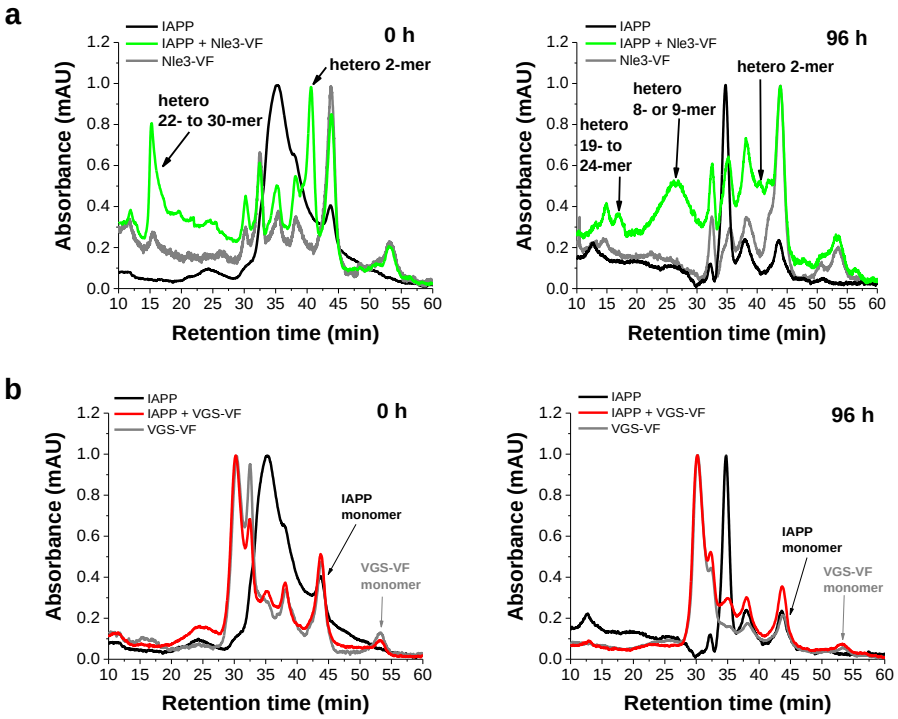

Figure 4-34: SEC elution profiles of mixtures containing IAPP and Nle3-VF or VGS-VF. Incubations of IAPP (16.5 µM), Nle3-VF (33 µM) and VGS-VF (33 µM) or their mixtures (1:2) were prepared in ThT assay buffer with 0.5 % HFiP. After the indicated incubation times, samples were centrifuged for 1 min at 20000 g and supernatants were loaded onto a Superdex 75 10/300 GL column and chromatographed using ThT assay buffer as mobile phase (0.5 ml/min). Results are shown for IAPP/Nle3-VF mixtures and corresponding control incubations in (**a**) and accordingly for VGS-VF in (**b**). After setting the lowest absorbance value within the time frame 10-60 min to 0, chromatograms were normalised to their highest value. Arrows highlight LMW and HMW heterocomplexes in (a) and monomeric IAPP or monomeric VGS-VF in (b). Data is representative of 3 assays. Data of a) is part of a figure in reference [140].

4.5.3 Early and late IAPP/Nle3-VF assemblies differ from IAPP assemblies in their structure in solution

Structural properties of early and late IAPP/Nle3-VF assemblies in solution were determined by CD experiments. For this, IAPP (16.5 µM), Nle3-VF (33 µM) or their mixture (1:2) were prepared as for IAPP inhibition experiments in ThT assay buffer (0.5 % HFIP) and examined directly after, after 1 h of aging (0 h/ 1 h, “early assemblies”) or after 7 days of aging (“late assemblies”). Identical mixtures with the non-inhibitor VGS-VF were incubated and analysed in parallel as control.

As previously shown[28], freshly prepared (0 h) and 1 h aged solutions containing only IAPP show mainly random coil content, 7 days aged solutions show high amounts of β-sheet/β-turn structure (Figure 4-35). This agrees with IAPP’s transition from an intrinsically disordered polypeptide into β-sheet rich fibrils[28]. Early IAPP/Nle3-VF as well as early IAPP/VGS-VF assemblies present structures mainly consistent of random coil content (Figure 4-35). In both cases, experimentally determined CD spectra of the mixtures differ from the theoretical spectra obtained by mathematical addition of the spectra of the single peptides, indicating that structural changes are taking place upon interaction of IAPP with the peptide. This finding further confirms results from CL and SEC experiments (see chapters 4.5.2.1 and 4.5.2.2) showing that heterocomplexes with IAPP are formed by Nle3-VF and VGS-VF at early stages. Importantly, the structure of 7 days aged assemblies of IAPP with the inhibitor Nle3-VF

(considered to be heterofibrils) is totally different from 7 days aged IAPP assemblies (Figure 4-35a), while 7 days aged IAPP/VGS-VF assemblies show a β-sheet/β-turn rich structure similar to IAPP's (Figure 4-35b), indicating these are fibrils formed by IAPP only. Further investigations to prove the heterogenic nature of fibrils in 7 days aged IAPP/Nle3-VF mixtures will be presented in the following chapter.

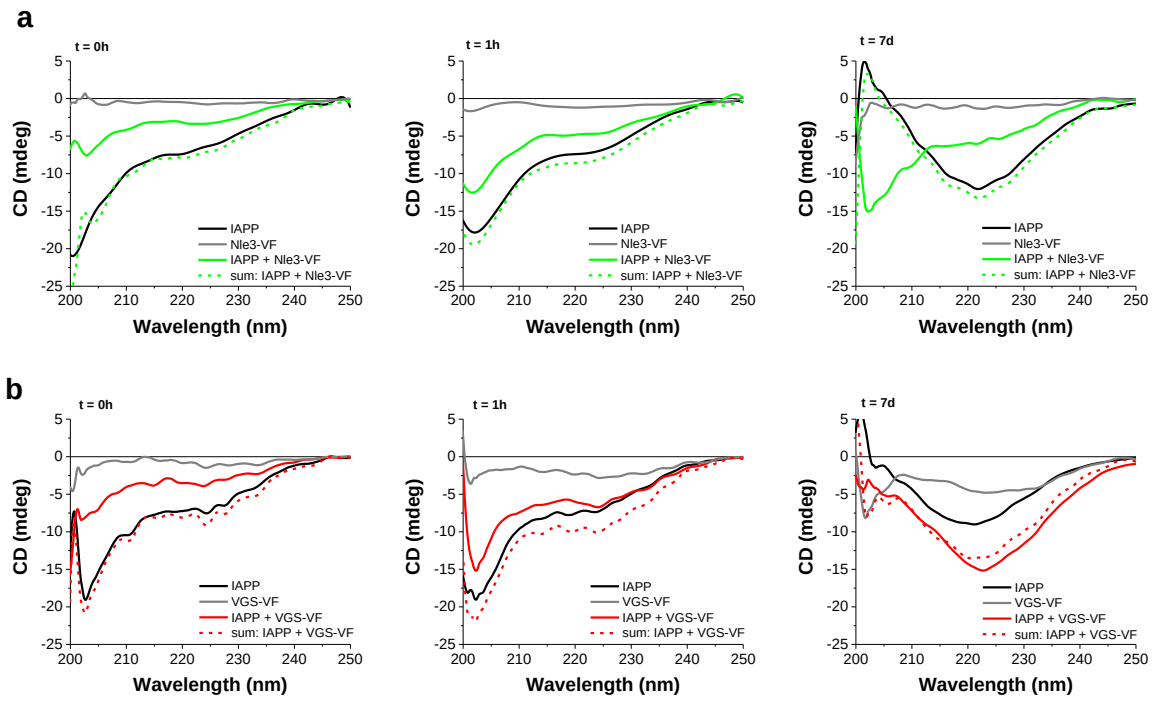

Figure 4-35: Structure of early and late IAPP/Nle3-VF and IAPP/VGS-VF assemblies in solution determined by CD. Incubations of IAPP (16.5 µM), Nle3-VF/VGS-VF (33 µM) or their mixture (1:2) were prepared as for corresponding inhibition studies in ThT assay buffer (0.5 % HFIP) and incubated for the indicated times. To measure CD signals, solutions were transferred into cuvettes. Baseline measurements were subtracted from all measurements. Results for early (0 h, 1 h) and late (7 days) assemblies are shown for Nle3-VF (a) and VGS-VF (b). Studies for Nle3-VF are representative of 2 assays, studies for VGS-VF control were performed once. Data of a) (0 h IAPP control and 7 d measurements) is part of a figure in reference [140].

4.6 ACMs form fibrillar co-assemblies with IAPP

4.6.1 Immunogold-TEM and pulldown assays indicate heterofibril formation

Since fibrils observed in IAPP/ACM mixtures were considered to consist of both peptides, it was first checked for observable differences in fibril morphology on a nanoscopic level. For this purpose, lengths and widths of fibrils originating from IAPP were directly compared to fibrils found when IAPP was co-incubated with ACMs or corresponding non-inhibitory controls. Fibrillar IAPP showed a characteristic fibril length of 161 ± 46 nm and width of 9.7 ± 2.3 nm. Identical fibril dimensions were found for mixtures of IAPP and the non-inhibitory ADP VGS-VF (length: 180 ± 75 nm, width: 8.5 ± 2.0 nm). Also mixtures with ACMs were found to contain fibrils of very similar dimensions. For detailed measurement results see Table 4-12. Thus, single-fibrils formed by IAPP and ACMs do not strikingly differ from fibrils formed by IAPP alone (Figure 4-36). However, immunogold-TEM (IG-TEM) provided support for the existence of heterogenous fibrils. For this experiment, samples of 7 days aged IAPP (16.5 µM, in ThT assay

Table 4-12: Fibril dimensions of fIAPP and heterofibrils formed with ACMs. Fibril lengths and width were measured from representative TEM pictures of 7 days aged incubations (IAPP 16.5 µM, mixtures IAPP/ADP 1/2, ThT buffer with 0.5 % HFIP). Data are means ± SD from 20-47 fibrils (see also Table 7-21 and Table 7-22 in Appendix). Data of fibril widths is included in a table in reference [140].

Peptide or peptide mixture	Fibril length (nm)	Fibril width (nm)
IAPP	161 ± 46	9.7 ± 2.3
IAPP+VGS-VF	180 ± 75	8.5 ± 2.0
IAPP+Nle3-VF	182 ± 74	8.3 ± 1.9
IAPP+L3-VF	172 ± 41	7.7 ± 1.5
IAPP+F3-VF	197 ± 66	8.7 ± 1.8
IAPP+Nle3-LF	158 ± 56	6.1 ± 1.1
IAPP+L3-LF	163 ± 47	7.9 ± 1.8
IAPP+F3-LF	159 ± 58	6.6 ± 1.2

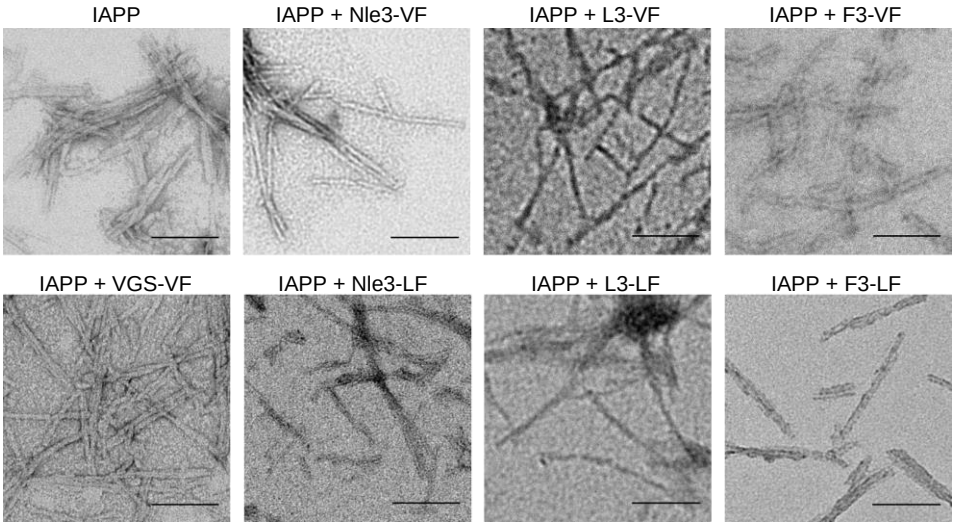

Figure 4-36: Comparison of fibril morphologies found for fIAPP and heterofibrils formed with ACMs. Samples for negative stain TEM imaging were prepared in ThT assay buffer with 0.5 % HFiP. IAPP (16.5 µM) or its mixture with peptides (1:2) were aged for 7 days prior to sample preparation. Scale bars are 100 nm.

buffer with 0.5 % HFiP) or its mixture with peptide (1:2) were loaded onto TEM grids and stained afterwards using the anti-fIAPP antibody and/or an anti-Aβ antibody (to detect the ACM) in combination with appropriate gold-labelled secondary antibodies (5 nm gold for IAPP, 10 nm gold for ACM). Both antibodies were found to be suitable for the experiment in preliminary studies, since the anti-fIAPP antibody efficiently detected fibrillar IAPP and the anti-Aβ antibody was able to bind to amorphous aggregates formed by Nle3-VF (Figure 4-37a). When staining 7 days aged IAPP/Nle3-VF mixtures with either the anti-Aβ antibody or the anti-fIAPP antibody it was found that the present fibrillar species can be bound by both (Figure 4-37b). To investigate if this means that separate filaments are formed by IAPP and Nle3-VF or if both peptides are also contained in the same fibril or fibrillar bundle, samples were stained with both antibodies in parallel in a next step. Gold particles of 5 and 10 nm were found to be bound to many areas in fibrillar assemblies and to closely associate on single fibrillar bundles (Figure 4-37c). The ratio of anti-fIAPP:anti-Aβ antibody binding was ~60:40. Despite that

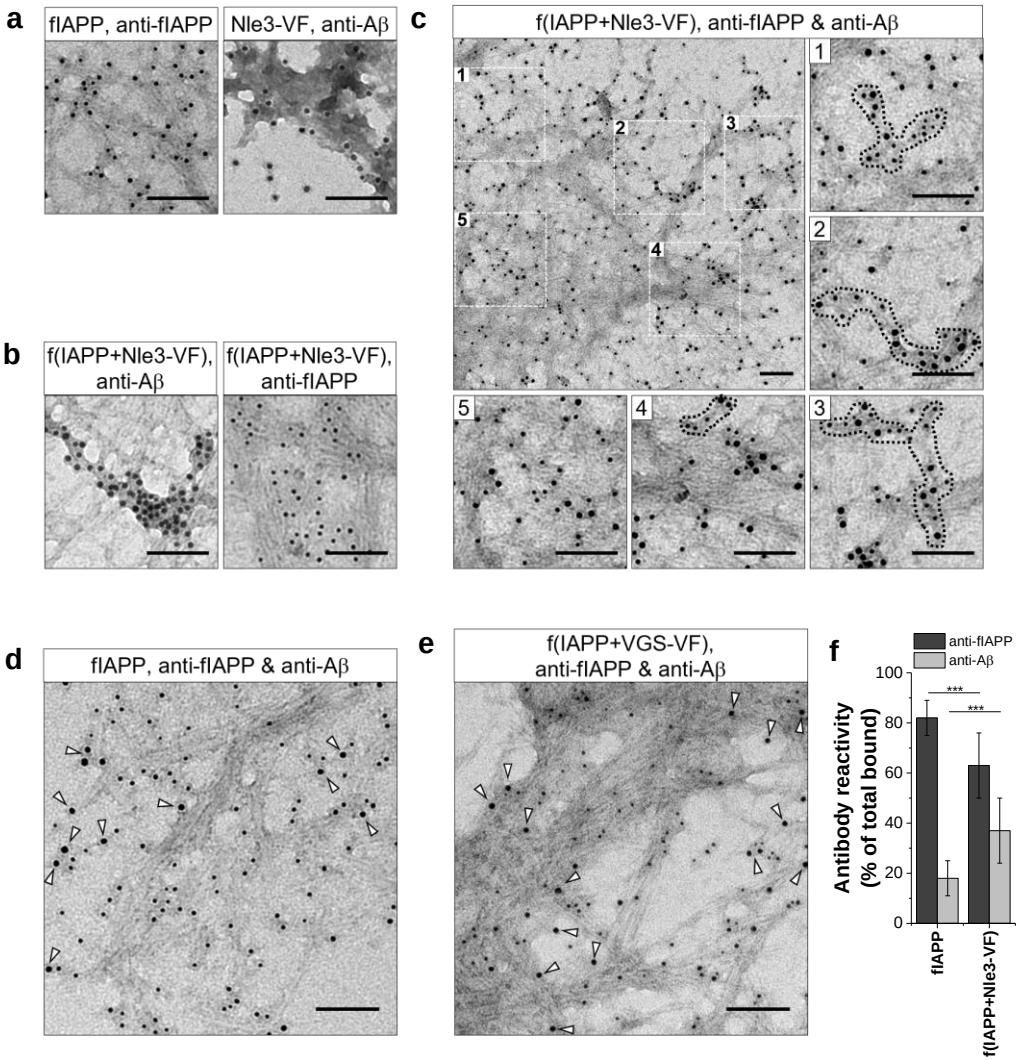

Figure 4-37: Immunogold-TEM as proof for the existence of IAPP/ACM heterofibrils. Negative stain TEM imaging was applied to examine immunogold reactions of 7 days aged IAPP (16.5 µM), Nle3-VF (33 µM) and mixtures of IAPP and Nle3-VF or VGS-VF (ratio 1:2) using an anti-IAPP antibody (fibril-specific; anti-fIAPP) and an anti-Aβ antibody with corresponding gold-labelled secondary antibodies. 10 nm gold particles indicate the presence of Nle3-VF or VGS-VF, 5 nm gold particles indicate the presence of IAPP. (**a**) Suitability test of applied antibodies. Fibrils originating from IAPP can be efficiently detected by the anti-fIAPP antibody. Amorphous aggregates found in 7 days aged solutions of Nle3-VF stain positive for the anti-Aβ antibody. (**b**) Staining of heterofibrils by different antibodies. Fibrils found in 7 days aged mixtures containing IAPP and Nle3-VF stain positive for the anti-fIAPP antibody and the anti-Aβ antibody, respectively. (**c**) Parallel staining of heterofibrils with anti-fIAPP antibody and anti-Aβ antibody. Shown are exemplary areas (1-5) of a representative sample of a 7 days aged IAPP/Nle3-VF mixture stained for both peptides in parallel. Highlighted areas show presence of both peptides within the same fibril bundle. (**d**) Unspecific binding of the anti-Aβ antibody. Fibrillar IAPP was stained with anti-fIAPP antibody and anti-Aβ antibody in parallel. Arrows indicate unspecifically bound 10 nm gold particles (~20 %). (**e**) Parallel staining of fibrils found in 7 days aged mixtures containing IAPP and the negative control peptide VGS-VF with anti-fIAPP antibody and anti-Aβ antibody. Arrows highlight binding of anti-Aβ antibody (10 nm gold particles). (**f**) Quantification of antibody reactivity observed for fIAPP and heterofibrils formed by IAPP and Nle3-VF. fIAPP mainly stains for the anti-fIAPP antibody (~80 %) and shows weak unspecific binding of the anti-Aβ antibody (~20 %). Heterofibrils display a significantly different antibody reactivity (anti-fIAPP:anti-Aβ = 60:40 % approx.). Error bars show mean ± SD. For quantification, gold particles in 12 fibril-containing areas with a size of 0.4 µm^2 (n=10) or 2.5 µm^2 (n=2) each were counted for fIAPP and in 24 fibril-containing areas with a size of 0.4 µm^2 (n=15) or 2.5 µm^2 (n=9) each for f(IAPP+Nle3-VF). *** P<0.001 by one-way ANOVA and Bonferroni. Scale bars are 100 nm. Data of c) is part of a figure in reference [140] (adapted figure version).

approximately 20 % of unspecific binding of the anti-Aβ antibody to IAPP fibrils was observed, the antibody reactivity found for IAPP/Nle3-VF fibrils differed significantly from IAPP fibrils (Figure 4-37d,f). Additionally, unspecifically bound 10 nm gold particles often seemed to be more randomly spread all over sample instead of being associated in a defined way. Fibrils formed in solutions containing IAPP and the non-inhibitory ADP VGS-VF were also stained by the anti-Aβ antibody but to a lower extent than IAPP/Nle3-VF fibrils (anti-fIAPP:anti-Aβ ~70:30; similar to fIAPP (~80:20)) (Figure 4-37e).

The hypothesis that fibrils in mixtures contain IAPP and Nle3-VF was further supported by a pulldown assay combined with NuPAGE gel electrophoresis and Western blotting. Streptavidin-coated magnetic beads were used to specifically capture species containing N^{α}-terminal biotinylated IAPP (Biotin-IAPP) from 7 days aged incubations either made from Biotin-IAPP alone (16.5 µM) or mixtures with Nle3-VF (1:2). Heterocomplex components on the membrane were disclosed after dissociation and release from the beads. Of note, inhibitory properties of Nle3-VF did not change when biotinylated IAPP was used instead (Figure 4-38a). Also, fibrils were still found to be the main species in the incubations after 7 days aging. Pulldown analysis of such fibrils revealed that both Nle3-VF and Biotin-IAPP were co-isolated by the streptavidin-coated beads (Figure 4-38b), confirming IG-TEM findings and the heterogenous nature of these fibrils.

In conclusion, the IG-TEM and pulldown experiments supported the hypothesis that ACMs inhibit IAPP by co-assembling into heteromeric fibrils which are ThT-invisible and non-toxic in contrast to fIAPP.

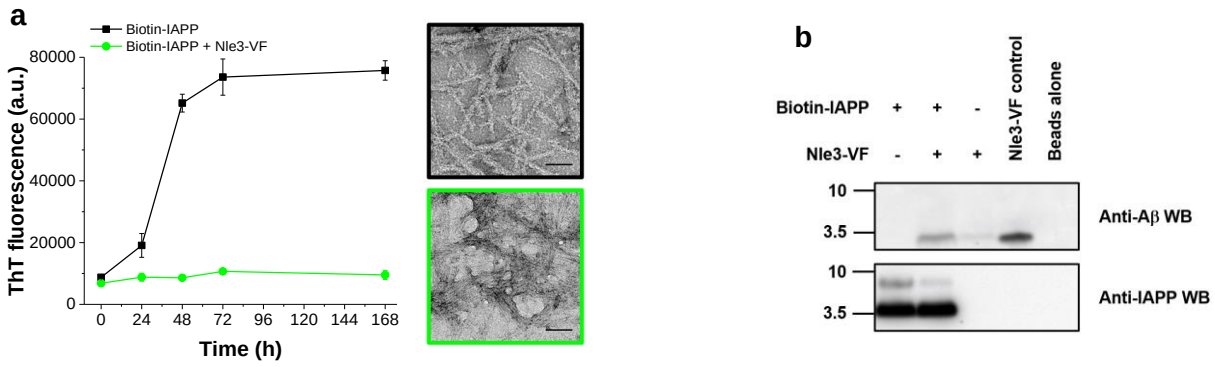

Figure 4-38: Inhibition assay and pulldown experiment using biotinylated IAPP. (**a**) Inhibition of Biotin-IAPP by Nle3-VF. Fibril formation of biotinylated IAPP (16.5 µM) was followed in presence and absence of Nle3-VF (1:2). Incubations were prepared in ThT assay buffer containing 0.5 % HFiP and analysed over 7 days. Error bars represent means ± SD from three assays. TEM analysis was performed of 7 days aged solutions, colours correspond to colours in ThT binding assay. Scale bars are 100 nm. (**b**) Co-isolation of Nle3-VF with Biotin-IAPP by pulldown via streptavidin-coated magnetic beads. Incubations containing Biotin-IAPP (16.5 µM) or its mixture with Nle3-VF (1:2) were prepared in 1xb and aged for 7 days. Following dissociation from the beads, NuPAGE gel electrophoresis and Western blotting, complexes were revealed using an anti-Aβ and an anti-IAPP antibody. Species of interest between 3.5 and 10 kDa are shown. Equal amounts of peptide were loaded in each lane (100 % input: 11.2 µg Biotin-IAPP, 14.5 µg Nle3-VF). Loaded amounts for Nle3-VF control (freshly dissolved peptide without bead-incubation) was 1.8 µg (12.5 %). Results are representative of 2 assays. Data of b) is part of a figure in reference [140].

4.6.2 High-resolution advanced laser-scanning microscopy provides evidence for heteromeric fibril co-assemblies

By using different advanced laser-scanning microscopy techniques[126] to examine aged IAPP/ACM mixtures containing fluorescently labelled peptides, the heterogenous nature of fibril co-assemblies could be proven.

4.6.2.1 Evidence from 2-photon microscopy (2-PM)

For 2-photon microscopy (2-PM) studies, N^{α}-terminal 5,6-carboxytetramethylrhodamine (TAMRA)-labelled IAPP (TAMRA-IAPP) and N^{α}-terminal 5,6-carboxyfluorescein-labelled ACMs (Fluos-ACM) were used. Incubations were prepared in 1xb instead of ThT assay buffer with 0.5 % HFiP to reduce salt content which might disturb microscoping. In pre-liminary trials, inhibitory properties of Nle3-VF towards IAPP were found to be the same under both buffer

conditions (data not shown). Importantly, the introduction of the N-terminal label does not alter IAPP's ability to form fibrils, does not induce fibril formation properties to Nle3-VF, and aged mixtures still contain fibrils according to TEM (Figure 7-49 in Appendix). 2-PM experiments showed for TAMRA-IAPP samples the presence of large fiber-like structures, 36.6 ± 19.8 µm in length with a width of 3.1 ± 1.9 µm (Figure 4-39a). Additionally, thinner fibrillar assemblies (widths ~600 nm) were observed. Morphologically similar (lengths: 12.2 ± 5.9 µm, widths: 1.3 ± 0.3 µm) IAPP nanofibers were also found in mixtures containing TAMRA-IAPP and the non-inhibitory ADP Fluos-VGS-VF (Figure 4-39b). In contrast, mixtures of TAMRA-IAPP and Fluos-Nle3-VF proved to contain fibrillar co-assemblies of diverse nature. They were assigned to the following categories (Figure 4-39c): 1) double-stranded straight nanofibers with different strand colour, width ~700 nm – 1 µm, 2) bicolored straight nanofibers with an approximate width of 700 nm to 1 µm. Additionally, a third category consisting of double-stranded, twisted nanofibers with different strand colour (~400 µm – 1 µm wide) seemed to be present, but their twisted character was hard to be judged due to resolution issues. Furthermore, it was observed that even larger assemblies are formed in these mixtures (>500 µm long). These „loop-shaped macro assemblies" (Figure 4-39d,e and Figure 7-52 in Appendix) were found to be comprised of the previously mentioned fibrillar species, indicating that this is not a discrete fourth category of possible assemblies but the final end point of a multi-step arrangement and re-arrangement of diverse fibrillar species formed by IAPP and ACMs into a novel supramolecular nanofibre co-assembly. Many of the nanofibers building up the supramolecular co-assemblies were also found to run in parallel. Additionally, nanofibers showing a successive order of IAPP and Nle3-VF segments (red-green-red) were found, where IAPP also acts as a connector between nanofiber strands (Figure 4-39f). IAPP was in general often found to link or wrap around different nanofiber components within the assembly (Figure 4-39g).

Since TEM studies revealed fibril formation in mixtures for all ACMs, two additional IAPP inhibitors, L3-VF and F3-VF, were labelled with carboxyfluorescein and their mixture with TAMRA-IAPP was examined via 2-PM. As expected, also TAMRA-IAPP/Fluos-L3-VF mixtures (1:2, 7 days) contained big fibrillar co-assemblies (~280 µm in length) composed of smaller nanofiber units, which resembled those found for Nle3-VF mixtures, namely, double-stranded straight nanofibers and bicolored straight nanofibers (Figure 4-40a). Similar nanofibers were also observed in TAMRA-IAPP/Fluos-F3-VF mixtures (1:2, 7 days) (Figure 4-40b). Taken together, using 2-PM made it possible to visualise fibrillar hetero-assemblies formed by IAPP and three different ACMs and thereby to proof their existence conclusively. Notably, the applied advanced fluorescence microscopy techniques cannot provide a resolution on the level of a single fibril (width ~6-10 nm, see chapter 4.6.1) and the species observed by 2-PM are much thicker than this. Therefore, these fibrillar hetero-assemblies will be further referred to as "nanofibres" instead of "fibrils" to underline that they represent bundles of several fibrils joint together. Fibrillar co-assemblies will be abbreviated by "hf-IAPP/ACM". The observed species were different hetero-nanofibers and supramolecular nanofibre co-assemblies composed of the smaller nanofiber units, suggesting maybe a multi-stage arrangement process of the final assemblies. Two findings support the hypothesis that the formation of fibrillar hetero-assemblies is part of the mechanism by which ACMs inhibit IAPP. First, all three investigated ACMs showed hetero-nanofiber formation with IAPP when mixed in 1:2. And second, no hetero-nanofibers were found in 1:2 mixtures with the non-inhibitor VGS-VF.

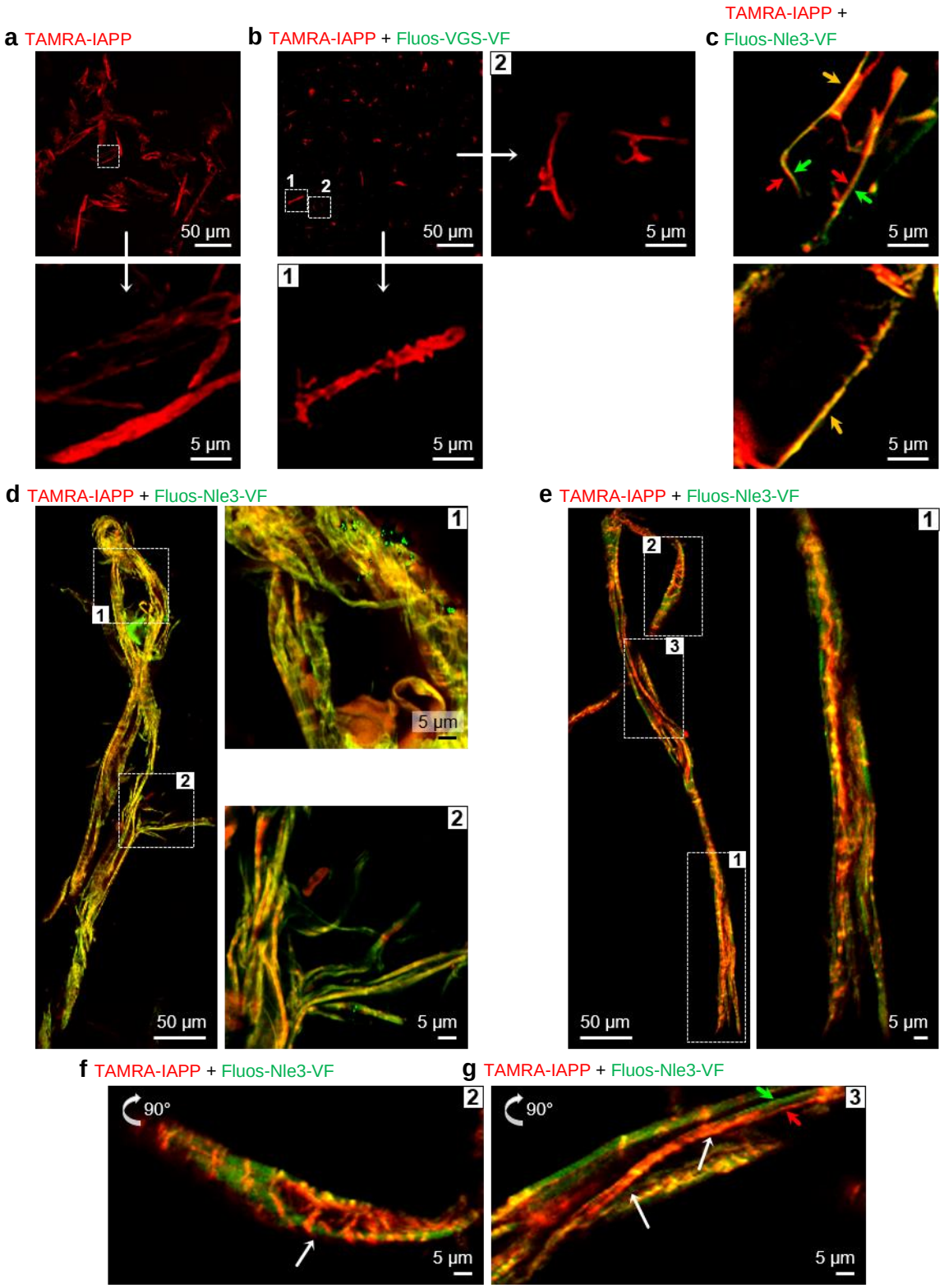

Figure 4-39: 2-photon microscopy of fibrillar co-assemblies formed by TAMRA-IAPP and TAMRA-IAPP/Fluos-Nle3-VF mixtures. For fluorescence microscopy, TAMRA-labelled IAPP (red) and Fluos-labelled Nle3-VF (green) were used. (**a**) TAMRA-IAPP nanofibers (16.5 µM, 7 days, in 1xb). (**b**) TAMRA-IAPP nanofibers formed in 1:2 mixtures of TAMRA-IAPP/Fluos-VGS-VF (7 days, 1xb). (**c**) Fibrillar hetero-assemblies formed in 1:2 mixtures of TAMRA-IAPP/Fluos-Nle3-VF (6-7 days, 1xb). Two distinct categories are shown: bicolored straight nanofibers (→) and double-stranded straight nanofibers with different strand colour (→ and →). (**d,e**) Loop-shaped macro-assemblies found in 1:2 mixtures of TAMRA-IAPP/Fluos-Nle3-VF (6-7 days, 1xb). Magnified areas show that macro-assemblies are composed of various smaller nanofiber units. Areas 2 and 3 of e) are magnified in f) and g). (**f**) Magnified area 2 of the nanofibre co-assembly shown in e). Arrow highlights successive order of IAPP and Nle3-VF segments (red-green-red) and the interconnection between strands by IAPP. (**g**). Magnified area 3 of the nanofibre co-assembly shown in e). White arrows terminate a region where two nanofiber strands (→ and →) are linked/wrapped by IAPP. Images are part of a figure in reference [140] (adapted figure version).

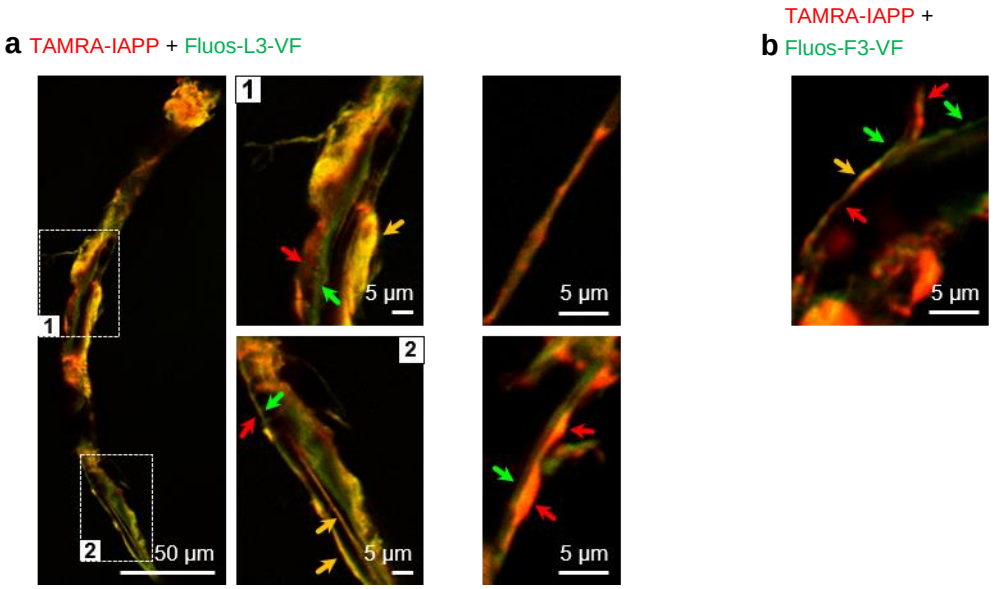

Figure 4-40: 2-photon microscopy of fibrillar co-assemblies formed by TAMRA-IAPP and Fluos-L3-VF or Fluos-F3-VF. For fluorescence microscopy, TAMRA-labelled IAPP (red) and Fluos-labelled L3-VF or F3-VF (green) were used. (**a**) Fibrillar hetero-assemblies formed in 1:2 mixtures of TAMRA-IAPP/Fluos-L3-VF (7 days, 1xb). Magnified areas 1 and 2 show regions of the nanofibre co-assembly composed of smaller nanofiber units. Pictures on the right show additional nanofibers found in this sample. (**b**) Fibrillar hetero-assemblies formed in 1:2 mixtures of TAMRA-IAPP/Fluos-F3-VF (7 days, 1xb). Coloured arrows denote bicolored straight nanofibers (→) and double-stranded straight nanofibers with different strand colour (→ and →). Images are part of a figure in reference [140].

4.6.2.2 Similarities of IAPP/Aβ40 and IAPP/Aβ42 hetero-nanofibers with IAPP/Nle3-VF hetero-nanofibers revealed by 2-PM

Previous studies indicated that initially non-fibrillar and non-toxic IAPP-Aβ heterooligomers can misfold and aggregate further into fibrillar and cytotoxic co-assemblies[80,84]. Therefore, 2-PM was next used to confirm the existence of IAPP-Aβ hetero-nanofibers and to investigate if they share any similarities with IAPP-ACM hetero-nanofibers. For this purpose, fluorescein isothiocyanate (FITC)-labelled Aβ42 and 7-diethylaminocoumarin-3-carbonyl (DAC)-labelled Aβ40 were incubated with TAMRA-IAPP (2:1) similar to ACMs. Since the IAPP-Aβ interaction only delays but does not completely block the self-association of both polypeptides, samples were not taken at 7 days but at 24 h where the mixture is not ThT-reactive yet but already contains some fibrillar species[80] in order to guarantee similar conditions as for IAPP-ACM mixtures. Hetero-nanofibers containing both peptides were found for both TAMRA-IAPP/FITC-Aβ42 and TAMRA-IAPP/DAC-Aβ40 mixtures. They were either double-stranded with two strands of different strand colours running in parallel (red & green) or bicoloured one-stranded (yellow) as observed for TAMRA-IAPP/Fluos-ACM mixtures (Figure 4-41). Also, width (~500 nm to 1 µm) and morphology resembled IAPP/ACM hetero-nanofibers. This could be due to the peptides' design concept since ACMs were generated to mimic the Aβ40 structure in its fibrillar context.

Thus, ACMs may have kept the parent peptide's intrinsic feature to co-aggregate with IAPP into a composite amyloid. In contrast to IAPP/Aβ40 or IAPP/Aβ42 heterofibrils/-nanofibers, heterofibrils/-nanofibers formed by IAPP and ACMs seem to appear later (not present at 24 h, see chapter 4.4) but to be more persistent. This is likely due to the constrained nature of the ACMs. ThT-negative and non-toxic fibrillar IAPP/ACM co-assemblies are still present after two

weeks (see chapter 4.4) whereas IAPP/Aβ40 mixtures turn ThT-positiv and cytotoxic from 3 days onward[80,84].

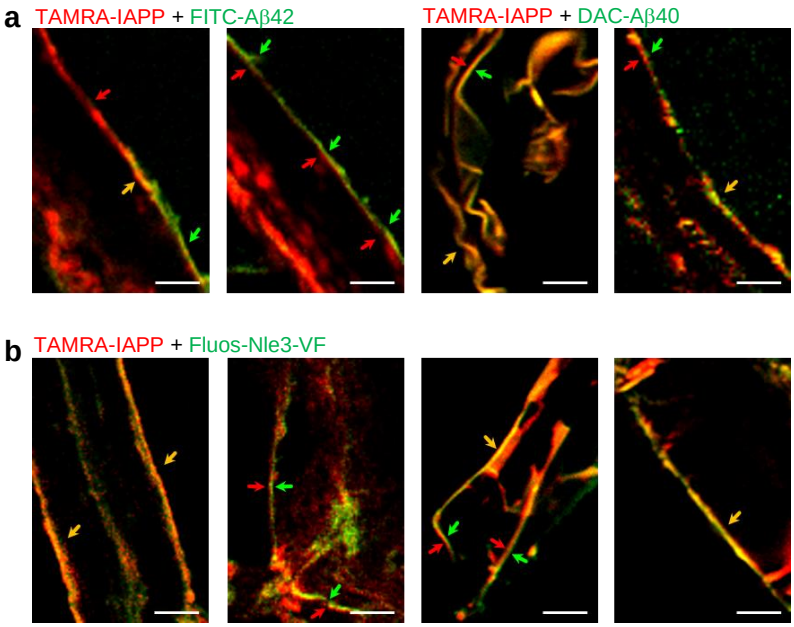

Figure 4-41: 2-photon microscopy to compare fibrillar assemblies formed by fluorescently labelled IAPP and Aβ40 or Aβ42 or Nle3-VF. TAMRA-labelled IAPP (red) and FITC-labelled Aβ42 or DAC-labelled Aβ40 or Fluos-labelled Nle3-VF (green) were used for fluorescence microscopy. All mixtures were prepared in 1xb. Incubations containing TAMRA-IAPP (16.5 µM) and FITC-Aβ42 or DAC-Aβ40 (1:2, respectively) were analysed after 24 h (**a**), incubations containing TAMRA-IAPP (16.5 µM) and Fluos-Nle3-VF (1:2) were analysed after 6-7 days (**b**). Coloured arrows denote areas showing bicolored straight nanofibers (→) and double-stranded straight nanofibers with different strand colour (→ and →). Scale bars are 5 µm.

4.6.2.3 Evidence from CLSM and STED imaging

Since the supramolecular co-assemblies formed by IAPP and ACMs are built up by smaller nanofiber units, the nature and morphology of these species should be investigated in more detail. For this purpose, confocal laser scanning microscopy (CLSM) and stimulated emission depletion (STED) imaging were performed because the achievable resolution can be improved using especially the latter[149]. To conduct these experiments, solutions of IAPP (16.5 µM) and Nle3-VF (1:2) containing 10 % TAMRA-IAPP and 10 % Atto647N-labelled Nle3-VF were prepared and aged for 7 days (in 1xb) before sample preparation. CLSM and STED imaging showed that such IAPP/Nle3-VF mixtures contained bicoloured hetero-nanofibers of different sizes and appearance (Figure 4-42). Larger hetero-nanofiber structures were assembled by several smaller nanofiber units (Figure 4-42). Strand widths were measured from confocal and STED images to compare characteristic features of IAPP homo-nanofibres and IAPP/Nle3-VF hetero-nanofibers (Table 4-13). As the measurements from confocal images are pretty close to the resolution limit of CLSM[126], measurements from STED are the more precise ones. Bicoloured hetero-nanofibers presented a total width of 232 ± 76 nm. The IAPP-containing strand area showed a width of 192 ± 59 nm, the Nle3-VF-containing strand area was 187 ± 74 nm thick. IAPP control samples contained nanofibers with a width of 124 ± 23 nm.

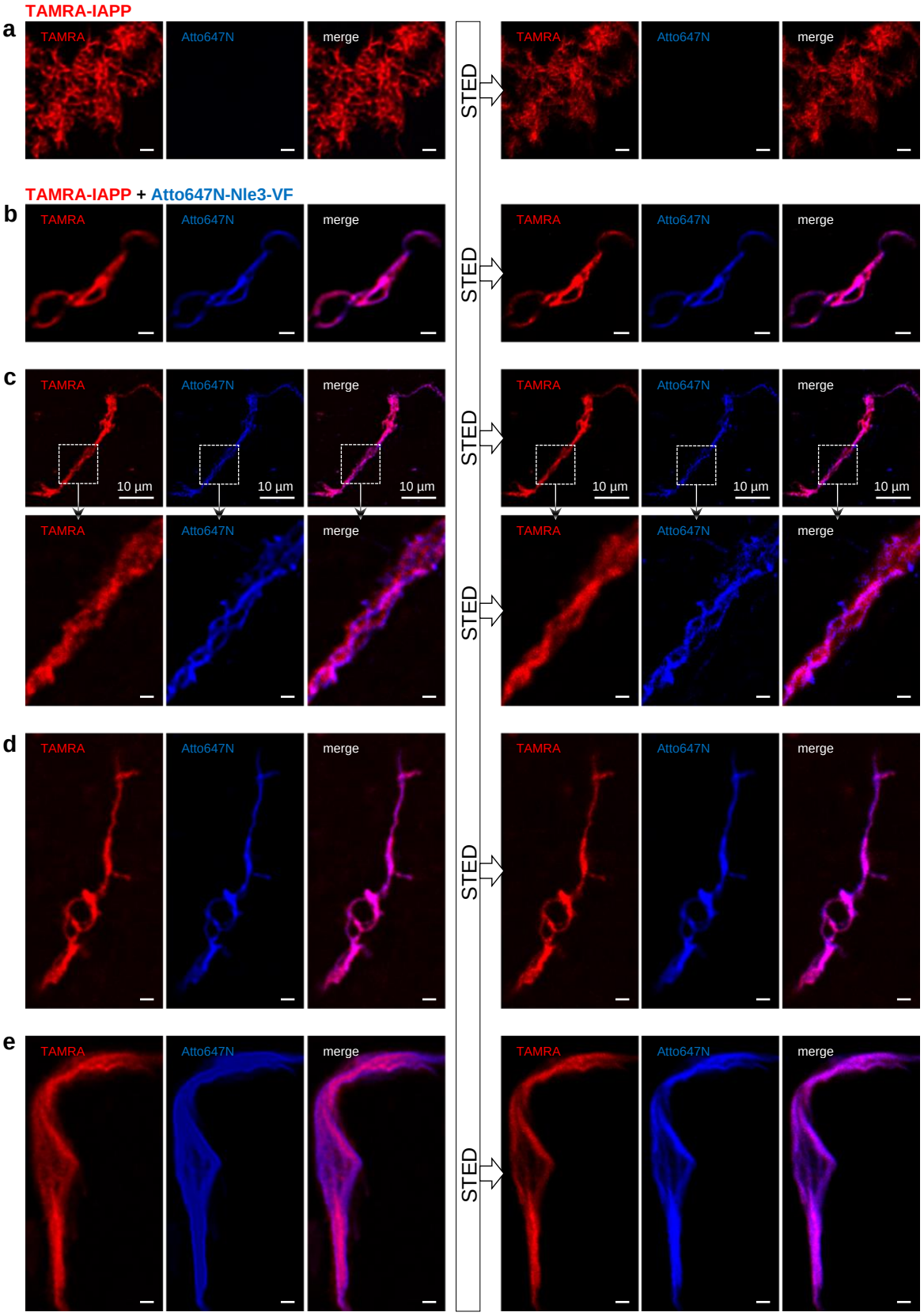

Figure 4-42: CLSM and STED imaging of fibrillar assemblies formed by TAMRA-IAPP and Atto647N-Nle3-VF. For CLSM and STED imaging, incubations of IAPP (total: 16.5 µM, (**a**)) or its mixture with Nle3-VF (1:2, (**b-e**)) containing 10 % TAMRA-labelled IAPP (1.65 µM, red) and 10 % Atto647N-labelled Nle3-VF (3.3 µM, blue) were aged for 7 days in 1xb. Left panels show CLSM pictures, right panels show the same areas analyzed by STED. Hetero-nanofibers are assembled by several inter-twined smaller nanofiber units. Scale bars are 1 µm if not stated otherwise. Images of a), b), and d) are part of a figure in reference [140].

The following conclusions can be drawn from the widths measurements obtained by STED imaging: First, IAPP nanofibers are significantly thinner than hetero-nanofibers (A vs. D in Table 4-13; *** P<0.001). Second, the IAPP strand in IAPP nanofibers is significantly thinner than the IAPP-containing strand area in fHetero (A vs. B in Table 4-13; * P<0.05). This could indicate that there might be a different arrangement and/or folding of IAPP monomer units in hetero-nanofibers compared to homo-nanofibres. Third, the IAPP-containing strand area and the Nle3-VF-containing strand area in hetero-nanofibers have the same width (B vs. C in Table 4-13; ns). In addition, the total width of hetero-nanofibers is identical to the width of the IAPP-containing and the Nle3-VF-containing strand areas (D vs. B/C in Table 4-13; ns). Moreover, the sum of widths of the IAPP-containing and the Nle3-VF-containing strand area in hetero-nanofibers is significantly larger than the total width of hetero-nanofibers that was measured (D vs. E in Table 4-13; *** P<0.001). At first sight, this might indicate that IAPP/Nle3-VF hetero-nanofibers do not form by lateral but by axial co-assembly of the peptides. Importantly, these measurements were performed on two-dimensional images and thus do not take into account the third dimension. Hence, the measurement of the total widths of hetero-nanofibers is biased by the viewing angle in which the image was taken. To gain more reliable insights into the IAPP/Nle3-VF hetero-nanofiber assembly mode, z-stacked images were taken using CLSM and 3D reconstructions of hetero-nanofibers were performed. The analyses showed that IAPP-containing and Nle3-VF-containing nanofiber bundles were parallelly arranged and partly intertwined (Figure 4-43).

In conclusion, the CLSM and STED data suggests that single IAPP/ACM hetero-nanofiber bundles assemble by a co-lateral stacking of IAPP and ACM molecules and that these “protofilament”-like stacks form the basic units of the supramolecular nanofibre co-assemblies. Of note, none of the applied imaging techniques can provide a resolution high enough to draw conclusions on the single-fibril level (~10 nm thick). Thus, further investigations are necessary to finally conclude on a co-lateral or a co-axial assembly mode.

Table 4-13: Widths of IAPP/Nle3-VF hetero-nanofibers obtained by CLSM and STED imaging. Values were obtained from CLSM and STED images by measuring widths of fluorescence signal intensities at half-maximum height using the LAS-X software. Error bars: means ± SD from 12-33 nanofibers (see Table 7-27 in Appendix). The diagram on the right graphically represents the STED-widths depicted in the table. “IAPP strand, fIAPP”: width of the IAPP strand in fIAPP; “IAPP strand, fHetero”: width of the IAPP strand in hetero-nanofibers; “Nle3-VF strand, fHetero”: width of the Nle3-VF strand in hetero-nanofibers; “total, fHetero (observed)”: total width of IAPP and Nle3-VF strand in the hetero-nanofibers; “total, fHetero (calculated)”: width obtained by mathematical addition of the single widths of IAPP and Nle3-VF strands in hetero-nanofibers. ns: not significant; *** P<0.001, * P<0.05 by one-way ANOVA and Bonferroni.

		CLSM	STED
A	IAPP strand, fIAPP	182 ± 16 nm	124 ± 23 nm
B	IAPP strand, fHetero	266 ± 95 nm	192 ± 59 nm
C	Nle3-VF strand, fHetero	257 ± 47 nm	187 ± 74 nm
D	Total width, fHetero (observed)	315 ± 73 nm	232 ± 76 nm
E	Total width, fHetero (calculated; sum A+B)	523 ± 124 nm	379 ± 117 nm

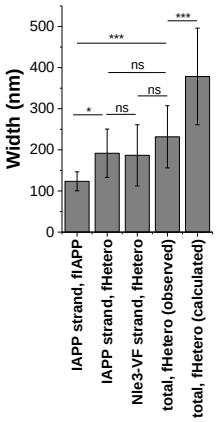

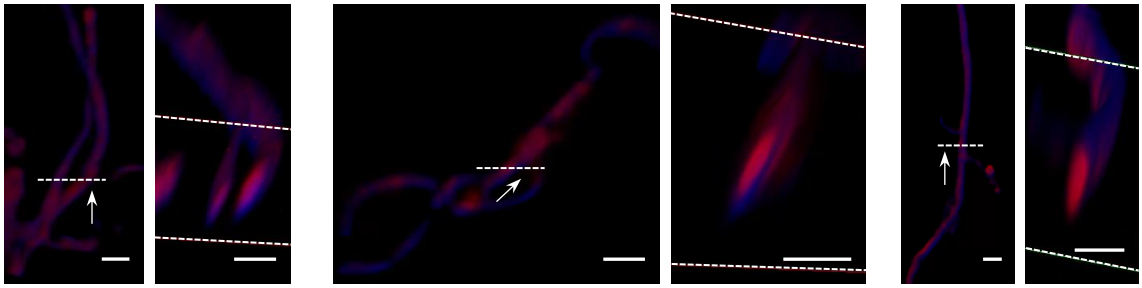

Figure 4-43: Co-lateral assembly of IAPP and Nle3-VF in heteromeric nanofibre bundles. 3D reconstructions of z-stacks of three different hetero-nanofibers (**a-c**) from CLSM imaging. Incubations were prepared in 1xb, aged for 7 days, and contained 14.85 µM IAPP, 1.65 µM TAMRA-IAPP, 29.7 µM Nle3-VF and 3.3 µM Atto647N-Nle3-VF (labelled peptides are 10 % of total). Dashed lines and arrows in the left panels show the view of the sections depicted on the right panels, respectively. Scale bars: 1 µm.

4.6.2.4 Evidence from FLIM-FRET analyses

Further evidence for a close interaction of IAPP with Nle3-VF within the fibrillar hetero-assemblies was obtained using fluorescence lifetime imaging (FLIM). Fluorescence lifetime is an intrinsic characteristic of a fluorophore and reflects the mean time for a fluorescent molecule to stay in the excited state before returning to the ground state after absorbing light. FLIM can be used for Förster resonance energy transfer (FRET) applications as the occurrence of FRET leads to the quenching of the donor fluorescence. Thus, by measuring the shortening of the fluorescence decay time of the donor in close proximity of an acceptor, FRET can be determined. To have a comparison, the lifetime (τ) of the donor, in this case Fluos-Nle3-VF, must be determined in absence of the acceptor in a first step. For this, Fluos-Nle3-VF (33 µM) was incubated for 6 days in 1xb and analysed after via 2-PM. A suitable area within the sample was chosen and lifetime was measured using the Leica SP8 FALCON application. The obtained decay curve can be found in Figure 4-44a. The data was fitted using a n-exponential reconvolution model implemented in the FALCON software. Three exponential components had to be used to obtain a suitable fit, meaning that the donor molecule shows a multi-exponential decay behaviour. The corresponding FLIM image and the lifetime distribution are shown in Figure 4-44b,c.

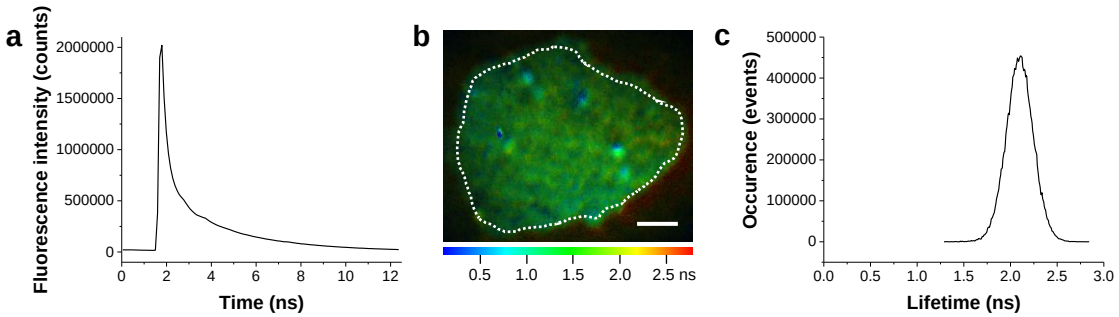

Figure 4-44: Donor lifetime determination of Fluos-Nle3-VF. For measuring the donor lifetime, a sample of 6 days aged Fluos-Nle3-VF (33 µM in 1xb) was analysed using the Leica SP8 FALCON application. A n-exponential reconvolution model using three exponential components was used to fit the data of the obtained decay curve. (**a**) Decay curve. (**b**) FLIM image. The highlighted area was used to determine the lifetime distribution in c. Coloured bar shows the lifetime. Scale bar is 10 µm. (**c**) Lifetime distribution in the sample area highlighted in b. Figure is part of a figure in reference [140].

In a next step, a similar FLIM-FRET analysis was performed for the loop-shaped macro-assemblies formed by IAPP and Nle3-VF where the donor Fluos-Nle3-VF is supposed to be in close proximity of the acceptor TAMRA-IAPP within the hetero-nanofibers. The same macro-assemblies as already shown in Figure 4-39 were analysed. In both cases, Fluos-Nle3-VF showed a shortened fluorescence decay time compared to the donor-alone control and the lifetime decreased from ~2.1 ns to ~0.8 ns and ~1.0 ns, respectively. A shortened lifetime and a high FLIM-FRET efficiency (~50-60 %) were observed throughout the whole fibrillar assemblies. Both the reduced donor lifetime in presence of the acceptor and the high FRET efficiency indicate that donor and acceptor are close enough for good energy transfer. As a prerequisite for FRET to occur is that donor and acceptor molecule are less than 10 nm separated from each other, it can be concluded that the distance between TAMRA-IAPP and Fluos-Nle3-VF within the hetero-nanofibers is not more than 10 nm, consistent with a close interaction between the two peptides in the hetero-assemblies. As the Förster's radius R_0 of the TAMRA/Fluos FRET pair is known to be 5.5 nm[150], the spatial separation of the two

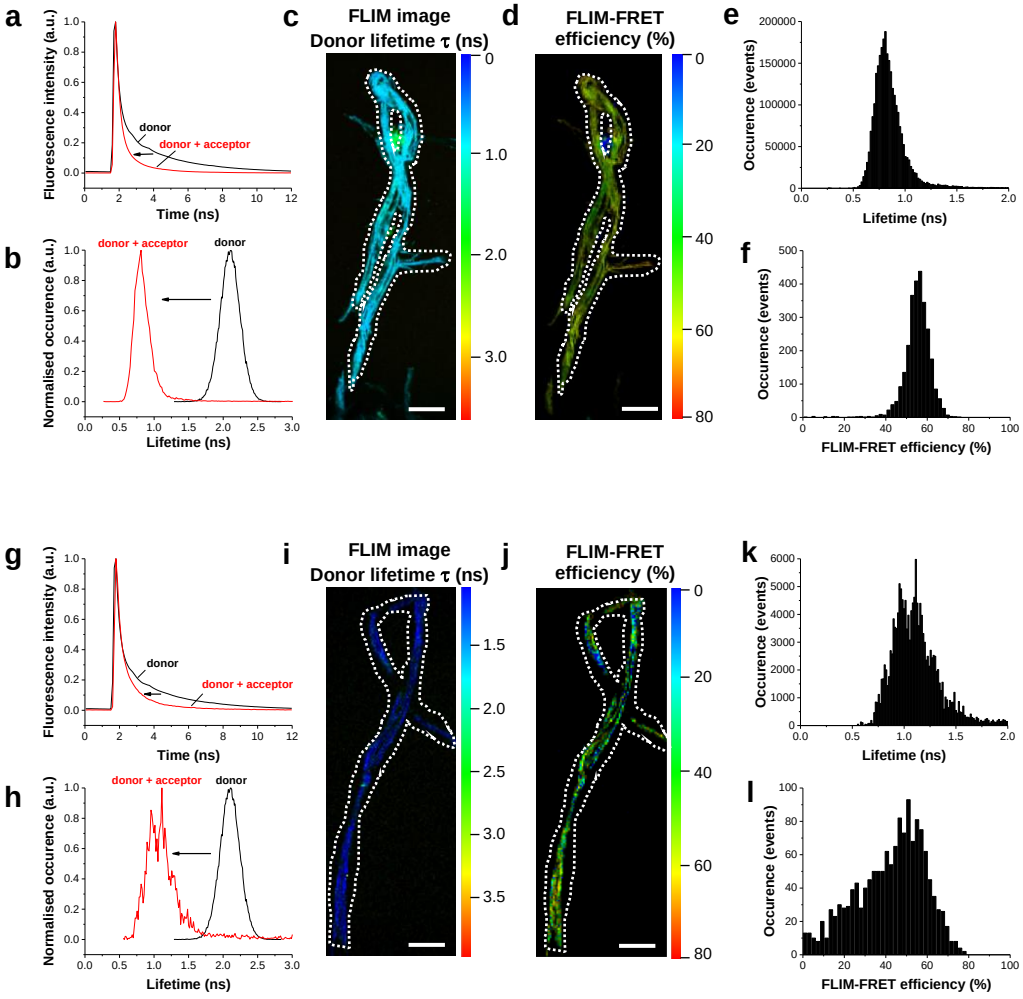

Figure 4-45: FLIM-FRET analysis of hetero-nanofibers formed by TAMRA-IAPP and Fluos-Nle3-VF from two different samples. Sample 1 (**a-f**) contained 6 days aged and sample 2 (**g-l**) contained 7 days aged mixtures of TAMRA-IAPP (16.5 µM) and Fluos-Nle3-VF (1:2) (in 1xb). (**a.g**) Decay curves of donor fluorescence in presence and absence of acceptor. (**b,h**) Lifetime of donor in presence and absence of acceptor. (**c,i**) FLIM image. Dotted lines highlight analysed area. Coloured bar represents the lifetime. Scale bar is 50 µm. (**d,j**) FLIM-FRET efficiency. Dotted lines highlight analysed area. Coloured bar represents the calculated efficiency. Scale bar is 50 µm. (**e,k**) Lifetime distributions of the hetero-nanofibers shown in c, and i, respectively. (**f,l**) FLIM-FRET efficiency distrubutions of the hetero-nanofibers shown in d, and j, respectively. Data of a-f) is part of a figure in reference [140].

peptides can be narrowed down even more precisely. R_0 is defined as the distance at which the energy transfer efficiency of a specific FRET pair is 50 %. For the hetero-nanofiber macro-assemblies an efficiency of ~50-60 % was determined. Thus, IAPP and Nle3-VF are most probably separated by ~5.5 nm or even less.

Of note, similar results were obtained for FLIM-FRET analyses of IAPP/Aβ40 and IAPP/Aβ42 hetero-nanofibers, indicating that ACMs are indeed mimicking Aβ's natural interaction with IAPP as intended by their design concept (Figure 7-53 and Figure 7-54 in Appendix).

4.6.3 IAPP/ACM amorphous aggregates transform into fibrillar co-assemblies

The findings presented earlier in this thesis showed that both the formation of amorphous heterocomplexes at early time points and the formation of heterofibrils/-nanofibers at later time points are necessary for IAPP inhibition by ACMs (see chapters 4.4 and 4.5). One remaining question was: How are these two separate states linked to each other and what are the basic prerequisites for heterofibril/-nanofiber formation? The hypothesis was that heterocomplexes convert into fibrillar co-assemblies.

To test this hypothesis, morphologies of assemblies of IAPP (16.5 µM) aged in presence and absence of Nle3-VF (ratio 1:2) was followed and analysed via TEM. Incubations for these studies were prepared in the two most frequently used buffers applied in other studies, 1xb and ThT assay buffer with 0.5 % HFIP. IAPP contained amorphous aggregates at time 0 h and was completely turned into fibrils after 24 h (Figure 4-46a,b). As expected, IAPP/Nle3-VF mixtures showed amorphous aggregates in the beginning still being present after 24 h and starting to convert into fibrils at or after 48 h depending on the buffer system. Full transition into fibrils was observed at 72 h in both cases. This result was further confirmed by CLSM imaging: 24 h aged IAPP (containing 10 % TAMRA-IAPP) was completely fibrillated already whereas 24 h/ 48 h aged mixtures of IAPP and Nle3-VF (1:2; containing 10 % TAMRA-IAPP and 10 % Fluos-Nle3-VF or Atto647N-Nle3-VF) still showed amorphous aggregates starting to convert into hetero-nanofibers (Figure 4-46c).

In conclusion, TEM and 2-PM analyses suggested that fibrillar IAPP/ACM co-assemblies emerge from amorphous hetero-assemblies. A similar trend for the conversion of amorphous aggregates into fibrils was also observed for all other IAPP/ACM mixtures (see TEM Figure 4-21 in chapter 4.4).

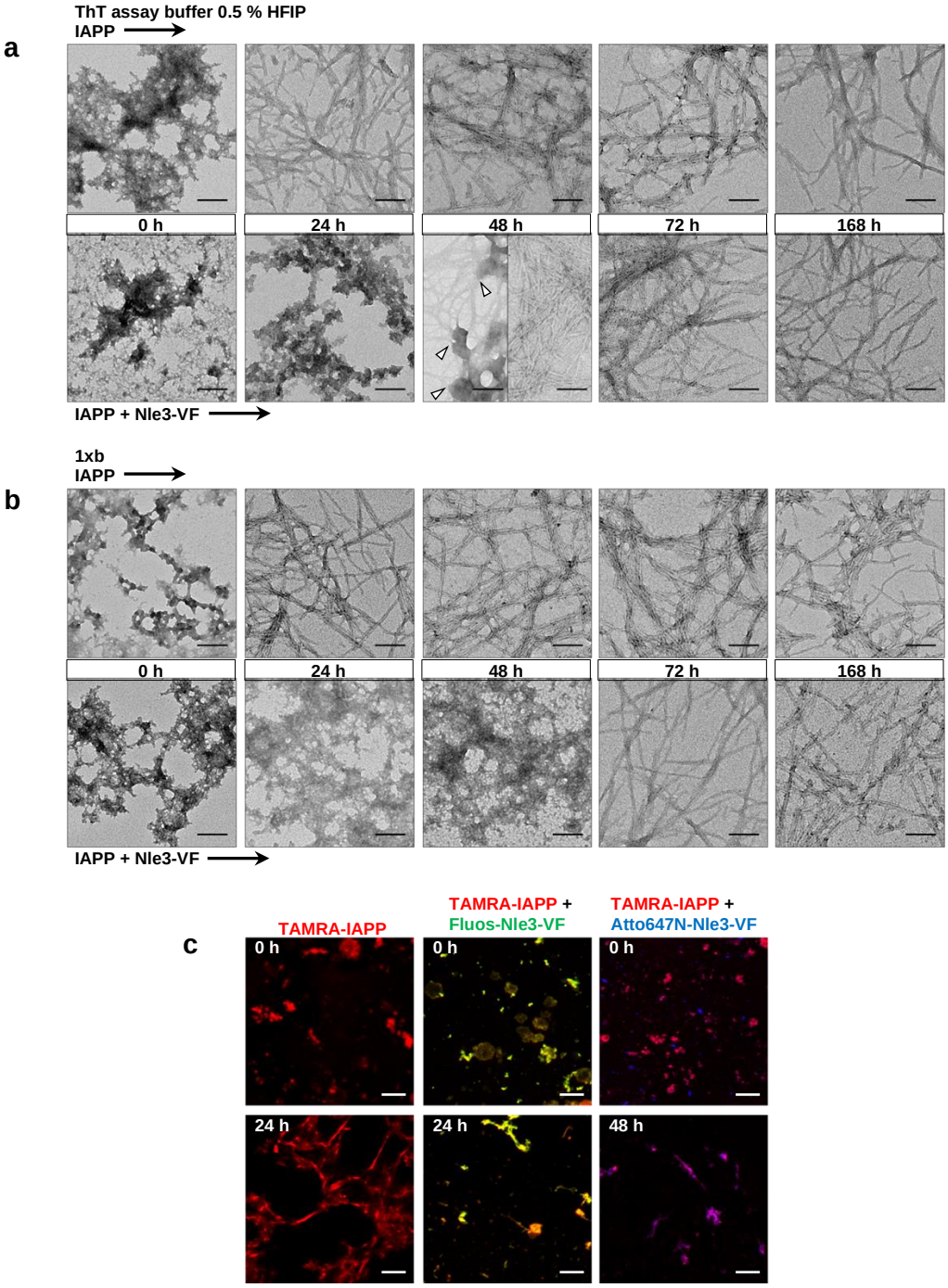

Figure 4-46: Transformation of IAPP/Nle3-VF amorphous co-assemblies into fibrillar ones. (**a,b**) TEM imaging. Aliquots of solutions containing either IAPP (16.5 µM) or its mixture with Nle3-VF (1:2) were taken at indicated time points during the aging process. Samples were prepared under two different buffer conditions, ThT assay buffer with 0.5 % HFIP (a) and 1xb (b). Full transition into fibrils was found after 72 h in both cases. Arrow heads in a, highlight fibrils emerging from amorphous aggregates. Scale bars are 100 nm. (**c**) CLSM imaging. Samples were prepared as in b, but contained 10 % TAMRA-labelled IAPP (red) and 10 % Fluos-labelled Nle3-VF (green) or 10 % Atto647N-labelled Nle3-VF (blue). IAPP/Nle3-VF mixtures show bicolored amorphous aggregates at 0 h which start transforming into hetero-nanofibers at 24 h/ 48 h, respectively. IAPP is already full fibrillated at 24 h. Scale bars are 10 µm. Images of b) are part of a figure in reference [140].

4.7 Studies on the requirements for the formation of fibrillar IAPP/ACM co-assemblies

4.7.1 IAPP/ACM fibrillar co-assemblies are not formed by deposition of ACM onto the IAPP fibril surface

The first aim was to exclude that heterofibrils/-nanofibers are simply generated by deposition of inhibitor on fIAPP. In fact, dot blot experiments performed by Christina Lindner during her Master thesis[140,151] showed that ACMs can bind to preformed IAPP fibrils. Therefore, the following experiment was performed: IAPP was aged, mixed after with Nle3-VF and incubated for another 4 days prior to sample preparation. IG-TEM showed that fibrils are still present after incubation with peptide but changed antibody-reactivity (Figure 4-47a). IAPP fibrils stained positively for the anti-fIAPP antibody whereas fibrils analysed 4 days after mixing stained mostly positively for the anti-Aβ antibody, further confirming peptide binding on the IAPP fibrils' surface. The ratio of anti-fIAPP:anti-Aβ antibody binding in the heterofibrils-containing control incubation was similar to previous findings (~55:45) (see chapter 4.6.1) and thus significantly different from the antibody-reactivity of Nle3-VF-"coated" IAPP fibrils, indicating that the two species are not the same.

Possible morphological differences between hetero-nanofibers derived from mixtures of monomeric IAPP with inhibitor and mixtures of fibrillar IAPP with inhibitor (termed "coated" fIAPP) were examined via 2-PM. 2-PM showed that fibrillar species found in samples containing TAMRA-fIAPP (16.5 µM) coated by Fluos-Nle3-VF (33 µM) were similar in size and shape to untreated TAMRA-fIAPP and that inhibitor is bound to the nanofibers' surface (Figure 4-47b). The appearance of coated fIAPP is thus clearly different from IAPP/Nle3-VF hetero-nanofibers which are composed of diverse smaller hetero-nanofiber units. Additionally, TAMRA-fIAPP (16.5 µM) coated by the non-inhibitor Fluos-VGS-VF (33 µM) were examined (Figure 4-47b). Their appearance was identical to the ones observed when the treatment was done with Fluos-Nle3-VF. To further prove the coating of fIAPP by Nle3-VF, another label combination was chosen. Atto647N-labelled Nle3-VF was used instead of Fluos-Nle3-VF and solutions contained mixtures of labelled and unlabelled peptides (IAPP total 16.5 µM, including 10 % TAMRA-IAPP; Nle3-VF total 33 µM, including 10 % Atto647N-Nle3-VF). The observed fibrillar species resembled those found when TAMRA-IAPP and Fluos-Nle3-VF were used. The Nle3-VF peptide layer covering parts of the nanofiber surface could be clearly detected (Figure 4-47c).

In addition to their different morphology and antibody-reactivity compared to heterofibrils/-nanofibers, ACM-coated fIAPP are – in contrast to heterofibrils/-nanofibers – still binding ThT (see Figure 4-24f in chapter 4.4) and exhibit cytotoxic effects on RIN cells (Figure 4-48a). Furthermore, fIAPP coated by the ACMs Nle3-VF, L3-VF or F3-VF still can seed IAPP fibril formation as efficient as untreated fIAPP seeds (Figure 4-48b), meaning that ACMs cannot interfere with secondary nucleation events. Analogue results were found for seeds-coating by the non-inhibitor control VGS-VF, indicating that fibrillar species resulting from coating by inhibitors and non-inhibitors have similar properties as fIAPP. Lastly, ACMs can only exhibit inhibitory effects on IAPP fibril formation when they are added prior to aggregation but not

when they are added during IAPP's growth or saturation phase, where IAPP is partly or fully in its fibrillar state (Figure 4-48c,d).

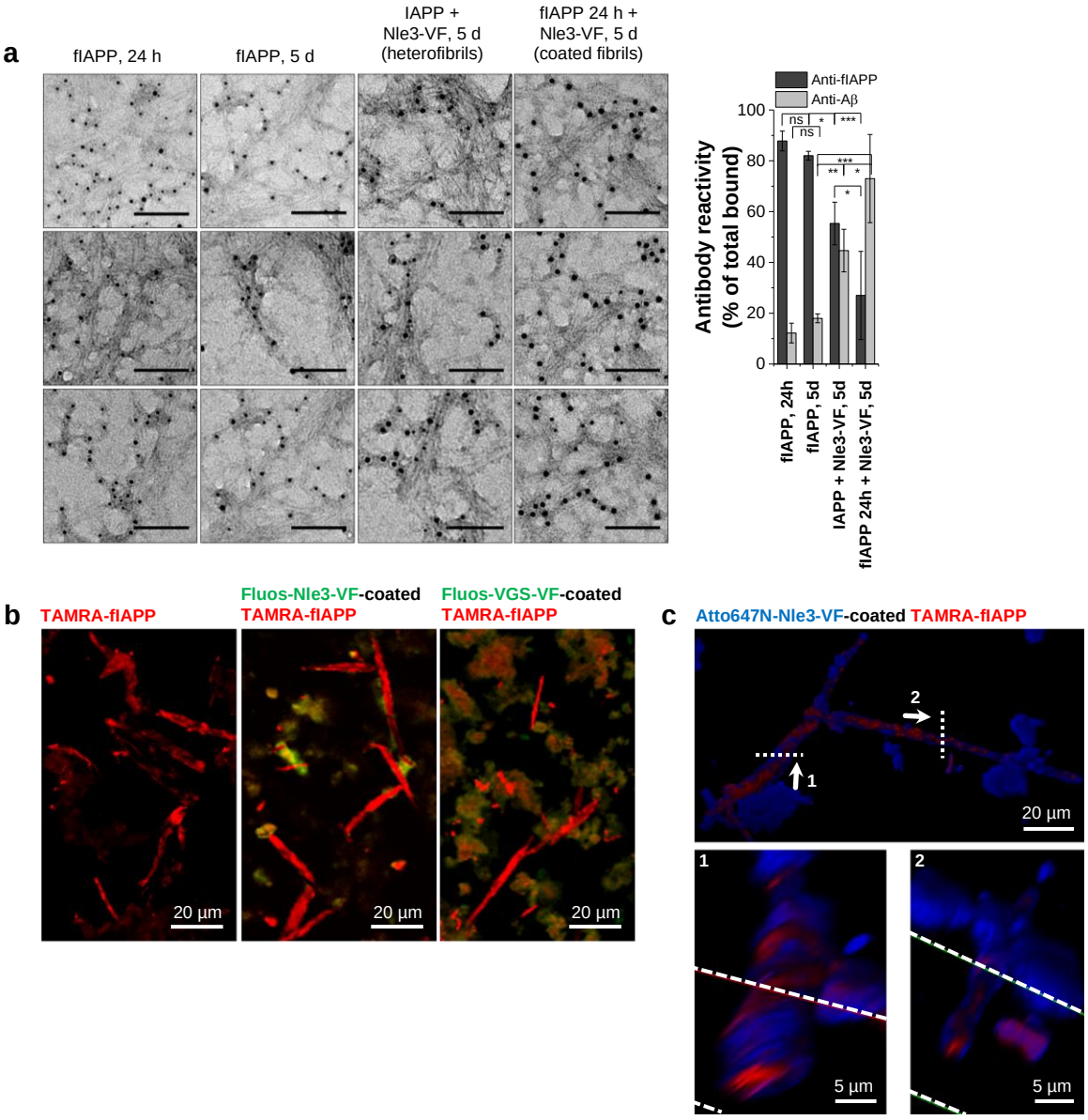

Figure 4-47: "Coating" of fIAPP by ACMs. (**a**) Differences in antibody-reactivity of Nle3-VF-coated fIAPP and IAPP/Nle3-VF heterofibrils elucidated by IG-TEM. Immunogold reactions were examined by TEM using the anti-fIAPP antibody and an anti-Aβ antibody. (IAPP 5 nm gold; Nle3-VF 10 nm gold). Due to unspecific anti-Aβ antibody binding to fIAPP (~ 10-20 %) samples containing only fIAPP show week staining by 10 nm gold particles. Mixtures of Nle3-VF with monomeric IAPP (16.5 µM, mix 1:2, ThT assay buffer 0.5 % HFIP, "heterofibrils") and fIAPP (24 h aged, 16.5 µM, coated 1:2, "coated fibrils")) present different antibody reactivity compared to fIAPP and compared to each other showing that either heterofibrils are formed or peptide is binding to the IAPP fibril surface. For quantification (see bar diagram right), gold particles in 4 fibril-containing areas with a size of 0.4 µm^2 each were counted for "fIAPP, 24h"; in 3 fibril-containing areas with a size of 0.4 µm^2 (n=2) or 2.5 µm^2 (n=1) each were counted for "fIAPP, 5 d"; in 3 fibril-containing areas with a size of 0.4 µm^2 each were counted for "IAPP+Nle3-VF, 5 d (heterofibrils)"; in 3 fibril-containing areas with a size of 2.5 µm^2 each were counted for "fIAPP 24 h+Nle3-VF, 5 d (coated fibrils)". Error bars show mean ± SD. *** P<0.001, ** P<0.01, ** P<0.05, ns: not significant, by one-way ANOVA and Bonferroni. Scale bars are 100 nm. (**b**) Coating of fIAPP by ADPs visualised by 2-PM. Labelled nanofibers were generated by incubating 16.5 µM TAMRA-IAPP for 7 days in 1xb. Nanofibers were incubated thereafter for 1 day using a 2-fold Fluos-peptide excess (33 µM). (**c**) 3D representation of an inhibitor-coated IAPP nanofiber analysed via 2-PM. Labelled nanofibers were generated by incubating 16.5 µM IAPP containing 10 % TAMRA-IAPP for 2 days in 1xb. After, nanofibers were incubated for 1 day using a 2-fold excess of Nle3-VF (33 µM, containing 3.3 µM Atto647N-Nle3-VF (10 %)). Lower images show nanofiber cross-sections indicated by the dotted lines and numbers. Selected images and bar graph of a), and images of c) are part of a figure in reference [140].

Taken together, the findings that 1) the treatment of preformed fIAPP with inhibitor does neither result in the antibody-reactivity nor in the nanofiber morphology expected for heterofibrils/-nanofibers, 2) the species present after coating by inhibitory and non-inhibitory ADPs are similar, 3) coated fIAPP show ThT binding and cytotoxicity which is not found for heterofibrils/-nanofibers, 4) ACM-coated fIAPP accelerate IAPP aggregation as untreated fIAPP and 5) Nle3-VF and F3-VF only block IAPP aggregation when mixed with non-fibrillar IAPP, further support the notion that IAPP/ACM heterofibrils/-nanofibers are not formed by deposition of inhibitor on the fIAPP surface.

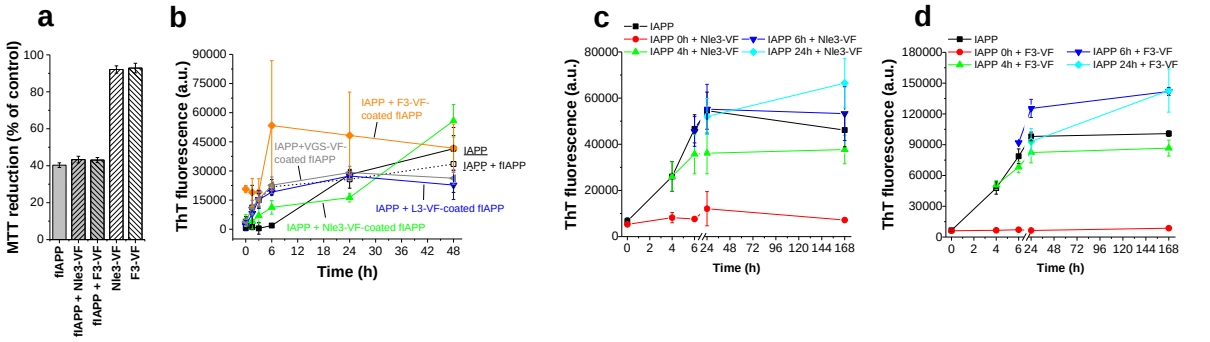

Figure 4-48: Studies on the effects of coating of fIAPP by ACMs. (**a**) For determining the cytotoxicity of ACM-coated fIAPP, 7 days aged IAPP (16.5 µM in ThT assay buffer 0.5 % HFIP) was mixed 1:2 with ACMs and left 1 day for incubation. Coated fIAPP were applied onto RIN5fm cells (500 nM IAPP). ACMs alone were used as controls. Error bars represent mean ± SD from two assays each performed in triplicate (for fIAPP and mixtures) and mean ± SD from one assay performed in triplicate for ACM controls. (**b**) Effects of ACM-coating on fIAPP seeding ability were studied via the ThT binding assay. fIAPP were coated by ACMs via pre-incubation (1:2) for 1 day prior to experiment. IAPP (16.5 µM) fibril formation was followed over 48 h in absence and presence of 10 % fIAPP pre-incubated with respective ACM. Non-coated fIAPP seeds were used as control. Error bars represent mean ± SD from three assays (n=4 for unseeded IAPP). (**c,d**) Inhibition of aged IAPP was performed using 16.5 µM IAPP. Fresh IAPP was either directly mixed with Nle3-VF or F3-VF (ratio 1:2) or aged for the indicated time prior to peptide application. Aggregation kinetics were followed using the ThT binding assay. Error bars represent mean ± SD from three assays. Data in a) and c) is part of a figure in reference [140].

4.7.2 IAPP/ACM fibrillar co-assemblies is induced by prefibrillar IAPP species

Having proven that fibrillar IAPP/ACM co-assemblies emerge from heterocomplexes and are not formed by ACM deposition on fIAPP, additional studies were performed to shed more light on basic prerequisites or triggers of fibrillar co-assembly. One possibility could be that the inhibitor (in non-aged/non-fibrillar form) acts as a template (seed) for heterofibril-nanofiber generation. This was excluded by the fact that sub-stoichiometric amounts of ACMs did not inhibit IAPP (see IC_{50}s, chapter 7.3 in Appendix). Furthermore, inhibitors alone were not found to form fibrils which may seed IAPP amyloid formation or act as template up to a concentration of 100 µM (see Figure 4-22 in chapter 4.4). Another possibility could be that fIAPP which forms during the incubation acts as a seed of ACM-IAPP co-fibrillation thus templating by itself the heterofibril/-nanofiber generation. The finding that ThT fluorescence did not decrease when Nle3-VF or F3-VF were added to aged IAPP (see Figure 4-48c,d) indicates that this is not the case. To further address this issue, peptides were incubated in presence of small amounts of preformed fIAPP seeds. As samples should be analysed via 2-PM, the labelled peptides Fluos-Nle3-VF or Fluos-VGS-VF and TAMRA-IAPP were used once more. Examination of freshly prepared samples (0 h) showed that seeded Fluos-Nle3-VF solutions contained bicolored fibrillar species, whereas seeded Fluos-VGS-VF solutions contained TAMRA-IAPP nanofibers

and unstructured peptide or peptide/IAPP aggregates (Figure 4-49a,b). Similar observations were made for this mixture after 48 h of incubation. The 48 h aged seeded Fluos-Nle3-VF solution contained different species compared to the fresh one, namely, TAMRA-IAPP nanofibers and amorphous peptide/IAPP aggregates which were very similar to the ones found in seeded Fluos-VGS-VF solutions. In some cases, Fluos-Nle3-VF was also found to be bound in the TAMRA-IAPP nanofiber surface (similar to "coated" fIAPP, see chapter 4.7.1). In conclusion, the fibrillar species resulting from seeding of Fluos-Nle3-VF with a sub-stoichiometric amount of TAMRA-fIAPP seeds do not resemble the previously described hetero-nanofibers even if initially some ordered structural arrangement of Fluos-Nle3-VF might take place in presence of TAMRA-fIAPP.

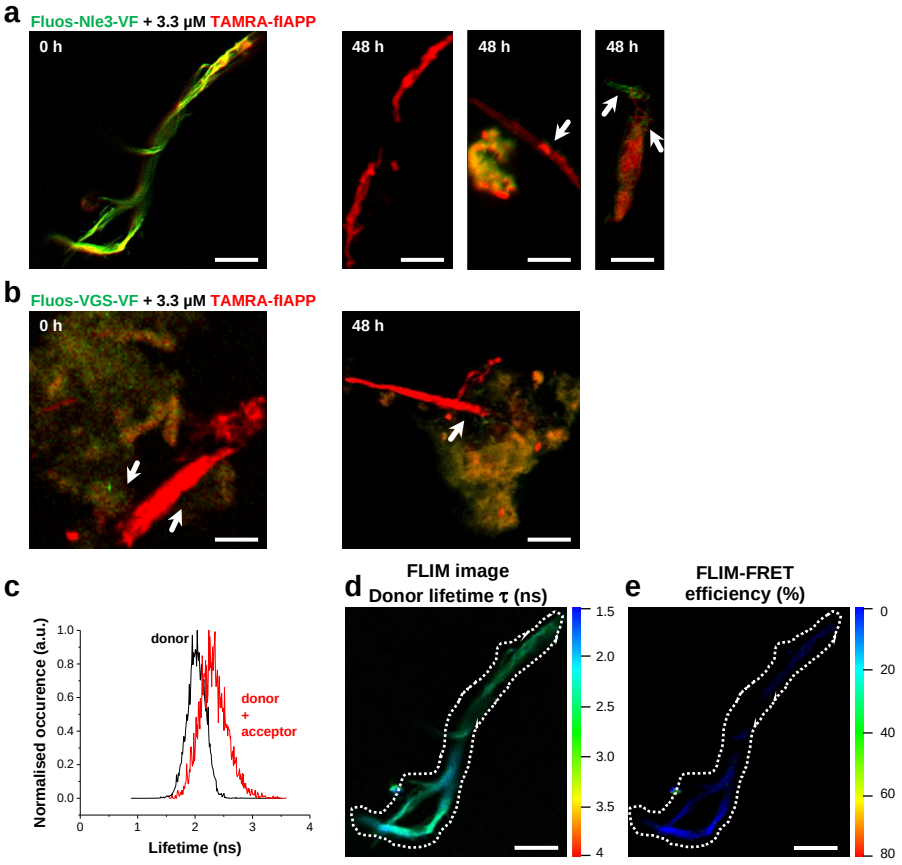

Figure 4-49: 2-PM and FLIM-FRET analysis of nanofibers found in fIAPP-seeded peptide solutions. (**a,b**) 2-PM analysis of species in TAMRA-fIAPP seeded Fluos-ADP solutions. Solutions of 33 µM Fluos-labelled ADPs (in 1xb, green) were seeded with preformed TAMRA-fIAPP (red) and analysed at indicated time points. A freshly prepared solution (0 h) of seeded inhibitor Fluos-Nle3-VF contained bicolored nanofiber structures whereas a freshly prepared solution of seeded non-inhibitor Fluos-VGS-VF contained TAMRA-IAPP fibrils and peptide or peptide/IAPP aggregates which were also present after 48 h aging. The 48 h aged sample of seeded Fluos-Nle3-VF contained TAMRA-IAPP fibrils as main species where peptide was bound to the surface in some cases and peptide or peptide/IAPP aggregates. Arrows indicate where peptide is in contact with TAMRA-fIAPP. Scale bars are 10 µm. (**c**) Lifetime of donor Fluos-Nle3-VF in absence and presence of acceptor TAMRA-fIAPP. Analysed were the bicolored nanofiber structures shown in a). Donor-alone data was kindly provided by Beatrice Dalla Volta[140,152]. (**d**) FLIM image of the nanofiber assembly shown in a). Coloured bar represents the lifetime. Scale bar is 10 µm. (**e**) FLIM-FRET efficiency of the nanofiber assembly shown in a). Coloured bar represents the calculated efficiency. Scale bar is 10 µm. Data in c-e) is part of a figure in reference [140].

To investigate if these early nanofiber species do have something in common with hetero-nanofibers formed in IAPP/Nle3-VF 1:2-mixtures, they were subjected to FLIM-FRET analysis. The determined lifetime of the donor Fluos-Nle3-VF within the examined nanofiber structure was very similar to the lifetime of the donor-alone control and little to no energy transfer was

observed (FLIM-FRET efficiency < 20 %) (Figure 4-49c-e). Both findings indicate that donor and acceptor molecule are not closely associated to each other within nanofibers resulting from seeding of Fluos-Nle3-VF with TAMRA-fIAPP seeds but are separated by more than 10 nm. In contrast, an efficient energy transfer and a significantly decreased donor lifetime was observed in context of hetero-nanofibers as described before. Taken together, seeding of ACMs by fIAPP does not result in fibrillar species similar to hetero-nanofibers and therefore the formation of fIAPP does not seem to be the leading trigger for subsequent generation of heterofibrils/-nanofibers in IAPP/ACM mixtures.

If fIAPP themselves are not triggering ACM/IAPP co-fibrillation, maybe IAPP in its prefibrillar form (monomeric or oligomeric) is the template which is initiating heterofibril/-nanofiber formation. This could be reasonable considering previous results showing that full inhibition of IAPP fibrillogenesis by Nle3-VF and F3-VF and heterofibril/-nanofiber formation is observed only when peptides are added prior to IAPP fibrillation. To address this issue, 2-PM studies were conducted on IAPP/ADP mixtures containing a 10-times reduced IAPP amount to investigate if hetero-nanofibers are still formed. At 48 h, both TAMRA-IAPP/Fluos-ADP mixtures (1.65 µM/33 µM) contained bicoloured fibrillar species (Figure 4-50). In case of the non-inhibitory ADP VGS-VF hetero-nanofiber formation is most likely due to the increased ADP:IAPP excess (20:1), giving the peptide some inhibitory properties. In addition, hetero-nanofibers found in the 7 days aged TAMRA-IAPP/Fluos-Nle3-VF mixtures look very similar to corresponding mixtures containing 10-times more TAMRA-IAPP (supramolecular nanofibre co-assemblies built up by smaller hetero-nanofiber units; Figure 4-50). To investigate similarities between hetero-nanofibers formed in IAPP/ACM mixtures containing 16.5 µM and mixtures containing 1.65 µM TAMRA-IAPP, fibrillar species in 48 h aged TAMRA-IAPP/Fluos-Nle3-VF (1.65 µM/33 µM) solutions were then subjected to FLIM-FRET analysis in a next step.

Within the analysed hetero-nanofiber, Fluos-Nle3-VF displayed a shortened fluorescence decay time compared to the donor-alone control and its lifetime decreased from ~2.2 ns to ~0.7 ns (Figure 4-51a-c), as it was also found for hetero-nanofibers originating from solutions containing 10-times more TAMRA-IAPP. Since the FLIM-FRET efficiency was determined to be ~75 % (Figure 4-51d) it can be assumed that both peptides are closer than the TAMRA/Fluos Förster's distance (5.5 nm) also in this case. These findings further indicate that IAPP in sub-stoichiometric amounts can induce the generation of similar hetero-nanofibers as when applied at significantly higher concentrations.

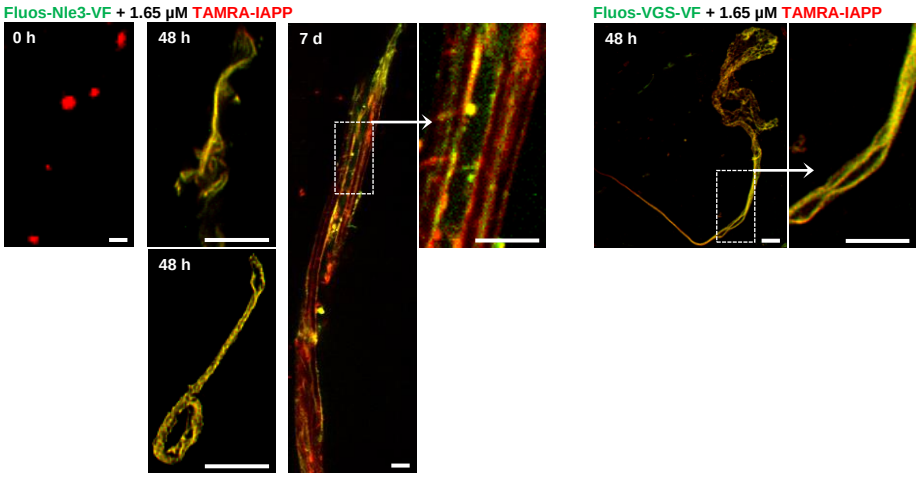

Figure 4-50: 2-PM analysis of species formed by peptides and sub-stoichiometric IAPP amounts. Incubations for fluorescence microscopy were freshly prepared in 1xb using 33 µM of Fluos-ADP (green) and 1.65 µM of TAMRA-IAPP and then aged for the indicated time. Freshly prepared TAMRA-IAPP/Fluos-Nle3-VF mixtures (0 h) did not contain fibrillar species. Both ADPs show hetero-nanofiber formation with IAPP at 48 h. Nanofiber species found in 7 days aged mixtures with Fluos-Nle3-VF contained huge macro-assemblies consisting of smaller nanofiber units. Scale bars are 10 µm. Images of "Fluos-Nle3-VF + 1.65 µM TAMRA-IAPP" are part of a figure in reference [140] (adapted figure version).

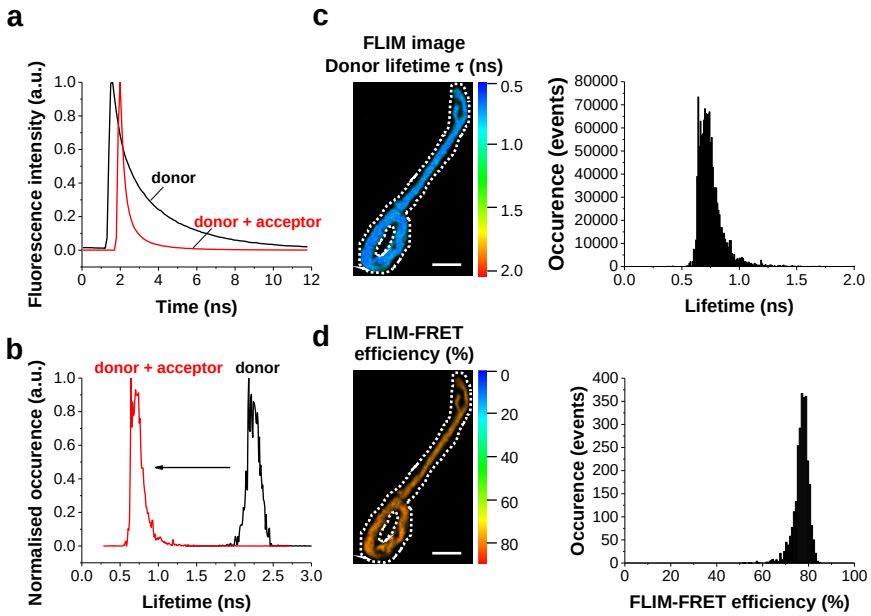

Figure 4-51: FLIM-FRET analysis of nanofibers formed in 48 h aged mixtures of Fluos-Nle3-VF and sub-stoichiometric TAMRA-IAPP amounts. Solutions were prepared in 1xb using 33 µM of Fluos-Nle3-VF and 1.65 µM of TAMRA-IAPP. Examined species were the ones presented in Figure 4-50. (**a**) Decay curves of the donor in presence and absence of the acceptor TAMRA-IAPP. Donor-alone data was kindly provided by Beatrice Dalla Volta[140,152]. (**b**) Lifetime of the donor in presence and absence of the acceptor TAMRA-IAPP. Donor-alone data was kindly provided by Beatrice Dalla Volta[140,152]. (**c**) FLIM image. Dotted lines highlight analysed area. Coloured bar represents the lifetime. Scale bar is 10 µm. Bar diagram on the right shows lifetime distribution corresponding to the FLIM image. (**d**) FLIM-FRET efficiency. Dotted lines highlight analysed area. Coloured bar represents the calculated efficiency. Scale bar is 10 µm. Bar diagram on the right shows efficiency distribution corresponding to the FLIM-FRET image. Figure is part of a figure in reference [140].

In addition, bicoloured fibrils found in 2-PM studies which were generated by different strategies – namely, by mixing TAMRA-IAPP with Fluos-ADPs either 16.5 µM : 33 µM or 1.65 µM : 33 µM or by seeding 33 µM Fluos-ADP solutions with 3.3 µM preformed TAMRA-fIAPP – were compared regarding their strand widths (Table 4-14). For this, widths of fluorescence signal intensities resulting from TAMRA-IAPP or Fluos-ADP were measured at half-maximum height using the LAS-X software to determine the width of the single

components and the total strand thickness. To reduce background noise influences as much as possible, pictures from 2-PM were deconvolved 2-3 times before the measurements were performed. Nanofiber assemblies found in solutions containing the standard mixture generating hetero-nanofibers (16.5 µM TAMRA-IAPP, 33 µM Fluos-Nle3-VF, 7 days aged) were found to be 455 ± 128 nm wide in total. The width resulting from measuring the Fluos-Nle3-VF component was 375 ± 50 nm, the one from TAMRA-IAPP was 348 ± 69 nm. In contrast, bicoloured nanofibers generated when Fluos-Nle3-VF (33 µM) is mixed with 10 % TAMRA-fIAPP show similar strand widths of the single components (370 ± 76 nm for Fluos-Nle3-VF, 337 ± 89 nm for TAMRA-IAPP) but the total width is much higher and corresponds approximately to the sum of both (622 ± 153 nm). This indicates that in this case the one peptide might deposit on the other. The difference in the peptides' arrangement is also supported by the previously discussed FLIM-FRET results where no reduction in donor lifetime and no energy transfer between donor and acceptor was observed for these nanofibers. Also, a greater distance between TAMRA-IAPP strand and Fluos-Nle3-VF strand was observed when analysing the 2-PM images in more detail (Figure 4-52). As found for mixtures containing 16.5 µM TAMRA-IAPP, hetero-nanofibers in mixtures with 1.65 µM TAMRA-IAPP and 33 µM Fluos-Nle3-VF showed a total strand width (370 ± 64 nm) similar to the single strand widths of both components (345 ± 70 nm and 342 ± 49 nm, respectively) (Table 4-14). The total strand width of hetero-nanofibers in mixtures of 1.65 µM TAMRA-IAPP with 33 µM Fluos-VGS-VF was higher (518 ± 95 nm) but this is most likely due to the higher width of the peptide signal (480 ± 79 nm). The increased width of the ADP component might be related to the peptide's conformation itself, since previous CD studies indicated a less ordered structure compared to Nle3-VF which might lead to a more extended arrangement within the hetero-nanofiber.

Table 4-14: Widths of hetero-nanofibers compared to nanofibers generated by peptides and sub-stoichiometric amounts of IAPP or fIAPP measured from 2-PM samples. Values were obtained from 2-PM images by measuring widths of fluorescence signal intensities at half-maximum height using the LAS-X software. For representative images of the different samples see Figure 4-52. Error bars represent means ± SD from 10-11 nanofibers (see Table 7-28 to Table 7-31 in the Appendix).

	width ADP strand (nm)	**width IAPP strand (nm)**	**total width (nm)**
Hetero-nanofibers (7 d)	375 ± 50	348 ± 69	455 ± 128
Fluos-Nle3-VF + 3.3 µM TAMRA-fIAPP (0 h)	370 ± 76	337 ± 89	622 ± 153
Fluos-Nle3-VF + 1.65 µM TAMRA-IAPP (48 h)	342 ± 49	345 ± 70	370 ± 64
Fluos-VGS-VF + 1.65 µM TAMRA-IAPP (48 h)	480 ± 79	351 ± 84	518 ± 95

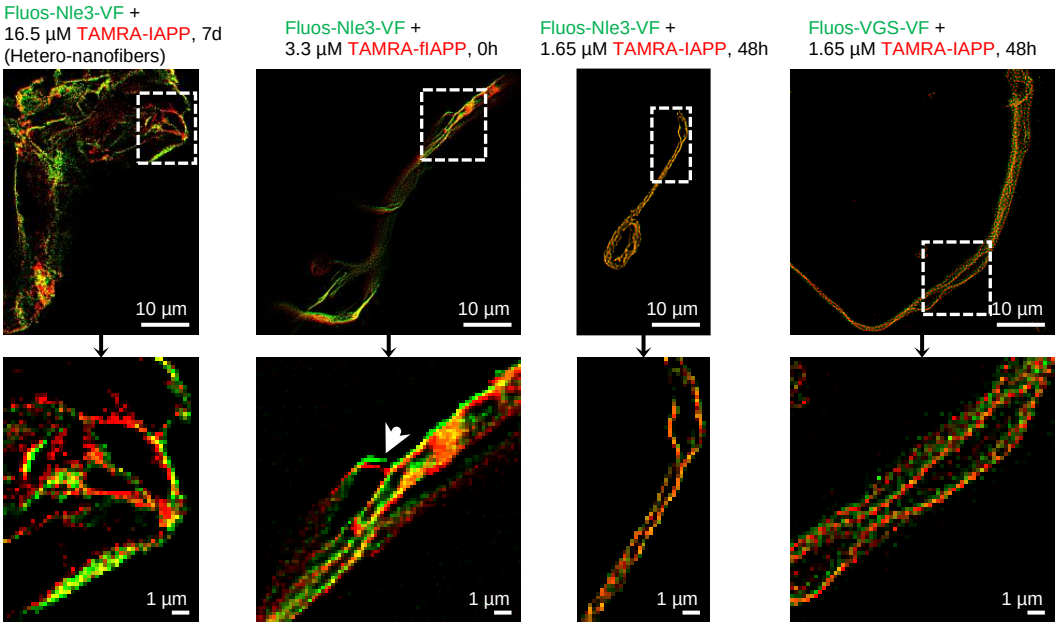

Figure 4-52: Comparison of hetero-nanofibers and nanofibers originating from mixtures of peptides with sub-stoichiometric amounts of IAPP or fIAPP by 2-PM. All incubations were made in 1xb and contained 33 µM of Fluos-labelled peptide with the indicated amount of TAMRA-IAPP or TAMRA-fIAPP. Nanofibers found in mixtures with sub-stoichiometric amounts of TAMRA-IAPP presented a similar total strand width compared to hetero-nanofibers whereas nanofibers found when Fluos-Nle3-VF was mixed with TAMRA-fIAPP were thicker. Arrow highlights the bigger strand separation in this sample. Dotted lines mark insets which are shown enlarged below.

In conclusion, bicoloured nanofibers found in mixtures containing sub-stoichiometric IAPP amounts were very similar to hetero-nanofibers generated under standard conditions using 10-times more IAPP with regards to their morphology (nanofibre co-assemblies formed from several smaller hetero-nanofiber units). Additionally, FLIM-FRET measurements indicated a separation of IAPP and ACM within the co-assembly smaller than 5.5 nm in both cases. The finding that no significant FRET events were detected in nanofibers formed in fIAPP-seeded ACM solutions indicates that the arrangement of the two peptide components is different in such nanofiber-species. This is additionally supported by strand widths measurements and the comparative 2-PM analysis (Table 4-14 and Figure 4-52). Hence, fibrillar IAPP is not templating heterofibril formation; the data suggests that it is rather induced by IAPP monomers or prefibrillar species.

4.7.3 Formation of fibrillar IAPP/ACM co-assemblies requires amyloidogenic IAPP

The findings presented in the previous chapter raised the question if heterofibrils/-nanofibers can be also formed by ACMs and non-amyloidogenic IAPP variants. To investigate this, IAPP-GI, a soluble non-toxic and non-amyloidogenic IAPP analogue[19] and rat IAPP which is also known to be weakly amyloidogenic[153], were incubated with Nle3-VF. 7 days aged samples usually containing heterofibrils were found to contain only amorphous aggregates in both cases when analysed by TEM (Figure 4-53a). Furthermore, 2-PM analysis of a 6 days aged incubation of TAMRA-IAPP-GI (16.5 µM) and Fluos-Nle3-VF (1:2) showed only roundish hetero-aggregates and no supramolecular hetero-nanofiber assemblies (Figure 4-53b) as

found for analogue TAMRA-IAPP mixtures. The findings so far indicate that IAPP amyloidogenicity is necessary for IAPP to act as a template for heterofibril formation with ACMs even though fIAPP is not the template.

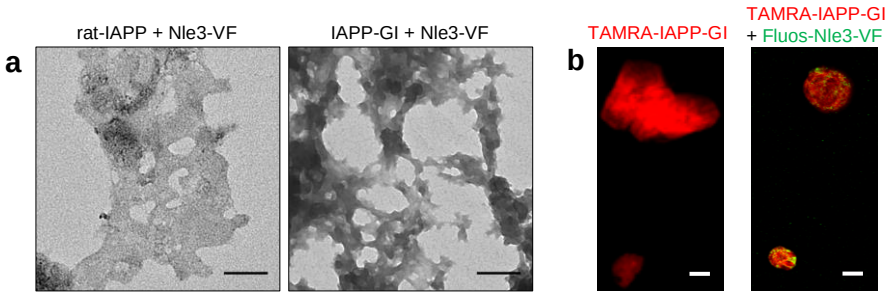

Figure 4-53: TEM and 2-PM of Nle3-VF mixtures with non-amyloidogenic IAPP. (**a**) Negative stain TEM imaging. Solutions containing either rat-IAPP or IAPP-GI (16.5 µM) and Nle3-VF (1:2) were prepared in ThT assay buffer (0.5 % HFIP), aged for 7 days and inspected after. Scale bars are 100 nm. (**b**) 2-PM imaging. Samples of TAMRA-IAPP-GI (16.5 µM, red)) or its mixture with Fluos-Nle3-VF (1:2, green) were prepared in 1xb and analysed after 6 days of aging. Scale bars are 10 µm. Images of a) are part of a figure in reference [140].

4.7.4 IAPP/ACM heterodimers might be the smallest building units of fibrillar co-assemblies

As previously discussed, binding to IAPP monomers and subsequent formation of hetero-dimers, -trimers/-tetramers and HMW heterocomplexes turned out to be of high importance for IAPP inhibition. By time-dependent CL experiments of IAPP/Nle3-VF mixtures it was found that hetero-dimers and -trimers/-tetramers are detected at all investigated time points (0 h, 24 h, 7 days). Since hf-IAPP/ACM were now determined to originate from amorphous heterocomplexes, the question arose why hetero-dimers/-trimers/-tetramers were still present at 7 days in CL experiments (see chapter 4.5.2.1). In case hf-IAPP/ACM are built up by former heterocomplexes one would not expect hetero-dimers/-trimers/-tetramers to be there still at 7 days. Then, transition into hf-IAPP/ACM is already accomplished and small heterocomplexes should be incorporated and be part of the fibrils. To investigate if this is due to the CL procedure itself, another CL experiment was performed in which the boiling step to denature folded species was skipped. Boiling could lead to partial or full destruction of hf-IAPP/ACM and thereby to the artificial release of heterodimer/-trimer/-tetramer units. Direct comparison of boiled and unboiled mixtures containing IAPP (30 µM) and Nle3-VF (60 µM; 1:2) crosslinked after 7 days shows that hetero-dimers and -trimers are indeed absent when boiling is avoided (Figure 4-54). Unboiled 7 days aged IAPP cannot be detected at all, indicating that fibrils which are most likely too big to enter the gel are still intact. Notably, in the unboiled 7 days aged IAPP/Nle3-VF mixture some HMW heterocomplexes can be detected even if they are significantly less compared to the boiled mixture. This suggests, that hf-IAPP/Nle3-VF are susceptible to the LDS (and the reducing agent) which is contained in the gel loading buffer and partially disassemble even without boiling in contrast to fIAPP. Comparing boiled and unboiled IAPP/Nle3-VF mixtures crosslinked at t = 0 h reveals that also in fresh solutions hetero-dimers and -trimers/-tetramers are only present when the boiling step is performed. Additionally, without boiling less HMW heterocomplexes are visible. Both findings suggest that IAPP and Nle3-VF form fast very big and relatively stable complexes which cannot enter the

gel without a boiling step. Additionally, the data supports the suggestion that hetero-dimers are the smallest building units of hf-IAPP/Nle3-VF.

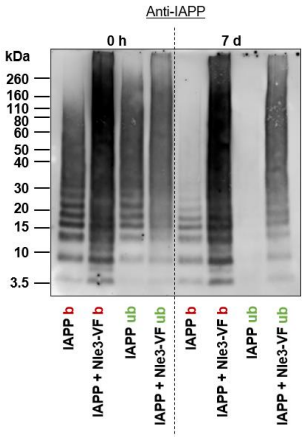

Figure 4-54: CL experiment of IAPP and its mixture with Nle3-VF performed with and without denaturing step. Characterisation of species was performed via cross-linking with glutaraldehyde, NuPAGE gel electrophoresis and Western blot (WB) using an anti-IAPP antibody. Solutions of IAPP (30 µM) and its mixture with Nle3-VF (1:2) were prepared in 1xb and incubated for the indicated time before cross linking. b: boiled; ub: unboiled. Experiment is representative of 2 similarly performed ones.

4.8 IAPP/ACM fibrillar co-assemblies show properties distinct from fIAPP

ThT binding and MTT reduction experiments previously showed that heterofibril-containing mixtures of IAPP and ACMs do not react with ThT and are not cytotoxic (see Figure 4-56a,b and chapter 4.3.2). This observation led to the assumption that these fibrils might differ also in other properties from IAPP fibrils and maybe even display more beneficial features. Since CL experiments indicated that cross-linked hetero-aggregates are less stable towards heat and denaturing agents (see chapter 4.7.4) compared to fIAPP, their thermostability should be further investigated in a next step. Firstly, species present in 7 days aged cross-linked incubations containing IAPP (30 µM, in 1xb) and mixtures with inhibitor (Nle3-VF, 1:2) or non-inhibitor (VGS-VF, 1:2) (compare Figure 4-27 and Figure 4-28 in chapter 4.5.2.1) were analysed by TEM after boiling in LDS- and DTT-containing sample buffer. These samples are identical to those which are normally loaded onto the gels for NuPAGE gel electrophoresis in context of CL experiments. As expected, cross-linked fIAPP and fibrils found in the mixture with the non-inhibitory ADP VGS-VF proved to be resistant to the harsh treatment whereas the IAPP/Nle3-VF mixture only contained amorphous aggregates, suggesting that heterofibrils dissociated (Figure 4-55a).

To further address this issue, IAPP was incubated under the ThT assay conditions (16.5 µM in ThT assay buffer with 0.5 % HFIP) in absence and presence of 2-fold molar excess of Nle3-VF or VGS-VF and samples were taken for TEM at 7 days (w/o cross-linking) before and after boiling the incubations for 5 min at 95 °C (Figure 4-55b). ThT-positive fibrils in IAPP and IAPP/VGS-VF incubations were still present on TEM grids after boiling, whereas ThT-negative

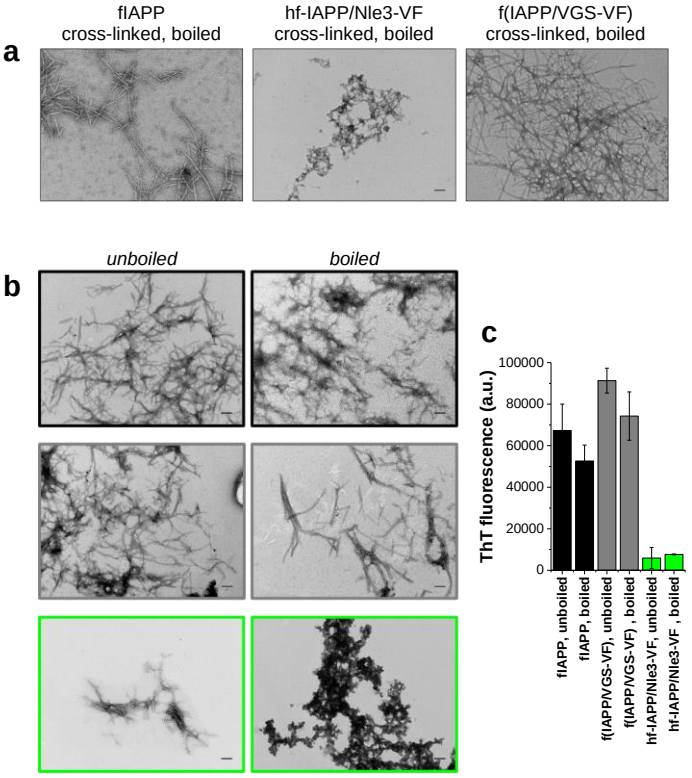

Figure 4-55: Thermostability of fIAPP and heterofibrils. (**a**) TEM analysis of cross-linked IAPP fibrils and heterofibrils after boiling. Cross-linking of species in 7 days aged solutions of IAPP (30 µM, in 1xb; "fIAPP") or IAPP/peptide mixtures (1:2; "hf-IAPP/Ne3-VF" and "f(IAPP/VGS-VF)" was performed using glutaraldehyde. After the CL procedure, precipitated pellets were resuspended in reducing LDS- and DTT-containing sample buffer, boiled 5 min at 95 °C and aliquots were loaded onto TEM grids. Scale bars are 100 nm. f, fibrils; hf, heterofibrils. (**b**) TEM analysis of IAPP fibrils and IAPP/Nle3-VF heterofibrils before and after boiling. Incubations of IAPP and its mixture with peptides were prepared under standard conditions (IAPP 16.5 µM, in ThT assay buffer 0.5 % HFIP, mixtures 1:2). After 7 days, aliquots were taken for TEM before and after boiling the solutions 5 min at 95 °C. Fibrils of the mixture of IAPP and the non-inhibitor VGS-VF were analysed in parallel as control. Colours correspond to colours in c. Scale bars are 100 nm. (**c**) ThT binding of IAPP fibrils and IAPP/Nle3-VF heterofibrils before and after boiling. Solutions were prepared as for b. ThT binding of the mixture of IAPP and the non-inhibitor VGS-VF were analysed in parallel as control. Error bars: means ± SD (n=3). Buffer values were subtracted from measurements. Data/images in b) and c) of IAPP and hf-IAPP/Nle3-VF are part of a figure in reference [140].

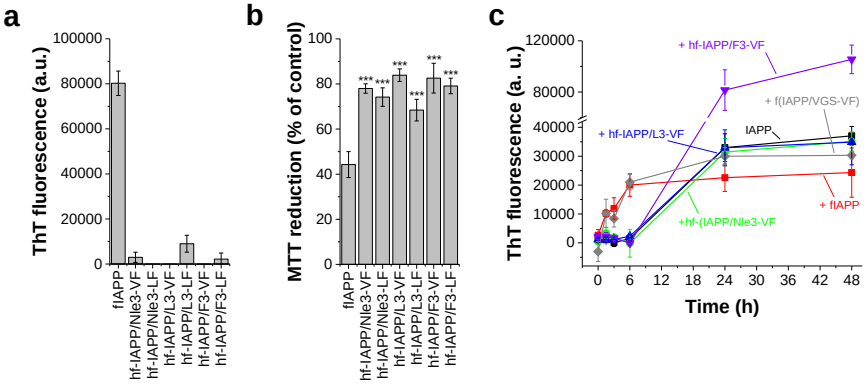

Figure 4-56: ThT binding, cytotoxicity and seeding capacity of fIAPP and heterofibrils. (**a**) ThT binding of fIAPP and heterofibrils. ThT fluorescence was measured of 7 days aged solutions containing either IAPP (16.5 µM; "fIAPP") or its mixture with ACMs (1:2 or 1:2.5 in case of L3-LF; "hf-IAPP/ACM"). Heterofibrils in mixtures did not show ThT binding. Incubations were prepared in ThT assay buffer with 0.5 % HFIP. Error bars represent mean ± SD from three assays. (**b**) Cytotoxic effects of fIAPP and heterofibrils on RIN5fm cells. Aliquots of 7 days aged incubations of IAPP (16.5 µM; "fIAPP") or IAPP/ACM mixtures (1:2 or 1:2.5 in case of L3-LF; "hf-IAPP/ACM") were made in ThT assay buffer (0.5 % HFIP) and diluted with cell medium and pipetted onto RIN5fm cells (final IAPP concentration: 500 nM). Heterofibrils showed significantly less toxicity. Error bars represent means ± SD from three assays, n=3 each. *** P<0.001 by one-way ANOVA and Bonferroni compared to fIAPP control. (**c**) IAPP seeding by fIAPP and heterofibrils. IAPP (12 µM, in ThT assay buffer 0.5 % HFIP) was seeded by 10 % (1.2 µM) fIAPP or heterofibril seeds and ThT binding was followed over 48 h. fIAPP seeds were generated by incubating IAPP at 12 or 16.5 µM for 4-7 days, heterofibril seeds ("hf-IAPP/ACM") were generated by incubating IAPP (16.5 µM) with 33 µM (1:2) ACMs for 7 days (both in ThT assay buffer with 0.5 % HFIP). Control seeds were prepared by similar incubations of IAPP with the non-inhibitor VGS-VF ("f(IAPP/VGS-VF)"). Error bars represent means ± SD from three assays, for IAPP and IAPP + fIAPP from four assays. Values of buffer and seeds alone were subtracted from all measurements. Data in c) is part of a figure in reference [140].

hf-IAPP/Nle3-VF were fully disassembled and only amorphous aggregates were found via TEM. Of note, IAPP and IAPP/VGS-VF solutions also contained amorphous aggregates after boiling, but fibrils could still be observed. The high thermostability of IAPP fibrils and fibrils in IAPP/VGS-VF mixtures could also be confirmed by a ThT binding assay in which 7 days aged species were found to react similarly with ThT before and after boiling (Figure 4-55c). Taken together, the above-mentioned results suggest that heterofibrils are indeed less resistant to chemical LDS/DTT- and thermal denaturation than fIAPP.

To investigate of hf-IAPP/ACM are better degradable than fIAPP, proteinase K (PK; 0.5 µg/ml) was added to incubations containing fIAPP or heterofibrils and samples were deposited on nitrocellulose membranes (Figure 4-57a,b). Membranes were probed with the anti-fIAPP antibody and an anti-Aβ40 antibody (anti-ACM). While fibrillar IAPP was still resistant to digestion by proteinase K after a 30 h treatment, hf-IAPP/Nle3-VF showed already a significant reduction in spot intensity after 1 h and were almost completely cleaved after 6 h. Probing the membrane with the anti-Aβ40 specific antibody showed that also the ACM contained in the heterofibrils is degraded. As a control, similar degradation experiments were performed with fIAPP which were coated by Nle3-VF prior to digestion. For this, IAPP (16.5 µM) was incubated for 6 days to generate fibrils. fIAPP was mixed thereafter with Nle3-VF (1:2) and incubated for 1 day more to allow coating of the fibril surface by the ACM. PK (0.5 µg/ml) was added to the fibril solution and dotting and detection of samples was performed as described above. 7 days aged fIAPP (16.5 µM) were digested in the same way for comparison. As expected, Nle3-VF-coated fIAPP could not be degraded by the proteinase and remained unchanged even after a 30-h treatment (Figure 4-57c,d). Nle3-VF was not detectable anymore after 1 h, which is reasonable as it is easily accessible for the proteinase when bound to the fibril surface. In conclusion, the proteinase can remove the ACM layer deposited on the IAPP fibril but cannot degrade the IAPP fibril structure itself, whereas the hf-IAPP/ACM structure seems to have a different and more instable architecture which can be readily disrupted.

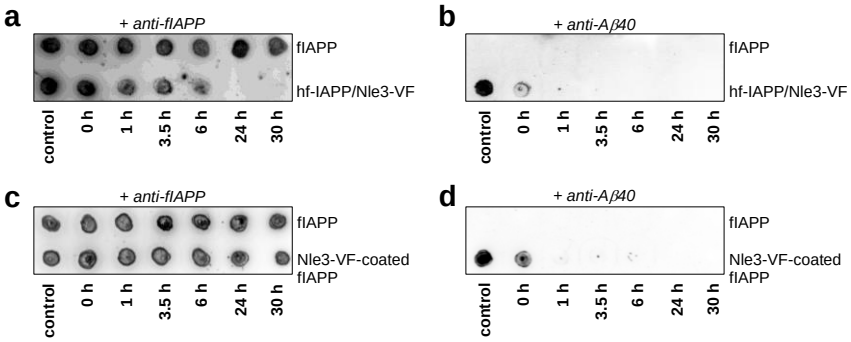

Figure 4-57: Proteolytic degradation of fIAPP and heterofibrils. (**a,b**) Proteinase K digestion of fIAPP and heterofibrils. Digestion of fIAPP and heterofibrils was performed by addition of proteinase K (PK) (0.5 µg/ml) to 7-8 days aged solutions containing IAPP alone (16.5 µM, in 1xb) or 1:2-mixtures with Nle3-VF. At indicated time points, aliquots of these solutions were dotted onto 0.2 µm nitrocellulose membranes (0.6 µg IAPP per spot). Aliquots of the solutions before addition of PK were spotted as control. Presence of fIAPP was revealed using the anti-fIAPP antibody (1:500) (a), presence of Nle3-VF was revealed using an anti-Aβ40 antibody (1:2000) (b). Results in a) are representative of 6 experiments, results in b) are representative of 3 experiments. Developments with different antibodies were done with independent membranes (no stripping in between). (**c,d**) Proteinase K digestion of fIAPP fibrils and Nle3-VF-coated fIAPP. fIAPP were generated by incubation of 16.5 µM IAPP in 1xb for 7 days. For Nle3-VF-coated fIAPP, 6 days aged IAPP (16.5 µM, in 1xb) was mixed 1:2 with dried Nle3-VF and incubated for one more day prior to digestion experiment. Digestion with PK, dotting and antibody development was performed as described in a) and b). Results in c) are representative of 3 experiments, experiment shown in d) was performed once. Developments with different antibodies were done with independent membranes (no stripping in between). Data of a) and b) is part of a figure in reference [140] (adapted figure version).In summary, thermal and proteolytical degradation experiments showed that whereas the hf-IAPP/ACM are more instable than fIAPP. Additionally, the non-

toxic heterofibrils cannot seed IAPP. Thus, by the formation of heterofibrils, ACMs drive IAPP into a fibrillar assembly which is easier clearable and seeding-incompetent and therefore more desirable than the fibrillar assembly usually formed by IAPP.

4.9 Peptide array data indicate an inhibitor-specific IAPP/ACM interaction interface

For deeper investigations on possible differences in the interaction interface of inhibitors and non-inhibitors with IAPP, peptide array analysis was performed. The generated peptide set comprised: deca-peptides spanning the entire IAPP sequence with a frameshift of one amino acid between successive sequences, single-alanine substituted IAPP fragments, 9- to 15-meric overlapping segments of inhibitors and non-inhibitors and corresponding alanine substituted segments. CelluSpot microarrays were incubated with N^{α}-terminal biotinylated peptides to detect biding to different IAPP or inhibitor/non-inhibitor segments.

In a first step, binding of full-length biotinylated IAPP to different sequence segments of Nle3, Nle3-GG, Nle3-VF and VGS-VF was tested. For Nle3 and Nle3-VF, the following segments were investigated (see Figure 4-58): 15-23, 15-29, 18-32, 21-35, 24-38 and 27-40. For VGS-VF, 15-23, 15-29, 18-32 and 27-40 were used and 15-23, 21-35, 24-38 and 27-40 for Nle3-GG. IAPP bound to all examined Nle3 fragments but showed strongest interactions with N-terminal fragments 15-23, 15-29 and 18-32, leading to the assumption that region 15-23 (QKLVFFAED) represents the main binding interface of this peptide (Figure 4-58a). This is further supported by the fact that a similar binding pattern of IAPP was observed when C-terminal methylations are introduced into the peptide (Nle3-GG), which do not hinder the interaction of the N-terminus with IAPP (Figure 4-58b). Consequently, a complete loss of IAPP binding to segment 15-23 was observed when N-terminal methylations are present in Nle3-VF (Figure 4-58c). Binding was in this case observed for segments comprising central and C-terminal Nle3-VF regions. The common core of all fragments are amino acids 27-32, the NKGAII-region. Introducing N-terminal methylations thus leads to a shift of the binding interface with IAPP from the N-terminal QKLVFFAED-region to the C-terminal NKGAII-region. A similar binding behaviour of IAPP was found in case of VGS-VF segments (Figure 4-58d).

To study the peptides' self-assembly interface, the array was incubated with biotinylated Nle3, Nle3-GG, Nle3-VF or VGS-VF and the binding to the same sequence fragments as for IAPP was analysed. In case of Nle3, both the N-terminal QKLVFF and the C-terminal VGGVV-region seem to be involved in self-association, since the central 21-35 fragment lacking these two segments was binding worst of all tested Nle3 15-mers (Figure 4-58a). Of note, the N-terminal 9-mer QKLVFFAED alone was not bound by Biotin-Nle3, indicating that part of the linker might be also involved in the N-terminal self-assembly interface. For Nle3-VF, VGS-VF and Nle3-GG, the region important for self- association is located in the C-terminus comprising amino acids 36-40 (VGGVV) (Figure 4-58b-d). Compared to the region important for IAPP binding, the interface for self-recognition lies closer to the peptides' C-terminus. Thus, self-assembly might not compete with IAPP binding (Figure 4-58).

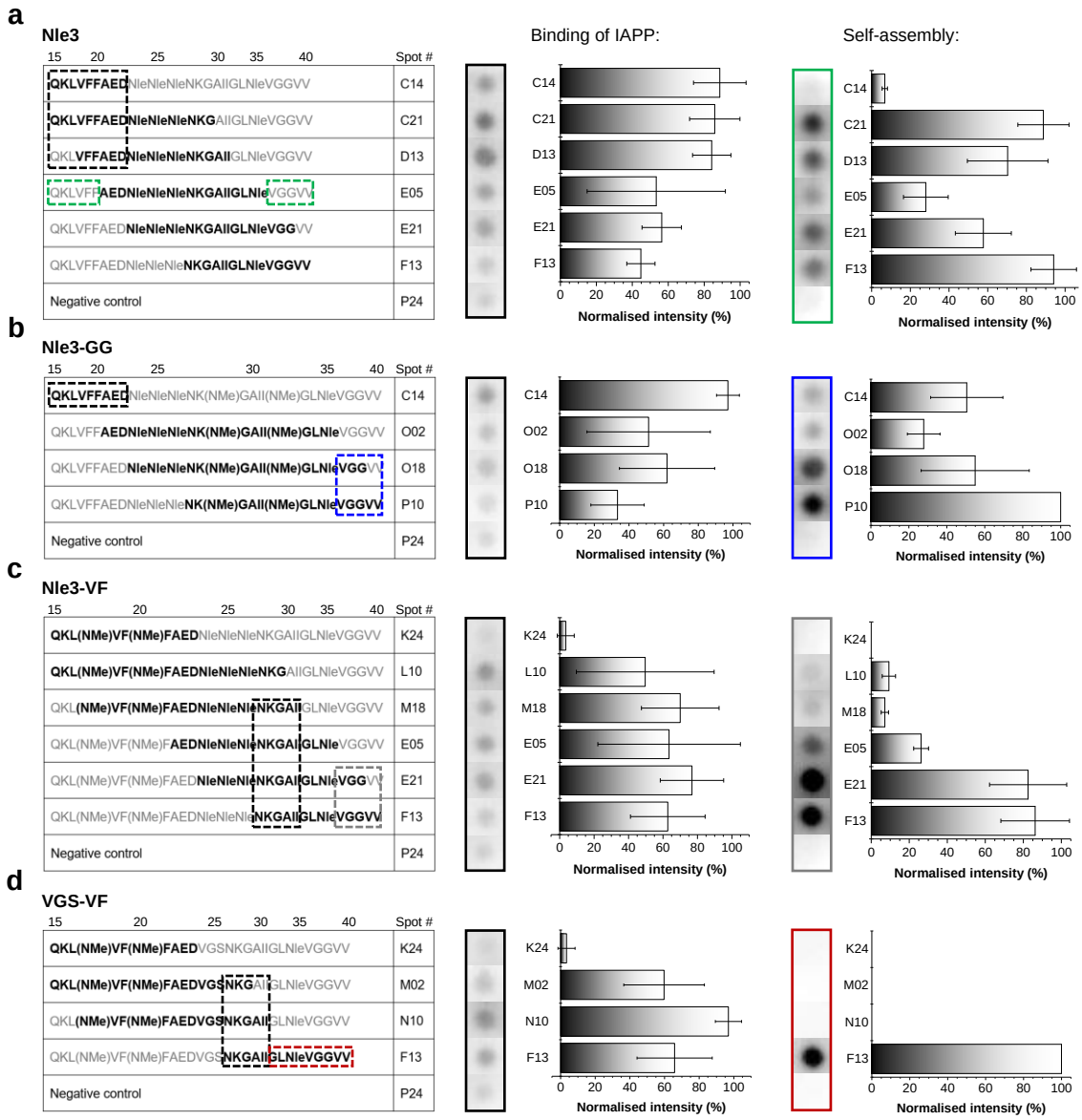

Figure 4-58: Identification of ADP segments important for their binding to IAPP and their self-recognition using peptide microarrays. Glass slides with ADP segments (bold) were incubated with 0.5 µM Biotin-IAPP (for testing "Binding of IAPP" to the segments) or with Biotin-ADPs (3 µM Biotin-Nle3 or 3 µM Biotin-Nle3-GG or 0.5 µM Biotin-Nle3-VF or 0.5 µM Biotin-VGS-VF) (for determining "Self-assembly" regions). Bound biotinylated peptides were detected after incubation with streptavidin-POD and development with ECL. Bar diagrams represent spot intensities obtained from different developments (mean ± SD; 6 assays for Biotin-IAPP binding, 3 assays for Biotin-Nle3-GG binding, 4 assays for the other self-recognition studies; see also Figure 7-62 and Figure 7-63 in Appendix). Depicted membranes are from one of these assays, respectively. Dashed black frames: Identified core regions for IAPP binding; dashed coloured frames: identified core regions for self-recognition. "Spot #" gives the location of the corresponding segment on the peptide array slide. NMe: *N*-methylation. Results are shown for binding to segments of Nle3 (**a**), Nle3-GG (**b**), Nle3-VF (**c**) and VGS-VF (**d**).

For investigating the IAPP-peptide interfaces in more detail, IAPP binding to the single-alanine mutants of the previously mentioned inhibitor/non-inhibitor fragments was quantified in order to obtain information about specific amino acids of the peptides involved in IAPP recognition. For all four peptides, no single amino acid could be determined the substitution of which by alanine leads to a significant reduction of IAPP binding, indicating that more than one residue must be replaced to disrupt the interaction interface (Figure 4-59 to Figure 4-61 and Figure 7-55 to Figure 7-61 in Appendix). In case of Nle3-VF and VGS-VF, amino acids Glu22 and Asp23 seem to strongly hinder the interaction with IAPP, as a highly improved binding to segments 15-23, 15-29 and 18-32 was observed upon their substitution by alanine (Figure

4-59, Figure 4-60; Figure 7-55, Figure 7-56 in Appendix). Additionally, exchange of Lys28 in Nle3-VF segment 15-29 and of Ile31 in Nle3-VF segment 18-32 to alanine caused a significantly increased binding of IAPP to these fragments. For Nle3-GG, improved IAPP binding was observed when Ile32 or Val39/Val40 in segment 27-40 were replaced by alanine (Figure 7-58 in Appendix). Furthermore, IAPP showed stronger binding to Nle3 segment 15-29 upon alanine substitution of Leu17 or Val18 and to Nle3 segment 18-32 upon alanine substitution of Nle26 (Figure 7-59, Figure 7-60 in Appendix). Gly29 was found to be crucial for IAPP interaction with Nle3 segment 15-29 (Figure 7-59 in Appendix) but for none of the other segments containing this amino acid.

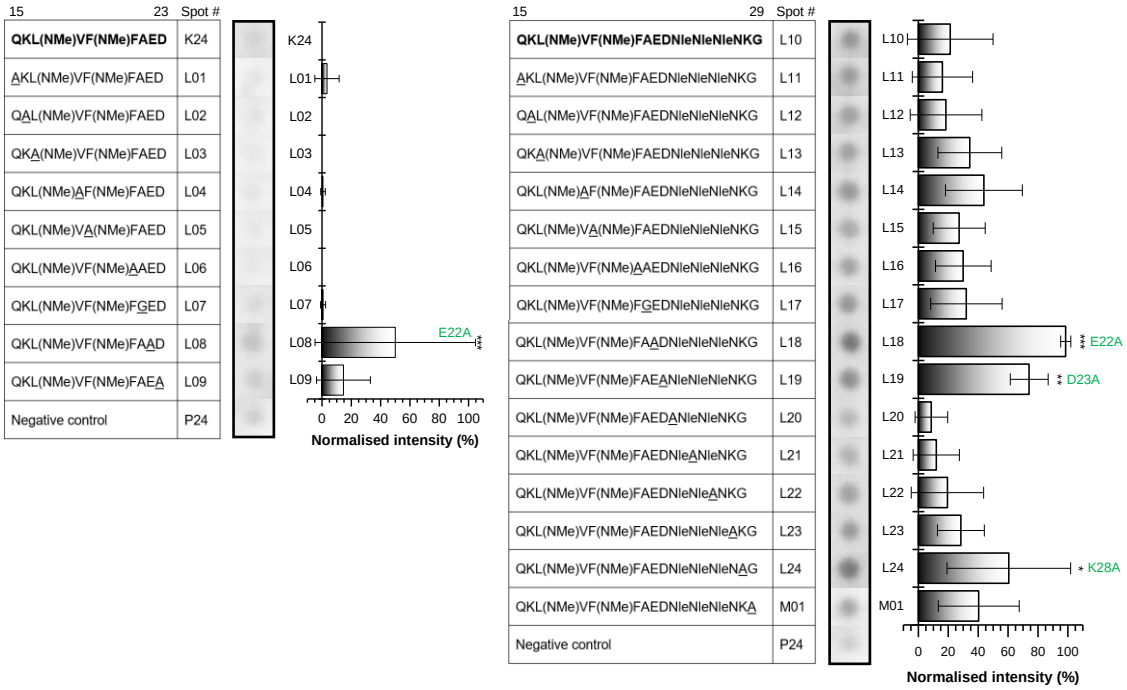

Figure 4-59: Identification of amino acids in N-terminal Nle3-VF segments important for IAPP binding by sequential alanine scanning using peptide microarrays. Glass slides with the wild-type segments (bold; no alanine substitution) and the corresponding alanine-substituted segments (position of alanine mutation underlined) were incubated with Biotin-IAPP (0.5 µM). Bound Biotin-IAPP was detected after incubation with streptavidin-POD and development with ECL. Bar diagrams represent spot intensities obtained from different developments (mean ± SD; 6 assays; see also Figure 7-62 in Appendix). Depicted membranes are from one of these assays. Green letters indicate alanine mutations causing stronger binding of the mutated segment compared to the wild-type segment. Asterisks mark spot intensities significantly different from the wild-type segment. *** P<0.001, ** P<0.01, * P<0.05 (by one-way ANOVA & Bonferroni). "Spot #" gives the location of the corresponding segment on the peptide array slide. NMe: *N*-methylation.

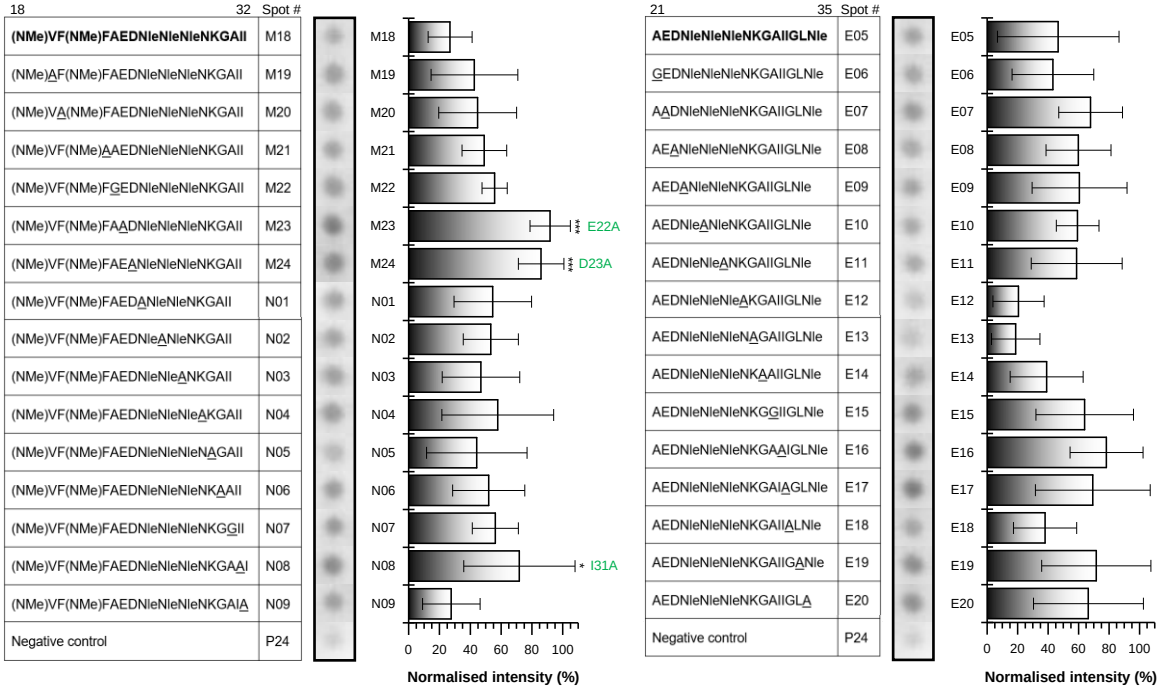

Figure 4-60: Identification of amino acids in central Nle3-VF segments important for IAPP binding by sequential alanine scanning using peptide microarrays. Incubations of glass slides with the wild-type segments (bold; no alanine substitution) and the corresponding alanine-substituted segments (position of alanine mutation underlined) were performed using Biotin-IAPP (0.5 µM). Bound Biotin-IAPP was detected following incubation with streptavidin-POD and development with ECL. Bar diagrams represent spot intensities obtained from different developments (mean ± SD; 6 assays; see also Figure 7-62 in Appendix). Depicted membranes are from one of these assays. Alanine mutations causing stronger binding of the mutated segment compared to the wild-type segment. Asterisks mark spot intensities significantly different from the wild-type segment. *** P<0.001, * P<0.05 (by one-way ANOVA & Bonferroni). "Spot #" gives the location of the corresponding segment on the peptide array slide. NMe: *N*-methylation.

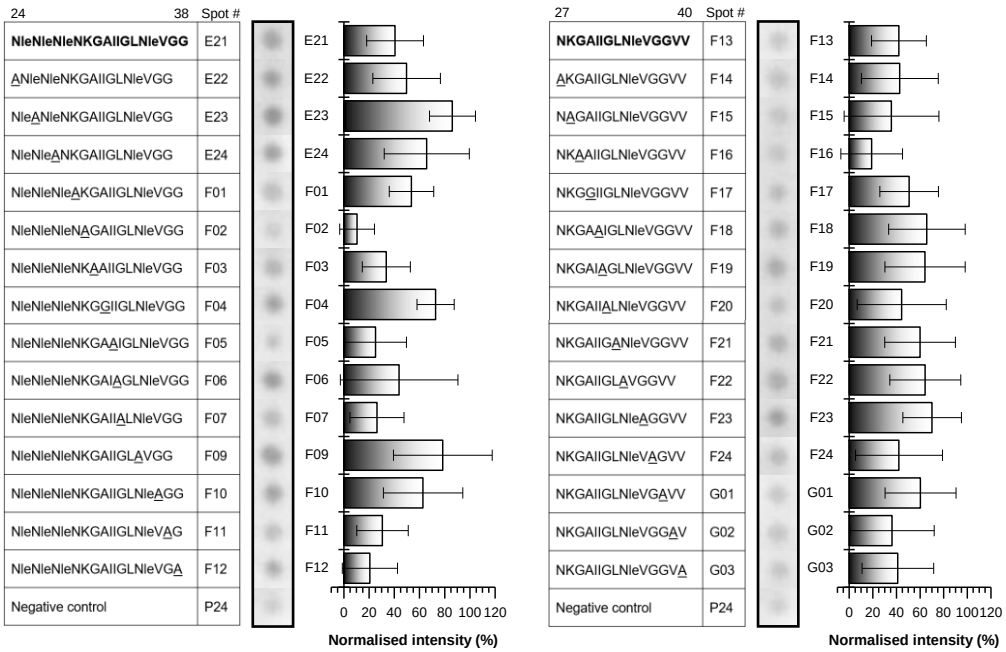

Figure 4-61: Identification of amino acids in C-terminal Nle3-VF segments important for IAPP binding by sequential alanine scanning using peptide microarrays. Glass slides containing the wild-type segments (bold; no alanine substitution) and the corresponding alanine-substituted segments (position of alanine mutation underlined) were incubated with Biotin-IAPP (0.5 µM). Detection of bound Biotin-IAPP was done after incubation with streptavidin-POD and development with ECL. Bar diagrams show spot intensities obtained from different developments (mean ± SD; 6 assays; see also Figure 7-62 in Appendix). Depicted membranes are from one of these assays. No significant impacts on binding strength of Biotin-IAPP were detected for single alanine mutations in the C-terminal segments. "Spot #" gives the location of the corresponding segment on the peptide array slide.

In conclusion, the first peptide array analyses revealed different interaction interfaces of Nle3, Nle3-GG, Nle3-VF and VGS-VF with IAPP. Nle3 and Nle3-GG can bind to IAPP with both N- and C-terminus, but preferentially do so with their N-terminal part involving amino acids 15-23 (QKLVFFAED). In contrast, the core segment of Nle3-VF and VGS-VF for IAPP recognition is located in the C-terminal NKGAII-region (amino acids 27-32) (Figure 4-62). The changes within the interaction interface between Nle3, Nle3-GG and Nle3-VF might explain the peptides' different potential to inhibit IAPP: Nle3 detects IAPP with both termini and is a medium inhibitor able to delay its aggregation for some days. In Nle3-VF, the *N*-methylations were introduced within the N-terminus. This might restrict the binding of IAPP to the N-terminal Nle3-VF part. Thus, binding of IAPP is only possible via the C-terminal Nle3-VF part. Since Nle3-VF is a potent full-inhibitor of IAPP amyloidogenicity, this selective recognition appears to favour the inhibition potential. As the NKGAII-region was found to be of special importance in Nle3-VF to bind IAPP, it is also comprehensible why Nle3-GG completely lost the inhibitory properties observed for Nle3 because it carries the N-methylations in this region. Even though Nle3-VF and VGS-VF share a similar recognition area for IAPP, VGS-VF is a non-inhibitor in contrast to Nle3-VF. This difference in inhibitory potential might be due to a differently located binding site for the two peptides in the IAPP sequence.

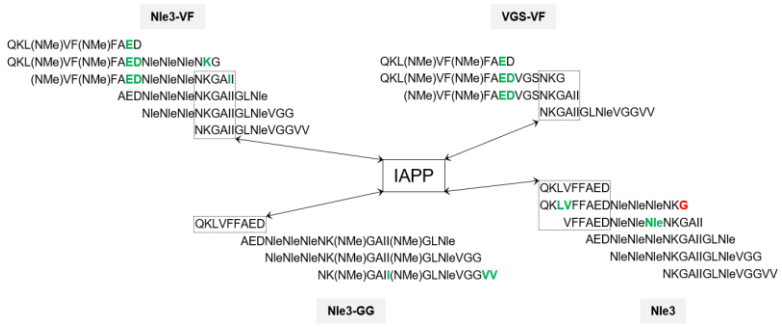

Figure 4-62: Binding sites in different ADPs important for IAPP recognition based on peptide array results. Depicted are sequence segments which were tested for IAPP binding in microarray experiments. Identified core regions in ADPs showing strongest interaction with IAPP are highlighted in the dashed frame boxes. Green: substitution of these residues by alanine leads to stronger IAPP binding to the corresponding fragment; red: substitution of these residues by alanine leads to weaker IAPP binding to the corresponding fragment; NMe: *N*-methylation.

To investigate this, the peptide array was next developed with biotinylated Nle3, Nle3-GG, Nle3-VF or VGS-VF and binding to IAPP decamers was analysed. Three distinct binding sites in IAPP were found for the non-methylated peptide Nle3 located in areas IAPP(8-24), IAPP(19-32) and IAPP(24-37) (Figure 4-63). Spot intensities of IAPP decamers were very fade in case of the development with Biotin-Nle3-GG. Binding was indicated to IAPP regions IAPP(9-22) and IAPP(20-32) (Figure 4-63). In contrast to Nle3, Nle3-VF did not bind to C-terminal IAPP decamers but binding was exclusively limited to IAPP decamers located within IAPP region 8-23, indicating that the introduction of N-terminal methylations strongly hinders the interaction with IAPP's C-terminus and favours specific interaction with IAPP's N-terminus (Figure 4-63). The above findings indicate that the methylations in Nle3-VF render its N-terminus incompatible for IAPP binding and on the other hand block interaction with IAPP's C-terminus, so that only a very specific interaction interface between the inhibitor's C-terminus

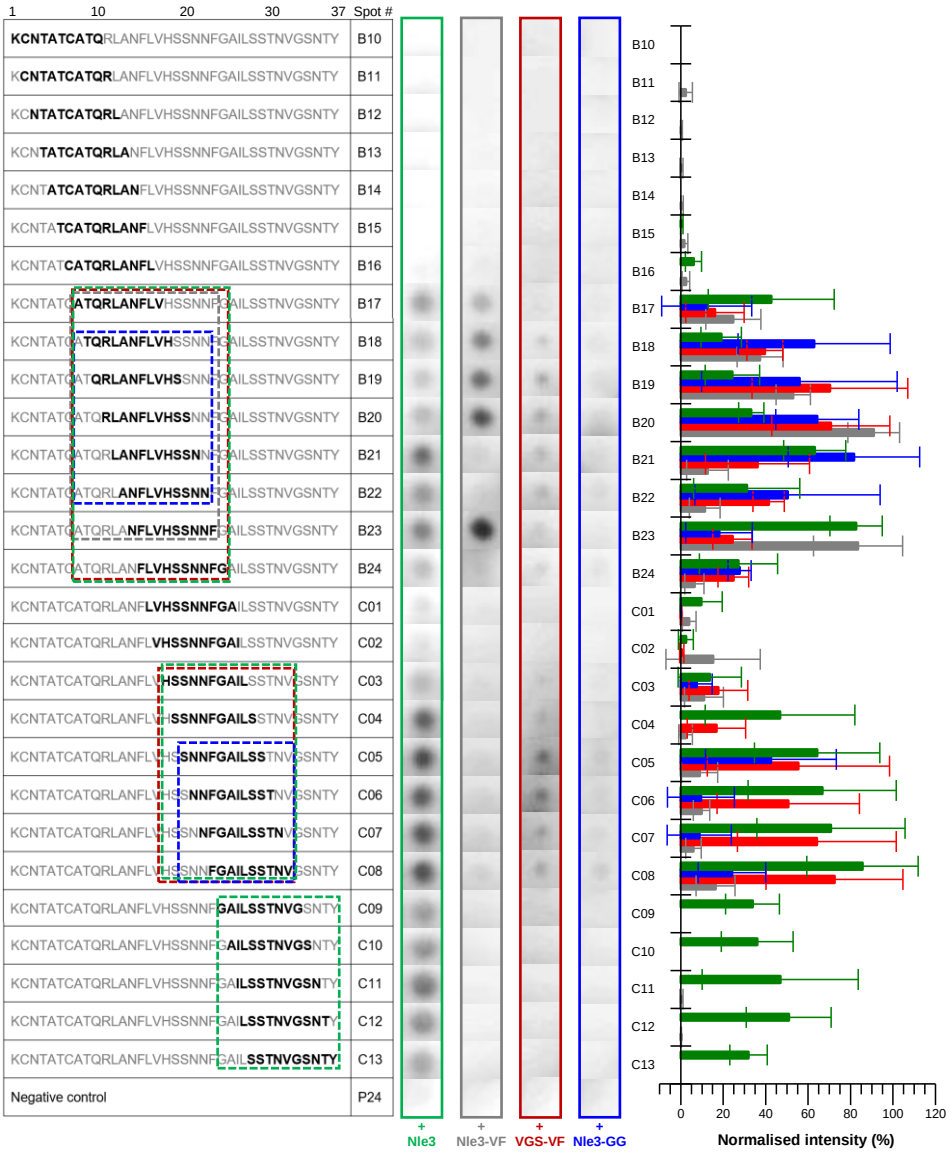

Figure 4-63: Identification of IAPP regions important for binding to ADPs using peptide microarrays. Glass slides with IAPP decamers (bold) were incubated with N-terminal biotinylated ADPs (3 µM Biotin-Nle3 or 3 µM Biotin-Nle3-GG or 0.5 µM Biotin-Nle3-VF or 0.5 µM Biotin-VGS-VF). Following incubation with streptavidin-POD and development with ECL, bound peptides were detected. Bar diagrams represent spot intensities obtained from different developments with the different Biotin-ADPs (mean ± SD; 3 assays for Biotin-Nle3-GG, 4 assays for the other Biotin-ADPs; see also Figure 7-63 in Appendix). Depicted membranes are from one of these assays, respectively. Dashed coloured frames: IAPP core regions for binding to ADPs. “Spot #” gives the location of the corresponding segment on the peptide array slide.

(core: NKGAII) and IAPP’s N-terminus (core: NFLVH) can be established. This interface can therefore be assumed the one necessary for the ADP in order to exhibit inhibitory function and might additionally be important for heterofibril formation. This would also be in good agreement with results obtained for VGS-VF: Peptide array analysis showed that VGS-VF lost binding to IAPP decamers within region 24-37 but could interact with both NFLVH- and NFGAILS-containing IAPP decamers, indicating that binding to IAPP is not as specific as observed for Nle3-VF (Figure 4-63). This might render VGS-VF a non-inhibitory ADP.

For obtaining further information about single amino acids in IAPP important for its interaction with the ADPs, the IAPP sequence was divided into five segments, namely, IAPP(1-10), IAPP(8-18), IAPP(14-28), IAPP(22-28) and IAPP(29-37). Binding of biotinylated ADPs to these segments and their alanine-substituted mutants was tested by peptide array analysis. Results

for binding to the non-mutated fragments were similar to results obtained from the decamer scan (Figure 4-64): None of the peptides bound to IAPP(1-10). Nle3 showed binding to the remaining four segments, with strongest interactions to the two segments containing the NFGAILS-region (IAPP(14-28), IAPP(22-28)). Nle3-VF only bound to the segments containing the NFLVH-region (IAPP(8-18), IAPP(14-28)), confirming the importance of this IAPP region for inhibitor interaction. VGS-VF bound strongest to IAPP(14-28) and IAPP(22-28), defining the NFGAILS-region as the important interaction surface. Spot intensities for development with Biotin-Nle3-GG were again very fade but the NFGAILS-region seemed to be the important one for interaction. Analysis of binding to alanine-substituted segments revealed Leu12, Phe15 and Leu16 in IAPP(8-18), Phe23 in IAPP(22-28) and Asn31 and Asn35 in IAPP(29-37) as crucial for Nle3 interaction with these segments (Figure 4-66 to Figure 4-68). Stronger binding of segments compared to their non-mutated wild-type segment was observed for Nle3 when Arg11 or Asn14 were replaced by alanine in IAPP(8-18), when Thr30, Ser31 or Thr36 were replaced in IAPP(29-37) or when Thr4 was replaced in IAPP(1-10) (Figure 4-66 to Figure 4-68). This indicates that these residues are hindering Nle3-binding to IAPP. The later substitution, Thr4Ala, was found to dramatically improve interaction of all four peptides with the IAPP(1-10) segment (Figure 4-66 to Figure 4-68). Thus, the presence of Thr4 in the native IAPP sequence might block the peptides' interaction with this IAPP region. Additionally, the following residues were found to be hindering for Nle3-VF binding: Phe15 in IAPP(8-18), Asn14, Val17, Phe23 and Ala25 in IAPP(14-28) as well as Asn22, Gly24 ans Ser28 in IAPP(22-28) (Figure 4-66 to Figure 4-68). Amino acids impeding VGS-VF binding were: Asn14 and His18 in IAPP(8-18), His18, Asn21, Asn22, Gly24 and Ser28 in IAPP(14-28), Gly24 in IAPP(22-28) and Tyr37 in IAPP(29-37) (Figure 4-66 to Figure 4-68). Similar observations were made in case of Nle3-GG (Figure 4-66 to Figure 4-68).

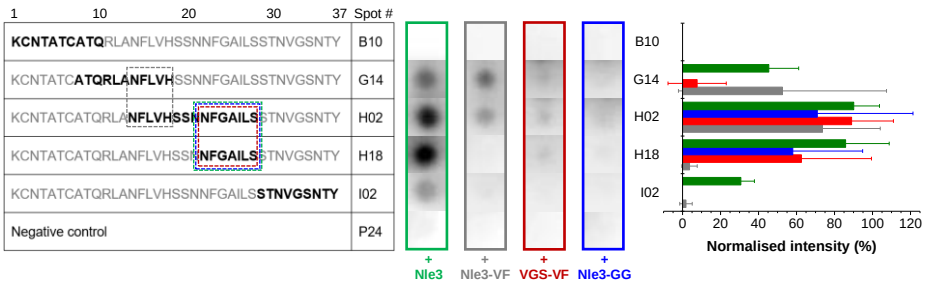

Figure 4-64: Binding of ADPs to IAPP(1-10), IAPP(29-37) segments and "hot regions". IAPP segments on glass slides (bold) were incubated with N-terminal biotinylated ADPs (3 µM Biotin-Nle3 or 3 µM Biotin-Nle3-GG or 0.5 µM Biotin-Nle3-VF or 0.5 µM Biotin-VGS-VF). Detection of bound Biotin-peptides was done after incubation with streptavidin-POD and development with ECL. Bar diagrams represent spot intensities obtained from different developments with the different Biotin-ADPs (mean ± SD; 3 assays for Biotin-Nle3-GG, 4 assays for the other Biotin-ADPs; see also Figure 7-63 in Appendix). Depicted membranes are from one of these assays, respectively. Dashed coloured frames: IAPP sequences mostly relevant for peptide binding. "Spot #" gives the location of the corresponding segment on the peptide array slide.

In summary, the following binding interfaces between IAPP and inhibitory/non-inhibitory ADPs were determined by the peptide array analysis: Nle3 and Nle3-GG can bind to IAPP with both their N- and C-termini, but preferentially do so via the N-terminally located QKLVFFAED-region. While strongest interaction was observed with IAPP's NFGAILS-region, Nle3 is also able to bind to the NFLVH-region and to C-terminal IAPP(29-37), suggesting a rather dynamic interaction interface (Figure 4-65). In contrast, binding of Nle3-VF to IAPP is very specified and

taking place between Nle3-VF's C-terminus (NKGAII) and IAPP's N-terminus (NFLVH). This interface is therefore considered to be the "inhibition-mediating" one. Also VGS-VF was found to interact via its C-terminus with IAPP, but binding was not limited to IAPP's N-terminus but also observed in the NFGAILS-region. Since the IAPP/VGS-VF interaction interface seems more dynamic and less restricted than the IAPP/Nle3-VF interface, this might explain why VGS-VF is a non-inhibitory ADP.

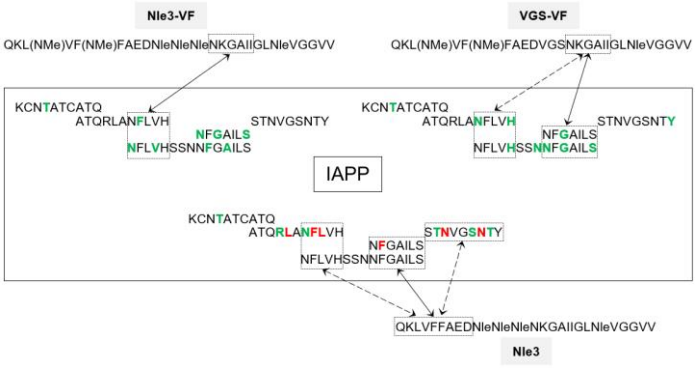

Figure 4-65: Binding sites in IAPP important for recognition of ADPs and determined IAPP/ADP interaction interfaces based on peptide array results. IAPP sequence segments which were tested for peptide binding in microarray experiments are depicted (see box). Identified core regions important for interaction with different peptides are highlighted in dashed frame boxes. Arrows indicate IAPP/peptide interaction interfaces (solid lines: main interface, dashed lines: secondary interaction interfaces). Green: replacement of residues by alanine causes stronger peptide binding to the corresponding fragment; red: replacement of residues by alanine causes weaker peptide binding to the corresponding fragment; NMe: *N*-methylation.

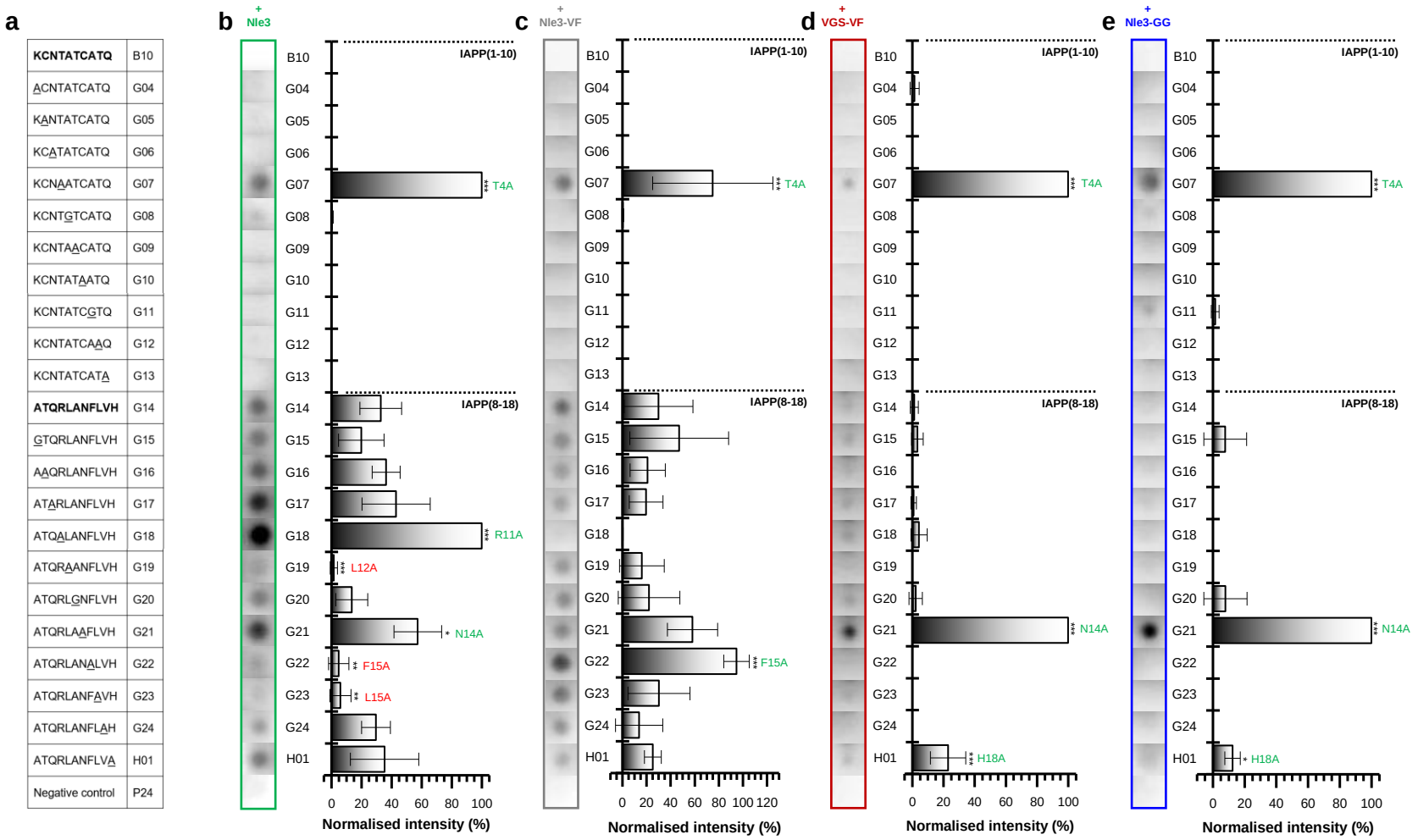

Figure 4-66: Identification of amino acids in IAPP(1-10) and IAPP(8-18) important for binding to ADPs by sequential alanine scanning using peptide microarrays. (**a**) IAPP wild-type segments IAPP(1-10) and IAPP(8-18) (bold; no alanine substitutions) and corresponding alanine-substituted segments (position of alanine mutation underlined) investigated in the microarray experiment. (**b-e**) Microarrays were incubated with N-terminal biotinylated ADPs (3 µM Biotin-Nle3 (b) or 3 µM Biotin-Nle3-GG (e) or 0.5 µM Biotin-Nle3-VF (c) or 0.5 µM Biotin-VGS-VF (d)). Detection of bound biotinylated ADPs was done after incubation with streptavidin-POD and development with ECL. Bar diagrams represent spot intensities obtained from different developments with the different Biotin-ADPs (mean ± SD; 3 assays for Biotin-Nle3-GG, 4 assays for the other peptides; see also Figure 7-63 in Appendix). Depicted membranes are from one of these assays, respectively. Green letters indicate alanine mutations causing stronger binding of the mutated segment compared to the wild-type segment, red letters indicate alanine mutations causing weaker binding. Asterisks mark spot intensities significantly different from the wild-type segment. *** P<0.001, ** P<0.01, * P<0.05 (by one-way ANOVA & Bonferroni).

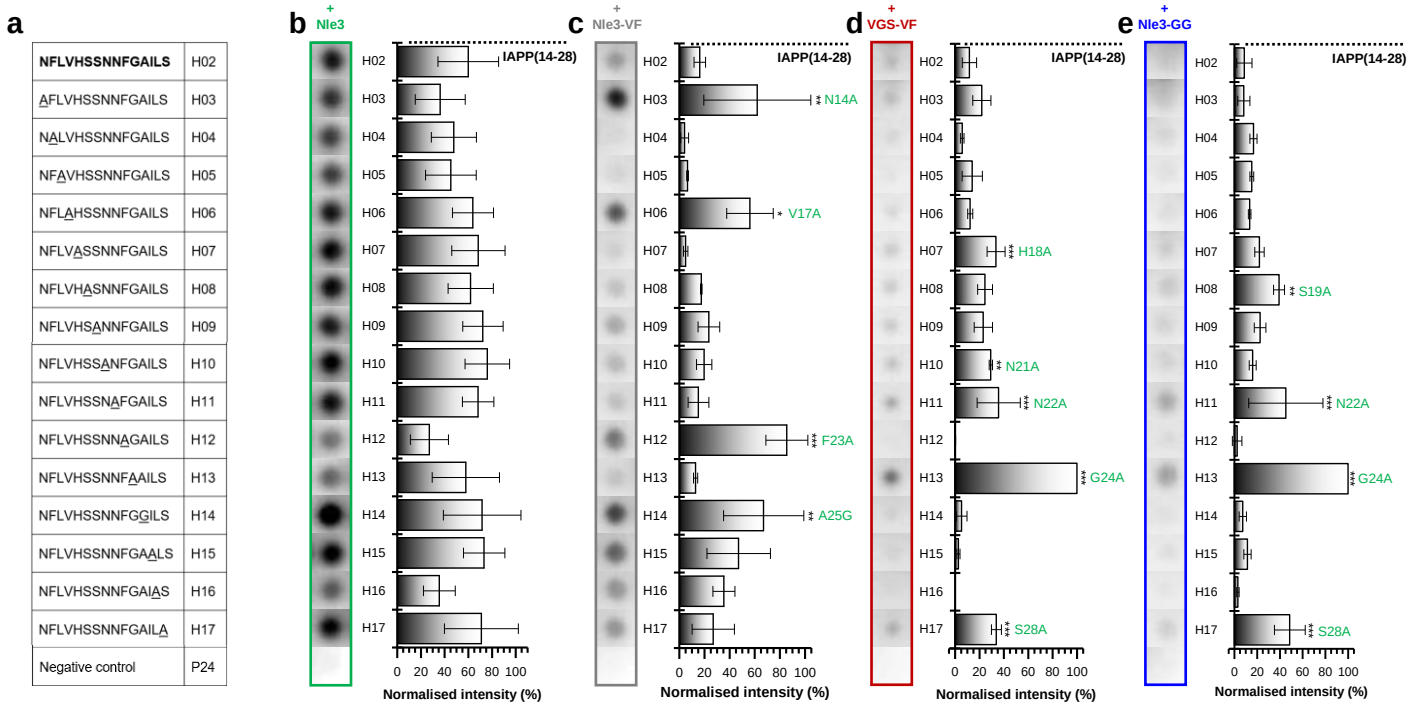

Figure 4-67: Identification of amino acids in IAPP(14-28) important for binding to ADPs by sequential alanine scanning using peptide microarrays. (**a**) IAPP wild-type segment IAPP(14-28) (bold; no alanine substitutions) and corresponding alanine-substituted segments (position of alanine mutation underlined) investigated in the microarray experiment. (**b-e**) N-terminal biotinylated ADPs (3 µM Biotin-Nle3 (b) or 3 µM Biotin-Nle3-GG (e) or 0.5 µM Biotin-Nle3-VF (c) or 0.5 µM Biotin-VGS-VF (d)) were used to incubate microarrays. After incubation with streptavidin-POD and development with ECL, detection of bound biotinylated ADPs was performed. Bar diagrams represent spot intensities obtained from different developments with the different Biotin-ADPs (mean ± SD; 3 assays for Biotin-Nle3-GG, 4 assays for the other peptides; see also Figure 7-63 in Appendix). Depicted membranes are from one of these assays, respectively. Green letters indicate alanine mutations causing stronger binding of the mutated segment compared to the wild-type segment. Asterisks mark spot intensities significantly different from the wild-type segment. *** P<0.001, ** P<0.01, * P<0.05 (by one-way ANOVA & Bonferroni).

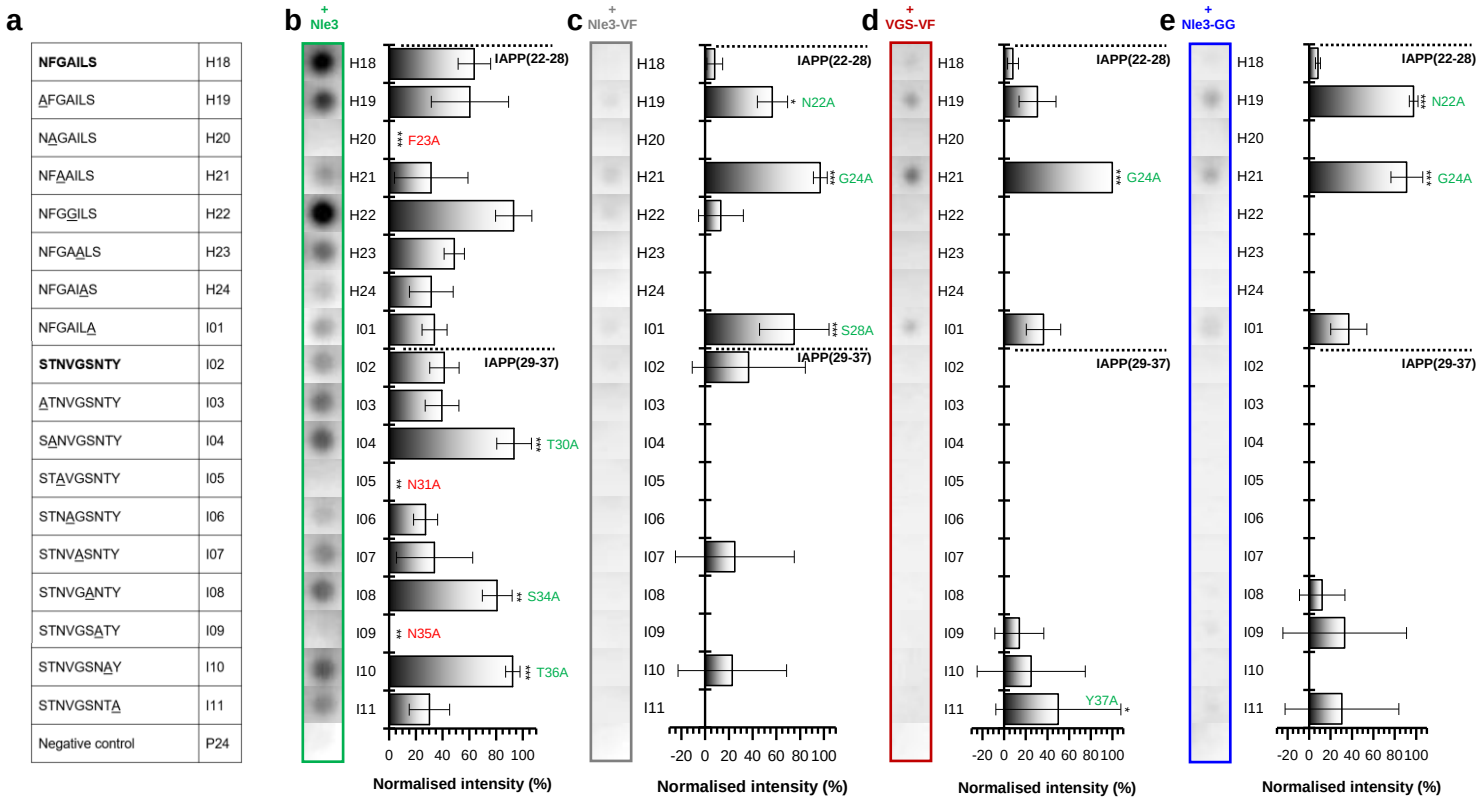

Figure 4-68: Identification of amino acids in IAPP(22-28) and IAPP(29-37) important for binding to ADPs by sequential alanine scanning using peptide microarrays. (**a**) IAPP wild-type segments IAPP(22-28) and IAPP(29-37) (bold; no alanine substitutions) and corresponding alanine-substituted segments (position of alanine mutation underlined) investigated in the microarray experiment. (**b-e**) Microarrays were incubated with N-terminal biotinylated ADPs (3 µM Biotin-Nle3 (b) or 3 µM Biotin-Nle3-GG (e) or 0.5 µM Biotin-Nle3-VF (c) or 0.5 µM Biotin-VGS-VF (d)). Following incubation with streptavidin-POD and development with ECL, bound biotinylated peptides were detected. Bar diagrams represent spot intensities obtained from different developments with the different Biotin-ADPs (mean ± SD; 3 assays for Biotin-Nle3-GG, 4 assays for the other peptides; see also Figure 7-63 in Appendix). Depicted membranes are from one of these assays, respectively. Green letters indicate alanine mutations causing stronger binding of the mutated segment compared to the wild-type segment, red letters indicate alanine mutations causing weaker binding. Asterisks mark spot intensities significantly different from the wild-type segment, *** P<0.001, ** P<0.01, * P<0.05 (by one-way ANOVA & Bonferroni).

4.10 ADPs interact with Aβ40 and Aβ42 and suppress their amyloid self-assembly

4.10.1 Interaction studies by fluorescence spectroscopic titrations and CD spectroscopy

ADPs are derived from the Aβ40 sequence and therefore expected to interact with and potentially inhibit Aβ40 and $Aβ42^{134-139}$. As fluorescence titration assays revealed, ACMs are indeed able to bind Aβ40 and Aβ42 with nano- to micromolar affinity. Titrations of FITC-Aβ42 (5 nM) or DAC-Aβ40 (10 nM) with unlabelled ACMs showed that binding to monomeric Aβ42 is stronger than binding to monomeric Aβ40 for all peptides (Table 4-15; Figure 7-31 and Figure 7-34 in Appendix). The two peptides carrying the phenylalanine linkers, F3-VF and F3-LF, showed weaker binding to both Aβ40 and Aβ42 compared to their Nle3- and L3-linked counterparts, indicating that the bulky aromatic rings within the loop region negatively influence binding. Taking into consideration the ACMs' self-assembly propensities reveals that interaction of monomeric Aβ42 is with monomeric Nle3-VF, Nle3-LF and L3-LF (app. k_D for self-assembly > app. k_D for FITC-Aβ42 binding), with monomeric or small oligomeric L3-VF and with oligomeric F3-VF and F3-LF (app. k_D for self-assembly < app. k_D for FITC-Aβ42 binding) (Table 4-15). Interaction of monomeric Aβ40 is with oligomeric ACM-species (Table 4-15). When titrations were performed with fluorescently labelled ACMs (1 or 5 nM) using increasing concentrations of Aβ40 or Aβ42, binding affinities were significantly weaker in almost all cases compared to binding affinities using FITC-Aβ42/DAC-Aβ40 (Table 4-15; Figure 7-32 and Figure 7-35 in Appendix). Since fluorescently labelled ACMs were used at a concentration lower than their app. k_D for self-assembly, interactions of monomeric ACMs with Aβ40 and Aβ42 are investigated using this assay system. Of note, the app. k_D obtained for Aβ42 self-assembly determined under the same conditions as app. k_Ds for Fluos-ACM/Aβ42 interactions was 11.8 ± 2.3 nM (Figure 7-33 in Appendix). The findings indicate that monomeric ACMs interact stronger with Aβ40 and Aβ42 monomers than with bigger oligomers.

Binding to monomeric and oligomeric Aβ40 was additionally studied for ADPs that were not able to inhibit IAPP. Comparing app. k_Ds of first-set ADPs without *N*-methylations (VGS, Nle3, L3) to DAC-Aβ40 reveals that changing the native LTS VGS to NleNleNle does not influence the peptide's binding affinity to monomeric Aβ40 (Table 4-16 and Figure 7-36, Figure 7-39, Figure 7-40 in Appendix). In contrast, substitution of VGS by LLL strongly impairs binding to monomeric Aβ40. Binding of monomeric peptides to oligomeric Aβ40 (assessed via titrating fluorescently labelled ADPs (5 nM) with unlabelled Aβ40) is weakened by both the NleNleNle and the LLL substitution. In case of the peptide VGS, introduction of N- and C-terminal *N*-methylations both dramatically impair interaction with monomeric Aβ40, while binding to oligomeric Aβ40 was not affected in all cases except for VGS-GG or even became stronger (Table 4-16, Figure 7-40 to Figure 7-44 in Appendix). C-terminal methylations additionally hindered the peptide's self-assembly while this effect was little to absent for N-terminal

Table 4-15: App. k_D values of interactions of ACMs with ACMs, Aβ40, and Aβ42 as determined by fluorescence spectroscopic titrations. Self-assembly was determined by titrations of synthetic N-terminal fluorescein-labelled ACMs (5 nM) with unlabelled ACMs. FITC-Aβ42 (5 nM) or DAC-Aβ40 (10 nM) was titrated with unlabelled ACMs. Synthetic N-terminal fluorescein-labelled ACMs (1 nM for Aβ42, 5 nM for Aβ40) were titrated with unlabelled Aβ40 or Aβ42. Experiments were performed in 1xb containing 1 % HFiP except for titrations of Fluos-ACMs with unlabelled Aβ42. These titrations were conducted in 50 mM ammonium acetate, pH 8.5 (1 % HFIP). App. k_Ds are means (± SD) from three binding curves. Corresponding fluorescence emission spectra and binding curves are shown in Figure 7-31, Figure 7-32, Figure 7-34, and Figure 7-35 in the Appendix. See Table 7-14, and Table 7-17 to Table 7-20in the Appendix for the three single app. k_D values. Data of titrations of FITC-Aβ42 with ACMs is included in a table in reference [140].

	Self-assembly	**FITC-Aβ42**	**Aβ42**	**DAC-Aβ40**	**Aβ40**
Peptide	app. k_D (±SD) (nM)				
Nle3-VF	51.9 ± 4.5	14.5 ± 8.0	> 25 µM	243.2 ± 2.0	572.7 ± 130.4
Nle3-LF	24.1 ± 1.4	11.1 ± 6.0	> 10 µM	358.1 ± 9.4	323.1 ± 20.0
L3-VF	20.2 ± 0.6	38.0 ± 2.0	> 10 µM	54.6 ± 7.5	578.9 ± 71.2
L3-LF	48.1 ± 1.8	2.6 ± 1.4	> 5 µM	220.8 ± 15.8	450.9 ± 54.0
F3-VF	64.9 ± 11.6	160.8 ± 12.9	> 10 µM	No binding (5 µM)	> 5 µM
F3-LF	47.0 ± 7.8	430.6 ± 7.1	> 5 µM	No binding (2.5 µM)	> 5 µM

methylations indicating that VGS's self-recognition is mediated by its C-terminus. Of note, this observation was not made for Nle3-GG and Nle3-GI, the two peptides carrying the same C-terminal methylations as VGS-GG and VGS-GI but comprise a different LTS (Table 4-16, Figure 7-37 and Figure 7-38 in Appendix). Obviously, the more hydrophobic NleNleNle LTS can compensate for the negative effect of C-terminal methylations on self-assembly ability. As observed for VGS-GI, also binding of Nle3-GI to monomeric Aβ40 was strongly impaired by the methylation but binding of Nle3-GG was not affected in contrast to VGS-GG. The two peptides carrying the hydrophilic arginine LTS R3-VF and R3-LF self-assembled and bound to monomeric and oligomeric Aβ40 with similar affinities (Table 4-16, Figure 7-45 and Figure 7-46 in Appendix). G3-VF was the only peptide with a N-terminal methylation that was not able to self-assemble in the investigated concentration range (0.5 nM – 5 µM) (Table 4-16, Figure 7-47 in Appendix). Similarly to VGS-VF, which is carrying the same methylation pair and also has a LTS comprised of rather small amino acids, it showed only very weak binding to DAC-Aβ40 whereas binding to oligomeric Aβ40 was strong (~44 nM vs. 33 nM for VGS-VF) (Table 4-16, Figure 7-47 in Appendix).

Potential conformational changes occurring upon interaction of Aβ40 and Aβ42 with ADPs were investigated by CD. For this, CD spectra of freshly prepared mixtures containing Aβ40 or Aβ42 (5 µM) and peptide (5 µM) were collected and compared to the theoretical spectra resulting from the mathematical addition of the experimentally obtained spectra from Aβ40 or Aβ42 and peptides alone. Experiments with Aβ40 were conducted in 1xb (1 % HFIP), experiments with Aβ42 were conducted in 20 mM ammonium acetate pH 8.5 (1 % HFIP). Of note, binding studies with monomeric Aβ40 (DAC-Aβ40 and unlabelled peptides) and oligomeric Aβ40 (Fluos-peptides and unlabelled Aβ40) were done in the same buffer as CD interaction experiments. Binding studies using Aβ42 were either done in 1xb containing 1 % HFIP (FITC-Aβ42 and unlabelled peptides) or in 50 mM ammonium acetate pH 8.5 (1 % HFIP) (Fluos-peptides and unlabelled Aβ42). Thus, CD interaction studies with Aβ42 are better comparable to binding experiments using fluorescently labelled peptides and unlabelled Aβ42.

Table 4-16 App. k_D values of interactions of ADPs with ADPs and Aβ40 as determined by fluorescence spectroscopic titrations. To determine self-assembly, titrations were performed using synthetic N-terminal fluorescein-labelled ADPs (5 nM). Bindings to DAC-Aβ40 (10 nM) were measured by titrating synthetic N-terminal fluorescently labelled Aβ40 with unlabelled ADPs. Bindings to unlabelled Aβ40 were determined by titrations of synthetic N-terminal fluorescein-labelled ADPs (5 nM) with Aβ40. Experiments were performed in 1xb containing 1 % HFiP. App. k_Ds are means (± SD) from three binding curves. * done by Sophia Kalpazidou during her Erasmus internship[147]. Corresponding fluorescence emission spectra and binding curves are shown in Figure 7-36 to Figure 7-47 in the Appendix. See Table 7-14, Table 7-19, and Table 7-20 in the Appendix for the three single app. k_D values.

	Self-assembly	**DAC-Aβ40**	**Aβ40**
Peptide		app. k_D (±SD) (nM)	
Nle3	198.1 ± 53.4	55.0 ± 10.2	1277.6 ± 154.7
Nle3-GG	81.7 ± 1.9	42.9 ± 16.1	300.3 ± 13.4
Nle3-GI	28.5 ± 1.9	No binding (10 µM)	418.5 ± 55.8
L3	34.1 ± 6.4	No binding (2.5 µM)	264.9 ± 26.4
VGS	16.8 ± 6.7	53.3 ± 10.0	31.5 ± 2.7
VGS-VF	24.2 ± 2.4	>10 µM	32.6 ± 1.8
VGS-LF	78.9 ± 32.5	No binding (5 µM)	0.240 ± 0.015
VGS-GG	No binding (5 µM)	>10 µM	>10 µM
VGS-GI	No binding (5 µM)	>10 µM	3.5 ± 1.8
R3-VF	37.7 ± 9.1	1126.1 ± 379.7	539.6 ± 56.5
R3-LF	20.8 ± 4.3	1596.1 ± 51.0	598.7 ± 74.5
G3-VF	No binding (5 µM)	>10 µM*	44.3 ± 8.1*

CD results correlated well with corresponding fluorescence titration experiments. Mixtures of Aβ40 with peptides displaying a strong binding affinity to both monomeric and oligomeric Aβ40 (Nle3-VF, Nle3-LF, L3-VF and L3-LF; Table 4-15) showed a much higher β-sheet/β-turn content than expectable from the mathematical addition of the peptides' single spectra (Figure 4-69a,b,d,e). This indicates that structural rearrangements are taking place upon interaction resulting in a higher ordered Aβ40/peptide-complex. CD spectra of mixtures of Aβ40 with VGS-VF and VGS-LF showed less random coil content than their mathematical sum of spectra but differences were less pronounced compared to effects of the previously mentioned peptides (Figure 4-69g,h). Both VGS-VF and VGS-LF strongly interact with oligomeric Aβ40 but show only weak to no binding affinity to monomeric Aβ40 (Table 4-16). When the peptides F3-VF, F3-LF or VGS-GG were mixed with Aβ40, resulting CD spectra did not or only little differ from the mathematical sum of the peptides' single spectra (Figure 4-69c,f,i). This is in good agreement with the lower binding affinity of these ADPs toward Aβ40 (Table 4-15, Table 4-16). Their weak interaction with Aβ40 does not lead to structural changes in the hetero-assemblies.

Interactions of ADPs with Aβ42 were studied via CD for three exemplary peptides, Nle3-VF, L3-VF and L3-LF (in 20 mM ammonium acetate pH 8.5, 1 % HFIP; RT). Spectra of all three mixtures did not strongly differ from the corresponding mathematical sum of spectra (Figure 4-70). Binding affinities obtained in a similar buffer system (50 mM ammonium acetate pH 8.5, 1 % HFIP; Fluos-peptides plus unlabelled Aβ42) were in the µM-range (Table 4-15). Taken together, both experiments indicate that also interactions of Aβ42 with Nle3-VF, L3-VF or L3-LF do not lead to structural changes in the hetero-assemblies under these buffer conditions.

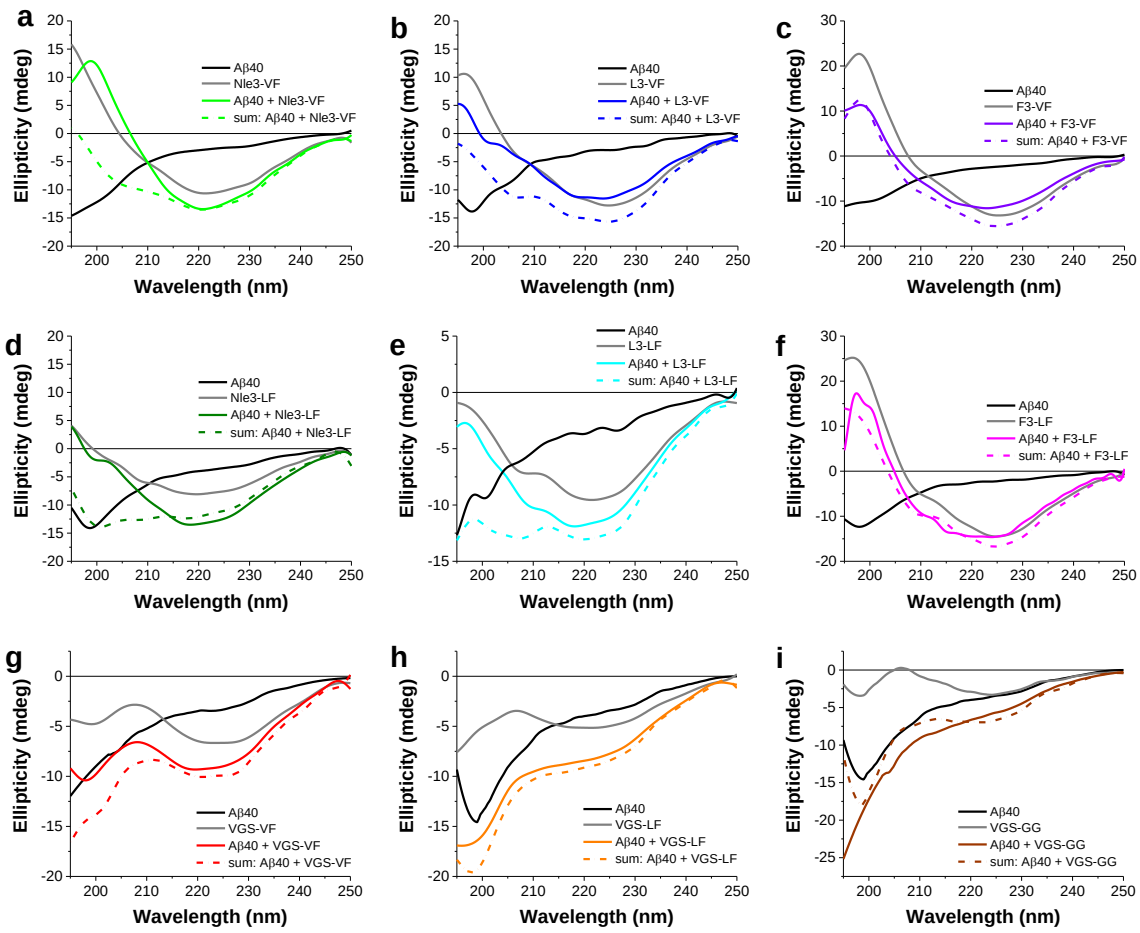

Figure 4-69: Investigations of interactions of Aβ40 with ACMs and other ADPs by CD. Solutions of Aβ40 (5 µM), ADPs (5 µM) or their mixtures (1:1) were freshly prepared in 1xb containing 1 % HFIP (pH 7.4). Sums of spectra (dashed lines) were obtained by mathematical addition of the single spectra measured for Aβ40 and ADP alone. Differences between experimental spectra of the mixture and the sum of spectra indicates conformational changes in the hetero-assembly upon interaction of Aβ40 and the partner peptide. Experiments using Nle3-VF (**a**), L3-VF (**b**), F3-VF (**c**), Nle3-LF (**d**), L3-LF (**e**), F3-LF (**f**), VGS-VF (**g**), VGS-LF (**h**) and VGS-GG (**i**) as interaction partners were performed.

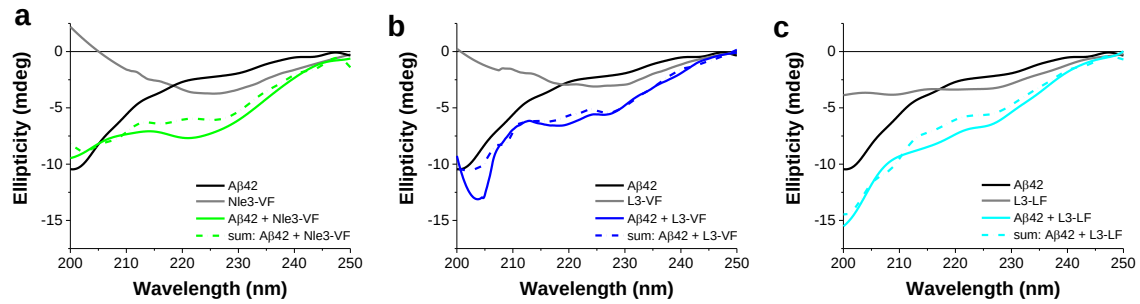

Figure 4-70: Investigations of interactions of Aβ42 with Nle3-VF, L3-VF and L3-LF by CD. Fresh solutions containing Aβ42 (5 µM), ACMs (5 µM) or their mixture (1:1) were made in 20 mM ammonium acetate, pH 8.5 (1 % HFIP). Sums of spectra (dashed lines) were obtained by mathematical addition of the single spectra measured for Aβ42 and ACM alone. Differences between experimental spectra of the mixture and the sum of spectra indicates conformational changes in the hetero-assembly upon interaction of Aβ42 and the partner peptide. Experiments were conducted using Nle3-VF (**a**), L3-VF (**b**) or L3-LF (**c**).

4.10.2 Inhibition of fibril formation and cytotoxicity of Aβ40 and Aβ42

In a first step, the 6 ACMs' effect on Aβ40 fibril formation and cytotoxicity was studied using the ThT binding and the MTT reduction assay. For this, Aβ40 (16.5 µM) was mixed with ACMs

(1:1) and fibril formation was followed over 8 days. Aβ40-mediated cell damage on PC-12 cells was assessed after 72 h and 8 days of aging. All 6 ACMs were able to suppress Aβ40 fibrillation and cytotoxicity (Figure 4-71a-c). Inhibition of cell damage was stronger at 72 h than at 8 days but mixtures were still less toxic than pure Aβ40 (Figure 4-71b,c). Except for VGS-GI, VGS-GG, and Nle3-GI, several other first and second set ADPs also showed inhibitory potential against Aβ40 (Figure 4-71d-l).

In a second step, ACMs' effects on Aβ42 amyloidogenicity were studied. For this, Aβ42 (5 µM) was mixed 1:1 with ACMs and aggregation kinetics were studied via ThT binding. Cytotoxicity of Aβ42 and mixtures were measured at 6 days. All ACMs could efficiently suppress Aβ42 fibrillation and cell damage (Figure 4-72a,b). Two IAPP non-inhibitors, namely VGS-VF and Nle3-GG, were additionally tested for their Aβ42 inhibition potential (in 1:1). While Nle3-GG could almost fully block Aβ42 fibril formation, VGS-VF only showed weak inhibitory effects (Figure 4-72c).

To investigate ADPs' aggregation propensities under the Aβ42 inhibition assay conditions (see Materials & Methods for details), ADPs were incubated in isolation (5 µM) and species were examined after 6 days via TEM (Figure 4-72d,e). Only two peptides – Nle3-LF and Nle3-GG – showed an increase in ThT fluorescence by time. TEM analysis proved the presence of fibrils in the 6 days aged Nle3-GG solution (Figure 4-72e). Thus, the small increase in ThT fluorescence observed for the Aβ42/Nle3-GG mixture could not only be due to a weakened inhibitory effect of Nle3-GG by time but also be due to fibril formation of the ADP alone under these conditions. The 6 days aged Nle3-LF solution did not contain fibrillar species but only amorphous aggregates (Figure 4-72e). This is in accordance with the ThT signal measured for Nle3-LF at 6 days (close to starting signal at t = 0 h). The temporary increase in ThT fluorescence could thus be due to the occurrence of β-rich oligomers (to which ThT is known to bind also to[154]) which might form during Nle3-LF self-aggregation and not due to the formation of fibrils. All other tested ADPs showed amorphous aggregates in TEM in accordance with ThT binding results (Figure 4-72d,e). For F3-VF and F3-LF, the aggregates were of rather roundish shape.

IC_{50}s of inhibitory effects on Aβ42 cytotoxicity were determined at 6 days for Nle3-VF, L3-VF, F3-VF and F3-LF. Values were in mid-nanomolar range for Nle3-VF, L3-VF and F3-LF and in low micromolar range for F3-VF (Table 4-17, Figure 7-10 in Appendix). IC_{50}s for Nle3-LF and L3-LF should also be determined but it turned out to be impossible due to an anormal inhibitor concentration-dependent behaviour of the mixtures. While no inhibitory effect was observed when Aβ42 was mixed with the peptides at 1:0.001 and strong inhibition was observed at 1:0.5 as expected, the inhibition potential of both peptides became weaker and not stronger with further increasing concentrations (Figure 4-73a,b). To investigate if this is due to the peptides themselves, all ACMs were incubated at increasing concentrations under the Aβ42 inhibition conditions and their ThT binding was followed to detect potential differences in their

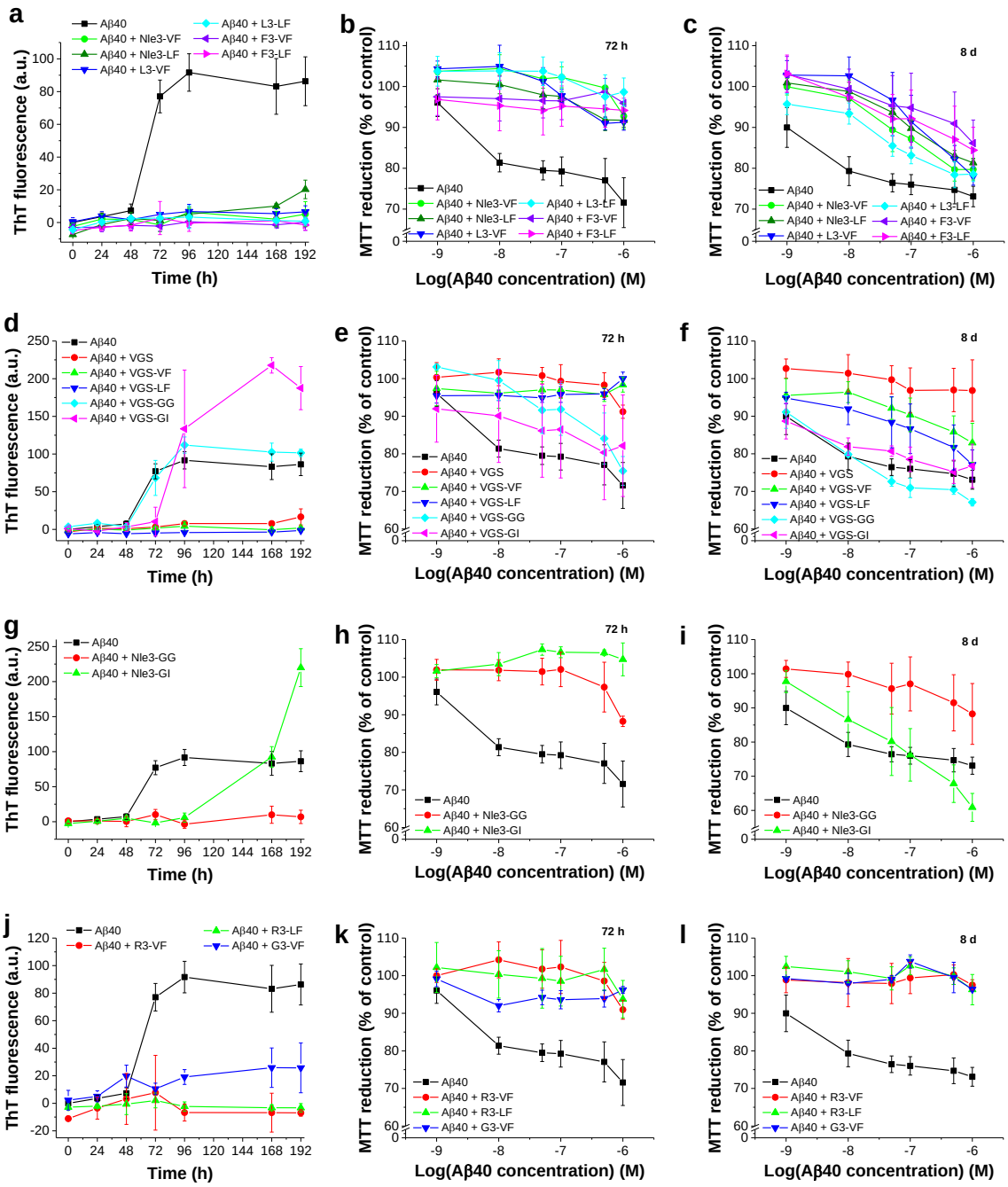

Figure 4-71: Effects of ACMs and other ADPs on Aβ40 amyloidogenicity. (**a,d,g,j**) ThT binding assays were conducted to follow Aβ40 (16.5 µM) fibril formation in presence and absence of peptides (1:1). Incubations were prepared in ThT assay buffer with 1 % HFIP. Error bars represent means ± SD (n=3-6 assays). Data was normalized to highest and lowest Aβ40 values in each assay. (**b,c,e,f,h,i,k,l**) Aliquots from corresponding incubations in a, d, g or j were taken at 72 h (b,e,h,k) and 8 days (c,f,i,l) and applied onto PC-12 cells after dilution with cell medium for assessing cell damage via the MTT reduction assay. Error bars represent means ± SD from three to six assays, n=3 each. Effects of R3-VF on Aβ40 fibril formation and cytotoxicity were also studied by Sophia Prem during her Bachelor thesis[146] (similar results); effects of G3-VF on Aβ40 fibril formation were also studied by Sophia Kalpazidou during her Erasmus internship[147].

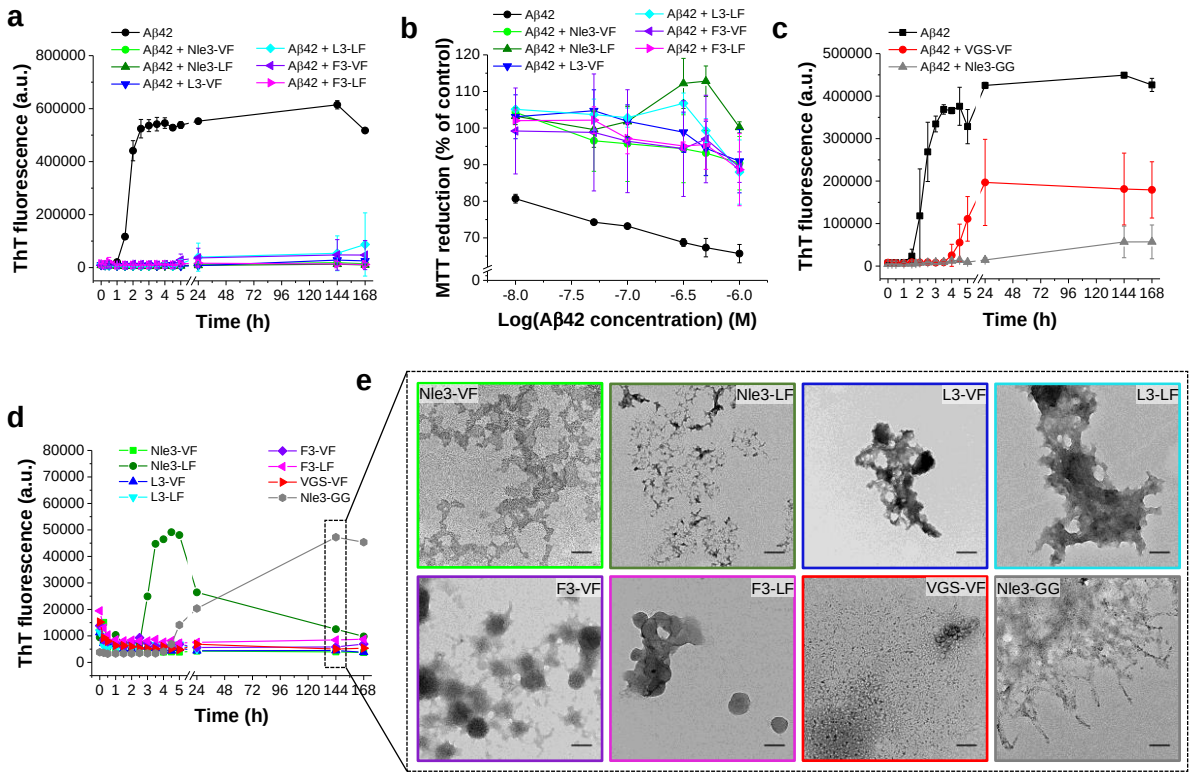

Figure 4-72: Studies on the effects of ACMs and other ADPs on Aβ42 amyloidogenicity and aggregation propensities of inhibitors. (**a,c**) Aβ42 (5 µM) fibril formation was followed in presence and absence of ADPs (1:1) by ThT binding. Solutions were prepared in 45 mM ammonium acetate (pH 8.5), contained 10 µM ThT and were incubated at 37 °C. Error bars represent means ± SD from three assays. (**b**) Incubations for the MTT reduction assay were prepared as in a, but did not contain ThT. Aliquots were taken at 6 days, diluted into cell medium and applied onto PC-12 cells for assessing cell damage. Error bars represent means ± SD from three assays, n=3 each. (**d**) Aggregation propensities of peptides incubated in isolation (5 µM) were studied in 45 mM ammonium acetate (pH 8.5, 10 µM ThT, 37 °C) Assays were performed once. (**e**) TEM imaging of 6 days aged peptide solutions (5 µM, from d). Scale bars are 100 nm. Data of a) and b) is part of a figure in reference [140].

Table 4-17: IC_{50} of inhibitory effects of ACMs on cytotoxic self-assembly of Aβ42. IC_{50} values are means (±SD) from 3 titration assays (n=3 each) (Aβ42, 1 µM) and were determined using 6 days aged Aβ42/ACM mixtures. *n.d.: could not be determined due to anormal peptide behaviour at higher concentrations. See Table 7-13 in Appendix for the three single IC_{50} values. Data is part of a table in reference [140].

ACM	IC_{50} (±SD) (nM) 6 d
Nle3-VF	367 (± 79)
Nle3-LF	n.d.*
L3-VF	261 (± 140)
L3-LF	n.d.*
F3-VF	1032 (± 297)
F3-LF	262 (± 115)

aggregation behaviour. No increase in ThT binding was observed for Nle3-VF and L3-VF which are directly related to Nle3-LF and L3-LF (Figure 4-73c,f). As just discussed, Nle3-LF showed an increasing ThT signal by time. This effect was found to be concentration-dependent (≥ 0.5 µM; Figure 4-73f). However, for lower concentrations ThT signals started to drop again with longer incubation times. Only at 10 µM the ThT-positive species were stably formed (Figure 4-73f). If the first increasing and later decreasing ThT fluorescence is due to β-rich oligomers which temporarily form during Nle3-LF's self-aggregation, this process might counteract the peptide's inhibitory effect. The finding that these potential β-rich oligomers form

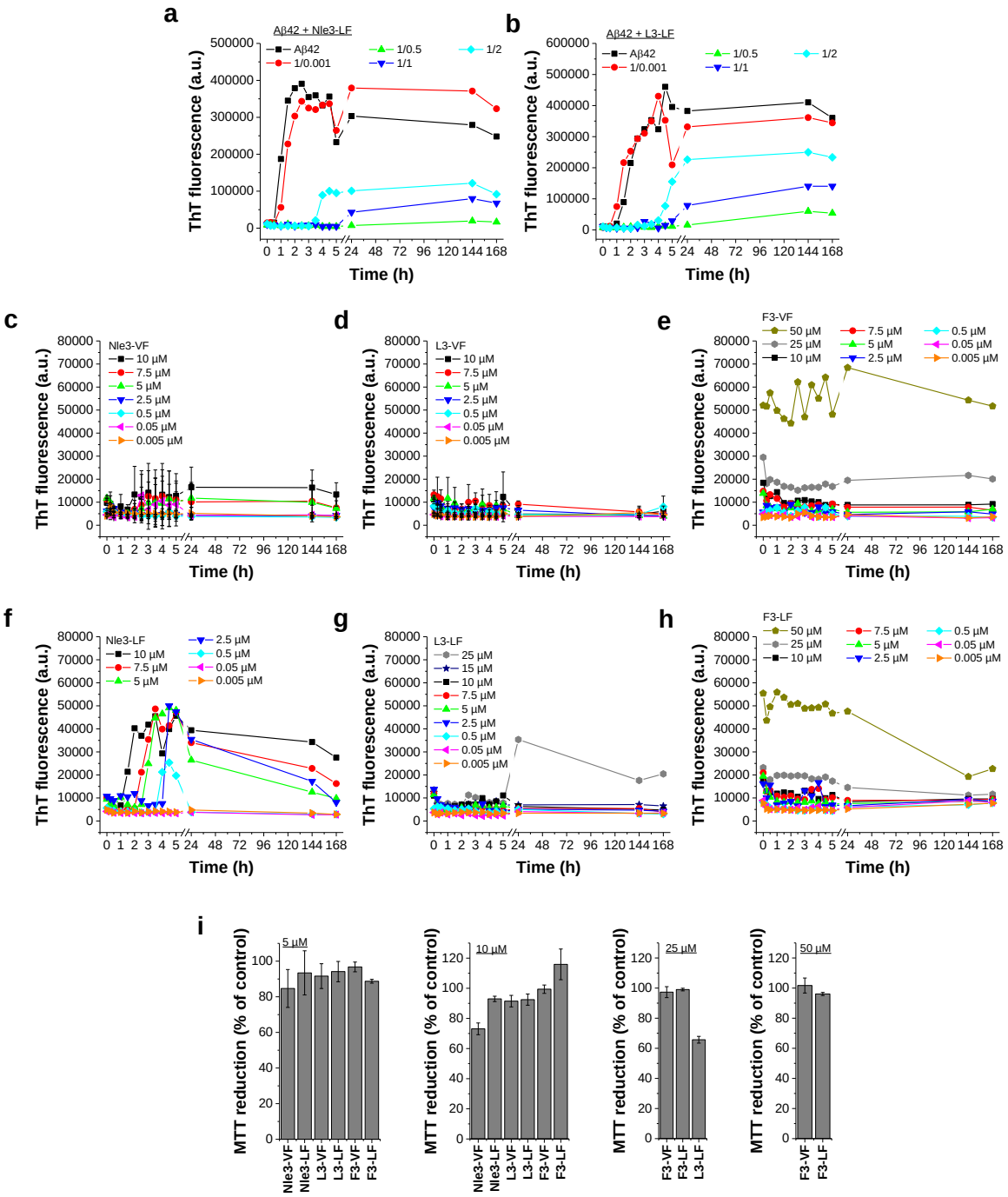

Figure 4-73: Concentration-dependent effects of Nle3-LF and L3-LF on Aβ42 fibril formation and ACM aggregation propensity under Aβ42 inhibition assay conditions. (**a,b**) Fibril formation of Aβ42 (5 μM) in presence and absence of Nle3-LF or L3-LF (ratios as indicated) was followed by ThT binding (in 45 mM ammonium acetate, pH 8.5, 10 μM ThT, 37 °C). One representative example for an IC_{50} assay (n=5-6 different IC_{50} assay trials using different Aβ42:ACM ratios) is shown for each peptide. (**c-h**) Aggregation behaviour of ACMs alone (concentrations as indicated) were studied under the same conditions as used for mixtures in a & b. Error bars in c & d represent means ± SD from three assays, assays in d-h were performed once. (**i**) Cytotoxicity of ACMs incubated in isolation at indicated concentrations. Solutions were prepared as in c-h but did not contain ThT. After 6 days of aging, aliquots were taken, diluted into cell medium and incubated with PC-12 cells. Final concentration on the cells for 5, 10, 25 and 50 μM incubations was 1, 2, 5 and 10 μM, respectively. Error bars represent means ± SD from three assays (n=3 each) for Nle3-VF and L3-VF and means ± SD from one assay (n=3; technical triplicate) for the other ACMs.

faster and become more stable with increasing peptide concentration would fit to the observation that inhibition also gets worse with increasing concentration. A similar concentration-dependent behaviour was observed for L3-LF, but higher concentrations were necessary (25 μM) (Figure 4-73g). However, increased ThT binding with increasing peptide concentration was also observed in case of F3-VF and F3-LF which behaved normally when

mixed at higher ratios with Aβ42 (Figure 4-73e,h). Of note, their ThT binding (at 25 and 50 µM) was already measurable in fresh solutions (t = 0 h) while for Nle3-LF and L3-LF a clear time-dependent kinetic was observed. These species might thus be of a different nature and might therefore not hinder Aβ42 inhibition. This was further confirmed by MTT reduction experiments: both F3-VF and F3-LF ThT-reactive species were not toxic, while L3-LF ThT-reactive species were (Figure 4-73i). ThT-reactive species of Nle3-LF were not toxic up to 10 µM (Figure 4-73i). Higher concentrations were not tested for this peptide. In conclusion, the experiments showed that both Nle3-LF and L3-LF form ThT-reactive species by time which differ in case of L3-LF in their cytotoxicity from other ThT-reactive species formed by F3-VF and F3-LF. The formation of these specific species might counteract the peptides' inhibitory effect and therefore their inhibitory potential weakens with increasing concentration in contrast to other ACMs.

Taken together, the rational design of ADPs did not only yield 6 potent inhibitors of IAPP but also yielded several inhibitors of Aβ40 and Aβ42. Importantly, all 6 ACMs were not only able to block IAPP amyloidogenicity but could also effectively suppress Aβ40 and Aβ42 fibrillation and cytotoxicity. ACMs were non-toxic and non-amyloidogenic at concentrations necessary for Aβ42 inhibition (5 µM) but showed unexpected aggregation into ThT-reactive species with increasing concentration.

4.11 ACMs form amorphous co-assemblies with Aβ40

To investigate if ACMs form fibrillar hetero-assemblies with Aβ40, samples from the end point of the aggregation kinetics were taken and analysed via TEM. 8 days aged samples from mixtures of Aβ40 with ACMs (1:1) presented amorphous aggregates as main species (Figure 4-74). Minor amounts of fibrils were observed in all mixtures except the Aβ40/L3-VF-mixture (only amorphous aggregates). Since the analysed 8 days aged Aβ40/ACM mixtures showed slightly increased toxicity compared to their toxicity after 72 h, it can be assumed that the small portion of fibrils observed via TEM are Aβ40 fibrils emerging due to inhibitor weakening by time (see Figure 4-71b,c). TEM images for mixtures of Aβ40 with other ADPs are shown in Figure 7-50 in the Appendix. TEM findings correlated with inhibition results from ThT binding and MTT reduction studies in case of the ADPs VGS, VGS-VF, VGS-GI, Nle3-GG, R3-VF and G3-VF. Mixtures with VGS-LF and R3-LF contained amorphous aggregates and fibrils even though ThT binding studies indicated full inhibition of both peptides at 8 days. The mixture with the non-inhibitor VGS-GG did not only contain fibrils but also amorphous aggregates, which might be due to the peptide itself and not due to the inhibition of Aβ40 fibril formation. Solely for Nle3-GI, TEM did not correlate at all with findings from ThT binding and MTT reduction studies. Instead of fibrils only amorphous aggregates were found in the mixture with this non-inhibitor. To investigate if these species might be cytotoxic β-rich (and therefore ThT-reactive) aggregates instead of amyloid fibrils more studies need to be conducted.

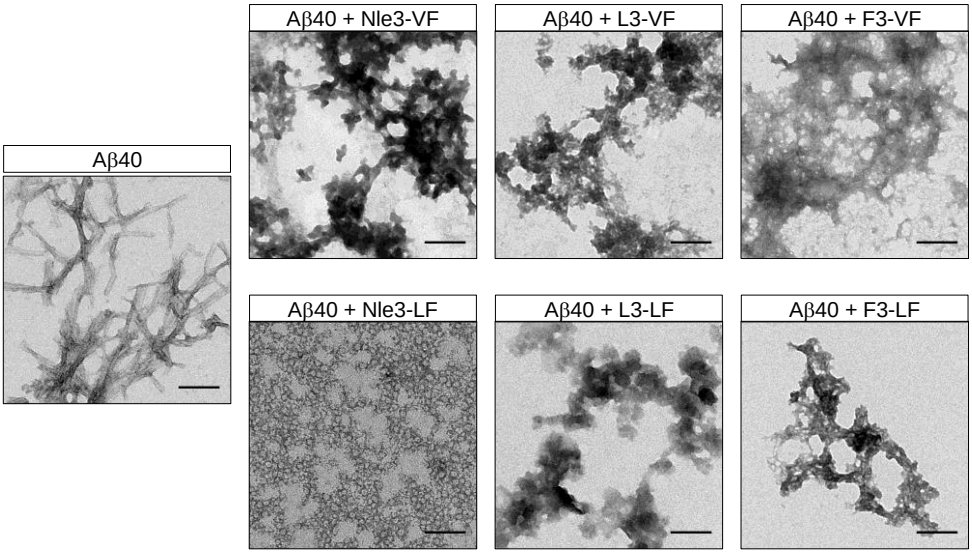

Figure 4-74: TEM imaging of Aβ40 and its mixtures with ACMs. Solutions containing Aβ40 (16.5 µM) or its mixtures with ACMs (1:1) were aged for 8 days before taking samples for TEM analysis (ThT assay buffer, 1 % HFIP). Amorphous aggregates were found as main species in 5 out of 6 mixtures, species in Aβ40/Nle3-LF mixtures were more roundish-shaped. Scale bars are 100 nm.

4.12 ACMs form fibrillar co-assemblies with Aβ42

4.12.1 Fibrils in Aβ42/ACM mixtures are longer than fAβ42

In a next step, samples from the end point of the aggregation kinetics of Aβ42 aged in presence and absence of ACMs were analysed by TEM to examine if ACMs form heterofibrils with Aβ42 ("hf-Aβ42/ACM"). In contrast to Aβ40/ACM mixtures, 6d aged Aβ42/ACM mixtures (1:1) contained fibrils as main species (Figure 4-75 and Figure 4-75 in Appendix). Of note, these fibrils display no ThT-reactivity (see Figure 4-72a), just as observed for IAPP/ACM heterofibrils. However, they clearly show morphological differences compared to Aβ42 fibrils (Figure 4-75). Aβ42 fibrils were found to have an average length of 154 ± 58 nm and an average width of 7.8 ± 1.6 nm (Table 4-18). In comparison, fibrils formed when Aβ42 is incubated with ACMs are significantly longer (~2-4 times) but share a similar width (Table 4-18, Figure 4-75). Thus, the presence of ACMs drives the Aβ42 aggregation process towards the formation of much longer fibrils. The generation of elongated fibrils is directly related to the inhibition mechanism, as samples containing inhibitors in a sub-stoichiometric ratio of 1:0.001 (Aβ42:ACM) where no inhibition is observed (see IC_{50} in Figure 7-10a in Appendix) do not contain them (Figure 4-75).

To confirm that fibrils – presumably heterofibrils – are formed as the main species Aβ42/ACM mixtures (1/1, 6 days, 5 µM Aβ42), fAβ42 and hf-Aβ42/ACM were prepared under the Aβ42 inhibition assay conditions. Thereafter, solutions were transferred from MTP wells into Eppendorf tubes and centrifuged for 20 min at 20000 g. With these centrifugation conditions, full precipitation of Aβ42 fibrils could be achieved in preliminary trials (Figure 4-76a). Peptide

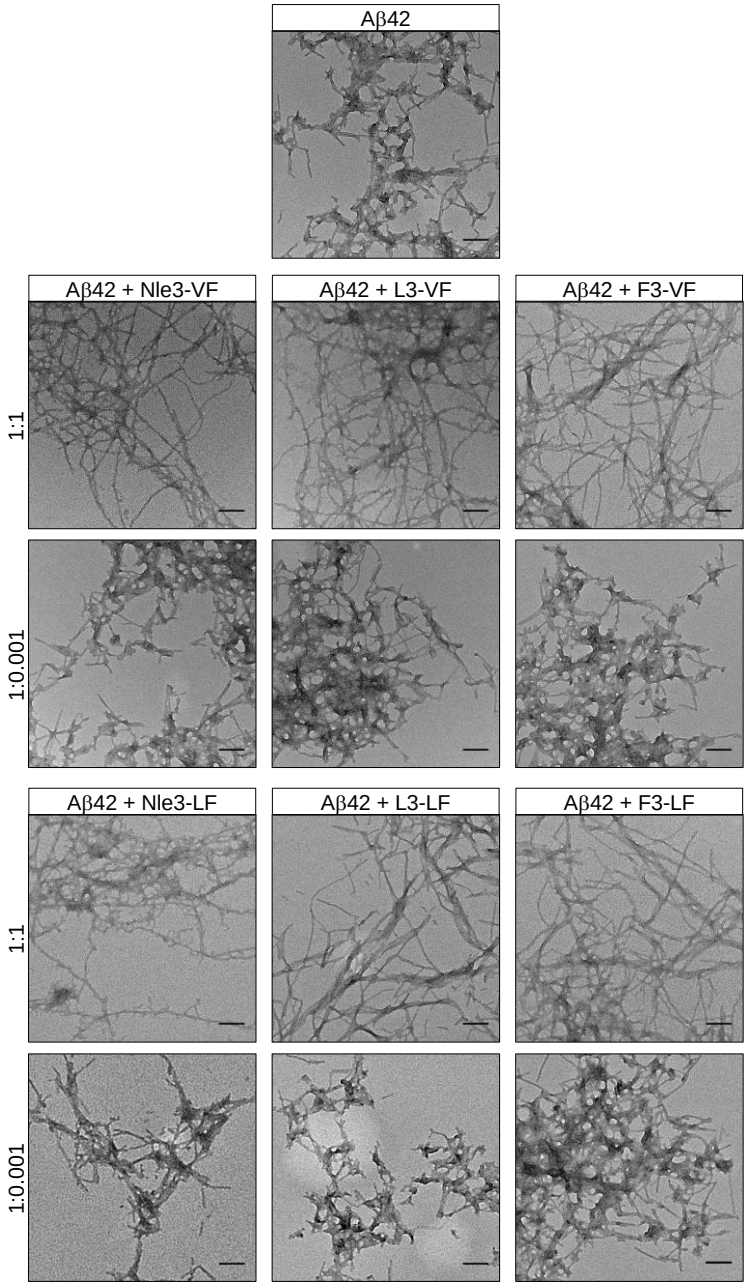

Figure 4-75: TEM imaging of Aβ42 and its mixtures with ACMs. TEM samples were taken from 6 days aged solutions containing Aβ42 (5 µM) or its mixtures with ACMs (1:1 or 1:0.001, as indicated; 45 mM ammonium acetate pH 8.5, 37 °C; corresponding to conditions of ThT binding/MTT reduction studies; w/o ThT). In presence of equimolar amounts (1:1) of ACMs, inhibition is observed in ThT binding and MTT reduction studies and TEM shows elongated fibrils. In presence of sub-stoichiometric inhibitor amounts (1:0.001), fibrils show the morphology of Aβ42 fibrils when Aβ42 is incubated in isolation (top picture). Scale bars are 100 nm. Images of Aβ42, Aβ42 + Nle3-VF, Aβ42 + L3-VF, Aβ42 + F3-VF, and Aβ42 + F3-LF are part of a figure in reference [140].

amounts in supernatant (SN) fractions of fAβ42 and hf-Aβ42/Nle3-VF were analysed via dot blot, peptide amounts in pellet fractions were quantified via BCA. The dot blot experiment showed that only very little peptide remained in solution after centrifugation for both fAβ42 and heterofibril samples (Figure 4-76b). This indicates that not only in the incubation containing pure Aβ42 but also in the Aβ42/Nle3-VF mixture fibrillar assemblies were formed as main species which can be precipitated by centrifugation. BCA analysis of the corresponding pellets revealed that peptide is indeed present in these fractions but to a much lower extent than expected assuming almost full precipitation of both fAβ42 and heterofibrils as indicated by dot

Table 4-18: Fibril dimensions of fAβ42 and heterofibrils formed with ACMs. Fibril lengths and widths were measured from representative TEM pictures of 6 days aged incubations (Aβ42 5 µM, mixtures 1:1). Error bars indicate mean ± SD from 15-23 fibrils (see Table 7-23 and Table 7-24 in the Appendix). The diagrams on the right graphically represent fibril lengths and widths depicted in the table. ns: not significant; *** P<0.001, by one-way ANOVA and Bonferroni. Data is part of a table in reference [140].

Sample	Fibril length (nm)	Fibril width (nm)
fAβ42	154 ± 58	7.8 ± 1.6
fHetero (Aβ42/Nle3-VF)	472 ± 138	7.3 ± 1.7
fHetero (Aβ42/L3-VF)	458 ± 106	6.9 ± 1.4
fHetero (Aβ42/F3-VF)	354 ± 117	6.9 ± 1.3
fHetero (Aβ42/Nle3-LF)	590 ± 268	7.5 ± 1.1
fHetero (Aβ42/L3-LF)	347 ± 72	7.0 ± 2.2
fHetero (Aβ42/F3-LF)	358 ± 118	7.3 ± 1.5

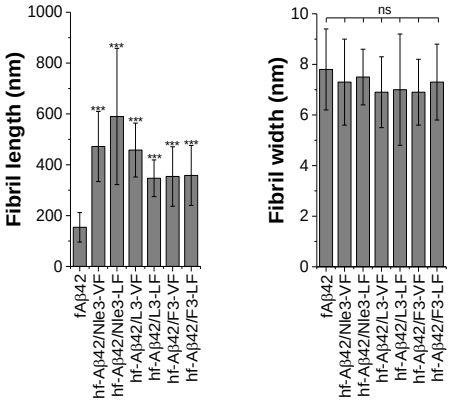

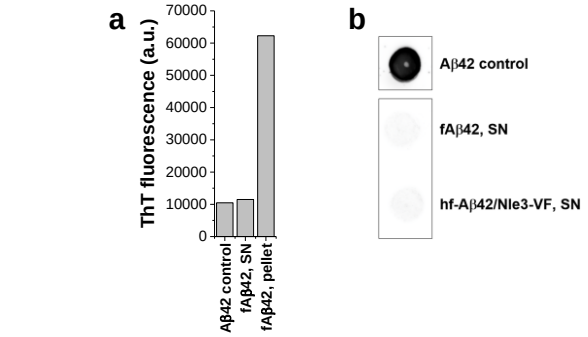

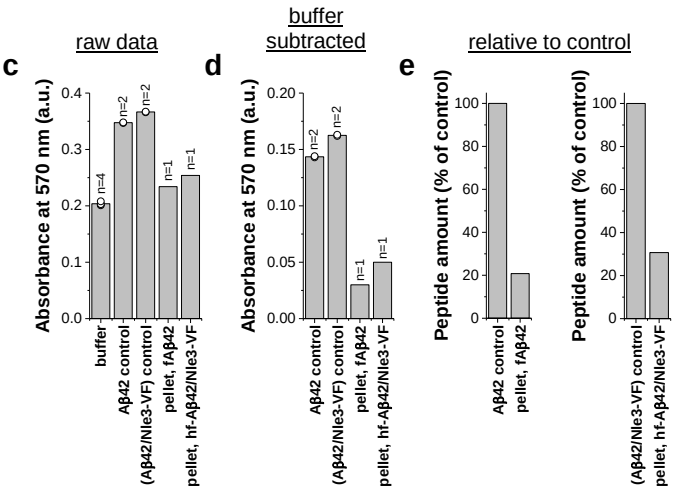

Figure 4-76: ThT binding, DB, and BCA analyses confirming that fibrils are main species in aged Aβ42/ACM mixtures (**a**) ThT-reactivity of supernatant (SN) and pellet fraction of an Aβ42 fibril solution. The incubation was prepared in 45 mM ammonium acetate, pH 8.5, and aged for 6 days (37 °C) using 5 µM Aβ42. Following centrifugation (20 min, 20000 g), SN and pellet fractions were separated. ThT was added to SN to a final concentration of 10 µM. The pellet fraction was re-dissolved in 45 mM ammonium acetate, pH 8.5, containing 10 µM ThT. Values are compared to a freshly prepared Aβ42-solution (5 µM, 45 mM ammonium acetate, pH 8.5) containing 10 µM ThT (w/o centrifugation; "Aβ42 control"). (**b**) Dot blot analysis of SN fractions of Aβ42 fibril ("fAβ42") and Aβ42/Nle3-VF heterofibril ("hf-Aβ42/Nle3-VF") solutions. Incubations were prepared as in a, Nle3-VF was applied in a 1:2-ratio in the mixture. After 8 days, solutions were centrifuged (20 min, 20000 g) and supernatants removed. SN solutions were spotted stepwise onto nitrocellulose membranes (4.5 µg Aβ42). Selective detection of Aβ42 was carried out using the mouse anti-Aβ(1-17) antibody (6E10). As control, a freshly prepared solution of Aβ42 (5 µM, w/o centrifugation) was spotted and analysed in parallel (4.5 µg Aβ42, "Aβ42 control"). (**c-e**) Quantification of peptide amounts in pellet fractions of Aβ42 fibril ("fAβ42") and Aβ42/Nle3-VF heterofibril ("hf-Aβ42/Nle3-VF") solutions via BCA. Remaining pellet fractions from b, were used. Results are presented as mean of raw data (c), after subtracting the buffer value (mean of n=4 measurements from c) (d) and as peptide amounts calculated relatively to the respective control sample (e). As controls, freshly prepared solutions of Aβ42 (5 µM) or an Aβ42/Nle3-VF mixture (1:2) were used (w/o centrifugation; "Aβ42 control" and "Aβ42/Nle3-VF control", respectively). Numbers (n) above bars indicate number of incubations that were analysed for each sample.

blot results (~20 % of control for Aβ42 fibrils and ~30 % of control for heterofibrils; controls were freshly prepared solutions of Aβ42 or its mixture with Nle3-VF) (Figure 4-76c-e). Maybe quantification via BCA is less reliable for peptides in their fibrillar form than for soluble peptides/proteins.

Taken together, based on dot blot results and the fact that fibrils found in Aβ42/Nle3-VF mixtures via TEM do not show ThT-reactivity, it can be concluded that heterofibrils are indeed formed as main species although this could not be ultimately confirmed by BCA quantification. Also, if these fibrils were mainly Aβ42 homofibrils, their ThT binding should be detectable. The heterogenic nature of fibrils formed in Aβ42/ACM mixtures was finally verified by 2-PM fluorescence microscopy as discussed in the next chapter.

4.12.2 2-photon microscopy and FLIM-FRET suggest heteromeric Aβ42/ACM fibrils

For investigating the composition of fibrillar assemblies formed in Aβ42/ACM mixtures, 2-PM was applied using N-terminal TAMRA-labelled Aβ42 and Fluos-labelled inhibitors. Solutions were prepared and incubated under ThT/MTT assay-equivalent conditions (5 µM Aβ42). Inhibitors were applied in 2-fold molar excess since inhibition studies with N^{α}-terminal biotinylated Nle3-VF showed that the peptide can only inhibit Aβ42 in 1:2 but not in 1:1 anymore when carrying an N-terminal label (Figure 7-65 in Appendix). Since the 5,6-carboxyfluorescein label for 2-PM studies is introduced in the same position, a similar effect was assumed. Incubations were prepared using 50 % labelled and 50 % unlabelled peptides, meaning that a solution to form potential Aβ42/ACM heterofibrils/-nanofibers contained 2.5 µM Aβ42, 2.5 µM TAMRA-Aβ42, 5 µM unlabelled ACM and 5 µM Fluos-ACM.

Such mixtures of (TAMRA-)Aβ42 and (Fluos-)Nle3-VF (4 days aged) contained bicoloured heterocomplexes and nanofibers (Figure 4-77). The observed nanofibers were of different appearance: Long (TAMRA-)Aβ42 nanofibers where heterocomplexes were associated with and maybe bridging separate shorter filaments into longer ones, and bicoloured hetero-nanofibers resembling a tube and presenting “islet-like” structures comprised by both peptides. Similar tube-like structures were also observed in mixtures of (TAMRA-)Aβ42 and (Fluos-)L3-VF (6 days aged) (Figure 4-78a,b). Moreover, large hetero-nanofibers were assembled by thinner hetero-nanofiber units, which seemed to be comprised of alternating (TAMRA-)Aβ42 (red) and (Fluos-)L3-VF (green) building blocks (see coloured arrows in Figure 4-78). Bicoloured hetero-nanofibers assembled from multiple smaller nanofiber-units were also observed in (TAMRA-)Aβ42/(Fluos-)F3-VF and (TAMRA-)Aβ42/(Fluos-)F3-LF mixtures (6 days aged) (Figure 4-78c,d). Of note, appearance of all observed hetero-nanofibers was different from nanofibers assembled by (TAMRA-)Aβ42 (Figure 4-77c, Figure 4-78e).

To study interactions of Aβ42 and ACMs within the hetero-nanofiber assembly in more detail, FLIM-FRET analysis was used. The (TAMRA-)Aβ42/(Fluos-)Nle3-VF hetero-nanofiber shown in Figure 4-77b was chosen as an example. Since 2-PM showed that this hetero-nanofiber is

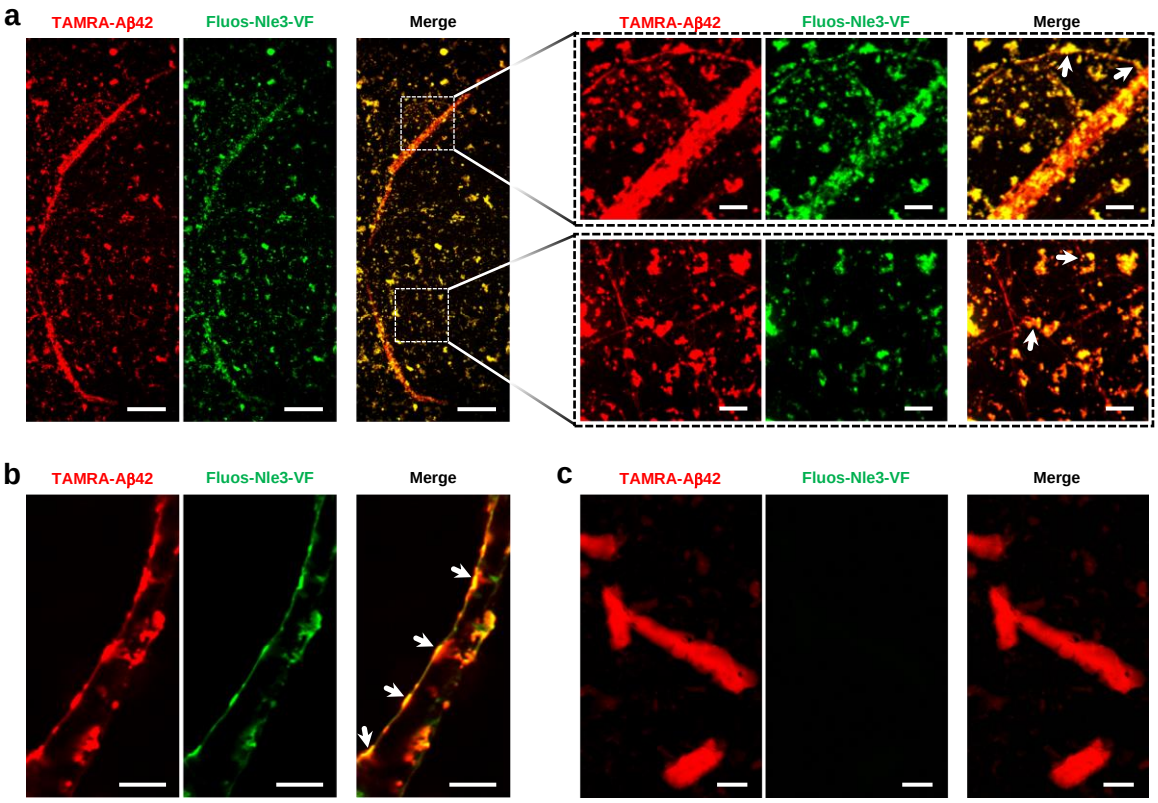

Figure 4-77: Hetero-nanofiber-species in (TAMRA-)Aβ42/(Fluos-)Nle3-VF mixtures visualised by 2-PM. Mixtures were prepared in 45 mM ammonium acetate, pH 8.5, aged for 4 days (37 °C) and contained 50 % labelled and 50 % unlabelled peptides, meaning 2.5 µM Aβ42, 2.5 µM TAMRA-Aβ42, 5 µM Nle3-VF and 5 µM Fluos-Nle3-VF (ratio 1:2). Control incubation of (TAMRA-)Aβ42 alone (c) was made in the same way without inhibitor. (**a**) (TAMRA-)Aβ42 fibrils bound and interconnected (see arrows) by heterocomplexes. Scale bars: 50 µm; 10 µm for magnifications. (**b**) Tube-like hetero-nanofiber containing islet-like regions (see arrows). Scale bars: 10 µm. (**c**) Nanofibers built by (TAMRA-)Aβ42 incubated in isolation. Scale bars: 10 µm**.** Images of b) are part of a figure in reference [140].

formed by bicoloured “islet-like” structures which are interconnected by thinner parts (“cable-like” structures), these two different regions were analysed separately by FLIM-FRET. In regions comprising the islets, the donor lifetime was remarkably more reduced than in interconnecting “cable-like” regions (Figure 4-79a). While the FLIM-FRET efficiency measured in islet-regions was 30-80 % (peaking at ~60 %), the efficiency in interconnecting regions showed a much broader distribution (0-80 %, peaking at ~20-40 %), meaning that energy from the donor molecule (Fluos) to the acceptor molecule (TAMRA) is less well transferred in these regions (Figure 4-79b). Both findings – more reduced donor lifetime and higher FLIM-FRET efficiency – indicate that Aβ42 and Nle3-VF are in very close contact within the islet-regions (<5.5 nm since Förster’s distance R_0 for TAMRA/Fluos is 5.5 nm and FRET efficiency is ~60 %) but their interaction is looser in the “cable-like” regions. This could be explained as follows: islets might be formed by a rearrangement of Aβ42/Nle3-VF heterocomplexes into fibrillar species or by the binding of Nle3-VF to Aβ42 fibrils which are emerging by time, resulting in a close interaction of the two peptides. Due to its relationship with Aβ40, the inhibitor’s amino acid sequence is highly similar to the Aβ42 sequence as well and might therefore be able to elongate the fibril units further, which is building up the interconnecting regions. Very probably, also additional Aβ42 molecules can be incorporated in a similar way but the spacing between inhibitor and Aβ42 might be bigger, leading to a less reduced donor

lifetime in these areas. More studies on Aβ42/ACM heterocomplexes formation and the fibril elongation mechanism will be presented in chapters 4.12.3 and 4.12.4.

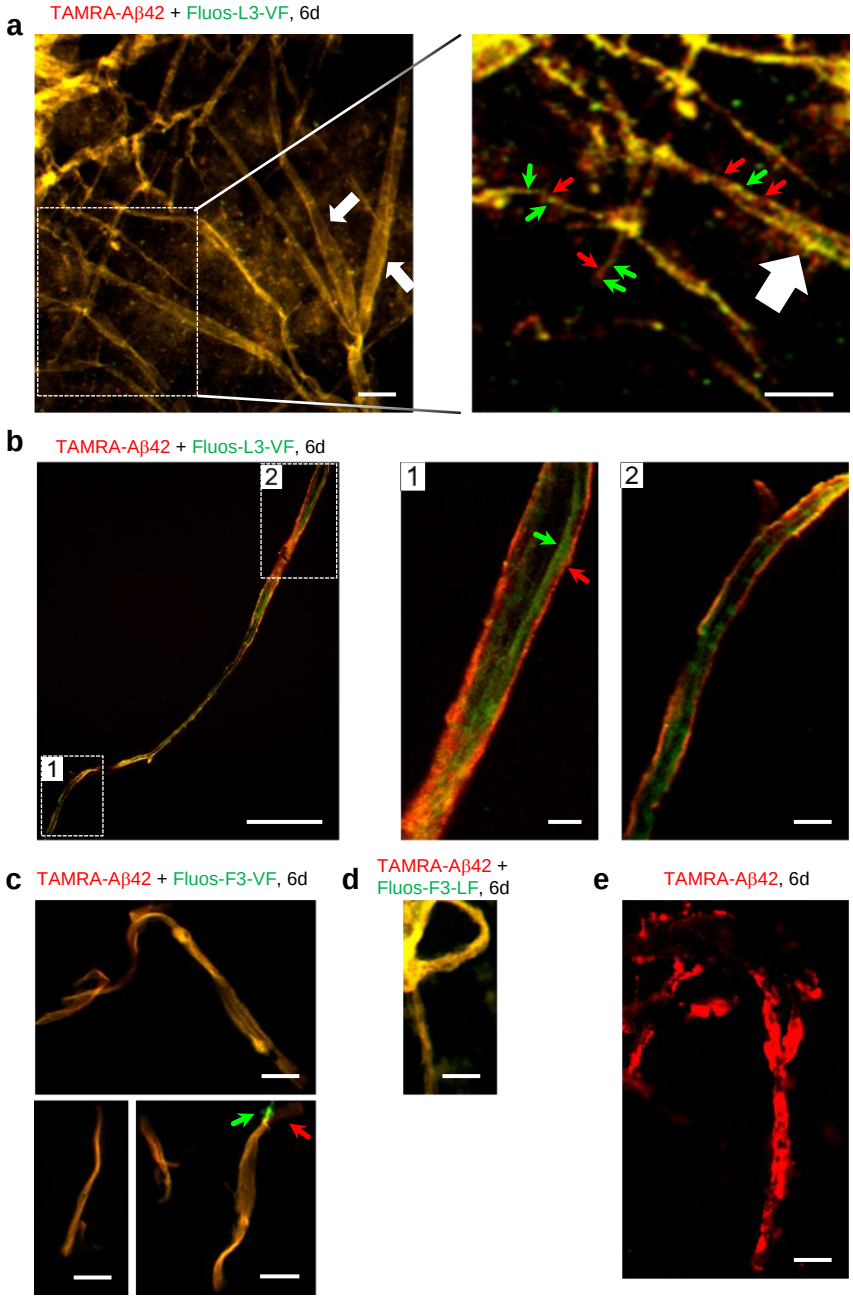

Figure 4-78: Hetero-nanofiber species in mixtures of (TAMRA-)Aβ42 with the ACMs (Fluos-)L3-VF, (Fluos-)F3-VF and (Fluos-)F3-LF visualised by 2-PM. Samples contained 50 % labelled and 50 % unlabelled peptides, meaning 2.5 µM Aβ42, 2.5 µM TAMRA-Aβ42, 5 µM unlabelled ACM and 5 µM Fluos-ACM (ratio 1:2) and were aged for 6 days (45 mM ammonium acetate, pH 8.5, 37 °C). Control incubation of (TAMRA-)Aβ42 alone (e) was made in the same way without inhibitor. (**a**) Hetero-nanofiber network observed in (TAMRA-)Aβ42/(Fluos-)L3-VF mixtures. White arrows indicate tube-like assemblies, coloured arrows mark alternating (TAMRA-)Aβ42 (red) and (Fluos-)L3-VF (green) building units. Scale bars: 10 µm. (**b**) Tube-like hetero-nanofiber assembled by (TAMRA-)Aβ42 and (Fluos-)L3-VF. Magnifications highlight two different areas of the tube. Coloured arrows indicate (TAMRA-)Aβ42- (red) and (Fluos-)L3-VF-containing (green) parts of the hetero-nanofiber. Scale bars: 100 µm for full hetero-nanofiber image, 10 µm for magnified areas. (**c,d**) Hetero-nanofibers assembled by (TAMRA-)Aβ42 and (Fluos-)F3-VF or (Fluos-)F3-LF, as indicated. Assemblies are composed of several thinner nanofiber units. Coloured arrows indicate (TAMRA-)Aβ42- (red) and (Fluos-)F3-VF building units. Scale bars: 10 µm. (**e**) (TAMRA-)Aβ42 nanofibers. Scale bar: 10 µm. Images of a-d) are part of a figure in reference [140] (adapted figure version).

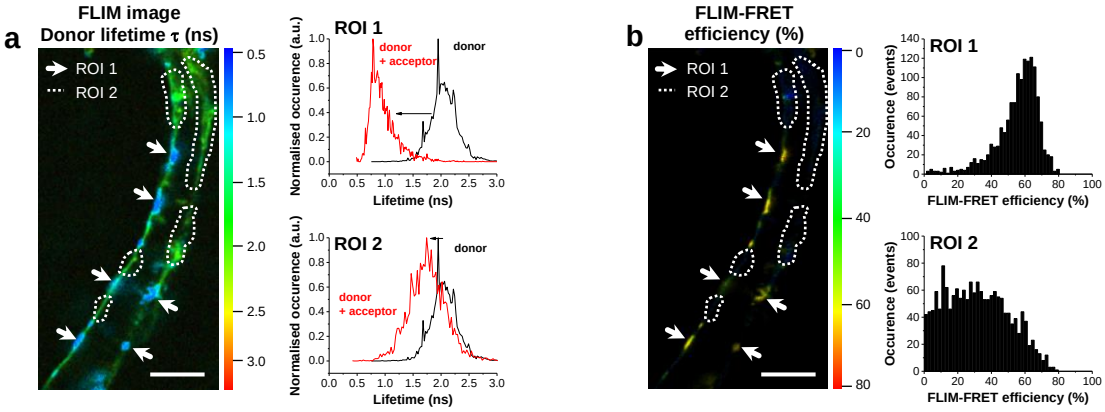

Figure 4-79: FLIM-FRET analysis of tube-like (TAMRA-)Aβ42/(Fluos-)Nle3-VF hetero-nanofiber. The sample was prepared by incubating 2.5 µM Aβ42 and 2.5 µM TAMRA-Aβ42 with 5 µM Nle3-VF and 5 µM Fluos-Nle3-VF (in 45 mM ammonium acetate, pH 8.5, 37 °C, 4 days). (**a**) FLIM image. Arrows mark ROI 1 ("islet-like" structures), dotted lines mark ROI 2 ("cable-like" structures). Coloured bar represents the lifetime. Scale bar is 10 µm. Diagrams on the right show lifetime distribution corresponding to the FLIM image for the two highlighted ROIs compared to the lifetime of the donor in absence of the acceptor. Donor-alone data was kindly provided by Beatrice Dalla Volta[140,152]. (**b**) FLIM-FRET efficiency. ROI areas are highlighted as in a,. Coloured bar represents the calculated efficiency. Scale bar is 10 µm. Bar diagrams on the right show efficiency distribution corresponding to the FLIM-FRET image for the two highlighted ROIs. ROI: region of interest. Figure is part of a figure in reference [140].

In conclusion, by using 2-PM and FLIM-FRET it was possible to verify the heterogenic nature of nanofibers formed in Aβ42/ACM mixtures. Thus, ACMs are not only able to assemble heterofibrils/-nanofibers with IAPP but also with Aβ42. Since FLIM-FRET analysis indicated that the distance between Aβ42 and Nle3-VF is <5.5 nm in hetero-nanofibers and their width was determined from TEM images to be ~7 nm, it can be concluded that the two peptides are indeed part of the same fibril.

4.12.3 Aβ42/ACM fibrillar co-assemblies evolve from amorphous co-aggregates

As previously presented fluorescence titration experiments revealed, ACMs strongly bind Aβ42 (see chapter 4.10.1). Analysis of complexes built upon interaction of Nle3-VF with Aβ42 was done by Christina Lindner during her Master thesis and showed that increasingly more heterodimers and -trimers were formed with rising inhibitor concentrations, accompanied by HMW species[151]. Notably, she found that heterodimer and -trimer are only formed in samples containing Nle3-VF in inhibition-competent quantity (1:1 and 1:2) which is consistent with fluorescence titration experiments and indicates that generation of specific heterocomplexes is essential for inhibition.

Based on these findings, time-dependent TEM studies were then performed to investigate what happens to the heterocomplexes after their formation. For this, solutions of Aβ42 (5 µM) and its mixture with inhibitor (1:1) were prepared and aged under the inhibition assay conditions. L3-VF was chosen as the exemplary inhibitor from the ACM family for these studies. Samples were taken from the incubations directly after preparation and at several time points during Aβ42's aggregation kinetics. TEM analysis showed that Aβ42 incubated in isolation completely aggregated into fibrils already after 3 h (Figure 4-80). The observed fibrillar species were rather short, as expected (compare Table 4-18 in chapter 4.12.1). In Aβ42/L3-VF mixtures, amorphous aggregates were found in freshly prepared solutions and after 1 h of

aging (Figure 4-80). At 3 h, amorphous heterocomplexes have transformed into short fibrils. From 5 h onward, transition into longer fibrils was observed. While after 5 h the main species were still short fibrils and only a minor portion of increased length was observed, the latter species was the dominant one at 48 h. At 6 days, only elongated fibrils were observed.

In summary, these findings indicate that Aβ42/ACM heterofibrils evolve by time from initially formed heterocomplexes. These heterocomplexes transform into elongated heterofibrils. Elongation could be for example caused by the joining of shorter fibril fragments or by addition of Aβ42 and/or ACMs onto the fibrils' ends.

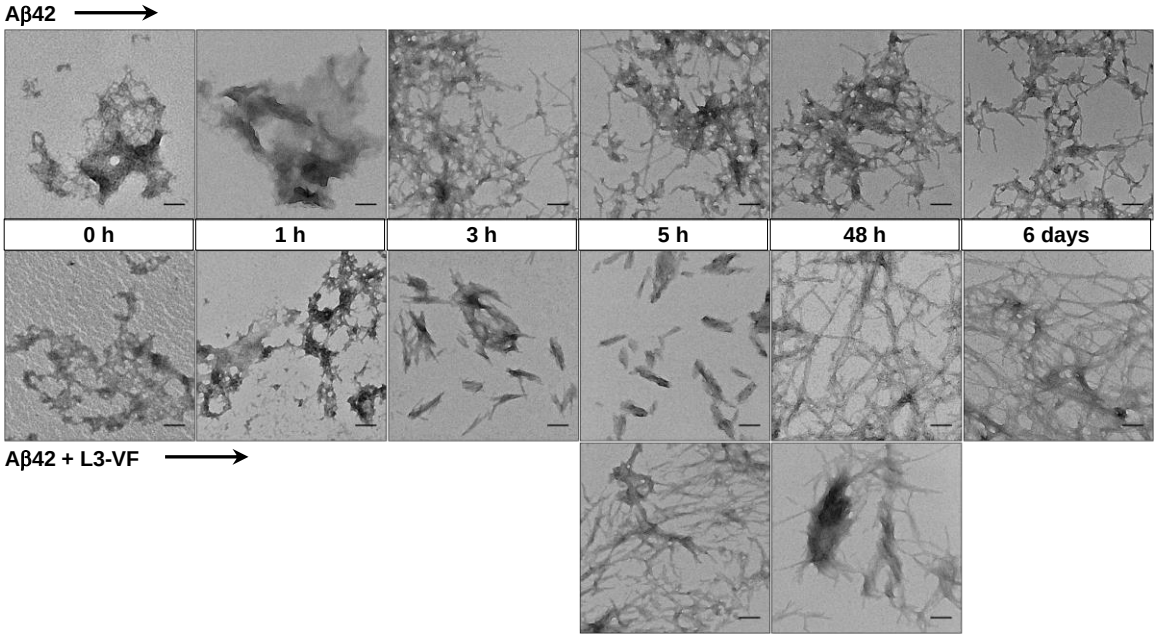

Figure 4-80: Transformation of Aβ42/L3-VF heterocomplexes into heterofibrils and fibril elongation process revealed by TEM. Samples for TEM imaging were taken at indicated time points from solutions containing 5 µM Aβ42 or its mixture with L3-VF (1:1) prepared in 45 mM ammonium acetate, pH 8.5 (37 °C) (corresponding to incubation conditions for ThT binding/MTT reduction studies; w/o ThT). Aβ42 transformed into typical short fibrils after 3 h, the Aβ42/L3-VF mixture showed transition of amorphous aggregates into fibrils after 3 h, which started to elongate from 5 h onward. Lower images at 5 h and 48 h show minor species observed in the mixture which were present in addition to major species (upper images). Scale bars are 100 nm.

4.12.4 Aβ42/ACM fibrillar co-assemblies elongate by integration of inhibitor or heterocomplexes into the growing fibril assembly

The next question was if for Aβ42/ACM heterofibril formation/ fibril elongation the presence of inhibitor is required from the beginning of the aggregation process or if pre-formed fAβ42 can also be extended further by ACMs. As dot blot experiments performed by Christina Lindner during her Master thesis revealed that ACMs can indeed bind to fibrillar Aβ42 species[151], ACMs' effects on fibril formation when added at post-nucleated stages were studied next. At this state, Aβ42-solutions are supposed to contain already fibrils but still also pre-fibrillar species. For this purpose, Aβ42 (5 µM; with 10 µM ThT inside the well) was aged under the ThT binding assay conditions for 105-135 min, added after to dried inhibitor (1:1 or 1:5) and ThT fluorescence was continued to be measured. These experiments revealed that fibril formation is significantly decelerated after aged Aβ42 was mixed with inhibitors in equimolar

concentration and even completely stopped when F3-VF was used at 5-fold molar excess (Figure 4-81a-e). The findings prove that ACMs can even act on Aβ42 fibril formation after its aggregation onset.

For TEM examination of species present at different time points after aged Aβ42 was mixed with inhibitor, identical solutions as above were prepared but without ThT. Nle3-VF was once more chosen as exemplary ACM. TEM analysis of samples taken at different time points after mixing 2 h-aged Aβ42 with Nle3-VF revealed that fibrils start elongating ~3 h after addition to Nle3-VF and were completely transformed into extended fibrils the next day (Table 4-19, Figure 4-82a,b). To investigate if Nle3-VF is even acting as an elongation promotor after Aβ42 fibrillation was fully completed, fAβ42 (5 µM, 7 days aged, w/o ThT) was added to the inhibitor (1:1). After 1 day of incubation, fibrils had indeed significantly increased in length (Table 4-20, Figure 4-82c). Similar results were obtained when samples were taken after 4 days of co-incubating fAβ42 with Nle3-VF.

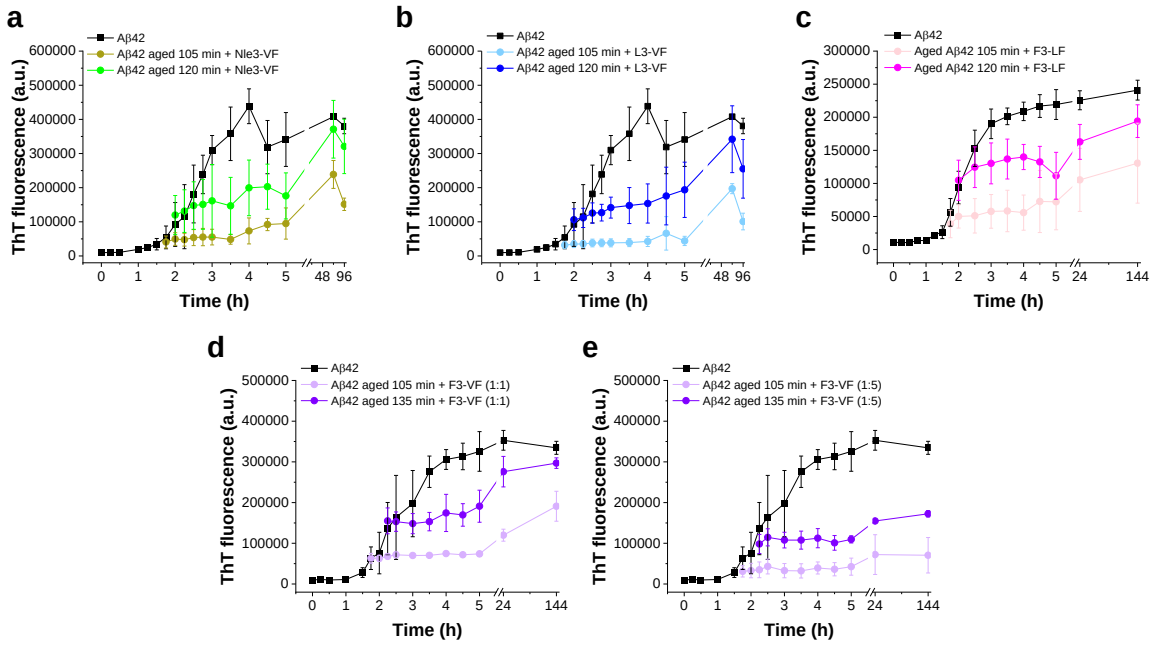

Figure 4-81: Effects of ACMs on nucleated Aβ42 aggregation. Effects of ACMs on Aβ42 fibril formation after nucleation were monitored by ThT binding. Aβ42 (5 µM, in 45 mM ammonium acetate, pH 8.5, 37 °C, with 10 µM ThT) was aged for the indicated time and added to dried inhibitors (1:1 if not stated otherwise). Error bars represent means ± SD (n=3-12 for Aβ42, n=3 for mixtures with ACMs). Results are shown for Nle3-VF (**a**), L3-VF (**b**), F3-LF (**c**), and F3-VF (**d,e**). Data of a) is part of a figure in reference [140].

Table 4-19: Fibril elongation in mixtures of nucleated Aβ42 with Nle3-VF. For TEM studies, Aβ42 (5 µM, in 45 mM ammonium acetate, pH 8.5, 37 °C, without ThT) was aged for 2 h and mixed after with Nle3-VF (1:1). Samples were taken from freshly prepared mixtures (2 h) and at several other time points during the aggregation process (3 h, 5 h, 24 h, 6 days; 37 °C) (see also Figure 4-82a,b). At the same time points, samples from Aβ42 incubated in isolation were taken and analysed as controls. Fibril lengths were measured from representative TEM images. Error bars indicate mean ± SD from 13-28 fibrils (see Table 7-25 in the Appendix).

	Fibril length (nm)				
	2 h	3 h	5 h	24 h	6 days
Aβ42	94.9 ± 32.8	116.8 ± 20.5	144.2 ± 39.8	133.7 ± 20.6	126.3 ± 26.2
Aβ42 (2 h) + Nle3-VF	96.0 ± 32.1	110.3 ± 22.5	169.8 ± 49.9	284.5 ± 137.7	251.4 ± 126.3

Table 4-20: Fibril elongation in mixtures of fibrillar Aβ42 with Nle3-VF. Aβ42 (5 µM) was aged in 45 mM ammonium acetate, pH 8.5 (37 °C, without ThT) for 7 days. Mature fAβ42 were mixed with 5 µM Nle3-VF (1:1) and further incubated (37 °C). TEM analysis was performed on fibrils before mixing with the inhibitor and after 1 and 4 days of co-incubation, respectively. Fibril lengths were measured from representative TEM images. Error bars indicate mean ± SD from 17-29 fibrils (see Table 7-26 in the Appendix).

	Fibril length (nm)
fAβ42, before mix with Nle3-VF	126.3 ± 26.2
fAβ42, 1 day after mix with Nle3-VF	257.9 ± 95.1
fAβ42, 4 days mix with Nle3-VF	204.9 ± 56.1

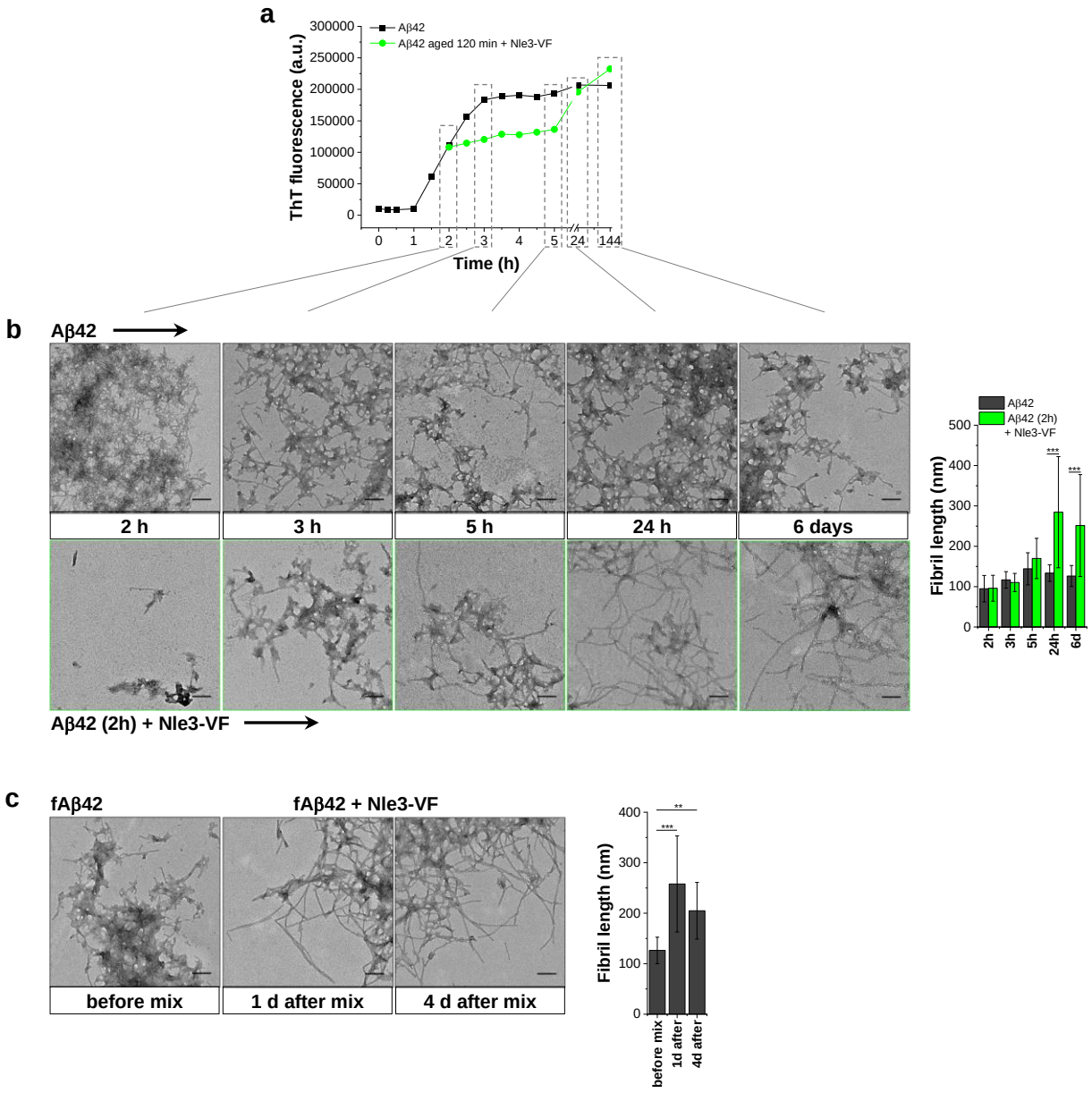

Figure 4-82: Fibril elongation in mixtures of aged Aβ42 and Nle3-VF. (**a**) ThT binding control experiment (n=1) for TEM studies shown in b. Aβ42 (5 µM, in 45 mM ammonium acetate, pH 8.5, 37 °C, with 10 µM ThT) was aged for 2 h and added to dried Nle3-VF (1:1). Dashed-line boxes highlight time points when TEM analysis was performed. (**b**) TEM imaging of Aβ42 and mixtures of aged Aβ42 with Nle3-VF. Incubations were prepared in parallel and similarly to ThT assay control incubations in a, but did not contain ThT. Bar diagram on the right shows time-dependent development of fibril lengths determined from TEM images. *** P<0.001 by one-way ANOVA and Bonferroni (n=13-28 fibrils used for the measurements, see Table 4-19). (**c**) TEM imaging of fAβ42 before and after co-incubation with Nle3-VF. fAβ42 were prepared as for b, (7 days aged). Fibrils were mixed with 5 µM dried Nle3-VF (1:1) and incubated further for the indicated time (37 °C). Bar diagram on the right compares fibril lengths measured from TEM images. *** P<0.001; ** P<0.01 by one-way ANOVA and Bonferroni (n=17-29 fibrils used for the measurements, see Table 4-20).

Since ACMs are derived from the Aβ40-sequence and therefore share a high degree of sequence-identity with Aβ42 as well, one can speculate that ACMs might be well integrable into an Aβ42-fibril scaffold leading to the observed fibril extension. To shed more light on how fibril elongation is processed, 2-PM analysis was performed. 105 min (= 1.75 h) aged, (TAMRA-)Aβ42 (incubated under the inhibition assay conditions) was mixed with (Fluos-)ACMs and samples were taken shortly after addition of peptide. The analysis showed that (Fluos-)Nle3-VF or (Fluos-)F3-VF or their heterocomplexes with (TAMRA-)Aβ42 attach to existing (TAMRA-)Aβ42 assemblies from both termini thereby initiating elongation (see white arrows in Figure 4-83). Additionally, (Fluos-)Nle3-VF was observed to associate with preformed (TAMRA-)Aβ42 nanofibers, joining them together into larger assemblies (Figure 4-83c). Rather large hetero-nanofiber assemblies comprised of several thinner nanofiber units were also observed (Figure 4-83d). Furthermore, in mixtures of (Fluos-)F3-VF with 1.75 h-aged (TAMRA-)Aβ42 many areas were seen in which several separate heterocomplexes started to obviously "self-sort" into structures resembling already fibrillar species (Figure 4-83b). This observation strongly supports the previously drawn conclusion from time-dependent TEM experiments that heterofibils/-nanofibers can evolve from initially formed heterocomplexes. Taken together, the presented results are in very good agreement with previous 2-PM findings when (Fluos-)Nle3-VF was mixed with (TAMRA-)Aβ42 at the pre-

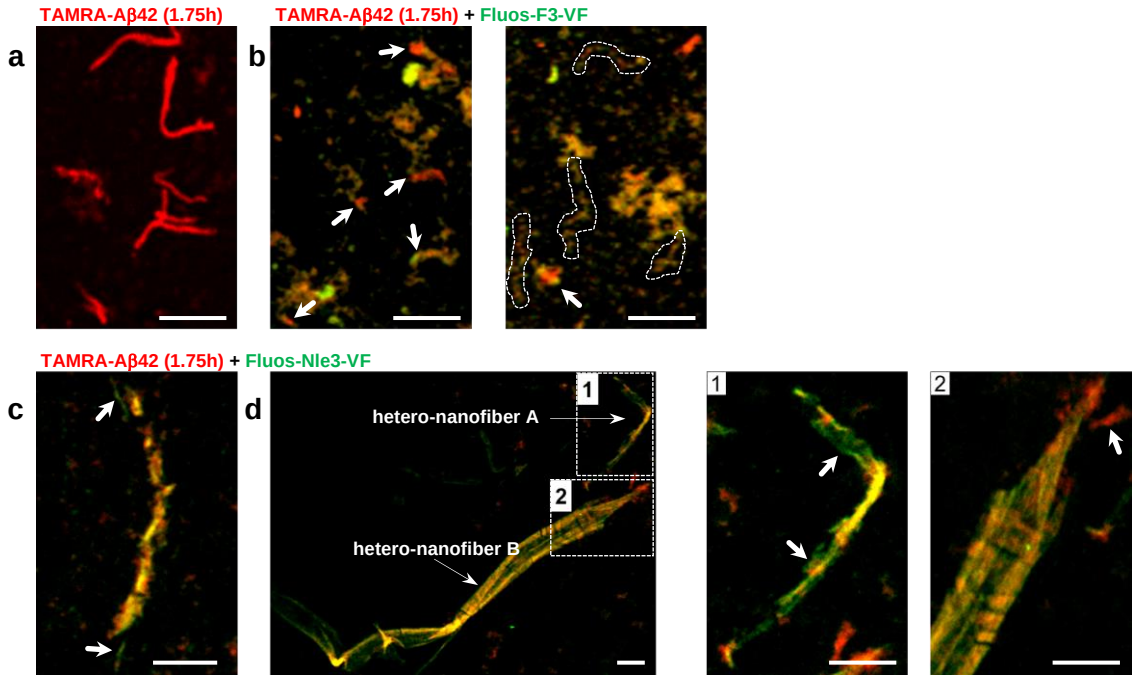

Figure 4-83: Hetero-nanofiber formation and nanofiber elongation in mixtures of aged (TAMRA-)Aβ42 with (Fluos-)ACMs monitored via 2-PM. Incubations were prepared in 45 mM ammonium acetate, pH 8.5 (37 °C) using 50 % labelled and 50 % unlabelled peptides (2.5 µM Aβ42 and 2.5 µM TAMRA-Aβ42; 5 µM unlabelled ACM and 5 µM Fluos-ACM). The (TAMRA-)Aβ42 solution was aged for 1.75 h (105 min) before mixing with dried inhibitor and samples were taken for 2-PM analysis thereafter. Scale bars are 10 µm. (**a**) (TAMRA-)Aβ42 nanofibers formed after 1.75 h of incubation. (**b**) Species found in mixtures of aged (TAMRA-)Aβ42 with (Fluos-)F3-VF. Arrows indicate regions in which existing (TAMRA-)Aβ42 species are bound by inhibitor or heterocomplexes to initiate elongation. Highlighted areas show multiple heterocomplexes starting to self-sort into fibrillar species. (**c,d**) Species found in mixtures of aged (TAMRA-)Aβ42 with (Fluos-)Nle3-VF. Image in c, shows a hetero-nanofiber assembly built from several smaller fragments which are "glued" and elongate (see arrows) by (Fluos-)Nle3-VF. Image in d, and corresponding magnifications 1 and 2 show two additional hetero-nanofibers (A and B) found in the sample. Arrows in 1 and 2 highlight nanofiber elongation regions.

nucleated stage: Initiation points for elongation strongly resemble the bicoloured “islets-like” structures (compare Figure 4-77b); long Aβ42 nanofibers with bound heterocomplexes (compare Figure 4-77a) could be the end product of the above-mentioned interconnection process.

Summarising, the results indicate that not only the ACMs‘ potential to bind to monomeric Aβ42 and form heterocomplexes is crucial for inhibition but also their ability to associate with fibrils and connect them into longer filaments is important. This association could additionally lead to the generation of “islets“ which seem to be a potent template for further addition of peptide or heterocomplex molecules.

4.13 ACMs inhibit self- and fIAPP-cross-seeded amyloid self-assembly of Aβ42

4.13.1 Studies on the effect of ACMs on fAβ42-mediated self-seeding of amyloid self-assembly of Aβ42

Since ACMs proved to be able to inhibit Aβ42 fibril formation and cytotoxicity, the next question arising was whether they might also interfere with fAβ42-mediated self-seeding of Aβ42. To address this, fAβ42 seeds (final concentration: 0.5 µM; 10 %) were added to fresh Aβ42 (5 µM), ACM (5 µM) or their mixture (1:1). Importantly, in this experimental setup, fresh Aβ42 was first mixed with ACMs before fAβ42 seeds were added to allow for Aβ42/ACM complex formation. Aβ42 fibril formation was significantly accelerated in presence of 10 % fAβ42 seeds, while fAβ42 had no effect on ACMs (Figure 4-84). When Aβ42 was mixed with the ACMs Nle3-VF, L3-VF, or F3-VF, self-seeding was completely suppressed and Aβ42’s fibril formation showed a highly increased lag phase (Figure 4-84). Even though ACMs were not able to fully inhibit self-seeded Aβ42 up to 7 days as it was observed for unseeded mixtures, they still could decrease the final fibril load. In conclusion, ACMs both inhibit unseeded Aβ42 and suppress fAβ42-self-seeded Aβ42.

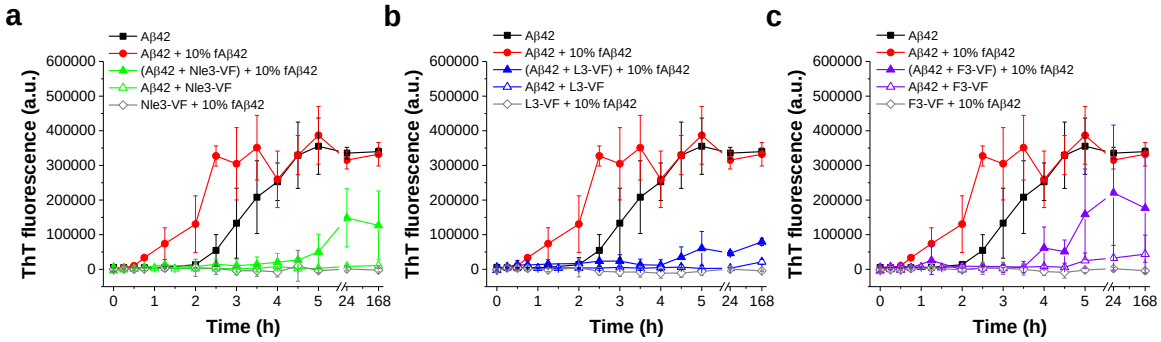

Figure 4-84: Effects of ACMs on fAβ42-mediated self-seeding of Aβ42. For self-seeding inhibition experiments, Aβ42 (5 µM), ACM (5 µM) or their mixture (1:1) were mixed with pre-formed Aβ42 fibrils (5 µM, 6 days aged; final concentration: 0.5 µM (10 %)). Aβ42 was mixed with ACMs before addition of fAβ42 seeds to allow complex formation (indicated by brackets). Unseeded Aβ42 and unseeded mixtures were incubated in parallel as controls. Incubation conditions were: 45 mM ammonium acetate, pH 8.5, 37 °C (5 h shaking at 500 rpm, non-agitated thereafter), with 10 µM ThT. Error bars: means ± SD (n=3). Results are shown for Nle3-VF (**a**), L3-VF (**b**) and F3-VF (**c**). Data is part of a figure in reference [140] (adapted figure version).

4.13.2 Studies on the effect of ACMs on fIAPP-mediated cross-seeding of of amyloid self-assembly of Aβ42

In a second step, ACMs' potential to suppress fIAPP-mediated cross-seeding of Aβ42 was investigated. Since Aβ42 at 5 µM could not be reproducibly seeded neither by 10 % nor by 20 % fIAPP seeds in preliminary trials, an assay system using 10 µM Aβ42 and 20 % fIAPP seeds (2 µM) was established and applied. As for self-seeding experiments, fresh Aβ42 was first mixed with ACMs before fIAPP seeds were added to facilitate Aβ42/ACM-complex formation. Firstly, ACMs were applied in an equimolar amount (1:1) with Aβ42. The investigated ACMs Nle3-VF, L3-VF, F3-VF, and F3-LF could all suppress the cross-seeding effect of fIAPP seeds on Aβ42 fibrillation and thereby were not seeded themselves (Figure 4-85). Next, ACMs were applied at 2-fold excess relative to Aβ42 to potentially improve their inhibitory properties. Effects of Nle3-VF, L3-VF and F3-VF were similarly strong as when applied in 1:1 (Figure 4-86a-c), while the inhibitory effect of F3-LF even slightly improved (lag phase of the fIAPP-cross-seeded Aβ42/F3-LF mixture increased to ~4.5 h compared to ~2.5 h with F3-LF in 1:1) (Figure 4-86d).

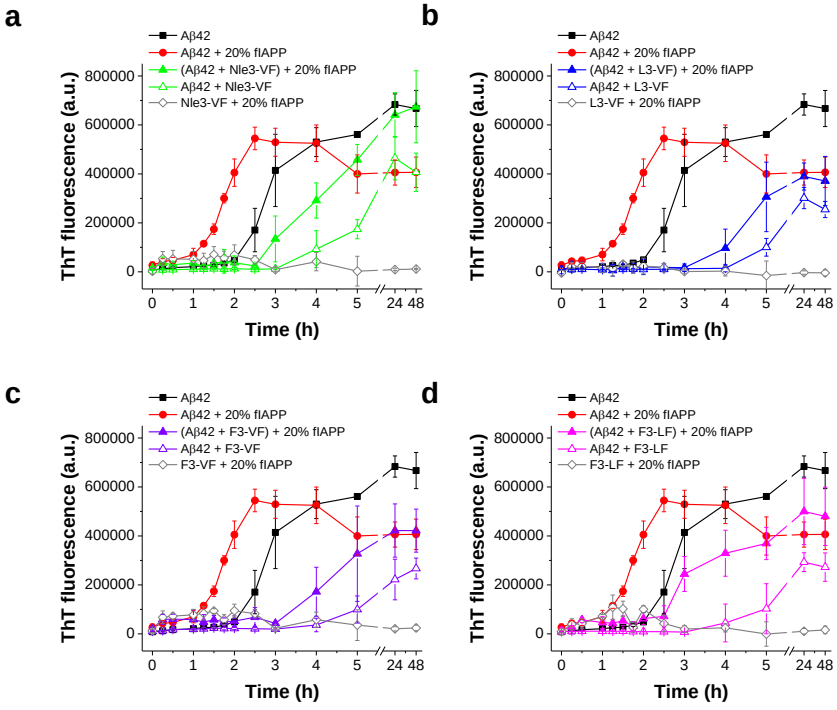

Figure 4-85: Effects of ACMs on fIAPP-mediated cross-seeding of Aβ42 at equimolar amounts. Cross-seeding experiments were performed in 45 mM ammonium acetate, pH 8.5, at 37 °C in presence of 10 µM ThT (5 h shaking at 500 rpm, non-agitated thereafter). Incubations contained a small amount (<2 %) of ThT assay buffer (with 0.5 % HFIP) resulting from the fIAPP seeds' incubation buffer. The same amount of ThT assay buffer (0.5 % HFIP) was also put to incubations not containing the fIAPP seeds. Aβ42 (10 µM) was mixed with ACMs (10 µM; 1:1) before addition of fIAPP seeds (incubated at 128 µM in ThT assay buffer with 0.5 % HFIP, aged for 5-12 days; final concentration: 2 µM (20 %)) to allow complex formation (indicated by brackets). As controls, unseeded Aβ42 and unseeded mixtures were incubated in parallel. Error bars: means ± SD (n=4). Results are shown for Nle3-VF (**a**), L3-VF (**b**), F3-VF (**c**) and F3-LF (**d**).

Thereafter, samples taken from 1.5 h-aged and 48 h-aged solutions from the cross-seeding experiments shown in Figure 4-86 were examined via TEM to study the species present in different incubations at time points in which ACMs (2-fold excess) show still inhibition (1.5 h) and in which they do not (48 h). As expected, the main species of unseeded 1.5 h-aged Aβ42

were amorphous aggregates accompanied by some short fibrils, while fIAPP-cross-seeded Aβ42 contained only fibrils already at this early time point (Figure 4-87). Both incubations contained only fibrils at 48 h. fIAPP-cross-seeded Aβ42/ACM mixtures showed amorphous aggregates as main species at 1.5 h but fibrillar species were also present (Figure 4-87a). The fibril portion might be heterofibrils, since the mixtures did not show ThT binding at this time point (Figure 4-86). After 48 h, the cross-seeded Aβ42/ACM mixtures contained short fibrils, many of them arranged in roundish/elliptic shapes (Figure 4-87b). The change of fibril morphology correlates with the finding that cross-seeded Aβ42/ACM mixtures also bind ThT at 48 h (Figure 4-86), so when ACMs' inhibitory effect weakens by time the fibrillar species seem to change. Of note, the roundish arrangement of fibrils in the cross-seeded Aβ42/ACM mixtures is somehow related to the presence of the fIAPP seeds since unseeded mixtures did not contain them (Figure 4-87b).

In conclusion, TEM studies correlated well with and further confirmed results from ThT binding experiments which showed ACMs' potential to inhibit fIAPP-mediated cross-seeding of Aβ42.

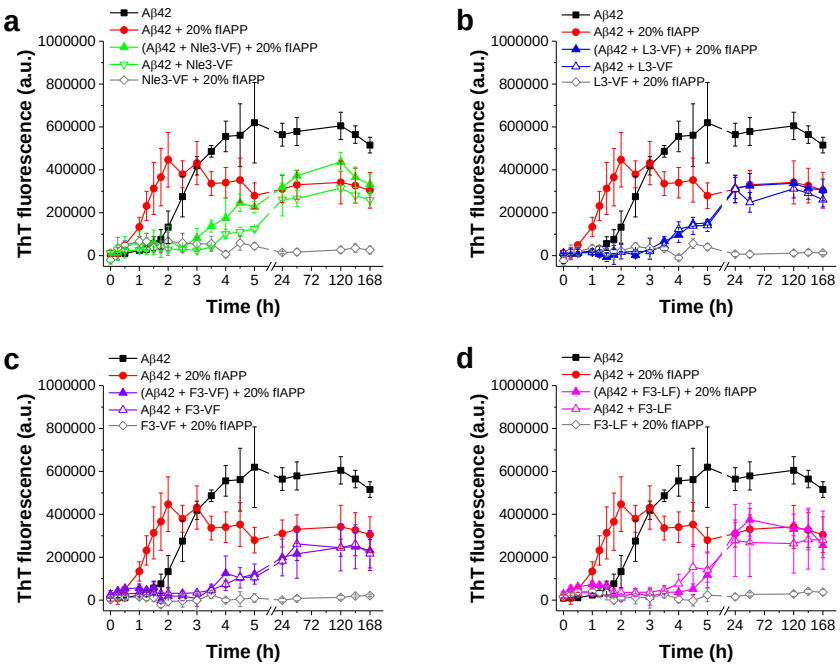

Figure 4-86: Effects of ACMs on fIAPP-mediated cross-seeding of Aβ42 at 2-fold excess. Aggregation kinetics were studied by ThT binding. Incubations were prepared in 45 mM ammonium acetate, pH 8.5, at 37 °C in presence of 10 µM ThT (5 h shaking at 500 rpm, non-agitated thereafter), using 10 µM Aβ42 and 20 µM ACMs (1:2). Incubations contained a small amount (<2 %) of ThT assay buffer (with 0.5 % HFIP) resulting from the fIAPP seeds' incubation buffer. The same amount of ThT assay buffer (0.5 % HFIP) was also added to unseeded incubations. Aβ42 was mixed with ACMs before fIAPP seeds (incubated at 128 µM in ThT assay buffer with 0.5 % HFIP, aged for 5-12 days; final concentration: 2 µM (20 %)) were added to allow complex formation (indicated by brackets). As controls, unseeded Aβ42 and unseeded mixtures were incubated in parallel. Error bars: means ± SD (n=4). Results are shown for Nle3-VF (**a**), L3-VF (**b**), F3-VF (**c**), and F3-LF (**d**). Data is part of a figure in reference [140] (adapted figure version).

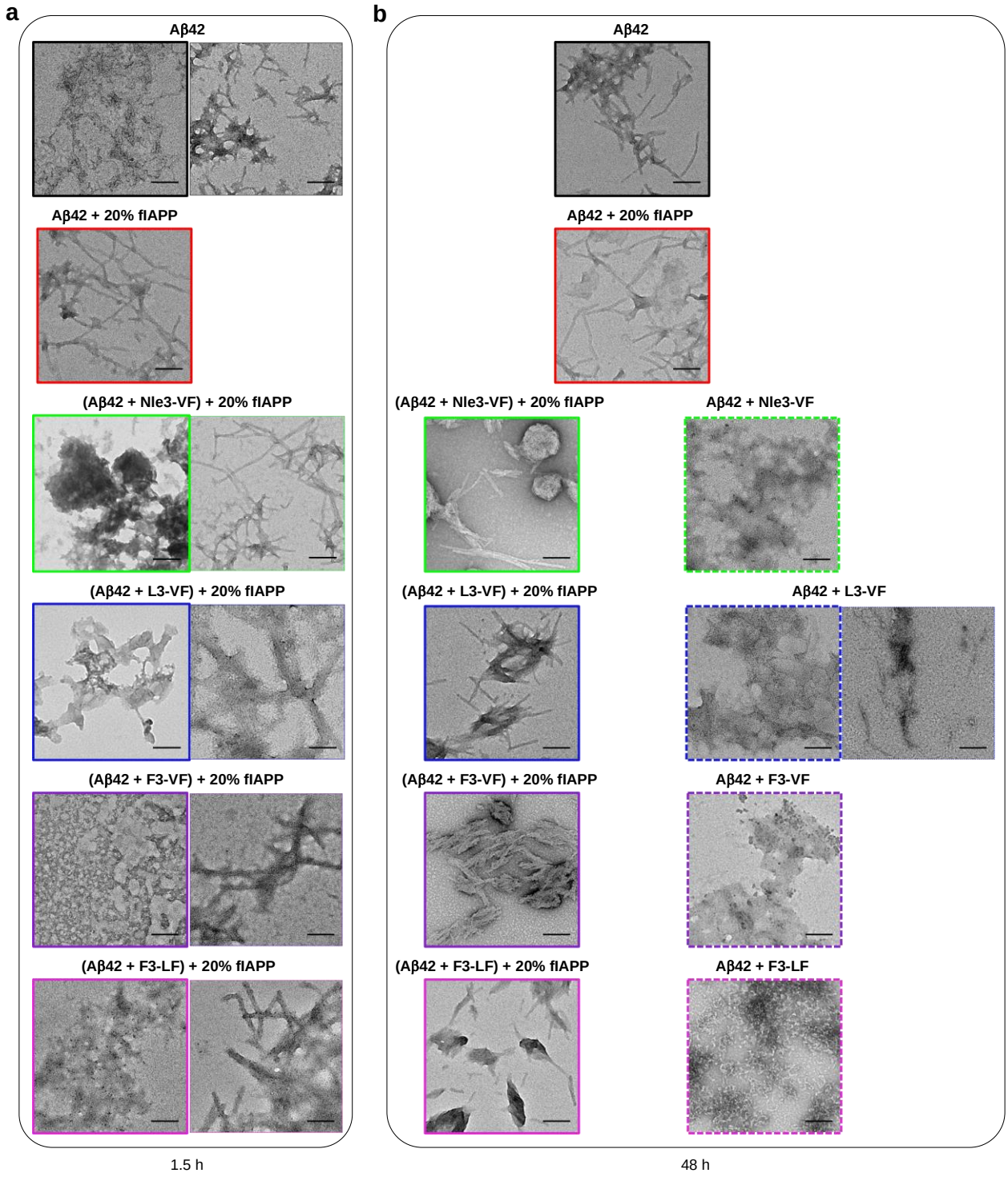

Figure 4-87: Species-analysis of fIAPP-cross-seeded Aβ42/ACM mixtures by TEM. Samples were taken after 1.5 h (**a**) or 48 h (**b**) of aging from solutions made as for ThT binding/MTT reduction assays (see Figure **4-86**) (45 mM ammonium acetate, pH 8.5, 37 °C, w/o ThT, 5 h shaking at 500 rpm, non-agitated thereafter; containing a small amount (<2 %) of ThT assay buffer (with 0.5 % HFIP) resulting from the fIAPP seeds' incubation buffer). Aβ42 (10 µM) was mixed with ACMs (20 µM; 1:2) before addition of fIAPP seeds (incubated at 128 µM in ThT assay buffer with 0.5 % HFIP, aged for 5-12 days; final concentration: 2 µM (20 %)) to allow complex formation (indicated by brackets). Colours correspond to colours in Figure **4-86**. When two images are shown for the same sample, the main species is framed with bold lines. Scale bars: 100 nm.

4.13.3 Studies on Nle3-VF's mechanism of action in inhibition of fIAPP-cross-seeded amyloid self-assembly of Aβ42

To shed more light on the mechanism by which ACMs inhibit cross-seeding of Aβ42 by fIAPP, the Aβ42 inhibitor Nle3-VF was chosen as exemplary ACM for further investigations by additional ThT binding experiments and 2-PM imaging. As previously mentioned, for cross-seeding experiments a ThT assay system using 10 µM Aβ42 was applied since preliminary trials showed that Aβ42 at 5 µM was not seedable by 10 % or 20 % IAPP fibrils. Therefore, inhibitory effects of Nle3-VF on fibril formation of 5 µM and 10 µM Aβ42 solutions were first compared. For this, Nle3-VF was mixed either with 5 µM Aβ42 in 1:1 or with 10 µM Aβ42 at 2-fold excess and incubated under inhibition assay conditions. The data showed that inhibition is weaker when 10 µM Aβ42 is used even if a 2-fold molar excess is applied (Figure 4-88). Similar observations were also made using other ACMs (compare Figure 4-86, unseeded mixtures). As Aβ42 is very aggregation prone, a possible explanation for this could be that a higher concentrated solution contains not only monomers or small aggregates but also bigger oligomers or pre-fibrillar species which cannot be blocked from transition into fibrils by the inhibitor. These larger species might be easier or preferentially seedable by fIAPP, explaining also why fIAPP (20%) could not seed 5 µM Aβ42 solutions but were able to seed 10 µM Aβ42 solutions.

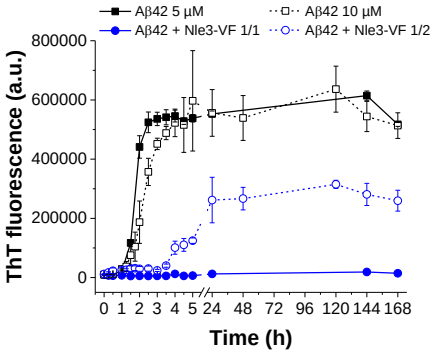

Figure 4-88: Changes in inhibitory potential of Nle3-VF toward Aβ42 at 5 µM vs. 10 µM. Inhibition of Aβ42 fibril formation was studied via the ThT binding assay using 5 or 10 µM Aβ42 (as indicated). Incubations were prepared in 45 mM ammonium acetate (pH 8.5, 37 °C) in presence and absence of Nle3-VF (equimolar or 2-fold excess). Error bars represent means ± SD, n=3-4.

Another experimental setup was used to perform additional cross-seeding experiments. In the first setup which was used for the experiments presented in chapter 4.13.2 (setup 1), Aβ42 (10 µM) was first mixed with dried ACMs (1:2) to allow complex formation and fIAPP seeds (2 µM; 20 %) were added thereafter. In the additional second setup (Setup 2), ACMs were first mixed (10-fold excess) with fIAPP seeds to allow interaction of the ACMs with the fibril surface. After, these pre-treated/coated seeds were mixed with Aβ42 as in the first setup. Final concentrations in both setups were: 10 µM Aβ42, 20 µM Nle3-VF, and 2 µM fIAPP (20 %).

When Aβ42 was pre-mixed with Nle3-VF (setup 1), fibril formation was accelerated in presence of fIAPP seeds compared to unseeded mixtures but was nevertheless much slower than for cross-seeded Aβ42 (Figure 4-89a). These results would fit with the above described scenario

in which 10 µM Aβ42 solutions contain portions of small and large species: the small Aβ42 species might be sequestered by the inhibitor and convert into heterofibrils by time whereas the larger species stay „free“ and accessible for cross-seeding by fIAPP or to form Aβ42 homofibrils. Since only a part of the Aβ42 molecules are therefore available for cross-seeding, the seeding effect in mixtures is less pronounced then for pure Aβ42 but fibril formation is still faster than in unseeded mixtures.

When fIAPP were pre-treated with Nle3-VF before addition to Aβ42 (setup 2), Nle3-VF‘s inhibitory effect was much stronger than in “setup 1” since fibril formation was fully blocked (Figure 4-89b). This change in inhibitory potential might be explained as follows: In setup 1 (Aβ42/Nle3-VF complex formation first) the ratio Aβ42:Nle3-VF is 1:2. Since the Nle3-VF excess is not very high, it can be assumed that basically all Nle3-VF is complexed with the small Aβ42 species while larger species might stay available for fIAPP-cross-seeding. In setup 2 (pre-treatment of fIAPP by Nle3-VF) the ratio fIAPP:Nle3-VF is 1:10. Since inhibition of secondary nucleation (via covering the fibril surface) by specific inhibitors is generally achieved with sub-stoichiometric inhibitor-amounts[155,156], it can be assumed that only a small portion of the Nle3-VF molecules are necessary to coat the IAPP fibril surface. The remaining portion can still interact with small Aβ42 species in the final mixture. In this way, small Aβ42 species could be sequestered by Nle3-VF and large Aβ42 species could not be seeded anymore since the fIAPP surface is blocked by inhibitor. Both effects acting in concert could lead to the complete suppression of Aβ42 fibril formation that was observed in the ThT binding assay.

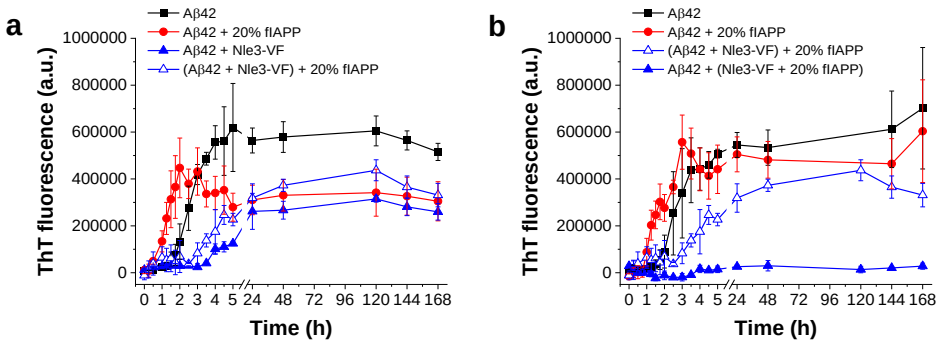

Figure 4-89: Studies on the effects of Nle3-VF on fIAPP-cross-seeded Aβ42 fibrillation using different assay setups. Setup 1: Aβ42/ACM-complexes formed first, “(Aβ42+Nle3-VF)+20% fIAPP)”; setup 2: seeds “coated” first, “Aβ42+(Nle3-VF+20% fIAPP)”. fIAPP seeds were prepared in ThT assay buffer with 0.5 % HFIP and diluted to a final concentration of 2 µM (20 %). Incubations were prepared in 45 mM ammonium acetate (pH 8.5; 37 °C; containing a small amount of ThT assay buffer (0.5 % HFIP) from the seeds’ incubation buffer) using 10 µM Aβ42 and a 2-fold excess of Nle3-VF (20 µM). Values for buffer or seeds were subtracted from the measurements. (**a**) Inhibition of Aβ42 fibril formation by Nle3-VF in presence and absence of seeds. Error bars: means ± SD, n=4-8. (**b**) Inhibitory effects of Nle3-VF on cross-seeding when Aβ42/ACM-complexes are formed before addition of seeds (setup 1) or when seeds are first “coated” by Nle3-VF (setup 2). Error bars: means ± SD, n=3-4.

Next, species from solutions equivalent to cross-seeding experiments were analysed by 2-PM. For preparing incubations for 2-PM analysis, HiLyte647-Aβ42, Fluos-Nle3-VF, and TAMRA-IAPP were used as labelled analogues. Seeds were generated using 100% labelled TAMRA-IAPP. Solutions of Aβ42 and Nle3-VF contained 50% labelled and 50% unlabelled peptides (i. e. 5 µM Aβ42, 5 µM HiLyte-Aβ42, 10 µM Fluos-Nle3-VF, 10 µM Nle3-VF). Samples were taken after 1.5 h of aging (done as described above for ThT binding studies but w/o ThT). Of

note, samples did not only contain nanofibers at this relatively early time point but also non-fibrillar aggregates, but special attention was given to nanofiber-species in the following analyses. 2-PM revealed binding of (HiLyte647-)Aβ42 to the TAMRA-IAPP fiber surface, presumably further leading to formation of the larger cross-seeded (HiLyte647-)Aβ42/TAMRA-IAPP nanofibers, which were also observed in the 1.5 h-incubation (Figure 4-90). These results are in very good agreement with ThT binding studies which also indicated fibril formation in fIAPP-cross-seeded Aβ42 solutions at 1.5 h but not in unseeded Aβ42 solutions (see chapter 4.13.2). 1.5 h-aged (HiLyte647-)Aβ42/(Fluos-)Nle3-VF mixtures contained aggregates and nanofibers consisting of the two peptides (Figure 4-91a). When TAMRA-fIAPP seeds were added to preformed (HiLyte647-)Aβ42/(Fluos-)Nle3-VF complexes ("setup 1"), mixtures contained (in addition to triple-coloured (HiLyte647-)Aβ42/(Fluos-)Nle3-VF/TAMRA-IAPP or bi-coloured (HiLyte647-)Aβ42/(Fluos-)Nle3-VF roundish aggregates) nanofibers of three different colours – thus consisting of Aβ42, Nle3-VF and IAPP (Figure 4-91b). 3D reconstructions of the 2-PM images indicated that fibrillar hetero-assemblies were formed by binding of ACM,

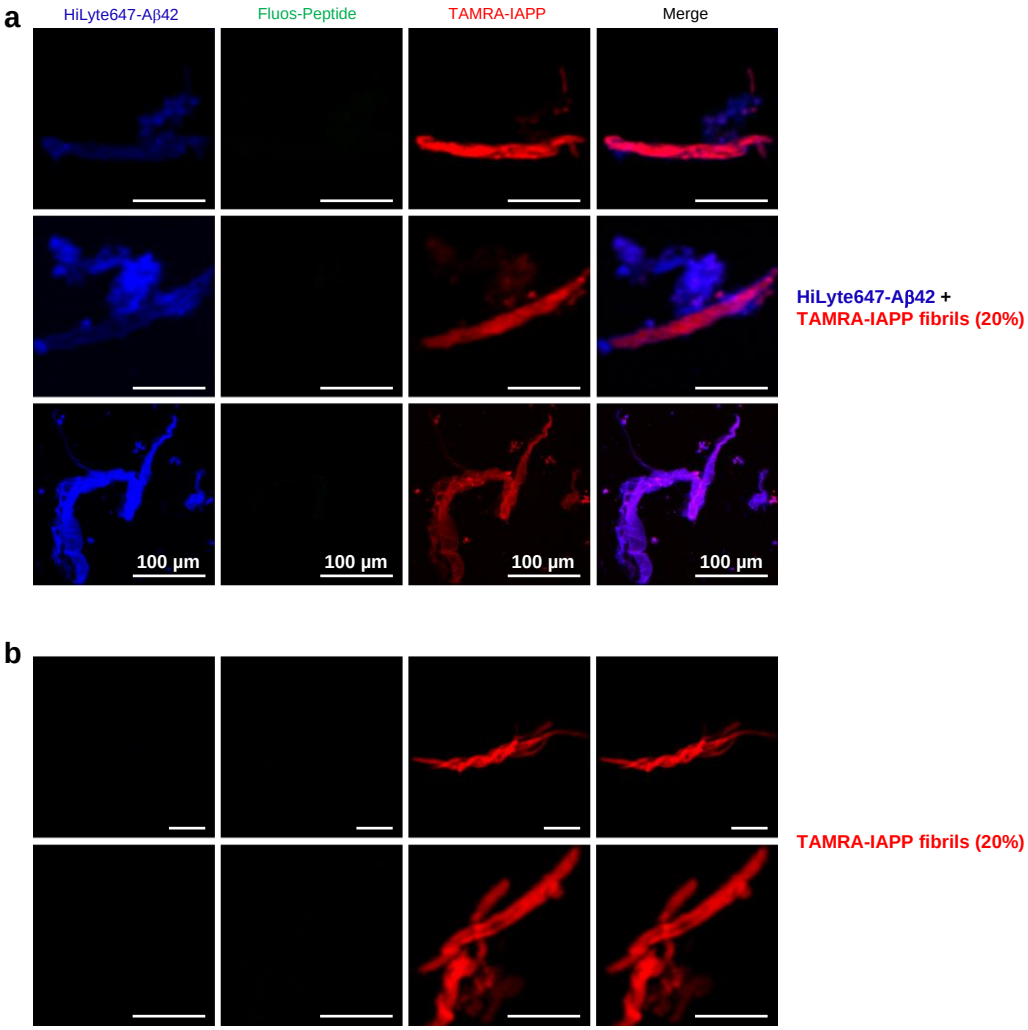

Figure 4-90: Cross-seeding of (HiLyte-)Aβ42 by fibrillar (TAMRA-)IAPP observed via 2-PM. Incubations contained a mixture of 50% unlabelled Aβ42 (5 µM) and 50 % HiLyte647-labelled Aβ42 (5 µM). TAMRA-fIAPP seeds were prepared using 100 % labelled peptide and diluted to a final concentration of 2 µM (20 %). Samples for 2-PM analysis were prepared after 1.5 h of aging (in 45 mM ammonium acetate (pH 8.5; 37 °C; containing a small amount of ThT assay buffer (0.5 % HFIP) from the seeds' incubation buffer). Scale bars are 10 µm if not stated otherwise. (**a**) Initiation of cross-seeding by binding of Aβ42 to the IAPP fibril surface (upper & middle panel) and resulting cross-seeded nanofibers (lower panel). (**b**) Appearance of the IAPP nanofibers used as seeds. Images of upper and middle panels in a) are part of a figure in reference [140] (adapted figure version).

Aβ42, or Aβ42/ACM heterocomplexes to fIAPP (Figure 4-92). Analysis of mixtures of TAMRA-fIAPP with (Fluos-)Nle3-VF (the solution that was used to pre-treat fIAPP seeds in "setup 2") showed that (Fluos-)Nle3-VF adhered to the seeds covering the nanofibers' surface (Figure 4-91c). Of note, 2-PM samples from incubations prepared under the ThT assay "setup 2"-conditions with (Fluos-)Nle3-VF contained also triple-coloured nanofibers (as observed for "setup 1"-samples) (Figure 4-91b, lower panel). Binding of (Fluos-)Nle3-VF to the TAMRA-fIAPP surface could be nicely observed (Figure 4-91b, lower panel).

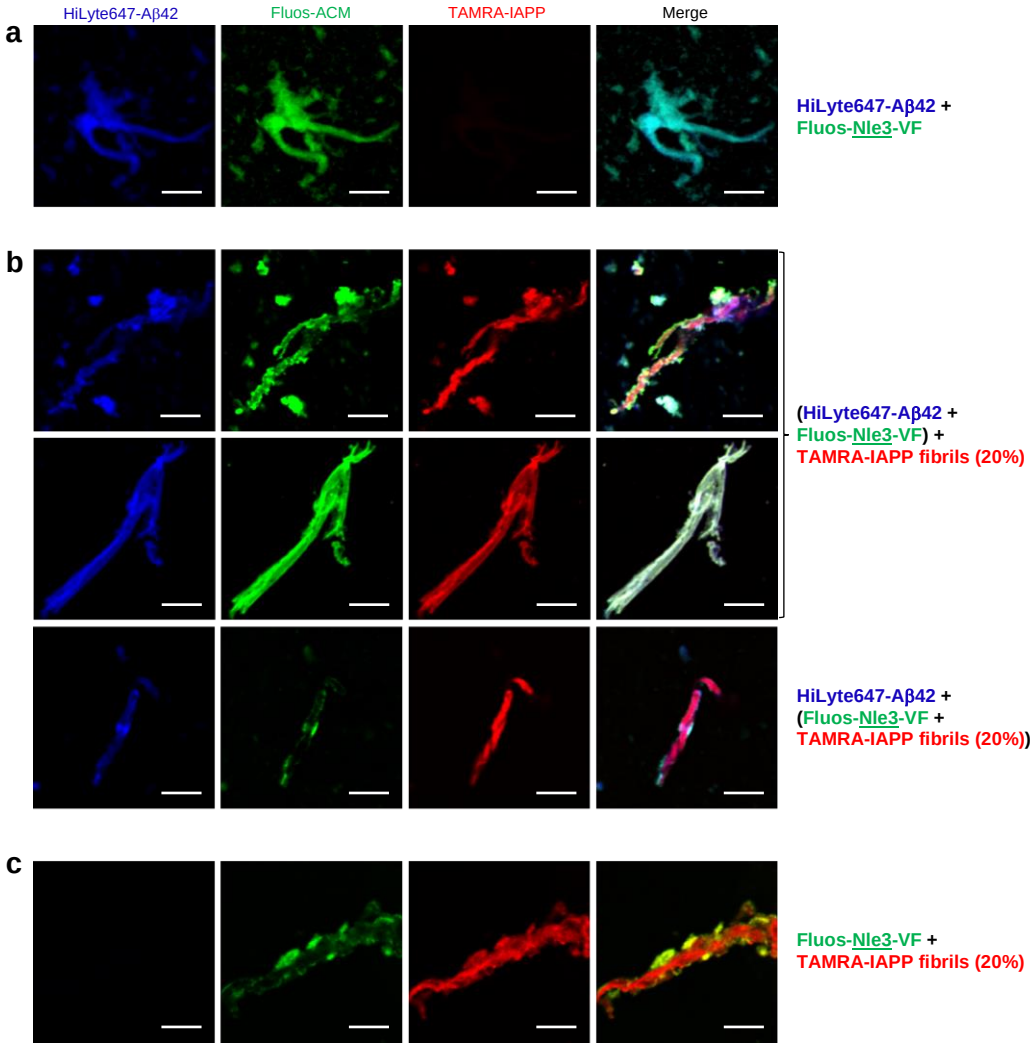

Figure 4-91: Fibrillar species in unseeded or fIAPP-cross-seeded (HiLyte647-)Aβ42/(Fluos-)Nle3-VF mixtures and (Fluos-)Nle3-VF solutions visualised by 2-PM. Incubations contained a mixture of 50 % unlabelled Aβ42 (5 µM) and 50 % HiLyte647-labelled Aβ42 (5 µM) with 50 % unlabelled inhibitor (10 µM) and 50 % Fluos-labelled inhibitor (10 µM). TAMRA-IAPP seeds were prepared using 100 % labelled peptide and diluted to a final concentration of 2 µM (20 %). Samples for 2-PM analysis were prepared after 1.5 h of aging (in 45 mM ammonium acetate (pH 8.5; 37 °C; containing a small amount of ThT assay buffer (0.5 % HFIP) from the seeds' incubation buffer). Scale bars are 10 µm. (**a**) Nanofibers formed by (HiLyte-)Aβ42 and (Fluos-)Nle3-VF in absence of TAMRA-fIAPP seeds. (**b**) Nanofibers formed by (HiLyte-)Aβ42/(Fluos-)peptide mixtures in presence of TAMRA-fIAPP seeds. Brackets indicate if inhibitor was first mixed with (HiLyte-)Aβ42 (Setup 1) or TAMRA-fIAPP seeds (Setup 2). (**c**) Appearance of TAMRA-fIAPP seeds after incubation with (Fluos-)Nle3-VF. Images of "(HiLyte647-Aβ42 + Fluos-Nle3-VF) + TAMRA-IAPP fibrils (20%)" in b) are part of a figure in reference [140] (adapted figure version).

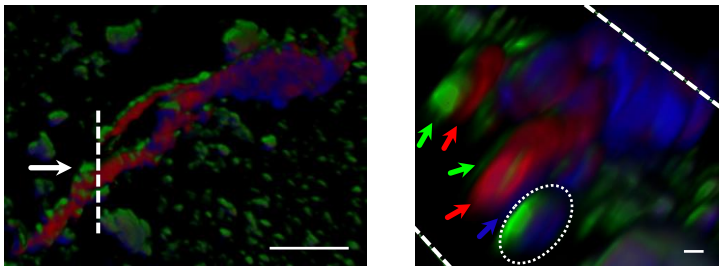

Figure 4-92: Ternary nanofiber co-assembly formed in fIAPP-cross-seeded Aβ42/Nle3-VF mixtures visualised by 2-PM. Incubations contained a mixture of 50 % unlabelled Aβ42 (5 µM) and 50 % HiLyte647-labelled Aβ42 (5 µM) with 50 % unlabelled inhibitor (10 µM) and 50 % Fluos-labelled inhibitor (10 µM). TAMRA-IAPP seeds were prepared using 100 % labelled peptide and diluted to a final concentration of 2 µM (20 %). Samples for were prepared after 1.5 h of aging (in 45 mM ammonium acetate (pH 8.5; 37 °C; containing a small amount of ThT assay buffer (0.5 % HFIP) from the seeds' incubation buffer). The 3D reconstruction was made from the image of the nanofibre co-assembly shown in Figure 4-91b (upper panels). Dashed line and white arrow in the left image indicate view of the section shown on the right. Red arrows: fIAPP; green and blue arrows: Nle3-VF and Aβ42 bound to fIAPP; encircled area: Aβ42/Nle3-VF co-assembly bound to fIAPP. Scale bars: 10 µm (left), 1 µm (right). Figure is part of a figure in reference [140] (adapted figure version).

In conclusion, ThT binding experiments showed that inhibition of fIAPP-mediated cross-seeding of Aβ42 by Nle3-VF is stronger when fIAPP seeds are pre-treated with the ACM before addition to Aβ42. Together with findings from 2-PM studies the results suggest a dual mechanism for Aβ42 cross-seeding suppression by ACMs: Firstly, ACMs sequester Aβ42 into Aβ42/ACM hetero-assemblies thereby preventing Aβ42 self-aggregation, and secondly, binding of ACMs and Aβ42/ACM hetero-assemblies to fIAPP results in cross-seeding incompetent ternary nanofiber co-assemblies.

4.14 Aβ42/ACM fibrillar co-assemblies show properties distinct from fAβ42

As previously observed for hf-IAPP/ACM, also hf-Aβ42/ACM are not cytotoxic and do not bind ThT (see chapter 4.10.2 and Figure 4-93). To investigate potential differences in the structure of hf-Aβ42/ACM and fAβ42, CD experiments were performed. Solutions of Aβ42 (5 µM), Nle3-VF (5 µM) or L3-VF (5 µM) or Aβ42/ACM-mixtures (1:1) were prepared under inhibition assay conditions and aged for 6 days to obtain heterofibrils/-nanofibers. Fresh solutions (t=0 h) containing heterocomplexes (see chapters 4.10.1 and 4.12.3) were analysed in parallel as controls. CD spectra of freshly prepared Aβ42/ACM-mixtures did not differ from the spectrum obtained by the mathematical addition of the peptides' single spectra (Figure 4-94a,c), indicating that there are no major structural re-arrangements taking place upon interaction of Aβ42 with Nle3-VF or L3-VF. These results are in very good agreement with previously presented CD interaction studies (chapter 4.10.1). Importantly, strong differences were observed between the spectra measured for hf-Aβ42/ACM (6 days) and the mathematical sum of Aβ42 and Nle3-VF or L3-VF spectra (6 days) (Figure 4-94b,d), leading to the conclusion that the transformation process from heterocomplexes into heterofibrils/-nanofibers involves structural re-arrangements of the two peptides. Additionally, hf-Aβ42/ACM show less β-sheet/β-turn structure than fAβ42 (Figure 4-94b,d). Thus, hf-Aβ42/ACM do not only differ in

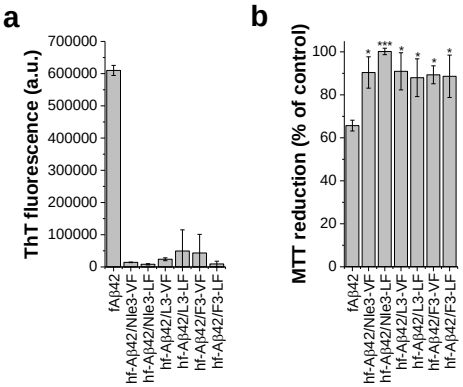

Figure 4-93: ThT binding and cytotoxicity of fAβ42 and hf-Aβ42/ACM. (**a**) ThT binding of fAβ42 and hf-Aβ42/ACM. Fibril-containing solutions (6 days aged, 37 °C) were prepared in 45 mM ammonium acetate (pH 8.5) in presence of 10 µM ThT using 5 µM Aβ42 ("fAβ42") or a mixture of Aβ42 and ACM (5 µM each; "hf-Aβ42/ACM"). Buffer values were subtracted from measurements. Error bars represent mean ± SD (n=3). (**b**) Cell damaging effects of fAβ42 and hf-Aβ42/ACM on PC-12 cells. fAβ42 fibrils and hf-Aβ42/ACM were prepared as in a, but w/o ThT. Aliquots were diluted with cell medium and administered to PC-12 cells (1 µM Aβ42 final). Error bars represent means ± SD from three assays, n=3 each. *** P<0.001; * P<0.05 by one-way ANOVA and Bonferroni compared to fAβ42 control.

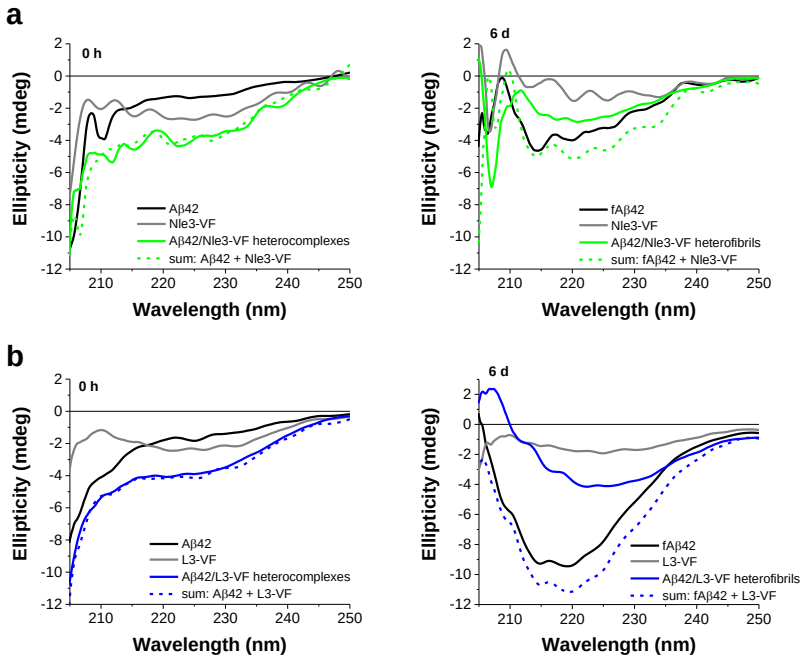

Figure 4-94: Structural features of Aβ42/ACM heterocomplexes and heterofibrils in solution determined by CD. Aβ42 (5 µM) or Aβ42/ACM-mixtures (5 µM each; 1:1) were made in 45 mM ammonium acetate, pH 8.5. ACM-alone controls (5 µM) were prepared accordingly in parallel. To examine structural features of heterocomplexes, solutions were freshly prepared and CD spectra were recorded directly after (t=0 h). Solutions to generate fAβ42 fibrils and hf-Aβ42/ACM were prepared as described above but were incubated for 6 days (37 °C) in parallel to ACM-alone controls (5 µM). Results are shown for Nle3-VF (**a**) and L3-VF (**b**). Sums of spectra (dashed lines in a and b) were obtained by mathematical addition of the single spectra measured for Aβ42 and ACMs alone. Data of b) is part of a figure in reference [140].

their ThT binding and cell damaging properties from fAβ42 but they are also structurally distinct from them.

In a next step, hf-Aβ42/ACM were also tested for other features such as seeding capacity toward Aβ42, and resistance to thermal denaturation and proteolytic digestion. To examine the seeding capacity of hf-Aβ42/ACM, the heterofibrils/-nanofibers were prepared by aging Aβ42/Nle3-VF- or Aβ42/L3-VF-mixtures (1:1, 5 µM each) for 6 days under inhibition assay

conditions. fAβ42 were prepared accordingly as control. Fibrils (10 %) were added to fresh Aβ42 solutions (5 µM). While fAβ42 seeds accelerated Aβ42 fibril formation, hf-Aβ42/Nle3-VF and hf-Aβ42/L3-VF were seeding incompetent (Figure 4-95a).

Next, thermostability of hf-Aβ42/Nle3-VF in comparison to fAβ42 was investigated. For this purpose, fAβ42 and hf-Aβ42/Nle3-VF were prepared under inhibition assay conditions in presence of 10 µM ThT. After 6 days, solutions were transferred into cuvettes and ThT fluorescence was determined. ThT measurements were repeated following boiling of the solutions for 5-15 min at 95 °C. ThT fluorescence of fAβ42 dropped to ~60 % after 5 min of boiling but then stayed approximately the same until the end of the experiment (Figure 4-95b). No ThT binding was observed when hf-Aβ42/Nle3-VF were boiled for 5 min (Figure 4-95b). To confirm that hf-Aβ42/Nle3-VF are destroyed by heating while fAβ42 stay intact, TEM studies of boiled and unboiled samples were performed. Of note, solutions for TEM samples were prepared identically to solutions used for the ThT binding studies but did not contain ThT. Even though ThT binding studies indicated that around half of fAβ42 might be dissociated after 15 min of boiling, TEM showed a large number of intact fibrils after this treatment (Figure 4-95d). To ensure that the drop in ThT fluorescence of fAβ42 is not due to the destruction of ThT during the boiling procedure, the experiment was repeated using fAβ42 and hf-Aβ42/Nle3-VF prepared in absence of ThT. ThT (10 µM) was added in this attempt after completion of the boiling step to avoid thermal harming of the dye, but results were very similar to the previous finding (Figure 4-95c). Heat-treatment might thus not destroy fAβ42 but impair their ThT binding on an invisible level. For example, boiling might induce changes in the fibril surface side-chain grooves where ThT is proposed to bind to[157]. In contrast to fAβ42, 5 min of boiling at 95 °C is enough to completely decompose hf-Aβ42/Nle3-VF as shown by TEM: Samples containing the typical elongated heterofibrils before boiling consisted only of amorphous aggregates after the treatment (Figure 4-95d). To assess the proteolytic stability of hf-Aβ42/Nle3-VF in comparison to fAβ42 (prepared as for the previous experiments), protease digestion by proteinase K (PK) was performed followed by dot blot analysis. Digestions were performed using two different PK concentrations, namely, 0.1 µg/ml and 0.5 µg/ml. Fibril degradation was probed using an anti-Aβ antibody specifically recognising the Aβ region 1-17 (6E10; anti-Aβ(1-17)) that is only present in Aβ42 but not in Nle3-VF. Using a 0.5 µg/ml PK working concentration, approximately half of hf-Aβ42/Nle3-VF was already degraded almost immediately after addition of the protease while fAβ42 resisted significantly longer (50 % degraded after ~23 min) (Figure 4-95e,f). When 0.1 µg/ml PK was used, fAβ42 were still completely intact after 30 min (Figure 4-95e,f). 50 % degradation was reached after ~1.5 h. Also hf-Aβ42/Nle3-VF were more persistent then, but their degradation was nevertheless much faster than fAβ42 degradation (50 % degraded after approximately 30 min) (Figure 4-95e,f).

In summary, the following beneficial features were observed by comparing the properties of hf-Aβ42/ACM with fAβ42: In contrast to fAβ42, hf-Aβ42/ACM do not bind ThT and are non-toxic and their CD structures show major differences. hf-Aβ42/ACM are incapable of seeding Aβ42 and more susceptible to thermal and proteolytical degradation.

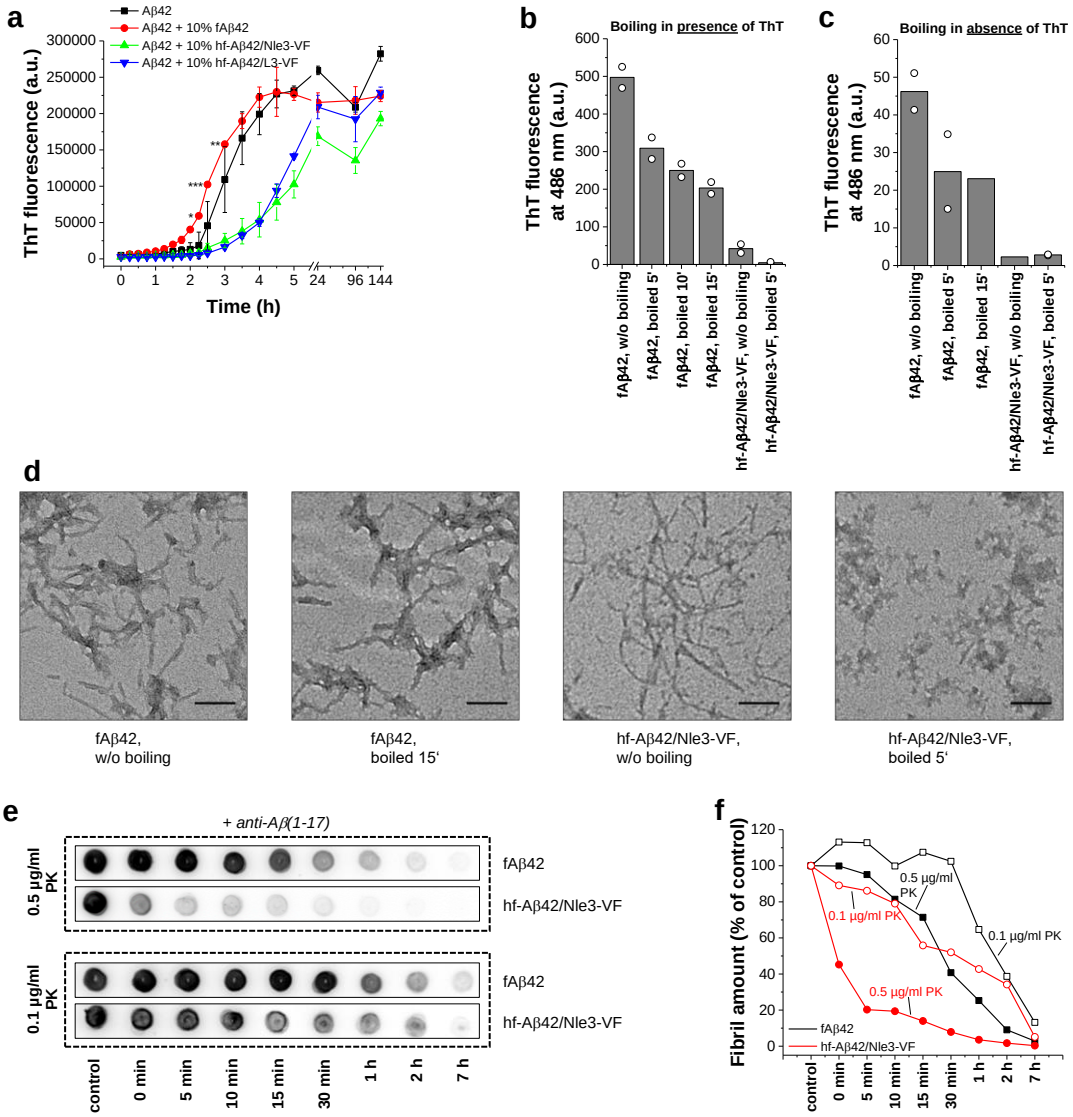

fAβ42, w/o boiling | fAβ42, boiled 15' | hf-Aβ42/Nle3-VF, w/o boiling | hf-Aβ42/Nle3-VF, boiled 5'

Figure 4-95: Properties of hf-Aβ42/ACM in comparison to fAβ42. (**a**) Seeding capacity. Aβ42 (5 µM, in 45 mM ammonium acetate pH 8.5, 10 µM ThT) was seeded by 10 % (0.5 µM) fAβ42 or hf-Aβ42/ACM seeds (37 °C). fAβ42 seeds were generated by incubating Aβ42 (5 µM) for 6 days, hf-Aβ42/ACM seeds were generated by incubating Aβ42 (5 µM) with 5 µM (1:1) Nle3-VF or L3-VF for 6 days (37 °C, in 45 mM ammonium acetate pH 8.5, w/o ThT). Error bars: means ± SD (n=3). Statistical differences between ThT fluorescence of fAβ42-seeded (**-**) and unseeded Aβ42 (**-**) at 0-5 h were assessed by one-way ANOVA and Bonferroni. *** P<0.001; ** P<0.01; * P<0.05. (**b,c**) Thermostability assessed by ThT fluorescence. fAβ42 fibrils and hf-Aβ42/Nle3-VF were prepared as in a). Boiling was performed at 95 °C for the indicated times in presence (b) or absence (c) of ThT. Incubations were prepared with ThT (10 µM) for b, and w/o ThT for c). In c, ThT (10 µM) was added after boiling was completed. (**d**) TEM images of samples corresponding to b, and c, (no ThT). Scale bars: 100 nm. (**e**) Proteolytic stability. Proteinase K (PK; 0.5 or 0.1 µg/ml final concentration) was added to fAβ42 and hf-Aβ42/Nle3-VF solutions (made as in a, no ThT, 6 days aged) and samples were dotted at indicated time points (0.44 µg Aβ42). Control sample was taken before addition of PK. Fibrils were probed using an anti-Aβ(1-17) antibody (6E10; 1:2000). Experiment using 0.5 µg/ml PK is representative of 3 assays, experiment using 0.1 µg/ml PK was performed once. (**f**) Densitometric analysis of the DB assays in e, (n=1). Data of a) and e) (membrane of samples using 0.5 µg/ml PK) and images of boiled samples in d) are part of a figure in reference [140].

4.15 Peptide array data indicate an Aβ/ADP interaction interface primarily established by the peptides' C-termini

Interaction interfaces built up by Aβ42 and the ACM Nle3-VF were investigated using peptide microarrays. Interfaces formed with Aβ40 and the two weaker inhibitors VGS-VF and Nle3-GG (see chapter 4.10.2) were studied for comparison. CelluSpot microarrays containing Aβ42 and

ADP segments were incubated with N^{α}-terminally biotinylated peptides and developed with horse-radish peroxidase (HRP)-streptavidin to detect binding.

In a first step, binding of biotinylated Aβ40, Nle3-VF, VGS-VF and Nle3-GG to Aβ42's N-terminal, central, and C-terminal regions was tested. The investigated Aβ42 segments were: Aβ(1-14), Aβ(15-26) and Aβ(27-42). All four peptides bound both to Aβ42's central and C-terminal segments (Figure 4-96). Interactions with the C-terminal segment Aβ(27-42) was strongest in all cases, while Aβ40 and ADPs did not bind to the N-terminal segment Aβ(1-14) (Figure 4-96). For gaining more detailed information on Aβ42 regions important for interactions with Nle3-VF, VGS-VF, Nle3-GG, and Aβ40, binding of biotinylated peptides to various deca-peptides spanning the entire Aβ42 sequence (frameshift of one amino acid between successive sequences) was tested next. While Aβ40, VGS-VF and Nle3-GG bound to decameric peptides included in identical Aβ42 regions, namely, Aβ(11-26) and Aβ(26/27-42), Nle3-VF's binding sites seemed to be slightly more expanded (decamers in Aβ(7-28) and Aβ(23-42)) (Figure 4-97). Additionally, Nle3-VF showed interaction with a more N-terminally located region, namely, two segments of Aβ42 region 4-14 (Figure 4-97). Since no binding to the previously tested Aβ(1-14) segment was observed, this interaction is maybe less stable. In general, results obtained from interaction studies using decameric Aβ42 fragments confirmed previous results on binding of Aβ42's N-terminal, central and C-terminal segments. Thus, it can be concluded that Nle3-VF, but also VGS-VF, Nle3-GG, and Aβ40, preferably bind to Aβ42's central and C-terminal regions and strongest interaction is observed with Aβ42's C-terminus. Of note, the regions involved in Aβ self-association were already previously determined[43]. Experiments were repeated for this thesis to have a direct comparison with Nle3-VF, VGS-VF and Nle3-GG binding sites. The obtained results presented here for Aβ/Aβ interaction reproduced previously published findings.

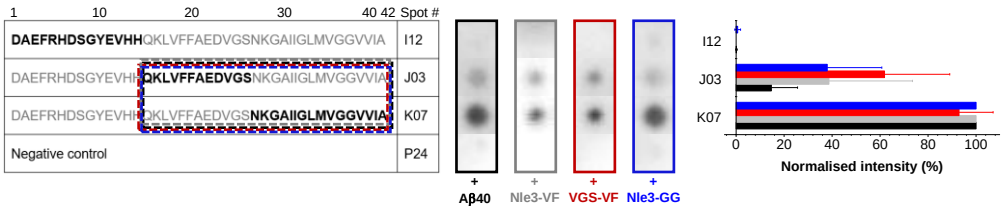

Figure 4-96: Binding of ADPs to Aβ(1-14), Aβ(15-26) and Aβ(27-42) segments. Aβ42 segments on glass slides (bold) were incubated with N-terminal biotinylated Aβ40 or ADPs (0.5 µM). Detection of bound Biotin-peptides was done after incubation with streptavidin-POD and development with ECL. Bar diagrams represent spot intensities obtained from different developments with the different Biotin-peptides (mean ± SD; n=4 assays; see also Figure 7-64 in Appendix). Depicted membranes are from one of these assays, respectively. Dashed coloured frames: Aβ42 sequences mostly relevant for Aβ40 and ADP binding. "Spot #" gives the location of the corresponding segment on the peptide array slide.

In a second step, regions in Nle3-VF, VGS-VF and Nle3-GG important for interaction of Aβ42 were studied. For this, binding to the following peptide segments was investigated via the peptide microarray: Nle3-VF(15-23), Nle3-VF(15-29), Nle3-VF(18-32), Nle3-VF(21-35), Nle3-VF(24-38), Nle3-VF(27-40); VGS-VF(15-23), VGS-VF(15-29), VGS-VF(18-32), VGS-VF(27-40); Nle3-GG(15-23), Nle3-GG(21-35), Nle3-GG(24-38), Nle3-GG(27-40).

Instead of biotinylated Aβ42, biotinylated Aβ40 was used to incubate the microarrays. Since Aβ42 is highly aggregation prone, the peptide could easily aggregate during the incubation time, leading to potentially false results. As Aβ40 is less aggregation prone but only differs from Aβ42 in two C-terminal amino acids, its interaction interface with the studied ADPs should be very similar to Aβ42's and was therefore chosen as an adequate alternative. For both Nle3-VF

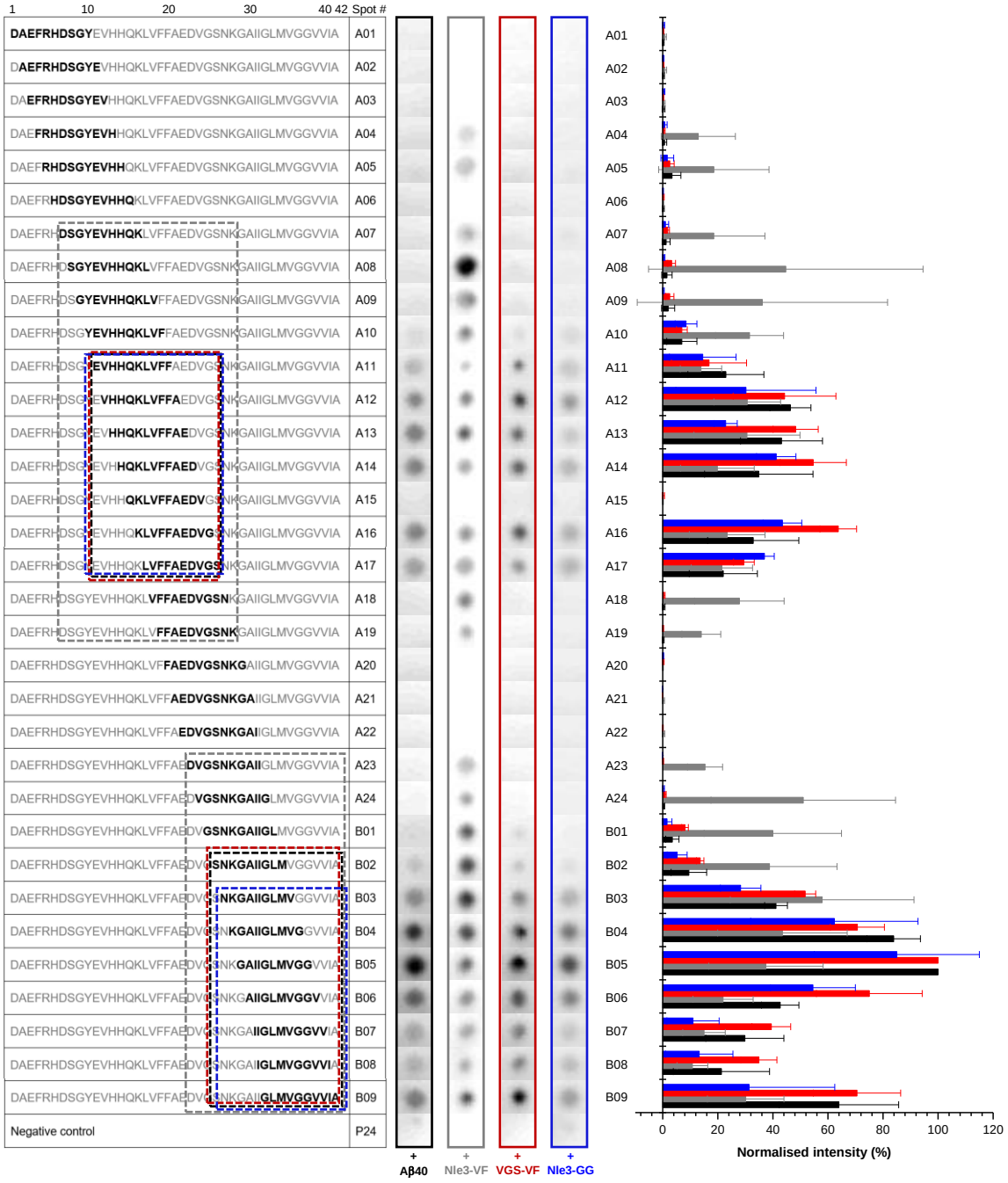

Figure 4-97: Identification of Aβ42 regions important for binding to ADPs using peptide microarrays. Glass slides with Aβ42 decamers (bold) were incubated with N-terminal biotinylated ADPs (0.5 µM). Following incubation with streptavidin-POD and development with ECL, bound peptides were detected. Bar diagrams represent spot intensities obtained from different developments with the different Biotin-peptides (mean ± SD; n=4 assays; see also Figure 7-64 in Appendix). Depicted membranes are from one of these assays, respectively. Dashed coloured frames: Aβ42 core regions for for binding to Aβ40 and ADPs. "Spot #" gives the location of the corresponding segment on the peptide array slide.

and VGS-VF and Nle3-GG, binding of Aβ40 was detected at the C-terminal peptide parts involving region 27-40 (Figure 4-98). Of note, comparisons of the interaction interfaces involved in the peptides' self-assembly with the ones involved in hetero-association with Aβ40 reveals that these binding sites are very similar (Figure 4-98). This is expected since the peptides initially were derived from Aβ40 and might thus also share still some of its self-association interfaces.

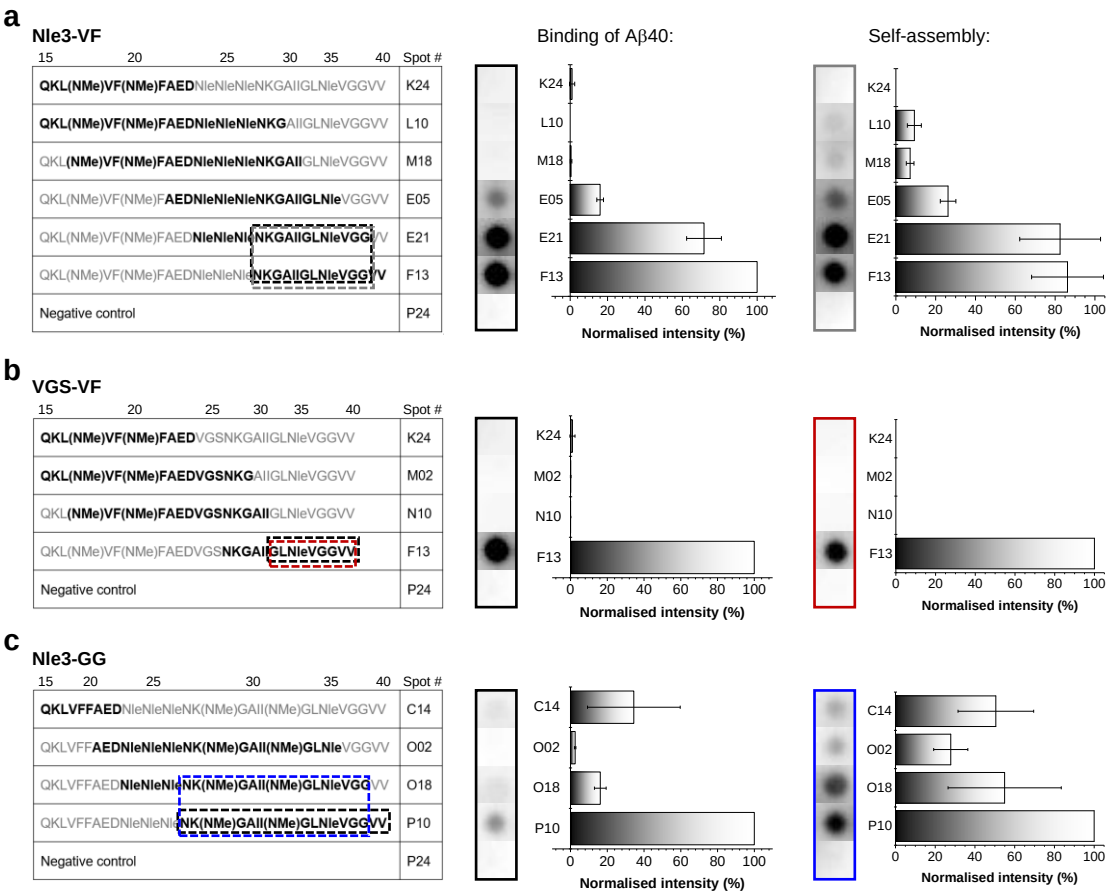

Figure 4-98: Identification of ADP segments important for their binding to Aβ42 and their self-recognition using peptide microarrays. Glass slides with ADP segments (bold) were incubated with 0.5 µM Biotin-Aβ40 (for testing "Binding of Aβ40" to the segments) or Biotin-ADPs (3 µM Biotin-Nle3-GG or 0.5 µM Biotin-Nle3-VF or 0.5 µM Biotin-VGS-VF) (for determining "Self-assembly" regions). Bound biotinylated peptides were detected after incubation with streptavidin-POD and development with ECL. Bar diagrams represent spot intensities obtained from different developments (mean ± SD; 4 assays for Biotin-Aβ40 binding, 3 assays for Biotin-Nle3-GG binding, 4 assays for the other self-recognition studies; see also Figure 7-63 and Figure 7-64 in Appendix). Depicted membranes are from one of these assays, respectively. Dashed black frames: Identified core regions for Aβ40 binding; dashed coloured frames: identified core regions for self-recognition. "Spot #" gives the location of the corresponding segment on the peptide array slide. NMe: *N*-methylation. Results are shown for binding to segments of Nle3-VF (**a**), VGS-VF (**b**) and Nle3-GG (**c**).

In conclusion, peptide microarrays showed that Nle3-VF, VGS-VF and Nle3-GG all bind to Aβ42 in similar regions, namely, its central and C-terminal parts, with preferences for the C-terminus. Vice versa, Aβ40 and Aβ42 interact with the ADPs' C-terminal region ADP(27-40). Thus, the main interaction interface between Aβ40 or Aβ42 and the ADPs is built up by their C-termini.

5 Discussion

In this work, the Aβ(15-40) sequence was used as a template to rationally design potent inhibitors of both IAPP and Aβ40(42) self-assembly. ADPs were designed to mimic the amyloid core Aβ(15-40) of Aβ40 in an alternative amyloid-like but non-amyloidogenic fold. Six peptides, termed Aβ amyloid core mimics (ACMs), turned out to be efficient amyloid inhibitors of IAPP, Aβ40 and Aβ42 while being themselves non-toxic and non-amyloidogenic. Shared features of all ACMs were their hydrophobic LTS and their N-terminally located *N*-methylation pair. ACMs showed ordered β-sheet/β-turn structure, were high-affinity binders of IAPP, Aβ40 and Aβ42, and inhibited IAPP cytotoxic self-assembly with nanomolar IC_{50}s and Aβ42 cytotoxic self-assembly with nano- to micromolar IC_{50}s. In addition, ACMs could not only block IAPP and Aβ42 self-seeding but also fIAPP-mediated cross-seeding of Aβ42 and even the reciprocal fAβ40- and fAβ42-mediated cross-seeding of IAPP. These properties place ACMs among the most effective inhibitors of *in vitro* amyloid self-assembly of IAPP and/or Aβ40(42) reported to date[96,158]. Moreover, the potential physiological relevance of the *in vitro* results is supported by the findings that ACMs efficiently inhibit Aβ42 in *ex vivo* studies on hippocampal synaptic long-term potentiation (LTP) performed by Xènia Puig-Bosch (group of Prof. G. Rammes, Department of Anesthesiology and Intensive Care/ Klinikum rechts der Isar of TUM). These experiments demonstrated that ACMs suppress the LTP deficit caused by Aβ42 aggregates[140]. Since ACMs formed mixed fibrils and higher ordered supramolecular nanofiber co-assemblies with both IAPP and Aβ42, our results revealed a novel inhibition mechanism. Importantly, fibrillar IAPP/ACM ad Aβ42/ACM hetero-assemblies differed in their properties from both fIAPP and fAβ42. A more detailed discussion of findings concerning the hf-IAPP/ACM and hf-Aβ42/ACM formation mechanism and their properties is presented in the following chapters.

5.1 IAPP/ACM heterocomplex formation and IAPP-templated transition into heterofibrils as inhibitory mechanism of ACMs toward IAPP amyloid self-assembly

The following important observations were made in context of inhibition and heterofibril formation of ACMs with IAPP:

1) A stabilised β-sheet/β-turn ACM conformation is possibly required for inhibition (structures determined by CD, ThT binding/MTT reduction inhibition assays; chapters 4.3.2, 4.3.3).
2) Strong binding to monomeric IAPP is important (shown by fluorescence titration experiments; chapter 4.5.1); but strong binding alone is not sufficient.
3) Inhibition of IAPP amyloid formation by ACMs is a conformation-specific mechanism (chapters 4.3.2, 4.3.3, 4.5.1).
4) Hetero-dimers seem to be the smallest building units instantly assembling into bigger species and their formation seems to be required for inhibition (CL and SEC; chapters 4.5.2, 4.7.4)
5) The amyloid character of IAPP is likely necessary to template IAPP/ACM heterofibril/ -nanofibers (chapter 4.7.3)

6) Heterofibril/ -nanofiber formation cannot be induced by “seed”-amounts of preformed fIAPP but by “seed-amounts” of monomeric or prefibrillar IAPP, indicating that interaction of ACMs with IAPP monomer/prefibrillar species is crucial (2-PM and FLIM-FRET; chapter 4.7.2)
7) Binding of ACMs to fIAPP does not result in heterofibrils but leads to a coating of the fibril surface by peptide (IG-TEM and 2-PM; chapter 4.7.1)
8) A time-dependent transition of amorphous aggregates into fibrillar assemblies is observed in IAPP/ACM mixtures (TEM and 2-PM; chapter 4.6.3)
9) FLIM-FRET analyses show that IAPP and Nle3-VF are close enough (<5.5 nm) to be part of the same fibril (fibril width by TEM: 8.3 ± 1.9 nm; chapter 4.6.1) (chapter 4.6.2.4)
10) 3D reconstructions from CLSM images of hetero-nanofibers indicate that IAPP/ACM hetero-nanofiber bundles assemble by a co-lateral stacking of IAPP and ACM molecules. These “protofilament”-like bundles build up the supramolecular nanofibre co-assemblies. A co-axial assembly mode nevertheless cannot be finally excluded as none of the applied methods can provide sufficient resolution for this discrimination and therefore must also be considered (chapter 4.6.2.3).

The above-mentioned points lead to the following suggested mechanism for the generation of IAPP/ACM heterofibrils/-nanofibers: ACMs bind to specific IAPP conformers and thereby sequester early prefibrillar precursors of amyloidogenic IAPP assemblies (Figure 5-1). Upon interaction, hetero-dimeric and -trimeric/-tetrameric species are formed which are rapidly further mounted into larger complexes, competing with IAPP self-association. By time, heterocomplexes might convert into heterofibrils which further co-assemble into supramolecular nanofibers. As an amyloidogenic IAPP variant is crucial to form heterofibrils/-nanofibers, maybe a remaining IAPP sequence part which is not involved in interaction with ACMs induces the structural re-arrangements necessary for the conversion into fibrillar species. This conversion can only take place if heterocomplexes were formed prior to IAPP fibrillation, interactions of ACMs with fibrillar IAPP do not result in heterofibrils/-nanofibers but in ACM-coated fIAPP.

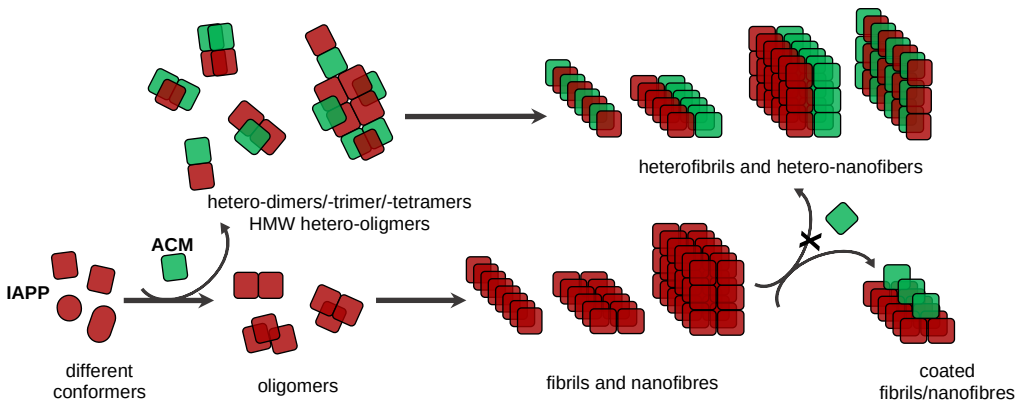

Figure 5-1: Supported mechanism of heterofibril/-nanofiber formation. ACMs sequester IAPP by formation of hetero-dimers, -trimers/-tetramers and HMW hetero-oligomers and thereby block generation of toxic IAPP oligomers and fibrils. By time, heterocomplexes transform into heterofibrils which further assemble into supramolecular nanofibres. A lateral co-assembly of “protofilament”-like IAPP and ACM stacks is most supported by the data. Binding of ACMs to fibrillar IAPP does not result in heterofibril/-nanofiber formation but in surface coating.

An ESI-IMS-MS study published by Young *et al.* has investigated the nature of complexes formed upon interaction of IAPP with ACMs' parent peptide Aβ40[159]. Their IAPP/Aβ40 mixture co-assembled into distinct hetero-oligomers, namely, 1:1 IAPP:Aβ40 dimers and 2:1 or 1:2 IAPP:Aβ40 trimers. As a consequence of co-polymerisation, unique oligomer conformations were observed that presented different stabilities and amyloid formation rates compared to homo-oligomers formed by the single peptides. MD simulations by Ge *et al.* further confirmed these findings[160]. The study showed that formation of an IAPP/Aβ42 hetero-dimer is the first step toward their co-aggregation. The hetero-dimer was the most populated species during the early assembly process, while later in time higher order oligomers were also observed. Similar observations were also made for the interaction of IAPP and the Aβ segment 25-35. A series of hetero-oligomers was formed in their mixture in the early stages as shown by ESI-IMS-MS, the most frequent among them being the hetero-dimer[161]. The relative abundance of hetero-dimers also gradually decreased by time when aggregation proceeded. The IAPP/Aβ42 hetero-dimer was investigated in more detail via MD simulations performed by Li *et al.*[162]. The authors found that IAPP and Aβ42 co-aggregate into predominantly disordered coils and, to a lesser extent, β-sheet rich conformations, and concluded that these ordered IAPP/Aβ42 β-sheet-rich conformations may be on the pathway of hetero-oligomers toward the IAPP/Aβ42 heterofibril formation since ordered β-sheets are the scaffold of amyloid fibrils[162]. In conclusion, the types of heterocomplexes formed by IAPP and ACMs are very similar to the types of heterocomplexes formed by IAPP and Aβ40(42) or its segment Aβ(25-35). This highlights the success of the ACM design concept which aimed at generating inhibitors mimicking the naturally occurring IAPP-Aβ cross-interaction (see chapter 4.1).

Although similar types of heterocomplexes are formed by IAPP and ACMs compared to IAPP and Aβ, they differ in their properties. For instance, previous studies from our group showed that seeding with fIAPP or fAβ40 and cytotoxic assemblies accelerates formation of fibrils and cytotoxic aggregates in IAPP/Aβ40 mixtures[84]. On the contrary, IAPP/ACM mixtures cannot be seeded neither by fIAPP nor by fAβ40 or fAβ42 (see chapter 4.3.4). Additionally, IAPP/Aβ42 heterocomplexes were described to be significantly more toxic than IAPP or Aβ42 alone by Bharadwaj *et al.* and their co-polymerisation was key to the enhanced cytotoxicity[163]. In contrast, earlier studies from our group showed that IAPP/Aβ40 hetero-association leads to the formation of less toxic early hetero-oligomers[80]. The findings by Bharadwaj *et al.* could be contradictory because the peptides might have been toxic or fibrillar already before their co-polymerisation was initiated. In accordance with our previous data on IAPP/Aβ40 heterocomplexes[80], IAPP/ACM heterocomplexes (and also heterofibrils) do not cause cell damage (see chapters 4.3.2 and 4.8). Thus, ACMs might be efficiently mimicking the naturally occurring IAPP/Aβ cross-interaction by combining inherited binding and complex formation behaviour with design-attributed introduction of beneficial changes to the resulting heterocomplexes. The findings are also in very good agreement with previous studies of the Kapurniotu group on IAPP-GI and other IAPP-derived cross-amyloid inhibitors (ISMs) of Aβ40(42)[80,111].

Based on the results of this thesis, IAPP seems to to template hf-IAPP/ACM formation and IAPP's amyloidogenic character seems crucial for this process. This could be supported by

findings suggesting that interpeptide interactions of IAPP with Aβ42 in the hetero-dimer cause structural changes of Aβ42 in its central hydrophobic core Aβ(16-22), and thus promote co-aggregation[160]. Another indication that IAPP could initiate co-fibrillation with non-amyloidogenic ACMs is provided in a study conducted by Middleton *et al.*[164]. Here, an equimolar mixture of the only weakly amyloidogenic rIAPP (as inhibitor) and hIAPP was used and the two peptides were suggested to interact as monomers or early-stage oligomers, similar to what is considered important for IAPP/ACM interactions and ACMs' inhibition. MD simulations studies suggested that rIAPP initially becomes incorporated in hIAPP's N-terminal β-sheet but due to structural re-arrangement the IAPP fibril structure forms[164]. Mature hIAPP fibrils could not cause rIAPP to aggregate or form its own β-sheets[164], an observation that is similar to ACMs which need to be mixed with prefibrillar IAPP to form IAPP/ACM heterofibrils/-nanofibers. Therefore, the authors assumed that a transient hIAPP/rIAPP complex serves as a seed for rIAPP amyloid β-sheet formation[164]. Overall, the role of IAPP in the formation of the hypothetical joint IAPP/rIAPP fibril assemblies suggested by Middleton *et al.*[164] seem similar to its role in the formation of hf-IAPP/ACM that was concluded by the findings of this thesis. In both cases, inhibitor peptides with little or no self-amyloidogenic properties interact with IAPP, structural re-arrangements of the heterocomplexes take place subsequently, and non-fibrillar IAPP templates and promotes the further formation of mixed fibril assemblies. In accordance with this, also other amyloidogenic peptides (except for IAPP/Aβ, IAPP/rIAPP) were described to promote each others co-aggregation. For example, αSynuclein can induce tau fibril formation and was shown to cross-interact with tau and form fibrillar co-assemblies[165]. Also, the formation of αSynuclein/tau heterocomplexes was shown to promote maturation into fibrils through binding-induced misfolding and aggregation[166]. Furthermore, studies conducted by Nespovitaya *et al.* demonstrated that the amyloid aggregation promotor heparin can co-aggregate with the neuropeptide β-endorphine into composite amyloid fibrils and thereby alters stability and structural properties of the fibrillar co-assemblies[167,168].

5.2 The proposed inhibitory interaction interface between IAPP's N-terminus and Nle3-VF's C-terminus

Full-length Aβ40 interacts with IAPP with an app. k_D of 48.5 nM[80]. Binding of the Aβ40 C-terminus 29-40 is slightly weaker but still about ten-times stronger than binding of the N-terminus 1-28 to IAPP (200 nM vs. 2.5 µM)[43]. This indicates a crucial role of the hydrophobic C-terminal part Aβ(29-40) in the Aβ40-IAPP interaction. The N-terminal segment 1-18 and the C-terminal segment 19-37 of IAPP interact with similar nM affinities with Aβ40[43]. Aβ(19-22) (FFAE), Aβ(27-40) (NKGAII), Aβ(35-40) (MVGGVV), IAPP(8-18) (ATQRLANFLVH), and IAPP(22-28) (NFGAILS) were identified as "hot regions" crucial for both self-association and cross-interaction of the two peptides[43] (Figure 5-2a). Comparable regions for cross-interaction were also found by Li *et al.* who simulated the Aβ-IAPP interface specifically for a hetero-dimer scenario[162]. Within IAPP "hot regions", residues F15, L16, F23, and I26 were found to act in concert to function as key molecular determinants of IAPP hetero-assembly with Aβ40(42)[117].

Peptide array experiments showed that Nle3 can bind to IAPP with both its N- and C-terminus, but it preferentially does so with its N-terminal part involving amino acids 15-23 (QKLVFFAED) (see chapter 4.9 and Figure 5-2b). In comparison to Aβ40, truncation of amino acids 1-14, exchange of the LTS, and the M35Nle substitution in Nle3 thus did not completely change the peptide's interaction behaviour with IAPP since it still binds with both N- and C-terminus but led to a preferential binding of the N-terminus while for Aβ40 stronger binding is observed for the C-terminus[43]. This is also in good agreement with the inhibitory effect observed for Aβ40 and Nle3 toward IAPP: both peptides detect IAPP with both termini and are medium inhibitors able to delay IAPP's aggregation by some days (see reference [80] and chapter 4.3.1). In contrast to Nle3, the core segment of Nle3-VF and VGS-VF for IAPP recognition lies in their C-terminal NKGAII-region, indicating that the introduction of N-terminal methylations leads to a shift of the binding interface with IAPP from the N-terminal QKLVFFAED-region selectively to the C-terminal NKGAII-region (Figure 5-2c,d).

Nle3 was found to interact with both IAPP "hot regions" identified by Andreetto *et al.*[43] and additionally with another IAPP region 29-37 that was also reported to be important for Aβ-IAPP cross-interaction by Li *et al.*[162]. Strongest interaction was observed with IAPP's NFGAIL-region 22-28 (see chapter 4.9 and Figure 5-2b). In contrast, Nle3-VF did not bind to C-terminal IAPP decamers of the peptide array but binding was exclusively limited to IAPP decamers located within IAPP region 8-23, indicating that the introduction of N-terminal methylations strongly hinders the interaction with IAPP's C-terminus and favours specific interaction with IAPP's N-terminus (see chapter 4.9 and Figure 5-2c). Thus, methylations in Nle3-VF on the one hand render its N-terminus incompatible for IAPP binding and on the other hand block interaction with IAPP's C-terminus. Consequently, only a very specific interaction interface between the inhibitor's C-terminus (core: NKGAII) and IAPP's N-terminus (core: NFLVH) can be established (Figure 5-2c). Even though Nle3-VF and VGS-VF share a similar recognition site for IAPP, namely, their NKGAII-region, peptide array analysis showed that VGS-VF could interact with both NFLVH- and NFGAILS-containing IAPP regions, indicating that binding to IAPP is not as specific as observed for Nle3-VF (see chapter 4.9 and Figure 5-2d). Furthermore, VGS-VF interacted more strongly with IAPP's NFGAILS-region than with its NFLVH-region. Since VGS-VF differs from Nle3-VF only in its LTS, the hydrophobic Nle3-tripeptide appears to be the reason for the specific NKGAII-NFLVH Nle3-VF/IAPP recognition site. VGS-VF seems to obtain some inhibitory activity toward IAPP fibril formation when applied at higher molar excess (5-fold) while Nle3-GG does not show inhibitory effects even at 20-fold excess (see chapter 4.3.2). Thus, it is maybe possible that binding to IAPP's NFLVH-region might get favoured over binding to IAPP's NFGAILS-region with increasing VGS-VF concentration (leading to increased structural order, see Figure 4-18 in chapter 4.3.3), rendering the peptide more inhibition-competent subsequently, while the presence of the Gly29Gly33-methylation in Nle3-GG's NKGAIIG-region permanently suppresses formation of the NKGAII-NFLVH inhibitory interface due to the location of the methylation pair.

Taken together, ADPs like Nle3 and VGS-VF that bind to both "hot regions" IAPP(8-18) and IAPP(22-28) in a similar way as also their parent Aβ40 does, are only weak to medium inhibitors of IAPP aggregation. Similarly, mixing of Aβ40 with IAPP was found to attenuate cytotoxic self-assembly of both polypeptides but could not completely block it[80]. In contrast,

Nle3-VF's interaction with IAPP is less "promiscuous" and strictly limited to IAPP's N-terminal region. This interaction is specifically mediated by Nle3-VF's C-terminus (NKGAII-region). Therefore, the NKGAII-NFLVH interface can be considered the "inhibition-mediating" one in the Nle3-VF/IAPP interaction and might render Nle3-VF a very potent Aβ-derived inhibitor of IAPP. Notably, a parallel assembly with a hybrid interface formed via the C-terminal β-sheet of Aβ and the N-terminal β-sheet of IAPP was found as the most energetically favourable packing for MD simulated double-layer cross-seeding assemblies of Aβ and IAPP[169]. This might be a hint that such an arrangement might also occur in heterologous IAPP-Aβ fibril assemblies and, more importantly, also in hf-IAPP/Nle3-VF that are a very important part of the mechanism by which Nle3-VF inhibits IAPP.

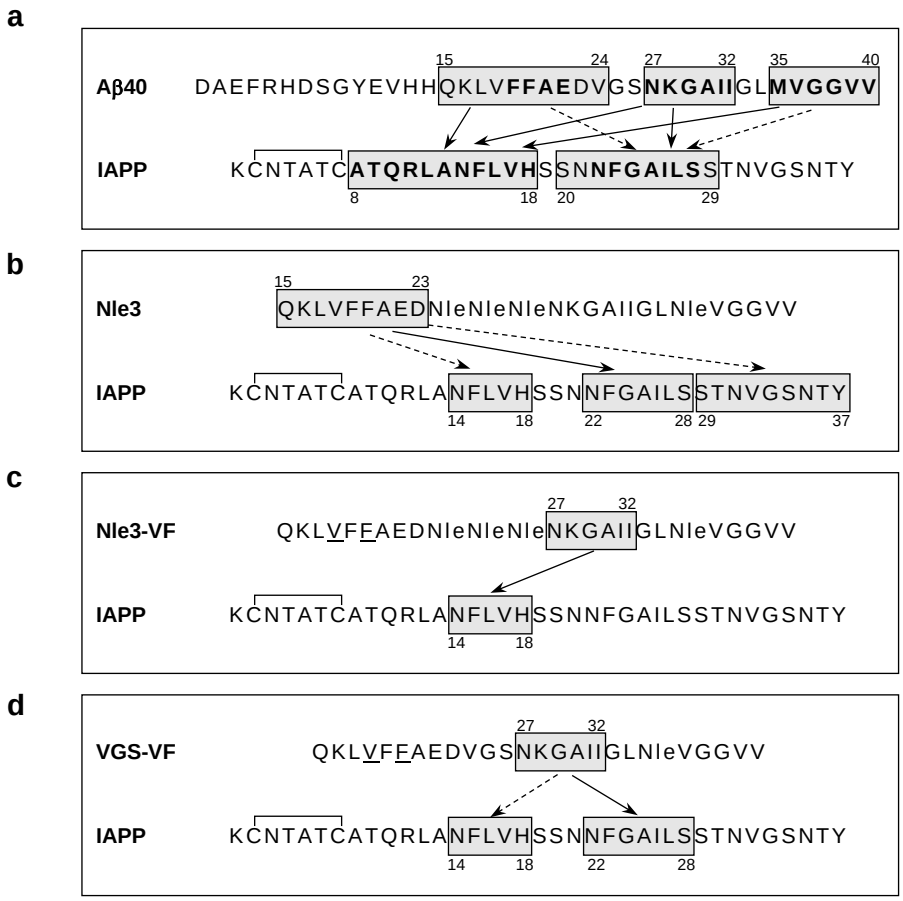

Figure 5-2: Suggested interaction interfaces of IAPP with Aβ40, Nle3, Nle3-VF, and VGS-VF. (**a**) Cross-interactions between the hot (bold) and slightly longer sequences (grey boxes) of Aβ40 and IAPP suggested by Andreetto *et al.*[43]. Solid-line arrows indicate interactions between "hot segments", dashed-line arrows indicate interactions between slightly longer sequences. (**b-d**) Interaction interfaces of IAPP with Nle3 (b), Nle3-VF (c) and VGS-VF (d) as revealed by peptide array experiments (see chapter 4.9). Grey boxes mark core peptide segments involved in cross-interaction. Bold-line arrows highlight the main interaction interface between the two peptides, dashed-line arrows indicate less dominant secondary interaction interfaces (if existing).

A study performed by Eisenberg and co-workers[30] further supports the finding that Nle3-VF's specific interaction with the N-terminal IAPP region IAPP(14-18) (NFLVH) is of high importance. Using and IAPP-MBP (maltose-binding protein) fusion protein to crystallise IAPP, the authors found that IAPP contains two α-helical segments, namely, 8-18 and 22-27. Importantly, IAPP homo-dimers were formed via helix-helix interactions between residues 8-18 and this dimerization was assumed to be on the pathway of fibrillation. The authors

suggested that IAPP dimerization initiates alignment of C-termini which subsequently form the steric zipper spine of the fibril before alignment of the N-terminal strand occurs[30]. Insulin was suggested to inhibit the initial IAPP dimerization step by binding via a helical motif to the same helical motif of residues IAPP(8-18) and thereby competing with homo-dimerization[30]. In this scenario, insulin would inhibit IAPP aggregation by blocking a potential self-interaction interface located in IAPP's N-terminus. Obviously, there are several parallels to the here-suggested inhibition mechanism for Nle3-VF and other ACMs. First, formation of specific hetero-dimers seems to be key for IAPP inhibition. Second, the interaction interface of Nle3-VF's NKGAII-region with IAPP's NFLVH-region was determined the "inhibition-mediating" one. Thus, Nle3-VF interacts with the same binding site of IAPP as insulin and might therefore also have a similar inhibitory effect, namely, competing with IAPP's helix-helix homo-dimerization that is mediated by segment 8-18. Third, Eisenberg and co-workers' model suggests that alignment of IAPP C-termini mediated by homo-dimerization is the initiation step toward further fibril formation[30]. If Nle3-VF interacts with IAPP's N-terminus during initial hetero-dimer/heterocomplex formation, this would potentially leave free IAPP's C-terminus at this point, leading to a remaining surface in IAPP which is competent for amyloid formation[21,123,170]. The free C-terminus might be capable of inducing structural re-arrangements which promote the formation of hf-IAPP/ACM, although one IAPP segment responsible for self-recognition is blocked for further self-aggregation by interaction with Nle3-VF (see also chapter 5.3 on this).

5.3 Proposed model of IAPP/ACM heterofibrils

For proposing an hf-IAPP/Nle3-VF model based on results of this thesis, known structures of IAPP and Aβ40(42) were taken into consideration additionally. Recently, three different cryo-EM structures of fibrillar IAPP were published[33-35]. The two structures presented by Schröder and co-workers[33] and Ranson, Radford and co-workers[34] show a highly similar, S-shaped fold of the fibril core (Figure 5-3a). The structure reported by Eisenberg and co-workers is also S-shape-like but shows significant differences compared to the other two, which might be due to the SUMO-tag attached to the peptide favouring maybe another IAPP polymorph[35]. During the last years, several structures of Aβ42 fibrils were found, the majority of them indicating an S-shaped arrangement of the fibril core[56,171-176]. Structure alignment shows high similarity of amino acids 17-42 in all S-shape folds (Figure 5-3b). Differences are mainly observed within the peptide's N-terminus. Several studies found Aβ40 adopting a U-turn fold within its fibril structure. Two- and three-fold symmetries were described[54,55,132,177]. As for Aβ42, structure alignment indicates high folding similarities among different models (Figure 5-3c).

Röder *et al.* described high similarity of S-shapes in IAPP and Aβ42 fibrils[33]. IAPP and Aβ42 fibril structures indeed align well in sequence segments IAPP(13-37) and Aβ42(15-40) (Figure 5-4a). Of note, the Aβ(15-40)-segment is exactly what was taken for designing Aβ-derived IAPP inhibitors in this work. Since peptide array experiments showed that the "inhibition-mediating" interface with IAPP is formed with Nle3-VF's NKGAII-region (amino acids 27-32), structure alignment was repeated using only the C-terminal (27-40) part of the Aβ42 fibril model

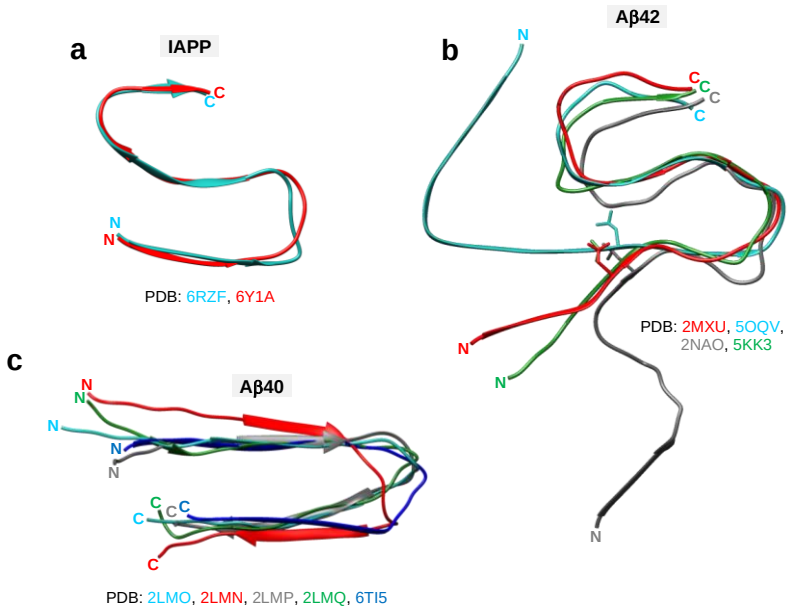

Figure 5-3: Alignment of different IAPP, Aβ40 and Aβ42 fibril structures. Multiple structure alignments were performed using Chimera. Results are shown for IAPP (**a**), Aβ42 (**b**) and Aβ40 (**c**). PDB entries used for the alignments: 6ZRF[34], 6Y1A[33] (IAPP); 2MXU[173], 5OQV[56], 2NAO[171], 5KK3[172] (Aβ42); 2LMN[55], 2LMO[55], 2LMP[55], 2LMQ[55], 6TI5[177] (Aβ40). IAPP structures comprise residues 13-37, Aβ42 structures comprise residues 11-42 except for 5OQV (1-42), Aβ40 structures comprise residues 11-40. Leu17 is shown in stick-representation in the different Aβ42 models (b) to highlight the position where structures start to become similar.

(Figure 5-4b). Best matching peptide segments are then IAPP(14-27) and Aβ42(27-40), leading to a change in the orientation of Aβ42 relative to IAPP. Similar alignments were performed for Aβ40. A chain from the PDB model 2LMQ was chosen as an example since it aligned well with parts of the IAPP fibril structure (Figure 5-4c). Aβ40(14-23) matches IAPP(23-32), Aβ40(30-39) matches IAPP(13-22). Of note, one Aβ40 molecule aligns with its N- and C-terminal segments with two IAPP molecules located in different fibrils layers. The orientation of the Aβ40 molecule remains very similar when only Aβ40(27-40) is taken into consideration for the alignment (Figure 5-4d).

Based on the assumption that Nle3-VF might match IAPP similarly to its parents Aβ40(42) in an IAPP/Nle3-VF heterofibril, two artificial Nle3-VF constructs were generated from the Aβ40(42) model structures and overlayed with the IAPP fibril structure to match similar regions. Nle3-VF was constructed from PDB models 5OQV (Aβ42) and 2LMQ (Aβ40) by deleting residues 1-14 and 41-42 or residues 11-14, respectively, and replacing residues V24, G25, S26 and M35 by norleucine using Chimera[128] and the SwissSidechain[129] database (Figure 5-5). Most probable norleucine rotamers were inserted that did not clash with surrounding atoms in the structure. Nevertheless, the real structure of Nle3-VF is most likely different from such constructs since especially the substitution of the small residues V24, G25, and S26 by bulky, hydrophobic norleucines is assumed to cause structural changes. As these constructs are only meant as a first rough approximation, no further energetic minimisations etc. were performed. PDB model 5OQV was chosen representatively among the different S-shaped Aβ42 fibrils for building the Nle3-VF construct, since all models are rather similar concerning amino acids 17-42. Since Nle3-VF is based on Aβ-residues 15-40, choosing another model should not greatly influence the overall outcome. Both model constructs were manually

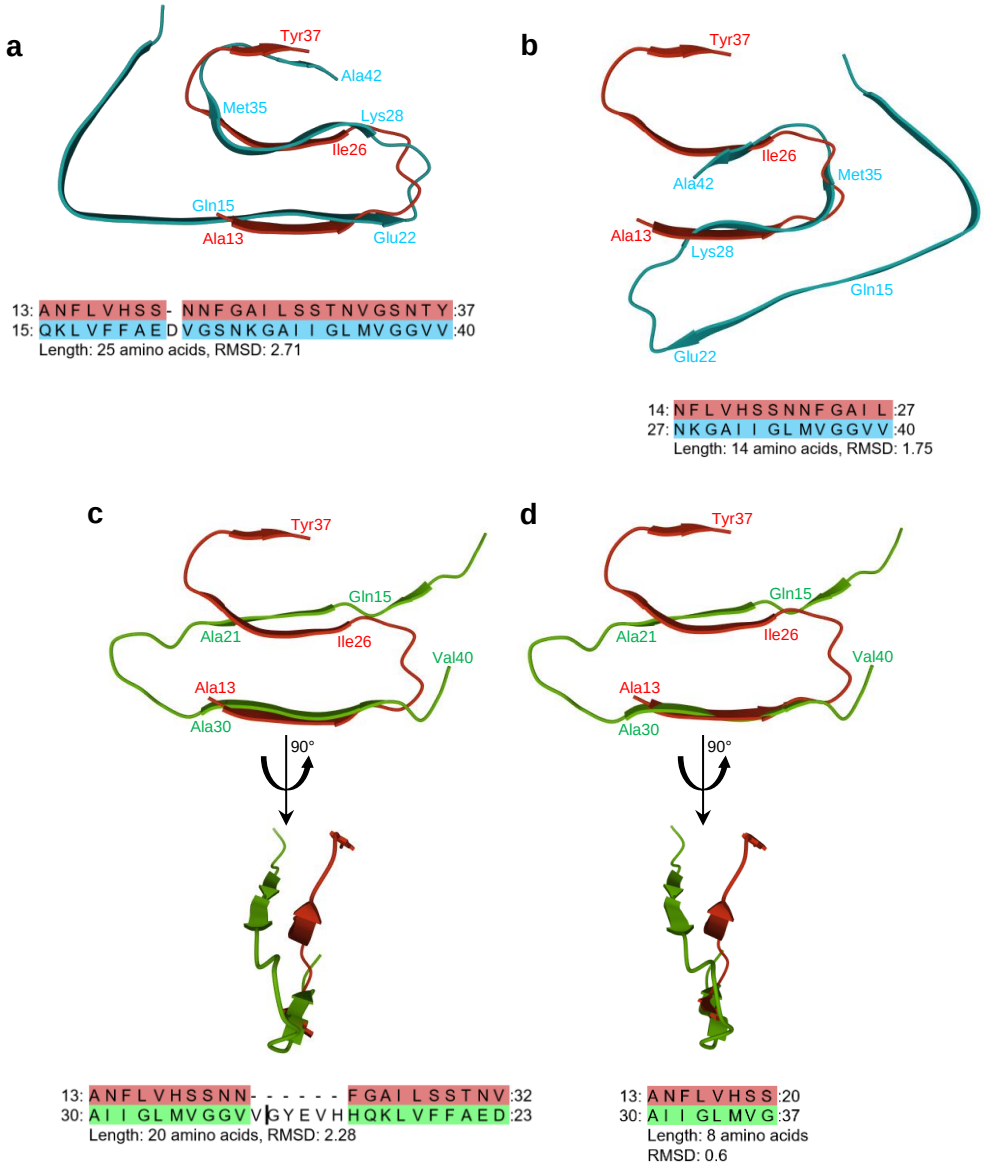

Figure 5-4: Structure alignments of IAPP and Aβ40(42) fibrils. (**a**) Alignment of IAPP with full-length Aβ42. (**b**) Alignment of IAPP with Aβ42 segment 27-40. (**c**) Alignment of IAPP with full-length Aβ40. (**d**) Alignment of IAPP with Aβ40 segment 27-40. Aligned IAPP/Aβ40 fibrils (c,d) are additionally depicted after turning by 90° to show that one Aβ40 molecule is aligning with two IAPP molecules located in two different fibril layers. Pairwise structure alignments were performed using the protein structure alignment tool from the PDB webpage (jFATCAT (flexible) alignment method). Coloured sequences highlight matching segments. Length of matches and corresponding RMSD is given below the sequences. PDB entries: 6Y1A[33] (IAPP), 5OQV[56] (Aβ42), 2LMQ[55] (Aβ40).

overlayed in parallel and antiparallel direction with the IAPP fibril structure to match IAPP's NFLVH-segment with Nle3-VF's NKGAII-segment since peptide array results indicated this to be the crucial interaction interface and it was also part of the IAPP/Aβ40(42) fibril structure alignments (Figure 5-6). The Aβ40-based Nle3-VF construct was additionally flipped horizontally by 180° (compared to the IAPP/Aβ40 alignment, see Figure 5-4c,d) to avoid overlay of the IAPP fibril with Nle3-VF's QKLVFF-region, based on the hypothesis that it is most likely not part of the inner hf-IAPP/ACM core due to its N-methylations. Based on the parallel overlays, two hypothetical IAPP/Nle3-VF heterofibrils were built, one representing a heterofibril co-assembled by mixed protofilaments consisting of both peptides (Figure 5-7a) and the other representing a heterofibril built up by two self-sorted protofilaments forming a

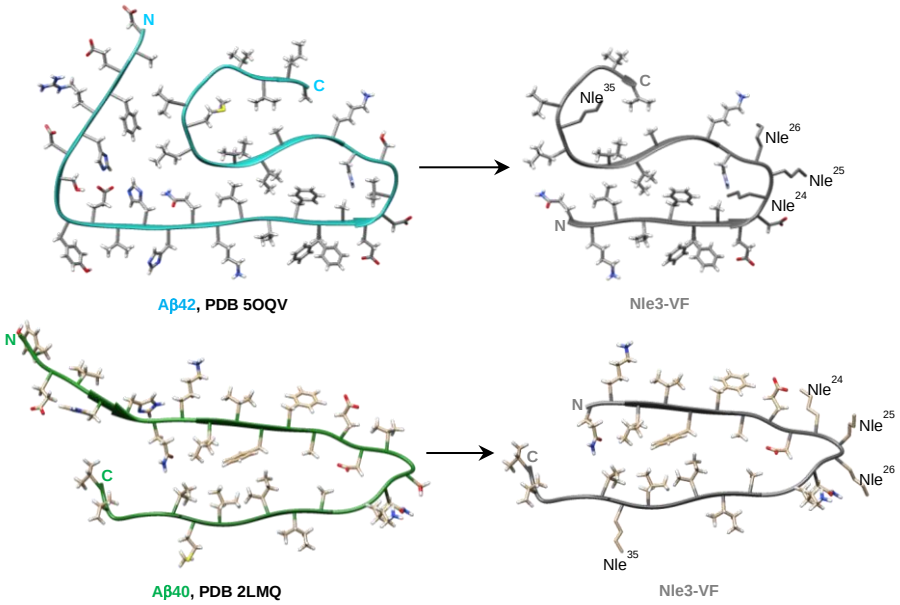

Figure 5-5: Nle3-VF model structures generated from published Aβ40(42) fibril structures. Nle3-VF constructs were obtained by deleting amino acids 1-14 and 41/42 from the Aβ42 fibril structure (PDB 5OQV[56]) or amino acids 11-14 from the Aβ40 fibril structure (PDB 2LMQ[55]) and replacing residues 24, 25, 26 and 35 by Norleucin (Nle). Most probable norleucine rotamers which did not cause clashes with other atoms within the structure were inserted from the SwissSidechain database using Chimera. Of note, structures were not energetically minimised.

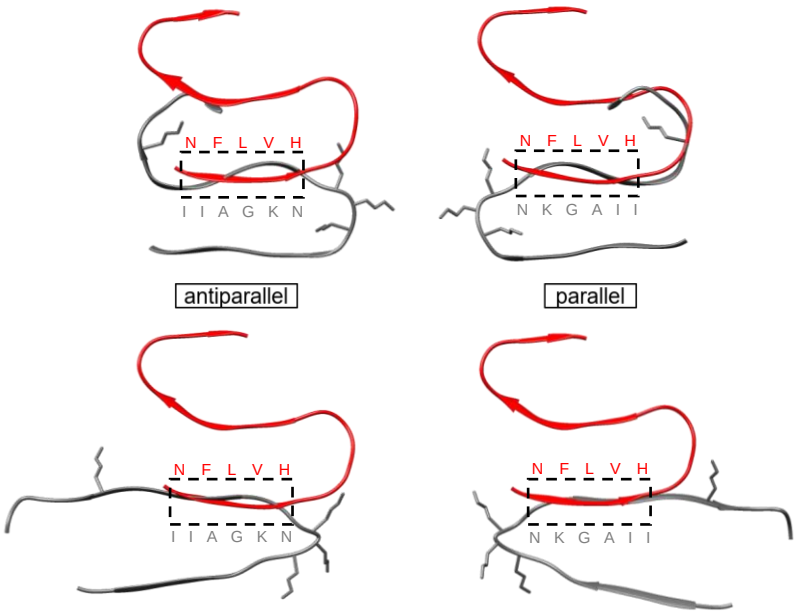

Figure 5-6: Overlay of Nle3-VF with the IAPP fibril structure. Nle3-VF constructs generated from an Aβ42 fibril structure (PDB 5OQV[56]; upper panels) and an Aβ40 fibril structure (PDB 2LMQ[55]; lower panels) were manually overlayed in parallel and antiparallel manner with an IAPP fibril structure (PDB 6Y1A[33]) to match Nle3-VF's NFLVH-region with IAPP's NKGAII-region. Nle3-residues in Nle3-VF are shown as sticks.

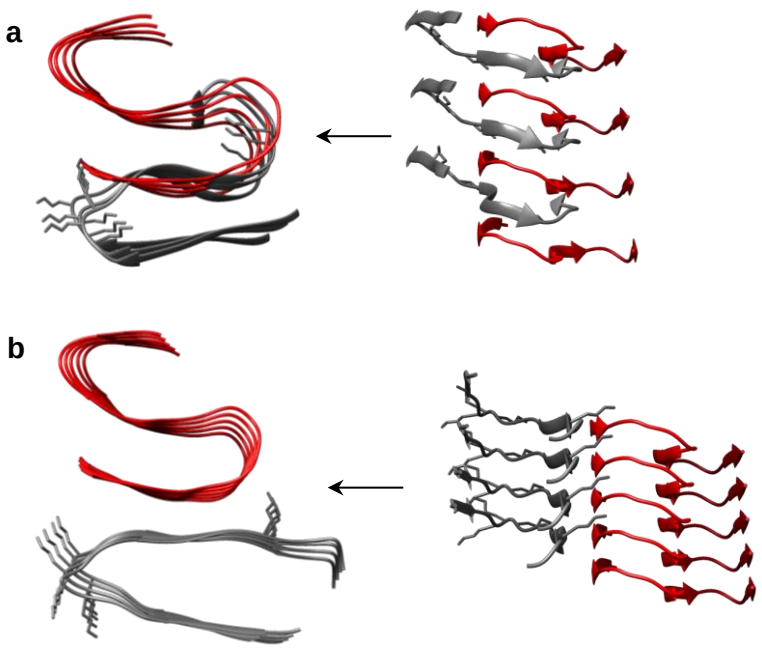

Figure 5-7: Potential appearance of IAPP/Nle3-VF heterofibrils. (**a**) Heterofibril derived from a mixed protofilament. The Nle3-VF construct generated from the Aβ42 fibril structure (PDB 5OQV[56]) was inserted into the IAPP fibril structure (PDB 6Y1A[33]) by manually replacing an IAPP molecule in every second layer by an Nle3-VF molecule. (**b**) Heterofibril derived from a laterally co-assembled protofilament. The Nle3-VF construct generated from the Aβ40 fibril structure (PDB 2LMQ[55]) was manually placed strand-by-strand next to the IAPP fibril structure (PDB 6Y1A[33]) to match Nle3-VF's NKGAII-region with IAPP's NFLVH-region.

joint lateral assembly (Figure 5-7b). Both models can give a notion for how IAPP/ACM heterofibrils might look like. Nevertheless, non-negligible differences might occur in real structures, especially concerning the N-terminal Nle3-VF region. The N-terminus of Nle3-VF within the heterofibril is most probably less well sorted or stacked, due to the disturbed H-bonding caused by the V18/F20-methylations. Experiments on *N*-methylated Aβ40 by Meredith and co-workers showed that Aβ40's two β-sheet domains fold in a semiautonomous manner since incorporation of two *N*-methylated residues into one of the β-sheets is enough to disrupt that sheet while the other, unmodified β-sheet stays intact and able to form fibrils[137]. Thus, kind of a self-sorting ability necessary for a laterally assembled hf-IAPP/Nle3-VF as suggested in Figure 5-7b can be considered possible also for Nle3-VF even though H-bonding is disrupted in its N-terminal part.

Another important observation from the conducted experiments in this work was that an amyloidogenic IAPP variant is necessary to form hf-IAPP/ACM, since non-amyloidogenic IAPP and rat-IAPP did not form fibrillar assemblies with Nle3-VF. Rat-IAPP differs from human IAPP at six positions, five of which are located in the 20-29 region, including three proline replacements. IAPP-GI carries two N-methylations in the 20-29 region at positions Gly24 and Ile26[19]. Both features prevent IAPP fibrillation[19,153]. Together with the finding that IAPP mainly interacts via its NFLVH-region with Nle3-VF this led to the assumption that initially formed IAPP/ACM heterocomplexes are re-converted into heterofibrils due to a remaining surface in IAPP which is competent for amyloid formation and not blocked upon interaction. Already early studies indicated that the ability of IAPP to form amyloid is determined by its 20-29 region and this segment has been intensively studied for its fibril formation properties and has been suggested to form the core of IAPP fibrils[14,123,153,170,178,179]. However, also peptides comprised

of residues from regions 8-20, 28-33 and 30-37 were found to be capable of forming fibrils, arguing that IAPP(20-29) is not the only amyloidogenic segment[20-25]. Moreover, Goldsbury *et al.* stated that IAPP(20-29) is sufficient for fibril formation but other N- and C-terminal fragments of the molecule clearly influence the mode of fibril assembly and the final fibril morphology[180]. Peptide array results presented in this work revealed Nle3-VF's NKGAII-region and IAPP's NFLVH-region (amino acids 14-18) as core recognition sites for their interaction. Thus, even though one IAPP segment responsible for self-recognition is blocked for further self-aggregation by interaction with Nle3-VF, the C-terminal IAPP segment 22-37 might be at least partly free and capable of inducing structural re-arrangements into heterofibrils. This would also be in good agreement with both suggested heterofibril models in which the IAPP segment 22-37 is mainly or even fully free from direct interactions with Nle3-VF. This could also explain why heterofibrils cannot be assembled with IAPP-GI or rat-IAPP: in these cases, two out of three amyloidogenic IAPP regions are blocked, one by interaction with Nle3-VF and the other one by methylations (IAPP-GI) or proline-substitutions (rat-IAPP) within the 20-29 segment. The remaining amyloidogenic segment 30-37 might not be enough anymore to induce structural re-arrangements.

5.4 Heterocomplex and heterofibril formation and fibril elongation as inhibitory mechanism of ACMs toward Aβ42

Fluorescence titration experiments showed that ACMs interact with Aβ42 monomers with nanomolar affinities and bind to oligomeric Aβ42 with micromolar affinities (see chapter 4.10.1). Studies conducted by Christina Lindner during her Master thesis confirmed fluorescence titration experiments by showing that ACMs form hetero-dimers/-trimers and HMW heterocomplexes with Aβ42[151]. The former were only observed in presence of an inhibition-competent ACM quantity[151], indicating that generation of these specific heterocomplexes is essential for the inhibitory effect. Furthermore, the results presented in this thesis showed that hf-Aβ42/ACM evolve by time from initially formed heterocomplexes, but heterofibril formation and fibril elongation can also be initiated from oligomeric and fibrillar forms of Aβ42 by ACMs. Notably, ACMs did not co-fibrillise with Aβ40 (see chapter 4.11). This might be due to the fact that Aβ40 is less amyloidogenic than Aβ42[181]. As discussed before, an amyloidogenic IAPP variant was also necessary to form hf-IAPP/ACM.

Interestingly, not only ADPs but also the ACMs' parent peptide full-length Aβ40 has been described to show inhibitory effects on Aβ42[182-186]. Studies on the interaction of Aβ40 and Aβ42 conducted by Frost *et al.* suggested that Aβ42 and Aβ40 co-assemble early in the fibrillogenesis pathway since Aβ42 and Aβ40 were found to associate into unstructured mixed aggregates immediately upon mixture[187]. By time, these early aggregates converted into larger and structured assemblies. Early aggregates of Aβ40 and Aβ42 were also studied by Murray *et al.*[184]. Using mass spectrometry and ion-mobility spectrometry, freshly prepared 1:1-mixtures were investigated. While Aβ42 was found to produce oligomers of order up to dodecamers, mixed Aβ40/Aβ42 solutions contained hetero-oligomers with a oligomer

distribution extending to tetramers[184]. These tetramers contained equal parts of Aβ42 and Aβ40 and the authors' results supported the formation of the mixed tetramer via dimer condensation rather than monomer addition. Additional atomic details on the effect of Aβ40/Aβ42 interaction on oligomer formation were provided by Viet *et al.*[183]. Their MD simulations indicated that Aβ42 becomes less ordered in the mixed Aβ40/Aβ42 system compared to the monomer case and that the presence of Aβ40 increases the flexibility of segment 18-33 in Aβ42 and of its D23/K28 salt bridge. Thus, the formation of early complexes between Aβ40 and Aβ42 strongly resembles the heterocomplex assembly pattern observed by ACMs and Aβ42, namely, immediate formation of mixed species – most importantly of hetero-dimers[151] – and subsequent conversion into larger oligomers. Of course, no atomic details are available on the effect of ACMs on the Aβ42 structure or flexibility upon their interaction but, notably, hf-Aβ42/ACM showed less β-sheet/β-turn content in CD experiments than Aβ42 fibrils (see chapter 4.14). Hence, ACMs seem to have at least partly inherited Aβ40's interaction behaviour toward Aβ42. Nevertheless, their mechanism of action regarding Aβ42 inhibition might still partly or even fully differ from Aβ40's due to the sequence truncations and changes that were made during their design.

Effects of Aβ40 on Aβ42 monomers, protofibrils, and mature fibrils have been investigated by Jan *et al.*[182]. When monomers of Aβ40 and Aβ42 were mixed, Aβ40 inhibited Aβ42 fibrillogenesis in a concentration-dependent manner. Co-incubation of the two peptides favoured the formation short protofibrillar structures but suppressed further conversion into mature elongated fibrils. Thus, Aβ40 monomers interfere with the ability of Aβ42 monomers to form mature fibrils but do not interfere with their ability to form higher order prefibrillar aggregates[182]. In addition, mixing of monomeric Aβ40 with Aβ42 protofibrils blocked the formation of mature Aβ42 fibrils and led to the formation of mixed Aβ40/Aβ42 protofibrillar assemblies[182]. Furthermore, addition of Aβ40 monomers to mature but mechanically fragmented Aβ42 fibrils retarded their growth and blocked fibril reassembly[182]. These findings on the effect of monomeric Aβ40 on different Aβ42 species reported by Jan *et al.* are contrary to the observations that were made for effects of Aβ(15-40)-derived ACMs on Aβ42. While the presence of Aβ40 suppresses the formation of mature Aβ42 fibrils, ACMs rather drive elongation and maturation of heterofibrils. Nevertheless, both Aβ40 and ACMs show effects on different Aβ42 species and lead to the formation of a specific kind of fibrils independently of being mixed with prefibrillar or fibrillar Aβ42, namely, short protofibrils or elongated heterofibrils, respectively. In conclusion, Aβ40 and ACMs might form early heterocomplexes with Aβ42 of similar order, but their subsequent mechanism of Aβ42 inhibition is obviously different. This seems reasonable considering the significant changes in peptide length and sequence that were made to design ACMs derived from the Aβ40 template.

Of note, a series of peptides originating from Aβ segment 14-23 was designed by Mihara and co-workers and their effects on Aβ42 oligomers and fibrils were investigated[188,189]. Out of a first set, two peptides (named "LF" and "VF") were found to be able to co-assemble into amyloid-like fibrils when mixed with fibrillar Aβ42[188]. One of them ("LF") also formed amyloid-like mixed fibrils with oligomeric Aβ42. This peptide was later shown to also act on Aβ42 toxicity by

transforming more toxic species of Aβ42 into less toxic ones through its co-assembly with Aβ42 to form fibrils[189]. This mechanism of inhibition is reminiscent to that described for ACMs in this thesis, although fibrillar species formed in mixtures of Aβ42 oligomers/fibrils with the ADPs designed by Mihara and co-workers were ThT-reactive[188] (in contrast to Aβ42/ACM heterofibrils). However, when a second set of these peptides was designed based on the "LF"-peptide, two of these new compounds produced only minor increases in ThT fluorescence when incubated with Aβ42 oligomers but TEM still showed formation of fibrils[189]. Cytotoxicity in both mixtures was reduced compared to Aβ42 alone and one of the peptides also proved to suppress Aβ42's apoptotic activity. Thus, these peptides captured toxic Aβ42 oligomers into a less toxic form by transforming them into amyloid-like but way less ThT-reactive mixed fibrils. These findings indicate that Aβ-derived peptides are in principle able to act on Aβ42 aggregation by inducing the formation of heteromeric and less toxic fibrillar assemblies that do not react with ThT. ACMs might be especially effective in this since they could trigger heterofibril formation independently of being mixed with Aβ42 monomers, oligomers, or mature fibrils.

One important point that was not discussed so far considering the ThT-binding experiments and related time-dependent TEM studies of mixtures of aged Aβ42 with ACMs (see Figure 4-81 and Figure 4-82 in chapter 4.12.4) is the following: the comparison of ThT binding and TEM results show that when fibrils begin to extend (form 5 h onward) an increase in ThT-binding is observed whereas elongated hf-Aβ42/ACM actually did not display ThT-reactivity. This is a rather unexpected finding since one would anticipate that ThT signals either stay constant at the level they are before the addition of aged Aβ42 to ACMs (if only the rest of not-yet fibrillated Aβ42 is interacting with inhibitors for forming the long heterofibrils) or that the ThT signal is reducing (if already present Aβ42 fibrils become part of longer heterofibrils which do normally not show ThT-reactivity). One hypothesis could be: Fibrils in the aged Aβ42-solution could be "dynamic" structures and able to exchange Aβ42 molecules with inhibitor molecules by time leading in the end to mixed fibrils. Thus, when inhibitors are added during Aβ42's growth phase, two things might happen in parallel: 1) existing fibrils elongate by addition of more inhibitor and/or Aβ42 molecules or heterocomplexes, and 2) exchanges take place in already formed Aβ42 fibril parts. The Aβ42 molecules which are released from its fibrils could start to build new homomeric fibrils which are supposed to be able to bind ThT. This process might not be preventable by the inhibitor since it is already complexed, bound to previously present fAβ42 or incorporated into the heterofibril assembly. Such a scenario of dynamic fibrils exchanging monomers by time until a thermodynamic equilibrium is reached was already described by Pujais *et al.* for diphenylalanine-based nanostructures[190] and molecule recycling was also observed for Aβ40(42) fibrils[191], so it seems to be a possible mechanism. A further hint that this could be true is that when aged Aβ42 is added to a 5-fold excess of F3-VF instead of to an equimolar amount, there is no increase in ThT fluorescence observable anymore in the specified time frame (5 h onward; see Figure 4-81). Since more ACM is available in this case, the inhibitor might be able to block also new Aβ42 homofibril formation starting from released Aβ42 molecules. Since no more studies were conducted on this issue, the exact mechanism remains elusive for this specific case and is open for further

investigations. In addition, cytotoxicity studies on mixtures of aged Aβ42 with ACM should be conducted to address the question to what extent the resulting fibrillar co-assemblies differ from hf-Aβ42/ACM which are formed by interaction with monomeric Aβ42.

A more general mechanism for Aβ42 inhibition and heterofibril formation of ACMs based on the findings described in chapters 4.10 – 4.12.4 and discussed above is shown in Figure 5-8. ACMs can interact with Aβ42 at its monomeric or pre-aggregated state to form hetero-dimers, -trimers and HMW hetero-oligomers. By time, these heterocomplexes undergo structural rearrangements to form heterofibrils. Furthermore, ACMs do also impact on Aβ42 at its post-nucleated state, when Aβ42 oligomers and/or protofibrils have already formed, by delaying Aβ42 homo-fibrillation and inducing fibril elongation and heterofibril formation. ACMs are even able to act as fibril elongation promotors on mature Aβ42 fibrils, maybe by interconnecting separate Aβ42 fibril segments, by addition of ACM molecules onto Aβ42 fibril ends, or both.

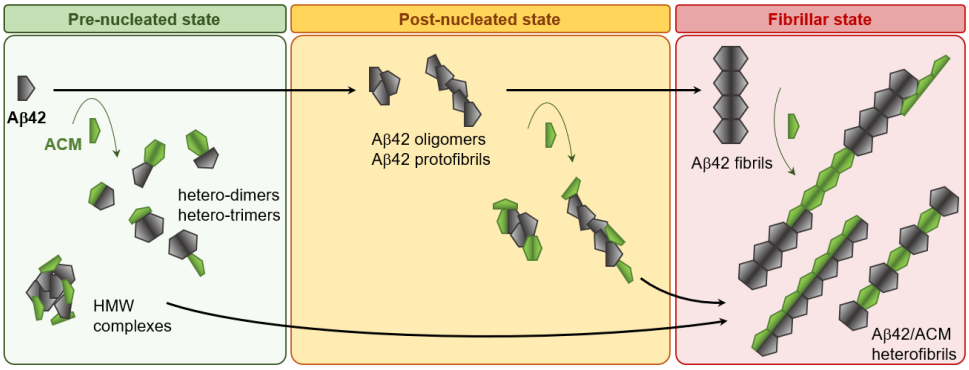

Figure 5-8: Suggested mechanism for the inhibition of Aβ42 fibrillogenesis by ACMs. ACMs can act on Aβ42 fibril formation at its pre-nucleated, post-nucleated and fibrillar sate. Heterofibrils are either formed from Aβ42/ACM heterocomplexes at an early stage which transform by time or by interaction of ACMs with Aβ42 oligomers and fibrils. Preformed Aβ42 aggregates (non-fibrillar, protofibrils or fibrils) could be interconnected by ACMs or Aβ42/ACM heterocomplexes to form elongated fibrils or elongate by addition of molecules to the fibril ends.

5.5 Proposed model of Aβ42/ACM heterofibrils

While Aβ40 is typically found in an U-shaped conformation in its fibril, the characteristic conformation of Aβ42 in this context is S-shaped[56,171-173]. Nevertheless, there are also studies reporting an U-shaped arrangement of the Aβ42 monomer unit within fibrils[175,176]. Recently, Cerofolini *et al.* could show that Aβ40 and Aβ42 can co-assemble and form structurally-uniform 1:1 mixed fibrillar species which differ from both pure fibrils[177]. Of note, Aβ42 adopts an U-shape fold within these heterogenous fibrils, indicating that it might adapt its shape to Aβ40 to be able to form mixed assemblies. Since ACMs are derived from Aβ40, it seems possible that Aβ42 arranges in a similar way with them when Aβ42/ACM heterofibrils are built up. When both Aβ42 and inhibitor would adopt an U-shaped fold, there are 12 different possibilities for hetero-dimeric building units to form either collateral or coaxial assemblies (Figure 5-9). Peptide array experiments revealed that Nle3-VF interacts with both Aβ40(42)'s central (aa 15-26) and C-terminal (aa 27-40/42) regions, but the C-terminus is preferred (see chapter

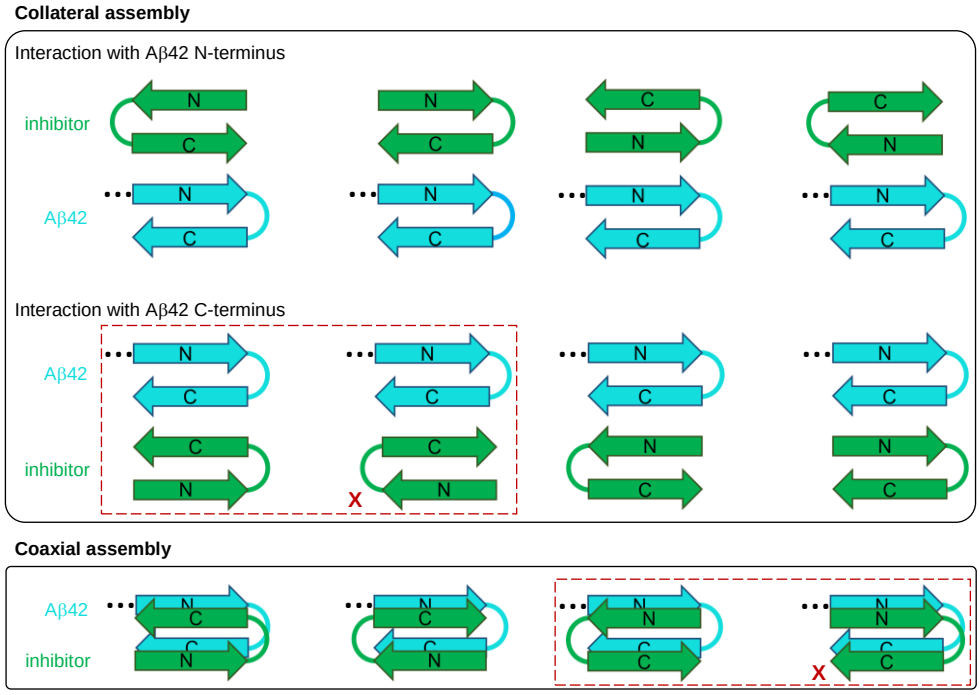

Figure 5-9: Possible hetero-dimeric building units for U-shaped Aβ42 and inhibitor folds in collateral and coaxial heterofibril assemblies. Different possible arrangements of U-shaped inhibitor with Aβ42's N-terminus or C-terminus or both (coaxial assemblies) are shown. Dots at the Aβ42 N-terminus indicate the sequence part that is not part of homomeric Aβ42 fibrils. Red boxes highlight structural arrangements fitting best with peptide array data presented in this thesis. Red crosses mark structural arrangement of Aβ42 and Aβ40 in Aβ42/Aβ40 heterofibrils as published by Cerofolini *et al.*[177]

4.15). Aβ40 was found to bind strongest to Nle3-VF's C-terminus. Assigning these findings to potential heterofibril arrangements, collateral or coaxial assemblies between Aβ42 and inhibitor involving interactions of both peptides' C-termini are the most probable ones (Figure 5-9). Cerofolini *et al.* reported two equally possible arrangements of Aβ42/Aβ40 heterofibrils both assembled from interlaced protofilaments showing either a paired or a staggered cross-β structure[177] (Figure 5-10). In both models the peptides' antiparallelly arranged C-termini interact and form the inner fibril core (Figure 5-10). A heterofibril assembly originating from two homogenous protofilaments could be excluded by the NMR data[177]. Aβ42/Nle3-VF building blocks of heterofibrils not directly involving Nle3-VF's N-terminus in the fibril core, considering additionally the peptide array data and structure suggestions from Cerofolini *et al.*, are shown in Figure 5-11. Possible arrangements include homo- and hetero-dimeric layers, interconnected by an Aβ42 molecule of the subsequent layer. Strands of the Aβ42 connector-molecule could run parallelly or antiparallelly to the subjacent C-terminal strands of the homo-/hetero-dimer units. In all such models the inhibitor N-terminus is pointing outwards the fibril core so that *N*-methylation would not disturb the fibril assembly. Furthermore, the inhibitor could interact with both Aβ42's N- and C-terminus and does so via its own C-terminus as it was indicated by peptide arrays (see chapter 4.15). The findings that ACMs inhibit Aβ42 when applied at an equimolar ratio but strong or even full inhibition is also observed when an Aβ42:inhibitor ratio of 0.5:1 is used (see Figure 7-10 in Appendix), rather supports heterofibril models involving hetero-dimeric layers in the building units than models with homo-dimeric inhibitor-layers connected by Aβ42.

In fact, it is known that only the introduction of *N*-methylations into both β-sheets fully disrupts Aβ40 fibril formation while their incorporation into only one sheet leaves the other one intact and able to form fibrils[137]. Since ACMs are derived from Aβ40 and thus share a very high sequence identity with Aβ42, inhibitors could possibly be incorporated into the heterofibril similarly as Aβ40 despite their *N*-methylations: Compared to an Aβ42/Aβ40 heterofibril, an Aβ42/Nle3-VF heterofibril would lack two H-bonds (pointing into the same direction) interconnecting Nle3-VF's N-terminus and Aβ42's N-terminus. Accordingly, an Aβ42/Nle3-LF heterofibril would lack the two H-bonds between N-terminal strands pointing to the other side.

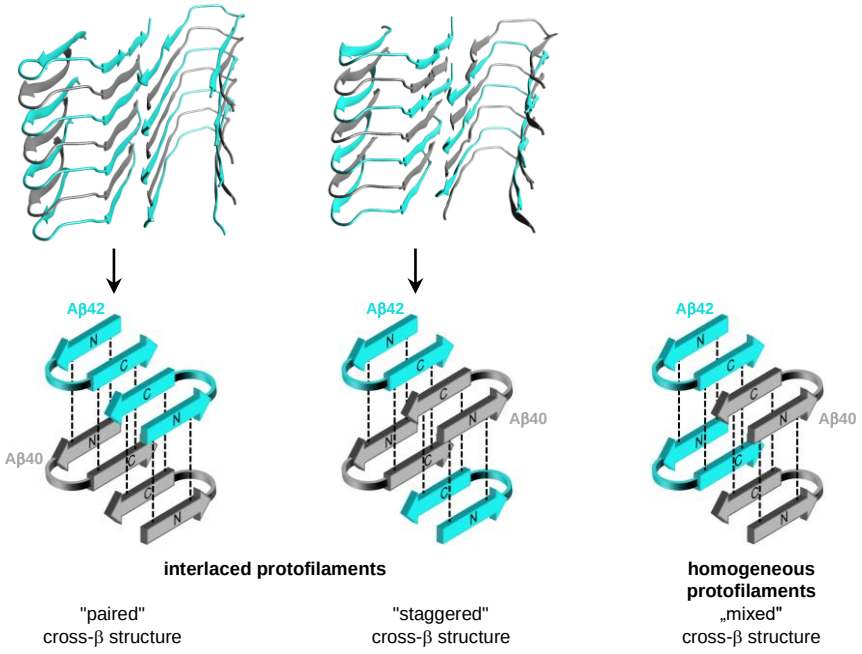

Figure 5-10: Possible arrangements of Aβ40/Aβ42 heterofibrils as reported by Cerofolini *et al.* [177] Interlaced protofilaments showing either a paired or a staggered cross-β structure were determined to by equally possible by Cerofolini *et al.*[177]. The inner fibril core is formed by the peptides' antiparallel arranged C-termini. NMR data excluded a heterofibril assembly originating from two homogenous protofilaments as shown on the right. Dashed lines indicate H-bonding between strands. The two fibril structures shown on top are the ones published by Cerofolini *et al.* (PDB entries: 6TI6 and 6TI7).

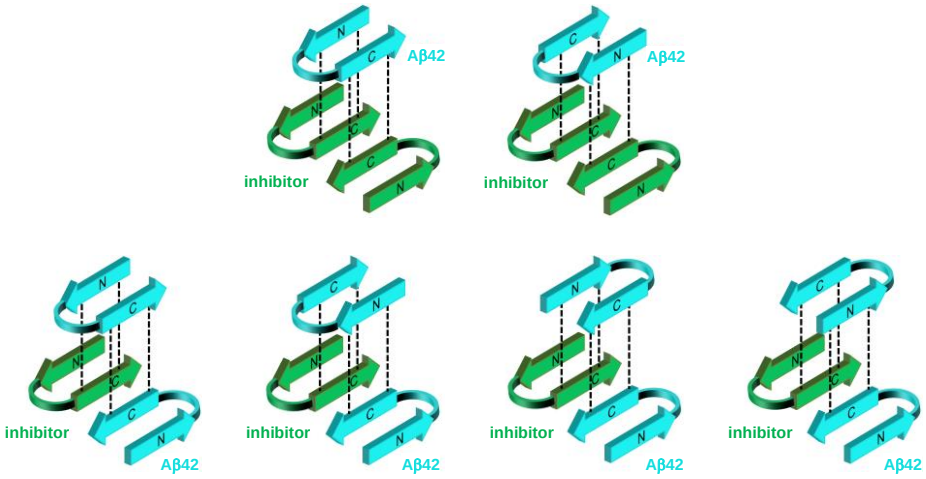

Figure 5-11: Potential building blocks of hf-Aβ42/Nle3-VF based on peptide array data of this thesis and structure suggestions from Cerofolini *et al.* [177] Possible arrangements including homo- and hetero-dimeric layers are shown. Layers are interconnected by an Aβ42 molecule of the subsequent layer. Strands of the Aβ42 connector-molecule could run parallelly or antiparallelly to the subjacent C-terminal strands of the homo-/hetero-dimer units. Inhibitor N-terminus is pointing outwards the fibril core. Dashed lines indicate H-bonding between strands.

In the Aβ42/Aβ40 heterofibril model suggested by Cerofolini *et al.* there are 23 possibilities for H-bonding of the Aβ40 N-terminus with the adjacent Aβ42 N-terminal strands (10 upwards, 13 downwards) (Figure 5-12). Thus, the lack of two of them might not be enough to fully disrupt the fibril assembly when assuming that the other H-bonds can be kept due to the high degree of similarity/identity between Aβ40 and ACMs. Suggested models of heterofibrils assembled by Aβ42 and Nle3-VF and Nle3-LF are depicted in Figure 5-13. Homo- and hetero-dimeric fibril layers were considered as proposed by Cerofolini *et al.*[177] for Aβ42/Aβ40 heterofibrils.

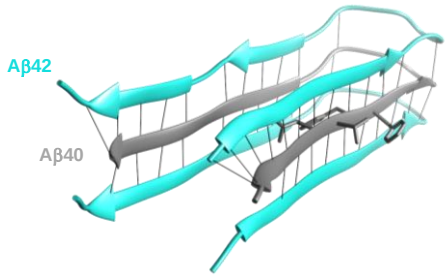

Figure 5-12: H-bonding in Aβ40/Aβ42 heterofibrils. A part of the Aβ40/Aβ42 heterofibril model published by Cerofolini *et al.*[177] is shown (PDB entry: 6TI6). Hydrogen bonding between Aβ40 and Aβ42 molecules is indicated by black lines. Side chains of region 17LVFF20 in Aβ40 are shown in stick representation.

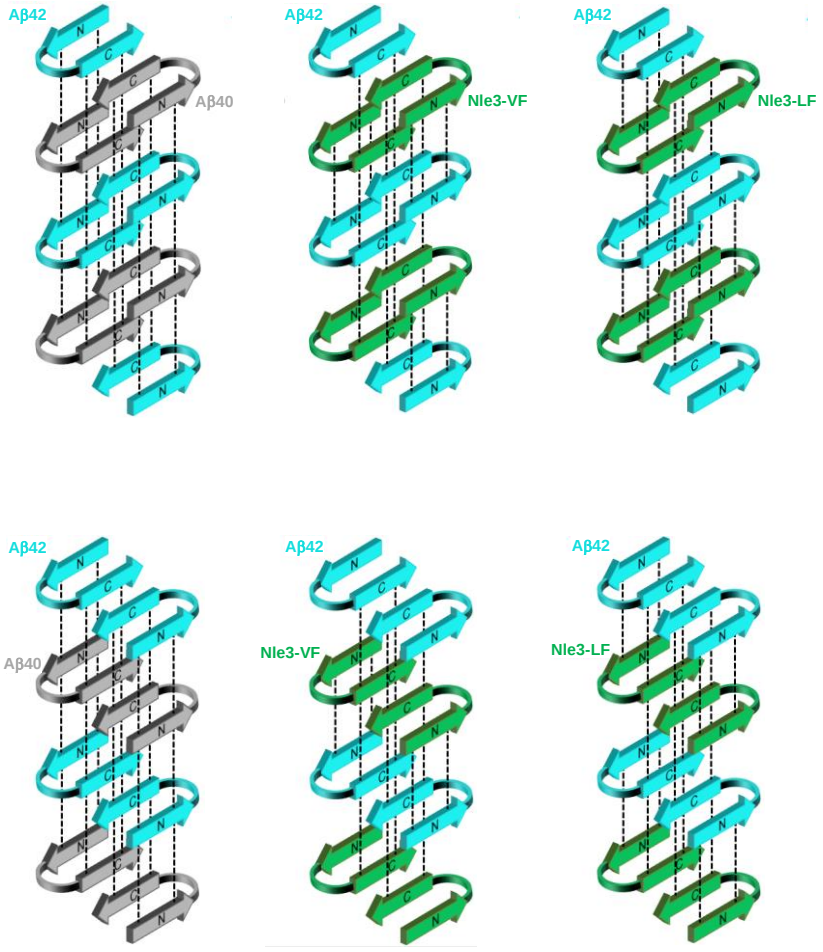

Figure 5-13: Suggested models of heterofibrils formed by Nle3-VF and Nle3-LF. Top images show potential heterofibrils assembled from hetero-dimeric building layers, bottom images show potential heterofibrils assembled from homo-dimeric building layers. Corresponding arrangement in Aβ40/Aβ42 heterofibrils as published by Cerofolini *et al.*[177] are depicted on the left. Dashed lines indicate H-bonding between strands. For clarity, not all possibly H-bonds are shown but only two representative per strand. Due to the *N*-methylations in the inhibitors' N-termini, Aβ42/inhibitor heterofibrils lack 2 positions for structure-stabilising H-bonding, indicated by the absence of dashed lines compared to the Aβ40/Aβ42 heterofibril model.

Of note, peptide array experiments indicated similar Aβ42/ADP interaction interfaces for Nle3-VF and VGS-VF that shares the same *N*-methylation with Nle3-VF but comprises a different linker sequence, and Nle3-GG that shares the same linker sequence with Nle3-VF but carries its *N*-methylation pair C-terminally. This is most likely due to the fact that both peptides are not complete non-inhibitors but show some partial inhibitory effects toward Aβ42 (see chapter 4.10.2). Also, elongated heterofibrils could be at least in part be assembled with them (see Figure 7-51 in Appendix). Thus, they might also be able to establish similar interaction interfaces with Aβ42 as Nle3-VF, but these are possibly weaker or less favourable. For Nle3-GG, the reduced inhibitory potential might be explained by the fact that its *N*-methylations are located in the C-terminus, the inner core of the potential heterofibril. A loss of two stabilising H-bonds might therefore be more dramatic. Additionally, Nle3-GG is more structurally disordered than Nle3-VF (at 5 µM) judged by CD (Figure 5-14) but this also holds true for Nle3-LF. Nevertheless, if structural disorder is induced by the *N*-methylations in the corresponding peptide segment, C-terminal disorder might be of higher impact than N-terminal disorder due to the involvement of the C-terminus in the potential heterofibril core. Also VGS-VF is less structured than Nle3-VF (Figure 5-14) and might therefore be less well integratable into the heterofibril, resulting in a reduced inhibitory potential. Since it differs from Nle3-VF only in its LTS, it is conceivable that the three norleucine residues comprising the LTS in Nle3-VF undergo hydrophobic interactions which additionally stabilise the heterofibril assembly.

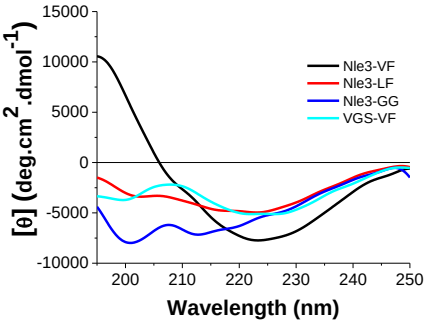

Figure 5-14: Structure comparison of Nle3-VF, Nle3-LF, Nle3-GG and VGS-VF by CD. CD spectra of 5 µM peptides were recorded in 1xb containing 1 % HFIP, pH 7.4. Baseline signals were subtracted from all measurements.

5.6 Properties of IAPP/ACM and Aβ42/ACM heterofibrils

5.6.1 Fibrillar IAPP/ACM and Aβ42/ACM co-assemblies do not bind ThT

Various properties of hf-IAPP/ACM and hf-Aβ42/ACM were investigated during this thesis with the aim to identify heterofibril-specific and/or potentially beneficial features distinguishing heterofibrils from fibrils formed by pure IAPP or Aβ42, respectively. One of the first observations that were made for heterofibrils was the fact that they do not bind ThT (see chapters 4.8 and 4.14). ThT is known to bind to the cross-β structure of amyloid fibrils and to enhance its fluorescence thereby significantly[192,193]. Therefore, the dye is frequently used to monitor and follow amyloid fibril formation. The most commonly accepted explanation to this significant increase in quantum yield is that rotational freedom about the carbon-carbon bond

is lost upon binding of ThT to channel-like motifs or grooves formed by side chains on the surface of cross-β amyloid fibrils, thereby enhancing fluorescence emission[157]. However, the exact correlation between ThT fluorescence intensity, quantum yields, spectral shifts, and its assumed binding mode is rather complex and not entirely understood yet[194]. For instance, Lindberg *et al.* demonstrated that ThT emission intensity can differ substantially even when it is bound to amyloid fibrils formed by the two highly similar Aβ isoforms Aβ40 and Aβ42[195]. They showed that the total emission intensity largely depends on binding site availability, whereas the quantum yield depends on the exact nature of the preferred fibril binding site. Another investigation by Sidhu *et al.* revealed that two chemically identical but morphologically distinct αSynuclein fibril polymorphs present type-specific ThT intensity behaviour despite similar β-sheet contents[196]. This study shows the high specificity of fibril-ThT interactions for fibril morphology. Although ThT binds an extraordinary variety of amyloid[197] it possesses e. g. some level of amino acid sequence specificity, and ThT binding sites show specific size requirements[194].

If ThT binding and fluorescence intensity can substantially vary between fibrils formed from two isoforms of the same peptide (Aβ40 vs. Aβ42[195]) or even between fibrils formed from the same peptide but with different morphologies (αSynuclein[196]), it is reasonable to conclude that heterogenic fibril formation by peptides from two different sources (IAPP & Aβ-derived inhibitors) might have even a higher impact on ThT binding an that also ThT reactivity of Aβ42/ACM heterofibrils can be influenced although both peptides originate from the same source (Aβ42 vs. Aβ40). The heterogenic composition of hf-IAPP/ACM and hf-Aβ42/ACM might change ThT binding sites in size, composition or yet unknown important features or lead to a re-arrangement in fibril morphologies in a way such that ThT binding is unfavoured. Nevertheless, some other examples of fibrillar co-assemblies – assembled from peptides of the same but also from different sources – have been published already, e. g. IAPP/rat-IAPP[164], Aβ42/Aβ(14-23)-derivatives[188], Aβ40/Aβ42[177], Aβ/IAPP[84], and αSynuclein/tau[166], but to the best of my knowledge, all of them were ThT-reactive.

Another explanation for the loss of ThT binding of amyloid fibrils in presence of inhibitors would of course be the competition of binding sites. As an example, the antibiotic rifampicin can be invoked, which was initially believed to be a potent IAPP inhibitor but was later disclosed to not prevent amyloid fibril formation by IAPP but does interfere with fibril-ThT interactions[198]. This possibility was ruled out by several control experiments for the IAPP/ACM and Aβ42/ACM fibrils discovered in this thesis and their heterogenic nature was irrevocably proven in addition by 2-PM, CLSM, FLIM-FRET and IG-TEM.

5.6.2 Fibrillar IAPP/ACM and Aβ42/ACM co-assemblies are non-toxic and easy degradable

Despite that mixing of Aβ42 or IAPP with ACMs still leads to the formation of fibrils instead of amorphous aggregates, these fibrillar co-assemblies were found to be non-toxic and to bear additional advantageous features (see chapters 4.8 and 4.14). Thus, inhibitors can displace detrimental amyloid fibril formation of IAPP and Aβ42 by heterofibril formation and thereby

“trapping” them in a beneficial structural arrangement. While amyloid fibrils were initially believed to constitute the toxic forms of Aβ and IAPP[199], subsequent studies indicated that it is rather the small, oligomeric IAPP and Aβ species (forming as intermediates during aggregation) instead of fibrils that constitute the harmful species[200,201], but this issue is still debated[202,203]. Increasing fibril stability by fibril-binding compounds and thereby shifting the equilibrium from oligomers to fibrils, has already been proposed as measure to decrease Aβ42 toxicity[204]. Thus, if fibrils can act as protective reservoirs that scavenge and store potentially toxic oligomers, accelerating and/or enhancing fibril formation could be a strategy to protect from IAPP and Aβ toxicity. ACMs are assumed to work in a very similar manner: by interacting with prefibrillar IAPP species, ACMs form heterocomplexes that are converted into non-toxic heterfibrils/-nanofibers and thereby hinder IAPP from cytotoxic self-assembly processes. In case of Aβ42, ACMs do not only interact with prefibrillar species but also with mature fibrils and induce heterofibril/-nanofiber formation and elongation, a process that traps and stores potentially toxic Aβ42 species in non-toxic structures.

Examples of peptide-based compounds leading to an enhancement of Aβ fibrillation and thereby to a reduced cytotoxicity are scarce but existing[205,206]. For instance, Ghanta *et al.* used a hybrid peptide created by combining the N-terminal Aβ segment Aβ(15-25) as recognition element with an oligolysine attachment as disrupting element to specifically recognise Aβ and alter its self-assembly. This peptide (named H2) did not prevent fibril formation but did change fibril morphology and completely suppressed Aβ toxicity. Of note, ThT fluorescence dropped simultaneously by a factor of 2 in the mixture. According to the authors, this result “suggests that ThT fluorescence may serve as an effective means of identifying inhibitors of Aβ toxicity [even though] complete inhibition of ThT fluorescence […] was clearly not a prerequisite for complete inhibition of toxicity”[205]. The authors concluded that their hybrid peptide compound acts by disrupting fibril elongation processes by binding to the growing Aβ fibril. Heterofibril formation between Aβ and the hybrid peptide was of course not considered or investigated but nevertheless findings resembled the ones presented in this thesis for hf-Aβ42/ACM, namely, a drop in ThT reactivity and a change in fibril morphology.

Several small molecule compounds have also been shown to decrease the toxic effect of Aβ or IAPP by stimulating their fibrillation[207-212], for example, sulfonated dendrimers or glycosaminoglycans in case of IAPP. Civitelli *et al.* reported that the luminescent oligothiophene p-FTAA decreases Aβ42 toxicity via accelerating the formation of non-toxic and insoluble Aβ42 fibrils[210]. In contrast to the findings presented in this thesis for hf-Aβ42/ACM (and also hf-IAPP/ACM), their fibrils were more resistant to proteinase K digestion than pure fAβ42 and not vice versa. The authors suggested that increased proteolytic resistance is a beneficial feature, since by accelerating the fibril formation process and thereby sequestering toxic Aβ species into more stable and inert fibrils, p-FTAA could hypothetically shift the Aβ species equilibrium toward plaques[210]. Conversely, induction of the formation of hf-Aβ42/ACM or hf-IAPP/ACM which are less proteolytically stable than their homomeric counterpart fAβ42 or fIAPP could be considered disadvantageous. On the other hand, several studies confirmed a significant correlation between antemortem cognitive impairment and Aβ plaque load[213]. Thus, plaque formation might not be exclusively beneficial or might only have a protecting

effect until a certain time point in disease progression. Still, the exact role of Aβ plaques in AD pathogenesis or rather the clinicopathological correlation of dementia severity and plaque formation is debated[213,214].

Importantly, work by Yuan Tian (Prof. J. Bernhagen group) demonstrated that both hf-IAPP/ACM and hf-Aβ42/ACM are better phagocytosed by bone marrow-derived macrophages and microglia compared to fIAPP and fAβ42[140]. Thus, induction of heterofibril formation with Aβ42 and IAPP by ACMs could be beneficial in more than one way, when considering that they also proved to be better degradable (see chapters 4.8 and 4.14). First, the formation of potentially cytotoxic oligomeric Aβ and IAPP species is avoided since the molecules are sequestered in non-toxic fibrillar species (or plaques in a prospective medical application). Second, these heterofibrils/plaques could be less persisting as they are easier to degrade and become phagocytosed. Thus, clearence of potentially toxic or harmful plaques would be more efficient. Of course, a number of studies should be done in order to further develop ACMs as candidates for anti-amyloid drugs.

Additionally, properties like non-toxicity, proteolytic degradability, and easy disassembly are in contrast to “pathogenic amyloids” often observed in so-called reversible “functional amyloids” and are crucial to maintain/exert their biological function, controlled formation, and reversibility[5,215,216]. Hence, it might be speculated that additionally to pathogenic IAPP/Aβ hetero-amyloids also other hetero-amyloid structures exist which might naturally prevent cytotoxic self-assembly and related cell damage caused by both peptides. Such structures might be efficiently mimicked by IAPP/ACM heterofibrillar assemblies, in particular since ACMs were intended to imitate the Aβ amyloid core in a benign alternative fold by design.

5.7 Suggested mechanism for the inhibition of fIAPP-cross-seeded Aβ42 by ACMs

Cross-seeding of Aβ42 by fIAPP accelerates amyloid self-assembly of Aβ42[86,87]. Reciprocal induction and promotion of the two polypeptides’ co-aggregation might be also disease-relevant and provides a potential molecular link for T2D and AD onset and pathologies[89-91]. ThT binding studies showed that ACMs can efficiently suppress fIAPP-mediated cross-seeding of Aβ42 (see chapter 4.13.2 and 4.13.3). Since preliminary trials showed that Aβ42 at 5 µM could not be cross-seeded by 10 % or 20 % fIAPP these experiments were conducted with 10 µM Aβ42. Usage of two different assay setups revealed that inhibition is even more effective when Nle3-VF is first mixed with fIAPP to allow coating of the fibril surface before addition to Aβ42. Additional 2-PM studies showed that fIAPP-cross-seeded Aβ42 solutions contained large ternary nanofibre co-assemblies and divers roundish complexes consisting of Aβ42/IAPP/Nle3-VF or Aβ42/Nle3-VF in presence of Nle3-VF.

Based on the presented results, the following mechanism on how Nle3-VF is inhibiting fIAPP-mediated cross-seeding of Aβ42 is suggested: In a solution of 5 µM Aβ42 (used for non-seeded inhibition studies), Aβ42 is present in its monomeric or small oligomeric form in the beginning. By time, these species further aggregate and form fibrils. In presence of Nle3-VF, Aβ42 is sequestered from this pathway and forms hetero-aggregates and later on fibrillar co-

assemblies with the inhibitor, respectively (Figure 5-15a). A solution containing 10 µM Aβ42 might not only consist of small Aβ42 species but also contain some larger aggregates and/or pre-fibrillar species (Figure 5-15b). In presence of Nle3-VF, small Aβ42 species might still be sequestered from their usual aggregation pathway while larger aggregates might stay partly "free" to form Aβ42 fibrils in case Nle3-VF preferentially interacts with smaller species. This suggestion is supported by the observation that inhibition by Nle3-VF gets significantly worse when 10 µM Aβ42 is used instead of 5 µM (see Figure 4-88 in chapter 4.13.3). In assay "setup 1", Aβ42 is first mixed with Nle3-VF, meaning that complex formation of small Aβ42 species with Nle3-VF can take place before IAPP fibrils are added. Since the molar excess of Nle3-VF is only 2-fold it can be assumed that most Nle3-VF molecules are complexed with these species. The "remaining" larger species would then at least in part be available for cross-seeding by fIAPP, explaining why ThT signal rise faster in cross-seeded then in unseeded mixtures (Figure 4-89a, Figure 5-15c). Triple-coloured nanofibers as observed via 2-PM could form both by interaction of fIAPP seeds with Aβ42/Nle3-VF hetero-aggregates or heterofibrils/-nanofibers and by interaction of cross-seeded Aβ42 fibrils with other species in the solution (Figure 5-15). In assay "setup 2", IAPP fibrils are treated with Nle3-VF before addition to Aβ42. Since Nle3-VF is in 10-fold excess of IAPP fibrils and generally only a sub-stoichiometric inhibitor amount is necessary to block secondary nucleation on the fibril surface[155,156], it can be assumed that a large portion of Nle3-VF molecule is still free for interaction the moment the Nle3-VF/seed solution is added to Aβ42. The remaining Nle3-VF molecules can therefore maybe complex with small Aβ42 species and suppress homofibril formation while larger Aβ42 species cannot be cross-seeded anymore by the IAPP fibrils since their surface is blocked by inhibitor (Figure 5-15d). In this way, Aβ42 is completely blocked from fibril formation and full inhibition is observed in ThT binding assays. The triple-coloured nanofibers which were seen via 2-PM could originate from interaction of the Nle3-VF-coated IAPP fibrils with Aβ42 aggregates or interactions with Aβ42/Nle3-VF hetero-aggregates or heterofibrils/-nanofibers.

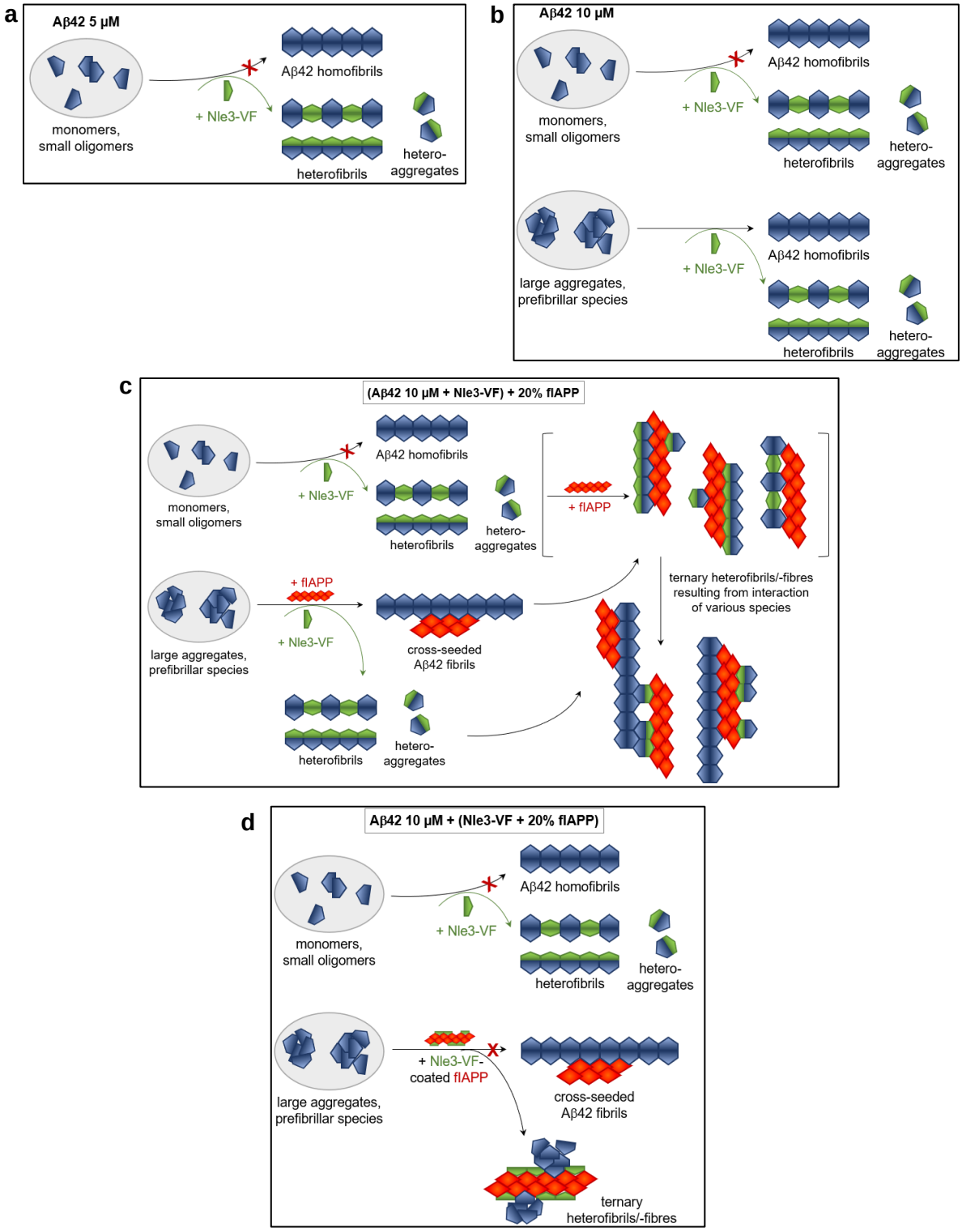

Figure 5-15: Suggested mechanism of Nle3-VF's inhibition of fIAPP-cross-seeded Aβ42 fibril formation. (**a**) Inhibition of 5 µM Aβ42. Aβ42 is present in monomeric or small oligomeric forms with which Nle3-VF strongly interacts to built heterocomplexes and heterofibrils/ -nanofibers later on. (**b**) Inhibition of 10 µM Aβ42. Aβ42 solutions do not only contain small species but also larger or pre-fibrillar species. Nle3-VF might preferentially bind smaller species to form heterocomplexes and after heterofibrils/ -nanofibers. Larger species might remain partly free and can associate into Aβ42 homofibrils. (**c**) Inhibition of fIAPP-cross-seeded Aβ42 when IAPP seeds were added to preformed Aβ42/Nle3-VF complexes ("setup 1"). Nle3-VF preferentially interacts with small Aβ42 species while larger species can be cross-seeded by IAPP fibrils. Thus, the inhibitory effect is smaller than in unseeded conditions. Ternary nanofibers observed in 2-PM studies could originate from various interactions of the different fibrillar species present in the mixture. (**d**) Inhibition of fIAPP-cross-seeded Aβ42 when IAPP fibrils were pre-treated with Nle3-VF before addition to Aβ42 ("setup 2"). IAPP seeds are rendered seeding-incompetent since Nle3-VF is bound to their surface. Excess amounts of Nle3-VF not bound to the fibril surface can additionally interact with small Aβ42 species present in the solution, leading to a dual effect and to strong inhibition under these conditions. Ternary nanofibers observed in 2-PM studies could be assembled by addition of Aβ42 onto the coated fIAPP surface or by multiple other possible interactions of the different species present in the mixture. An adapted version of this figure is part of a figure in reference [140].

6 Conclusions

Designed Aβ amyloid core mimics (ACMs) are potent inhibitors of both IAPP and Aβ amyloidogenicity and exert their inhibitory effect on IAPP and Aβ42 by co-assembling with the two polypeptides into fibrils and supramolecular hetero-nanofiber structures (hf-IAPP/ACM, hf-Aβ42/ACM). Hf-IAPP/ACM and hf-Aβ42/ACM are non-toxic, less thermostable, easier degradable by proteinase K, easier phagocytosed by BMDMs and microglia cells, and seeding-incompetent in contrast to fIAPP and fAβ42.

In conclusion, this thesis provides a novel class of rationally designed peptides that are highly effective in suppressing both amyloid self-assembly and reciprocal cross-seeding of IAPP and Aβ42. Their properties thus expand their functional profile over previously reported cross-amyloid inhibitors. Therefore, ACMs are promising leads for anti-amyloid drugs applicable in the two strongly related protein misfolding diseases T2D and AD as future “two-in-one” strategy targeting both diseases. Additionally, this thesis suggests that inducing the formation of non-toxic and degradable fibrillar co-assemblies of amyloid polypeptides with designed peptides could be a feasible molecular approach to hinder their pathogenic amyloid self-assembly.

7 Appendix

7.1 SPPS protocols

Table 7-1: Synthesis plan of region 27-40 for ADPs without C-terminal *N*-methylations. Abbreviations: AA, amino acid; eq., equivalents; Fmoc, fluorenylmethoxycarbonyl; HBTU, 2-(1H-Benzotriazol-1-yl)-1,1,3,3-tetramethyluronium-hexafluorophosphate; HOBt, Hydroxybenzotriazole; HATU, 2-(7-aza-1H-benzotriazole-1-yl)-1,1,3,3-tetramethyluronium-hexafluorophosphate; DIEA, *N,N*-diisopropylethylamine; Boc, tert-butyloxycarbonyl; Trt, trityl. Amino acids are abbreviated with 3-letter code.

Position	Amino acid (AA)	Number of couplings		AA excess	Activator excess	Base excess	Coupling time
40	Fmoc-Val-OH	1	1	3 eq.	3 eq. HBTU 3 eq. HOBt	6 eq. DIEA	2 h
39	Fmoc-Val-OH	2	1 2	3 eq. 3 eq.	3 eq. HBTU 3 eq. HBTU	4.5 eq. DIEA 4.5 eq. DIEA	40 min 40 min
38	Fmoc-Gly-OH	2	1 2	3 eq. 3 eq.	3 eq. HBTU 3 eq. HBTU	4.5 eq. DIEA 4.5 eq. DIEA	40 min 40 min
37	Fmoc-Gly-OH	2	1 2	3 eq. 3 eq.	3 eq. HBTU 3 eq. HBTU	4.5 eq. DIEA 4.5 eq. DIEA	40 min 40 min
36	Fmoc-Val-OH	2	1 2	3 eq. 3 eq.	3 eq. HBTU 3 eq. HBTU	4.5 eq. DIEA 4.5 eq. DIEA	40 min 40 min
35	Fmoc-Nle-OH	2	1 2	3 eq. 3 eq.	3 eq. HBTU 3 eq. HBTU	4.5 eq. DIEA 4.5 eq. DIEA	40 min 40 min
34	Fmoc-Leu-OH	2	1 2	3 eq. 3 eq.	3 eq. HBTU 3 eq. HBTU	4.5 eq. DIEA 4.5 eq. DIEA	40 min 40 min
33	Fmoc-Gly-OH	2	1 2	3 eq. 3 eq.	3 eq. HBTU 3 eq. HBTU	4.5 eq. DIEA 4.5 eq. DIEA	40 min 40 min
32	Fmoc-Ile-OH	3	1 2 3	3 eq. 3 eq. 3 eq.	3 eq. HATU 3 eq. HBTU 3 eq. HBTU	4.5 eq. DIEA 4.5 eq. DIEA 4.5 eq. DIEA	40 min 40 min 40 min
31	Fmoc-Ile-OH	3	1 2 3	3 eq. 3 eq. 3 eq.	3 eq. HATU 3 eq. HATU 3 eq. HBTU	4.5 eq. DIEA 4.5 eq. DIEA 4.5 eq. DIEA	40 min 40 min 40 min
30	Fmoc-Ala-OH	2	1 2	3 eq. 3 eq.	3 eq. HBTU 3 eq. HBTU	4.5 eq. DIEA 4.5 eq. DIEA	40 min 40 min
29	Fmoc-Gly-OH	2	1 2	3 eq. 3 eq.	3 eq. HBTU 3 eq. HBTU	4.5 eq. DIEA 4.5 eq. DIEA	40 min 40 min
28	Fmoc-Lys(Boc)-OH	2	1 2	3 eq. 3 eq.	3 eq. HBTU 3 eq. HBTU	4.5 eq. DIEA 4.5 eq. DIEA	40 min 40 min
27	Fmoc-Asn(Trt)-OH	2	1 2	3 eq. 3 eq.	3 eq. HBTU 3 eq. HBTU	4.5 eq. DIEA 4.5 eq. DIEA	40 min 40 min

Table 7-2: Synthesis plan of region 27-40 for ADPs with C-terminal Gly29Gly33 *N*-methylations. Abbreviations: AA, amino acid; eq., equivalents; Fmoc, fluorenylmethoxycarbonyl; HBTU, 2-(1H-Benzotriazol-1-yl)-1,1,3,3-tetramethyluronium-hexafluorophosphate; HOBt, Hydroxybenzotriazole; HATU, 2-(7-aza-1H-benzotriazole-1-yl)-1,1,3,3-tetramethyluronium-hexafluorophosphate; DIEA, *N,N*-diisopropylethylamine; Boc, tert-butyloxycarbonyl; Trt, trityl; NMe, *N*-methylation. Amino acids are abbreviated with 3-letter code.

Position	Amino acid (AA)	Number of couplings		AA excess	Activator excess	Base excess	Coupling time
40	Fmoc-Val-OH	1	1	3 eq.	3 eq. HBTU 3 eq. HOBt	6 eq. DIEA	2 h
39	Fmoc-Val-OH	2	1	3 eq.	3 eq. HBTU	4.5 eq. DIEA	40 min
			2	3 eq.	3 eq. HBTU	4.5 eq. DIEA	40 min
38	Fmoc-Gly-OH	2	1	3 eq.	3 eq. HBTU	4.5 eq. DIEA	40 min
			2	3 eq.	3 eq. HBTU	4.5 eq. DIEA	40 min
37	Fmoc-Gly-OH	2	1	3 eq.	3 eq. HBTU	4.5 eq. DIEA	40 min
			2	3 eq.	3 eq. HBTU	4.5 eq. DIEA	40 min
36	Fmoc-Val-OH	2	1	3 eq.	3 eq. HBTU	4.5 eq. DIEA	40 min
			2	3 eq.	3 eq. HBTU	4.5 eq. DIEA	40 min
35	Fmoc-Nle-OH	2	1	3 eq.	3 eq. HBTU	4.5 eq. DIEA	40 min
			2	3 eq.	3 eq. HBTU	4.5 eq. DIEA	40 min
34	Fmoc-Leu-OH	2	1	3 eq.	3 eq. HBTU	4.5 eq. DIEA	40 min
			2	3 eq.	3 eq. HBTU	4.5 eq. DIEA	40 min
33	Fmoc-NMeGly-OH	2	1	4 eq.	4 eq. HATU	6 eq. DIEA	1 h
			2	3 eq.	3 eq. HBTU	4.5 eq. DIEA	40 min
32	Fmoc-Ile-OH	2	1	6 eq.	6 eq. HATU	9 eq. DIEA	1 h
			2	3 eq.	3 eq. HBTU	4.5 eq. DIEA	40 min
31	Fmoc-Ile-OH	2	1	3 eq.	3 eq. HBTU	4.5 eq. DIEA	40 min
			2	3 eq.	3 eq. HBTU	4.5 eq. DIEA	40 min
30	Fmoc-Ala-OH	2	1	3 eq.	3 eq. HBTU	4.5 eq. DIEA	40 min
			2	3 eq.	3 eq. HBTU	4.5 eq. DIEA	40 min
29	Fmoc-NMeGly-OH	2	1	4 eq.	4 eq. HATU	6 eq. DIEA	1 h
			2	3 eq.	3 eq. HATU	4.5 eq. DIEA	40 min
28	Fmoc-Lys(Boc)-OH	2	1	6 eq.	6 eq. HATU	9 eq. DIEA	1 h
			2	6 eq.	6 eq. HATU	9 eq. DIEA	40 min
27	Fmoc-Asn(Trt)-OH	2	1	3 eq.	3 eq. HBTU	4.5 eq. DIEA	40 min
			2	3 eq.	3 eq. HBTU	4.5 eq. DIEA	40 min

Table 7-3: Synthesis plan of region 27-40 for ADPs with C-terminal Gly29Ile31 *N*-methylations. Abbreviations: AA, amino acid; eq., equivalents; Fmoc, fluorenylmethoxycarbonyl; HBTU, 2-(1H-Benzotriazol-1-yl)-1,1,3,3-tetramethyluronium-hexafluorophosphate; HOBt, Hydroxybenzotriazole; HATU, 2-(7-aza-1H-benzotriazole-1-yl)-1,1,3,3-tetramethyluronium-hexafluorophosphate; DIEA, *N,N*-diisopropylethylamine; Boc, tert-butyloxycarbonyl; Trt, trityl; NMe, *N*-methylation. Amino acids are abbreviated with 3-letter code.

Position	Amino acid (AA)	Number of couplings		AA excess	Activator excess	Base excess	Coupling time
40	Fmoc-Val-OH	1	1	3 eq.	3 eq. HBTU 3 eq. HOBt	6 eq. DIEA	2 h
39	Fmoc-Val-OH	2	1	3 eq.	3 eq. HBTU	4.5 eq. DIEA	40 min
			2	3 eq.	3 eq. HBTU	4.5 eq. DIEA	40 min
38	Fmoc-Gly-OH	2	1	3 eq.	3 eq. HBTU	4.5 eq. DIEA	40 min
			2	3 eq.	3 eq. HBTU	4.5 eq. DIEA	40 min
37	Fmoc-Gly-OH	2	1	3 eq.	3 eq. HBTU	4.5 eq. DIEA	40 min
			2	3 eq.	3 eq. HBTU	4.5 eq. DIEA	40 min
36	Fmoc-Val-OH	2	1	3 eq.	3 eq. HBTU	4.5 eq. DIEA	40 min
			2	3 eq.	3 eq. HBTU	4.5 eq. DIEA	40 min
35	Fmoc-Nle-OH	2	1	3 eq.	3 eq. HBTU	4.5 eq. DIEA	40 min
			2	3 eq.	3 eq. HBTU	4.5 eq. DIEA	40 min
34	Fmoc-Leu-OH	2	1	3 eq.	3 eq. HBTU	4.5 eq. DIEA	40 min
			2	3 eq.	3 eq. HBTU	4.5 eq. DIEA	40 min
33	Fmoc-Gly-OH	2	1	3 eq.	3 eq. HBTU	4.5 eq. DIEA	40 min
			2	3 eq.	3 eq. HBTU	4.5 eq. DIEA	40 min
32	Fmoc-Ile-OH	2	1	3 eq.	3 eq. HBTU	4.5 eq. DIEA	40 min
			2	3 eq.	3 eq. HBTU	4.5 eq. DIEA	40 min
31	Fmoc-NMeIle-OH	2	1	4 eq.	4 eq. HATU	6 eq. DIEA	1 h
			2	3 eq.	3 eq. HBTU	4.5 eq. DIEA	40 min
30	Fmoc-Ala-OH	5	1	6 eq.	6 eq. HATU	9 eq. DIEA	1 h
			2	6 eq.	6 eq. HATU	9 eq. DIEA	1 h
			3	6 eq.	6 eq. HATU	9 eq. DIEA	1 h
			4	6 eq.	6 eq. HATU	9 eq. DIEA	1 h
			5	6 eq.	6 eq. HATU	9 eq. DIEA	1 h
29	Fmoc-NMeGly-OH	2	1	4 eq.	4 eq. HATU	6 eq. DIEA	1 h
			2	3 eq.	3 eq. HBTU	4.5 eq. DIEA	40 min
28	Fmoc-Lys(Boc)-OH	2	1	6 eq.	6 eq. HATU	9 eq. DIEA	1 h
			2	3 eq.	3 eq. HBTU	4.5 eq. DIEA	40 min
27	Fmoc-Asn(Trt)-OH	2	1	3 eq.	3 eq. HBTU	4.5 eq. DIEA	40 min
			2	3 eq.	3 eq. HBTU	4.5 eq. DIEA	40 min

Table 7-4: Synthesis plan for the different loop tripeptide segments (LTS) in region Aβ(24-26) of ADPs. Abbreviations: AA, amino acid; eq., equivalents; Fmoc, fluorenylmethoxycarbonyl; HBTU, 2-(1H-Benzotriazol-1-yl)-1,1,3,3-tetramethyluronium-hexafluorophosphate; HATU, 2-(7-aza-1H-benzotriazole-1-yl)-1,1,3,3-tetramethyluronium-hexafluorophosphate; DIEA, *N,N*-diisopropylethylamine; tBu, tert-butyl; Pbf, 2,2,4,6,7-pentamethyldihydrobenzofuran-5-sulfonyl. Amino acids are abbreviated with 3-letter code.

Position	Amino acid (AA)	Number of couplings		AA excess	Activator excess	Base excess	Coupling time
ValGlySer (VGS, native) linker							
26	Fmoc-Ser(tBu)-OH	2	1	3 eq.	3 eq. HBTU	4.5 eq. DIEA	40 min
			2	3 eq.	3 eq. HBTU	4.5 eq. DIEA	40 min
25	Fmoc-Gly-OH	2	1	3 eq.	3 eq. HBTU	4.5 eq. DIEA	40 min
			2	3 eq.	3 eq. HBTU	4.5 eq. DIEA	40 min
24	Fmoc-Val-OH	2	1	3 eq.	3 eq. HBTU	4.5 eq. DIEA	40 min
			2	3 eq.	3 eq. HBTU	4.5 eq. DIEA	40 min
ArgArgArg (RRR) linker							
26	Fmoc-Arg(Pbf)-OH	2	1	3 eq.	3 eq. HATU	4.5 eq. DIEA	40 min
			2	3 eq.	3 eq. HATU	4.5 eq. DIEA	40 min
25	Fmoc-Arg(Pbf)-OH	3	1	6 eq.	6 eq. HATU	9 eq. DIEA	40 min
			2	3 eq.	3 eq. HATU	4.5 eq. DIEA	40 min
			3	3 eq.	3 eq. HATU	4.5 eq. DIEA	40 min
24	Fmoc-Arg(Pbf)-OH	3	1	6 eq.	6 eq. HATU	9 eq. DIEA	40 min
			2	6 eq.	6 eq. HATU	9 eq. DIEA	40 min
			3	6 eq.	6 eq. HATU	9 eq. DIEA	40 min
GlyGlyGly (GGG) linker							
26	Fmoc-Gly-OH	2	1	3 eq.	3 eq. HBTU	4.5 eq. DIEA	40 min
			2	3 eq.	3 eq. HBTU	4.5 eq. DIEA	40 min
25	Fmoc-Gly-OH	3	1	3 eq.	3 eq. HATU	4.5 eq. DIEA	40 min
			2	3 eq.	3 eq. HBTU	4.5 eq. DIEA	40 min
			3	3 eq.	3 eq. HBTU	4.5 eq. DIEA	40 min
24	Fmoc-Gly-OH	3	1	3 eq.	3 eq. HATU	4.5 eq. DIEA	40 min
			2	3 eq.	3 eq. HATU	4.5 eq. DIEA	40 min
			3	3 eq.	3 eq. HATU	4.5 eq. DIEA	40 min
NleNleNle linker							
26	Fmoc-Nle-OH	2	1	3 eq.	3 eq. HATU	4.5 eq. DIEA	40 min
			2	3 eq.	3 eq. HATU	4.5 eq. DIEA	40 min
25	Fmoc-Nle-OH	3	1	6 eq.	6 eq. HATU	9 eq. DIEA	40 min
			2	3 eq.	3 eq. HATU	4.5 eq. DIEA	40 min
			3	3 eq.	3 eq. HATU	4.5 eq. DIEA	40 min
24	Fmoc-Nle-OH	3	1	6 eq.	6 eq. HATU	9 eq. DIEA	40 min
			2	6 eq.	6 eq. HATU	9 eq. DIEA	40 min
			3	3 eq.	3 eq. HATU	4.5 eq. DIEA	40 min
LeuLeuLeu (LLL) linker							
26	Fmoc-Leu-OH	2	1	3 eq.	3 eq. HATU	4.5 eq. DIEA	40 min
			2	3 eq.	3 eq. HATU	4.5 eq. DIEA	40 min
25	Fmoc-Leu-OH	2	1	3 eq.	3 eq. HATU	4.5 eq. DIEA	40 min
			2	3 eq.	3 eq. HATU	4.5 eq. DIEA	40 min
24	Fmoc-Leu-OH	2	1	3 eq.	3 eq. HATU	4.5 eq. DIEA	40 min
			2	3 eq.	3 eq. HATU	4.5 eq. DIEA	40 min
PhePhePhe (FFF) linker							
26	Fmoc-Phe-OH	2	1	3 eq.	3 eq. HATU	4.5 eq. DIEA	40 min
			2	3 eq.	3 eq. HATU	4.5 eq. DIEA	40 min
25	Fmoc-Phe-OH	3	1	6 eq.	6 eq. HATU	9 eq. DIEA	40 min
			2	3 eq.	3 eq. HATU	4.5 eq. DIEA	40 min
			3	3 eq.	3 eq. HATU	4.5 eq. DIEA	40 min
24	Fmoc-Phe-OH	3	1	6 eq.	6 eq. HATU	9 eq. DIEA	40 min
			2	6 eq.	6 eq. HATU	9 eq. DIEA	40 min
			3	3 eq.	3 eq. HATU	4.5 eq. DIEA	40 min

Table 7-5: Synthesis plan of region 15-23 for ADPs without N-terminal *N*-methylations. Abbreviations: AA, amino acid; eq., equivalents; Fmoc, fluorenylmethoxycarbonyl; HBTU, 2-(1H-Benzotriazol-1-yl)-1,1,3,3-tetramethyluronium-hexafluorophosphate; HATU, 2-(7-aza-1H-benzotriazole-1-yl)-1,1,3,3-tetramethyluronium-hexafluorophosphate; DIEA, *N,N*-diisopropylethylamine; Boc, tert-butyloxycarbonyl; Trt, trityl; tBu, tert-butyl. Amino acids are abbreviated with 3-letter code.

Position	Amino acid (AA)	Number of couplings		AA excess	Activator excess	Base excess	Coupling time
23	Fmoc-Asp(tBu)-OH	2	1	3 eq.	3 eq. HBTU	4.5 eq. DIEA	40 min
			2	3 eq.	3 eq. HBTU	4.5 eq. DIEA	40 min
22	Fmoc-Glu(tBu)-OH	2	1	3 eq.	3 eq. HBTU	4.5 eq. DIEA	40 min
			2	3 eq.	3 eq. HBTU	4.5 eq. DIEA	40 min
21	Fmoc-Ala-OH	2	1	3 eq.	3 eq. HBTU	4.5 eq. DIEA	40 min
			2	3 eq.	3 eq. HBTU	4.5 eq. DIEA	40 min
20	Fmoc-Phe-OH	2	1	3 eq.	3 eq. HBTU	4.5 eq. DIEA	40 min
			2	3 eq.	3 eq. HBTU	4.5 eq. DIEA	40 min
19	Fmoc-Phe-OH	2	1	3 eq.	3 eq. HATU	4.5 eq. DIEA	50 min
			2	3 eq.	3 eq. HBTU	4.5 eq. DIEA	50 min
18	Fmoc-Val-OH	2	1	3 eq.	3 eq. HATU	4.5 eq. DIEA	50 min
			2	3 eq.	3 eq. HBTU	4.5 eq. DIEA	50 min
17	Fmoc-Leu-OH	2	1	3 eq.	3 eq. HATU	4.5 eq. DIEA	50 min
			2	3 eq.	3 eq. HATU	4.5 eq. DIEA	50 min
16	Fmoc-Lys(Boc)-OH	2	1	3 eq.	3 eq. HATU	4.5 eq. DIEA	50 min
			2	3 eq.	3 eq. HATU	4.5 eq. DIEA	50 min
15	Fmoc-Gln(Trt)-OH	2	1	3 eq.	3 eq. HBTU	4.5 eq. DIEA	50 min
			2	3 eq.	3 eq. HBTU	4.5 eq. DIEA	50 min

Table 7-6: Synthesis plan of region 15-23 for ADPs with N-terminal Leu17Phe19 *N*-methylations. Abbreviations: AA, amino acid; eq., equivalents; Fmoc, fluorenylmethoxycarbonyl; HBTU, 2-(1H-Benzotriazol-1-yl)-1,1,3,3-tetramethyluronium-hexafluorophosphate; HATU, 2-(7-aza-1H-benzotriazole-1-yl)-1,1,3,3-tetramethyluronium-hexafluorophosphate; DIEA, *N,N*-diisopropylethylamine; Boc, tert-butyloxycarbonyl; Trt, trityl; tBu, tert-butyl; NMe, *N*-methylation. Amino acids are abbreviated with 3-letter code.

Position	Amino acid (AA)	Number of couplings		AA excess	Activator excess	Base excess	Coupling time
23	Fmoc-Asp(tBu)-OH	2	1	3 eq.	3 eq. HBTU	4.5 eq. DIEA	40 min
			2	3 eq.	3 eq. HBTU	4.5 eq. DIEA	40 min
22	Fmoc-Glu(tBu)-OH	2	1	3 eq.	3 eq. HBTU	4.5 eq. DIEA	40 min
			2	3 eq.	3 eq. HBTU	4.5 eq. DIEA	40 min
21	Fmoc-Ala-OH	2	1	3 eq.	3 eq. HBTU	4.5 eq. DIEA	40 min
			2	3 eq.	3 eq. HBTU	4.5 eq. DIEA	40 min
20	Fmoc-Phe-OH	2	1	3 eq.	3 eq. HBTU	4.5 eq. DIEA	40 min
			2	3 eq.	3 eq. HBTU	4.5 eq. DIEA	40 min
19	Fmoc-NMePhe-OH	2	1	6 eq.	6 eq. HATU	9 eq. DIEA	50 min
			2	3 eq.	3 eq. HATU	4.5 eq. DIEA	50 min
18	Fmoc-Val-OH	2	1	6 eq.	6 eq. HATU	9 eq. DIEA	50 min
			2	3 eq.	3 eq. HATU	4.5 eq. DIEA	50 min
17	Fmoc-NMeLeu-OH	2	1	6 eq.	6 eq. HATU	9 eq. DIEA	50 min
			2	3 eq.	3 eq. HATU	4.5 eq. DIEA	50 min
16	Fmoc-Lys(Boc)-OH	3	1	6 eq.	6 eq. HATU	9 eq. DIEA	50 min
			2	6 eq.	6 eq. HATU	9 eq. DIEA	50 min
			3	3 eq.	3 eq. HATU	4.5 eq. DIEA	50 min
15	Fmoc-Gln(Trt)-OH	2	1	3 eq.	3 eq. HATU	4.5 eq. DIEA	50 min
			2	3 eq.	3 eq. HBTU	4.5 eq. DIEA	50 min

Table 7-7: Synthesis plan of region 15-23 for ADPs with N-terminal Val18Phe20 *N*-methylations. Abbreviations: AA, amino acid; eq., equivalents; Fmoc, fluorenylmethoxycarbonyl; HBTU, 2-(1H-Benzotriazol-1-yl)-1,1,3,3-tetramethyluronium-hexafluorophosphate; HATU, 2-(7-aza-1H-benzotriazole-1-yl)-1,1,3,3-tetramethyluronium-hexafluorophosphate; DIEA, *N,N*-diisopropylethylamine; Boc, tert-butyloxycarbonyl; Trt, trityl; tBu, tert-butyl; NMe, *N*-methylation. Amino acids are abbreviated with 3-letter code.

Position	Amino acid (AA)	Number of couplings		AA excess	Activator excess	Base excess	Coupling time
23	Fmoc-Asp(tBu)-OH	2	1	3 eq.	3 eq. HBTU	4.5 eq. DIEA	40 min
			2	3 eq.	3 eq. HBTU	4.5 eq. DIEA	40 min
22	Fmoc-Glu(tBu)-OH	2	1	3 eq.	3 eq. HBTU	4.5 eq. DIEA	40 min
			2	3 eq.	3 eq. HBTU	4.5 eq. DIEA	40 min
21	Fmoc-Ala-OH	2	1	3 eq.	3 eq. HBTU	4.5 eq. DIEA	40 min
			2	3 eq.	3 eq. HBTU	4.5 eq. DIEA	40 min
20	Fmoc-NMePhe-OH	2	1	6 eq.	6 eq. HATU	9 eq. DIEA	40 min
			2	3 eq.	3 eq. HATU	4.5 eq. DIEA	40 min
19	Fmoc-Phe-OH	2	1	3 eq.	3 eq. HATU	4.5 eq. DIEA	50 min
			2	3 eq.	3 eq. HATU	4.5 eq. DIEA	50 min
18	Fmoc-NMeVal-OH	2	1	6 eq.	6 eq. HATU	9 eq. DIEA	50 min
			2	3 eq.	3 eq. HATU	4.5 eq. DIEA	50 min
17	Fmoc-Leu-OH	3	1	6 eq.	6 eq. HATU	9 eq. DIEA	50 min
			2	6 eq.	6 eq. HATU	9 eq. DIEA	50 min
			3	3 eq.	3 eq. HATU	4.5 eq. DIEA	50 min
16	Fmoc-Lys(Boc)-OH	3	1	6 eq.	6 eq. HATU	9 eq. DIEA	50 min
			2	6 eq.	6 eq. HATU	9 eq. DIEA	50 min
			3	3 eq.	3 eq. HATU	4.5 eq. DIEA	50 min
15	Fmoc-Gln(Trt)-OH	2	1	3 eq.	3 eq. HATU	4.5 eq. DIEA	50 min
			2	3 eq.	3 eq. HBTU	4.5 eq. DIEA	50 min

7.2 MALDI-TOF-MS and ESI-IT-MS of purified ADPs

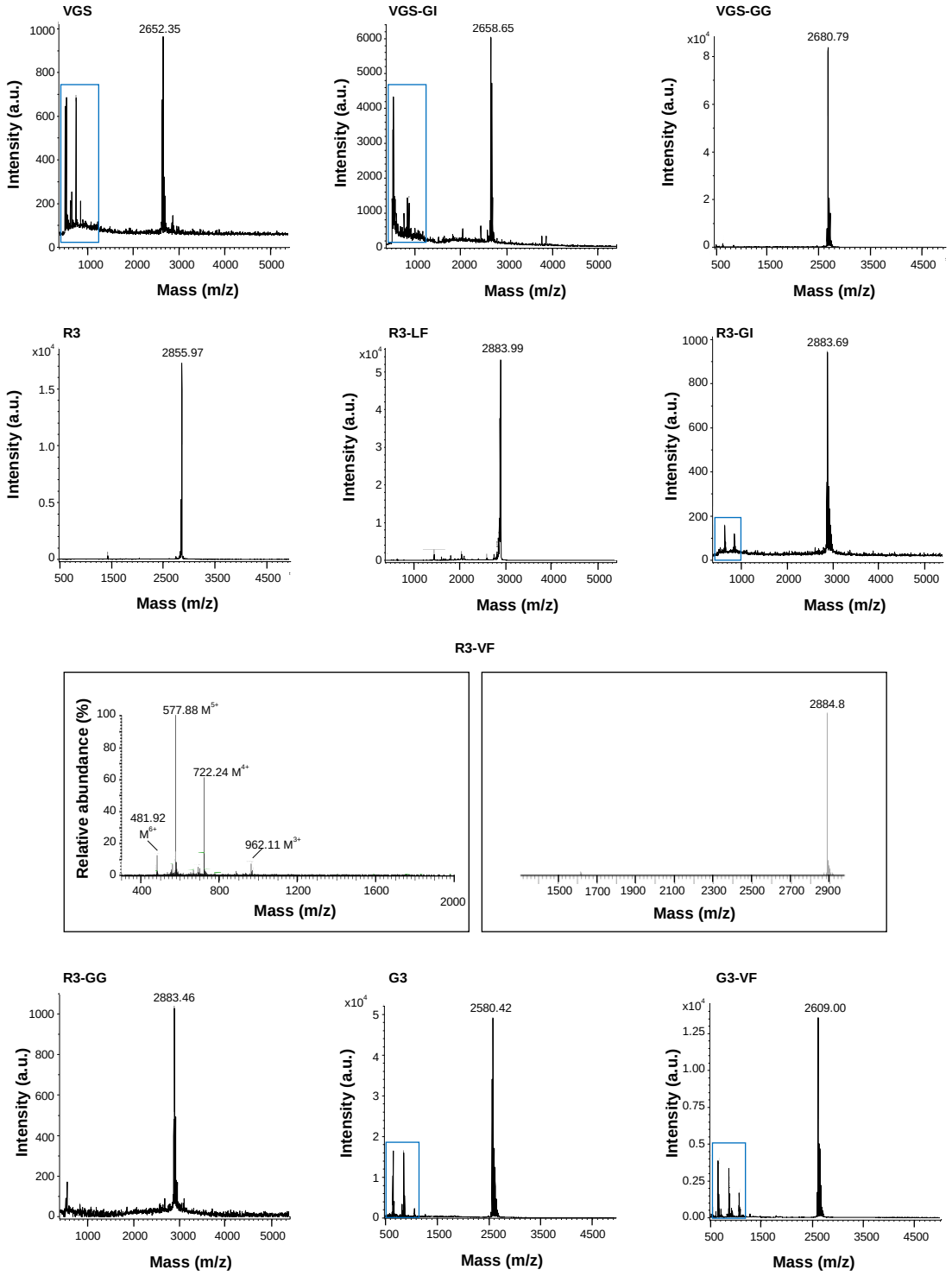

Figure 7-1: Mass spectrometric characterisation of ADPs comprising VGS-, R3-, and G3-loop tripeptide segments. MALDI-TOF-MS and ESI-IT-MS spectra of the peptides that were HPLC-purified according to the strategies presented in Table 4-3 in chapter 4.2. Only R3-VF was characterised by ESI-IT-MS (left: measured spectrum, right: deconvolved spectrum), all other ADPs were characterised by MALDI-TOF-MS. The sample of R3-VF was dissolved in 80 % ACN in ddH_2O, samples of VGS-GI and R3 were dissolved in 30 % ACN in ddH_2O with 0.1 % TFA, and samples of all other ADPs were dissolved in 97 % acetone in ddH_2O with 0.1 % TFA. The theoretical calculated masses ($M+H^+$) are summarised in Table 4-3 in chapter 4.2. Blue boxes indicate peaks that are due to the matrix (see Figure 7-5 in Appendix).

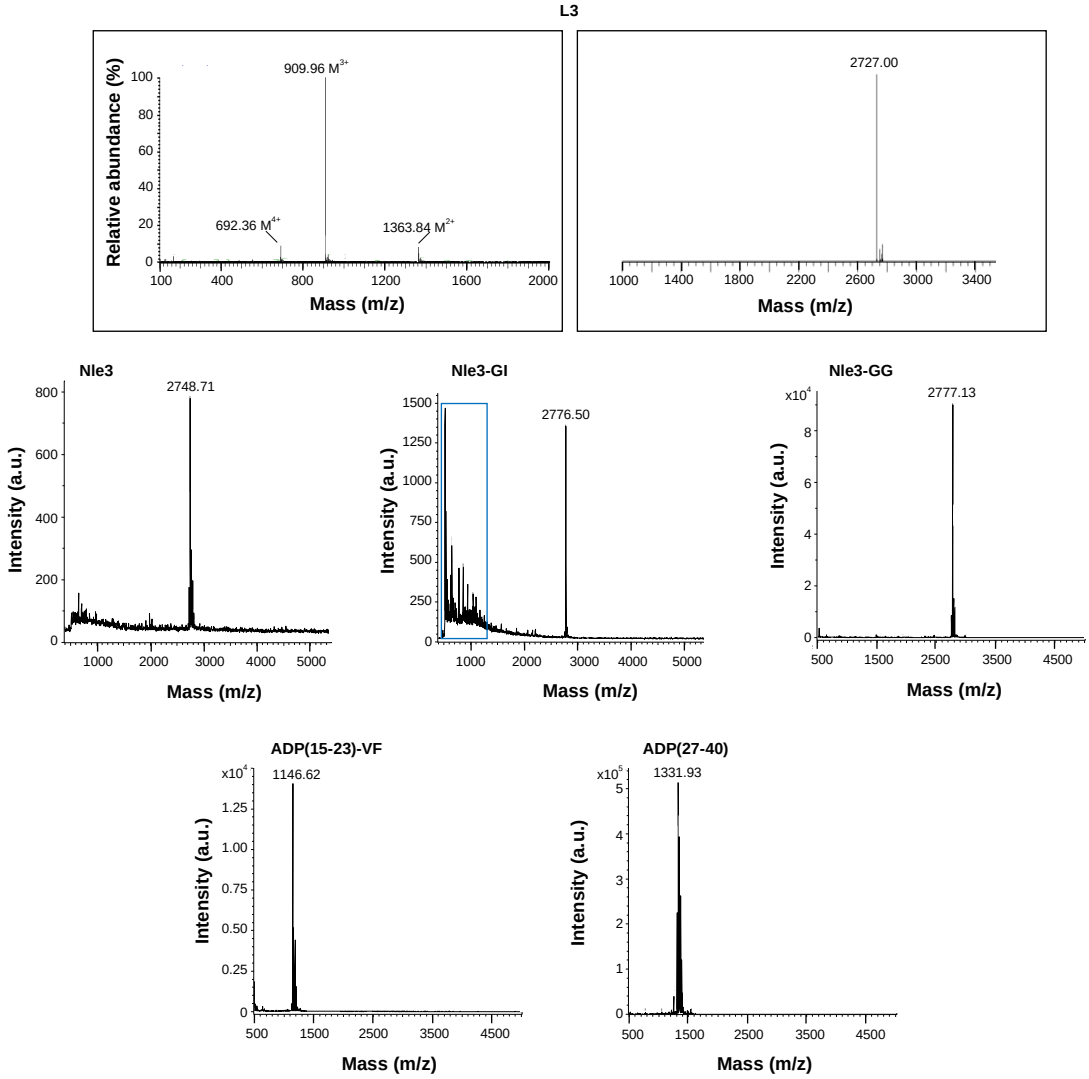

Figure 7-2: Mass spectrometric characterisation of ADPs comprising L3- and Nle3-loop tripeptide segments, and of ADP fragments ADP(15-23)-VF and ADP(27-40). MALDI-TOF-MS and ESI-IT-MS spectra of the peptides that were HPLC-purified according to the strategies presented in Table 4-3 in chapter 4.2. Only L3 was characterised by ESI-IT-MS (left: measured spectrum, right: deconvolved spectrum), all other ADPs were characterised by MALDI-TOF-MS. The sample of L3 was dissolved in 80 % ACN in ddH_2O, samples of all other ADPs were dissolved in 97 % acetone in ddH_2O with 0.1 % TFA. The theoretical calculated masses ($M+H^+$) are summarised in Table 4-3 in chapter 4.2. Blue boxes indicate peaks that are due to the matrix (see Figure 7-5 in Appendix).

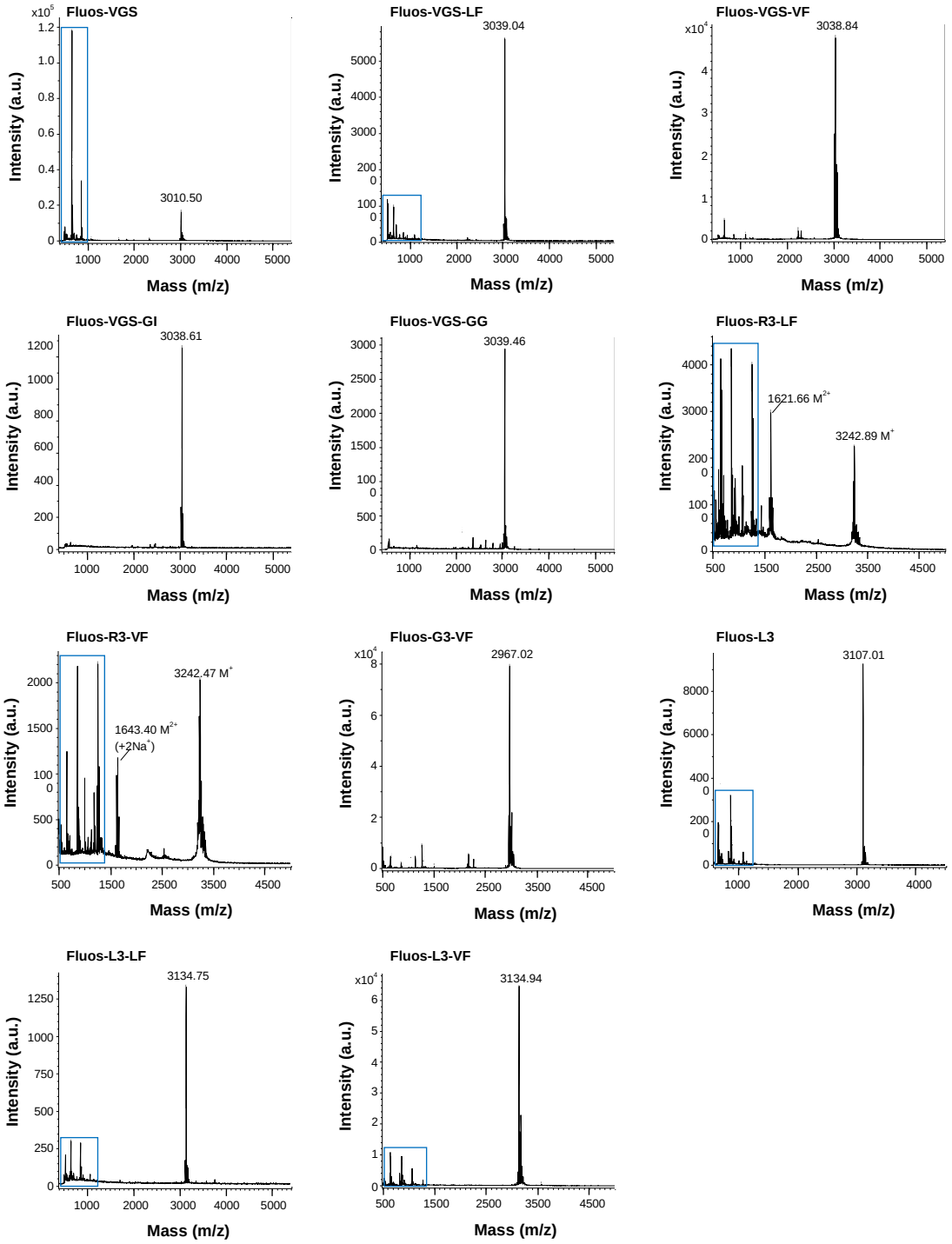

Figure 7-3: Mass spectrometric characterisation of Fluos-labelled ADPs comprising VGS-, R3-, G3-, and L3-loop tripeptide segments. MALDI-TOF-MS spectra of the peptides that were HPLC-purified according to the strategies presented in Table 4-4 in chapter 4.2. Samples were dissolved in 97 % acetone in ddH_2O with 0.1 % TFA. The theoretical calculated masses ($M+H^+$) are summarised in Table 4-4 in chapter 4.2. Blue boxes indicate peaks that are due to the matrix (see Figure 7-5 in Appendix).

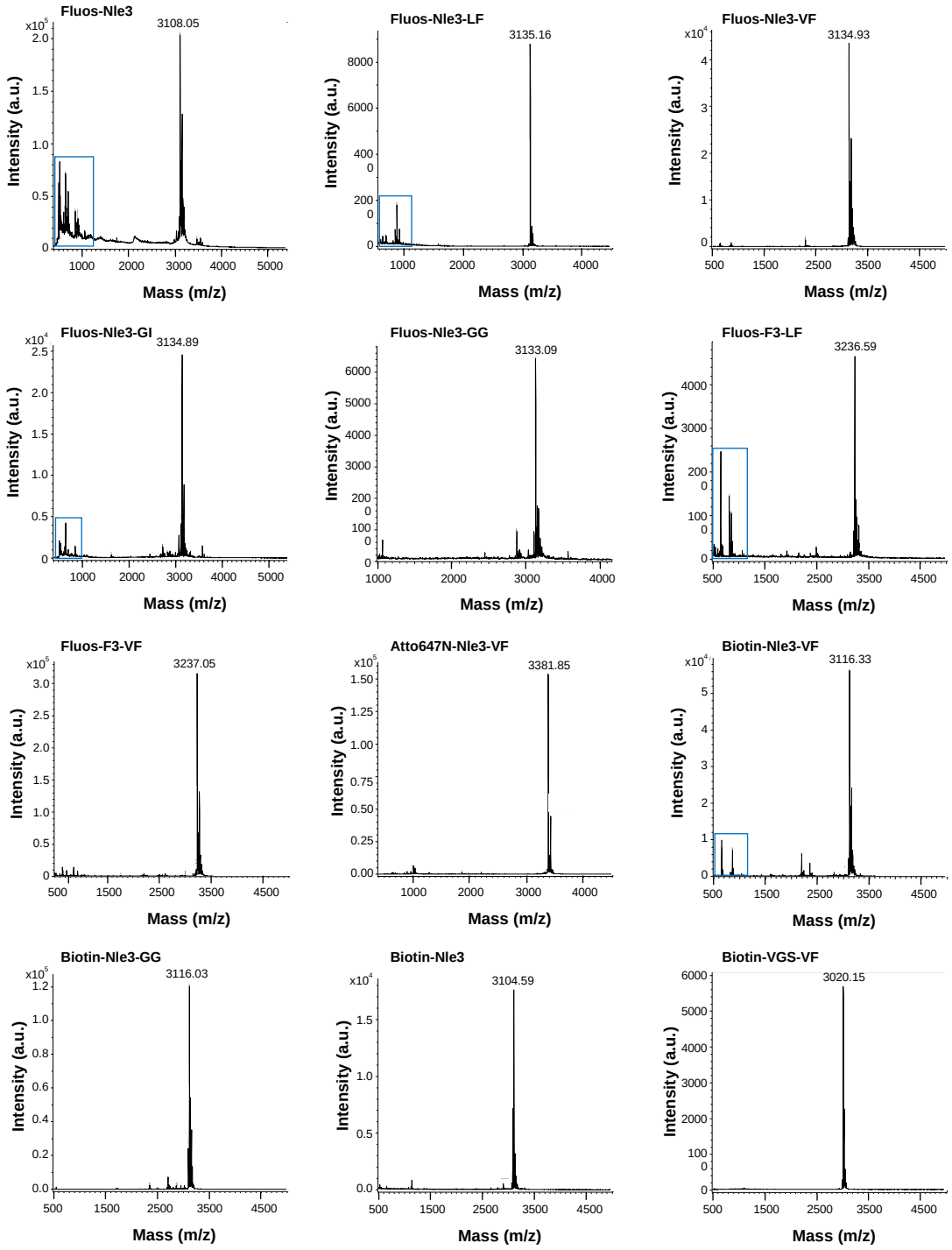

Figure 7-4: Mass spectrometric characterisation of Fluos-labelled ADPs comprising Nle3-, and F3-loop tripeptide segments, of biotinylated ADPs, and of Atto647N-Nle3-VF. MALDI-TOF-MS spectra of the peptides that were HPLC-purified according to the strategies presented in Table 4-4 in chapter 4.2. Samples were dissolved in 97 % acetone in ddH_2O with 0.1 % TFA. The theoretical calculated masses ($M+H^+$) are summarised in Table 4-4 in chapter 4.2. Blue boxes indicate peaks that are due to the matrix (see Figure 7-5 in Appendix).

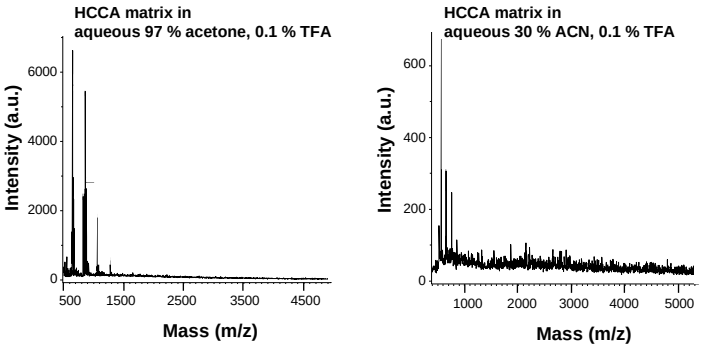

Figure 7-5: MALDI-TOF-MS spectra of α-Cyano-4-hydroxycinnamic acid (HCCA) matrix in MALDI solvents without peptide. HCCA matrix was dissolved in the MALDI solvents that were also used to dissolve peptide samples. HCCA matrix alone was analysed by MALDI-TOF-MS in parallel to the peptide samples to define background peaks caused by the matrix.

7.3 IC_{50} of inhibitory effects of ACMs on IAPP and Aβ42 cytotoxicity

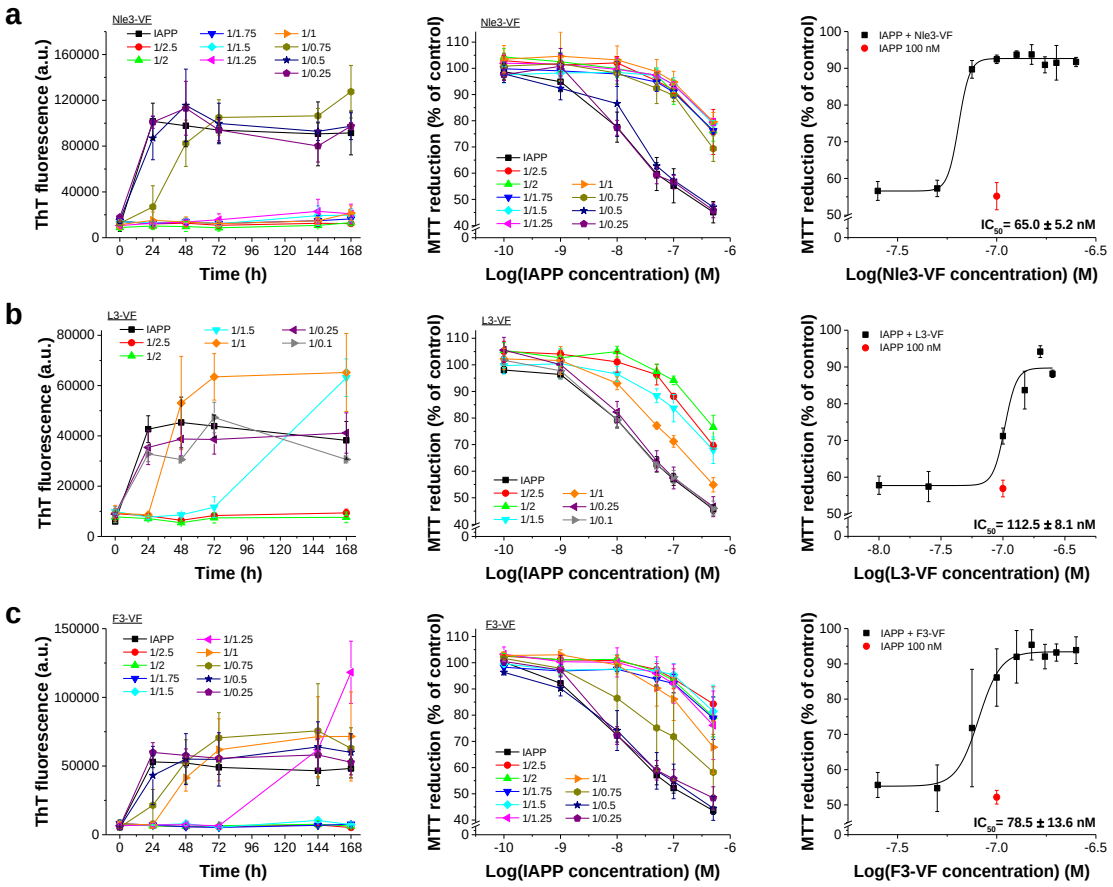

Figure 7-6: IC_{50}s of inhibitory effects of V18F20 methylated ACMs on IAPP cytotoxicity at 24 h. For assessing concentration dependent effects of ACMs on IAPP fibril formation, IAPP (16.5 µM) was incubated in presence of ACMs at indicated ratios and aggregation kinetics were followed over 7 days by ThT binding (left panels: means ± SD, n=3-8). Concentration dependent effects of ACMs on IAPP cell toxicity were studied via the MTT reduction assay by treating RIN5fm cells with 24 h aged solutions from ThT assays (middle panels; means ± SD, 3 assays, n=3 each). IC_{50} curves are means ± SD from three different assays (n = 3 each). IC_{50} values were calculated for IAPP = 100 nM (right panels). Cytotoxicity of IAPP control at 100 nM is depicted as a red dot for comparison. Shown is data for Nle3-VF (**a**), L3-VF (**b**) and F3-VF (**c**). Data in left and right panels is part of a figure in reference [140].

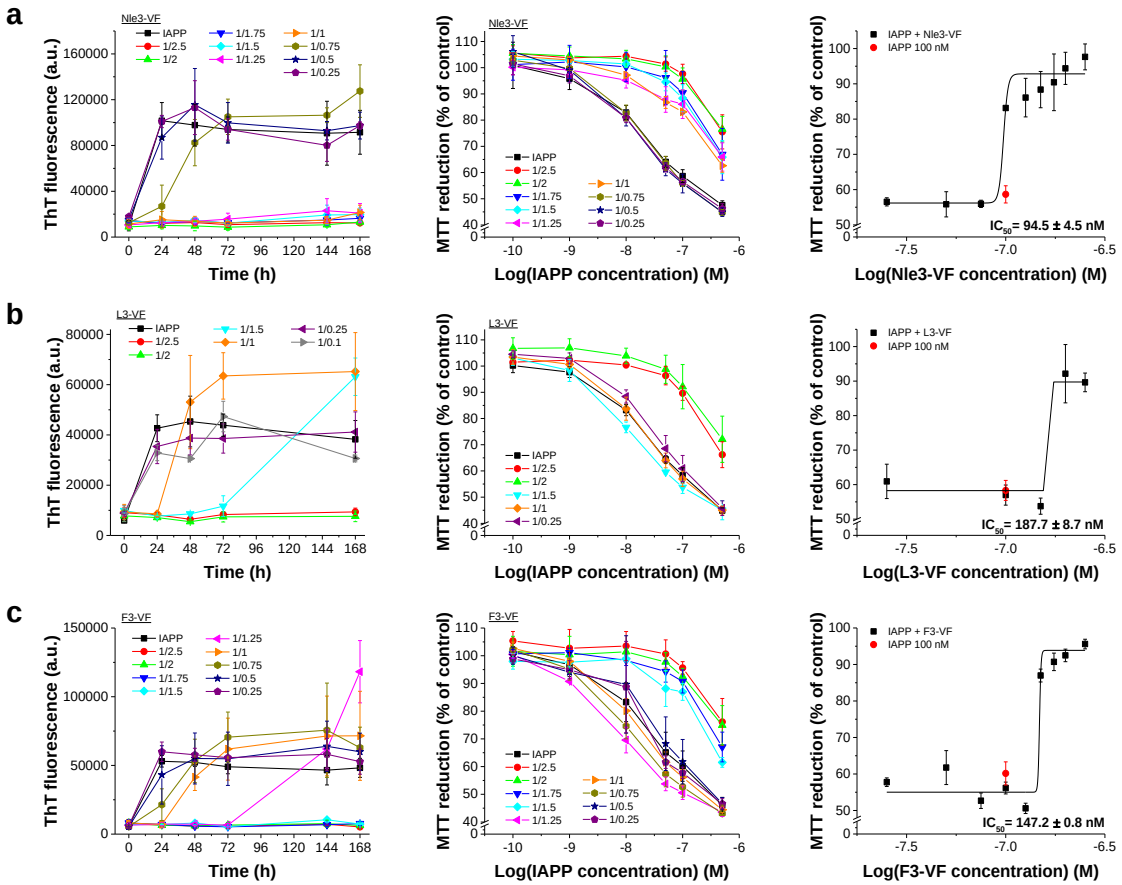

Figure 7-7: IC_{50}s of inhibitory effects of V18F20 methylated ACMs on IAPP cytotoxicity at 7 d. For assessing concentration dependent effects of ACMs on IAPP fibril formation, IAPP (16.5 µM) was incubated in presence of ACMs at indicated ratios and aggregation kinetics were followed over 7 days by ThT binding (left panels; means ± SD, n=3-8). Concentration dependent effects of ACMs on IAPP cell toxicity were studied via the MTT reduction assay by treating RIN5fm cells with 7 days aged solutions from ThT assays (middle panels; means ± SD, 3 assays, n=3 each). IC_{50} curves are means ± SD from three different assays (n = 3 each). IC_{50} values were calculated for IAPP = 100 nM (right panels). Cytotoxicity of IAPP control at 100 nM is depicted as a red dot for comparison. Shown is data for Nle3-VF (**a**), L3-VF (**b**) and F3-VF (**c**).

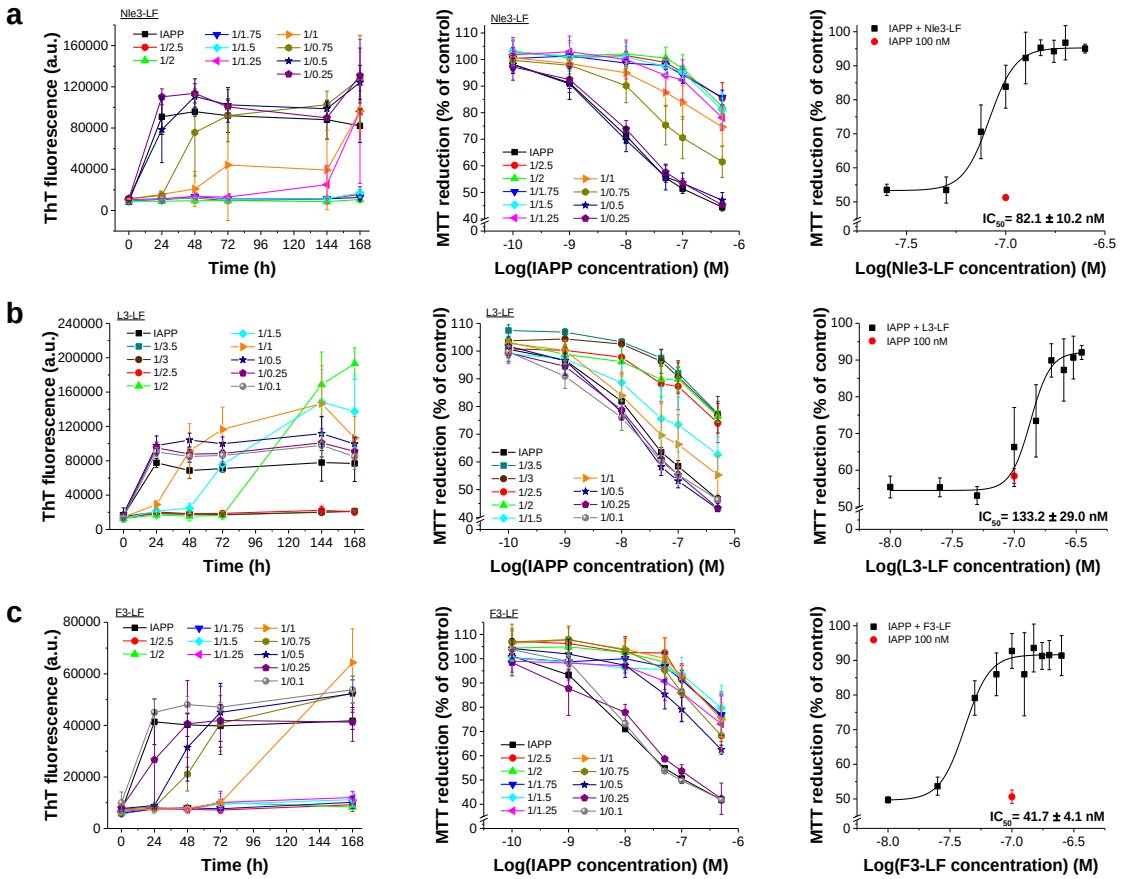

Figure 7-8: IC_{50}s of inhibitory effects of L17F19 methylated ACMs on IAPP cytotoxicity at 24 h. For assessing concentration dependent effects of ACMs on IAPP fibril formation, IAPP (16.5 µM) was incubated in presence of ACMs at indicated ratios and aggregation kinetics were followed over 7 days by ThT binding (left panels; means ± SD, n=3-8). Concentration dependent effects of ACMs on IAPP cell toxicity were studied via the MTT reduction assay by treating RIN5fm cells with 24 h aged solutions from ThT assays (middle panels; means ± SD, 3 assays, n=3 each). IC_{50} curves are means ± SD from three different assays (n = 3 each). IC_{50} values were calculated for IAPP = 100 nM (right panels). Cytotoxicity of IAPP control at 100 nM is depicted as a red dot for comparison. Shown is data for Nle3-LF (**a**), L3-LF (**b**) and F3-LF (**c**). Data in left and right panels is part of a figure in reference [140].

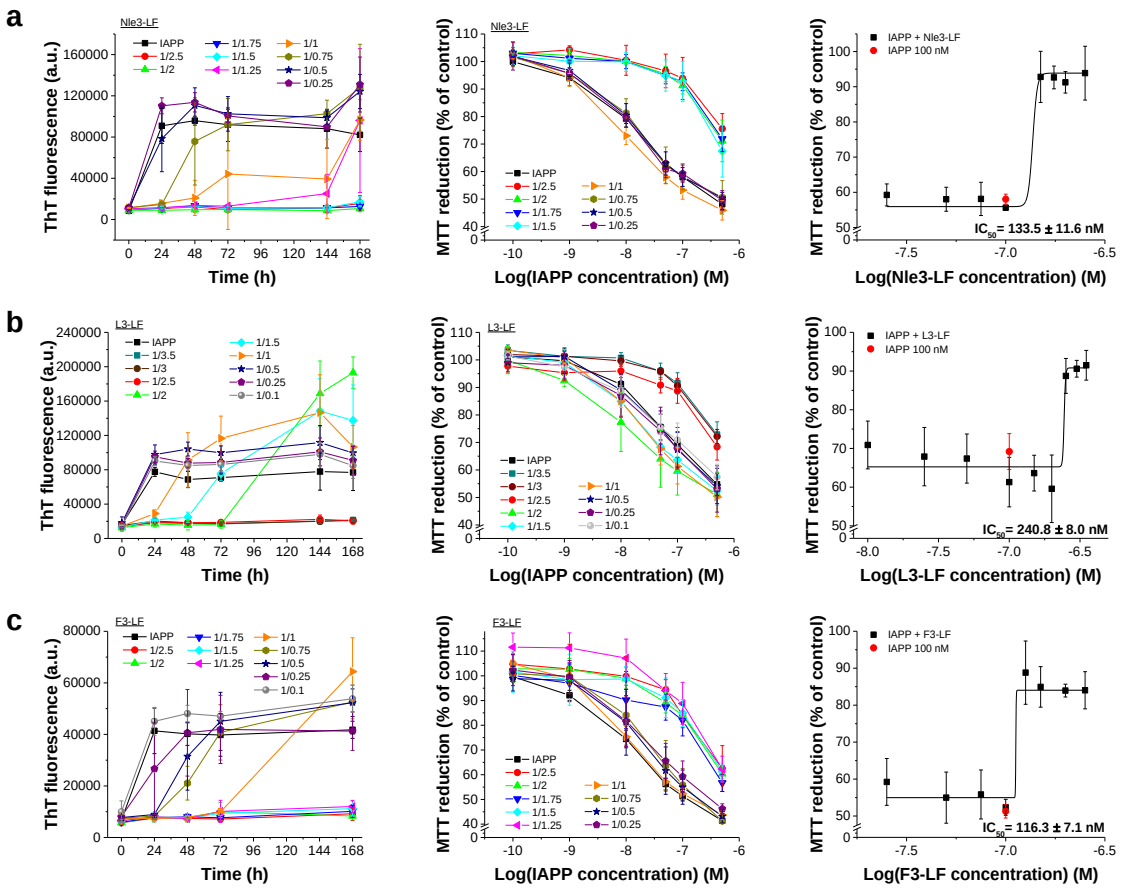

Figure 7-9: IC_{50}s of inhibitory effects of L17F19 methylated ACMs on IAPP cytotoxicity at 7 d. For assessing concentration dependent effects of ACMs on IAPP fibril formation, IAPP (16.5 µM) was incubated in presence of ACMs at indicated ratios and aggregation kinetics were followed over 7 days by ThT binding (left panels; means ± SD, n=3-8). Concentration dependent effects of ACMs on IAPP cell toxicity were studied via the MTT reduction assay by treating RIN5fm cells with 7 days aged solutions from ThT assays (middle panels; means ± SD, 3 assays, n=3 each). IC_{50} curves are means ± SD from three different assays (n = 3 each). IC_{50} values were calculated for IAPP = 100 nM (right panels). Cytotoxicity of IAPP control at 100 nM is depicted as a red dot for comparison. Shown is data for Nle3-LF (**a**), L3-LF (**b**) and F3-LF (**c**).

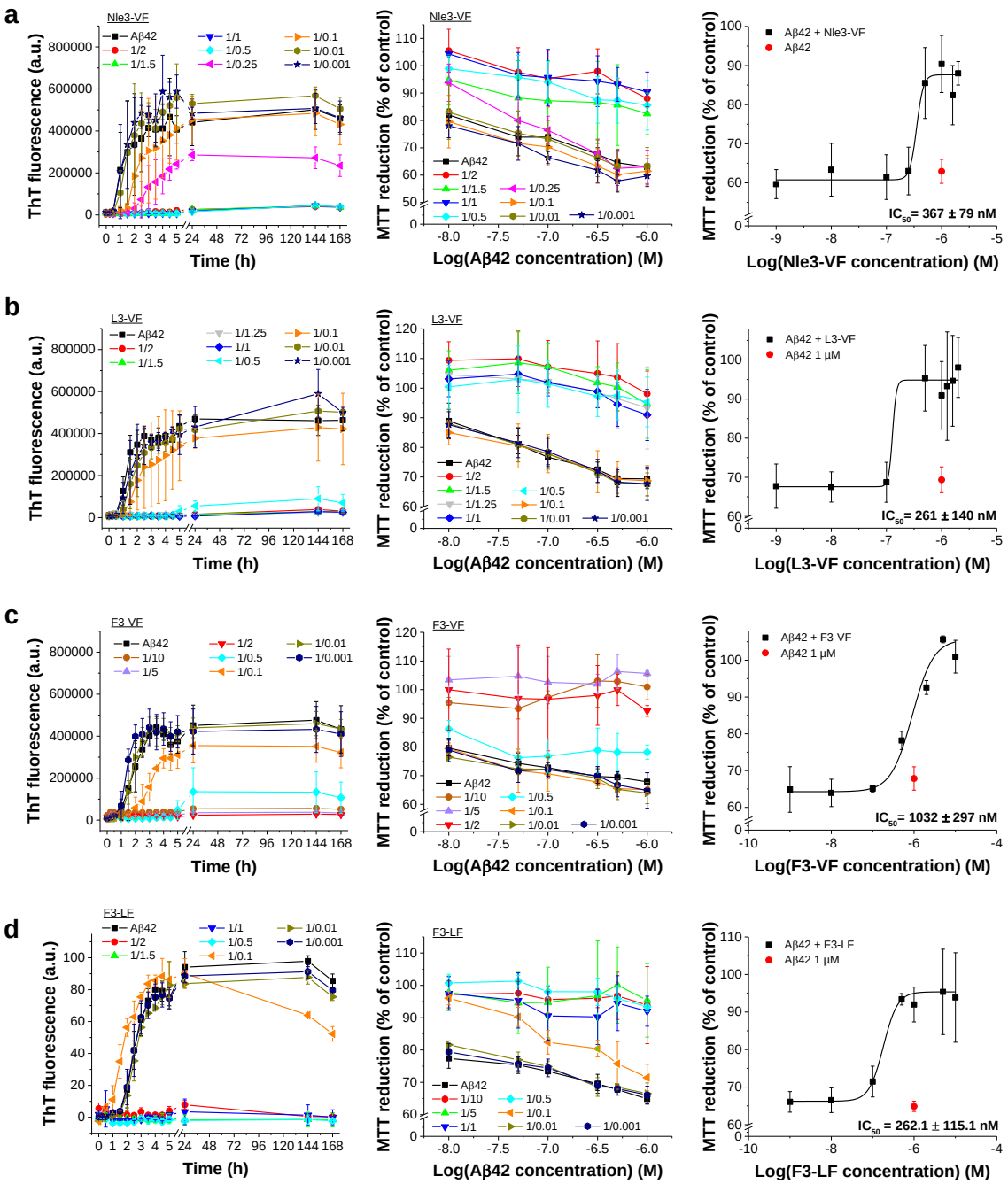

Figure 7-10: IC_{50}s of inhibitory effects of ACMs on Aβ42 cytotoxicity at 6 d. Aβ42 (5 µM) was incubated with ACMs at indicated ratios and fibril formation was followed over 7 days by ThT binding to investigate concentration dependent effects of ACMs on Aβ42 fibrillation (left panels; means ± SD, n=3). Concentration dependent effects of ACMs on Aβ42 cytotoxicity were studied via the MTT reduction assay. PC-12 cells were treated with 6 days aged solutions (w/o ThT) (middle panels; means ± SD, 3 assays, n=3 each). IC_{50} curves are means ± SD from three different assays (n = 3 each). IC_{50} values were calculated for Aβ42 = 1 µM (right panels). Cytotoxicity of Aβ42 control at 1 µM is depicted as a red dot for comparison. Shown is data for Nle3-VF (**a**), L3-VF (**b**), F3-VF (**c**) and F3-LF (**d**). Data in right panels is part of a figure in reference [140].

7.4 Cytotoxicity of Nle3-linked peptides with different methylation pairs

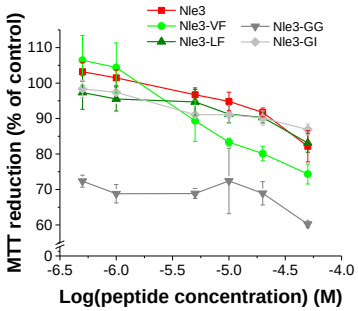

Figure 7-11: Effects of different *N*-methylations on cytotoxic properties of ADPs with the Nle3 loop tripeptide segment. Peptides were incubated at 1 mM for 4 days in 1xb containing 1 % HFiP. Following dilution into cell medium, peptides were applied onto PC-12 cells at indicated concentrations. Error bars represent means ± SD from three assays, n=3 each.

7.5 Fluorescence spectroscopic titration – spectra and binding curves

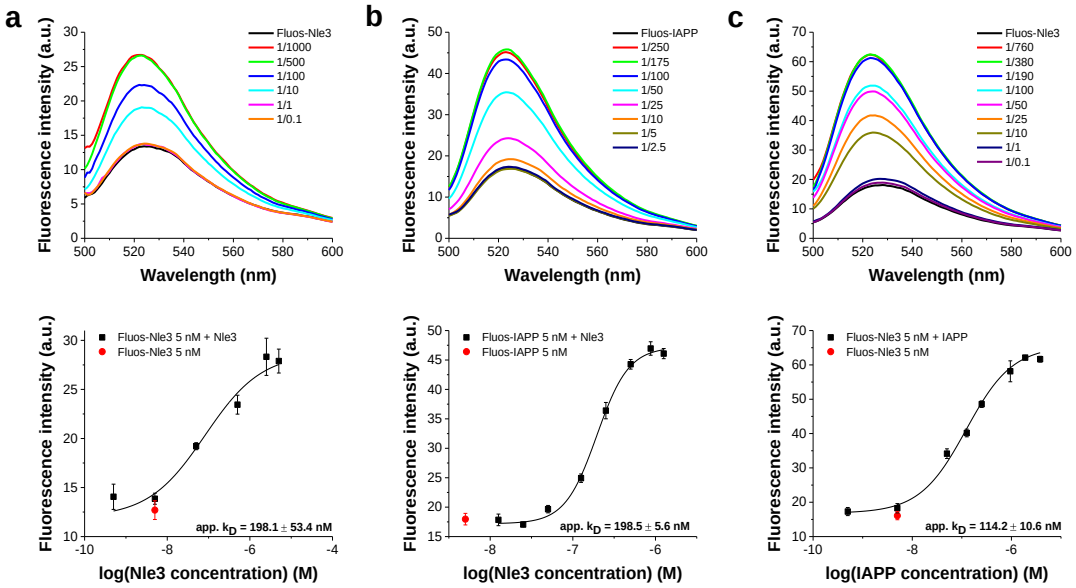

Figure 7-12: Fluorescence spectroscopic titrations with Nle3. Titrations were performed using 5 nM Fluos-labelled peptide. Fluorescence emission spectra of Fluos-peptide alone and after titration with the binding partner were recorded in 1xb containing 1 % HFiP, pH 7.4. Shown is one representative data set for the fluorescence emission spectra (top) and the binding curve (bottom). App. k_D values (means ± SD) were calculated from three different binding curves. Fluorescence emissions of Fluos-peptides alone are shown as red dot for comparison. Data is shown for Nle3 self-assembly (**a**), binding of Nle3 to Fluos-IAPP (**b**) and binding of IAPP to Fluos-Nle3 (**c**). App. k_Ds are summarised in Table 4-7.

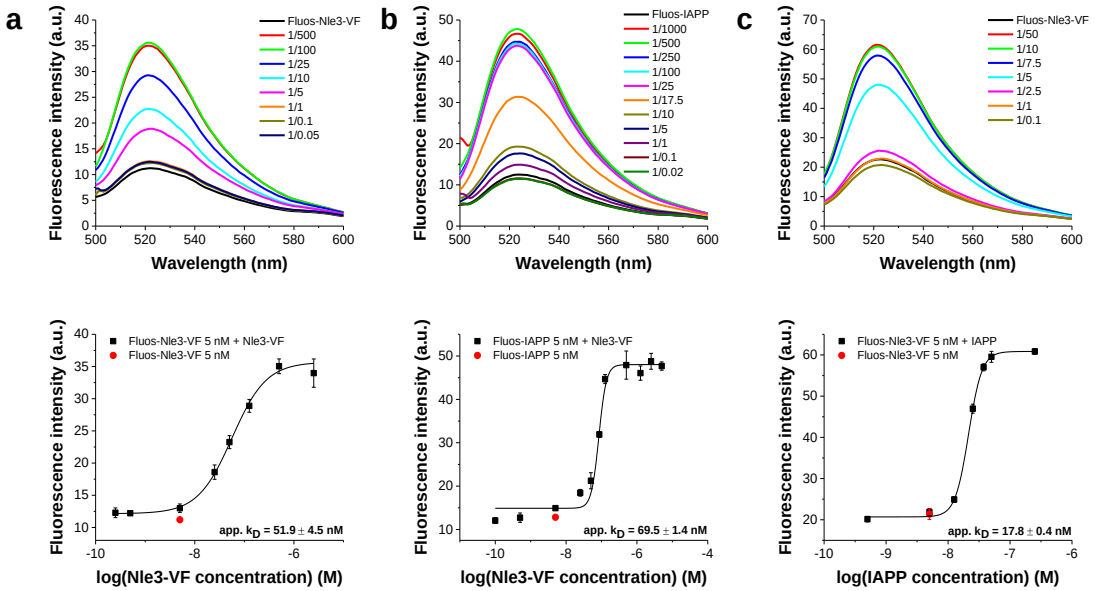

Figure 7-13: Fluorescence spectroscopic titrations with Nle3-VF. Titrations were performed using 5 nM Fluos-labelled peptide. Fluorescence emission spectra of Fluos-peptide alone and after titration with the binding partner were recorded in 1xb containing 1 % HFiP, pH 7.4. Shown is one representative data set for the fluorescence emission spectra (top) and the binding curve (bottom). App. k_D values (means ± SD) were calculated from three different binding curves. Fluorescence emissions of Fluos-peptides alone are shown as red dot for comparison. Data is shown for Nle3-VF self-assembly (**a**), binding of Nle3-VF to Fluos-IAPP (**b**) and binding of IAPP to Fluos-Nle3-VF (**c**). App. k_Ds are summarised in Table 4-7. Data of a) and b) is part of a figure in reference [140].

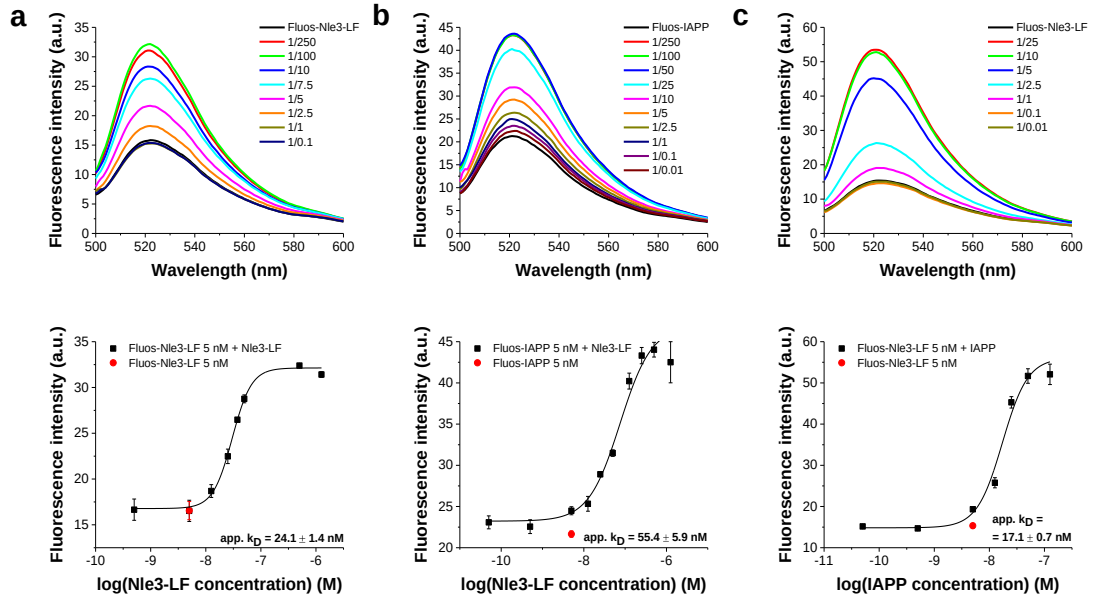

Figure 7-14: Fluorescence spectroscopic titrations with Nle3-LF. Titrations were performed using 5 nM Fluos-labelled peptide. Fluorescence emission spectra of Fluos-peptide alone and after titration with the binding partner were recorded in 1xb containing 1 % HFiP, pH 7.4. Shown is one representative data set for the fluorescence emission spectra (top) and the binding curve (bottom). App. k_D values (means ± SD) were calculated from three different binding curves. Fluorescence emissions of Fluos-peptides alone are shown as red dot for comparison. Data is shown for Nle3-LF self-assembly (**a**), binding of Nle3-LF to Fluos-IAPP (**b**) and binding of IAPP to Fluos-Nle3-LF (**c**). App. k_Ds are summarised in Table 4-7. Data of b) is part of a figure in reference [140].

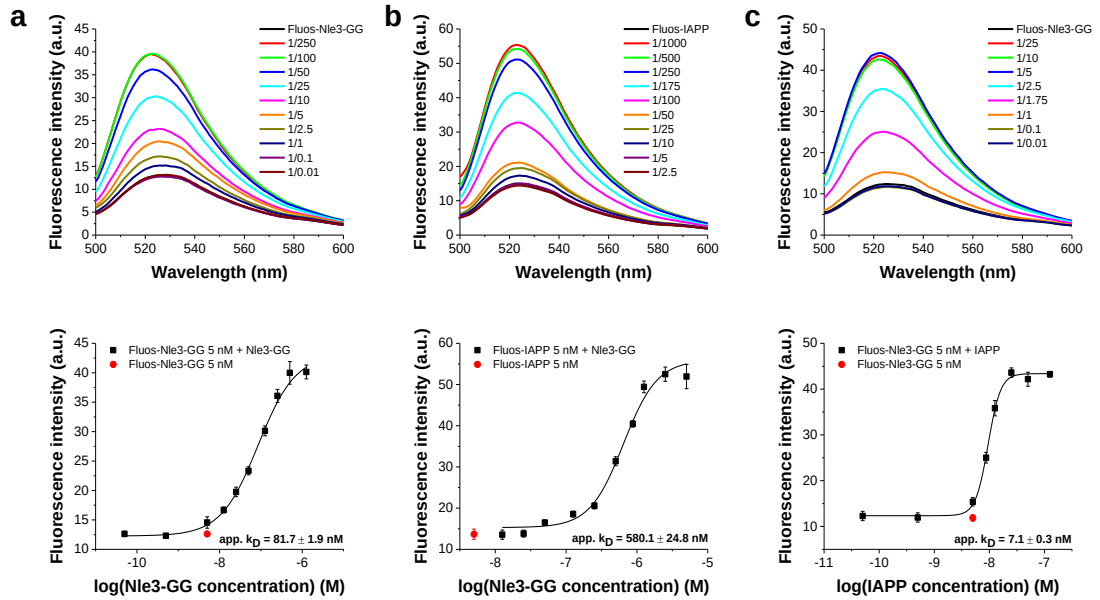

Figure 7-15: Fluorescence spectroscopic titrations with Nle3-GG. Titrations were performed using 5 nM Fluos-labelled peptide. Fluorescence emission spectra of Fluos-peptide alone and after titration with the binding partner were recorded in 1xb containing 1 % HFiP, pH 7.4. Shown is one representative data set for the fluorescence emission spectra (top) and the binding curve (bottom). App. k_D values (means ± SD) were calculated from three different binding curves. Fluorescence emissions of Fluos-peptides alone are shown as red dot for comparison. Data is shown for Nle3-GG self-assembly (**a**), binding of Nle3-GG to Fluos-IAPP (**b**) and binding of IAPP to Fluos-Nle3-GG (**c**). App. k_Ds are summarised in Table 4-7.

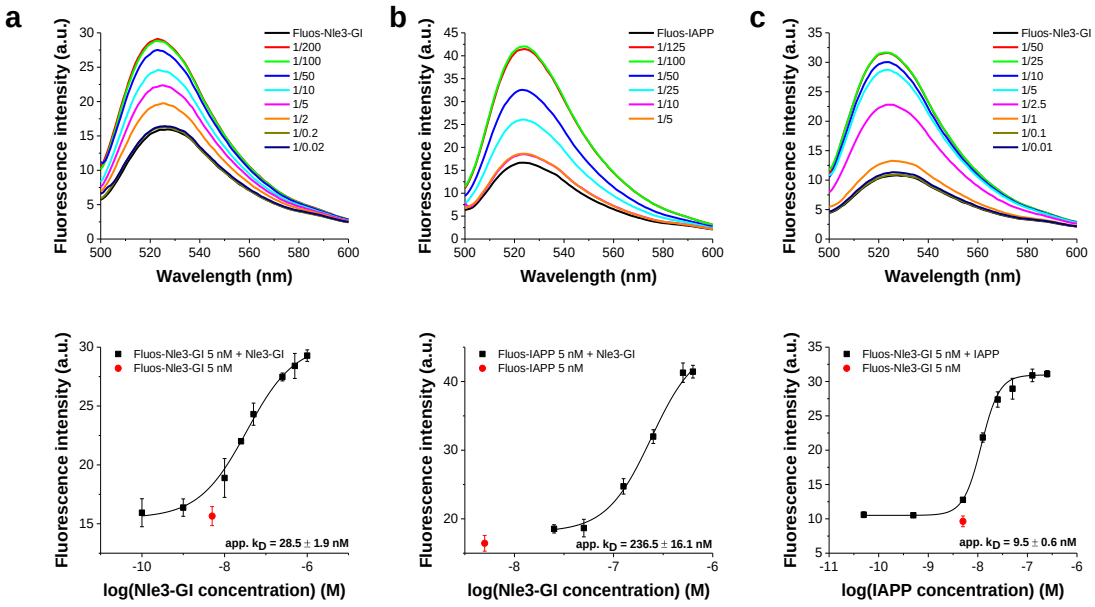

Figure 7-16: Fluorescence spectroscopic titrations with Nle3-GI. Titrations were performed using 5 nM Fluos-labelled peptide. Fluorescence emission spectra of Fluos-peptide alone and after titration with the binding partner were recorded in 1xb containing 1 % HFiP, pH 7.4. Shown is one representative data set for the fluorescence emission spectra (top) and the binding curve (bottom). App. k_D values (means ± SD) were calculated from three different binding curves. Fluorescence emissions of Fluos-peptides alone are shown as red dot for comparison. Data is shown for Nle3-GI self-assembly (**a**), binding of Nle3-GI to Fluos-IAPP (**b**) and binding of IAPP to Fluos-Nle3-GI (**c**). App. k_Ds are summarised in Table 4-7.

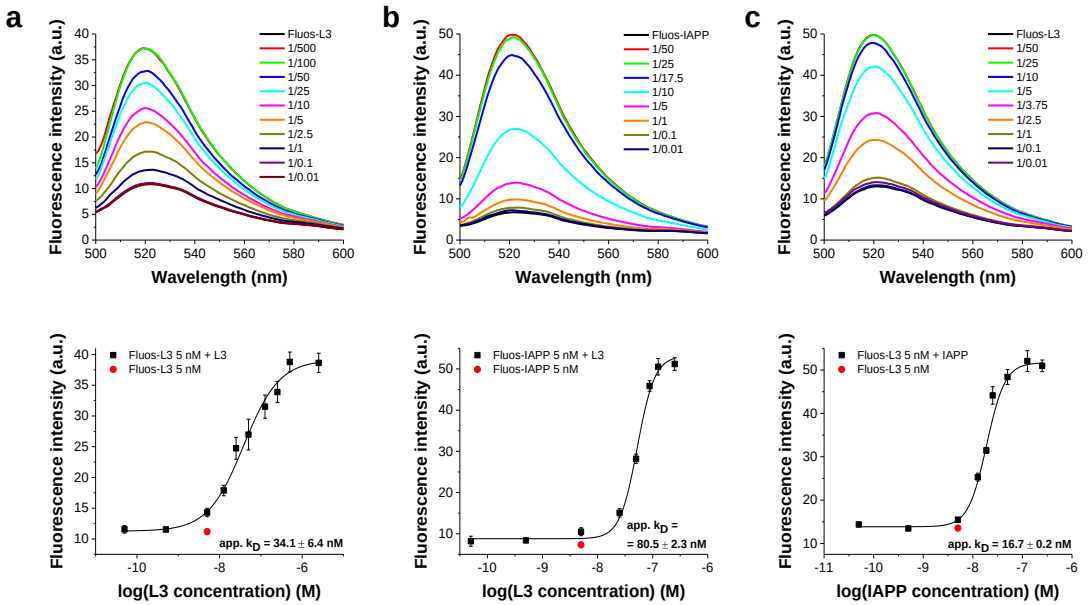

Figure 7-17: Fluorescence spectroscopic titrations with L3. Titrations were performed using 5 nM Fluos-labelled peptide. Fluorescence emission spectra of Fluos-peptide alone and after titration with the binding partner were recorded in 1xb containing 1 % HFiP, pH 7.4. Shown is one representative data set for the fluorescence emission spectra (top) and the binding curve (bottom). App. k_D values (means ± SD) were calculated from three different binding curves. Fluorescence emissions of Fluos-peptides alone are shown as red dot for comparison. Data is shown for L3 self-assembly (**a**), binding of L3 to Fluos-IAPP (**b**) and binding of IAPP to Fluos-L3 (**c**). App. k_Ds are summarised in Table 4-7.

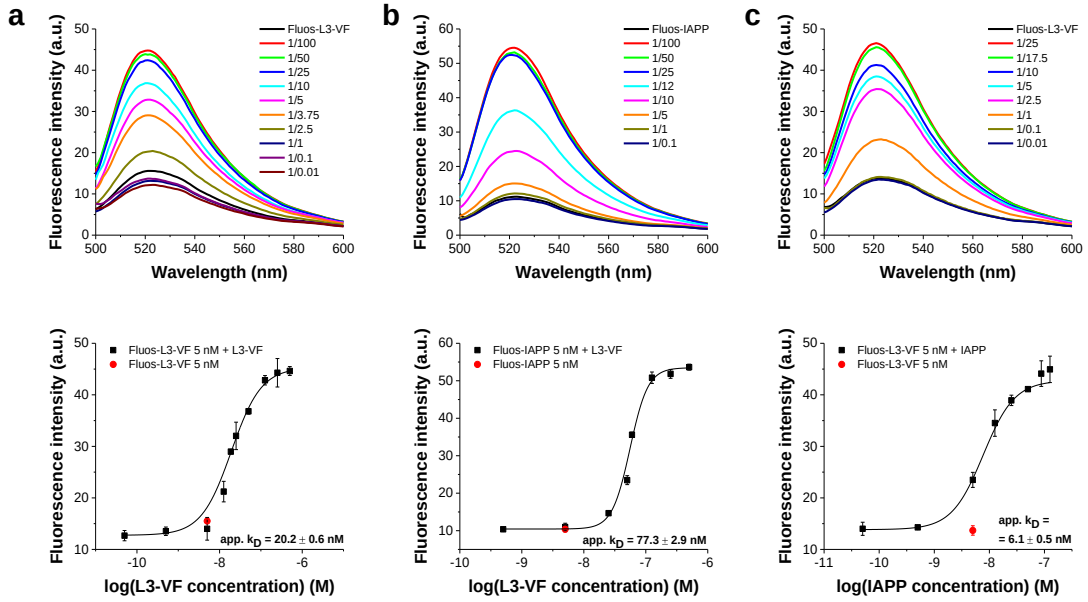

Figure 7-18: Fluorescence spectroscopic titrations with L3-VF. Titrations were performed using 5 nM Fluos-labelled peptide. Fluorescence emission spectra of Fluos-peptide alone and after titration with the binding partner were recorded in 1xb containing 1 % HFiP, pH 7.4. Shown is one representative data set for the fluorescence emission spectra (top) and the binding curve (bottom). App. k_D values (means ± SD) were calculated from three different binding curves. Fluorescence emissions of Fluos-peptides alone are shown as red dot for comparison. Data is shown for L3-VF self-assembly (**a**), binding of L3-VF to Fluos-IAPP (**b**) and binding of IAPP to Fluos-L3-VF (**c**). App. k_Ds are summarised in Table 4-7. Data of b) is part of a figure in reference [140].

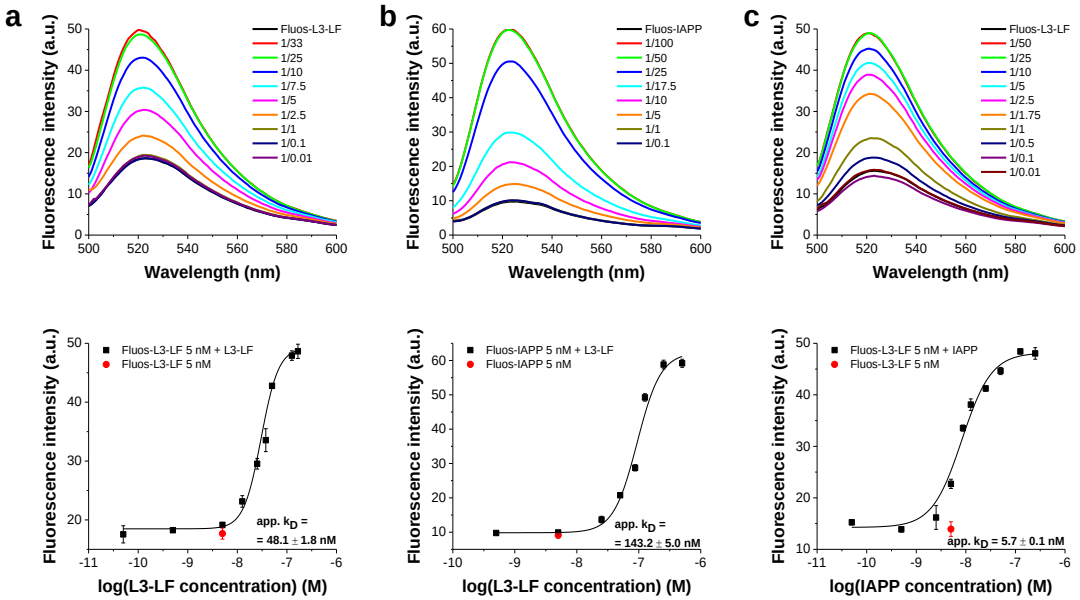

Figure 7-19: Fluorescence spectroscopic titrations with L3-LF. Titrations were performed using 5 nM Fluos-labelled peptide. Fluorescence emission spectra of Fluos-peptide alone and after titration with the binding partner were recorded in 1xb containing 1 % HFiP, pH 7.4. Shown is one representative data set for the fluorescence emission spectra (top) and the binding curve (bottom). App. k_D values (means ± SD) were calculated from three different binding curves. Fluorescence emissions of Fluos-peptides alone are shown as red dot for comparison. Data is shown for L3-LF self-assembly (**a**), binding of L3-LF to Fluos-IAPP (**b**) and binding of IAPP to Fluos-L3-LF (**c**). App. k_Ds are summarised in Table 4-7. Data of b) is part of a figure in reference [140].

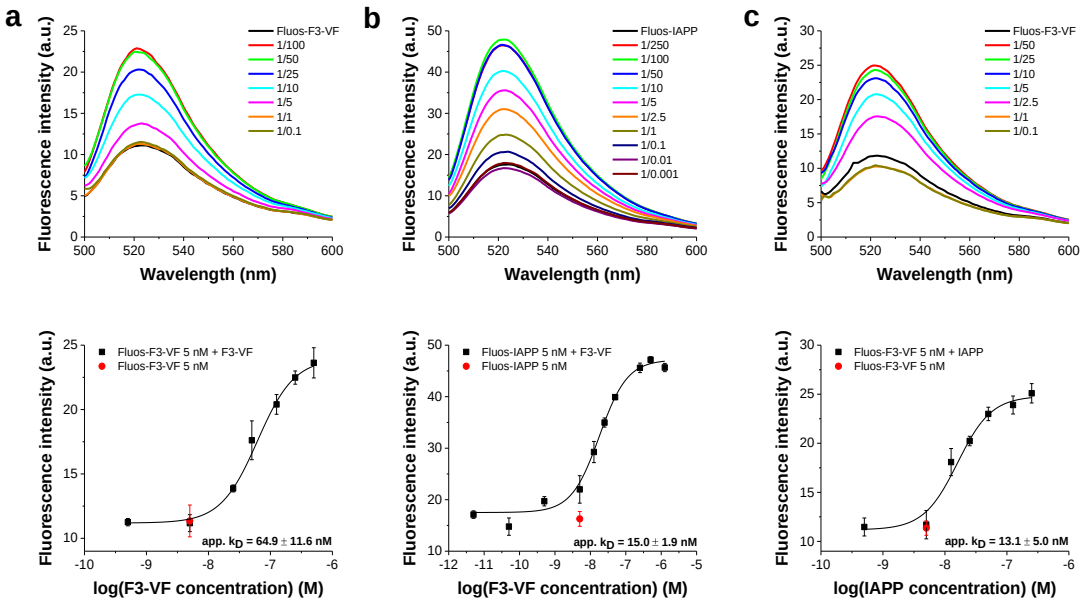

Figure 7-20: Fluorescence spectroscopic titrations with F3-VF. Titrations were performed using 5 nM Fluos-labelled peptide. Fluorescence emission spectra of Fluos-peptide alone and after titration with the binding partner were recorded in 1xb containing 1 % HFiP, pH 7.4. Shown is one representative data set for the fluorescence emission spectra (top) and the binding curve (bottom). App. k_D values (means ± SD) were calculated from three different binding curves. Fluorescence emissions of Fluos-peptides alone are shown as red dot for comparison. Data is shown for F3-VF self-assembly (**a**), binding of F3-VF to Fluos-IAPP (**b**) and binding of IAPP to Fluos-F3-VF (**c**). App. k_Ds are summarised in Table 4-7. Data of b) is part of a figure in reference [140].

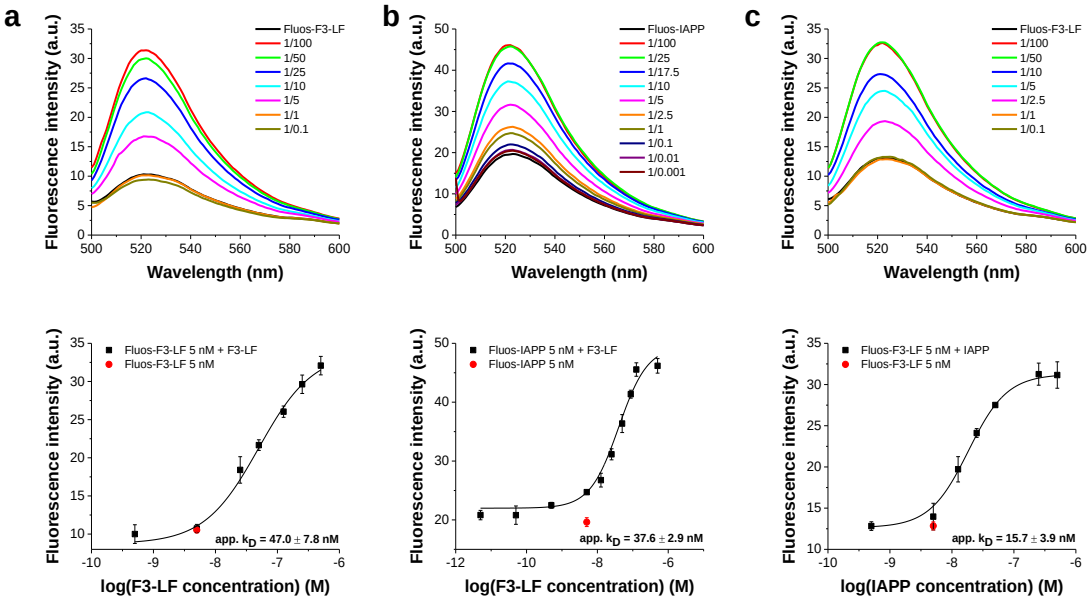

Figure 7-21: Fluorescence spectroscopic titrations with F3-LF. Titrations were performed using 5 nM Fluos-labelled peptide. Fluorescence emission spectra of Fluos-peptide alone and after titration with the binding partner were recorded in 1xb containing 1 % HFiP, pH 7.4. Shown is one representative data set for the fluorescence emission spectra (top) and the binding curve (bottom). App. k_D values (means ± SD) were calculated from three different binding curves. Fluorescence emissions of Fluos-peptides alone are shown as red dot for comparison. Data is shown for F3-LF self-assembly (**a**), binding of F3-LF to Fluos-IAPP (**b**) and binding of IAPP to Fluos-F3-LF (**c**). App. k_Ds are summarised in Table 4-7. Data of b) is part of a figure in reference [140].

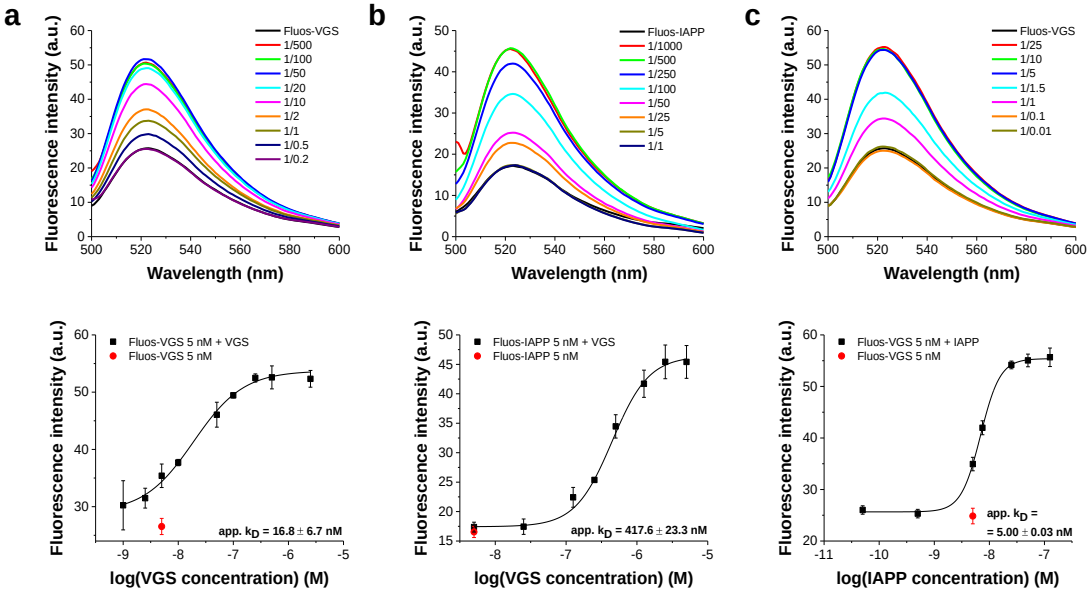

Figure 7-22: Fluorescence spectroscopic titrations with VGS. Titrations were performed using 5 nM Fluos-labelled peptide. Fluorescence emission spectra of Fluos-peptide alone and after titration with the binding partner were recorded in 1xb containing 1 % HFiP, pH 7.4. Shown is one representative data set for the fluorescence emission spectra (top) and the binding curve (bottom). App. k_D values (means ± SD) were calculated from three different binding curves. Fluorescence emissions of Fluos-peptides alone are shown as red dot for comparison. Data is shown for VGS self-assembly (**a**), binding of VGS to Fluos-IAPP (**b**) and binding of IAPP to Fluos-VGS (**c**). App. k_Ds are summarised in Table 4-7.

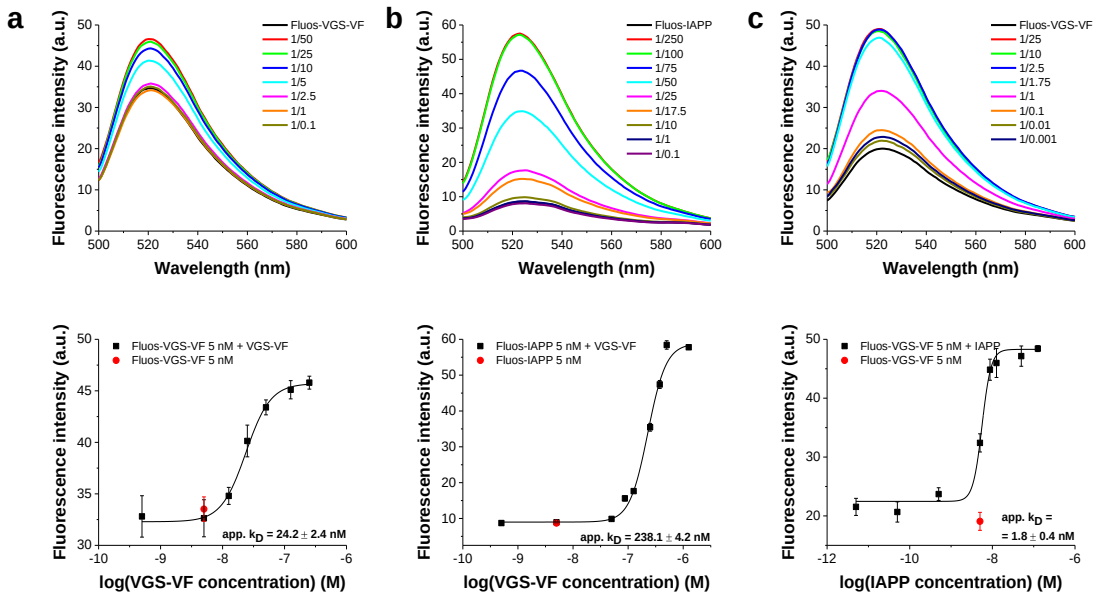

Figure 7-23: Fluorescence spectroscopic titrations with VGS-VF. Titrations were performed using 5 nM Fluos-labelled peptide. Fluorescence emission spectra of Fluos-peptide alone and after titration with the binding partner were recorded in 1xb containing 1 % HFiP, pH 7.4. Shown is one representative data set for the fluorescence emission spectra (top) and the binding curve (bottom). App. k_D values (means ± SD) were calculated from three different binding curves. Fluorescence emissions of Fluos-peptides alone are shown as red dot for comparison. Data is shown for VGS-VF self-assembly (**a**), binding of VGS-VF to Fluos-IAPP (**b**) and binding of IAPP to Fluos-VGS-VF (**c**). App. k_Ds are summarised in Table 4-7.

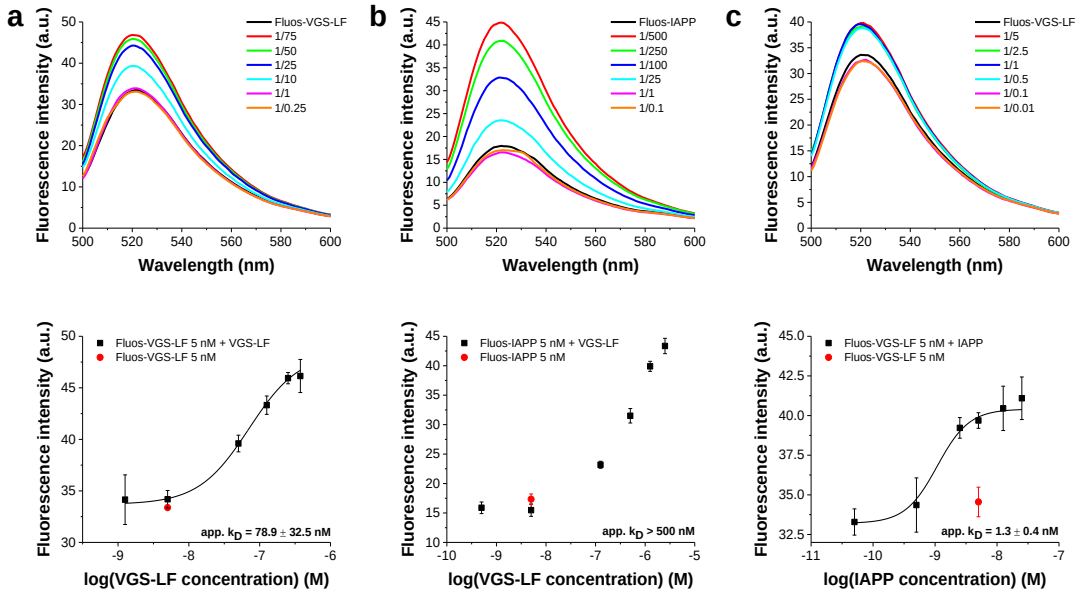

Figure 7-24: Fluorescence spectroscopic titrations with VGS-LF. Titrations were performed using 5 nM Fluos-labelled peptide. Fluorescence emission spectra of Fluos-peptide alone and after titration with the binding partner were recorded in 1xb containing 1 % HFiP, pH 7.4. Shown is one representative data set for the fluorescence emission spectra (top) and the binding curve (bottom). App. k_D values (means ± SD) were calculated from three different binding curves. Fluorescence emissions of Fluos-peptides alone are shown as red dot for comparison. Data is shown for VGS-LF self-assembly (**a**), binding of VGS-LF to Fluos-IAPP (**b**) and binding of IAPP to Fluos-VGS-LF (**c**). App. k_Ds are summarised in Table 4-7.

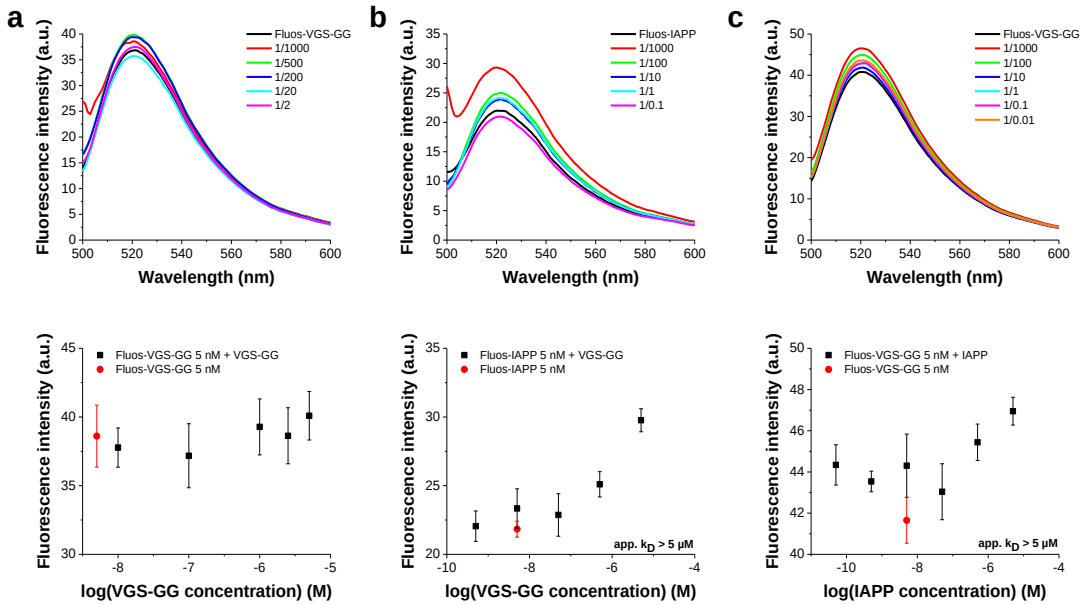

Figure 7-25: Fluorescence spectroscopic titrations with VGS-GG. Titrations were performed using 5 nM Fluos-labelled peptide. Fluorescence emission spectra of Fluos-peptide alone and after titration with the binding partner were recorded in 1xb containing 1 % HFiP, pH 7.4. Shown is one representative data set for the fluorescence emission spectra (top) and the binding curve (bottom). App. k_D values (means ± SD) were calculated from three different binding curves. Fluorescence emissions of Fluos-peptides alone are shown as red dot for comparison. Data is shown for VGS-GG self-assembly (**a**), binding of VGS-GG to Fluos-IAPP (**b**) and binding of IAPP to Fluos-VGS-GG (**c**). App. k_Ds are summarised in Table 4-7.

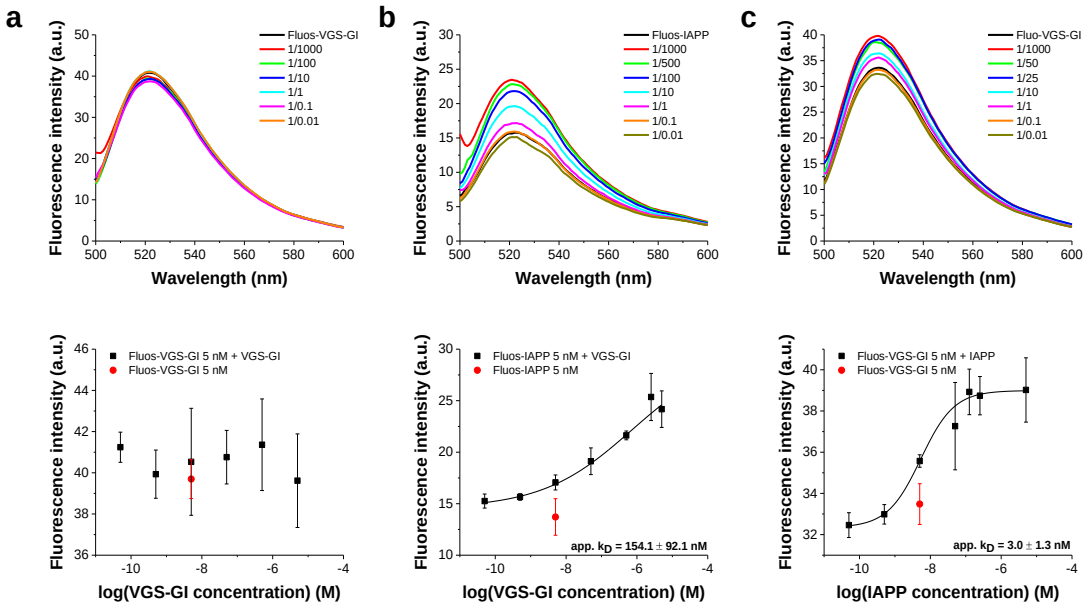

Figure 7-26: Fluorescence spectroscopic titrations with VGS-GI. Titrations were performed using 5 nM Fluos-labelled peptide. Fluorescence emission spectra of Fluos-peptide alone and after titration with the binding partner were recorded in 1xb containing 1 % HFiP, pH 7.4. Shown is one representative data set for the fluorescence emission spectra (top) and the binding curve (bottom). App. k_D values (means ± SD) were calculated from three different binding curves. Fluorescence emissions of Fluos-peptides alone are shown as red dot for comparison. Data is shown for VGS-GI self-assembly (**a**), binding of VGS-GI to Fluos-IAPP (**b**) and binding of IAPP to Fluos-VGS-GI (**c**). App. k_Ds are summarised in Table 4-7.

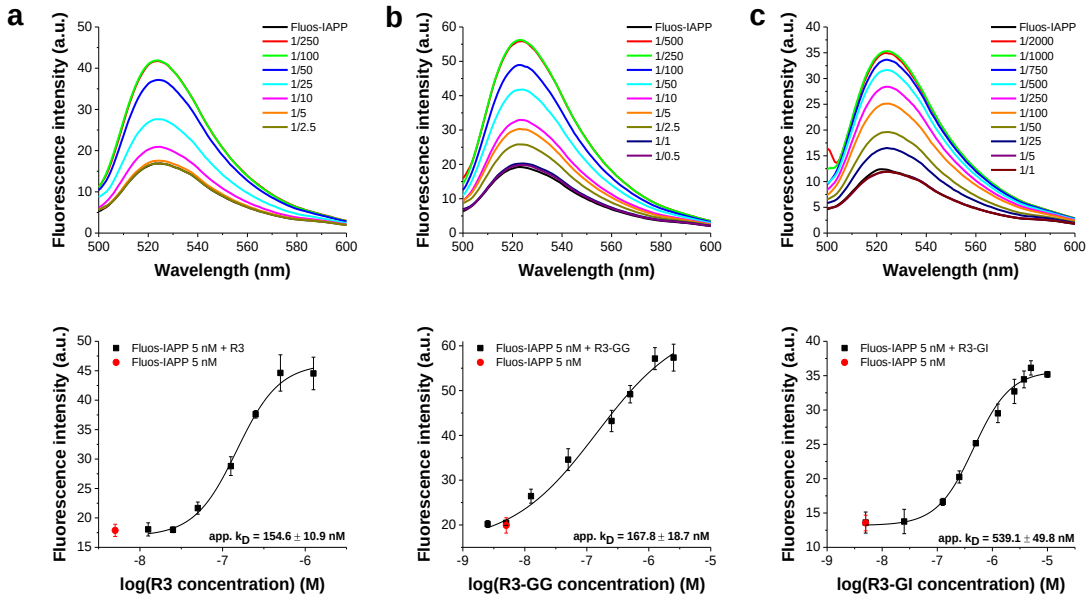

Figure 7-27: Fluorescence spectroscopic titrations with R3, R3-GG and R3-GI. Titrations were performed using 5 nM Fluos-labelled IAPP. Fluorescence emission spectra of Fluos-IAPP alone and after titration with the binding partner were recorded in 1xb containing 1 % HFiP, pH 7.4. Shown is one representative data set for the fluorescence emission spectra (top) and the binding curve (bottom). App. k_D values (means ± SD) were calculated from three different binding curves. Fluorescence emission of Fluos-IAPP alone is shown as red dot for comparison. Data is shown for R3 (**a**), R3-GG (**b**) and R3-GI (**c**). App. k_Ds are summarised in Table 4-7.

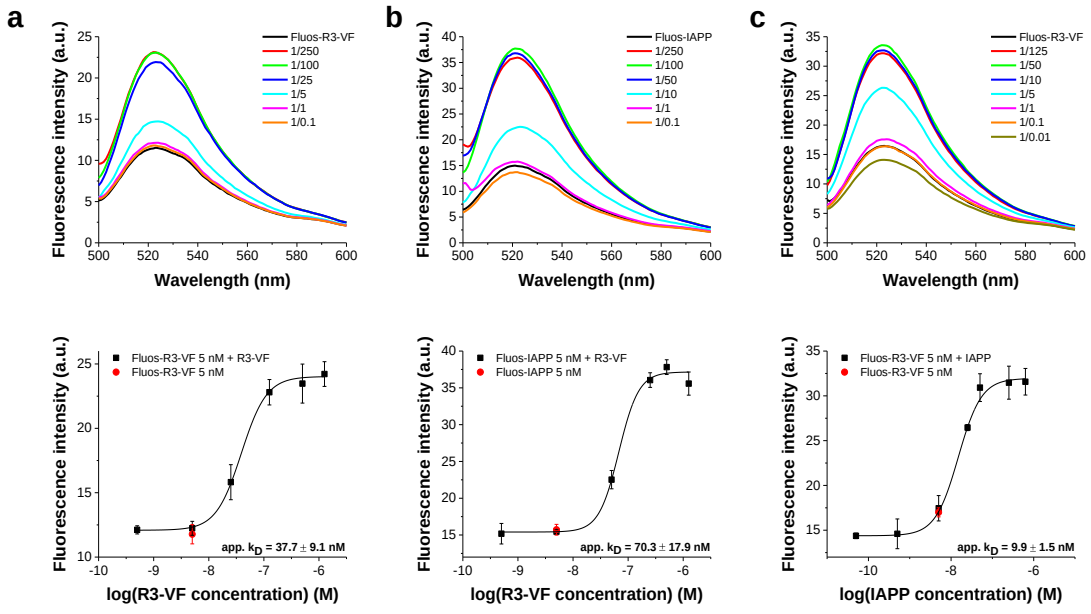

Figure 7-28: Fluorescence spectroscopic titrations with R3-VF. Titrations were performed using 5 nM Fluos-labelled peptide. Fluorescence emission spectra of Fluos-peptide alone and after titration with the binding partner were recorded in 1xb containing 1 % HFiP, pH 7.4. Shown is one representative data set for the fluorescence emission spectra (top) and the binding curve (bottom). App. k_D values (means ± SD) were calculated from three different binding curves. Fluorescence emissions of Fluos-peptides alone are shown as red dot for comparison. Data is shown for R3-VF self-assembly (**a**), binding of R3-VF to Fluos-IAPP (**b**) and binding of IAPP to Fluos-R3-VF (**c**). App. k_Ds are summarised in Table 4-7.

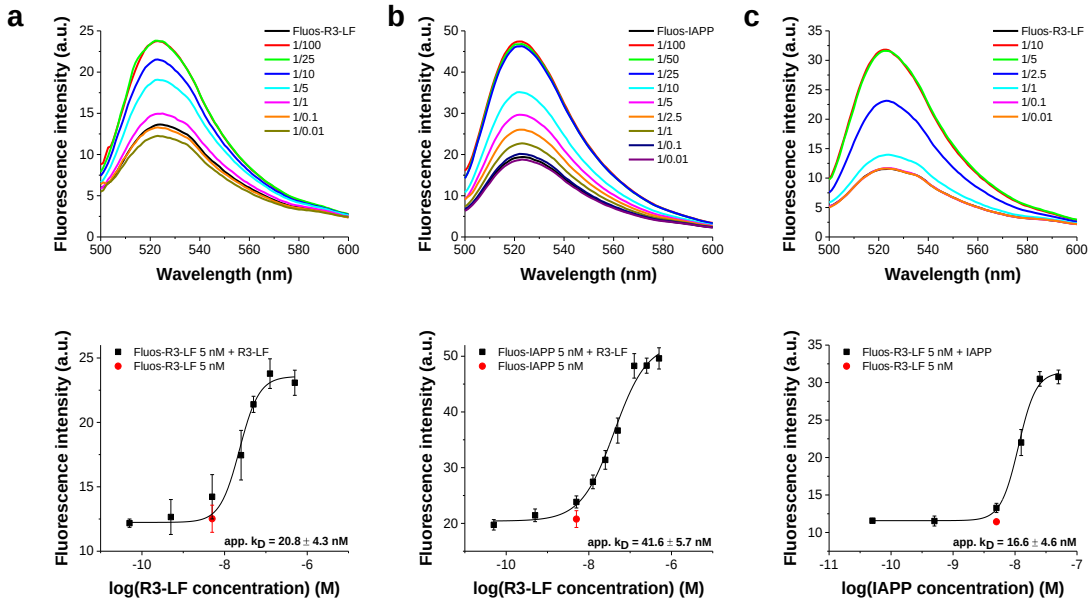

Figure 7-29: Fluorescence spectroscopic titrations with R3-LF. Titrations were performed using 5 nM Fluos-labelled peptide. Fluorescence emission spectra of Fluos-peptide alone and after titration with the binding partner were recorded in 1xb containing 1 % HFiP, pH 7.4. Shown is one representative data set for the fluorescence emission spectra (top) and the binding curve (bottom). App. k_D values (means ± SD) were calculated from three different binding curves. Fluorescence emissions of Fluos-peptides alone are shown as red dot for comparison. Data is shown for R3-LF self-assembly (**a**), binding of R3-LF to Fluos-IAPP (**b**) and binding of IAPP to Fluos-R3-LF (**c**). App. k_Ds are summarised in Table 4-7.

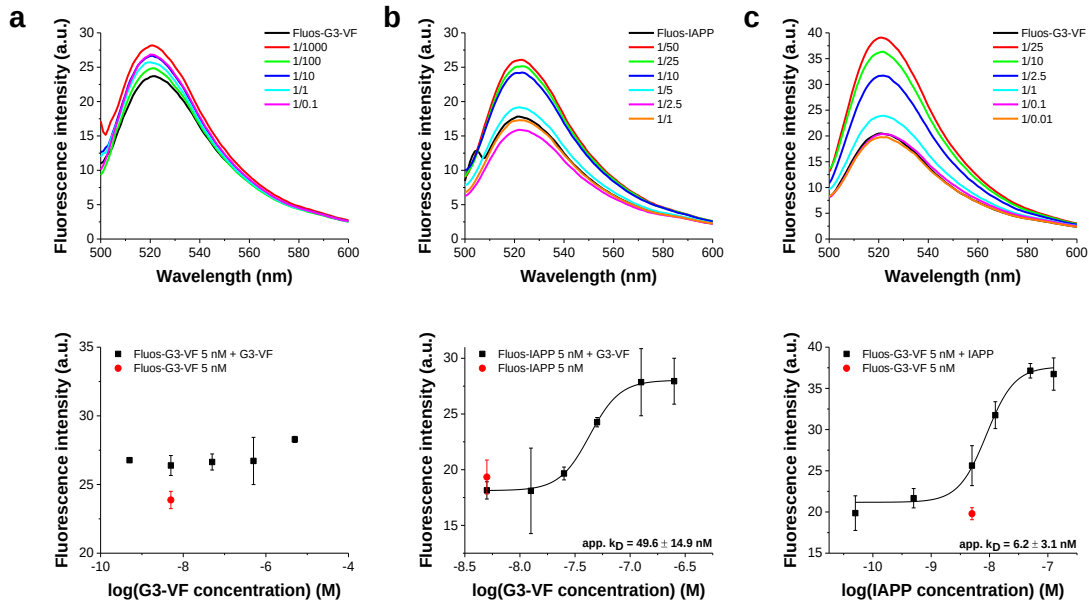

Figure 7-30: Fluorescence spectroscopic titrations with G3-VF. Titrations were performed using 5 nM Fluos-labelled peptide. Fluorescence emission spectra of Fluos-peptide alone and after titration with the binding partner were recorded in 1xb containing 1 % HFiP, pH 7.4. Shown is one representative data set for the fluorescence emission spectra (top) and the binding curve (bottom). App. k_D values (means ± SD) were calculated from three different binding curves. Fluorescence emissions of Fluos-peptides alone are shown as red dot for comparison. Data is shown for G3-VF self-assembly (**a**), binding of G3-VF to Fluos-IAPP (**b**) and binding of IAPP to Fluos-G3-VF (**c**). Titrations in (b) and (c) were done by Sophia Kalpazidou during her Erasmus internship[147]. App. k_Ds are summarised in Table 4-7.

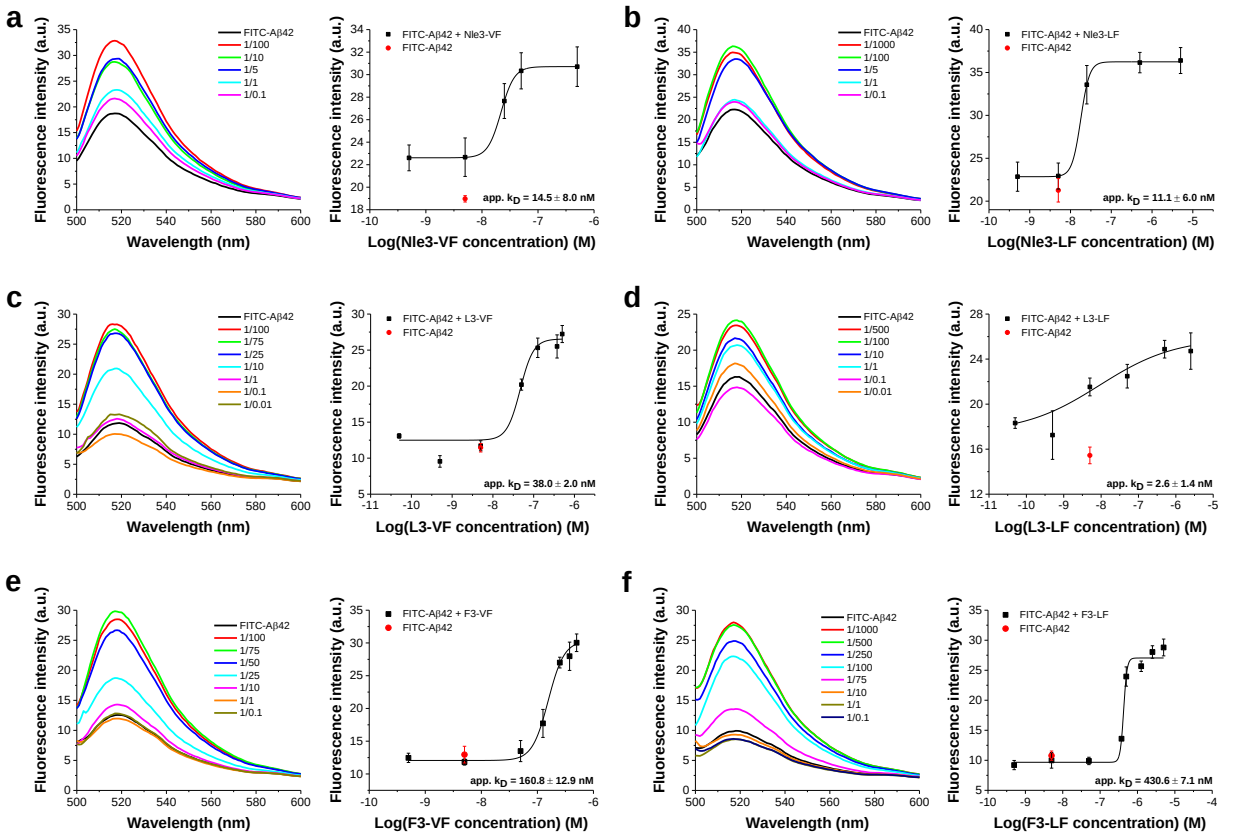

Figure 7-31: Fluorescence spectroscopic titrations of FITC-Aβ42 with ACMs. Fluorescence emission spectra of FITC-Aβ42 (5 nM) alone and after titration with ACMs were recorded in 1xb containing 1 % HFiP, pH 7.4. Shown is one representative data set for the fluorescence emission spectra (left) and the binding curve (right). App. k_D value (mean ± SD) was calculated from three different binding curves. Fluorescence emission of FITC-Aβ42 alone is shown as red dot for comparison. Data is presented for Nle3-VF (**a**), Nle3-LF (**b**), L3-VF (**c**), L3-LF (**d**), F3-VF (**e**) and F3-LF (**f**). App. k_Ds are summarised in Table 4-15. Data in a) is part of a figure in reference [140].

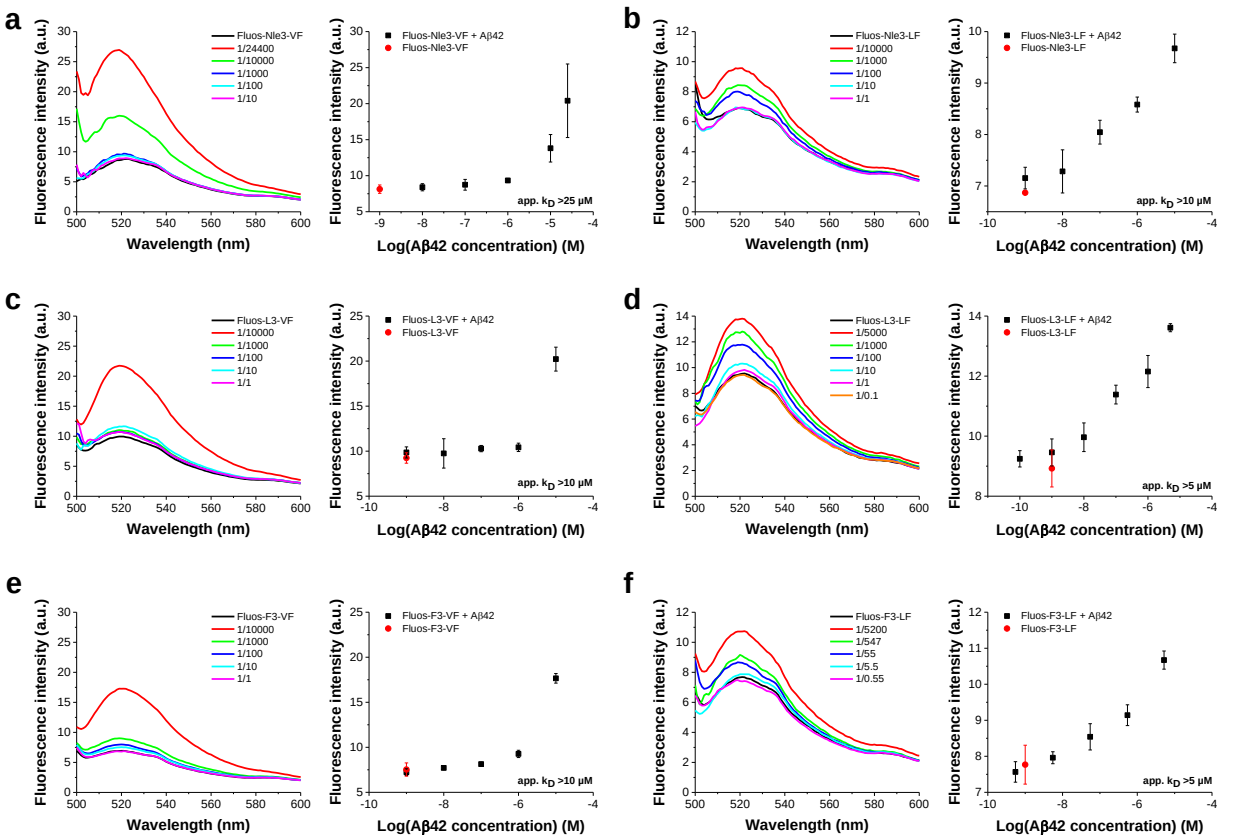

Figure 7-32: Fluorescence spectroscopic titrations of Fluos-ACMs with Aβ42. Titrations were performed using 1 nM Fluos-ACMs. Fluorescence emission spectra of Fluos-ACMs alone and after titration with Aβ42 were collected in 50 mM ammonium acetate containing 1 % HFiP, pH 8.5. Shown is one representative data set for the fluorescence emission spectra (left) and the binding curve (right). App. k_D values (mean ± SD) were estimated from three different binding curves. Fluorescence emissions of Fluos-ACMs alone are shown as red dot for comparison. Data is shown for Nle3-VF (**a**), Nle3-LF (**b**), L3-VF (**c**), L3-LF (**d**), F3-VF (**e**) and F3-LF (**f**). App. k_Ds are summarised in Table 4-15.

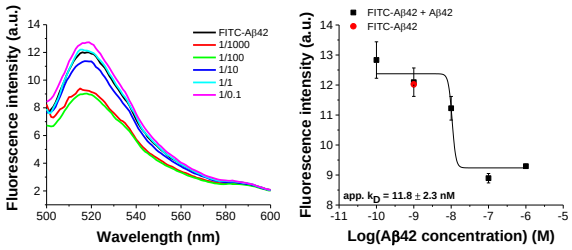

Figure 7-33: Fluorescence spectroscopic titrations of FITC-Aβ42 with Aβ42. Titrations were performed using 1 nM FITC-Aβ42. Fluorescence emission spectra of FITC-Aβ42 alone and after titration with Aβ42 were collected in 50 mM ammonium acetate containing 1 % HFiP, pH 8.5. Shown is one representative data set for the fluorescence emission spectra (left) and the binding curve (right). App. k_D value (mean ± SD) was estimated from three different binding curves. Fluorescence emissions of FITC-Aβ42 alone is shown as red dot for comparison.

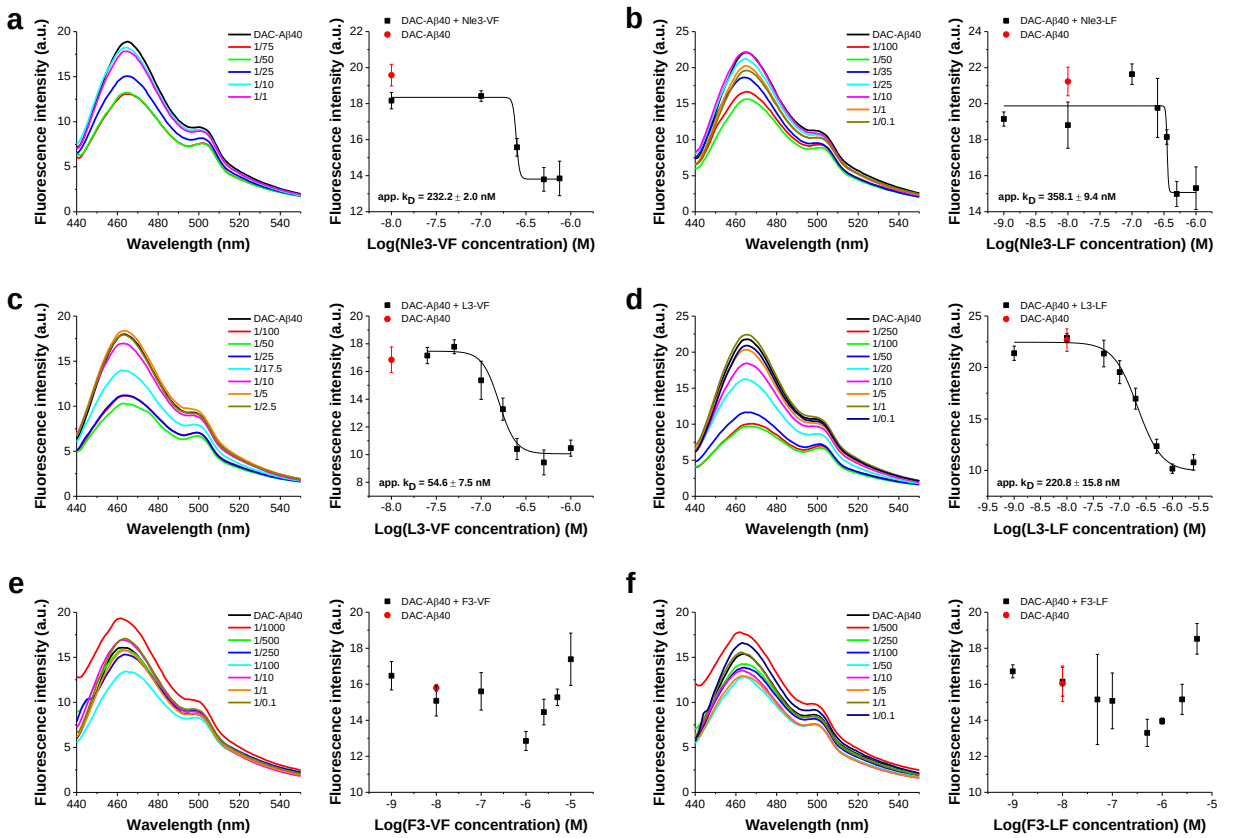

Figure 7-34: Fluorescence spectroscopic titrations of DAC-Aβ40 with ACMs. Titrations were performed using 10 nM DAC-Aβ40 and fluorescence emission spectra of DAC-Aβ40 alone and after titration with ACMs were recorded in 1xb containing 1 % HFiP, pH 7.4. Shown is one representative data set for the fluorescence emission spectra (left) and the binding curve (right). App. k_D value (mean ± SD) was calculated from three different binding curves. Fluorescene emission of DAC-Aβ40 alone is shown as red dot for comparison. Data is shown for Nle3-VF (**a**), Nle3-LF (**b**), L3-VF (**c**), L3-LF (**d**), F3-VF (**e**) and F3-LF (**f**). App. k_Ds are summarised in Table 4-15.

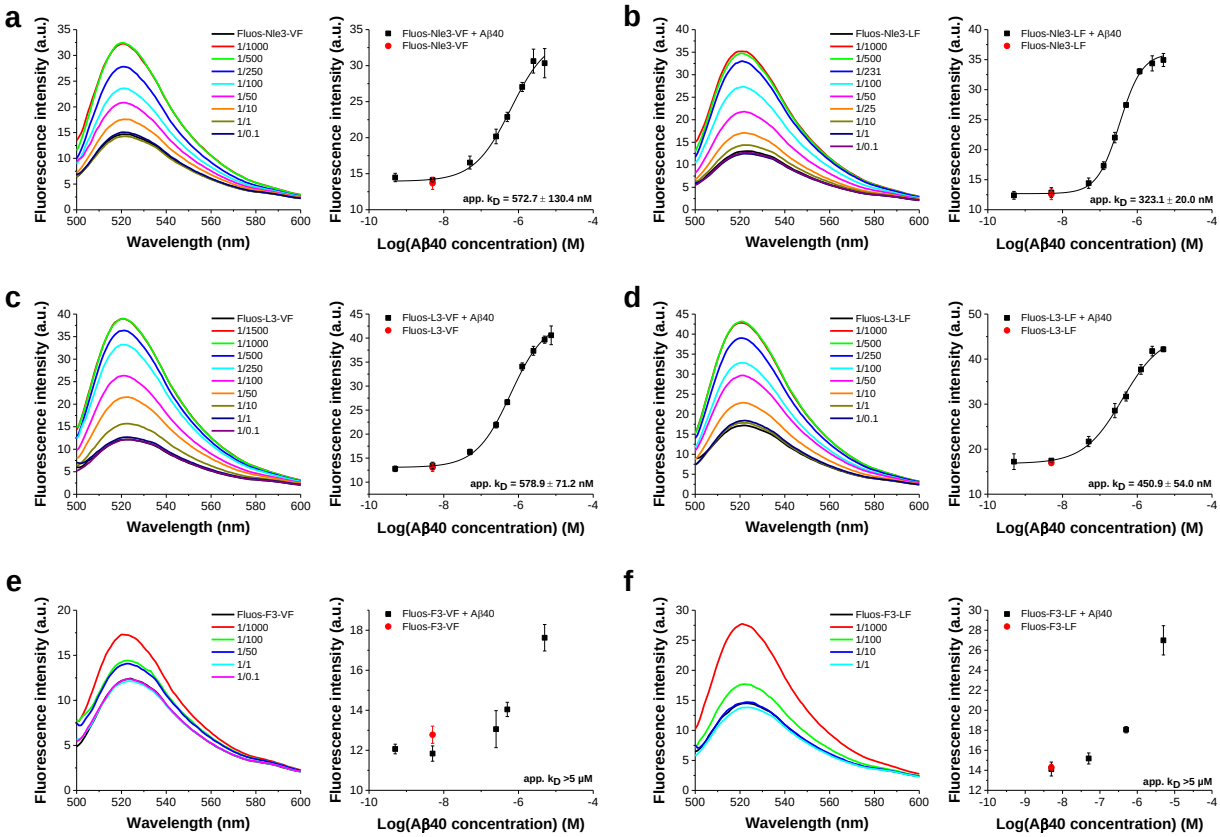

Figure 7-35: Fluorescence spectroscopic titrations of Fluos-ACMs with Aβ40. Fluorescence emission spectra of Fluos-ACMs (5 nM) alone and after titration with ACMs were measured in 1xb containing 1 % HFiP, pH 7.4. Shown is one representative data set for the fluorescence emission spectra (left) and the binding curve (right). App. k_D value (mean ± SD) was calculated from three different binding curves. Fluorescence emissions of Fluos-ACMs alone are sown as red dot for comparison. Data is presented for Nle3-VF (**a**), Nle3-LF (**b**), L3-VF (**c**), L3-LF (**d**), F3-VF (**e**) and F3-LF (**f**). App. k_Ds are summarised in Table 4-15.

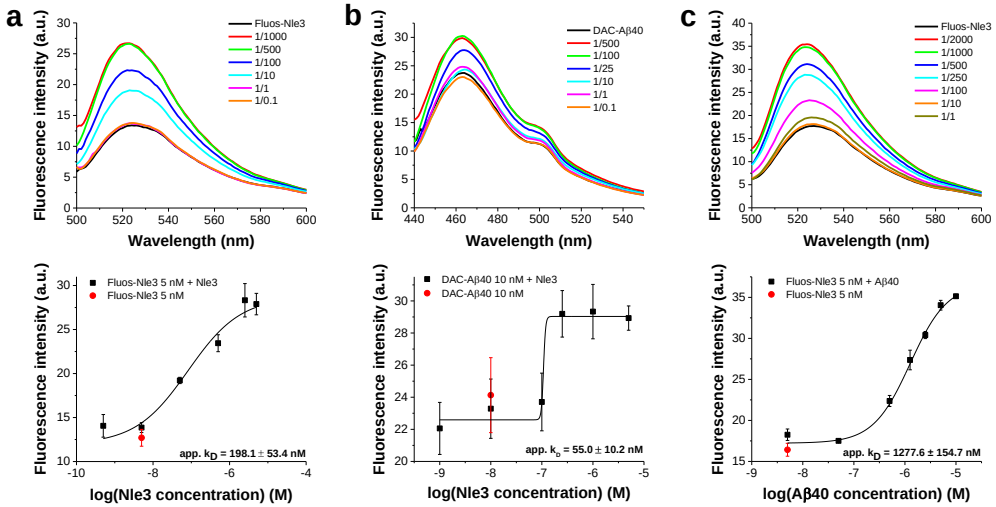

Figure 7-36: Fluorescence spectroscopic titrations of Fluos-Nle3 with Nle3 and Aβ40 and of DAC-Aβ40 with Nle3. Titrations were performed using 5 nM Fluos-Nle3 or 10 nM DAC-Aβ40. Fluorescence emission spectra of Fluos-Nle3 or DAC-Aβ40 alone and after titration with the binding partner were recorded in 1xb containing 1 % HFiP, pH 7.4. Shown is one representative data set for the fluorescence emission spectra (top) and the binding curve (bottom). App. k_D values (means ± SD) were calculated from three different binding curves. Fluorescence emissions of Fluos-Nle3 or DAC-Aβ40 alone are shown as red dot for comparison. Data is shown for Nle3 self-assembly (**a**), binding of Nle3 to DAC-Ab40 (**b**) and binding of Aβ40 to Fluos-Nle3 (**c**). App. k_Ds are summarised in Table 4-16.

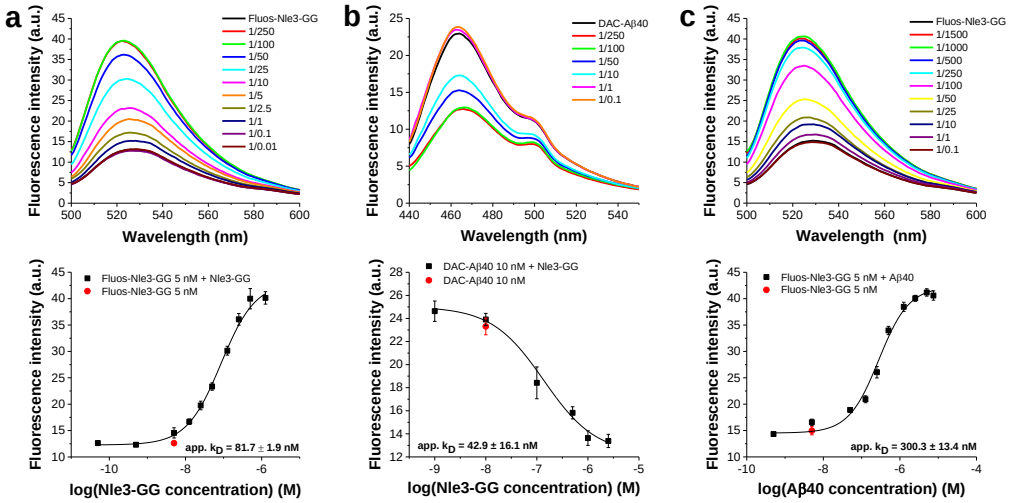

Figure 7-37: Fluorescence spectroscopic titrations of Fluos-Nle3-GG with Nle3-GG and Aβ40, and of DAC-Aβ40 with Nle3-GG. Titrations were performed using 5 nM Fluos-Nle3-GG or 10 nM DAC-Aβ40. Fluorescence emission spectra of Fluos-Nle3-GG or DAC-Aβ40 alone and after titration with the binding partner were recorded in 1xb containing 1 % HFiP, pH 7.4. Shown is one representative data set for the fluorescence emission spectra (top) and the binding curve (bottom). App. k_D values (means ± SD) were calculated from three different binding curves. Fluorescence emissions of Fluos-Nle3-GG or DAC-Aβ40 alone are shown as red dot for comparison. Data is shown for Nle3-GG self-assembly (**a**), binding of Nle3-GG to DAC-Ab40 (**b**) and binding of Aβ40 to Fluos-Nle3-GG (**c**). App. k_Ds are summarised in Table 4-16.

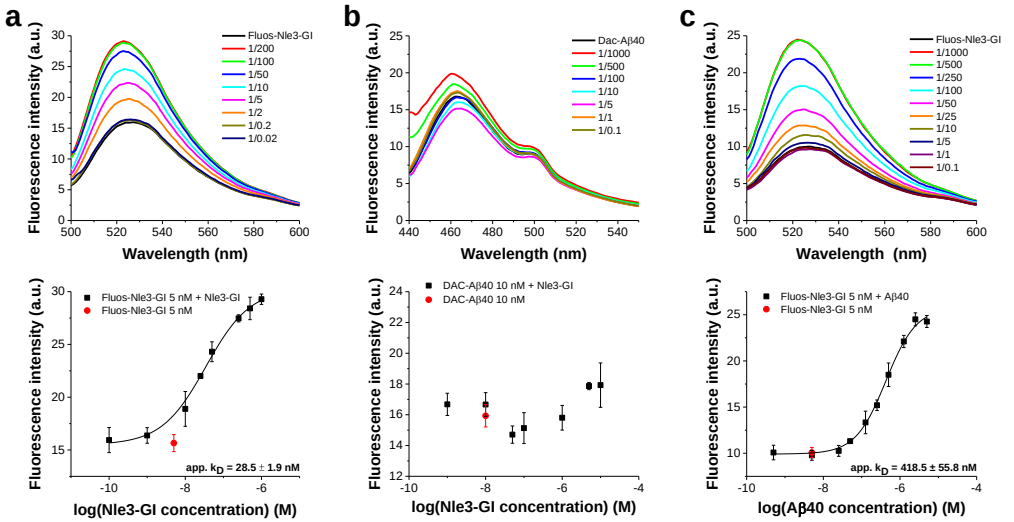

Figure 7-38: Fluorescence spectroscopic titrations of Fluos-Nle3-GI with Nle3-GI and Aβ40, and of DAC-Aβ40 with Nle3-GI. Titrations were performed using 5 nM Fluos-Nle3-GI or 10 nM DAC-Aβ40. Fluorescence emission spectra of Fluos-Nle3-GI or DAC-Aβ40 alone and after titration with the binding partner were recorded in 1xb containing 1 % HFiP, pH 7.4. Shown is one representative data set for the fluorescence emission spectra (top) and the binding curve (bottom). App. k_D values (means ± SD) were calculated from three different binding curves. Fluorescence emissions of Fluos-Nle3-GI or DAC-Aβ40 alone are shown as red dot for comparison. Data is shown for Nle3-GI self-assembly (**a**), binding of Nle3-GI to DAC-Ab40 (**b**) and binding of Aβ40 to Fluos-Nle3-GI (**c**). App. k_Ds are summarised in Table 4-16.

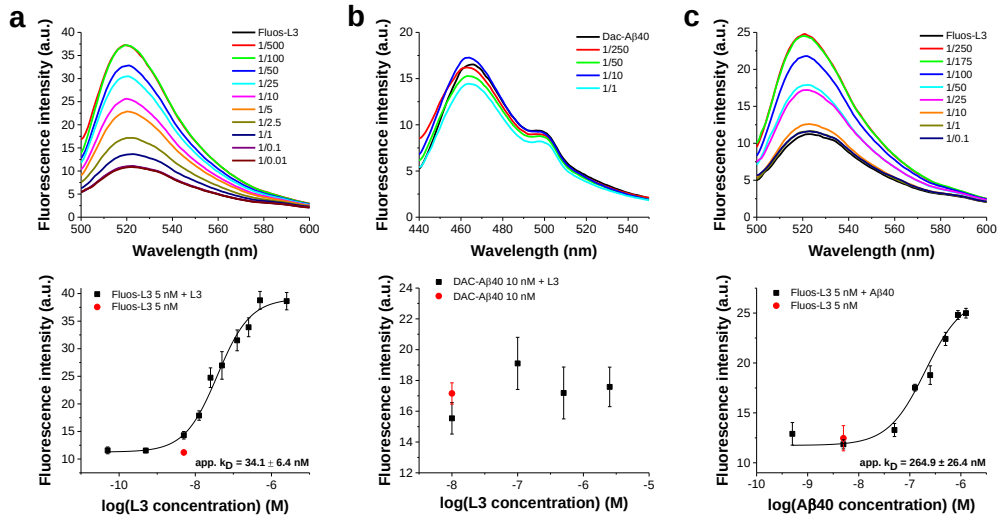

Figure 7-39: Fluorescence spectroscopic titrations of Fluos-L3 with L3 and Aβ40, and of DAC-Aβ40 with L3. Titrations were performed using 5 nM Fluos-L3 or 10 nM DAC-Aβ40. Fluorescence emission spectra of Fluos-L3 or DAC-Aβ40 alone and after titration with the binding partner were recorded in 1xb containing 1 % HFiP, pH 7.4. Shown is one representative data set for the fluorescence emission spectra (top) and the binding curve (bottom). App. k_D values (means ± SD) were calculated from three different binding curves. Fluorescence emissions of Fluos-L3 or DAC-Aβ40 alone are shown as red dot for comparison. Data is shown for L3 self-assembly (**a**), binding of L3 to DAC-Ab40 (**b**) and binding of Aβ40 to Fluos-L3 (**c**). App. k_Ds are summarised in Table 4-16.

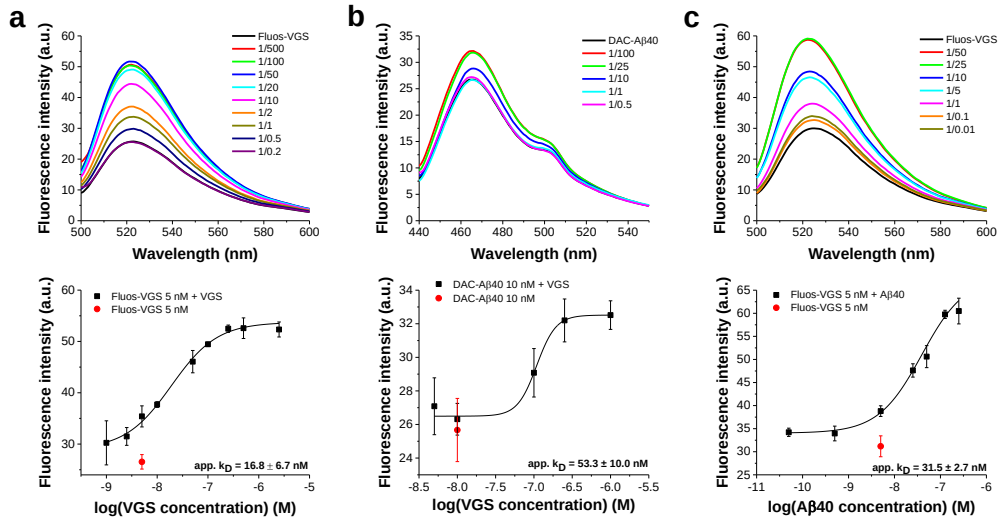

Figure 7-40: Fluorescence spectroscopic titrations of Fluos-VGS with VGS and Aβ40, and of DAC-Aβ40 with VGS. Titrations were performed using 5 nM Fluos-VGS or 10 nM DAC-Aβ40. Fluorescence emission spectra of Fluos-VGS or DAC-Aβ40 alone and after titration with the binding partner were recorded in 1xb containing 1 % HFiP, pH 7.4. Shown is one representative data set for the fluorescence emission spectra (top) and the binding curve (bottom). App. k_D values (means ± SD) were calculated from three different binding curves. Fluorescence emissions of Fluos-VGS or DAC-Aβ40 alone are shown as red dot for comparison. Data is shown for VGS self-assembly (**a**), binding of VGS to DAC-Ab40 (**b**) and binding of Aβ40 to Fluos-VGS (**c**). App. k_Ds are summarised in Table 4-16.

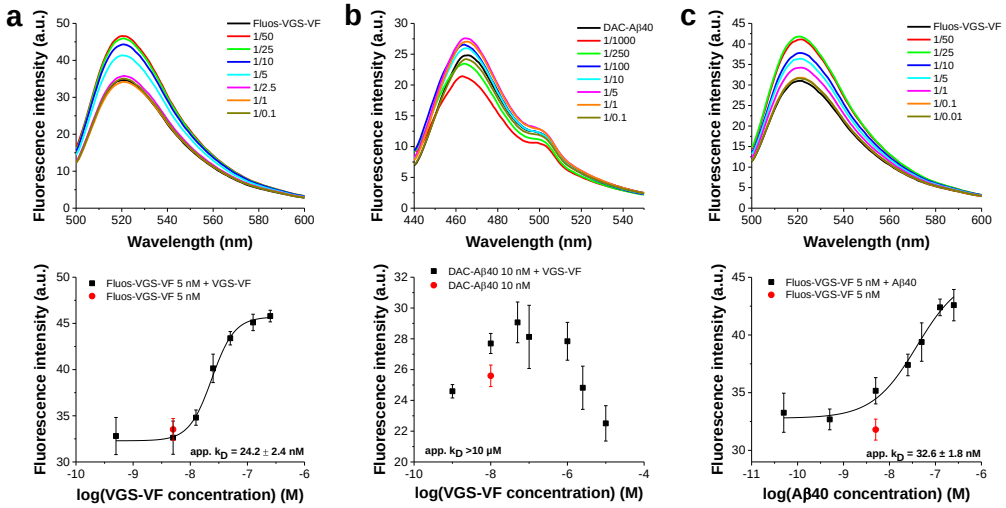

Figure 7-41: Fluorescence spectroscopic titrations of Fluos-VGS-VF with VGS-VF and Aβ40, and of DAC-Aβ40 with VGS-VF. Titrations were performed using 5 nM Fluos-VGS-VF or 10 nM DAC-Aβ40. Fluorescence emission spectra of Fluos-VGS-VF or DAC-Aβ40 alone and after titration with the binding partner were recorded in 1xb containing 1 % HFiP, pH 7.4. Shown is one representative data set for the fluorescence emission spectra (top) and the binding curve (bottom). App. k_D values (means ± SD) were calculated from three different binding curves. Fluorescence emissions of Fluos-VGS-VF or DAC-Aβ40 alone are shown as red dot for comparison. Data is shown for VGS-VF self-assembly (**a**), binding of VGS-VF to DAC-Ab40 (**b**) and binding of Aβ40 to Fluos-VGS-VF (**c**). App. k_Ds are summarised in Table 4-16.

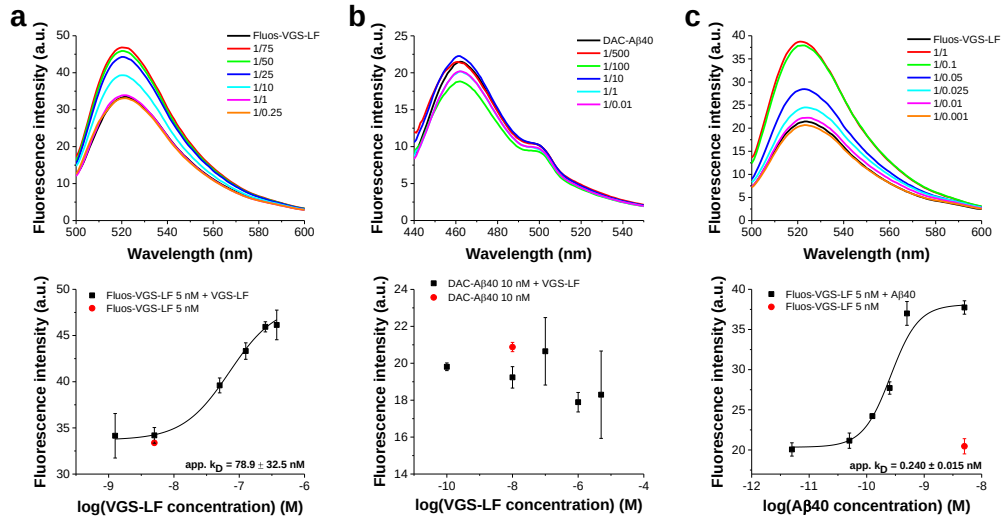

Figure 7-42: Fluorescence spectroscopic titrations of Fluos-VGS-LF with VGS-LF and Aβ40, and of DAC-Aβ40 with VGS-LF. Titrations were performed using 5 nM Fluos-VGS-LF or 10 nM DAC-Aβ40. Fluorescence emission spectra of Fluos-VGS-LF or DAC-Aβ40 alone and after titration with the binding partner were recorded in 1xb containing 1 % HFiP, pH 7.4. Shown is one representative data set for the fluorescence emission spectra (top) and the binding curve (bottom). App. k_D values (means ± SD) were calculated from three different binding curves. Fluorescence emissions of Fluos-VGS-LF or DAC-Aβ40 alone are shown as red dot for comparison. Data is shown for VGS-LF self-assembly (**a**), binding of VGS-LF to DAC-Ab40 (**b**) and binding of Aβ40 to Fluos-VGS-LF (**c**). App. k_Ds are summarised in Table 4-16.

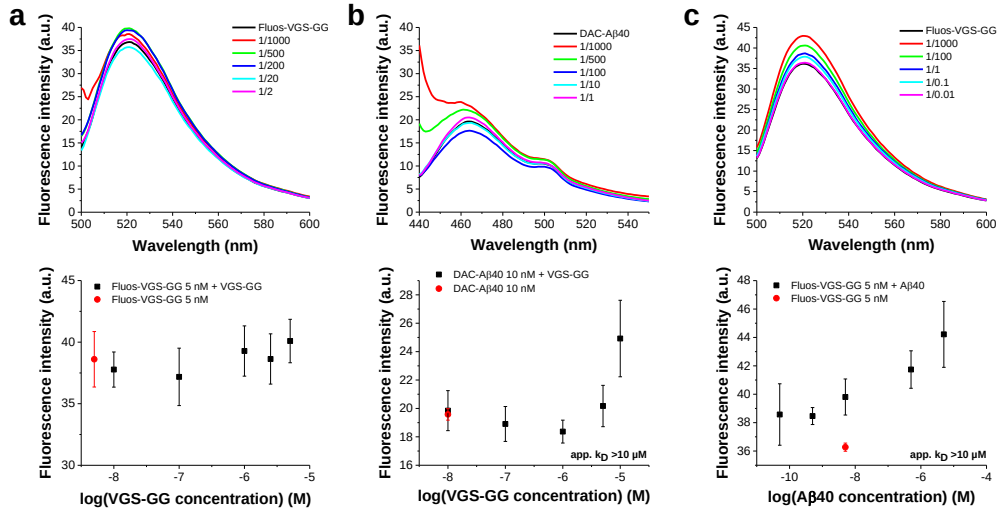

Figure 7-43: Fluorescence spectroscopic titrations of Fluos-VGS-GG with VGS-GG and Aβ40, and of DAC-Aβ40 with VGS-GG. Titrations were performed using 5 nM Fluos-VGS-GG or 10 nM DAC-Aβ40. Fluorescence emission spectra of Fluos-VGS-GG or DAC-Aβ40 alone and after titration with the binding partner were recorded in 1xb containing 1 % HFiP, pH 7.4. Shown is one representative data set for the fluorescence emission spectra (top) and the binding curve (bottom). App. k_D values (means ± SD) were calculated from three different binding curves. Fluorescence emissions of Fluos-VGS-GG or DAC-Aβ40 alone are shown as red dot for comparison. Data is shown for VGS-GG self-assembly (**a**), binding of VGS-GG to DAC-Ab40 (**b**) and binding of Aβ40 to Fluos-VGS-GG (**c**). App. k_Ds are summarised in Table 4-16.

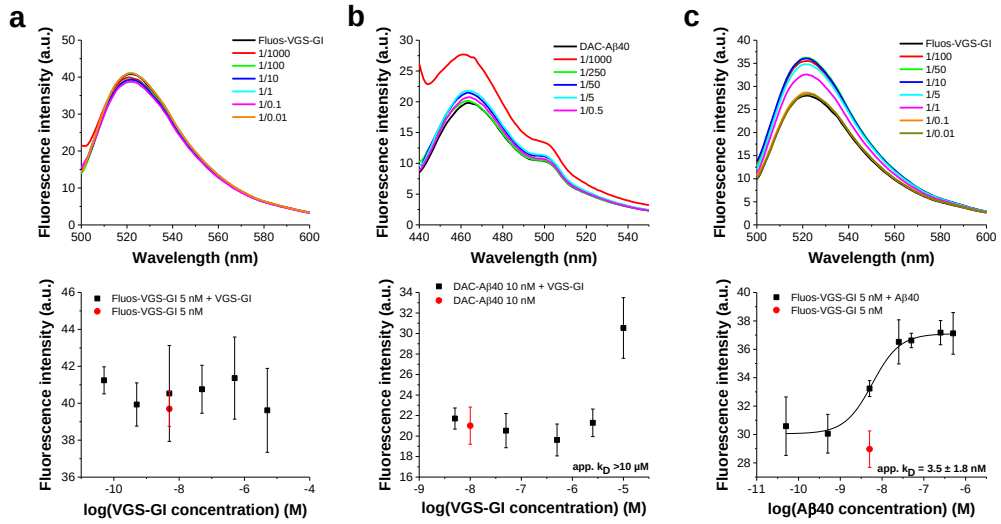

Figure 7-44: Fluorescence spectroscopic titrations of Fluos-VGS-GI with VGS-GI and Aβ40, and of DAC-Aβ40 with VGS-GI. Titrations were performed using 5 nM Fluos-VGS-GI or 10 nM DAC-Aβ40. Fluorescence emission spectra of Fluos-VGS-GI or DAC-Aβ40 alone and after titration with the binding partner were recorded in 1xb containing 1 % HFiP, pH 7.4. Shown is one representative data set for the fluorescence emission spectra (top) and the binding curve (bottom). App. k_D values (means ± SD) were calculated from three different binding curves. Fluorescence emissions of Fluos-VGS-GI or DAC-Aβ40 alone are shown as red dot for comparison. Data is shown for VGS-GI self-assembly (**a**), binding of VGS-GI to DAC-Ab40 (**b**) and binding of Aβ40 to Fluos-VGS-GI (**c**). App. k_Ds are summarised in Table 4-16.

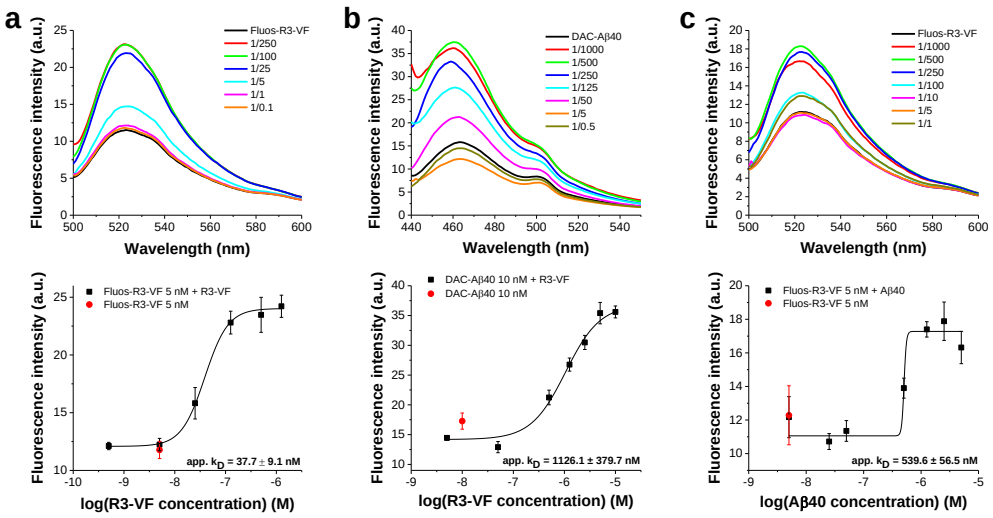

Figure 7-45: Fluorescence spectroscopic titrations of Fluos-R3-VF with R3-VF and Aβ40, and of DAC-Aβ40 with R3-VF. Titrations were performed using 5 nM Fluos-R3-VF or 10 nM DAC-Aβ40. Fluorescence emission spectra of Fluos-R3-VF or DAC-Aβ40 alone and after titration with the binding partner were recorded in 1xb containing 1 % HFiP, pH 7.4. Shown is one representative data set for the fluorescence emission spectra (top) and the binding curve (bottom). App. k_D values (means ± SD) were calculated from three different binding curves. Fluorescence emissions of Fluos-R3-VF or DAC-Aβ40 alone are shown as red dot for comparison. Data is shown for R3-VF self-assembly (**a**), binding of R3-VF to DAC-Ab40 (**b**) and binding of Aβ40 to Fluos-R3-VF (**c**). App. k_Ds are summarised in Table 4-16.

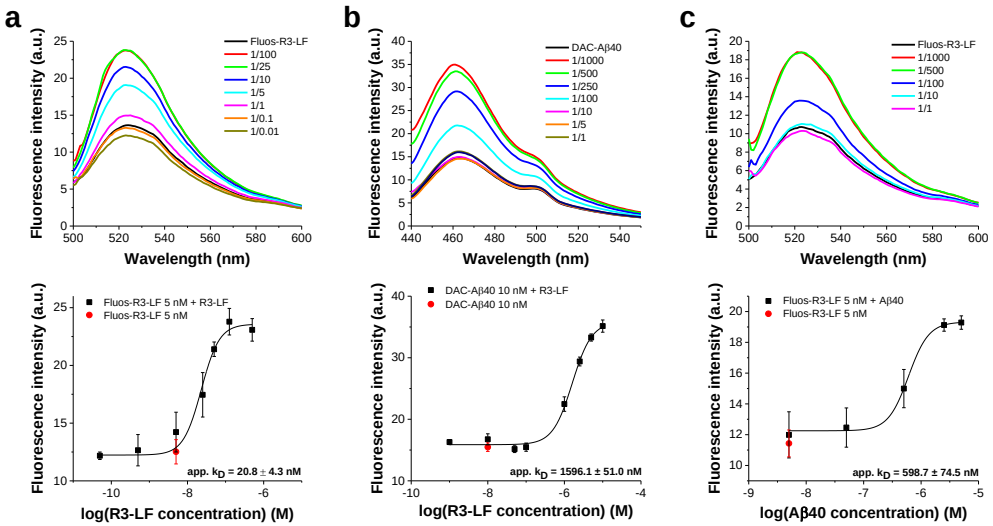

Figure 7-46: Fluorescence spectroscopic titrations of Fluos-R3-LF with R3-LF and Aβ40, and of DAC-Aβ40 with R3-LF. Titrations were performed using 5 nM Fluos-R3-LF or 10 nM DAC-Aβ40. Fluorescence emission spectra of Fluos-R3-LF or DAC-Aβ40 alone and after titration with the binding partner were recorded in 1xb containing 1 % HFiP, pH 7.4. Shown is one representative data set for the fluorescence emission spectra (top) and the binding curve (bottom). App. k_D values (means ± SD) were calculated from three different binding curves. Fluorescence emissions of Fluos-R3-LF or DAC-Aβ40 alone are shown as red dot for comparison. Data is shown for R3-LF self-assembly (**a**), binding of R3-LF to DAC-Ab40 (**b**) and binding of Aβ40 to Fluos-R3-LF (**c**). App. k_Ds are summarised in Table 4-16.

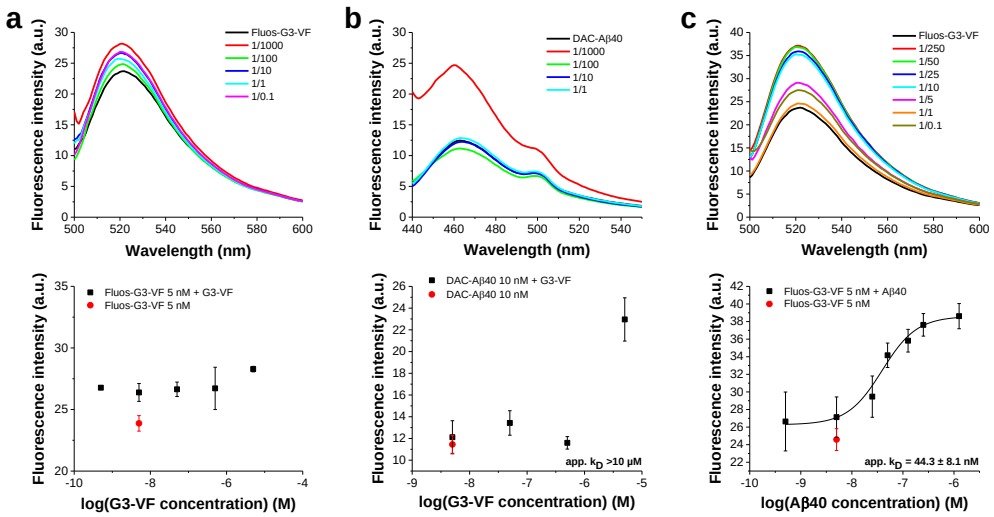

Figure 7-47: Fluorescence spectroscopic titrations of Fluos-G3-VF with G3-VF and Aβ40, and of DAC-Aβ40 with G3-VF. Titrations were performed using 5 nM Fluos-G3-VF or 10 nM DAC-Aβ40. Fluorescence emission spectra of Fluos-G3-VF or DAC-Aβ40 alone and after titration with the binding partner were recorded in 1xb containing 1 % HFiP, pH 7.4. Shown is one representative data set for the fluorescence emission spectra (top) and the binding curve (bottom). App. k_D values (means ± SD) were calculated from three different binding curves. Fluorescence emissions of Fluos-G3-VF or DAC-Aβ40 alone are shown as red dot for comparison. Data is shown for G3-VF self-assembly (**a**), binding of G3-VF to DAC-Ab40 (**b**) and binding of Aβ40 to Fluos-G3-VF (**c**). Titrations in (b) and (c) were done by Sophia Kalpazidou during her Erasmus internship[147]. App. k_Ds are summarised in Table 4-16.

7.6 Cross linking experiments

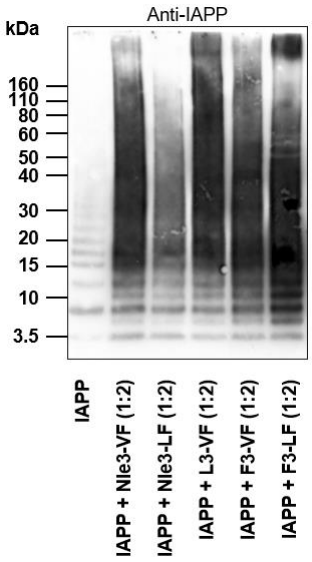

Figure 7-48: Comparison of species found in aged solutions containing IAPP or its mixtures with different ACMs. Glutaraldehyde-mediated cross linking was performed of 7 days aged solutions containing either IAPP (30 µM) or its mixture with indicated ACMs (1:2). Species were analysed by NuPAGE gel electrophoresis followed by Western blot analysis using an anti-IAPP specific antibody. All ACMs show similar hetero-dimer and -trimer/-tetramer formation as well as HMW hetero-assemblies. Data is representative of $\geq$ 2 membranes and is part of a figure in reference [140].

7.7 TEM pictures

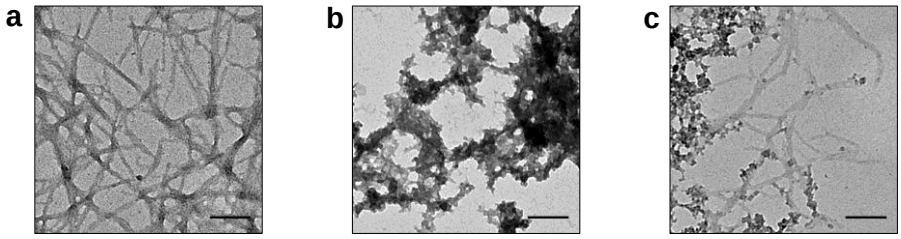

Figure 7-49: TEM images of aged TAMRA-IAPP, Fluos-Nle3-VF, and their 1:2-mixture. Incubations were prepared in 1xb and contained 16.5 µM TAMRA-IAPP or 33 µM Fluos-Nle3-VF or their 1:2-mixture, as for 2-PM studies. TEM samples were taken after 6 days of incubation. Results are shown for TAMRA-IAPP (**a**), Fluos-Nle3-VF (**b**), and their 1:2-mixture (**c**). Scale bars are 100 nm.

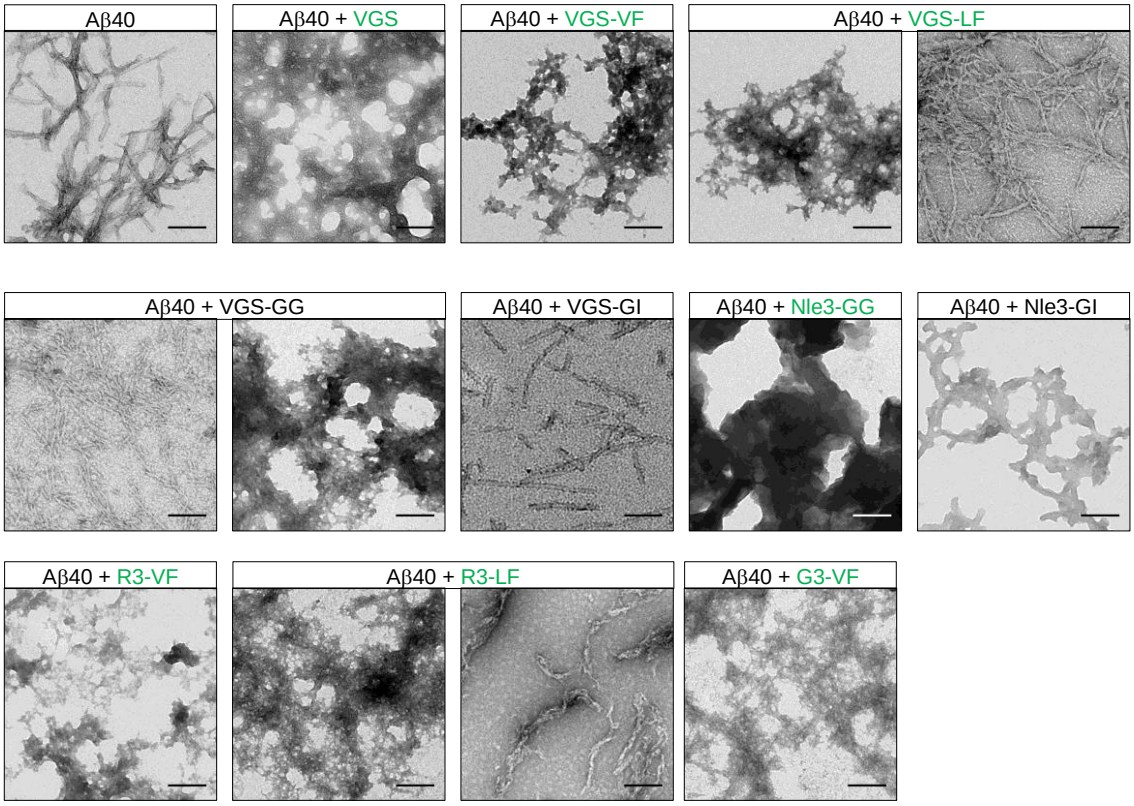

Figure 7-50: TEM images of mixtures of Aβ40 with ADPs. Samples for TEM analysis were taken from solutions of Aβ40 (16.5 µM) or Aβ40/peptide mixtures 1:1 after 8 days of aging (ThT assay buffer 1 % HFIP). Peptides still inhibiting Aβ40 after 8 days are highlighted in green. When two images are shown of the same sample, both species were observed in approximately equal amounts on the TEM grid. Scale bars are 100 nm.

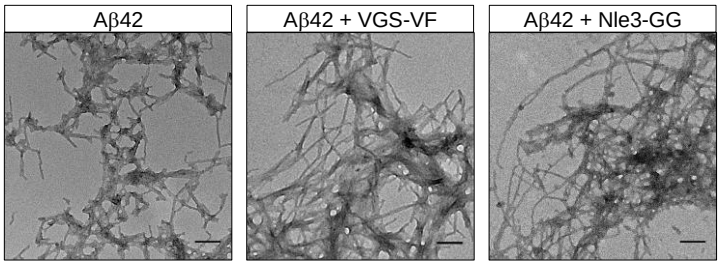

Figure 7-51: TEM images of mixtures of Aβ42 with VGS-VF and Nle3-GG. Solutions containing Aβ42 (5 µM) or 1:1-mixtures with VGS-VF or Nle3-GG, respectively, were aged for 6 days (45 mM ammonium acetate pH 8.5, 37 °C) before taking samples for TEM. Formation of elongated fibrils could be observed although both peptides show only partial inhibition in ThT binding assays after 6 days. Scale bars are 100 nm.

7.8 Light microscopy pictures

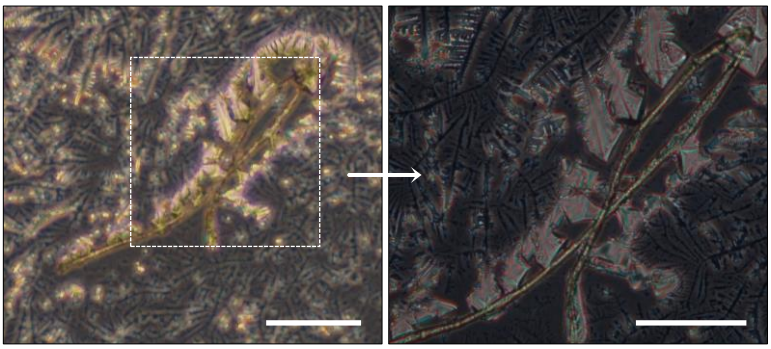

Figure 7-52: Loop-shaped macro-assembly formed by IAPP and Nle3-VF observed via light microscopy. Aliquots of a 7 days aged solution containing IAPP (16.5 µM) and Nle3-VF (1:2 mixture) were spotted onto a microscope slide and analysed by light microscopy after drying. The loop structure resembles the ones found in 2-PM microscopy. Structures around the loop are salt crystals from the incubation buffer (ThT assay buffer with 0.5 % HFiP). The left picture represents 100x magnification, the right one 400x. Scale bars are 100 µm.

7.9 FLIM-FRET analyses

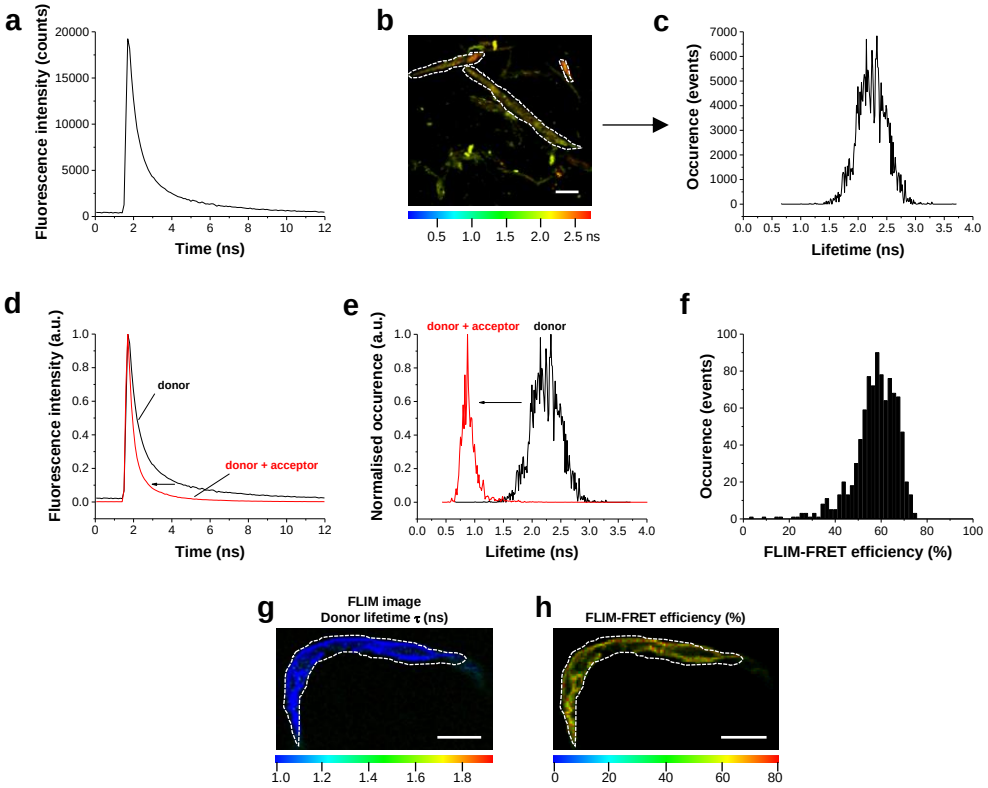

Figure 7-53: Donor lifetime determination for Dac-Aβ40 and FLIM-FRET analysis of TAMRA-IAPP/Dac-Aβ40 hetero-nanofibers. (**a**) Decay curve of Dac-Aβ40. A sample of 7 days aged Dac-Aβ40 (33 µM in 1xb) was analysed using the Leica SP8 FALCON application. A n-exponential reconvolution model using three exponential components was used to fit the data of the obtained decay curve. (**b**) FLIM image of Dac-Aβ40 nanofibers. The highlighted area was used to determine the lifetime distribution in c. Coloured bar shows the lifetime. Scale bar is 10 µm. (**c**) Lifetime distribution in the sample area highlighted in b. (**d**) Overlay of decay curves of Dac-Aβ40 alone (donor) and TAMRA-IAPP/Dac-Aβ40 hetero-nanofibers (donor+acceptor). Hetero-nanofibers were obtained by aging incubations containing TAMRA-IAPP (16.5 µM) and Dac-Aβ40 (33 µM) for 24 h before microscope slide preparation. Arrow indicates faster decay of donor in presence of acceptor. (**e**) Lifetime of donor in presence and absence of acceptor. Arrow indicates reduced donor lifetime in TAMRA-IAPP/Dac-Aβ40 hetero-nanofibers. (**f**) FLIM-FRET efficiency measured in TAMRA-IAPP/Dac-Aβ40 hetero-nanofiber samples. Diagram shows efficiency distribution corresponding to the FLIM-FRET image shown in h,. (**g**) FLIM image of TAMRA-IAPP/Dac-Aβ40 hetero-nanofibers. Scale bar is 10 µm. Coloured bar represents the lifetime. (**h**) FLIM-FRET efficiency image of TAMRA-IAPP/Dac-Aβ40 hetero-nanofibers. Scale bar is 10 µm. Coloured bar represents the calculated efficiency.

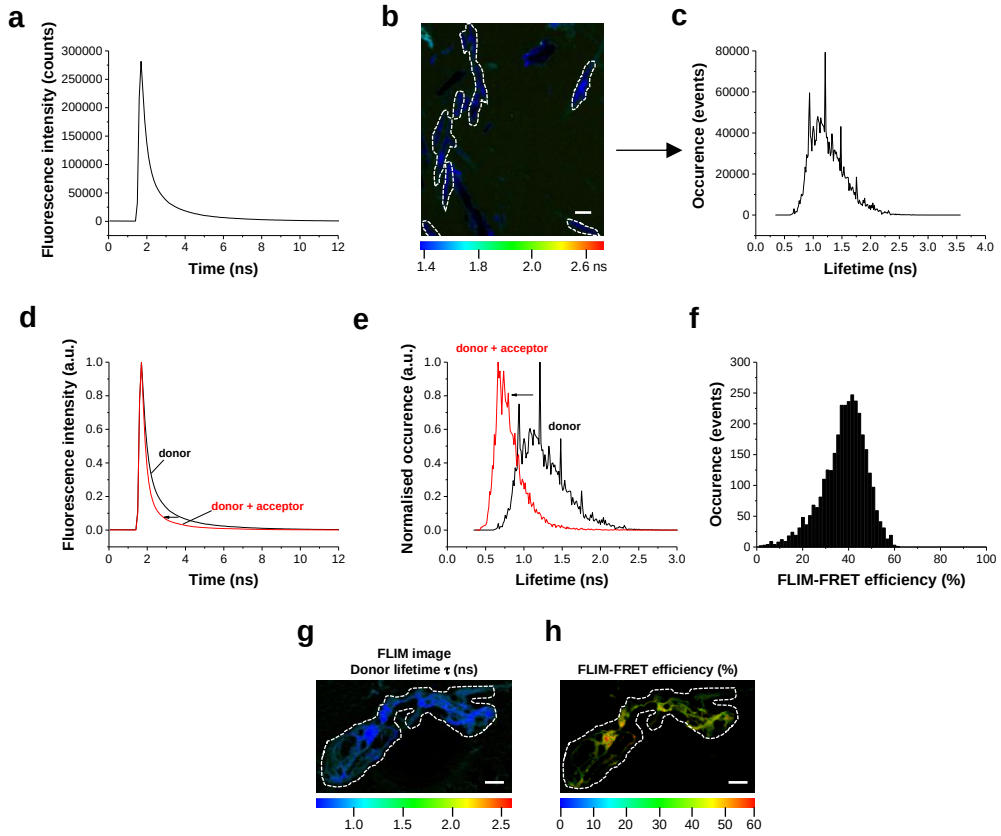

Figure 7-54: Donor lifetime determination for FITC-Aβ42 and FLIM-FRET analysis of TAMRA-IAPP/FITC-Aβ42 hetero-nanofibers. (**a**) Decay curve of FITC-Aβ42. A sample of 7 days aged FITC-Aβ42 (33 µM in 1xb) was analysed using the Leica SP8 FALCON application. A n-exponential reconvolution model using four exponential components was used to fit the data of the obtained decay curve. (**b**) FLIM image of FITC-Aβ42 nanofibers. The marked area was used to determine the lifetime distribution in c. Coloured bar shows the lifetime. Scale bar is 10 µm. (**c**) Lifetime distribution of the sample area highlighted in b. (**d**) Overlay of decay curves of FITC-Aβ42 alone (donor) and TAMRA-IAPP/FITC-Aβ42 hetero-nanofibers (donor+acceptor). Hetero-nanofibers were generated by aging incubations containing TAMRA-IAPP (16.5 µM) and FITC-Aβ42 (33 µM) for 24 h before microscope slide preparation. Arrow indicates faster decay of donor in presence of acceptor. (**e**) Lifetime of donor in presence and absence of acceptor. Arrow indicates reduced donor lifetime in TAMRA-IAPP/FITC-Aβ42 hetero-nanofibers. (**f**) FLIM-FRET efficiency measured in TAMRA-IAPP/FITC-Aβ42 hetero-nanofiber samples. Diagram shows efficiency distribution corresponding to the FLIM-FRET image shown in h. (**g**) FLIM image of TAMRA-IAPP/FITC-Aβ42 hetero-nanofibers. Scale bar is 10 µm. Coloured bar represents the lifetime. (**h**) FLIM-FRET efficiency image of TAMRA-IAPP/FITC-Aβ42 hetero-nanofibers. Scale bar is 10 µm. Coloured bar represents the calculated efficiency.

7.10 Peptide array results

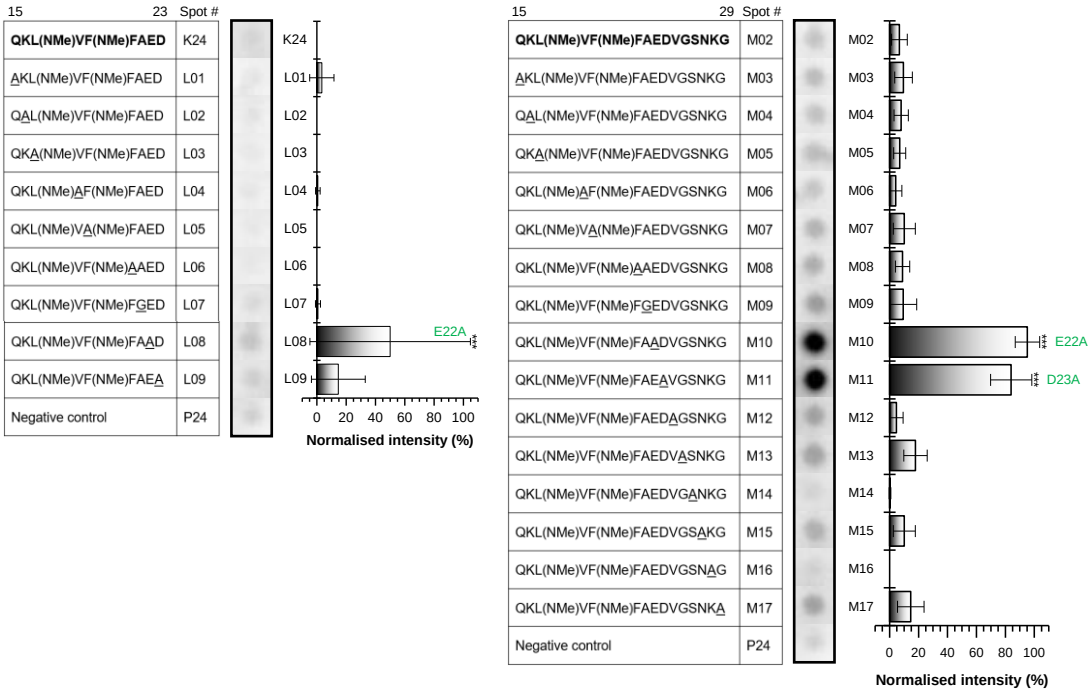

Figure 7-55: Identification of amino acids in N-terminal VGS-VF segments important for IAPP binding by sequential alanine scanning using peptide microarrays. Glass slides with the wild-type segments (bold; no alanine substitution) and the corresponding alanine-substituted segments (position of alanine mutation underlined) were incubated with Biotin-IAPP (0.5 µM). Bound Biotin-IAPP was detected after incubation with streptavidin-POD and development with ECL. Bar diagrams represent spot intensities obtained from different developments (mean ± SD; 6 assays). Depicted membranes are from one of these assays. Green letters indicate alanine mutations causing stronger binding of the mutated segment compared to the wild-type segment. Asterisks mark spot intensities significantly different from the wild-type segment. *** P<0.001 (by one-way ANOVA & Bonferroni). "Spot #" gives the location of the corresponding segment on the peptide array slide. NMe: *N*-methylation.

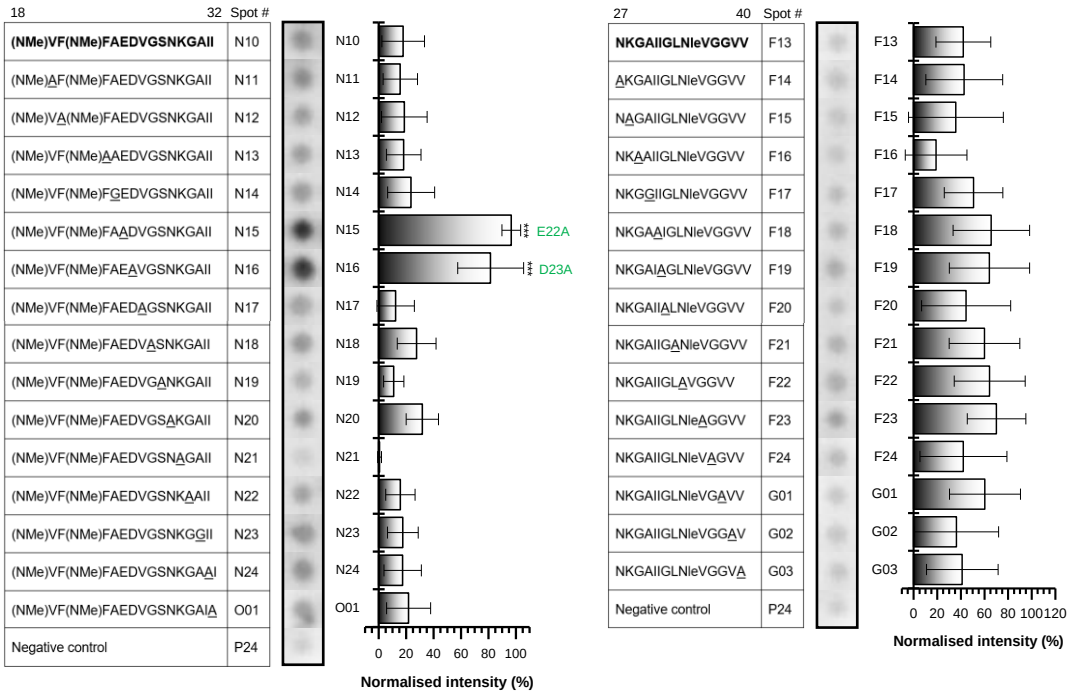

Figure 7-56: Identification of amino acids in central and C-terminal VGS-VF segments important for IAPP binding by sequential alanine scanning using peptide microarrays. Glass slides with the wild-type segments (bold; no alanine substitution) and the corresponding alanine-substituted segments (position of alanine mutation underlined) were incubated with Biotin-IAPP (0.5 µM). Bound Biotin-IAPP was detected after incubation with streptavidin-POD and development with ECL. Bar

diagrams represent spot intensities obtained from different developments (mean ± SD; 6 assays). Depicted membranes are from one of these assays. Green letters indicate alanine mutations causing stronger binding of mutated segment compared to the wild-type segment. Asterisks mark spot intensities significantly different from the wild-type segment. *** P<0.001 (by one-way ANOVA & Bonferroni). “Spot #” gives the location of the corresponding segment on the peptide array slide. NMe: *N*-methylation.

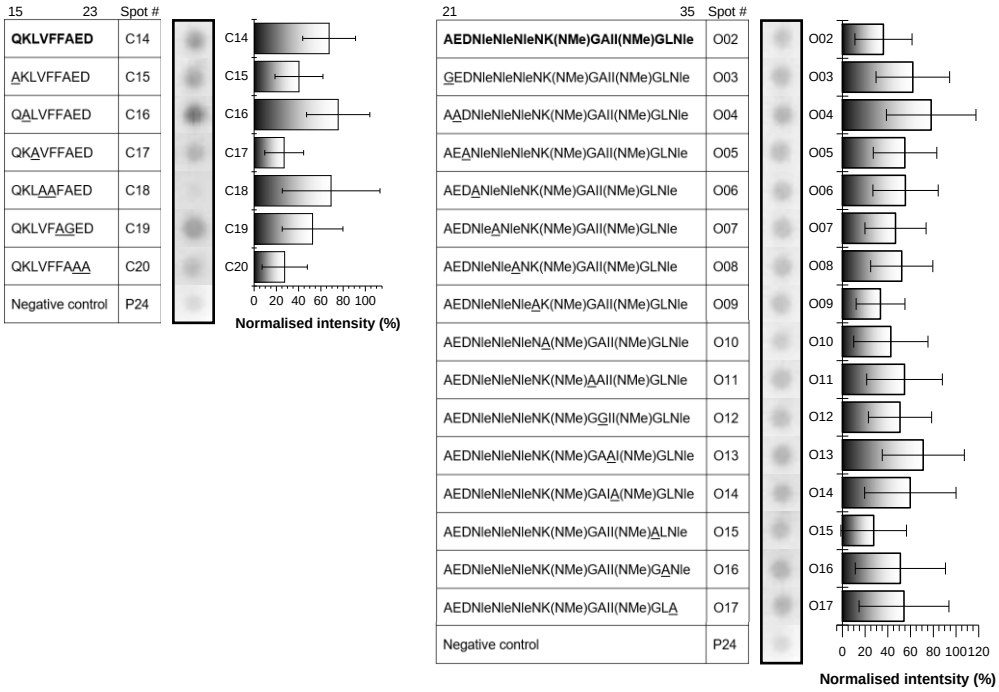

Figure 7-57: Identification of amino acids in N-terminal and central Nle3-GG segments important for IAPP binding by sequential alanine scanning using peptide microarrays. Glass slides with the wild-type segments (bold; no alanine substitution) and the corresponding alanine-substituted segments (position of alanine mutation underlined) were incubated with Biotin-IAPP (0.5 µM). Bound Biotin-IAPP was detected after incubation with streptavidin-POD and development with ECL. Bar diagrams represent spot intensities obtained from different developments (mean ± SD; 6 assays). Depicted membranes are from one of these assays. No significant impacts on binding strength of Biotin-IAPP were detected for alanine mutations in these segments. “Spot #” gives the location of the corresponding segment on the peptide array slide. NMe: *N*-methylation.

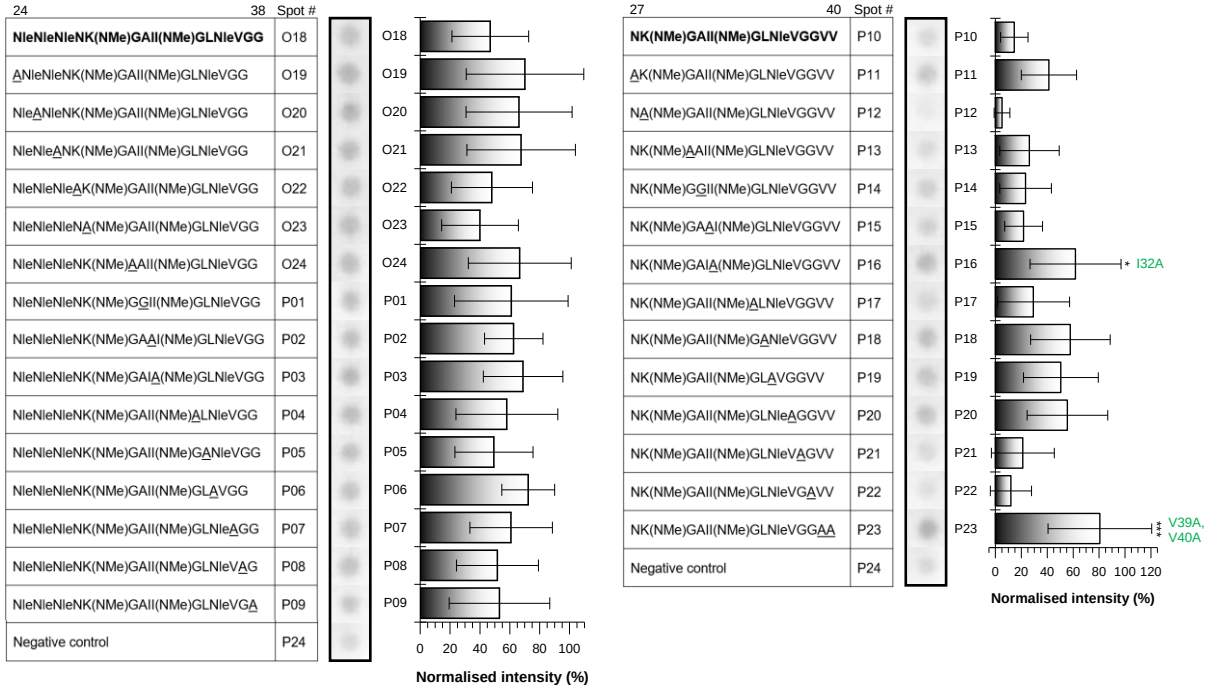

Figure 7-58: Identification of amino acids in C-terminal Nle3-GG segments important for IAPP binding by sequential alanine scanning using peptide microarrays. Glass slides with the wild-type segments (bold; no alanine substitution) and the corresponding alanine-substituted segments (position of alanine mutation underlined) were incubated with Biotin-IAPP (0.5 µM). Bound Biotin-IAPP was detected after incubation with streptavidin-POD and development with ECL. Bar diagrams represent spot intensities obtained from different developments (mean ± SD; 6 assays). Depicted membranes are from one of these assays. Green letters indicate alanine mutations causing stronger binding of the mutated segment compared to the wild-type segment. Asterisks mark spot intensities significantly different from the wild-type segment. *** P<0.001, * P<0.05 (by one-way ANOVA & Bonferroni). "Spot #" gives the location of the corresponding segment on the peptide array slide. NMe: *N*-methylation.

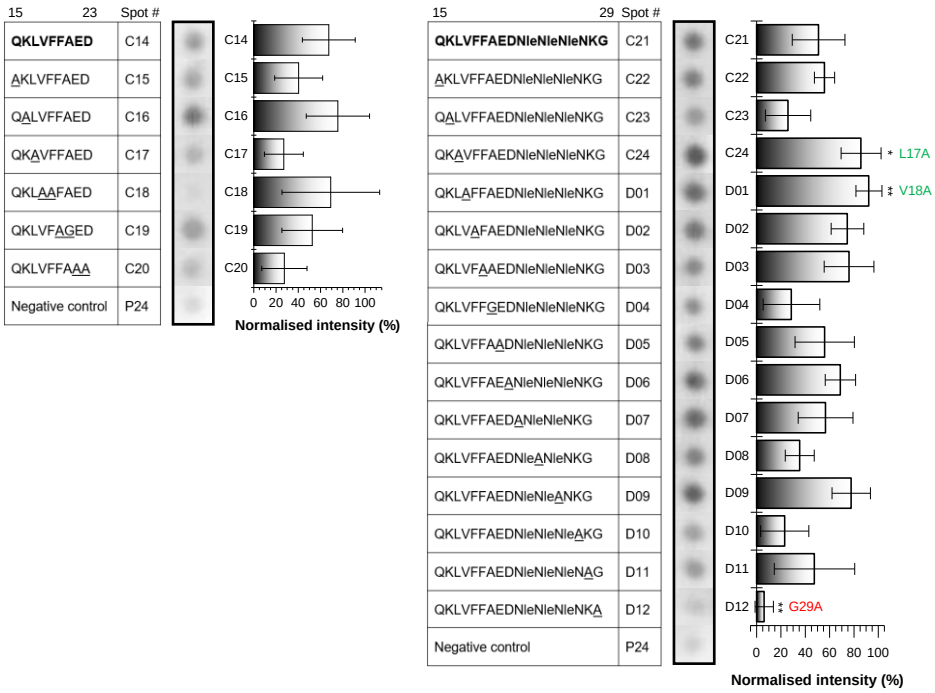

Figure 7-59: Identification of amino acids in N-terminal Nle3 segments important for IAPP binding by sequential alanine scanning using peptide microarrays. Glass slides with the wild-type segments (bold; no alanine substitution) and the corresponding alanine-substituted segments (position of alanine mutation underlined) were incubated with Biotin-IAPP (0.5 µM). Bound Biotin-IAPP was detected after incubation with streptavidin-POD and development with ECL. Bar diagrams represent spot intensities obtained from different developments (mean ± SD; 6 assays). Depicted membranes are from one of these assays. Green letters indicate alanine mutations causing stronger binding of the mutated segment compared to the wild-type segment, red letters indicate alanine mutations causing weaker binding. Asterisks mark spot intensities significantly different from the wild-type segment. ** P<0.01, * P<0.05 (by one-way ANOVA & Bonferroni). "Spot #" gives the location of the corresponding segment on the peptide array slide.

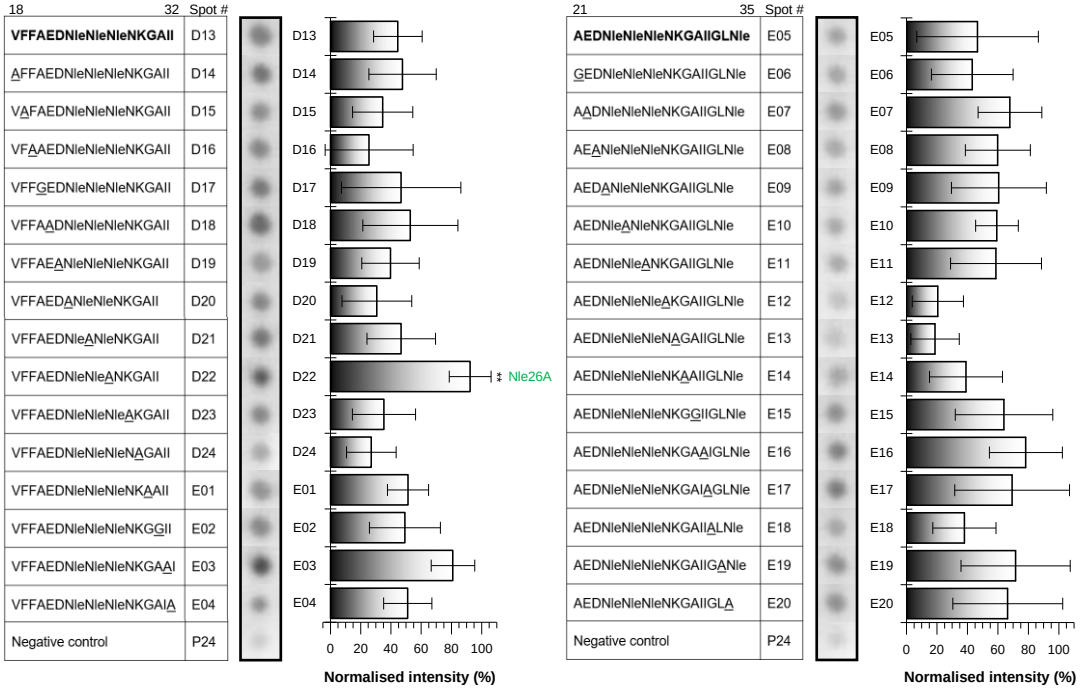

Figure 7-60: Identification of amino acids in central Nle3 segments important for IAPP binding by sequential alanine scanning using peptide microarrays. Glass slides with the wild-type segments (bold; no alanine substitution) and the corresponding alanine-substituted segments (position of alanine mutation underlined) were incubated with Biotin-IAPP (0.5 µM). Bound Biotin-IAPP was detected after incubation with streptavidin-POD and development with ECL. Bar diagrams represent spot intensities obtained from different developments (mean ± SD; 6 assays). Depicted membranes are from one of these assays. Green letters indicate alanine mutations causing stronger binding of the mutated segment compared to the wild-type segment. Asterisks mark spot intensities significantly different from the wild-type segment. ** P<0.01 (by one-way ANOVA & Bonferroni). "Spot #" gives the location of the corresponding segment on the peptide array slide.

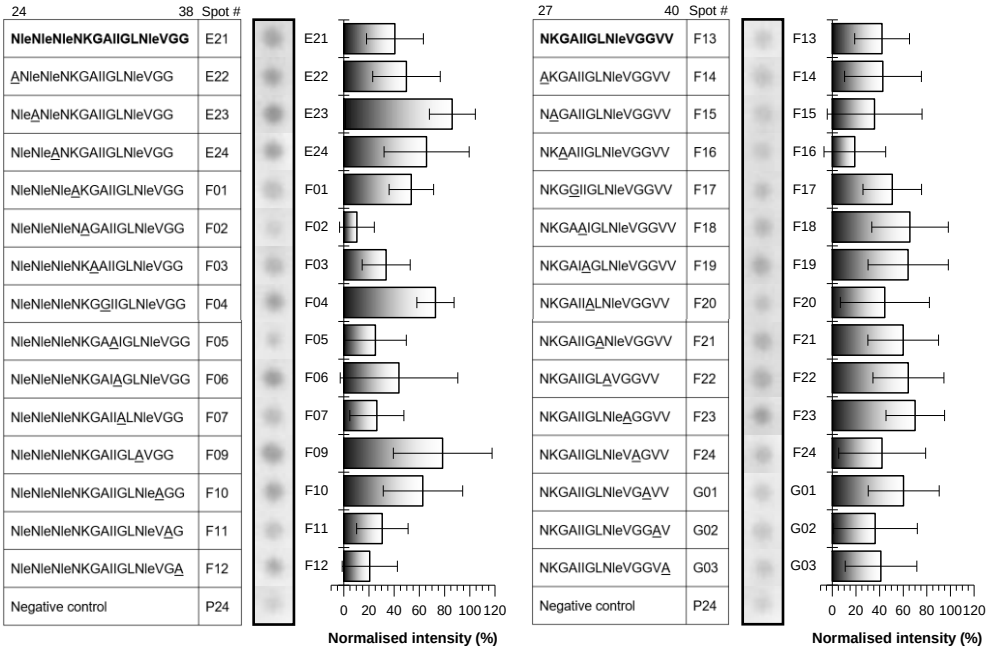

Figure 7-61: Identification of amino acids in C-terminal Nle3 segments important for IAPP binding by sequential alanine scanning using peptide microarrays. Glass slides with the wild-type segments (bold; no alanine substitution) and the corresponding alanine-substituted segments (position of alanine mutation underlined) were incubated with Biotin-IAPP (0.5 µM). Bound Biotin-IAPP was detected after incubation with streptavidin-POD and development with ECL. Bar diagrams represent spot intensities obtained from different developments (mean ± SD; 6 assays). Depicted membranes are from one of these assays. No significant impacts on binding strength of Biotin-IAPP were detected for single alanine mutations in these segments. "Spot #" gives the location of the corresponding segment on the peptide array slide.

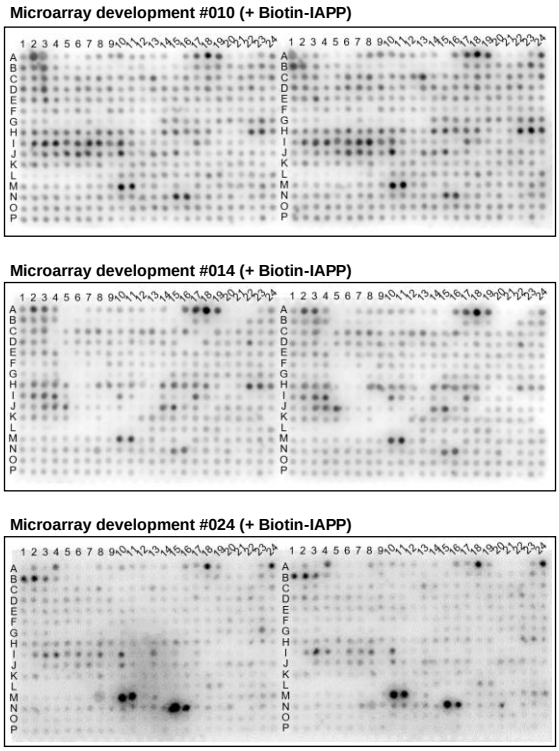

Figure 7-62: Peptide microarray developments with biotinylated IAPP used for analyses of binding of IAPP to ADP segments. Microarrays were incubated with biotinylated IAPP (0.5 µM). One microarray contains two subarrays (2 assays). Letters and numbers define the location of the peptides on the microarray. For corresponding peptide sequences refer to Table 7-8 - Table 7-10.

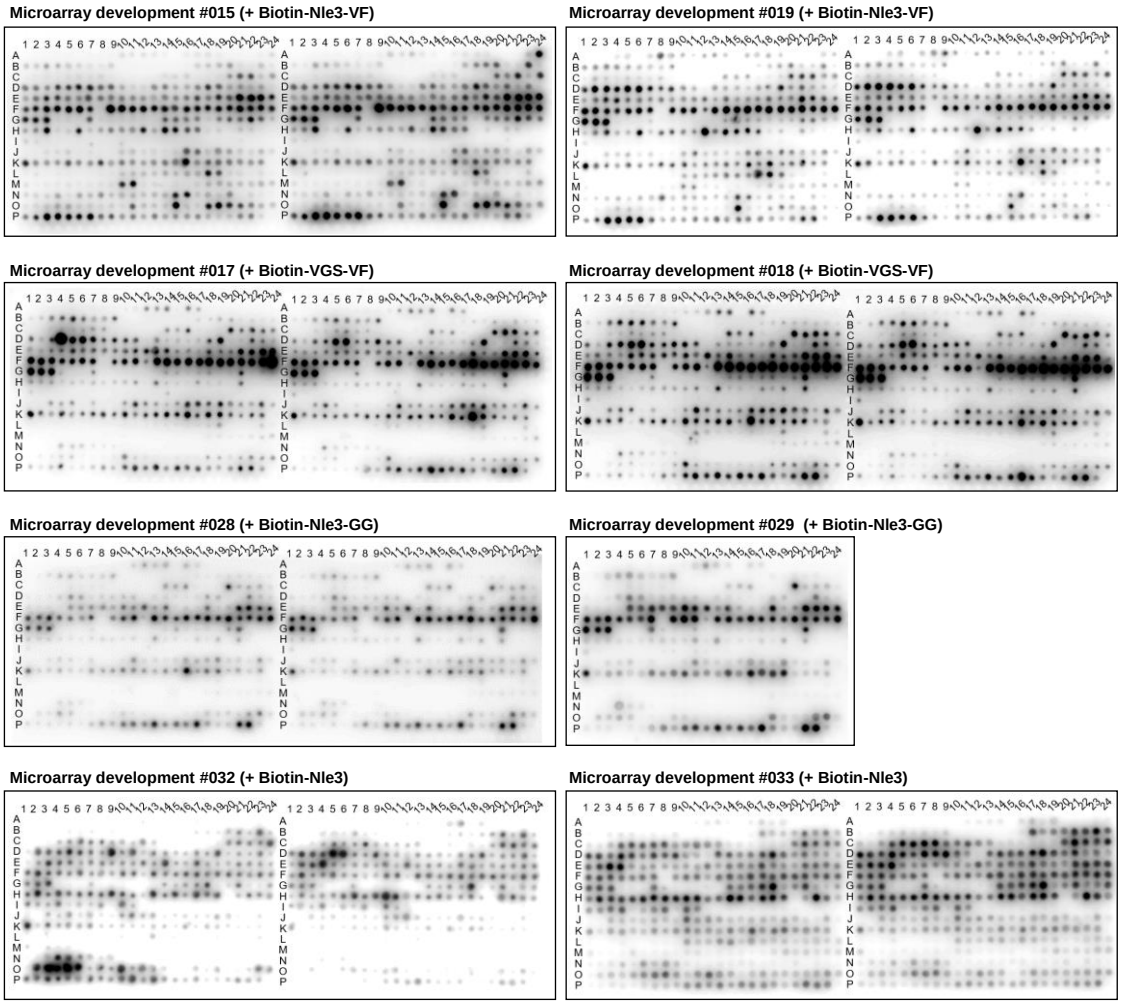

Figure 7-63: Peptide microarray developments with biotinylated ADPs used for analyses of binding of ADPs to IAPP segments and of ADP self-assembly recognition sites. Microarrays were incubated with biotinylated ADPs (3 µM Biotin-Nle3 or 3 µM Biotin-Nle3-GG or 0.5 µM Biotin-Nle3-VF or 0.5 µM Biotin-VGS-VF). One microarray usually contains two subarrays (2 assays). In case of development #029 (Biotin-Nle3-GG) only one subarray is shown since the second development failed. Letters and numbers define the location of the peptides on the microarray. For corresponding peptide sequences refer to Table 7-8 - Table 7-10.

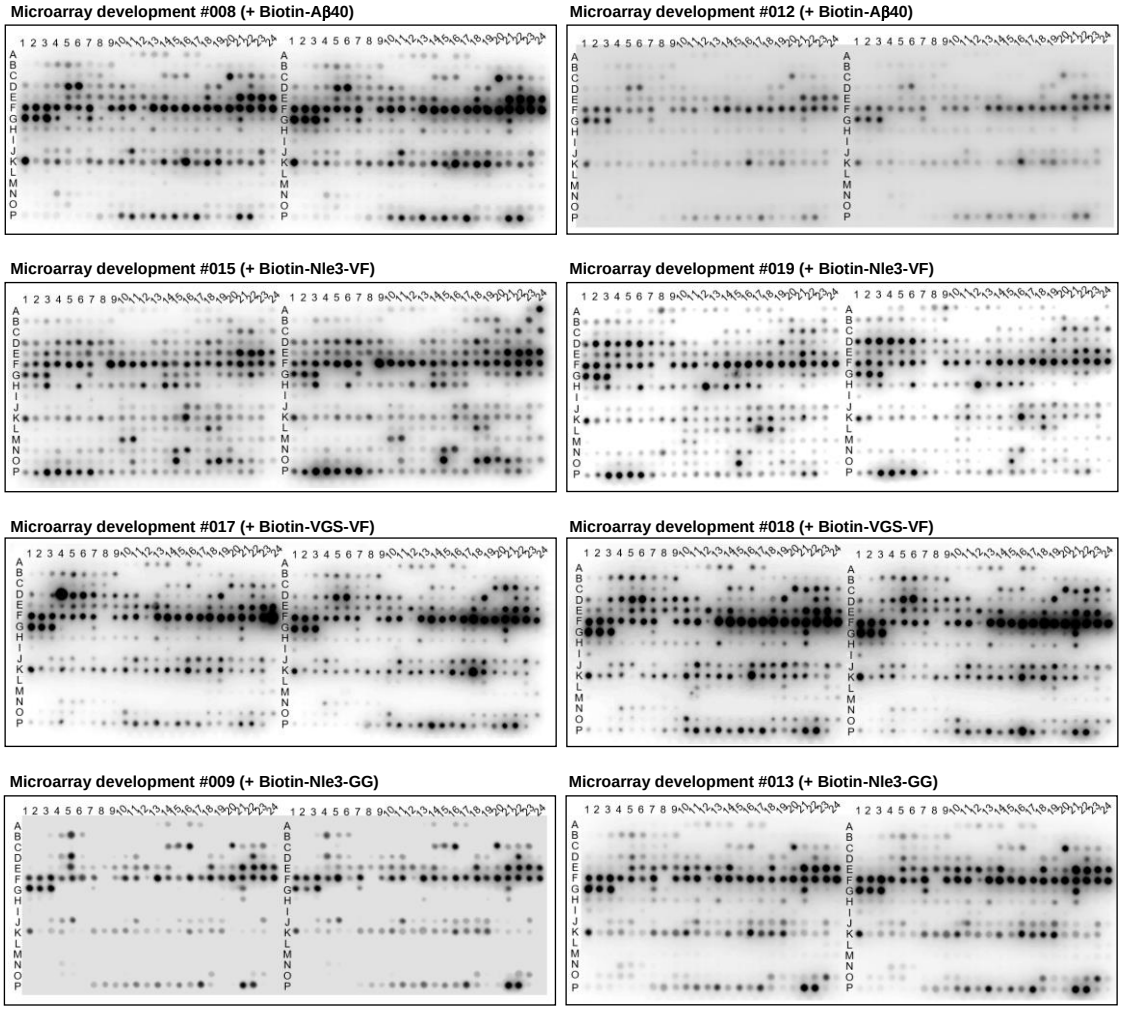

Figure 7-64: Peptide microarray developments with biotinylated Aβ40 or ADPs used for analyses of binding of Aβ to ADP segments, of ADPs to Aβ segments, and of Aβ self-assembly recognition sites. Microarrays were incubated with biotinylated Aβ40 or ADPs (0.5 µM). One microarray contains two subarrays (2 assays). Letters and numbers define the location of the peptides on the microarray. For corresponding peptide sequences refer to Table 7-8 - Table 7-10.

Table 7-8: Peptide sequences and corresponding spot numbers on microarrays – spot numbers A01 to G03. "Spot #" gives the location of the corresponding peptide segment on the microarray slides (see Figure 7-62 - Figure 7-64).

Peptide sequence	Spot #
DAEFRHDSGY	A01
AEFRHDSGYE	A02
EFRHDSGYEV	A03
FRHDSGYEVH	A04
RHDSGYEVHH	A05
HDSGYEVHHQ	A06
DSGYEVHHQK	A07
SGYEVHHQKL	A08
GYEVHHQKLV	A09
YEVHHQKLVF	A10
EVHHQKLVFF	A11
VHHQKLVFFA	A12
HHQKLVFFAE	A13
HQKLVFFAED	A14
QKLVFFAEDV	A15
KLVFFAEDVG	A16
LVFFAEDVGS	A17
VFFAEDVGSN	A18
FFAEDVGSNK	A19
FAEDVGSNKG	A20
AEDVGSNKGA	A21
EDVGSNKGAI	A22
DVGSNKGAII	A23
VGSNKGAIIG	A24
GSNKGAIIGL	B01
SNKGAIIGLM	B02
NKGAIIGLMV	B03
KGAIIGLMVG	B04
GAIIGLMVGG	B05
AIIGLMVGGV	B06
IIGLMVGGVV	B07
IGLMVGGVVI	B08
GLMVGGVVIA	B09

Peptide sequence	Spot #
KCNTATCATQ	B10
CNTATCATQR	B11
NTATCATQRL	B12
TATCATQRLA	B13
ATCATQRLAN	B14
TCATQRLANF	B15
CATQRLANFL	B16
ATQRLANFLV	B17
TQRLANFLVH	B18
QRLANFLVHS	B19
RLANFLVHSS	B20
LANFLVHSSN	B21
ANFLVHSSNN	B22
NFLVHSSNNF	B23
FLVHSSNNFG	B24
LVHSSNNFGA	C01
VHSSNNFGAI	C02
HSSNNFGAIL	C03
SSNNFGAILS	C04
SNNFGAILSS	C05
NNFGAILSST	C06
NFGAILSSTN	C07
FGAILSSTNV	C08
GAILSSTNVG	C09
AILSSTNVGS	C10
ILSSTNVGSN	C11
LSSTNVGSNT	C12
SSTNVGSNTY	C13

Peptide sequence	Spot #
QKLVFFAED	C14
AKLVFFAED	C15
QALVFFAED	C16
QKAVFFAED	C17
QKLAAFAED	C18
QKLVFAGED	C19
QKLVFFAAA	C20
QKLVFFAEDNleNleNleNKG	C21
AKLVFFAEDNleNleNleNKG	C22
QALVFFAEDNleNleNleNKG	C23
QKAVFFAEDNleNleNleNKG	C24
QKLAFFAEDNleNleNleNKG	D01
QKLVAFAEDNleNleNleNKG	D02
QKLVFAAEDNleNleNleNKG	D03
QKLVFFGEDNleNleNleNKG	D04
QKLVFFAADNleNleNleNKG	D05
QKLVFFAEANleNleNleNKG	D06
QKLVFFAEDANleNleNKG	D07
QKLVFFAEDNleANleNKG	D08
QKLVFFAEDNleNleANKG	D09
QKLVFFAEDNleNleNleAKG	D10
QKLVFFAEDNleNleNleNAG	D11
QKLVFFAEDNleNleNleNKA	D12
VFFAEDNleNleNleNKGAII	D13
AFFAEDNleNleNleNKGAII	D14
VAFAEDNleNleNleNKGAII	D15
VFAAEDNleNleNleNKGAII	D16
VFFGEDNleNleNleNKGAII	D17
VFFAADNleNleNleNKGAII	D18
VFFAEANleNleNleNKGAII	D19
VFFAEDANleNleNKGAII	D20
VFFAEDNleANleNKGAII	D21
VFFAEDNleNleANKGAII	D22

Peptide sequence	Spot #
VFFAEDNleNleNleAKGAII	D23
VFFAEDNleNleNleNAGAII	D24
VFFAEDNleNleNleNKAAII	E01
VFFAEDNleNleNleNKGGII	E02
VFFAEDNleNleNleNKGAAI	E03
VFFAEDNleNleNleNKGAIA	E04
AEDNleNleNleNKGAIIGLNle	E05
GEDNleNleNleNKGAIIGLNle	E06
AADNleNleNleNKGAIIGLNle	E07
AEANleNleNleNKGAIIGLNle	E08
AEDANleNleNKGAIIGLNle	E09
AEDNleANleNKGAIIGLNle	E10
AEDNleNleANKGAIIGLNle	E11
AEDNleNleNleAKGAIIGLNle	E12
AEDNleNleNleNAGAIIGLNle	E13
AEDNleNleNleNKAAIIGLNle	E14
AEDNleNleNleNKGGIIGLNle	E15
AEDNleNleNleNKGAAIGLNle	E16
AEDNleNleNleNKGAIAGLNle	E17
AEDNleNleNleNKGAIIALNle	E18
AEDNleNleNleNKGAIIGANle	E19
AEDNleNleNleNKGAIIGLA	E20
NleNleNleNKGAIIGLNleVGG	E21
ANleNleNKGAIIGLNleVGG	E22
NleANleNKGAIIGLNleVGG	E23
NleNleANKGAIIGLNleVGG	E24
NleNleNleAKGAIIGLNleVGG	F01
NleNleNleNAGAIIGLNleVGG	F02
NleNleNleNKAAIIGLNleVGG	F03
NleNleNleNKGGIIGLNleVGG	F04
NleNleNleNKGAAIGLNleVGG	F05
NleNleNleNKGAIAGLNleVGG	F06
NleNleNleNKGAIIALNleVGG	F07

Peptide sequence	Spot #
NleNleNleNKGAIIGANleVGG	F08
NleNleNleNKGAIIGLAVGG	F09
NleNleNleNKGAIIGLNleAGG	F10
NleNleNleNKGAIIGLNleVAG	F11
NleNleNleNKGAIIGLNleVGA	F12
NKGAIIGLNleVGGVV	F13
AKGAIIGLNleVGGVV	F14
NAGAIIGLNleVGGVV	F15
NKAAIIGLNleVGGVV	F16
NKGGIIGLNleVGGVV	F17
NKGAAIGLNleVGGVV	F18
NKGAIAGLNleVGGVV	F19
NKGAIIALNleVGGVV	F20
NKGAIIGANleVGGVV	F21
NKGAIIGLAVGGVV	F22
NKGAIIGLNleAGGVV	F23
NKGAIIGLNleVAGVV	F24
NKGAIIGLNleVGAVV	G01
NKGAIIGLNleVGGAV	G02
NKGAIIGLNleVGGVA	G03

Table 7-9: Peptide sequences and corresponding spot numbers on microarrays – spot numbers G04 to M17. "Spot #" gives the location of the corresponding peptide segment on the microarray slides (see Figure 7-62 - Figure 7-64).

Peptide sequence	Spot #
ACNTATCATQ	G04
KANTATCATQ	G05
KCATATCATQ	G06
KCNAATCATQ	G07
KCNTGTCATQ	G08
KCNTAACATQ	G09
KCNTATAATQ	G10
KCNTATCGTQ	G11
KCNTATCAAQ	G12
KCNTATCATA	G13
ATQRLANFLVH	G14
GTQRLANFLVH	G15
AAQRLANFLVH	G16
ATARLANFLVH	G17
ATQALANFLVH	G18
ATQRAANFLVH	G19
ATQRLGNFLVH	G20
ATQRLAAFLVH	G21
ATQRLANALVH	G22
ATQRLANFAVH	G23
ATQRLANFLAH	G24
ATQRLANFLVA	H01
NFLVHSSNNFGAILS	H02
AFLVHSSNNFGAILS	H03
NALVHSSNNFGAILS	H04
NFAVHSSNNFGAILS	H05
NFLAHSSNNFGAILS	H06
NFLVASSNNFGAILS	H07
NFLVHASNNFGAILS	H08
NFLVHSANNFGAILS	H09
NFLVHSSANFGAILS	H10
NFLVHSSNAFGAILS	H11

Peptide sequence	Spot #
NFLVHSSNNAGAILS	H12
NFLVHSSNNFAAILS	H13
NFLVHSSNNFGGILS	H14
NFLVHSSNNFGAALS	H15
NFLVHSSNNFGAIAS	H16
NFLVHSSNNFGAILA	H17
NFGAILS	H18
AFGAILS	H19
NAGAILS	H20
NFAAILS	H21
NFGGILS	H22
NFGAALS	H23
NFGAIAS	H24
NFGAILA	I01
STNVGSNTY	I02
ATNVGSNTY	I03
SANVGSNTY	I04
STAVGSNTY	I05
STNAGSNTY	I06
STNVASNTY	I07
STNVGANTY	I08
STNVGSATY	I09
STNVGSNAY	I10
STNVGSNTA	I11
DAEFRHDSGYEVHH	I12
AAEFRHDSGYEVHH	I13
DGEFRHDSGYEVHH	I14
DAAFRHDSGYEVHH	I15
DAEARHDSGYEVHH	I16
DAEFAHDSGYEVHH	I17
DAEFRADSGYEVHH	I18
DAEFRHASGYEVHH	I19

Peptide sequence	Spot #
DAEFRHDAGYEVHH	I20
DAEFRHDSAYEVHH	I21
DAEFRHDSGAEVHH	I22
DAEFRHDSGYAVHH	I23
DAEFRHDSGYEAHH	I24
DAEFRHDSGYEVAH	J01
DAEFRHDSGYEVHA	J02
QKLVFFAEDVGS	J03
AKLVFFAEDVGS	J04
QALVFFAEDVGS	J05
QKAVFFAEDVGS	J06
QKLAFFAEDVGS	J07
QKLVAFAEDVGS	J08
QKLVFAAEDVGS	J09
QKLVFFGEDVGS	J10
QKLVFFAADVGS	J11
QKLVFFAEAVGS	J12
QKLVFFAEDAGS	J13
QKLVFFAEDVAS	J14
QKLVFFAEDVGA	J15
NKGAIIGLMVGGVV	J16
AKGAIIGLMVGGVV	J17
NAGAIIGLMVGGVV	J18
NKAAIIGLMVGGVV	J19
NKGGIIGLMVGGVV	J20
NKGAAIGLMVGGVV	J21
NKGAIAGLMVGGVV	J22
NKGAIIALMVGGVV	J23
NKGAIIGAMVGGVV	J24
NKGAIIGLAVGGVV	K01
NKGAIIGLMAGGVV	K02
NKGAIIGLMVAGVV	K03

Peptide sequence	Spot #
NKGAIIGLMVGAVV	K04
NKGAIIGLMVGGAV	K05
NKGAIIGLMVGGVA	K06
NKGAIIGLMVGGVVIA	K07
AKGAIIGLMVGGVVIA	K08
NAGAIIGLMVGGVVIA	K09
NKAAIIGLMVGGVVIA	K10
NKGGIIGLMVGGVVIA	K11
NKGAAIGLMVGGVVIA	K12
NKGAIAGLMVGGVVIA	K13
NKGAIIALMVGGVVIA	K14
NKGAIIGAMVGGVVIA	K15
NKGAIIGLAVGGVVIA	K16
NKGAIIGLMAGGVVIA	K17
NKGAIIGLMVAGVVIA	K18
NKGAIIGLMVGAVVIA	K19
NKGAIIGLMVGGAVIA	K20
NKGAIIGLMVGGVAIA	K21
NKGAIIGLMVGGVVAA	K22
NKGAIIGLMVGGVVIG	K23
QKL(NMe)VF(NMe)FAED	K24
AKL(NMe)VF(NMe)FAED	L01
QAL(NMe)VF(NMe)FAED	L02
QKA(NMe)VF(NMe)FAED	L03
QKL(NMe)AF(NMe)FAED	L04
QKL(NMe)VA(NMe)FAED	L05
QKL(NMe)VF(NMe)AAED	L06
QKL(NMe)VF(NMe)FGED	L07
QKL(NMe)VF(NMe)FAAD	L08
QKL(NMe)VF(NMe)FAEA	L09

Peptide sequence	Spot #
QKL(NMe)VF(NMe)FAEDNleNleNleNKG	L10
AKL(NMe)VF(NMe)FAEDNleNleNleNKG	L11
QAL(NMe)VF(NMe)FAEDNleNleNleNKG	L12
QKA(NMe)VF(NMe)FAEDNleNleNleNKG	L13
QKL(NMe)AF(NMe)FAEDNleNleNleNKG	L14
QKL(NMe)VA(NMe)FAEDNleNleNleNKG	L15
QKL(NMe)VF(NMe)AAEDNleNleNleNKG	L16
QKL(NMe)VF(NMe)FGEDNleNleNleNKG	L17
QKL(NMe)VF(NMe)FAADNleNleNleNKG	L18
QKL(NMe)VF(NMe)FAEANleNleNleNKG	L19
QKL(NMe)VF(NMe)FAEDANleNleNKG	L20
QKL(NMe)VF(NMe)FAEDNleANleNKG	L21
QKL(NMe)VF(NMe)FAEDNleNleANKG	L22
QKL(NMe)VF(NMe)FAEDNleNleNleAKG	L23
QKL(NMe)VF(NMe)FAEDNleNleNleNAG	L24
QKL(NMe)VF(NMe)FAEDNleNleNleNKA	M01
QKL(NMe)VF(NMe)FAEDVGSNKG	M02
AKL(NMe)VF(NMe)FAEDVGSNKG	M03
QAL(NMe)VF(NMe)FAEDVGSNKG	M04
QKA(NMe)VF(NMe)FAEDVGSNKG	M05
QKL(NMe)AF(NMe)FAEDVGSNKG	M06
QKL(NMe)VA(NMe)FAEDVGSNKG	M07
QKL(NMe)VF(NMe)AAEDVGSNKG	M08
QKL(NMe)VF(NMe)FGEDVGSNKG	M09
QKL(NMe)VF(NMe)FAADVGSNKG	M10
QKL(NMe)VF(NMe)FAEAVGSNKG	M11
QKL(NMe)VF(NMe)FAEDAGSNKG	M12
QKL(NMe)VF(NMe)FAEDVASNKG	M13
QKL(NMe)VF(NMe)FAEDVGANKG	M14
QKL(NMe)VF(NMe)FAEDVGSAKG	M15
QKL(NMe)VF(NMe)FAEDVGSNAG	M16
QKL(NMe)VF(NMe)FAEDVGSNKA	M17

Table 7-10: Peptide sequences and corresponding spot numbers on microarrays – spot numbers M18 to P24. "Spot #" gives the location of the corresponding peptide segment on the microarray slides (see Figure 7-62 - Figure 7-64).

Peptide sequence	Spot #
(NMe)VF(NMe)FAEDNleNleNleNKGAII	M18
(NMe)AF(NMe)FAEDNleNleNleNKGAII	M19
(NMe)VA(NMe)FAEDNleNleNleNKGAII	M20
(NMe)VF(NMe)AAEDNleNleNleNKGAII	M21
(NMe)VF(NMe)FGEDNleNleNleNKGAII	M22
(NMe)VF(NMe)FAADNleNleNleNKGAII	M23
(NMe)VF(NMe)FAEANleNleNleNKGAII	M24
(NMe)VF(NMe)FAEDANleNleNKGAII	N01
(NMe)VF(NMe)FAEDNleANleNKGAII	N02
(NMe)VF(NMe)FAEDNleNleANKGAII	N03
(NMe)VF(NMe)FAEDNleNleNleAKGAII	N04
(NMe)VF(NMe)FAEDNleNleNleNAGAII	N05
(NMe)VF(NMe)FAEDNleNleNleNKAAII	N06
(NMe)VF(NMe)FAEDNleNleNleNKGGII	N07
(NMe)VF(NMe)FAEDNleNleNleNKGAAI	N08
(NMe)VF(NMe)FAEDNleNleNleNKGAIA	N09
(NMe)VF(NMe)FAEDVGSNKGAII	N10
(NMe)AF(NMe)FAEDVGSNKGAII	N11
(NMe)VA(NMe)FAEDVGSNKGAII	N12
(NMe)VF(NMe)AAEDVGSNKGAII	N13
(NMe)VF(NMe)FGEDVGSNKGAII	N14
(NMe)VF(NMe)FAADVGSNKGAII	N15
(NMe)VF(NMe)FAEAVGSNKGAII	N16
(NMe)VF(NMe)FAEDAGSNKGAII	N17
(NMe)VF(NMe)FAEDVASNKGAII	N18
(NMe)VF(NMe)FAEDVGANKGAII	N19
(NMe)VF(NMe)FAEDVGSAKGAII	N20
(NMe)VF(NMe)FAEDVGSNAGAII	N21
(NMe)VF(NMe)FAEDVGSNKAAII	N22
(NMe)VF(NMe)FAEDVGSNKGGII	N23
(NMe)VF(NMe)FAEDVGSNKGAAI	N24
(NMe)VF(NMe)FAEDVGSNKGAIA	O01

Peptide sequence	Spot #
AEDNleNleNleNK(NMe)GAII(NMe)GLNle	O02
GEDNleNleNleNK(NMe)GAII(NMe)GLNle	O03
AADNleNleNleNK(NMe)GAII(NMe)GLNle	O04
AEANleNleNleNK(NMe)GAII(NMe)GLNle	O05
AEDANleNleNK(NMe)GAII(NMe)GLNle	O06
AEDNleANleNK(NMe)GAII(NMe)GLNle	O07
AEDNleNleANK(NMe)GAII(NMe)GLNle	O08
AEDNleNleNleAK(NMe)GAII(NMe)GLNle	O09
AEDNleNleNleNA(NMe)GAII(NMe)GLNle	O10
AEDNleNleNleNK(NMe)AAII(NMe)GLNle	O11
AEDNleNleNleNK(NMe)GGII(NMe)GLNle	O12
AEDNleNleNleNK(NMe)GAAI(NMe)GLNle	O13
AEDNleNleNleNK(NMe)GAIA(NMe)GLNle	O14
AEDNleNleNleNK(NMe)GAII(NMe)ALNle	O15
AEDNleNleNleNK(NMe)GAII(NMe)GANle	O16
AEDNleNleNleNK(NMe)GAII(NMe)GLA	O17
NleNleNleNK(NMe)GAII(NMe)GLNleVGG	O18
ANleNleNK(NMe)GAII(NMe)GLNleVGG	O19
NleANleNK(NMe)GAII(NMe)GLNleVGG	O20
NleNleANK(NMe)GAII(NMe)GLNleVGG	O21
NleNleNleAK(NMe)GAII(NMe)GLNleVGG	O22
NleNleNleNA(NMe)GAII(NMe)GLNleVGG	O23
NleNleNleNK(NMe)AAII(NMe)GLNleVGG	O24
NleNleNleNK(NMe)GGII(NMe)GLNleVGG	P01
NleNleNleNK(NMe)GAAI(NMe)GLNleVGG	P02
NleNleNleNK(NMe)GAIA(NMe)GLNleVGG	P03
NleNleNleNK(NMe)GAII(NMe)ALNleVGG	P04
NleNleNleNK(NMe)GAII(NMe)GANleVGG	P05
NleNleNleNK(NMe)GAII(NMe)GLAVGG	P06
NleNleNleNK(NMe)GAII(NMe)GLNleAGG	P07
NleNleNleNK(NMe)GAII(NMe)GLNleVAG	P08
NleNleNleNK(NMe)GAII(NMe)GLNleVGA	P09

Peptide sequence	Spot #
NK(NMe)GAII(NMe)GLNleVGGVV	P10
AK(NMe)GAII(NMe)GLNleVGGVV	P11
NA(NMe)GAII(NMe)GLNleVGGVV	P12
NK(NMe)AAII(NMe)GLNleVGGVV	P13
NK(NMe)GGII(NMe)GLNleVGGVV	P14
NK(NMe)GAAI(NMe)GLNleVGGVV	P15
NK(NMe)GAIA(NMe)GLNleVGGVV	P16
NK(NMe)GAII(NMe)ALNleVGGVV	P17
NK(NMe)GAII(NMe)GANleVGGVV	P18
NK(NMe)GAII(NMe)GLAVGGVV	P19
NK(NMe)GAII(NMe)GLNleAGGVV	P20
NK(NMe)GAII(NMe)GLNleVAGVV	P21
NK(NMe)GAII(NMe)GLNleVGAVV	P22
NK(NMe)GAII(NMe)GLNleVGGAA	P23
Negative control (no peptide)	P24

7.11 ThT binding studies

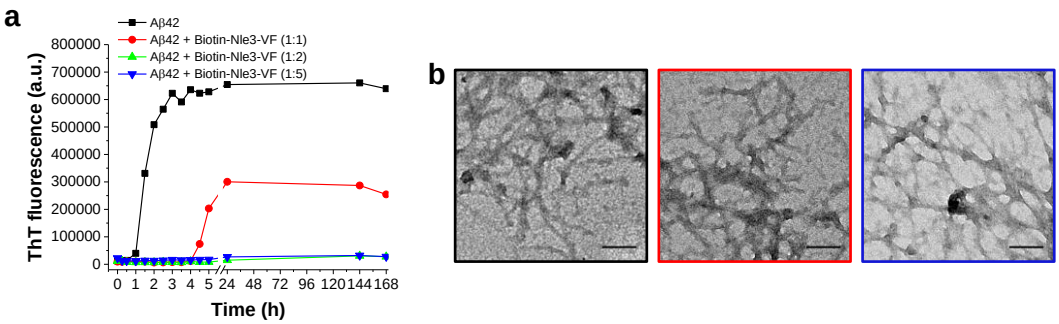

Figure 7-65: Aβ42 inhibition by Nᵅ-terminal biotinylated Nle3-VF. (**a**) Effect of Biotin-Nle3-VF on Aβ42 fibril formation studied via ThT binding. Incubations contained 5 µM Aβ42 and indicated molar excess of Biotin-Nle3-VF and were prepared in 45 mM ammonium acetate (pH 8.5) with 10 µM ThT (37 C°). Of note, Nᵅ-terminal labelling reduces the ACM's inhibitory potential since an equimolar amount (1:1) is not enough anymore to fully inhibit Aβ42 fibril formation. Shown is a representative experiment (n=2). (**b**) TEM images of Aβ42 and its mixtures (1:1 or 1:5) with Biotin-Nle3-VF after 6 days aging. Incubations were prepared as in a, but did not contain ThT. Colours correspond to colours in a. Scale bars: 100 nm.

7.12 Single values underlying means and errors calculated for IC_{50}s, app. kDs, and fibril dimension measurements

Table 7-11: Single values for calculating the mean IC_{50}s of inhibitory effects of ACMs on cytotoxic self-assembly of IAPP at 24 h. IAPP 100 nM; means (± SD) from 3 titration assays.

IC_{50} (nM)					
ACM	Value 1	Value 2	Value 3	Mean	SD
Nle3-VF	62.95	70.85	61.15	65.0	5.2
Nle3-LF	91.60	83.17	71.39	82.1	10.2
L3-VF	105.62	121.49	110.34	112.5	8.1
L3-LF	103.11	161.02	135.49	133.2	29.0
F3-VF	77.44	92.61	65.51	78.5	13.6
F3-LF	43.80	37.0	44.35	41.7	4.1

Table 7-12: Single values for calculating the mean IC_{50}s of inhibitory effects of ACMs on cytotoxic self-assembly of IAPP at 7 days. IAPP 100 nM; means (± SD) from 3 titration assays.

IC_{50} (nM)					
ACM	Value 1	Value 2	Value 3	Mean	SD
Nle3-VF	98.81	89.84	94.84	94.5	4.5
Nle3-LF	145.26	122.09	133.17	133.5	11.6
L3-VF	177.81	191.12	194.13	187.7	8.7
L3-LF	244.83	231.51	245.96	240.8	8.0
F3-VF	147.68	146.31	147.75	147.2	0.8
F3-LF	122.25	108.43	118.24	116.3	7.1

Table 7-13: Single values for calculating the mean IC_{50}s of inhibitory effects of ACMs on cytotoxic self-assembly of Aβ42 at 6 days. Aβ42 1 µM; means (± SD) from 3 titration assays.

IC_{50} (nM)					
ACM	Value 1	Value 2	Value 3	Mean	SD
Nle3-VF	341.21	303.23	455.00	366.48	79.0
L3-VF	380.52	295.07	106.13	260.57	140.41
F3-VF	1366.68	800.44	929.95	1032.36	296.69
F3-LF	308.08	347.02	131.12	262.08	115.07

Table 7-14: Single values for calculating the mean app. k_Ds for self-assemblies of ADPs. Measurements performed in 1xb with 1 % HFIP; Fluos-ADPs at 5 µM; n.d.: not determined.

	App. kDs (nM) for self-assembly of ADPs				
Peptide	Value 1	Value 2	Value 3	Mean	SD
Nle3	252.88	146.17	195.25	198.10	53.41
Nle3-VF	47.98	56.85	50.93	51.92	4.52
Nle3-LF	22.57	25.45	24.25	24.09	1.44
Nle3-GG	81.38	80.01	83.83	81.74	1.93
Nle3-GI	28.99	26.47	30.11	28.52	1.87
L3	35.69	39.43	27.02	34.05	6.37
L3-VF	20.85	19.66	19.96	20.16	0.62
L3-LF	48.21	49.90	46.26	48.12	1.82
F3-VF	64.15	53.75	76.92	64.94	11.60
F3-LF	51.95	51.00	38.03	47.00	7.78
VGS	9.09	21.43	19.84	16.79	6.71
VGS-VF	23.88	21.95	26.78	24.20	2.43
VGS-LF	52.89	68.46	115.35	78.90	32.51
VGS-GG	No binding up to 5 µM				
VGS-GI	No binding up to 5 µM				
R3	n.d.				
R3-VF	41.49	44.23	27.25	37.66	9.12
R3-LF	16.76	20.28	25.33	20.79	4.31
R3-GG	n.d.				
R3-GI	n.d.				
G3-VF	No binding up to 5 µM				

Table 7-15: Single values for calculating the mean app. k_Ds for binding of Fluos-ADPs to IAPP. Measurements performed in 1xb with 1 % HFIP; Fluos-ADPs at 5 µM; n.d.: not determined; * done by Sophia Kalpazidou during her Erasmus internship[147].

	App. kDs (nM) for binding of Fluos-ADPs to IAPP				
Peptide	Value 1	Value 2	Value 3	Mean	SD
Nle3	110.93	125.94	105.58	114.15	10.56
Nle3-VF	17.96	17.94	17.37	17.75	0.34
Nle3-LF	16.64	17.90	16.86	17.13	0.67
Nle3-GG	7.32	7.15	6.69	7.05	0.32
Nle3-GI	9.77	9.98	8.79	9.51	0.64
L3	16.85	16.89	16.46	16.73	0.24
L3-VF	6.11	6.62	5.55	6.09	0.53
L3-LF	5.81	5.75	5.53	5.70	0.15
F3-VF	18.71	9.10	11.53	13.11	4.99
F3-LF	19.94	12.34	14.92	15.73	3.87
VGS	4.97	5.03	5.00	5.00	0.03
VGS-VF	1.86	2.09	1.38	1.77	0.36
VGS-LF	1.06	1.72	1.17	1.32	0.35
VGS-GG	>5000	>5000	>5000	n.d.	n.d.
VGS-GI	1.57	3.29	4.11	2.99	1.30
R3	n.d.				
R3-VF	11.59	8.87	9.29	9.92	1.46
R3-LF	14.69	21.93	13.32	16.65	4.62
R3-GG	n.d.				
R3-GI	n.d.				
G3-VF*	8.76	2.83	7.12	6.24	3.06

Table 7-16: Single values for calculating the mean app. k_Ds for binding of Fluos-IAPP to ADPs. Measurements performed in 1xb with 1 % HFIP; Fluos-IAPP at 5 µM; n.d.: not determined; * done by Sophia Kalpazidou during her Erasmus internship[147].

	App. kDs (nM) for binding of Fluos-IAPP to ADPs				
Peptide	Value 1	Value 2	Value 3	Mean	SD
Nle3	200.75	202.62	192.18	198.51	5.57
Nle3-VF	70.87	68.17	69.47	69.50	1.35
Nle3-LF	50.66	53.68	62.01	55.45	5.87
Nle3-GG	557.64	575.94	606.75	580.11	24.82
Nle3-GI	250.59	218.95	239.83	236.46	16.08
L3	82.88	78.19	80.34	80.47	2.35
L3-VF	80.51	75.07	76.19	77.25	2.87
L3-LF	142.89	148.31	138.28	143.16	5.02
F3-VF	17.10	13.48	14.43	15.00	1.88
F3-LF	38.97	34.36	39.59	37.64	2.86
VGS	393.13	420.01	439.63	417.59	23.34
VGS-VF	238.45	242.09	233.75	238.09	4.18
VGS-LF	>500	>500	>500	n.d.	n.d.
VGS-GG	>5000	>5000	>5000	n.d.	n.d.
VGS-GI	192.15	49.10	220.99	154.08	92.05
R3	142.19	162.42	159.18	154.60	10.87
R3-VF	90.10	65.42	55.34	70.29	17.88
R3-LF	41.53	47.35	35.88	41.59	5.74
R3-GG	166.73	187.00	149.61	167.78	18.72
R3-GI	491.50	590.83	535.12	539.15	49.79
G3-VF*	63.07	52.09	33.62	49.59	14.88

Table 7-17: Single values for calculating the mean app. k_Ds for binding of FITC-Aβ42 to ADPs. Measurements performed in 1xb with 1 % HFIP; FITC-Aβ42 at 5 µM.

	App. kDs (nM) for binding of FITC-Aβ42 to ADPs				
Peptide	Value 1	Value 2	Value 3	Mean	SD
Nle3-VF	23.08	7.36	13.00	14.48	7.96
Nle3-LF	18.02	7.03	8.22	11.09	6.03
L3-VF	35.81	39.61	38.53	37.98	1.96
L3-LF	1.65	2.06	4.20	2.64	1.37
F3-VF	175.75	152.99	153.80	160.85	12.92
F3-LF	430.81	423.35	437.63	430.60	7.14

Table 7-18: Single values for calculating the mean app. k_Ds for binding of Fluos-ADPs to Aβ42. Measurements performed in 50 mM ammonium acetate, pH 8.5 (1 % HFIP); Fluos-ADPs at 1 µM; n.d.: not determined.

	App. kDs (nM) for binding of Fluos-ADPs to Aβ42				
Peptide	Value 1	Value 2	Value 3	Mean	SD
Nle3-VF	>25000	>25000	>25000	n.d.	n.d.
Nle3-LF	>10000	>10000	>10000	n.d.	n.d.
L3-VF	>10000	>10000	>10000	n.d.	n.d.
L3-LF	>5000	>5000	>5000	n.d.	n.d.
F3-VF	>10000	>10000	>10000	n.d.	n.d.
F3-LF	>5000	>5000	>5000	n.d.	n.d.

Table 7-19: Single values for calculating the mean app. k_Ds for binding of DAC-Aβ40 to ADPs. Measurements performed in 1xb with 1 % HFIP; DAC-Aβ40 at 10 µM; n.d.: not determined; * done by Sophia Kalpazidou during her Erasmus internship[147].

	App. kDs (nM) for binding of DAC-Aβ40 to ADPs				
Peptide	Value 1	Value 2	Value 3	Mean	SD
Nle3	64.46	56.48	44.14	55.03	10.24
Nle3-VF	240.87	243.92	244.67	243.15	2.01
Nle3-LF	368.69	354.86	350.66	358.07	9.43
Nle3-GG	35.55	31.72	61.33	42.86	16.10
Nle3-GI	No binding up to 10 µM				
L3	No binding up to 10 µM				
L3-VF	46.02	58.81	59.08	54.64	7.46
L3-LF	212.76	210.64	239.09	220.83	15.85
F3-VF	No binding up to 5 µM				
F3-LF	No binding up to 2.5 µM				
VGS	58.44	59.62	41.69	53.25	10.03
VGS-VF	>10000	>10000	>10000	n.d.	n.d.
VGS-LF	No binding up to 5 µM				
VGS-GG	>10000	>10000	>10000	n.d.	n.d.
VGS-GI	>10000	>10000	>10000	n.d.	n.d.
R3-VF	885.01	1563.81	929.51	1126.11	379.71
R3-LF	1579.48	1653.34	1555.42	1596.08	51.03
G3-VF*	>10000	>10000	>10000	n.d.	n.d.

Table 7-20: Single values for calculating the mean app. k_Ds for binding of Fluos-ADPs to Aβ40. Measurements performed in 1xb with 1 % HFIP; Fluos-ADPs at 5 µM; n.d.: not determined; * done by Sophia Kalpazidou during her Erasmus internship[147].

	App. kDs (nM) for binding of Fluos-ADPs to Aβ40				
Peptide	Value 1	Value 2	Value 3	Mean	SD
Nle3	1422.40	1295.82	1114.56	1277.59	154.73
Nle3-VF	434.14	590.94	692.95	572.68	130.37
Nle3-LF	300.06	335.06	334.32	323.15	20.00
Nle3-GG	315.35	295.60	289.90	300.28	13.35
Nle3-GI	434.33	464.59	356.46	418.46	55.78
L3	291.59	264.16	238.81	264.85	26.40
L3-VF	516.19	564.28	656.27	578.91	71.17
L3-LF	506.40	447.90	398.52	450.94	54.01
F3-VF	>5000	>5000	>5000	n.d.	n.d.
F3-LF	>5000	>5000	>5000	n.d.	n.d.
VGS	33.31	28.33	32.76	31.47	2.73
VGS-VF	30.67	34.19	32.98	32.61	1.79
VGS-LF	0.25	0.22	0.24	0.24	0.01
VGS-GG	>10000	>10000	>10000	n.d.	n.d.
VGS-GI	1.80	5.43	3.40	3.55	1.82
R3-VF	600.27	488.58	530.00	539.62	56.46
R3-LF	668.92	520.52	606.71	598.71	74.52
G3-VF*	34.96	49.30	48.70	44.32	8.11

Table 7-21: Single values for calculating the mean fibril widths of fIAPP and hf-IAPP/ACM as observed by TEM. Widths were measured from TEM images of 7 days aged IAPP (16.5 µM, ThT buffer with 0.5 % HFIP) or its mixtures with ADPs (1:2) using Image J.

Fibril widths (nm)								
	IAPP	IAPP + VGS-VF	IAPP + Nle3-VF	IAPP + Nle3-LF	IAPP + L3-VF	IAPP + L3-LF	IAPP + F3-VF	IAPP + F3-LF
	9.7	7.8	9.5	4.5	11.8	7.8	11.7	6.3
	15.4	9.4	9.5	6.1	10.2	12.2	6.4	4.3
	13.6	8.2	8.9	5.6	6.7	9.6	9.9	7
	13.8	6.2	8	5.3	8.2	7.3	10.5	6.3
	10.7	8.1	8.7	6.2	7.1	7.4	8.9	8.2
	7.4	9	10.1	6.4	7.6	7.8	6.7	7
	7.2	9	8	4.5	7.6	5.9	6	6.8
	9.7	9.7	8.4	4.1	8.5	8.9	7.4	8.2
	11.1	7	11.1	6	6.2	7.8	5	6.6
	8	6.4	7.4	7	6.8	10	9.2	5.6
	9.9	5.7	10.2	7.3	9	9.5	7.5	6.1
	7.2	6.7	10.9	8.1	9.1	7.1	8.7	8.6
	9.7	10.7	12.5	5.5	7	10.7	10.8	7.9
	7.5	10	11.4	6.2	7.6	6.8	9.5	8
	9.4	5.4	8.6	5.3	6.4	9.1	9.3	5.2
	8.7	7.6	9.5	5.8	5	8.9	9.5	5.1
	9.9	5.6	11.8	5	9.1	5.7	8	8.4
	13.3	6.2	8.4	7.3	6.8	6.8	7.1	6.2
	9.2	9.4	8.9	7.3	9.2	7	9.5	5.1
	10.8	13.1	9.5	8.3	6.4	5.6	11.9	5.6
	12.4	11.5	7.2	6.3	7.3	5.6	9.3	6.5
	8.9	7.1	7.2	6.0	7.6	6.9		6.5
	6.5	11.1	5		6.1	9.2		
	7.8	11.1	5.9		7.6	4.8		
	8.1	10.3	7.1		8.3			
	6.6	10	6.3					
	10.2	7.8	5.2					
	10.4	9	5.5					
	6.6	7.6	5					
	12.9	9.6	8.3					
	7.4		6.5					
	12.2		7.7					
	8.9		7.8					
	7.8		4.5					
	7.4		8.9					
	9.7		7.3					
	11.2		6.3					
	6.8		11.1					
	13.3		9.2					
	9		7					
	9.6		7.3					
	10.9		10.4					
			7.4					
			9.6					
			10.5					
			9.1					
			6.3					
mean:	9.69	8.54	8.32	6.10	7.73	7.85	8.70	6.61
SD:	2.26	1.97	1.94	1.12	1.46	1.82	1.84	1.21

Table 7-22: Single values for calculating the mean fibril lengths of fIAPP and hf-IAPP/ACM as observed by TEM. Lengths were measured from TEM images of 7 days aged IAPP (16.5 µM, ThT buffer with 0.5 % HFIP) or its mixtures with ADPs (1:2) using Image J.

Fibril lengths (nm)								
	IAPP	IAPP + VGS-VF	IAPP + Nle3-VF	IAPP + Nle3-LF	IAPP + L3-VF	IAPP + L3-LF	IAPP + F3-VF	IAPP + F3-LF
	190.1	315.5	234.6	284.5	271.5	130.6	214.9	298
	172.6	252	93.6	262.7	161	136.6	285.7	160.5
	100.4	152.4	214.1	190.1	173.9	180.4	244	80.2
	143.8	142.4	165.7	157.8	140.4	235.8	277.2	171
	161.6	104.5	338.8	237.3	158	206.6	229.2	142
	94.6	201.9	333.5	120.2	190.2	151.7	252.1	106.6
	97.9	406.5	108.4	178.2	162.9	172.5	283	207
	206.8	110.7	145.4	149.9	171.6	130	106.6	208.8
	197.2	220	106	115.1	158.3	259.5	111.2	223
	236.6	189.9	116.8	203.6	261.1	94.4	181.7	134
	200.4	115.1	72.3	101.3	163.9	166.3	143.6	154.4
	189	254.6	113	143.3	121.4	176.3	126.2	114.8
	86.9	204.4	102.9	160.3	188.6	132.1	132.8	189.8
	138	214.6	131.8	96.2	151	142	239.5	137
	168.4	178.9	229.5	139	193.8	111.7	149.5	137.6
	151.3	236.4	259.1	123.9	138.5	115.7	106.4	130.4
	91.1	339.4	337.4	124.7	119.2	74.8	132.2	118.4
	80.4	120.5	269.3	206.9	117.5	155.3	299.4	162.3
	132.5	87.1	286.2	85.3	199.4	156.8	206.2	119.2
	203.1	104.8	305.1	84.6	198.1	160.9	222.1	139
	125.7	144.8	285.7	145.3		223.6		312.2
	152.4	142.7	179.6			157.8		105.9
	276.6	161.5	191.7			254.1		115.5
	171.2	128.3	148.5			177.1		
	109.1	171.1	165.3					
	181.7	156	172.3					
	176.7	101.5	161					
	133.2	153.6	179.8					
	189.8	151.3	175.6					
	150.7	129.7	112.7					
	154.9		153.4					
	174.4		130.4					
	159		103.8					
	149.7		147.1					
	183		192.2					
	249.4		149.3					
			152.9					
			137.8					
mean:	160.56	179.74	181.65	157.63	172.02	162.61	197.18	159.46
SD:	45.81	75.25	73.55	56.22	40.97	47.14	66.38	58.28

Table 7-23: Single values for calculating the mean fibril widths of fAβ42 and hf-Aβ42/ACM as observed by TEM. Widths were measured from TEM images of 6 days aged Aβ42 (5 µM, 45 mM ammonium acetate pH 8.5, 37 °C, w/o ThT) or its mixtures with ACMs (1:1) using Image J.

Fibril widths (nm)							
	Aβ42	Aβ42 + Nle3-VF	Aβ42 + Nle3-LF	Aβ42 + L3-VF	Aβ42 + L3-LF	Aβ42 + F3-VF	Aβ42 + F3-LF
	6.8	9.8	6.3	6.3	6.3	8.3	5.8
	10.3	7.4	6.4	6.6	12.8	9.2	5.2
	6.6	9.3	8.9	7.9	7.3	8.1	10.4
	8.1	5.9	9.1	8.2	7.3	7.1	7.8
	5.9	10.6	8.5	4.9	4.9	6.1	7.5
	8	7.4	7.1	10.2	4.7	6.3	4.9
	6.8	7.7	6.3	4.5	6.1	7.4	5
	7.3	6.3	6.6	6.1	11.4	7.2	8.7
	9.5	7.2	7.1	5.6	5.9	7.4	6.5
	8.9	7.2	7.3	7.7	6.6	9	8.1
	7.8	4.4	7	6.9	4.6	6.6	8.6
	8.7	7.2	5.5	6.5	7.1	5.4	6.7
	5	9.4	8.9	7.5	6.5	5.3	6.5
	6.1	7.5	6.4	7.5	7.2	6.3	9.4
	8.6	4.7	8.2	8.9	3.5	7.4	8
	9.6	6.3	7.2	5.5	9.1	4.8	8.2
	9.5	8.6	7.6	7	7.1	9.1	8.5
	6.7	6	6.8	5.1	7	5.7	7.3
	6.9	4.6	8.9	7.8	8.9	6.9	6.2
	5.8	8.6	9.2	7.3	6.6	5.5	6.8
	10.6	7		8.2		6.5	5.3
				5.2		6.8	8.6
				7			8.9
mean:	7.79	7.29	7.47	6.89	7.05	6.93	7.34
SD:	1.58	1.69	1.13	1.39	2.20	1.25	1.51

Table 7-24: Single values for calculating the mean fibril lengths of fAβ42 and hf-Aβ42/ACM as observed by TEM. Lengths were measured from TEM images of 6 days aged Aβ42 (5 µM, 45 mM ammonium acetate pH 8.5, 37 °C, w/o ThT) or its mixtures with ACMs (1:1) using Image J.

Fibril lengths (nm)							
	Aβ42	Aβ42 + Nle3-VF	Aβ42 + Nle3-LF	Aβ42 + L3-VF	Aβ42 + L3-LF	Aβ42 + F3-VF	Aβ42 + F3-LF
	155.4	372.8	1242.2	334.4	419.8	300	699.2
	166.6	666.9	731.8	331.9	296.9	230.2	366.1
	168.9	478.5	773	606.5	356.8	422.2	501.5
	130	540.7	669.8	399	354.8	663.3	255.9
	87.5	577	507.1	512.4	278	440.6	204
	153.1	442	263.8	363.9	251.1	588.5	236.6
	203.3	410.6	499.3	458.2	228.9	327.4	394.7
	169	326.6	432.4	422	283.7	406.3	412.8
	126	404.7	436.9	627.9	245.9	495.9	391.1
	135.2	681	573.5	373.9	334.6	244.6	566.7
	149.9	704	289.5	485.5	482.3	223.6	272.9
	109.5	429.8	392	624.9	391.2	272.9	414.3
	112.8	351	728.7	335.3	378.1	247.7	316.8
	113	424	394.2	442.1	367.7	250.4	307.1
	82.1	404.6	351.8	544.8	404.7	352.2	315.2
	133.8	407.7	828.8		470.4	323.9	281.3
	324.5	541.4	1104.1		325.2	370.3	253.3
	293.3	257.6	245.4		419.9	258	434.9
	166.9	301.1	606		340.4	323.8	329
	111.4	726.1	734.4		300.7	254.3	358.2
	124.6					360.6	225.3
	172.2					306.6	340.2
						474.2	
mean:	154.05	472.41	590.24	457.51	346.56	353.80	358.05
SD:	58.46	138.30	267.58	105.97	71.98	116.81	118.12

Table 7-25: Single values for calculating the mean lengths of elongated fibrils found in mixtures of nucleated Aβ42 with Nle3-VF by TEM. Lengths were measured from TEM images of mixtures of nucleated 2 h-aged Aβ42 (5 µM, 45 mM ammonium acetate pH 8.5, 37 °C, w/o ThT) with Nle3-VF (1:1) using Image J. Samples were taken directly after preparation of the mixture (2 h) and at several other time points during the aggregation process (3 h, 5 h, 24 h, 6 days). Samples of the Aβ42 control incubation were taken at the same time points.

Fibril lengths (nm)										
	Aβ42					Aβ42 (2h) + Nle3-VF				
	2h	3h	5h	24h	6d	2h	3h	5h	24h	6d
	82.1	111.6	127.5	149.6	182.3	156.4	169.4	148.6	308.2	117.3
	79.4	133.1	105.9	147.1	81.2	119.1	87.5	176.2	437.3	150.5
	56	120.2	114.3	128.4	104.9	115.1	103.4	160.9	292.9	118.7
	84.3	98.9	131.7	155.3	117.3	75.7	99.8	205.3	300	135
	64.8	103	159.4	105.1	113.4	140	67.9	139.5	355.4	188
	71.5	90	109.5	163.8	120.2	126.8	98.9	92.9	227.6	139.5
	95.2	126.8	128	105.2	124.6	109.3	111.9	141.6	376.4	138.3
	79.3	101.5	169.6	155.7	109.5	62.9	93.4	138.9	405.7	637.2
	170.9	113.3	145.5	137.1	134.7	144.1	115.8	165.2	271.4	185.5
	114.2	138.6	142	143.6	164	68.2	125.2	100.2	278.3	202.7
	83.6	117.6	169	120.5	159.7	93.2	124.1	102.5	294.3	308.5
	79.4	131.7	127.7	109.8	145.9	70.8	118.8	174.2	226.9	318.1
	115.5	73.5	108	116.3	108.5	70.8	117.6	236.6	238.5	385
	152.4	107.9	182.5		100.2	81.2	89.2	141.6	321.9	333.4
		145.7	139.9		148.5	64.5	67.7	344.1	858.3	252.6
		106.8	270.5		122.8	59.4	119.1	153.6	363.8	407.6
		123.8	120		109.6	75.1	104.4	184.1	300.4	267
		112.8					113.4	184.5	230.5	279
		161.5					144.4	148.6	200.9	474.5
							115.5	176.2	255	213.6
							108.6	193.3	263.9	185.7
							144.5	231.3	205.7	223.2
							92.1	209.2	165.9	176.3
							118.3	125.7	152.6	196
							106.4	154.6	130.1	
								176.7	182	
								178.4	160.7	
									162.4	
mean:	94.9	116.75	144.18	133.65	126.31	96.04	110.29	169.80	284.54	251.38
SD:	32.79	20.45	39.82	20.63	26.19	32.08	22.46	49.93	137.71	126.31

Table 7-26: Single values for calculating the mean lengths of elongated fibrils found in mixtures of fibrillar Aβ42 with Nle3-VF by TEM. Lengths were measured from TEM images of mixtures of fibrillar Aβ42 (5 µM, 45 mM ammonium acetate pH 8.5, 37 °C, 7 days aged, w/o ThT) with Nle3-VF (1:1) after 1 day or 4 days of co-incubation using Image J. Lengths of fAβ42 before co-incubation with Nle3-VF is given for comparison.

Fibril lengths (nm)			
	fAβ42, before mix with Nle3-VF	fAβ42, 1d after mix with Nle3-VF	fAβ42, 4d after mix with Nle3-VF
	182.3	258.3	284
	81.2	268.2	209.8
	104.9	294.2	242.9
	117.3	307.4	304.1
	113.4	239.1	252.2
	120.2	261.2	157.5
	124.6	261.5	278.8
	109.5	227.2	206.1
	134.7	226.9	136.3
	164	235.2	258.4
	159.7	240.8	106.8
	145.9	166.5	133.9
	108.5	185.9	167.6
	100.2	254.7	259.7
	148.5	239.5	206
	122.8	172.6	243.2
	109.6	180.1	117.8
		211.8	189.1
		136.3	201.8
		365.2	206.6
		232.3	164.4
		438.1	222.3
		200	220.5
		149.6	115
		250.2	173.9
		611.5	268.1
		328.7	
		189.7	
		346.3	
mean:	126.31	257.90	204.88
SD:	26.19	95.13	56.10

Table 7-27: Single values for calculating the mean widths of IAPP/Nle3-VF hetero-nanofibers observed via CLSM and STED imaging. Widths were measured from CLSM and STED images of 7 days aged mixtures of 14.85 µM IAPP, 1.65 µM TAMRA-IAPP, 29.7 µM Nle3-VF and 3.3 µM Atto647N-Nle3-VF (in 1xb; labelled peptides are 10 % of total peptide amount) using LAS-X. Widths observed for the IAPP control incubation (containing 14.85 µM IAPP and 1.65 µM TAMRA-IAPP) are given for comparison.

Nanofibre widths (nm)										
	IAPP strand, fIAPP		IAPP strand, fHetero		Nle3-VF strand, fHetero		total width, fHetero (observed)		total width, fHetero (calculated)	
	CLSM	STED	CLSM	STED	CLSM	STED	CLSM	STED	CLSM	STED
	169.95	107.31	280.58	211.67	221.51	147.68	280.58	211.67	502.10	359.34
	213.53	91.05	176.53	294.22	288.87	160.48	288.87	337.02	465.40	454.70
	172.66	141.37	171.18	240.73	304.92	240.73	304.92	310.27	476.10	481.45
	211.28	133.87	234.42	192.06	228.77	189.23	271.14	200.53	463.19	381.29
	181.61	131.90	266.74	273.01	222.80	194.56	288.70	285.56	489.54	467.57
	190.70	172.14	216.17	315.25	274.72	229.68	310.75	315.25	490.89	544.93
	180.79	119.06	245.44	249.22	222.79	196.36	294.53	249.22	468.23	445.58
	163.91	127.36	294.80	258.45	230.18	209.99	294.80	258.45	524.98	468.44
	180.36	118.48	587.40	310.98	334.01	460.71	610.44	472.23	921.42	771.69
	163.21	103.58	112.68	117.38	291.09	234.75	291.09	234.75	403.78	352.13
	180.88	125.80	482.65	189.28	397.48	359.62	482.65	369.09	880.13	548.90
	178.31	108.93	124.91	164.52	243.73	115.77	243.73	164.52	368.64	280.29
		146.00	210.74	179.51	266.84	101.88	320.21	208.62	477.58	281.40
		107.14	168.61	182.66	252.92	147.54	252.92	182.66	421.53	330.20
		175.71	317.35	248.73	291.62	291.62	317.35	325.93	608.97	540.35
		122.52	360.23	188.69	308.77	205.85	385.97	265.89	669.01	394.54
		93.49	261.93	132.12	178.48	155.30	275.84	155.30	440.42	287.43
		104.76	283.18	149.31	283.18	190.50	370.71	195.65	566.36	339.81
		116.33	235.36	139.30	264.18	124.89	312.22	139.30	499.55	264.18
			226.32	181.87	262.69	137.41	270.78	181.87	489.02	319.27
			196.95	147.72	246.19	181.57	273.89	240.04	443.15	329.28
			287.52	128.17	284.06	103.92	353.34	152.42	571.58	232.10
			368.78	108.46	319.97	92.19	406.74	130.16	688.74	200.66
			311.29	113.89	235.82	108.46	311.29	135.58	547.11	222.35
			311.29	188.66	273.56	207.53	311.29	254.69	584.84	396.18
			276.34	245.26	212.92	198.09	276.34	245.26	489.25	443.35
			282.15	172.15	193.25	197.06	282.15	197.06	475.41	369.21
			314.67	189.39	210.89	150.74	314.67	224.18	525.56	340.13
			294.03	184.11	236.43	147.29	319.88	241.02	530.46	331.41
			218.54	171.53	191.96	194.71	248.07	231.80	410.50	366.24
			156.66	126.99	211.28	126.99	256.66	141.76	367.95	253.98
			243.75	105.64	235.35	162.15	268.97	162.15	479.10	267.79
				226.94		197.52		226.94		424.47
mean:	182.27	123.52	266.23	191.75	256.91	186.75	315.34	231.72	523.14	378.50
SD:	16.12	23.16	95.14	58.80	46.68	74.40	73.22	75.59	123.55	117.49

Table 7-28: Single values for calculating the mean widths of IAPP/Nle3-VF hetero-nanofibers observed via 2-PM imaging. hf-IAPP/Nle3-VF were prepared by aging a mixture of 16.5 µM TAMRA-IAPP with 33 µM Fluos-Nle3-VF for 7 days in 1xb. Widths were measured from 2-PM imaging using LAS-X.

Nanofibre widths (nm)			
	Nle3-VF strand	IAPP strand	total
	314.99	334.67	590.60
	469.74	489.73	529.70
	325.75	315.93	325.75
	396.35	386.91	603.96
	407.08	416.13	651.33
	324.43	249.56	311.96
	376.41	321.05	365.34
	340.57	280.16	338.80
	422.52	347.96	447.38
	377.45	337.42	388.89
mean:	375.53	347.95	455.37
SD:	49.99	68.78	128.17

Table 7-29: Single values for calculating the mean widths of fibrillar co-assemblies observed in mixtures of Nle3-VF with sub stoichiometric amounts of fIAPP via 2-PM imaging. Fibrillar co-assemblies were obtained by mixing a 33 µM Fluos-Nle3-VF solution (in 1xb) with TAMRA-fIAPP (3.3 µM final). The sample for 2-PM was taken from a freshly prepared solution (0 h). TAMRA-fIAPP was prepared in 1xb (16.5 µM, 5 days aged). Widths were measured from 2-PM imaging using LAS-X.

Nanofibre widths (nm)			
	Nle3-VF strand	IAPP strand	total
	220.48	203.07	705.20
	374.10	386.57	506.74
	287.04	423.01	648.89
	515.29	286.27	459.79
	372.16	343.53	540.93
	386.47	486.67	405.70
	332.58	291.00	837.77
	415.72	443.43	851.73
	386.94	330.03	766.17
	361.55	277.19	510.17
	421.81	241.03	609.71
mean:	370.38	337.44	622.07
SD:	75.61	88.93	152.77

Table 7-30: Single values for calculating the mean widths of fibrillar co-assemblies observed in mixtures of Nle3-VF with sub stoichiometric amounts of monomeric/pre-fibrillar IAPP via 2-PM imaging. Fibrillar co-assemblies were obtained by aging a mixture of 1.65 µM TAMRA-IAPP with 33 µM Fluos-Nle3-VF for 48 h in 1xb. Widths were measured from 2-PM imaging using LAS-X.

Nanofibre widths (nm)			
	Nle3-VF strand	IAPP strand	total
	272.81	283.30	290.40
	346.26	377.74	365.16
	274.73	226.65	274.73
	377.76	336.55	357.15
	438.23	438.22	500.84
	375.63	323.46	386.06
	333.89	333.89	344.33
	341.87	379.85	367.19
	329.20	455.82	417.83
	329.20	291.22	392.51
mean:	341.96	344.67	369.62
SD:	48.76	70.41	63.63

Table 7-31: Single values for calculating the mean widths of fibrillar co-assemblies observed in mixtures of VGS-VF with sub stoichiometric amounts of monomeric/pre-fibrillar IAPP via 2-PM imaging. Fibrillar co-assemblies were obtained by aging a mixture of 1.65 µM TAMRA-IAPP with 33 µM Fluos-VGS-VF for 48 h in 1xb. Widths were measured from 2-PM imaging using LAS-X.

Nanofibre widths (nm)			
	Nle3-VF strand	IAPP strand	total
	526.31	297.78	526.31
	369.22	308.94	384.29
	530.69	464.35	530.69
	530.69	309.57	519.63
	499.71	271.03	550.53
	398.08	287.97	567.47
	457.37	398.08	491.24
	489.19	286.13	498.42
	378.43	369.20	387.66
	618.46	515.39	721.54
mean:	479.81	350.84	517.78
SD:	79.40	83.87	94.95

8 Contributions of other lab members or students to the results presented in my PhD thesis

Ricardo Keller contributed to the synthesis and purification of TAMRA-IAPP[114].

Sophia Kalpazidou contributed to the synthesis of Fluos-G3-VF and purification of Fluos-G3-VF and G3-VF, and to analysis of binding of G3-VF to IAPP and Aβ40[147] (Table 8-1).

Martin Ortner contributed to synthesis, purification, and structural analysis of non-methylated ADPs[141] (Table 8-1). Kathleen Hille performed re-syntheses of Nle3 and R3.

Sophia Prem contributed to synthesis, purification, and analysis of structure and cytotoxic properties of F3-VF, F3-LF, R3-VF, and R3-LF[146] (Table 8-1). Re-syntheses were done by Kathleen Hille.

Christina Lindner contributed to cross linking studies (Table 8-1).

Planning, preparation, and performance of the SPOT synthesis was carried out in our group together with Valentina Armiento, Kathleen Hille, and Christos Kontos. Cellulose disks were handed on to Christine Krammer (group of Vascular Biology, Prof. J. Bernhagen group; Institute for Stroke and Dementia Research) who performed disk work up, CelluSpot slide preparation, and microarray development. Raw data was returned to me for data evaluation and interpretation, which was done by me.

IAPP was provided for our group by Eleni Malideli, Denise Naltsas, Simon Hornung, and me.

Fluos-IAPP was provided for the research group by Kathleen Hille, Denise Naltsas, and Alexandros Grammatikopoulos.

Aβ40, Biotin-Aβ40, IAPP-GI, TAMRA-IAPP-GI, TAMRA-IAPP and Biotin-IAPP were provided by Kathleen Hille.

DAC-Aβ40 was provided by Kathleen Hille, Michael Kracklauer, or Alexandros Grammatikopoulos.

ADP(15-23)-VF, ADP(27-40), and G3-VF synthesis and re-syntheses of VGS-VF, Nle3-VF, and L3-VF were performed by Kathleen Hille, and she contributed to purification of several ADPs.

Atto647N-Nle3-VF was synthesised and purified by Kathleen Hille and she also assisted in purification of other labelled ADPs.

Contributions of other lb members or students to parts of figures shown in this PhD thesis are summarised in Table 8-1.

Table 8-1: Contributions of other lab members or students to data presented in figures of this thesis.

Contributor	Figure or table number	contributions
Martin Ortner[141]	Figure 4-10	Also analysed structure of VGS, Nle3, G3, and R3 by CD
Maria Bakou[144]	Figure 4-11	Performed preliminary studies on the effects of VGS, R3, G3, and Nle3 on IAPP fibril formation and cytotoxicity
Martin Ortner[141]	Figure 4-17a	Also analysed structure of Nle3 by CD
Sophia Prem[146]	Figure 4-17c,d	Also analysed structure of F3-LF and R3-LF by CD; experiment for R3-VF was taken over from her
Sophia Kalpazidou[147]	Figure 4-17d	Also analysed structure of G3-VF by CD
Sophia Prem[146]	Figure 4-18	Also analysed structure of F3-LF by CD
Sophia Prem[146]	Figure 4-19d	Experiment for R3-VF was taken over from her; she also tested cytotoxicity of R3-LF
Sophia Kalpazidou[147]	Table 4-7	Performed fluorescence spectroscopic titrations of Fluos-G3-VF with IAPP and of Fluos-IAPP with G3-VF
Christina Lindner	Figure 4-28, Figure 4-29, Figure 4-31	CL procedure, NuPAGE and WB were done by Christina Lindner when she was a working student in our lab; Incubations for the presented assay were prepared by me
Sophia Kalpazidou[147]	Table 4-16	Performed fluorescence spectroscopic titrations of Fluos-G3-VF with Aβ40 and of DAC-Aβ40 with G3-VF
Beatrice Dalla Volta[140,152]	Figure 4-49c	Provided lifetime distribution data of the correct donor alone control
Beatrice Dalla Volta[140,152]	Figure 4-51a,b	Provided fluorescence decay curve and lifetime distribution data of the correct donor alone control
Sophia Prem[146]	Figure 4-71j-l	Also studied effects of R3-VF on Aβ40 fibril formation and cytotoxicity
Sophia Kalpazidou[147]	Figure 4-71j	Also studied effects of G3-VF on Aβ40 fibril formation (preliminary results)
Beatrice Dalla Volta[140,152]	Figure 4-79a	Provided lifetime distribution data of the correct donor alone control

Literature

1 Dobson, C. M. Protein folding and misfolding. *Nature* **426**, 884-890, doi:10.1038/nature02261 (2003).

2 Chiti, F. & Dobson, C. M. Protein Misfolding, Amyloid Formation, and Human Disease: A Summary of Progress Over the Last Decade. *Annu Rev Biochem* **86**, 27-68, doi:10.1146/annurev-biochem-061516-045115 (2017).

3 Sunde, M. *et al.* Common core structure of amyloid fibrils by synchrotron X-ray diffraction. *J Mol Biol* **273**, 729-739, doi:10.1006/jmbi.1997.1348 (1997).

4 Eanes, E. D. & Glenner, G. G. X-ray diffraction studies on amyloid filaments. *J Histochem Cytochem* **16**, 673-677, doi:10.1177/16.11.673 (1968).

5 Otzen, D. & Riek, R. Functional Amyloids. *Cold Spring Harb Perspect Biol* **11**, doi:10.1101/cshperspect.a033860 (2019).

6 International Diabetes Federation. *IDF Diabetes Atlas, 10th edn.*, <https://www.diabetesatlas.org> (2021).

7 Milardi, D. *et al.* Proteostasis of Islet Amyloid Polypeptide: A Molecular Perspective of Risk Factors and Protective Strategies for Type II Diabetes. *Chem Rev* **121**, 1845-1893, doi:10.1021/acs.chemrev.0c00981 (2021).

8 Akter, R. *et al.* Islet Amyloid Polypeptide: Structure, Function, and Pathophysiology. *J Diabetes Res* **2016**, 2798269, doi:10.1155/2016/2798269 (2016).

9 Westermark, P., Andersson, A. & Westermark, G. T. Islet amyloid polypeptide, islet amyloid, and diabetes mellitus. *Physiol Rev* **91**, 795-826, doi:10.1152/physrev.00042.2009 (2011).

10 Röcken, C., Linke, R. P. & Saeger, W. Immunohistology of islet amyloid polypeptide in diabetes mellitus: semi-quantitative studies in a post-mortem series. *Virchows Arch A Pathol Anat Histopathol* **421**, 339-344, doi:10.1007/bf01660981 (1992).

11 Clark, A. *et al.* Islet amyloid, increased A-cells, reduced B-cells and exocrine fibrosis: quantitative changes in the pancreas in type 2 diabetes. *Diabetes Res* **9**, 151-159 (1988).

12 Westermark, P. *et al.* Amyloid fibrils in human insulinoma and islets of Langerhans of the diabetic cat are derived from a neuropeptide-like protein also present in normal islet cells. *Proc Natl Acad Sci U S A* **84**, 3881-3885, doi:10.1073/pnas.84.11.3881 (1987).

13 Cooper, G. J. *et al.* Amylin found in amyloid deposits in human type 2 diabetes mellitus may be a hormone that regulates glycogen metabolism in skeletal muscle. *Proc Natl Acad Sci U S A* **85**, 7763-7766, doi:10.1073/pnas.85.20.7763 (1988).

14 Betsholtz, C. *et al.* Sequence divergence in a specific region of islet amyloid polypeptide (IAPP) explains differences in islet amyloid formation between species. *FEBS Lett* **251**, 261-264, doi:10.1016/0014-5793(89)81467-x (1989).

15 Sakagashira, S. *et al.* Missense mutation of amylin gene (S20G) in Japanese NIDDM patients. *Diabetes* **45**, 1279-1281, doi:10.2337/diab.45.9.1279 (1996).

16 Sakagashira, S. *et al.* S20G mutant amylin exhibits increased in vitro amyloidogenicity and increased intracellular cytotoxicity compared to wild-type amylin. *Am J Pathol* **157**, 2101-2109, doi:10.1016/s0002-9440(10)64848-1 (2000).

17 Abedini, A., Meng, F. & Raleigh, D. P. A single-point mutation converts the highly amyloidogenic human islet amyloid polypeptide into a potent fibrillization inhibitor. *J Am Chem Soc* **129**, 11300-11301, doi:10.1021/ja072157y (2007).

18 Meng, F., Raleigh, D. P. & Abedini, A. Combination of kinetically selected inhibitors in trans leads to highly effective inhibition of amyloid formation. *J Am Chem Soc* **132**, 14340-14342, doi:10.1021/ja1046186 (2010).

19 Yan, L. M., Tatarek-Nossol, M., Velkova, A., Kazantzis, A. & Kapurniotu, A. Design of a mimic of nonamyloidogenic and bioactive human islet amyloid polypeptide (IAPP) as nanomolar affinity inhibitor of IAPP cytotoxic fibrillogenesis. *Proc Natl Acad Sci U S A* **103**, 2046-2051, doi:10.1073/pnas.0507471103 (2006).

20 Wiltzius, J. J. *et al.* Atomic structure of the cross-beta spine of islet amyloid polypeptide (amylin). *Protein Sci* **17**, 1467-1474, doi:10.1110/ps.036509.108 (2008).

21 Nilsson, M. R. & Raleigh, D. P. Analysis of amylin cleavage products provides new insights into the amyloidogenic region of human amylin. *J Mol Biol* **294**, 1375-1385, doi:10.1006/jmbi.1999.3286 (1999).

22 Scrocchi, L. A. *et al.* Identification of minimal peptide sequences in the (8-20) domain of human islet amyloid polypeptide involved in fibrillogenesis. *J Struct Biol* **141**, 218-227, doi:10.1016/s1047-8477(02)00630-5 (2003).

23 Gilead, S. & Gazit, E. The role of the 14-20 domain of the islet amyloid polypeptide in amyloid formation. *Exp Diabetes Res* **2008**, 256954, doi:10.1155/2008/256954 (2008).

24 Mazor, Y., Gilead, S., Benhar, I. & Gazit, E. Identification and characterization of a novel molecular-recognition and self-assembly domain within the islet amyloid polypeptide. *J Mol Biol* **322**, 1013-1024, doi:10.1016/s0022-2836(02)00887-2 (2002).

25 Jaikaran, E. T. *et al.* Identification of a novel human islet amyloid polypeptide beta-sheet domain and factors influencing fibrillogenesis. *J Mol Biol* **308**, 515-525, doi:10.1006/jmbi.2001.4593 (2001).

26 Paulsson, J. F., Andersson, A., Westermark, P. & Westermark, G. T. Intracellular amyloid-like deposits contain unprocessed pro-islet amyloid polypeptide (proIAPP) in beta cells of transgenic mice overexpressing the gene for human IAPP and transplanted human islets. *Diabetologia* **49**, 1237-1246, doi:10.1007/s00125-006-0206-7 (2006).

27 Iadanza, M. G., Jackson, M. P., Hewitt, E. W., Ranson, N. A. & Radford, S. E. A new era for understanding amyloid structures and disease. *Nat Rev Mol Cell Biol* **19**, 755-773, doi:10.1038/s41580-018-0060-8 (2018).

28 Kayed, R. *et al.* Conformational transitions of islet amyloid polypeptide (IAPP) in amyloid formation in vitro. *J Mol Biol* **287**, 781-796, doi:10.1006/jmbi.1999.2646 (1999).

29 Rodriguez Camargo, D. C. *et al.* The redox environment triggers conformational changes and aggregation of hIAPP in Type II Diabetes. *Sci Rep* **7**, 44041, doi:10.1038/srep44041 (2017).

30 Wiltzius, J. J., Sievers, S. A., Sawaya, M. R. & Eisenberg, D. Atomic structures of IAPP (amylin) fusions suggest a mechanism for fibrillation and the role of insulin in the process. *Protein Sci* **18**, 1521-1530, doi:10.1002/pro.145 (2009).

31 Knight, J. D., Hebda, J. A. & Miranker, A. D. Conserved and cooperative assembly of membrane-bound alpha-helical states of islet amyloid polypeptide. *Biochemistry* **45**, 9496-9508, doi:10.1021/bi060579z (2006).

32 Bishoyi, A. K. *et al.* Human islet amyloid polypeptide (hIAPP) - a curse in type II diabetes mellitus: insights from structure and toxicity studies. *Biol Chem* **402**, 133-153, doi:10.1515/hsz-2020-0174 (2021).

33 Röder, C. *et al.* Cryo-EM structure of islet amyloid polypeptide fibrils reveals similarities with amyloid-β fibrils. *Nat Struct Mol Biol* **27**, 660-667, doi:10.1038/s41594-020-0442-4 (2020).

34 Gallardo, R. *et al.* Fibril structures of diabetes-related amylin variants reveal a basis for surface-templated assembly. *Nat Struct Mol Biol* **27**, 1048-1056, doi:10.1038/s41594-020-0496-3 (2020).

35 Cao, Q., Boyer, D. R., Sawaya, M. R., Ge, P. & Eisenberg, D. S. Cryo-EM structure and inhibitor design of human IAPP (amylin) fibrils. *Nat Struct Mol Biol* **27**, 653-659, doi:10.1038/s41594-020-0435-3 (2020).

36 Patil, S. M., Xu, S., Sheftic, S. R. & Alexandrescu, A. T. Dynamic alpha-helix structure of micelle-bound human amylin. *J Biol Chem* **284**, 11982-11991, doi:10.1074/jbc.M809085200 (2009).

37 Nanga, R. P., Brender, J. R., Vivekanandan, S. & Ramamoorthy, A. Structure and membrane orientation of IAPP in its natively amidated form at physiological pH in a membrane environment. *Biochim Biophys Acta* **1808**, 2337-2342, doi:10.1016/j.bbamem.2011.06.012 (2011).

38 Wimalawansa, S. J. Amylin, calcitonin gene-related peptide, calcitonin, and adrenomedullin: a peptide superfamily. *Crit Rev Neurobiol* **11**, 167-239, doi:10.1615/critrevneurobiol.v11.i2-3.40 (1997).

39 Roh, J., Chang, C. L., Bhalla, A., Klein, C. & Hsu, S. Y. Intermedin is a calcitonin/calcitonin gene-related peptide family peptide acting through the calcitonin receptor-like receptor/receptor activity-modifying protein receptor complexes. *J Biol Chem* **279**, 7264-7274, doi:10.1074/jbc.M305332200 (2004).

40 Westermark, P., Li, Z. C., Westermark, G. T., Leckström, A. & Steiner, D. F. Effects of beta cell granule components on human islet amyloid polypeptide fibril formation. *FEBS Lett* **379**, 203-206, doi:10.1016/0014-5793(95)01512-4 (1996).

41 Marmentini, C., Branco, R. C. S., Boschero, A. C. & Kurauti, M. A. Islet amyloid toxicity: From genesis to counteracting mechanisms. *J Cell Physiol*, doi:10.1002/jcp.30600 (2021).

42 Ionescu-Tirgoviste C, G. C. Proinsulin, proamylin and the beta cell endoplasmic reticulum: the key for the pathogenesis of different diabetes phenotypes. *Proc Rom Acad Series B 2*, 113–139 (2007).

43 Andreetto, E. *et al.* Identification of hot regions of the Abeta-IAPP interaction interface as high-affinity binding sites in both cross- and self-association. *Angew Chem Int Ed Engl* **49**, 3081-3085, doi:10.1002/anie.200904902 (2010).

44 Alzheimer's Disease International. World Alzheimer Report 2015. The global impact of dementia: an analysis of prevalence, incidence, cost and trends., (2015).

45 Alzheimer, A. Über eine eigenartige Erkrankung der Hirnrinde. *Allg Z Psychiatr* **64**, 146-148 (1907).

46 Ferrari, C. & Sorbi, S. The complexity of Alzheimer's disease: an evolving puzzle. *Physiol Rev* **101**, 1047-1081, doi:10.1152/physrev.00015.2020 (2021).

47 Breijyeh, Z. & Karaman, R. Comprehensive Review on Alzheimer's Disease: Causes and Treatment. *Molecules* **25**, doi:10.3390/molecules25245789 (2020).

48 Ferrari, C. *et al.* Alzheimer's Disease Progression: Factors Influencing Cognitive Decline. *J Alzheimers Dis* **61**, 785-791, doi:10.3233/jad-170665 (2018).

49 Cohen, M. L. *et al.* Rapidly progressive Alzheimer's disease features distinct structures of amyloid-β. *Brain* **138**, 1009-1022, doi:10.1093/brain/awv006 (2015).

50 Ryan, N. S. *et al.* Clinical phenotype and genetic associations in autosomal dominant familial Alzheimer's disease: a case series. *Lancet Neurol* **15**, 1326-1335, doi:10.1016/s1474-4422(16)30193-4 (2016).

51 Chen, G. F. *et al.* Amyloid beta: structure, biology and structure-based therapeutic development. *Acta Pharmacol Sin* **38**, 1205-1235, doi:10.1038/aps.2017.28 (2017).

52 Coles, M., Bicknell, W., Watson, A. A., Fairlie, D. P. & Craik, D. J. Solution structure of amyloid beta-peptide(1-40) in a water-micelle environment. Is the membrane-spanning domain where we think it is? *Biochemistry* **37**, 11064-11077, doi:10.1021/bi972979f (1998).

53 Vivekanandan, S., Brender, J. R., Lee, S. Y. & Ramamoorthy, A. A partially folded structure of amyloid-beta(1-40) in an aqueous environment. *Biochem Biophys Res Commun* **411**, 312-316, doi:10.1016/j.bbrc.2011.06.133 (2011).

54 Petkova, A. T., Yau, W. M. & Tycko, R. Experimental constraints on quaternary structure in Alzheimer's beta-amyloid fibrils. *Biochemistry* **45**, 498-512, doi:10.1021/bi051952q (2006).

55 Paravastu, A. K., Leapman, R. D., Yau, W. M. & Tycko, R. Molecular structural basis for polymorphism in Alzheimer's beta-amyloid fibrils. *Proc Natl Acad Sci U S A* **105**, 18349-18354, doi:10.1073/pnas.0806270105 (2008).

56 Gremer, L. *et al.* Fibril structure of amyloid-β(1-42) by cryo-electron microscopy. *Science* **358**, 116-119, doi:10.1126/science.aao2825 (2017).

57 Hardy, J. A. & Higgins, G. A. Alzheimer's disease: the amyloid cascade hypothesis. *Science* **256**, 184-185, doi:10.1126/science.1566067 (1992).

58 Walsh, D. M. *et al.* Naturally secreted oligomers of amyloid beta protein potently inhibit hippocampal long-term potentiation in vivo. *Nature* **416**, 535-539, doi:10.1038/416535a (2002).

59 Kayed, R. & Lasagna-Reeves, C. A. Molecular mechanisms of amyloid oligomers toxicity. *J Alzheimers Dis* **33 Suppl 1**, S67-78, doi:10.3233/jad-2012-129001 (2013).

60 Tolar, M., Abushakra, S. & Sabbagh, M. The path forward in Alzheimer's disease therapeutics: Reevaluating the amyloid cascade hypothesis. *Alzheimers Dement* **16**, 1553-1560, doi:10.1016/j.jalz.2019.09.075 (2020).

61 Ray, W. J. & Buggia-Prevot, V. Novel Targets for Alzheimer's Disease: A View Beyond Amyloid. *Annu Rev Med* **72**, 15-28, doi:10.1146/annurev-med-052919-120219 (2021).

62 Sevigny, J. *et al.* The antibody aducanumab reduces Aβ plaques in Alzheimer's disease. *Nature* **537**, 50-56, doi:10.1038/nature19323 (2016).

63 Food and Drug Administration. *FDA Grants Accelerated Approval for Alzheimer's Drug.*, <https://www.fda.gov/news-events/press-announcements/fda-grants-accelerated-approval-alzheimers-drug> (2021).

64 Carrillo-Mora, P., Luna, R. & Colín-Barenque, L. Amyloid beta: multiple mechanisms of toxicity and only some protective effects? *Oxid Med Cell Longev* **2014**, 795375, doi:10.1155/2014/795375 (2014).

65 Puzzo, D., Gulisano, W., Arancio, O. & Palmeri, A. The keystone of Alzheimer pathogenesis might be sought in Aβ physiology. *Neuroscience* **307**, 26-36, doi:10.1016/j.neuroscience.2015.08.039 (2015).

66 Soscia, S. J. *et al.* The Alzheimer's disease-associated amyloid beta-protein is an antimicrobial peptide. *PLoS One* **5**, e9505, doi:10.1371/journal.pone.0009505 (2010).

67 Biessels, G. J., Staekenborg, S., Brunner, E., Brayne, C. & Scheltens, P. Risk of dementia in diabetes mellitus: a systematic review. *Lancet Neurol* **5**, 64-74, doi:10.1016/s1474-4422(05)70284-2 (2006).

68 Janson, J. *et al.* Increased risk of type 2 diabetes in Alzheimer disease. *Diabetes* **53**, 474-481, doi:10.2337/diabetes.53.2.474 (2004).

69 Verdile, G. *et al.* Inflammation and Oxidative Stress: The Molecular Connectivity between Insulin Resistance, Obesity, and Alzheimer's Disease. *Mediators Inflamm* **2015**, 105828, doi:10.1155/2015/105828 (2015).

70 Kandimalla, R., Thirumala, V. & Reddy, P. H. Is Alzheimer's disease a Type 3 Diabetes? A critical appraisal. *Biochim Biophys Acta Mol Basis Dis* **1863**, 1078-1089, doi:10.1016/j.bbadis.2016.08.018 (2017).

71 Rivera, E. J. *et al.* Insulin and insulin-like growth factor expression and function deteriorate with progression of Alzheimer's disease: link to brain reductions in acetylcholine. *J Alzheimers Dis* **8**, 247-268, doi:10.3233/jad-2005-8304 (2005).

72 Liu, Y., Liu, F., Grundke-Iqbal, I., Iqbal, K. & Gong, C. X. Deficient brain insulin signalling pathway in Alzheimer's disease and diabetes. *J Pathol* **225**, 54-62, doi:10.1002/path.2912 (2011).

73 Talbot, K. *et al.* Demonstrated brain insulin resistance in Alzheimer's disease patients is associated with IGF-1 resistance, IRS-1 dysregulation, and cognitive decline. *J Clin Invest* **122**, 1316-1338, doi:10.1172/jci59903 (2012).

74 Ferreira, S., Raimundo, A. F., Menezes, R. & Martins, I. C. Islet amyloid polypeptide & amyloid beta peptide roles in Alzheimer's disease: two triggers, one disease. *Neural Regen Res* **16**, 1127-1130, doi:10.4103/1673-5374.300323 (2021).

75 Rojas, M. *et al.* Alzheimer's disease and type 2 diabetes mellitus: Pathophysiologic and pharmacotherapeutics links. *World J Diabetes* **12**, 745-766, doi:10.4239/wjd.v12.i6.745 (2021).

76 Zhu, H. *et al.* Intraperitoneal injection of the pancreatic peptide amylin potently reduces behavioral impairment and brain amyloid pathology in murine models of Alzheimer's disease. *Mol Psychiatry* **20**, 252-262, doi:10.1038/mp.2014.17 (2015).

77 Wang, E. *et al.* Amylin Treatment Reduces Neuroinflammation and Ameliorates Abnormal Patterns of Gene Expression in the Cerebral Cortex of an Alzheimer's Disease Mouse Model. *J Alzheimers Dis* **56**, 47-61, doi:10.3233/jad-160677 (2017).

78 Raimundo, A. F., Ferreira, S., Martins, I. C. & Menezes, R. Islet Amyloid Polypeptide: A Partner in Crime With Aβ in the Pathology of Alzheimer's Disease. *Front Mol Neurosci* **13**, 35, doi:10.3389/fnmol.2020.00035 (2020).

79 O'Nuallain, B., Williams, A. D., Westermark, P. & Wetzel, R. Seeding specificity in amyloid growth induced by heterologous fibrils. *J Biol Chem* **279**, 17490-17499, doi:10.1074/jbc.M311300200 (2004).

80 Yan, L. M., Velkova, A., Tatarek-Nossol, M., Andreetto, E. & Kapurniotu, A. IAPP mimic blocks Abeta cytotoxic self-assembly: cross-suppression of amyloid toxicity of Abeta and IAPP suggests a molecular link between Alzheimer's disease and type II diabetes. *Angew Chem Int Ed Engl* **46**, 1246-1252, doi:10.1002/anie.200604056 (2007).

81 Sanke, T. *et al.* Plasma islet amyloid polypeptide (Amylin) levels and their responses to oral glucose in type 2 (non-insulin-dependent) diabetic patients. *Diabetologia* **34**, 129-132, doi:10.1007/bf00500385 (1991).

82 Banks, W. A., Kastin, A. J., Maness, L. M., Huang, W. & Jaspan, J. B. Permeability of the blood-brain barrier to amylin. *Life Sci* **57**, 1993-2001, doi:10.1016/0024-3205(95)02197-q (1995).

83 Ida, N. *et al.* Analysis of heterogeneous A4 peptides in human cerebrospinal fluid and blood by a newly developed sensitive Western blot assay. *J Biol Chem* **271**, 22908-22914, doi:10.1074/jbc.271.37.22908 (1996).

84 Yan, L. M., Velkova, A. & Kapurniotu, A. Molecular characterization of the hetero-assembly of β-amyloid peptide with islet amyloid polypeptide. *Curr Pharm Des* **20**, 1182-1191, doi:10.2174/13816128113199990064 (2014).

85 Wang, Y. & Westermark, G. T. The Amyloid Forming Peptides Islet Amyloid Polypeptide and Amyloid β Interact at the Molecular Level. *Int J Mol Sci* **22**, doi:10.3390/ijms222011153 (2021).

86 Ono, K. *et al.* Exogenous amyloidogenic proteins function as seeds in amyloid β-protein aggregation. *Biochim Biophys Acta* **1842**, 646-653, doi:10.1016/j.bbadis.2014.01.002 (2014).

87 Moreno-Gonzalez, I. *et al.* Molecular interaction between type 2 diabetes and Alzheimer's disease through cross-seeding of protein misfolding. *Mol Psychiatry* **22**, 1327-1334, doi:10.1038/mp.2016.230 (2017).

88 Oskarsson, M. E. *et al.* In vivo seeding and cross-seeding of localized amyloidosis: a molecular link between type 2 diabetes and Alzheimer disease. *Am J Pathol* **185**, 834-846, doi:10.1016/j.ajpath.2014.11.016 (2015).

89 Jackson, K. *et al.* Amylin deposition in the brain: A second amyloid in Alzheimer disease? *Ann Neurol* **74**, 517-526, doi:10.1002/ana.23956 (2013).

90 Martinez-Valbuena, I. *et al.* Amylin as a potential link between type 2 diabetes and alzheimer disease. *Ann Neurol* **86**, 539-551, doi:10.1002/ana.25570 (2019).

91 Miklossy, J. *et al.* Beta amyloid and hyperphosphorylated tau deposits in the pancreas in type 2 diabetes. *Neurobiol Aging* **31**, 1503-1515, doi:10.1016/j.neurobiolaging.2008.08.019 (2010).

92 Wijesekara, N. *et al.* Amyloid-β and islet amyloid pathologies link Alzheimer's disease and type 2 diabetes in a transgenic model. *Faseb j* **31**, 5409-5418, doi:10.1096/fj.201700431R (2017).

93 Krotee, P. *et al.* Common fibrillar spines of amyloid-β and human islet amyloid polypeptide revealed by microelectron diffraction and structure-based inhibitors. *J Biol Chem* **293**, 2888-2902, doi:10.1074/jbc.M117.806109 (2018).

94 Baram, M., Atsmon-Raz, Y., Ma, B., Nussinov, R. & Miller, Y. Amylin-Aβ oligomers at atomic resolution using molecular dynamics simulations: a link between Type 2 diabetes and Alzheimer's disease. *Phys Chem Chem Phys* **18**, 2330-2338, doi:10.1039/c5cp03338a (2016).

95 Zhang, M. *et al.* Polymorphic cross-seeding amyloid assemblies of amyloid-β and human islet amyloid polypeptide. *Phys Chem Chem Phys* **17**, 23245-23256, doi:10.1039/c5cp03329b (2015).

96 Armiento, V., Spanopoulou, A. & Kapurniotu, A. Peptide-Based Molecular Strategies To Interfere with Protein Misfolding, Aggregation, and Cell Degeneration. *Angew Chem Int Ed Engl* **59**, 3372-3384, doi:10.1002/anie.201906908 (2020).

97 Ehrnhoefer, D. E. *et al.* EGCG redirects amyloidogenic polypeptides into unstructured, off-pathway oligomers. *Nat Struct Mol Biol* **15**, 558-566, doi:10.1038/nsmb.1437 (2008).

98 Franko, A. *et al.* Epigallocatechin gallate (EGCG) reduces the intensity of pancreatic amyloid fibrils in human islet amyloid polypeptide (hIAPP) transgenic mice. *Sci Rep* **8**, 1116, doi:10.1038/s41598-017-18807-8 (2018).

99 Mishra, R., Sellin, D., Radovan, D., Gohlke, A. & Winter, R. Inhibiting islet amyloid polypeptide fibril formation by the red wine compound resveratrol. *Chembiochem* **10**, 445-449, doi:10.1002/cbic.200800762 (2009).

100 Tu, L. H. *et al.* Mutational analysis of the ability of resveratrol to inhibit amyloid formation by islet amyloid polypeptide: critical evaluation of the importance of aromatic-inhibitor and histidine-inhibitor interactions. *Biochemistry* **54**, 666-676, doi:10.1021/bi501016r (2015).

101 Willander, H. *et al.* BRICHOS domains efficiently delay fibrillation of amyloid β-peptide. *J Biol Chem* **287**, 31608-31617, doi:10.1074/jbc.M112.393157 (2012).

102 Poska, H. *et al.* Dementia-related Bri2 BRICHOS is a versatile molecular chaperone that efficiently inhibits Aβ42 toxicity in Drosophila. *Biochem J* **473**, 3683-3704, doi:10.1042/bcj20160277 (2016).

103 Oskarsson, M. E. *et al.* BRICHOS domain of Bri2 inhibits islet amyloid polypeptide (IAPP) fibril formation and toxicity in human beta cells. *Proc Natl Acad Sci U S A* **115**, E2752-e2761, doi:10.1073/pnas.1715951115 (2018).

104 Frydman-Marom, A., Shaltiel-Karyo, R., Moshe, S. & Gazit, E. The generic amyloid formation inhibition effect of a designed small aromatic β-breaking peptide. *Amyloid* **18**, 119-127, doi:10.3109/13506129.2011.582902 (2011).

105 Kellock, J., Hopping, G., Caughey, B. & Daggett, V. Peptides Composed of Alternating L- and D-Amino Acids Inhibit Amyloidogenesis in Three Distinct Amyloid Systems Independent of Sequence. *J Mol Biol* **428**, 2317-2328, doi:10.1016/j.jmb.2016.03.013 (2016).

106 Huggins, K. N. *et al.* Designed hairpin peptides interfere with amyloidogenesis pathways: fibril formation and cytotoxicity inhibition, interception of the preamyloid state. *Biochemistry* **50**, 8202-8212, doi:10.1021/bi200760h (2011).

107 Sun, Y. *et al.* Risk of Parkinson disease onset in patients with diabetes: a 9-year population-based cohort study with age and sex stratifications. *Diabetes Care* **35**, 1047-1049, doi:10.2337/dc11-1511 (2012).

108 Griner, S. L. *et al.* Structure-based inhibitors of amyloid beta core suggest a common interface with tau. *Elife* **8**, doi:10.7554/eLife.46924 (2019).

109 Yan, L. M. *et al.* Selectively N-methylated soluble IAPP mimics as potent IAPP receptor agonists and nanomolar inhibitors of cytotoxic self-assembly of both IAPP and Aβ40. *Angew Chem Int Ed Engl* **52**, 10378-10383, doi:10.1002/anie.201302840 (2013).

110 Velkova, A., Tatarek-Nossol, M., Andreetto, E. & Kapurniotu, A. Exploiting cross-amyloid interactions to inhibit protein aggregation but not function: nanomolar affinity inhibition of insulin aggregation by an IAPP mimic. *Angew Chem Int Ed Engl* **47**, 7114-7118, doi:10.1002/anie.200801499 (2008).

111 Andreetto, E. *et al.* A Hot-Segment-Based Approach for the Design of Cross-Amyloid Interaction Surface Mimics as Inhibitors of Amyloid Self-Assembly. *Angew Chem Int Ed Engl* **54**, 13095-13100, doi:10.1002/anie.201504973 (2015).

112 Spanopoulou, A. *et al.* Designed Macrocyclic Peptides as Nanomolar Amyloid Inhibitors Based on Minimal Recognition Elements. *Angew Chem Int Ed Engl* **57**, 14503-14508, doi:10.1002/anie.201802979 (2018).

113 Kapurniotu, A., Schmauder, A. & Tenidis, K. Structure-based design and study of non-amyloidogenic, double N-methylated IAPP amyloid core sequences as inhibitors of IAPP amyloid formation and cytotoxicity. *J Mol Biol* **315**, 339-350, doi:10.1006/jmbi.2001.5244 (2002).

114 Keller, R. *Synthesis of Aß-derived peptides and studies of their secondary structure and interactions.* Research internship thesis, TUM, (2018).

115 Kaiser, E., Colescott, R. L., Bossinger, C. D. & Cook, P. I. Color test for detection of free terminal amino groups in the solid-phase synthesis of peptides. *Anal Biochem* **34**, 595-598, doi:10.1016/0003-2697(70)90146-6 (1970).

116 Christensen, T., Eriksson, A. & Thornell, L. E. A Qualitative Test for Monitoring Coupling Completeness in Solid Phase Peptide Synthesis Using Chloranil. *Acta Chemica Scandinavica*, 763-766 (1979).

117 Bakou, M. *et al.* Key aromatic/hydrophobic amino acids controlling a cross-amyloid peptide interaction versus amyloid self-assembly. *J Biol Chem* **292**, 14587-14602, doi:10.1074/jbc.M117.774893 (2017).

118 Velkova, A. *Biochemische Charakterisierung der Wirkung peptidischer Inhibitoren auf die Aggregation der amyloidogenen Peptide Inselamyloid Polypeptid (IAPP), Amyloid-ß-Peptid (Aß) und Insulin.* PhD thesis, TUM, (2009).

119 Andreetto, E. *Identification of sequences of the interaction interface of β-amyloid peptide (Aβ) and islet amyloid polypeptide (IAPP) and synthesis and characterization of IAPP-derived inhibitors of Aβ aggregation.* PhD thesis, TUM, (2011).

120 Kazantzis, A., Waldner, M., Taylor, J. W. & Kapurniotu, A. Conformationally constrained human calcitonin (hCt) analogues reveal a critical role of sequence 17-21 for the oligomerization state and bioactivity of hCt. *Eur J Biochem* **269**, 780-791, doi:10.1046/j.0014-2956.2001.02689.x (2002).

121 Walsh, D. M. *et al.* A facile method for expression and purification of the Alzheimer's disease-associated amyloid beta-peptide. *Febs j* **276**, 1266-1281, doi:10.1111/j.1742-4658.2008.06862.x (2009).

122 Jan, A., Hartley, D. M. & Lashuel, H. A. Preparation and characterization of toxic Abeta aggregates for structural and functional studies in Alzheimer's disease research. *Nat Protoc* **5**, 1186-1209, doi:10.1038/nprot.2010.72 (2010).

123 Tenidis, K. *et al.* Identification of a penta- and hexapeptide of islet amyloid polypeptide (IAPP) with amyloidogenic and cytotoxic properties. *J Mol Biol* **295**, 1055-1071, doi:10.1006/jmbi.1999.3422 (2000).

124 Ladiwala, A. R. *et al.* Conformational differences between two amyloid β oligomers of similar size and dissimilar toxicity. *J Biol Chem* **287**, 24765-24773, doi:10.1074/jbc.M111.329763 (2012).

125 Cho, P. Y., Joshi, G., Johnson, J. A. & Murphy, R. M. Transthyretin-derived peptides as β-amyloid inhibitors. *ACS Chem Neurosci* **5**, 542-551, doi:10.1021/cn500014u (2014).

126 Megens, R. T., Bianchini, M., Schmitt, M. M. & Weber, C. Optical imaging innovations for atherosclerosis research: multiphoton microscopy and optical nanoscopy. *Arterioscler Thromb Vasc Biol* **35**, 1339-1346, doi:10.1161/atvbaha.115.304875 (2015).

127 Kontos, C. *et al.* Designed CXCR4 mimic acts as a soluble chemokine receptor that blocks atherogenic inflammation by agonist-specific targeting. *Nat Commun* **11**, 5981, doi:10.1038/s41467-020-19764-z (2020).

128 Pettersen, E. F. *et al.* UCSF Chimera--a visualization system for exploratory research and analysis. *J Comput Chem* **25**, 1605-1612, doi:10.1002/jcc.20084 (2004).

129 Gfeller, D., Michielin, O. & Zoete, V. SwissSidechain: a molecular and structural database of non-natural sidechains. *Nucleic Acids Res* **41**, D327-332, doi:10.1093/nar/gks991 (2013).

130 Petkova, A. T. *et al.* A structural model for Alzheimer's beta -amyloid fibrils based on experimental constraints from solid state NMR. *Proc Natl Acad Sci U S A* **99**, 16742-16747, doi:10.1073/pnas.262663499 (2002).

131 Bertini, I., Gonnelli, L., Luchinat, C., Mao, J. & Nesi, A. A new structural model of Aβ40 fibrils. *J Am Chem Soc* **133**, 16013-16022, doi:10.1021/ja2035859 (2011).

132 Scheidt, H. A., Morgado, I., Rothemund, S. & Huster, D. Dynamics of amyloid β fibrils revealed by solid-state NMR. *J Biol Chem* **287**, 2017-2021, doi:10.1074/jbc.M111.308619 (2012).

133 Bitan, G. *et al.* A molecular switch in amyloid assembly: Met35 and amyloid beta-protein oligomerization. *J Am Chem Soc* **125**, 15359-15365, doi:10.1021/ja0349296 (2003).

134 Hughes, E., Burke, R. M. & Doig, A. J. Inhibition of toxicity in the beta-amyloid peptide fragment beta -(25-35) using N-methylated derivatives: a general strategy to prevent amyloid formation. *J Biol Chem* **275**, 25109-25115, doi:10.1074/jbc.M003554200 (2000).

135 Gordon, D. J., Sciarretta, K. L. & Meredith, S. C. Inhibition of beta-amyloid(40) fibrillogenesis and disassembly of beta-amyloid(40) fibrils by short beta-amyloid congeners containing N-methyl amino acids at alternate residues. *Biochemistry* **40**, 8237-8245, doi:10.1021/bi002416v (2001).

136 Cruz, M. *et al.* Inhibition of beta-amyloid toxicity by short peptides containing N-methyl amino acids. *J Pept Res* **63**, 324-328, doi:10.1111/j.1399-3011.2004.00156.x (2004).

137 Sciarretta, K. L., Boire, A., Gordon, D. J. & Meredith, S. C. Spatial separation of beta-sheet domains of beta-amyloid: disruption of each beta-sheet by N-methyl amino acids. *Biochemistry* **45**, 9485-9495, doi:10.1021/bi0605585 (2006).

138 Pratim Bose, P. *et al.* Poly-N-methylated amyloid beta-peptide (Abeta) C-terminal fragments reduce Abeta toxicity in vitro and in Drosophila melanogaster. *J Med Chem* **52**, 8002-8009, doi:10.1021/jm901092h (2009).

139 Li, H., Zemel, R., Lopes, D. H., Monien, B. H. & Bitan, G. A two-step strategy for structure-activity relationship studies of N-methylated aβ42 C-terminal fragments as aβ42 toxicity inhibitors. *ChemMedChem* **7**, 515-522, doi:10.1002/cmdc.201100584 (2012).

140 Taş, K. *et al.* Designed peptides as nanomolar cross-amyloid inhibitors acting via supramolecular nanofiber co-assembly. *Nat Commun* (Under revision).

141 Ortner, M. *Untersuchungen zur Rolle der Loop-Region bei der Konformation und Amyloidbildung des Beta-Amyloidpeptids.* Bachelor thesis, TUM, (2014).

142 Feuerstein, K. *Synthesen und Untersuchungen von Analoga der Amyloid-β Sequenz Aβ(15-40) und ihrer Wechselwirkungen mit IAPP.* Master thesis, TUM, (2015).

143 Gore, M. *Spectrophotometry and Spectrofluorimetry: A Practical Approach*. (Oxford University Press, 2000).

144 Bakou, M. & Kapurniotu, A. *Unpublished data* (2014).

145 Micsonai, A. *et al.* Accurate secondary structure prediction and fold recognition for circular dichroism spectroscopy. *Proceedings of the National Academy of Sciences* **112**, E3095-E3103, doi:doi:10.1073/pnas.1500851112 (2015).

146 Prem, S. *Synthese und biophysikalische Untersuchungen von Analoga der Selbsterkennungssequenzen von ß-Amyloidpeptid (Aß).* Bachelor thesis, TUM, (2016).

147 Kalpazidou, S. *Synthesis of Aß40 derived analogues, investigation of their structural properties and examination of binding-essential residues in IAPP for interaction with the designed peptides.* Erasmus research internship thesis, TUM, (2018).

148 Walsh, D. M., Lomakin, A., Benedek, G. B., Condron, M. M. & Teplow, D. B. Amyloid beta-protein fibrillogenesis. Detection of a protofibrillar intermediate. *J Biol Chem* **272**, 22364-22372, doi:10.1074/jbc.272.35.22364 (1997).

149 Blom, H. & Brismar, H. STED microscopy: increased resolution for medical research? *J Intern Med* **276**, 560-578, doi:10.1111/joim.12278 (2014).

150 Ciubotaru, M., Kriatchko, A. N., Swanson, P. C., Bright, F. V. & Schatz, D. G. Fluorescence resonance energy transfer analysis of recombination signal sequence configuration in the RAG1/2 synaptic complex. *Mol Cell Biol* **27**, 4745-4758, doi:10.1128/mcb.00177-07 (2007).

151 Lindner, C. *Studies on the interactions of peptidic amyloid inhibitors with the islet amyloid polypeptide (IAPP) and beta-amyloid peptide (Aß).* Master thesis, TUM, (2020).

152 Dalla Volta, B. & Kapurniotu, A. *Unpublished data* (2022).

153 Westermark, P., Engström, U., Johnson, K. H., Westermark, G. T. & Betsholtz, C. Islet amyloid polypeptide: pinpointing amino acid residues linked to amyloid fibril formation. *Proceedings of the National Academy of Sciences of the United States of America* **87**, 5036-5040, doi:10.1073/pnas.87.13.5036 (1990).

154 Lindgren, M., Sörgjerd, K. & Hammarström, P. Detection and characterization of aggregates, prefibrillar amyloidogenic oligomers, and protofibrils using fluorescence spectroscopy. *Biophys J* **88**, 4200-4212, doi:10.1529/biophysj.104.049700 (2005).

155 Munke, A. *et al.* Phage display and kinetic selection of antibodies that specifically inhibit amyloid self-replication. *Proc Natl Acad Sci U S A* **114**, 6444-6449, doi:10.1073/pnas.1700407114 (2017).

156 Cohen, S. I. A. *et al.* A molecular chaperone breaks the catalytic cycle that generates toxic Aβ oligomers. *Nat Struct Mol Biol* **22**, 207-213, doi:10.1038/nsmb.2971 (2015).

157 Krebs, M. R., Bromley, E. H. & Donald, A. M. The binding of thioflavin-T to amyloid fibrils: localisation and implications. *J Struct Biol* **149**, 30-37, doi:10.1016/j.jsb.2004.08.002 (2005).

158 Ke, P. C. *et al.* Half a century of amyloids: past, present and future. *Chem Soc Rev* **49**, 5473-5509, doi:10.1039/c9cs00199a (2020).

159 Young, L. M. *et al.* Insights into the consequences of co-polymerisation in the early stages of IAPP and Aβ peptide assembly from mass spectrometry. *Analyst* **140**, 6990-6999, doi:10.1039/c5an00865d (2015).

160 Ge, X., Yang, Y., Sun, Y., Cao, W. & Ding, F. Islet Amyloid Polypeptide Promotes Amyloid-Beta Aggregation by Binding-Induced Helix-Unfolding of the Amyloidogenic Core. *ACS Chem Neurosci* **9**, 967-975, doi:10.1021/acschemneuro.7b00396 (2018).

161 Pang, B. *et al.* Studies on the cross-interaction between hIAPP and Aβ(25-35) and the aggregation process in binary mixture by electrospray ionization-ion mobility-mass spectrometry. *J Mass Spectrom* **55**, e4643, doi:10.1002/jms.4643 (2020).

162 Li, X. *et al.* Mechanistic Insights into the Co-Aggregation of Aβ and hIAPP: An All-Atom Molecular Dynamic Study. *J Phys Chem B* **125**, 2050-2060, doi:10.1021/acs.jpcb.0c11132 (2021).

163 Bharadwaj, P. *et al.* Amylin and beta amyloid proteins interact to form amorphous heterocomplexes with enhanced toxicity in neuronal cells. *Sci Rep* **10**, 10356, doi:10.1038/s41598-020-66602-9 (2020).

164 Middleton, C. T. *et al.* Two-dimensional infrared spectroscopy reveals the complex behaviour of an amyloid fibril inhibitor. *Nat Chem* **4**, 355-360, doi:10.1038/nchem.1293 (2012).

165 Giasson, B. I. *et al.* Initiation and synergistic fibrillization of tau and alpha-synuclein. *Science* **300**, 636-640, doi:10.1126/science.1082324 (2003).

166 Bhasne, K., Sebastian, S., Jain, N. & Mukhopadhyay, S. Synergistic Amyloid Switch Triggered by Early Heterotypic Oligomerization of Intrinsically Disordered α-Synuclein and Tau. *J Mol Biol* **430**, 2508-2520, doi:10.1016/j.jmb.2018.04.020 (2018).

167 Nespovitaya, N. *et al.* Dynamic Assembly and Disassembly of Functional β-Endorphin Amyloid Fibrils. *Journal of the American Chemical Society* **138**, 846-856, doi:10.1021/jacs.5b08694 (2016).

168 Nespovitaya, N., Mahou, P., Laine, R. F., Schierle, G. S. K. & Kaminski, C. F. Heparin acts as a structural component of β-endorphin amyloid fibrils rather than a simple aggregation promoter. *Chem Commun (Camb)* **53**, 1273-1276, doi:10.1039/c6cc09770g (2017).

169 Hu, R., Zhang, M., Chen, H., Jiang, B. & Zheng, J. Cross-Seeding Interaction between β-Amyloid and Human Islet Amyloid Polypeptide. *ACS Chem Neurosci* **6**, 1759-1768, doi:10.1021/acschemneuro.5b00192 (2015).

170 Glenner, G. G., Eanes, E. D. & Wiley, C. A. Amyloid fibrils formed from a segment of the pancreatic islet amyloid protein. *Biochem Biophys Res Commun* **155**, 608-614, doi:10.1016/s0006-291x(88)80538-2 (1988).

171 Wälti, M. A. *et al.* Atomic-resolution structure of a disease-relevant Aβ(1-42) amyloid fibril. *Proc Natl Acad Sci U S A* **113**, E4976-4984, doi:10.1073/pnas.1600749113 (2016).

172 Colvin, M. T. *et al.* Atomic Resolution Structure of Monomorphic Aβ42 Amyloid Fibrils. *J Am Chem Soc* **138**, 9663-9674, doi:10.1021/jacs.6b05129 (2016).

173 Xiao, Y. *et al.* Aβ(1-42) fibril structure illuminates self-recognition and replication of amyloid in Alzheimer's disease. *Nat Struct Mol Biol* **22**, 499-505, doi:10.1038/nsmb.2991 (2015).

174 Schmidt, M. *et al.* Peptide dimer structure in an Aβ(1-42) fibril visualized with cryo-EM. *Proc Natl Acad Sci U S A* **112**, 11858-11863, doi:10.1073/pnas.1503455112 (2015).

175 Lührs, T. *et al.* 3D structure of Alzheimer's amyloid-beta(1-42) fibrils. *Proc Natl Acad Sci U S A* **102**, 17342-17347, doi:10.1073/pnas.0506723102 (2005).

176 Ahmed, M. *et al.* Structural conversion of neurotoxic amyloid-beta(1-42) oligomers to fibrils. *Nat Struct Mol Biol* **17**, 561-567, doi:10.1038/nsmb.1799 (2010).

177 Cerofolini, L. *et al.* Mixing Aβ(1-40) and Aβ(1-42) peptides generates unique amyloid fibrils. *Chem Commun (Camb)* **56**, 8830-8833, doi:10.1039/d0cc02463e (2020).

178 Ashburn, T. T. & Lansbury, P. T. Interspecies sequence variations affect the kinetics and thermodynamics of amyloid formation: peptide models of pancreatic amyloid. *Journal of the American Chemical Society* **115**, 11012-11013, doi:10.1021/ja00076a078 (1993).

179 Azriel, R. & Gazit, E. Analysis of the minimal amyloid-forming fragment of the islet amyloid polypeptide. An experimental support for the key role of the phenylalanine residue in amyloid formation. *J Biol Chem* **276**, 34156-34161, doi:10.1074/jbc.M102883200 (2001).

180 Goldsbury, C. *et al.* Amyloid fibril formation from full-length and fragments of amylin. *J Struct Biol* **130**, 352-362, doi:10.1006/jsbi.2000.4268 (2000).

181 Jarrett, J. T., Berger, E. P. & Lansbury, P. T., Jr. The carboxy terminus of the beta amyloid protein is critical for the seeding of amyloid formation: implications for the pathogenesis of Alzheimer's disease. *Biochemistry* **32**, 4693-4697, doi:10.1021/bi00069a001 (1993).

182 Jan, A., Gokce, O., Luthi-Carter, R. & Lashuel, H. A. The ratio of monomeric to aggregated forms of Abeta40 and Abeta42 is an important determinant of amyloid-beta aggregation, fibrillogenesis, and toxicity. *J Biol Chem* **283**, 28176-28189, doi:10.1074/jbc.M803159200 (2008).

183 Viet, M. H. & Li, M. S. Amyloid peptide Aβ40 inhibits aggregation of Aβ42: evidence from molecular dynamics simulations. *J Chem Phys* **136**, 245105, doi:10.1063/1.4730410 (2012).

184 Murray, M. M. *et al.* Amyloid beta protein: Abeta40 inhibits Abeta42 oligomerization. *J Am Chem Soc* **131**, 6316-6317, doi:10.1021/ja8092604 (2009).

185 Kim, J. *et al.* Abeta40 inhibits amyloid deposition in vivo. *J Neurosci* **27**, 627-633, doi:10.1523/jneurosci.4849-06.2007 (2007).

186 Yan, Y. & Wang, C. Abeta40 protects non-toxic Abeta42 monomer from aggregation. *J Mol Biol* **369**, 909-916, doi:10.1016/j.jmb.2007.04.014 (2007).

187 Frost, D., Gorman, P. M., Yip, C. M. & Chakrabartty, A. Co-incorporation of A beta 40 and A beta 42 to form mixed pre-fibrillar aggregates. *Eur J Biochem* **270**, 654-663, doi:10.1046/j.1432-1033.2003.03415.x (2003).

188 Sato, J., Takahashi, T., Oshima, H., Matsumura, S. & Mihara, H. Design of peptides that form amyloid-like fibrils capturing amyloid beta1-42 peptides. *Chemistry* **13**, 7745-7752, doi:10.1002/chem.200700643 (2007).

189 Suzuki, M. *et al.* Designed short peptides that form amyloid-like fibrils in coassembly with amyloid beta-peptide (Abeta) decrease the toxicity of Abeta to neuronal PC12 cells. *Chembiochem* **11**, 1525-1530, doi:10.1002/cbic.201000181 (2010).

190 Pujals, S., Tao, K., Terradellas, A., Gazit, E. & Albertazzi, L. Studying structure and dynamics of self-assembled peptide nanostructures using fluorescence and super resolution microscopy. *Chem Commun (Camb)* **53**, 7294-7297, doi:10.1039/c7cc02176c (2017).

191 Sánchez, L. *et al.* Aβ40 and Aβ42 amyloid fibrils exhibit distinct molecular recycling properties. *J Am Chem Soc* **133**, 6505-6508, doi:10.1021/ja1117123 (2011).

192 Naiki, H., Higuchi, K., Hosokawa, M. & Takeda, T. Fluorometric determination of amyloid fibrils in vitro using the fluorescent dye, thioflavin T1. *Anal Biochem* **177**, 244-249, doi:10.1016/0003-2697(89)90046-8 (1989).

193 LeVine, H., 3rd. Thioflavine T interaction with synthetic Alzheimer's disease beta-amyloid peptides: detection of amyloid aggregation in solution. *Protein Sci* **2**, 404-410, doi:10.1002/pro.5560020312 (1993).

194 Biancalana, M. & Koide, S. Molecular mechanism of Thioflavin-T binding to amyloid fibrils. *Biochim Biophys Acta* **1804**, 1405-1412, doi:10.1016/j.bbapap.2010.04.001 (2010).

195 Lindberg, D. J., Wranne, M. S., Gilbert Gatty, M., Westerlund, F. & Esbjörner, E. K. Steady-state and time-resolved Thioflavin-T fluorescence can report on morphological differences in amyloid fibrils formed by Aβ(1-40) and Aβ(1-42). *Biochem Biophys Res Commun* **458**, 418-423, doi:10.1016/j.bbrc.2015.01.132 (2015).

196 Sidhu, A., Vaneyck, J., Blum, C., Segers-Nolten, I. & Subramaniam, V. Polymorph-specific distribution of binding sites determines thioflavin-T fluorescence intensity in α-synuclein fibrils. *Amyloid* **25**, 189-196, doi:10.1080/13506129.2018.1517736 (2018).

197 Groenning, M. Binding mode of Thioflavin T and other molecular probes in the context of amyloid fibrils-current status. *J Chem Biol* **3**, 1-18, doi:10.1007/s12154-009-0027-5 (2010).

198 Meng, F., Marek, P., Potter, K. J., Verchere, C. B. & Raleigh, D. P. Rifampicin does not prevent amyloid fibril formation by human islet amyloid polypeptide but does inhibit fibril thioflavin-T interactions: implications for mechanistic studies of beta-cell death. *Biochemistry* **47**, 6016-6024, doi:10.1021/bi702518m (2008).

199 Lorenzo, A. & Yankner, B. A. Amyloid fibril toxicity in Alzheimer's disease and diabetes. *Ann N Y Acad Sci* **777**, 89-95, doi:10.1111/j.1749-6632.1996.tb34406.x (1996).

200 Janson, J., Ashley, R. H., Harrison, D., McIntyre, S. & Butler, P. C. The mechanism of islet amyloid polypeptide toxicity is membrane disruption by intermediate-sized toxic amyloid particles. *Diabetes* **48**, 491-498, doi:10.2337/diabetes.48.3.491 (1999).

201 Haass, C. & Selkoe, D. J. Soluble protein oligomers in neurodegeneration: lessons from the Alzheimer's amyloid beta-peptide. *Nat Rev Mol Cell Biol* **8**, 101-112, doi:10.1038/nrm2101 (2007).

202 Zraika, S. *et al.* Toxic oligomers and islet beta cell death: guilty by association or convicted by circumstantial evidence? *Diabetologia* **53**, 1046-1056, doi:10.1007/s00125-010-1671-6 (2010).

203 Siddiqi, M. K., Malik, S., Majid, N., Alam, P. & Khan, R. H. Cytotoxic species in amyloid-associated diseases: Oligomers or mature fibrils. *Adv Protein Chem Struct Biol* **118**, 333-369, doi:10.1016/bs.apcsb.2019.06.001 (2019).

204 Jiang, L. *et al.* Structure-based discovery of fiber-binding compounds that reduce the cytotoxicity of amyloid beta. *Elife* **2**, e00857, doi:10.7554/eLife.00857 (2013).

205 Ghanta, J., Shen, C. L., Kiessling, L. L. & Murphy, R. M. A strategy for designing inhibitors of beta-amyloid toxicity. *J Biol Chem* **271**, 29525-29528, doi:10.1074/jbc.271.47.29525 (1996).

206 Dutta, S. *et al.* Suppression of Oligomer Formation and Formation of Non-Toxic Fibrils upon Addition of Mirror-Image Aβ42 to the Natural l-Enantiomer. *Angew Chem Int Ed Engl* **56**, 11506-11510, doi:10.1002/anie.201706279 (2017).

207 Bieschke, J. *et al.* Small-molecule conversion of toxic oligomers to nontoxic β-sheet-rich amyloid fibrils. *Nat Chem Biol* **8**, 93-101, doi:10.1038/nchembio.719 (2011).

208 Caesar, I., Jonson, M., Nilsson, K. P., Thor, S. & Hammarström, P. Curcumin promotes A-beta fibrillation and reduces neurotoxicity in transgenic Drosophila. *PLoS One* **7**, e31424, doi:10.1371/journal.pone.0031424 (2012).

209 Necula, M. *et al.* Methylene blue inhibits amyloid Abeta oligomerization by promoting fibrillization. *Biochemistry* **46**, 8850-8860, doi:10.1021/bi700411k (2007).

210 Civitelli, L. *et al.* The Luminescent Oligothiophene p-FTAA Converts Toxic Aβ1-42 Species into Nontoxic Amyloid Fibers with Altered Properties. *J Biol Chem* **291**, 9233-9243, doi:10.1074/jbc.M115.696229 (2016).

211 Nguyen, P. T. *et al.* Low generation anionic dendrimers modulate islet amyloid polypeptide self-assembly and inhibit pancreatic β-cell toxicity. *RSC Advances* **6**, 76360-76369, doi:10.1039/C6RA15373A (2016).

212 De Carufel, C. A., Nguyen, P. T., Sahnouni, S. & Bourgault, S. New insights into the roles of sulfated glycosaminoglycans in islet amyloid polypeptide amyloidogenesis and cytotoxicity. *Biopolymers* **100**, 645-655, doi:10.1002/bip.22243 (2013).

213 Nelson, P. T. *et al.* Correlation of Alzheimer disease neuropathologic changes with cognitive status: a review of the literature. *J Neuropathol Exp Neurol* **71**, 362-381, doi:10.1097/NEN.0b013e31825018f7 (2012).

214 Selkoe, D. J. & Hardy, J. The amyloid hypothesis of Alzheimer's disease at 25 years. *EMBO Mol Med* **8**, 595-608, doi:10.15252/emmm.201606210 (2016).

215 Jackson, M. P. & Hewitt, E. W. Why are Functional Amyloids Non-Toxic in Humans? *Biomolecules* **7**, doi:10.3390/biom7040071 (2017).

216 Chatani, E., Yuzu, K., Ohhashi, Y. & Goto, Y. Current Understanding of the Structure, Stability and Dynamic Properties of Amyloid Fibrils. *Int J Mol Sci* **22**, doi:10.3390/ijms22094349 (2021).